ADVANCED CONCRETE TECHNOLOGY

ZONGJIN LI

Advanced Concrete Technology

Advanced Concrete Technology

Zongjin Li

WILEY

JOHN WILEY & SONS, INC.

This book is printed on acid-free paper.

Published by John Wiley & Sons, Inc., Hoboken, New Jersey

Published simultaneously in Canada

Library of Congress Cataloging-in-Publication Data:

Li, Zongjin, Dr.
Advanced concrete technology / Zongjin Li.
p. cm.
Includes index.
ISBN 978-0-470-43743-8 (cloth); ISBN 978-0-470-90239-4 (ebk); ISBN 978-0-470-90241-7 (ebk);
ISBN 978-0-470-90243-1 (ebk); ISBN 978-0-470-95006-7 (ebk); ISBN 978-0-470-95166-8 (ebk);
ISBN 978-0-470-95188-0 (ebk)
1. Concrete. I. Title.
TP877.L485 2011
620.1′36—dc22

2010031083

Printed in the United States of America
10 9 8 7 6 5 4 3 2 1

To students, teachers, researchers, and engineers in the field of concrete, who are the driving forces for the development of the science and technology of concrete, including the personnel working on the China 973 project, Basic Study on Environmentally Friendly Contemporary Concrete (2009CB623200).

CONTENTS

PREFACE

Concrete is the most widely used material in the world. It plays an important role in infrastructure and private buildings construction. Understanding the basic behaviors of concrete is essential for civil engineering students to become civil engineering professionals. There have been some very good books regarding concrete, including *Concrete* by Mindess, Young, and Darwin, *Concrete: Structure, Properties, and Materials* by Mehta and Monteriro, and *Concrete Technology* by Neville and Brook. The motivation to write this book is to introduce new methodologies, new developments, and new innovations in concrete technology. The unique features of this book include the introduction of end use guided research strategy for concrete, unification of materials and structures studies, and an emphasize on fundamental exploration of concrete structures, state of art of concrete development, and innovations. This book provides more comprehensive knowledge on concrete technology, including the systematic introduction of concrete fracture mechanics and nondestructive evaluation for concrete engineering.

The book is divided into nine chapters. Chapter 1 gives a brief introduction of concrete, including its historic development and advantages. Chapter 2 provides the knowledge of raw materials used for making concrete, covering aggregates, binders, admixtures, and water. Chapter 3 discusses the properties of fresh concrete, including workability and the corresponding measurement methods. Chapter 4 focuses on the structure of concrete at different scales, especially the calcium silicate hydrate at nanometer scale. Chapter 5 covers the properties of hardened concrete, including strength, durability, stress–strain relation, and dimension stability. Chapter 6 provides updated knowledge on various cement-based composites, including self-consolidation concrete, ultra-high-strength concrete, and extruded and engineered cementitious composites. Chapter 7 focuses the fracture behavior of concrete and provides the basic knowledge of fracture mechanics of concrete. Chapter 8 covers the essential knowledge of nondestructive testing of concrete engineering, including wave propagation theory in 1-D case, detecting principles of different NDT methodologies and techniques of different NDT methods. In Chapter 9, the issues regarding the future and development trend of concrete have been discussed.

Although the book is designed and written primarily to meet the teaching needs for undergraduate students at senior level and graduate students at entry level, it can serve as a reference or a guide for professional engineers in their practice.

In the process of writing this book, the authors received enthusiastic help and invaluable assistance from many people, which is deeply appreciated. The authors would like to express his special thanks to Dr. Garrison C. K. Chau, Dr. Biwan Xu, and Dr. Jianzhong Shen for their help in editing the book draft. Mr. Mike Pomfret is acknowledged for his professional page proofreading. The photos provided by Profs. Wei Sun, Tongbo Sui, Linhai Han, and Zhen He; Drs. Xiaojian Gao, Herbert Zheng, and Jinyang Jiang; Mr. Peter Allen; and the companies of Ove Arup and Gammon are greatly appreciated.

The support from China Basic Research Grant, Basic Research on Environmentally Friendly Contemporary Concrete (2009CB623200) is greatly acknowledged.

Finally, I would like to thank for my wife, Xiuming Cui, my daughters Yexin Li and Aileen Li for their love, understanding, and support.

Advanced Concrete Technology

CHAPTER 1

INTRODUCTION TO CONCRETE

1.1 CONCRETE DEFINITION AND HISTORICAL DEVELOPMENT

Concrete is a manmade building material that looks like stone. The word "concrete" is derived from the Latin *concretus*, meaning "to grow together." Concrete is a composite material composed of coarse granular material (the aggregate or filler) embedded in a hard matrix of material (the cement or binder) that fills the space among the aggregate particles and glues them together. Alternatively, we can say that concrete is a composite material that consists essentially of a binding medium in which are embedded particles or fragments of aggregates. The simplest definition of concrete can be written as

$$\text{concrete} = \text{filler} + \text{binder} \tag{1-1}$$

Depending on what kind of binder is used, concrete can be named in different ways. For instance, if a concrete in made with nonhydraulic cement, it is called nonhydraulic cement concrete; if a concrete made of hydraulic cement, it is called hydraulic cement concrete; if a concrete is made of asphalt, it is called asphalt concrete; if a concrete is made of polymer, it is called polymer concrete. Both nonhydraulic and hydraulic cement need water to mix in and react. They differ here in the ability to gain strength in water. Nonhydraulic cement cannot gain strength in water, while hydraulic cement does.

Nonhydraulic cement concretes are the oldest used in human history. As early as around 6500 BC, nonhydraulic cement concretes were used by the Syrians and spread through Egypt, the Middle East, Crete, Cyprus, and ancient Greece. However, it was the Romans who refined the mixture's use. The nonhydraulic cements used at that time were gypsum and lime. The Romans used a primal mix for their concrete. It consisted of small pieces of gravel and coarse sand mixed with hot lime and water, and sometimes even animal blood. The Romans were known to have made wide usage of concrete for building roads. It is interesting to learn that they built some 5300 miles of roads using concrete. Concrete is a very strong building material. Historical evidence also points out that the Romans used pozzalana, animal fat, milk, and blood as admixtures for building concrete. To trim down shrinkage, they were known to have used horsehair. Historical evidence shows that the Assyrians and Babylonians used clay as the bonding material. Lime was obtained by calcining limestone with a reaction of

$$\text{CaCO}_3 \xrightarrow{1000^\circ\text{C}} \text{CaO} + \text{CO}_2 \tag{1-2}$$

When CaO is mixed with water, it can react with water to form

$$\text{CaO} + \text{H}_2\text{O} \xrightarrow{\text{ambient temperature}} \text{Ca}(\text{OH})_2 \tag{1-3}$$

and is then further reacted with CO_2 to form limestone again:

$$Ca(OH)_2 + CO_2 + H_2O \xrightarrow{\text{ambient temperature}} CaCO_3 + 2H_2O \tag{1-4}$$

The Egyptians used gypsum mortar in construction, and the gypsum was obtained by calcining impure gypsum with a reaction of

$$2CaSO_4 \cdot H_2O \xrightarrow{107-130^\circ C} 2CaSO_4 \cdot \tfrac{1}{2}H_2O + 3H_2O \tag{1-5}$$

When mixed with water, half-water gypsum could turn into two-water gypsum and gain strength:

$$2CaSO_4 \cdot \tfrac{1}{2}H_2O + 3H_2O \xrightarrow{\text{ambient temperature}} 2CaSO_4 \cdot 2H_2O \tag{1-6}$$

The Egyptians used gypsum instead of lime because it could be calcined at much lower temperatures. As early as about 3000 BC, the Egyptians used gypsum mortar in the construction of the Pyramid of Cheops. However, this pyramid was looted long before archeologists knew about the building materials used. Figure 1-1 shows a pyramid in Gaza. The Chinese also used lime mortar to build the Great Wall in the Qin dynasty (220 BC) (see Figure 1-2).

A hydraulic lime was developed by the Greeks and Romans using limestone containing argillaceous (clayey) impurities. The Greeks even used volcanic ash from the island of Santorin, while the Romans utilized volcanic ash from the Bay of Naples to mix with lime to produce hydraulic lime. It was found that mortar made of such hydraulic lime could resist water. Thus, hydraulic lime mortars were used extensively for hydraulic structures from second half of the first century BC to the second century AD However, the quality of cementing materials declined throughout the Middle Ages. The art of burning lime was almost lost and siliceous impurities were not added. High-quality mortars disappeared for a long period. In 1756, John Smeaton

Figure 1-1 Pyramid built with gypsum mortar in Gaza, Egypt

Figure 1-2 The Great Wall, built in the Qin dynasty

was commissioned to rebuild the Eddystone Light house off the coast of Cornwall, England. Realizing the function of siliceous impurities in resisting water, Smeaton conducted extensive experiments with different limes and pozzolans, and found that limestone with a high proportion of clayey materials produced the best hydraulic lime for mortar to be used in water. Eventually, Smeaton used a mortar prepared from a hydraulic lime mixed with pozzolan imported from Italy. He made concrete by mixing coarse aggregate (pebbles) and powdered brick and mixed it with cement, very close to the proportions of modern concrete. The rebuilt Eddystone Lighthouse lasted for 126 years until it was replaced with a modern structure.

After Smeaton's work, development of hydraulic cement proceeded quickly James Parker of England filed a patent in 1796 for a natural hydraulic cement made by calcining nodules of impure limestone containing clay. Vicat of France produced artificial hydraulic lime by calcining synthetic mixtures of limestone and clay. Portland cement was invented by Joseph Aspdin of England. The name Portland was coined by Aspdin because the color of the cement after hydration was similar to that of limestone quarried in Portland, a town in southern England. Portland cement was prepared by calcining finely ground limestone, mixing it with finely divided clay, and calcining the mixture again in a kiln until the CO_2 was driven off. This mixture was then finely ground and used as cement. However, the temperature claimed in Aspdin's invention was not high enough to produce true Portland cement. It was Isaac Johnson who first burned the raw materials to the clinkering temperature in 1845 to produce modern Portland cement. After that, the application of Portland cement spread quickly throughout Europe and North America. The main application of Portland cement is to make concrete. It was in Germany that the first systematic testing of concrete took place in 1836. The test measured the tensile and compressive strength of concrete. Aggregates are another main ingredient of concrete, and which include sand, crushed stone, clay, gravel, slag, and shale. Plain concrete made of Portland cement and aggregate is usually called the first generation of concrete. The second generation of concrete refers to steel bar-reinforced concrete. François Coignet was a pioneer in the development of reinforced concrete. (Day and McNeil, 1996). Coignet started experimenting with iron-reinforced concrete in 1852 and was the first builder ever to use this technique as a building material (Encyclopaedia

Britannica, 1991). He decided, as a publicity stunt and to promote his cement business, to build a house made of *béton armé*, a type of reinforced concrete. In 1853, he built the first iron-reinforced concrete structure anywhere; a four-story house at 72 Rue Charles Michels (Sutherland et al., 2001). This location was near his family cement plant in St. Denis, a commune in the northern suburbs of Paris. The house was designed by local architect Theodore Lachez (Collins, 2004).

Coignet had an exhibit at the 1855 Paris Exposition to show his technique of reinforced concrete. At the exhibit, he forecast that the technique would replace stone as a means of construction. In 1856 he patented a technique of reinforced concrete using iron tirants. In 1861 he put out a publication on his techniques.

Reinforced concrete was further developed by Hennebique at the end of the 19th century, and it was realized that performance could be improved if the bars could be placed in tension, thus keeping the concrete in compression. Early attempts worked, with the beams showing a reduced tendency to crack in tension, but after a few months the cracks reopened. A good description of this early work is given in Leonhardt (1964). The first reinforced concrete bridge was built in 1889 in the Golden Gate Park in San Francisco, California.

To overcome the cracking problem in reinforced concrete, prestressed concrete was developed and was first patented by a San Francisco engineer as early as 1886. Prestressed means that the stress is generated in a structural member before it carries the service load. Prestressed concrete was referred to as the third generation of concrete. Prestressing is usually generated by the stretched reinforcing steel in a structural member. According to the sequence of concrete casting, prestressing can be classified as pretensioning or post-tensioning. Pretensioning pulls the reinforcing steel before casting the concrete and prestress is added through the bond built up between the stretched reinforcing steel and the hardened concrete. In the post-tensioning technique, the reinforcing steel or tendon is stretched after concrete casting and the gaining of sufficient strength. In post-tensioning, steel tendons are positioned in the concrete specimen through prereserved holes. The prestress is added to the member through the end anchorage. Figure 1-3 shows the sequence of the pretensioning technique for prestressed concrete.

Prestressed concrete became an accepted building material in Europe after World War II, partly due to the shortage of steel. North America's first prestressed concrete structure, the Walnut

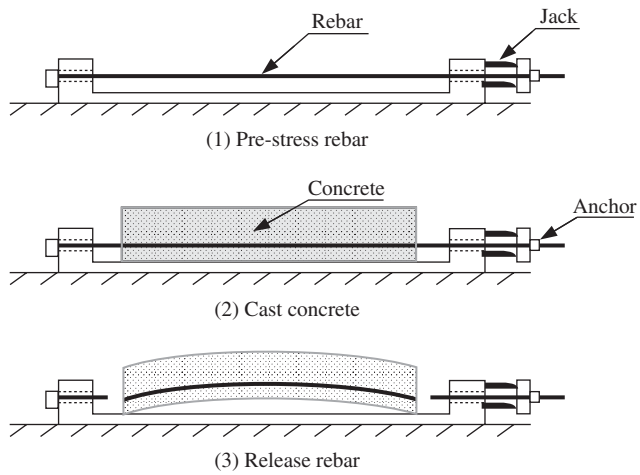

Figure 1-3 Pretensioning sequence for prestressing concrete

Lane Memorial Bridge in Philadelphia, Pennsylvania, was completed in 1951. Nowadays, with the development of prestressed concrete, long-span bridges, tall buildings, and ocean structures have been constructed. The Barrios de Lura Bridge in Spain is currently the longest-span prestressed concrete, cable-stayed bridge in the world, with a main span of 440 m. In Canada, the prestressed Toronto CN tower reaches a height of 553 m.

As a structural material, the compressive strength at an age of 28 days is the main design index for concrete. There are several reasons for choosing compressive strength as the representative index. First, concrete is used in a structure mainly to resist the compression force. Second, the measurement of compressive strength is relatively easier. Finally, it is thought that other properties of concrete can be related to its compressive strength through the microstructure. Pursuing high compressive strength has been an important direction of concrete development. As early as 1918, Duff Adams found that the compressive strength of a concrete was inversely proportional to the water-to-cement ratio. Hence, a high compressive strength could be achieved by reducing the w/c ratio. However, to keep a concrete workable, there is a minimum requirement on the amount of water; hence, the w/c ratio reduction is limited, unless other measures are provided to improve concrete's workability. For this reason, progress in achieving high compressive strength was very slow before the 1960s. At that time, concrete with a compressive strength of 30 MPa was regarded as high-strength concrete. Since the 1960s, the development of high-strength concrete has made significant progress due to two main factors: the invention of water-reducing admixtures and the incorporation of mineral admixtures, such as silica fume, fly ash, and slag. Water-reducing admixture is a chemical admixture that can help concrete keep good workability under a very low w/c ratio; the latter are finer mineral particles that can react with a hydration product in concrete, calcium hydroxide, to make concrete microstructure denser. Silica fume also has a packing effect to further improve the matrix density. In 1972, the first 52-MPa concrete was produced in Chicago for the 52-story Mid-Continental Plaza. In 1972, a 62-MPa concrete was produced, also in Chicago, for Water Tower Place, a 74-story concrete building, the tallest in the world at that time (see Figure 1-4). In the 1980s, the industry was able to produce a 95-MPa concrete to supply to the 225 West Whacker Drive building project in Chicago, as shown in Figure 1-5. The highest compressive strength of 130 MPa was realized in a 220-m-high, 58-story building, the Union Plaza constructed in Seattle, Washington (Caldarone, 2009).

Concrete produced after the 1980s usually contains a sufficient amount of fly ash, slag, or silica fume as well as many different chemical admixtures, so its hydration mechanism, hydration products, and other microstructure characteristics are very different from the concrete produced without these admixtures. Moreover, the mechanical properties are also different from the conventional concrete; hence, such concretes are referred to as contemporary concretes.

There have been two innovative developments in contemporary concrete: self-compacting concrete (SCC) and ultra-high-performance concrete (UHPC). SCC is a type of high-performance concrete. High-performance concrete is a concept developed in the 1980s. It is defined as a concrete that can meet special performance and uniformity requirements, which cannot always be achieved routinely by using only conventional materials and normal mixing, placing, and curing practices. The requirements may involve enhancement of the characteristics of concrete, such as placement and compaction without segregation, long-term mechanical properties, higher early-age strength, better toughness, higher volume stability, or longer service life in severe environments.

Self-compacting concrete is a typical example of high-performance concrete that can fill in formwork in a compacted manner without the need of mechanical vibration. SCC was initially developed by Professor Okamura and his students in Japan in the late 1980s (Ozama et al., 1989). At that time, concrete construction was blooming everywhere in Japan. Since Japan is in an

Figure 1-4 Water Tower Place in Chicago, Illinois, USA (Photo provided by Xiaojian Gao)

earthquake zone, concrete structures are usually heavily reinforced, especially at beam–column joints. Hence, due to low flowability, conventional concrete could hardly flow past the heavy reinforced rebars, leaving poor-quality cast concrete and leading to poor durability. Sometimes, the reinforcing steel was exposed to air immediately after demolding. To solve the problem, Professor Okamura and his students conducted research to develop a concrete with high flowability. With the help of the invention of the high-range water reducer or plasticizer, such a concrete was finally developed. They were so excited that they called this concrete "high-performance concrete" at the beginning. It was corrected later on to SCC, as HPC covers broader meanings. Durability is a main requirement of HPC. It has been found that many concrete structures could not fulfill the service requirement, due not to lack of strength, but to lack of durability. For this reason, concrete with high performance to meet the requirement of prolonging concrete service life was greatly needed.

In the 1990s, a new "concrete" with a compressive concrete strength higher than 200 MPa was developed in France. Due to the large amount of silica fume incorporated in such a material, it was initially called reactive powder concrete and later on changed to ultra-high-strength (performance) concrete (UHSC), due to its extremely high compressive strength (Richard and Cheyrezy, 1995). The ultra-high-strength concrete has reached a compressive strength of 800 MPa

Figure 1-5 The 225 West Whacker Drive building in Chicago, Illinois, USA (Photo provided by Xiaojian Gao)

with heating treatment. However, it is very brittle, hence, incorporating fibers into UHSC is necessary. After incorporating fine steel fibers, flexural strength of 50 MPa can be reached. The first trial application of UHSC was a footbridge built in Sherbrooke, Canada (Aitcin et al., 1998).

1.2 CONCRETE AS A STRUCTURAL MATERIAL

In this book, the term concrete usually refers to Portland cement concrete, if not otherwise specified. For this kind of concrete, the compositions can be listed as follows:

Portland cement
+ water (& admixtures) → cement **paste**
+ fine aggregate → **mortar**
+ coarse aggregate → **concrete**

Here we should indicate that admixtures are almost always used in modern practice and thus have become an essential component of contemporary concrete. Admixtures are defined as

materials other than aggregate (fine and coarse), water, and cement that are added into a concrete batch immediately before or during mixing. The use of admixtures is widespread mainly because many benefits can be achieved by their application. For instance, chemical admixtures can modify the setting and hardening characteristics of cement paste by influencing the rate of cement hydration. Water-reducing admixtures can plasticize fresh concrete mixtures by reducing surface tension of the water. Air-entraining admixtures can improve the durability of concrete, and mineral admixtures such as pozzolans (materials containing reactive silica) can reduce thermal cracking. A detailed description of admixtures is given in Chapter 2.

Concrete is the most widely used construction material in the world, and its popularity can be attributed to two aspects. First, concrete is used for many different structures, such as dams, pavements, building frames, or bridges, much more than any other construction material. Second, the amount of concrete used is much more than any other material. Its worldwide production exceeds that of steel by a factor of 10 in tonnage and by more than a factor of 30 in volume.

In a concrete structure, there are two commonly used structural materials: concrete and steel. A structural material is a material that carries not only its self-weight, but also the load passing from other members.

Steel is manufactured under carefully controlled conditions, always in a highly sophisticated plant; the properties of every type of steel are determined in a laboratory and described in a manufacturer's certificate. Thus, the designer of a steel structure need only specify the steel complying with a relevant standard, and the constructor needs only to ensure that the correct steel is used and that connections between the individual steel members are properly executed (Neville and Brooks, 1993).

On the other hand, concrete is produced in a cruder way and its quality varies considerably. Even the quality of cement, the binder of concrete, is guaranteed by the manufacturer in a manner similar to that of steel; however, the quality of concrete is hardly guaranteed because of many other factors, such as aggregates, mixing procedures, and skills of the operators of concrete production, placement, and consolidation.

It is possible to obtain concrete of specified quality from a ready-mix supplier, but, even in this case, it is only the raw materials that are bought for a construction job. Transporting, placing, and, above all, compacting greatly influence the quality of cast concrete structure. Moreover, unlike the case of steel, the choice of concrete mixes is virtually infinite and therefore the selection has to be made with a sound knowledge of the properties and behavior of concrete. It is thus the competence of the designer and specifier that determines the potential qualities of concrete, and the competence of the supplier and the contractor that controls the actual quality of concrete in the finished structure. It follows that they must be thoroughly conversant with the properties of concrete and with concrete making and placing.

In a concrete structure, concretes mainly carry the compressive force and shear force, while the steel carries the tension force. Moreover, concrete usually provides stiffness for structures to keep them stable.

Concretes have been widely used to build various structures. High-strength concrete has been used in many tall building constructions. In Hong Kong, grade 80 concrete (80 MPa) was utilized in the columns of the tallest building in the region. As shown in Figure 1-6, the 88-story International Finance Centre was built in 2003 and stands 415 m (1362 ft) tall.

Concrete has also been used in bridge construction. Figure 1-7 shows the recently built Sutong Bridge that spans the Yangtze River in China between Nantong and Changshu, a satellite city of Suzhou, in Jiangsu province. It is a cable-stayed bridge with the longest main span, 1088 meters, in the world. Its two side spans are 300 m (984 ft) each, and there are also four small cable spans.

Figure 1-6 International Finance Center, Hong Kong (Photo courtesy of user WiNG on Wikimedia Commons, http://commons.wikimedia.org/wiki/File:HK_ifc_Overview.jpg)

Figure 1-7 The Sutong Bridge in Suzhou, Jiangsu, China

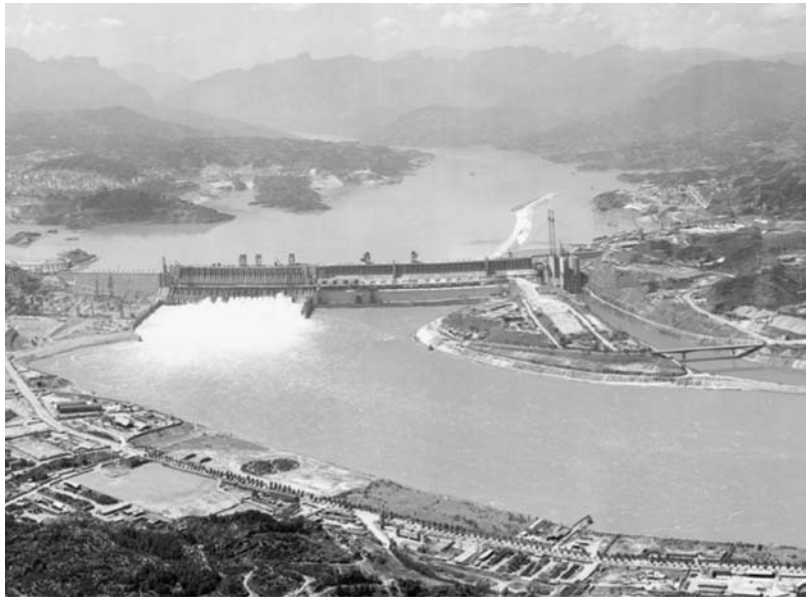

Figure 1-8 Three Gorges Dam, Hubei, China

Dams are other popular application fields for concrete. The first major concrete dams, the Hoover Dam and the Grand Coulee Dam, were built in the 1930s and they are still standing. The largest dam ever built is the Three Gorges Dam in Hubei province, China, as shown in Figure 1-8. The total concrete used for the dam was over 22 million m^3.

Concrete has also been used to build high-speed railways. Shinkansen, the world's first contemporary high-volume (initially 12-car maximum), "high-speed rail," was built in Japan in 1964. In Europe, high-speed rail was introduce during the International Transport Fair in Munich in June 1965. Nowadays, high-speed rail construction is blooming in China. According to planning, 17,000 km of high-speed rail will be built in China by 2012. Figure 1-9 shows a high-speed rail system in China.

In addition, concrete has been widely applied in the construction of airport runways, tunnels, highways, pipelines, and oil platforms. As of now, the annual world consumption of concrete has reached a value such that if concrete were edible, every person on earth would have 2000 kg per year to "eat." You may wonder why concrete has become so popular.

1.3 CHARACTERISTICS OF CONCRETE

1.3.1 Advantages of concrete

(a) *Economical*: Concrete is the most inexpensive and the most readily available material in the world. The cost of production of concrete is low compared with other engineered construction materials. The three major components in concrete are water, aggregate, and cement. Compared with steels, plastics, and polymers, these components are the most inexpensive, and are available in every corner of the world. This enables concrete to be produced worldwide at very low cost for local markets, thus avoiding the transport expenses necessary for most other materials.

Figure 1-9 High-speed rail

(b) *Ambient temperature-hardened material*: Because cement is a low-temperature bonded inorganic material and its reaction occurs at room temperature, concrete can gain its strength at ambient temperature. No high temperature is needed.

(c) *Ability to be cast*: Fresh concrete is flowable like a liquid and hence can be poured into various formworks to form different desired shapes and sizes right on a construction site. Hence, concrete can be cast into many different configurations. One good example to show concrete castability is the Baha'I Temple located in Wilmette, Illinois, USA, as shown in Figure 1-10. The very complex configurations of the different shapes of flowers in the wall and roof are all cast by concrete.

(d) *Energy efficient*: Compared with steel, the energy consumption of concrete production is low. The energy required to produce plain concrete is only 450–750 kWh/ton and that of reinforced concrete is 800–3200 kWh/ton, while structural steel requires 8000 kWh/ton or more to make.

(e) *Excellent resistance to water*: Unlike wood (timber) and steel, concrete can be hardened in water and can withstand the action of water without serious deterioration, which makes concrete an ideal material for building structures to control, store, and transport water, such as pipelines (Figure 1-11), dams, and submarine structures. A typical example of a pipeline application is the Central Arizona Project, which provides water from the Colorado river to central Arizona. The system contains 1560 pipe sections, each 6.7 m long, 7.5 m outside diameter, and 6.4 m inside diameter. Contrary to popular belief, water is not deleterious to concrete, even to reinforced concrete; it is the chemicals dissolved in water, such as chlorides, sulfates, and carbon dioxide, that cause deterioration of concrete structures.

(f) *High-temperature resistance*: Concrete conducts heat slowly and is able to store considerable quantities of heat from the environment. Moreover, the main hydrate that provides binding to aggregates in concrete, calcium silicate hydrate (C–S–H), will not be completely dehydrated until 910°C. Thus, concrete can withstand high temperatures much better than

Figure 1-10 Baha'i Temple

Figure 1-11 Pipeline under construction (Photo courtesy of Exponent, http://www.exponent.com/corrosion_analysis_of_pre_stressed_concrete_pipeline/)

wood and steel. Even in a fire, a concrete structure can withstand heat for 2–6 hours, leaving sufficient time for people to be rescued. This is why concrete is frequently used to build up protective layers for a steel structure.

(g) *Ability to consume waste*: With the development of industry, more and more by-products or waste has been generated, causing a serious environmental pollution problem. To solve the problem, people have to find a way to consume such wastes. It has been found that many industrial wastes can be recycled as a substitute (replacement) for cement or aggregate, such as fly ash, slag (GGBFS = ground granulated blast-furnaces slag), waste glass, and ground vehicle tires in concrete. Production of concrete with the incorporation of industrial waste not only provides an effective way to protect our environment, but also leads to better performance of a concrete structure. Due to the large amount of concrete produced annually, it is possible to completely consume most of industry waste in the world, provided that suitable techniques for individual waste incorporation are available.

(h) *Ability to work with reinforcing steel*: Concrete has a similar value to steel for the coefficient of thermal expansion (steel 1.2×10^{-5}; concrete $1.0–1.5 \times 10^{-5}$). Concrete produces a good protection to steel due to existence of CH and other alkalis (this is for normal conditions). Therefore, while steel bars provide the necessary tensile strength, concrete provides a perfect environment for the steel, acting as a physical barrier to the ingress of aggressive species and giving chemical protection in a highly alkaline environment (pH value is about 13.5), in which black steel is readily passivated.

(i) *Less maintenance required*: Under normal conditions, concrete structures do not need coating or painting as protection for weathering, while for a steel or wooden structure, it is necessary. Moreover, the coatings and paintings have to be replaced few years. Thus, the maintenance cost for concrete structures is much lower than that for steel or wooden structures.

1.3.2 Limitations

(a) *Quasi-brittle failure mode*: The failure mode of materials can be classified into three categories: brittle failure, quasi-brittle failure, and ductile failure, as shown in Figure 1-12. Glass is a typical brittle material. It will break as soon as its tension strength is reached. Materials exhibiting a strain-softening behavior (Figure 1-12b) are called quasi-brittle materials. Both brittle and quasi-brittle materials fail suddenly without giving a large deformation as a warning sign. Ductile failure is a failure with a large deformation that serves as a warning before collapse, such as low-carbon steel. Concrete is a type of quasi-brittle material with low fracture toughness. Usually, concrete has to be used with steel bars to form so-called reinforced concrete, in which steel bars are used to carry tension and the concrete

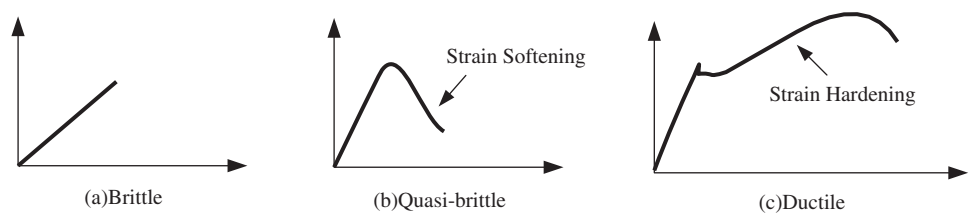

Figure 1-12 Three failure modes of materials

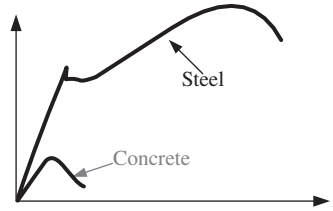

Figure 1-13 Toughness of steel and concrete

compression loads. Moreover, concrete can provide a structure with excellent stability. Reinforced concrete is realized as the second generation of concrete.

(b) *Low tensile strength*: Concrete has different values in compression and tension strength. Its tension strength is only about 1/10 of its compressive strength for normal-strength concrete, or lower for high-strength concrete. To improve the tensile strength of concrete, fiber-reinforced concrete and polymer concrete have been developed.

(c) *Low toughness (ductility)*: Toughness is usually defined as the ability of a material to consume energy. Toughness can be evaluated by the area of a load–displacement curve. Compared to steel, concrete has very low toughness, with a value only about 1/50 to 1/100 of that of steel, as shown in Figure 1-13. Adding fibers is a good way to improve the toughness of concrete.

(d) *Low specific strength (strength/density ratio)*: For normal-strength concrete, the specific strength is less than 20, while for steel it is about 40. There are two ways to increase concrete specific strength: one is to reduce its density and the other is to increase its strength. Hence, lightweight concrete and high-strength concrete have been developed.

(e) *Formwork is needed*: Fresh concrete is in a liquid state and needs formwork to hold its shape and to support its weight. Formwork can be made of steel or wood, as shown in Figure 1-14. The formwork is expensive because it is labor intensive and time-consuming. To improve efficiency, precast techniques have been developed.

(f) *Long curing time*: The design index for concrete strength is the 28-day compression strength. Hence, full strength development needs a month at ambient temperature. The improvement measure to reduce the curing period is steam curing or microwave curing.

(g) *Working with cracks*: Even for reinforced concrete structure members, the tension side has a concrete cover to protect the steel bars. Due to the low tensile strength, the concrete cover cracks. To solve the crack problem, prestressed concrete is developed, and it is also realized as a third-generation concrete. Most reinforced concrete structures have existing cracks on their tension sides while carrying the service load.

1.4 TYPES OF CONCRETE

1.4.1 Classification in accordance with unit weight

According to the unit weight of concretes, they can be classified into four categories, as shown in Table 1-1. Ultra-lightweight concrete can only be used to build up nonstructural members. Lightweight concrete can be used to build both nonstructural and structural members, depending on its specified composition. Normal-weight concretes are commonly used concretes in the

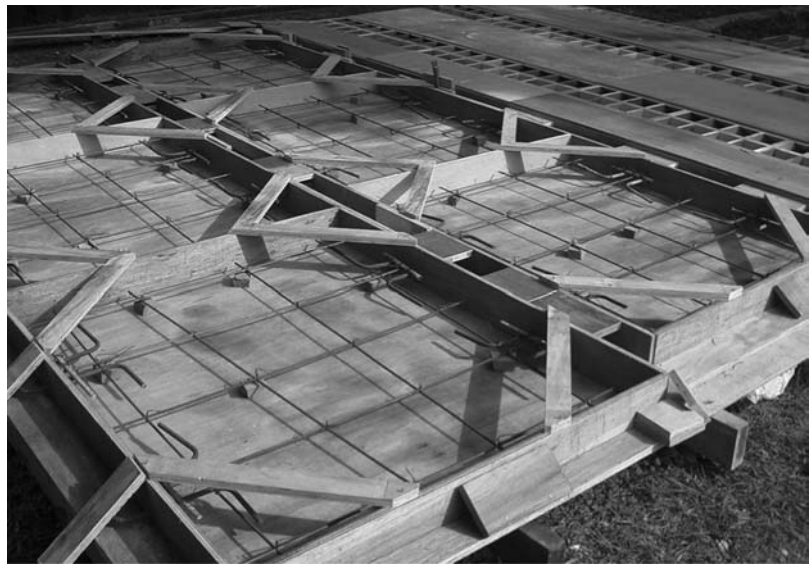

Figure 1-14 Formwork for concrete casting

Table 1-1 Classification of concrete in accordance with unit weight

Classification	Unit Weight (Kg/m^3)
Ultra-lightweight concrete	<1200
Lightweight concrete	1200 < UW < 1800
Normal-weight concrete	~2400
Heavyweight concrete	>3200

construction of infrastructures and buildings. Heavyweight concrete is used to build some special structures, such as laboratories, hospital examination rooms, and nuclear plant, where radioactive protection is needed to minimize its influence on people's health.

The main component that makes a concrete unit weight difference is the aggregate. As discussed in Chapter 2, the four types of concrete differentiated by UW correspond to four different types of aggregates.

1.4.2 Classification in accordance with compressive strength

According to its compressive strength, concrete can be classified into four categories, as listed in Table 1-2. Low-strength concrete is mainly used to construct mass concrete structures, subgrades of roads, and partitions. Moderate-strength concretes are the most commonly used concretes in buildings, bridges, and similar structures. High-strength concretes can be used to build tall building columns, bridge towers, and shear walls. Ultra-high-strength concretes have not yet been widely used in structural constructions. Only a few footbridges and some structural segments, such as girders, have been built using such concretes.

Table 1-2 Concrete classified in accordance with compressive strength

Classification	Compressive Strength (MPa)
Low-strength concrete	<20
Moderate-strength concrete	20–50
High-strength concrete	50–150
Ultra-high-strength concrete	>150

Table 1-3 Concrete classifications in accordance with additives

Classification	Additives
MDF	Polymers
Fiber-reinforced concrete	Different fibers
DSP concrete	Large amount silica fume
Polymer concrete	Polymers

1.4.3 Classification in accordance with additives

According to the materials other than cement, aggregate and water that are added into concrete mixtures as additives, concretes can be classified into different categories. Four examples are shown in Table 1-3. Fiber-reinforced concrete (FRC) is a type of concrete with fibers incorporated. Many different fibers have been used to produce fiber-reinforced concrete, including steel, glass, polymerics, and carbon. The purpose of incorporating fibers into concrete includes toughness enhancement, tension property improvement, shrinkage control, and decoration. Detailed information regarding FRC can be found in Chapter 6. Macro-defect-free (MDF) is a cement-based composite that incorporates a large amount of water-soluble polymer, produced in a twin-roll mixing process. It was developed to enhance the tensile and flexural properties of concrete. Concrete that has been densified with small particles. (DSP) has incorporated a large amount of silica fume, a mineral admixture with very small particles. DSP has excellent abrasion resistance and is mainly used to produce machine tools and industrial molds. Three methods have been developed to incorporate polymers into concrete: using the polymer as a binder, impregnating the polymer into normal Portland cement concrete members, and using the polymer as an admixture in ordinary Portland concrete. MDF, DSP, and polymer in concrete are discussed in detail in Chapter 6.

1.5 FACTORS INFLUENCING CONCRETE PROPERTIES

1.5.1 *w/c* ratio (or *w/b* or *w/p* ratio)

One property of concrete is the water/cement ratio. In contemporary concrete, w/c is frequently replaced with w/b (water/binder) or w/p (water/powder), since Portland cement is not the only binding material in such a concrete. The w/c or w/b ratio is one of the most important factors influencing concrete properties, such as compressive strength, permeability, and diffusivity. A lower w/c ratio will lead to a stronger and more durable concrete. The influence of w/c on the

concrete compressive strength has been known since the early 1900s (Abrams, 1927), leading to Abrams's law:

$$f_c = \frac{A}{B^{1.5(w/c)}} \tag{1-7}$$

where f_c is the compressive strength, A is an empirical constant (usually 97 MPa or 14,000 psi), and B is a constant that depends mostly on the cement properties (usually 4). It can be seen from the formula that the higher the w/c ratio, the lower the compressive strength. Another form to show the influence of the w/c ratio to compressive strength of a concrete can be written as

$$f_c = A f_{ce}\left(\frac{c}{w} - B\right) \tag{1-8}$$

where f_c is the compressive strength, A and B are empirical constants that depend on the aggregate, and f_{ce} is the compressive strength of a specified cement at 28 days. c/w is the reverse of w/c.

1.5.2 Cement content

When water is added a concrete mix, cement paste will be formed. Cement paste has three functions in concrete: binding, coating, and lubricating. Cement paste provides binding to individual aggregates, reinforcing bars, and fibers and glues them together to form a unique material. Cement paste also coats the surface of the aggregates and fibers during the fresh stage of concrete. The rest of the paste after coating can make the movement of the aggregates or fibers easier, rather like a lubrication agent. The cement content influences concrete workabilities in the fresh stage, heat release rate in the fast hydration stage, and volume stabilities in the hardened stage. The range of the amount of cement content in mass concrete is 160–200 kg/m^3, in normal strength concrete it is less than 400 kg/m^3, and in high strength concrete it is 400–600 kg/m^3.

1.5.3 Aggregate

(a) *Maximum aggregate size*: The maximum coarse aggregate size mainly influences the cement paste requirement in the concrete. For the same volume of aggregate, the ones with a large aggregate size will lead to a small total surface area and a lower amount of cement paste coating. Hence, if the same amount of cement is used, concrete with a larger maximum aggregate size will have more cement paste left as a lubricant and the fluidity of concrete can be enhanced, as compared to concrete with a smaller maximum aggregate size. For normal-strength concrete, at the same w/c ratio and with the same cement content, the larger the maximum sizes, the better the workability; at the same workability, the larger the maximum sizes, the higher the strength. However, a larger aggregate size has some drawbacks. First, a larger aggregate size may make the concrete appear nonhomogeneous. Second, a larger aggregate size may lead to a large interface that can influence the concrete transport properties and the mechanical properties.

Generally, the maximum size of coarse aggregate should be the largest that is economically available and consistent with the dimensions of the structure. In choosing the maximum aggregate size, the structural member size and spacing of reinforcing steel in a member have to be taken into consideration. In no event should the maximum size exceed one-fifth of the narrowest dimension in the sizes of the forms, one-third of the depth of slabs, or three-quarters of the minimum clear spacing between reinforcing bars.

(b) *Aggregate grading*: Aggregate grading refers to the size distribution of the aggregate. The grading mainly influences the space filling or particle packing. The classical idea of

particle packing is based on the Apollonian concept, in which the smaller particles fit into the interstices left by the large particles. Well-defined grading with an ideal size distribution of aggregate will decrease the voids in the concrete and hence the cement content. As the price of the aggregate is usually only one-tenth that of cement, well-defined grading not only will lead to a better compressive strength and low permeability, but also is more economical at lower cost.

(c) *Aggregate shape and texture*: The aggregate shape and texture can influence the workability, bonding, and compressive strength of concrete. At the same w/c ratio and with the same cement content, aggregates with angular shape and rough surface texture result in lower workability, but lead to a better bond and better mechanical properties. On the other hand, aggregates with spherical shape and smooth surface texture result in higher workability, but lead to a lower bond and lower mechanical properties.

(d) *Sand/coarse aggregate ratio*: The fine/coarse aggregate ratio will influence the packing of concrete. It also influences the workability of concrete in the fresh stage. Increase of the sand to coarse aggregate ratio can lead to an increase of cohesiveness, but reduces the consistency. Of all the measures for improving the cohesiveness of concrete, increasing the sand/coarse aggregate ratio has been proven to be the most effective one.

(e) *Aggregate/cement ratio*: The aggregate/cement ratio has an effect on the concrete cost, workability, mechanical properties, and volume stability. Due to the price difference between the aggregate and cement, increasing the aggregate/cement ratio will decrease the cost of concrete. From a workability point of view, an increase of the aggregate to cement ratio results in a lower consistency because of less cement paste for lubrication. As for mechanical properties, increase of the aggregate/cement ratio can lead to a high stiffness and compressive strength if proper compaction can be guaranteed. Increasing the aggregate/cement ratio will definitely improve concrete's dimension stability due to reduction of shrinkage and creep.

1.5.4 Admixtures

Admixtures (chemical admixtures and mineral admixtures) are important and necessary components for contemporary concrete technology. The concrete properties, both in fresh and hardened states, can be modified or improved by admixtures. For instance, concrete workability can be affected by air entraining agents, water reducers, and fly ash. Concrete strength can be improved by silica fume. More details regarding the effects of admixtures on concrete properties can be found in Chapter 2.

1.5.5 Mixing procedures

Mixing procedures refer to the sequence of putting raw materials into a mixer and the mixing time required for each step. Mixing procedures directly influence the workability of fresh concrete and indirectly influence some mature properties of concrete.

The following mixing procedure can be used to obtain a very good workability with a good coating on the coarse aggregate to protect alkali aggregate reaction.

Step 1: Coarse aggregate + 50% water + 50% cement: mixing for 30 sec to 1 min.

Step 2: Adding 50% cement + 25% water + superplasticizer + fine aggregate: mixing for 2 min.

Step 3: Adding 25% water: mixing for 3 min.

1.5.6 Curing

Curing is defined as the measures for taking care of fresh concrete right after casting. The main principle of curing is to keep favorable moist conditions under a suitable temperature range during the fast hydration process for concrete. It is a very important stage for the development of concrete strength and in controlling early volume changes. Fresh concrete requires considerable care, just like a baby. Careful curing will ensure that the concrete is hydrated properly, with good microstructure, proper strength, and good volume stability. On the other hand, careless curing always leads to improper hydration with defects in the microstructure, insufficient strength, and unstable dimensions. One of the common phenomena of careless curing is plastic shrinkage, which usually leads to an early age crack that provides a path for harmful ions and agents to get into the concrete body easily and causes durability problems. Curing is a simple measure to achieve a good quality of concrete. However, it is often ignored on construction sites.

Some methods could be helpful in curing:

(a) Moisten the subgrade and forms
(b) Moisten the aggregate
(c) Erect windbreaks and sunshades
(d) Cool the aggregate and mixing water
(e) Fog spray
(f) Cover
(g) High temperature (70–80°C) steam curing
(h) Use shrinkage compensating concrete

Recently, a new technique called internal curing has been developed, which utilizes the saturated porous aggregate to form a reservoir inside a concrete and provide water for concrete curing internally. Details of the relevant curing methods and the effects on properties of concrete are explained in Chapter 3.

1.6 APPROACHES TO STUDY CONCRETE

The scope of materials, including concrete, research, design, and development can be explained by the Chinese word 材料, which is pronounced *tsai liao* and means material. The first character, 材(pronounced *tsai*), is composed of two parts, 木(pronounced *mu*) and 才(pronounced *tsai*). The first part, 木, means wood and is real, while the second part, 才, means properties or performance and is virtual. The two parts 木 and 才 represent the hardware and software of materials research, development and design. Similarly, the second character in the Chinese word for material, 料 (pronounced *liao*), is also composed of two parts, 米(pronounced *mi*) and 斗(pronounced *dou*). The first part 米 means rice and is real and the second part 斗 means container and is virtual. The two parts 米 and 斗 also represents the hardware and software of materials research, development, and design. Basically, materials research, design, and development involve two aspects, hardware and software. Hardware includes material composition, microstructure, and synthesis/processing. Software includes characterization, measurement, properties, and performance.

As a structural material, the fundamental approach in materials study also applies to concrete. About 15 years ago, a pyramid diagram was used to describe the philosophy in materials research, as shown in Figure 1-15. In this pyramid, the top is performance and the base is

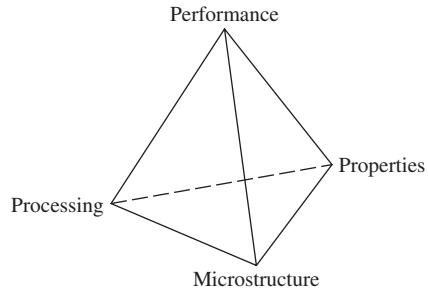

Figure 1-15 Fundamental approach of materials research, 1

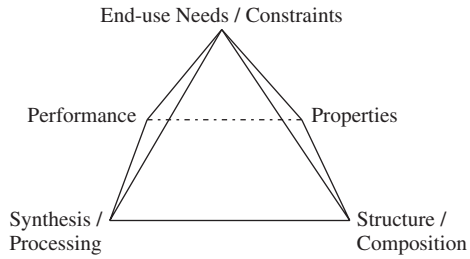

Figure 1-16 Fundamental approach of materials research, 2

a triangle formed by three points: properties, microstructure, and processing. The philosophy behind this pyramid is that the processing, microstructure, and properties of a material should be designed, developed, or investigated according its performance requirement.

This concept was changed in 1999. The U.S. National Research Council has developed a new pyramid for materials research, as shown in Figure 1-16. In this pyramid, the top is changed to End use needs/constraints and the base changed to a square with processing, properties, microstructure, and performance at each corner. The processing of concrete includes raw materials selection, mixing, placing, compacting, and curing. The properties of concrete include load-carrying capability, such as compressive strength, flexural strength, and fatigue strength, dimensional stability, such as shrinkage and creep, and stress–strain or load-deformation relationship. The structure of concrete consists of different phases with different amounts, sizes, and special arrangements. It covers the nanoscale, microscale, and millimeter scale, a typical multi phase composite. Performance of a concrete includes safety, durability, and serviceability.

The philosophy behind this pyramid is that the microstructure, processing, properties, and performance of a material have to be designed, investigated, or developed comprehensively to meet the requirement of the end use. In other words, it is the end use that governs the design, research, or development of a material, not material itself. Design and construction of the Eddystone Lighthouse by John Smeaton is a good example of an end use constraint. Since the structure to be built was a lighthouse, which must be able to withstand watery conditions, Smeaton designed the building materials according to the constraints of such end needs, in their composition, processing, properties, and performance, which turned out to be hydraulic cement. It is clear that the end requirements of a tall building are very different from those of a hydraulic dam. Hence, the materials' design and development must be very different for a tall building and for a hydraulic dam.

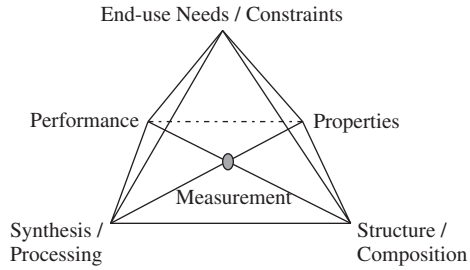

Figure 1-17 Measurement is an essential part of materials science and engineering

By adding measurement and characterization at the center of the base of the pyramid shown in Figure 1-16, the essential portion of materials science and engineering, the scope of materials design and development is complete, as demonstrated in Figure 1-17. With measurement and characterization, the materials structure/composition can be quantified, the properties can be specified, and synthesis/processing can be identified. Moreover, with measurement, the four corners of the base can be connected.

A close look at the historic development of concrete, shows that concrete has been applied in practice for more than 150 years without a systematic scientific background. Most practice followed empirical formulae and observations. Attention was paid mainly to the properties of concrete, especially compressive strength. Very limited understanding had been achieved on the material structure of concrete. In fact, concrete is a typical multiscale material, and its material structure covers the nanometer scale, the micrometer scale, and the millimeter scale. The concrete phases in the nanometer scale mainly constitute calcium silicate hydrate (C–S–H). It is believed that C–S–H contributes most to the binding strength, and understanding the nature of the C–S–H gel is a key to revealing the behavior of concrete. The structure of C–S–H on the atomic level determines the nature of the mechanical properties, transport mechanism, and dimensional stability of hydrated cement paste. However, due to the limitations in experimental techniques and computer simulation in the past, studies on C–S–H structure are very limited. Nowadays, with the fast development of microstructure measurement technology and powerful computer simulation methods, it is possible to study and develop concrete technology in a more scientific manner at the C–S–H level. The research activities aimed at understanding the nature of concrete hydrates at the nanometer-scale structure is growing very fast. A revolutionary breakthrough in concrete science is very likely. With such an understanding, it will be possible to design or develop concrete structures/compositions, properties, processing methods, and performance with solid knowledge to meet the every need of different end use.

DISCUSSION TOPICS

Why is concrete so popular?
What are the weaknesses of concrete?
What are the factors influencing concrete properties?
Give some examples for concrete applications.
Can you list a few topics for concrete research?
When you do a structural design, which failure mode should be applied?

How would you like to improve concrete workability (fluidity or cohesiveness)?

How can you enhance concrete compressive strength?

Which principles are you going to follow if you are involved in a concrete research?

REFERENCES

Abrams, D. A. (1927) "Water–cement ratio as a basis of concrete quality," *ACI Journal* 23(2), pp. 452–457.

Aitcin, P. C., Lachemi, M., Adeline, R., and Richard, P. (1998) "The Sherbrooke reactive powder concrete dootbridge," *Structural Engineering International* 8(2), 140–144.

Caldarone, M. A. (2009) *High-strength concrete: a practical guide*, London: Taylor & Francis.

Collins, P. (2004) *Concrete: the vision of a new architecture*, Montreal: McGill-Queen's University Press.

Day, L., and McNeil, I. (1996) *Biographical dictionary of the history of technology*, New York: Routledge.

Encyclopaedia Britannica, Inc. (1991) *The new encyclopaedia Britannica*, 15th edition, Chicago, IL: Encyclopaedia Britannica.

Leonhardt, F., (1964), *Prestressed Concrete: Design and Construction*, Berlin: Ernst & John.

Neville, A. M., and Brooks, J. J., (1993) *Concrete technology*, Essex, England: Longman Scientific and Technical.

Ozama K., Mekawa, K., Kunishima, M., and Okamura, H. (1989) "Development of high performance concrete based on durability design of concrete structure," *Proceedings of the second East-Asia and Pacific conference on structural engineering and construction (EASEC-2)*, 445–450.

Richard, P. and Cheyrezy M. (1995) "Composition of reactive powder concretes," *Cement and Concrete Research* 25(7), 1501–1511.

Sutherland, J., Humm, D., and Chrimes, M. (2001) *Historic concrete: background to appraisal*, London: Thomas Telford.

U. S. National Research Council (1999), "Material science and engineering: forging stronger links to Users."

CHAPTER 2

MATERIALS FOR MAKING CONCRETE

Concrete is one of the most versatile and widely produced construction materials in the world (Penttala, 1997). Its worldwide annual production exceeds 12 billion metric tons, i.e., more than two metric tons of concrete was produced each year for every person on earth in 2007. The ever-increasing population, living standards, and economic development lead to an increasing demand for infrastructure development and hence concrete materials. As a composite material, concrete is composed of different graded aggregates or fillers embedded in a hardened matrix of cementitious material. The properties of major constituents of concrete mixtures, such as aggregates, cementitious materials, admixtures, and water, should be understood first to better learn the properties and performance of concrete.

2.1 AGGREGATES

Aggregates constitute a skeleton of concrete. Approximately three-quarters of the volume of conventional concrete is occupied by aggregate. It is inevitable that a constituent occupying such a large percentage of the mass should contribute important properties to both the fresh and hardened product. Aggregate is usually viewed as an inert dispersion in the cement paste. However, strictly speaking, aggregate is not truly inert because physical, thermal, and, sometimes, chemical properties can influence the performance of concrete (Neville and Brooks, 1990).

2.1.1 Effects of aggregates

(a) *Aggregate in fresh and plastic concrete*: When concrete is freshly mixed, the aggregates are suspended in the cement–water–air bubble paste. The behavior of fresh concrete, such as fluidity, cohesiveness, and rheological behavior, is largely influenced by the amount, type, surface texture, and size gradation of the aggregate. The selection of aggregate has to meet the requirement of the end use, i.e., what type of structure to be built.

(b) *Aggregate in hardened concrete*: Although there is little chemical reaction between the aggregate and cement paste, the aggregate contributes many qualities to the hardened concrete. In addition to reducing the cost, aggregate in concrete can reduce the shrinkage and creep of cement paste. Moreover, aggregates have a big influence on stiffness, unit weight, strength, thermal properties, bond, and wear resistance of concrete.

2.1.2 Classification of aggregates

Aggregates can be divided into several categories according to different criteria, such as size, source, and unit weight.

(a) In accordance with size

Coarse aggregate: Aggregates predominately retained on a No. 4 (4.75-mm) sieve are classified as coarse aggregate. Generally, the size of coarse aggregate ranges from 5 to 150 mm. For normal concrete used for structural members such as beams and columns, the maximum size of coarse aggregate is about 25 mm. For mass concrete used for dams or deep foundations, the maximum size can be as large as 150 mm. Figure 2-1 shows some examples of coarse aggregates.

Fine aggregate (sand): Aggregates passing through a No. 4 (4.75 mm) sieve and predominately retained on a No. 200 (75 μm) sieve are classified as fine aggregate. River sand is the most commonly used fine aggregate. In addition, crushed rock fines can be used as fine aggregate. However, the finish of concrete with crushed rock fines is not as good as that with river sand. Figure 2-2 shows the profile of sand.

Figure 2-1 Different sizes of coarse aggregates

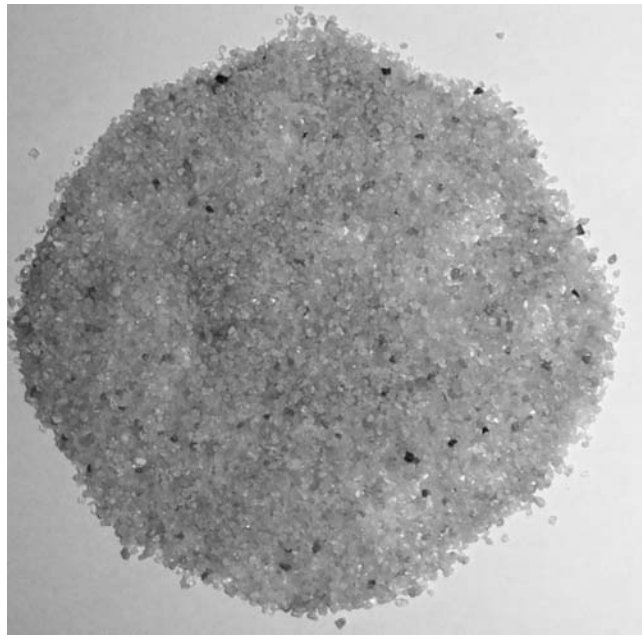

Figure 2-2 Profile of sand

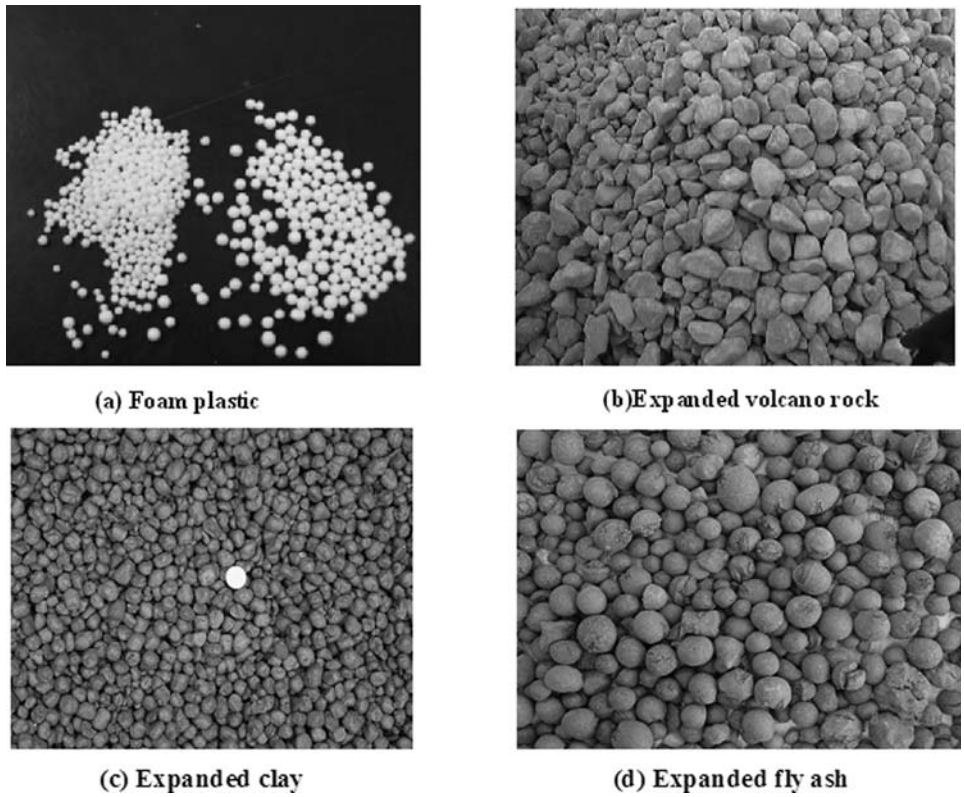

Figure 2-3 Synthetic aggregates

(b) In accordance with source

Natural aggregates: This kind of aggregate such as sand and gravel is taken from natural deposits without changing the nature during production.

Manufactured (synthetic) aggregates (see Figure 2-3): These kinds of aggregate are man-made materials, resulting from products or by-products of industry. Some examples are blast furnace slag and lightweight aggregate.

(c) In accordance with unit weight

Ultra-lightweight aggregate: The unit weight of such aggregates is less than 500 kg/m^3, including expanded perlite and foam plastic. The concrete made of ultra-lightweight aggregates has a bulk density from 800 to 1100 kg/m^3, depending on the volume fraction of aggregate. Such a concrete can be used only as nonstructural members, like partition walls.

Lightweight aggregate: The unit weight of such aggregates is between 500 and 1120 kg/m^3. Examples of lightweight aggregates include cinder, blast-furnace slag, volcanic pumice, and expanded clay. The concrete made of lightweight aggregate has a bulk density between 1200 and 1800 kg/m^3. Such concrete can be either a structural member or nonstructural member, depending what type of aggregate is used.

Normal-weight aggregate: An aggregate with a unit weight of 1520–1680 kg/m^3 is classified as normal-weight aggregate. Sand, gravel, and crushed rock belong to this category

and are most widely used. Concrete made with this type of aggregate has a bulk density of 2300–2400 kg/m^3. It is the main concrete used to produce important structural members.

Heavy-weight aggregate: If the unit weight of aggregate is greater than 2100 kg/m^3, it is classified as heavy-weight aggregate. Materials used as heavy-weight aggregate are iron ore, crashed steel pieces, and magnesite limonite. The bulk density of the corresponding concrete is greater than 3200 kg/m^3 and can reach 4000 kg/m^3. This kind of concrete has special usage, like radiation shields in nuclear power plants, hospitals, and laboratories. It can also be used as sound-shielding material.

2.1.3 Properties of aggregates

2.1.3.1 Moisture conditions

The moisture condition defines the presence and amount of water in the pores and on the surface of the aggregate. There are four moisture conditions, as demonstrated in Figure 2-4.

(a) *Oven dry (OD)*: This condition is obtained by keeping the aggregate in an oven at a temperature of 110°C long enough to drive all water out from internal pores and hence reach a constant weight.

(b) *Air dry (AD)*: This condition is obtained by keeping the aggregate at ambient temperature and ambient humidity. Under such condition, pores inside of aggregate are partly filled with water. When aggregate is under either the OD or AD condition, it will absorb water during the concrete mixing process until the internal pores are fully filled with water.

(c) *Saturated surface dry (SSD)*: In this situation, the pores of the aggregate are fully filled with water and the surface is dry. This condition can be obtained by immersing coarse aggregate in water for 24 h followed by drying of the surface with a wet cloth. When the aggregate is under the SSD condition, it will neither absorb water nor give out water during the mixing process. Hence, it is a balanced condition and is used as the standard index for concrete mix design.

(d) *Wet (W)*: The pores of the aggregate are fully filled with water and the surface of the aggregate has a film of water. When aggregate is in a wet condition, it will give out water to the concrete mix during the mixing process. Since sand is usually obtained from a river, it is usually in a wet condition.

2.1.3.2 Moisture content (MC) calculations

The moisture content of aggregates can be calculated with respect either the OD or SSD condition.

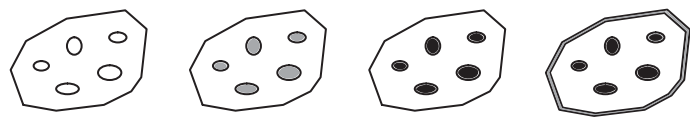

Figure 2-4 Moisture conditions of aggregates

(a) For the oven dry condition

$$\mathrm{MC\,(OD)} = \frac{W_{\mathrm{stock}} - W_{\mathrm{OD}}}{W_{\mathrm{OD}}} \times 100\% \tag{2-1}$$

where W_{stock} is the weight of aggregate in the stock condition, and W_{OD} the weight of oven-dried aggregates. It can be seen that $\mathrm{MC_{OD}}$ is a nonnegative value.

(b) For the saturated surface dry condition

$$\mathrm{MC\,(SSD)} = \frac{W_{\mathrm{stock}} - W_{\mathrm{SSD}}}{W_{\mathrm{SSD}}} \times 100\% \tag{2-2}$$

where W_{SSD} is the weight of aggregate in the SSD condition. As W_{stock} can be greater than, equal to, or less than W_{SSD}; $\mathrm{MC_{SSD}}$ can be greater than, equal to, or less than zero.

(c) Absorption capacity

$$\mathrm{AC} = \frac{W_{\mathrm{SSD}} - W_{\mathrm{OD}}}{W_{\mathrm{OD}}} \times 100\% \tag{2-3}$$

Absorption capability of an aggregate is defined as the total amount of water that can be taken by an aggregate from the OD to the SSD condition.

It should be noted that in designing a concrete mix, the moisture content usually uses the SSD condition as a reference, because it is an equilibrium condition at which the aggregate will neither absorb water nor give up water to the paste. Thus, if the $\mathrm{MC_{SSD}}$ value is positive, it means that the aggregate is under a surface moisture condition. If it is negative, it means that the pores in the aggregate are only partly filled with water. The amount of water used for mixing concrete has to be adjusted according to the $\mathrm{MC_{SSD}}$ value in order to keep a correct w/c ratio, especially for a high-strength concrete in which a small w/c ratio is used, and the amount of adjusted water involved in MC can easily be a large portion of the total amount of water in the mixture.

2.1.3.3 Density and specific gravity

Since aggregates are porous materials, even a single piece of aggregate contains both solid material volume and pores volume. Hence, two types of aggregate density are defined.

Density (D) is defined as the weight per unit volume of solid material only, excluding the pores volume inside a single aggregate:

$$D = \frac{\mathrm{weight}}{V_{\mathrm{solid}}} \tag{2-4}$$

Bulk density (BD) is defined as the weight per unit volume of both solid material and the pores volume inside a single aggregate:

$$\mathrm{BD} = \frac{\mathrm{weight}}{V_{\mathrm{solid}} + V_{\mathrm{pores}}} \tag{2-5}$$

where BD can be either $\mathrm{BD_{SSD}}$ or $\mathrm{BD_{AD}}$ according to the moisture condition of the aggregate when it is weighed.

Specific gravity (SG) is a ratio of density or bulk density of aggregate to density of water. Or SG is the mass of a given substance per unit mass of an equal volume of water. Depending

on the definition of volume, the specific gravity can be divided into absolute specific gravity (ASG) and bulk specific gravity (BSG).

$$\text{ASG} = \frac{\dfrac{\text{weight of aggregate}}{V_{\text{solid}}}}{\text{density of water}} = \frac{D}{\rho_{\text{w}}} \tag{2-6}$$

$$\text{and} \quad \text{BSG} = \frac{\dfrac{\text{weight of aggregate}}{V_{\text{solid}} + V_{\text{pores}}}}{\text{density of water}} = \frac{\text{BD}}{\rho_{\text{w}}} \tag{2-7}$$

In practice, the BSG value is the realistic one to use since the effective volume that an aggregate occupies in concrete includes its internal pores. The BSG of most rocks is in the range of 2.5 to 2.8. Similar to BD, BSG can be either BSG_{SSD} or BSG_{AD} according to the moisture condition of the aggregate. The BSG can be determined using the so-called displacement method. In this method, Archimedes' principle is utilized. The weight of aggregate is first measured in air, e.g., under the SSD condition, and is denoted as W_{SSD} in air. Then, the weight of the sample is measured in water, denoted as W_{SSD} in water. Thus, we have

$$\text{BSG}_{\text{SSD}} = \frac{W_{\text{SSD in air}}}{W_{\text{displacement}}} = \frac{W_{\text{SSD in air}}}{W_{\text{SSD in air}} - W_{\text{SSD in water}}} \tag{2-8}$$

where $W_{\text{displacement}}$ is the weight of water displaced by the aggregates.

2.1.3.4 Unit weight (UW)

The unit weight is defined as the weight per unit bulk volume for bulk aggregates. In addition to the pores inside each single aggregate, the bulk volume also includes the space among the particles. According to the weight measured at different conditions, the unit weight can be divided into UW(SSD) and UW(OD):

$$\text{UW (SSD)} = \frac{W_{\text{SSD}}}{V_{\text{solid}} + V_{\text{pores}} + V_{\text{spacing}}} \tag{2-9}$$

$$\text{and} \quad \text{UW (OD)} = \frac{W_{\text{OD}}}{V_{\text{solid}} + V_{\text{pores}} + V_{\text{spacing}}} \tag{2-10}$$

The percentage of spacing (voids) among the aggregates can be calculated as

$$\text{Spacing (void)} = \frac{\text{BD} - \text{UW}}{\text{BD}} \times 100\% \tag{2-11}$$

2.1.3.5 Measurement of moisture content

Once the BSG_{SSD} is obtained for a type of aggregate, the moisture content of the aggregate under different moisture conditions can be conveniently determined using the following equation:

$$\text{MC (SSD)} = \frac{W_{\text{stock}} - \dfrac{W_{\text{water}} \times \text{BSG}_{\text{SSD}}}{\text{BSG}_{\text{SSD}} - 1}}{\dfrac{W_{\text{water}} \times \text{BSG}_{\text{SSD}}}{\text{BSG}_{\text{SSD}} - 1}} \tag{2-12}$$

where W_{stock} is the weight of the sample under the stockpile condition, and W_{water} is the short form of W_{SSD} in water.

If AC is known for the aggregate, MC(SSD) can also be calculated using the absorption capability of aggregates as

$$\text{MC (SSD)} = \frac{W_{stock} - W_{OD}(1 + \text{AC})}{W_{OD}(1 + \text{AC})} \tag{2-13}$$

2.1.4 Grading aggregates

2.1.4.1 Grading and size distribution

The particle size distribution of aggregates is called grading. Grading determines the paste requirement for a workable concrete since the amount of voids among aggregate particles requires the same amount of cement paste to fill out in the concrete mixture. To obtain a grading curve for an aggregate, sieve analysis has to be conducted. The commonly used sieve designation is listed in Table 2-1.

As shown in Figure 2-5, five size distributions are generally recognized: dense, gap graded, well-graded, uniform graded, and open graded. The dense and well-graded types are essentially the wide size ranges with smooth distribution. They are the desired grading for making concrete. The dense graded is for coarse aggregate and well-graded for fine aggregate. Gap grading is a kind of grading that lacks one or more intermediate size; hence, a nearly flat horizontal region appears in the grading curve. For uniform grading, only a few sizes dominate the bulk materials, and the grading curve falls almost vertically at the dominating size. Open grading is defined as being under compact conditions, the voids among the aggregate are still relatively large. In open grading, usually the smaller size of aggregate dominates the bulk and can be easily disturbed by a small cavity. Open-grade material is not suitable to be used for subgrade construction of a road.

2.1.4.2 Fineness modulus

To characterize the overall *coarseness* or *fineness* of an aggregate, the concept of a fineness modulus is developed. The fineness modulus is defined as

$$\text{fineness modulus} = \frac{\sum(\text{cummulative retained percentage})}{100} \tag{2-14}$$

Table 2-1 Commonly used sieve designation and the corresponding opening size

Sieve Designation	Nominal Size of Sieve Opening
3 in.	75 mm
1.5 in.	37.5 mm
3/4 in.	19 mm
3/8 in.	9.5 mm
No. 4	4.75 mm
No. 8	2.36 mm
No. 16	1.18 mm
No. 30	600 μm
No. 50	300 μm
No. 100	150 μm
No. 200	75 μm

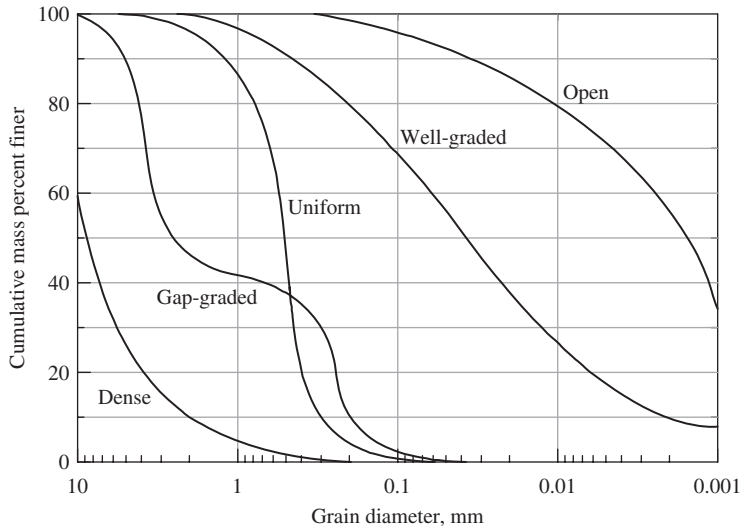

Figure 2-5 Five types of aggregate gradation

It can be seen from the formula that calculation of the fineness modulus requires that the sum of the cumulative percentages retained on a definitely specified set of sieves be determined, and the result divided by 100. The sieves specified to be used in determining the fineness modulus are No. 100, No. 50, No. 30, No. 16, No. 8, No. 4, 3/8", 3/4", 1.5", 3", and 6". It can be seen that the size of the opening in the above sieves has a common factor of 0.5 in any two adjacent ones. They are called full-size sieves. Any sieve size between full-size sieves is called half-size.

The fineness modulus for fine aggregate should lie between 2.3 and 3.1. A small number indicates a fine grading, whereas a large number indicates a coarse material. The fineness modulus can be used to check the constancy of grading when relatively small changes are expected, but it should not be used to compare the gradings of aggregates from two different sources. The fineness modulus of fine aggregates is required for the mix proportion since sand gradation has the largest effect on workability. A fine sand (low fineness modulus) has much higher paste requirements for good workability.

2.1.4.3 Fineness modulus for blending of aggregates

Blending of aggregates is undertaken for a variety of purposes, such as to remedy deficiencies in grading. A desired value of the fineness modulus can be calculated if the characteristics of the component aggregate are known. If two aggregates, designated A and B, are mixed together, having a fineness modulus of FM_A and FM_B, respectively, the resultant blend will have the following fineness modulus:

$$FM_{blend} = FM_A \times \frac{P_A}{100} + FM_B \times \frac{P_B}{100} \tag{2-15}$$

where P_A and P_B are the percentages, by weight, of aggregates A and B in the blend.

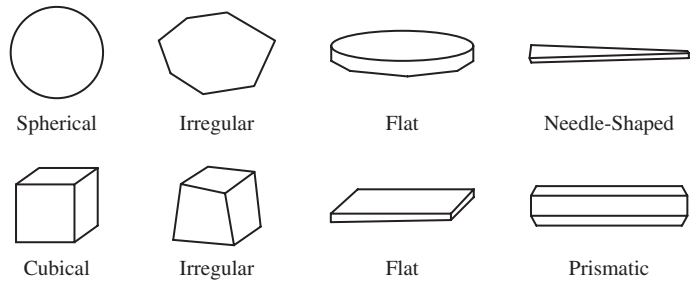

Figure 2-6 Different basic shapes of aggregates

Table 2-2 Effects of aggregate shape and surface texture on concrete strength

	Relative Effect (%) of	
Affected Strength	**Shape**	**Surface Texture**
Compressive	22	44
Flexural	31	26

2.1.5 Shape and texture of aggregates

2.1.5.1 Shape of aggregates

The aggregate shape affects the workability of concrete due to the differences in surface area caused by different shapes. Sufficient paste is required to coat the aggregate to provide lubrication. The typical shapes of aggregates are shown in Figure 2-6. Among these, spherical, cubical, and irregular shapes are good for application in concrete because they can benefit the strength. Flat, needle-shaped, and prismatic aggregates are weak in load-carrying ability and easily broken. Besides, the surface-to-volume ratio of a spherical aggregate is the smallest.

2.1.5.2 Texture of aggregates

The surface texture of aggregates can be classified in 6 groups: glassy, smooth, granular, rough, crystalline, and honeycombed. The surface texture of aggregates has significant influence on the fluidity of fresh concrete and the bond between aggregate and cement paste of hardened concrete. According to experimental statistics, the relative effects of the shape and surface texture of aggregates on concrete strength are summarized in Table 2-2 (Waddall and Dobrowolski, 1993).

2.2 CEMENTITIOUS BINDERS

2.2.1 Classification of binders

Based on the composition, the binder can be classified into organic and inorganic. An organic binder can be easily burned and thus cannot stand with fire. Polymer and asphalt are two

commonly used organic binders. Polymers consist of random chains of hydrocarbons and can be classified into thermoplastics, thermosets, and elastomers (or rubbers). Carbon atoms form the skeleton of the polymer chain. Along each chain, there are typically 1000 to 100,000 carbon atoms, held together by covalent bonds. The polymer chain is therefore very stiff and strong. The overall properties of a polymer, however, are governed by the interaction of individual polymer chains with one another. In thermoplastics, the chains interact with one another through weak van der Waal forces (Figure 2-7). In other words, while there is strong bonding along the polymer chain, making it very difficult to deform, there is very weak bonding between the chains, allowing easy relative movement of one chain from the other. The stiffness values of thermoplastics are therefore very low, and range from 0.15 to 3.5 GPa at room temperature (see examples in Table 2-3). In thermosets, the individual chains interact through van der Waal force as well as occasional cross-links. The cross-links are also hydrocarbon chains whose ends are bonded to the main polymer chains. Due to their presence, the stiffness of thermosets is higher than that of thermoplastics. At room temperature, it ranges from 1.3 to 8 GPa. Elastomers or rubbers are thermosets with a small number of cross-links. Also, they have very low glass transition temperatures, which means that the van der Waals force has disappeared at room temperature. Therefore, rubbers have very low stiffness values within the range of 0.002 to 0.1 GPa.

In concrete technology, the most widely used polymers are epoxy and latex. Epoxy is composed of resin and hardener and can be used to bind aggregate together or to repair cracks. Latex is mainly used to modify the concrete properties for repair.

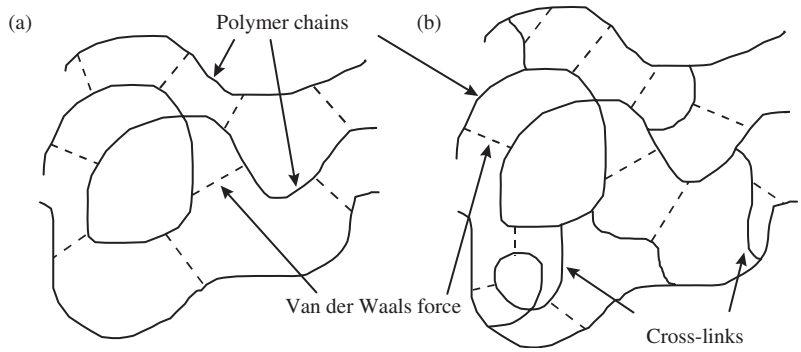

Figure 2-7 Difference between (a) thermoplastics and (b) thermosets

Table 2-3 Typical values of Young's modulus (E at room temperature), tensile strength, and glass transition temperature (T_g) for various polymers

Category	Material	E (GPa)	σ_T (MPa)	T_g (K)
Thermoplastic	Polyethylene (PE), low density	0.15–0.24	n/a	270
	Polyethylene, high density	0.55–1.0	20–37	300
	Polypropylene (PP)	1.2–1.7	50–70	253
	Polyvinyl chloride (PVC)	2.4–3.0	40–60	350
Thermosets	Polyesters	1.3–4.5	45–85	340
	Epoxies	2.1–5.5	40–85	380
Elastomers	Polyisoprene	0.002–0.1	~10	220
	Polybutadiene	0.004–0.1	n/a	171

Asphalt cement is mainly obtained from the distillation of crude oil. With very high molecular weight, asphalt is generally hard and relatively solid in its original form. Thus, it is easily distributed. To use it in practice, asphalt needs to be softened by heating. To reduce the need for heating, asphalt can be modified by the addition of volatile components or emulsifying agents. This will produce liquid asphalts (or cutbacks) and asphalt emulsions.

Depending on the added component, there are three different types of liquid asphalts: rapid-curing (RC) cutback, a mixture of asphalt and gasoline; medium-curing (MC), a mixture of asphalt and kerosene; and slow-curing (SC), a mixture of asphalt and diesel. Curing here refers to the hardening of the asphalt due to evaporation of the volatile component. When gasoline is used, evaporation occurs at the fastest rate and the curing is rapid. Also, in RC cutbacks, most of the volatile component vaporizes while in MC and SC, some stays with the asphalt. As a result, RC cutbacks produce a harder material, which is appropriate for hot weather. MC cutbacks give a softer material, which is less brittle under cold weather. SC cutbacks, which would produce too soft a material, are used only for dust binding. Asphalt can be used as binder to glue the aggregate together to form asphalt concrete for road construction. In asphalt concrete, the content of asphalt is only 4 to 6%.

Inorganic binders are usually made of different natural minerals. The inorganic binder can be further classified into nonhydaulic cement and hydaulic cement. However, nonhydraulic here does not mean that it does not need water. In fact, all inorganic binders need water for mixing and reacting to form bonds. Nonhydaulic cement also needs water for mixing. Nonhydraulic means only that such cement cannot harden and thus gain strength in water. Typical examples of nonhydraulic cement are gypsum and lime. They have been used since 6000 BC, as mentioned in Chapter 1. Gypsum is a soft mineral composed of calcium sulfate dihydrate, called two-water gypsum. Under a temperature of 130°C, two-water gypsum can change to half-water gypsum and release some water:

$$2CaSO_4 \cdot 2H_2O \xrightarrow{(130^\circ C)} 2CaSO_4 \cdot \tfrac{1}{2}H_2O + 3H_2O \tag{2-16}$$

When half-water gypsum is mixed with water, it can return to two water gypsum and form bonds. Lime is the product of calcination of limestone under 1000°C, and consists of the oxides of calcium:

$$CaCO_3 \xrightarrow{(1000^\circ C)} CaO + CO_2 \tag{2-17}$$

When CaO is mixed with water again, the following reactions occur:

$$CaO + CO_2 + H_2O \rightarrow Ca(OH)_2 + CO_2 \rightarrow CaCO_3 + H_2O \tag{2-18}$$

It can be seen that lime returns to limestone and forms bonds. Differing from nonhydraulic cement, hydraulic cement can harden and gain strength in water. The main difference in composition between two types of inorganic cements is that the hydraulic cement contains some amounts of clayey impurities (silicate composition). Examples of hydraulic cement include hydraulic lime, pozzolan cement, and Portland cement. Hydraulic lime is composed of lime and clayey impurities. The pozzolan cement contains lime and volcanic rock powders. The name pozzolan originated from the Romans, who used some volcanic tuff from Pozzuoli village, near Mt. Vesuvius. Since the history of the development of hydraulic cement has been discussed in Chapter 1, only the important events are briefly mentioned here.

In 1756, John Smeaton (the first person to style himself a civil engineer) was commissioned to rebuild the Eddystone Lighthouse off the coast of Cornwall, England). Recognizing that the normal lime mortars would not stand the action of water, Smeaton carried out an extensive series of experiments with different limes and pozzolans. He found that the high proportion of clayey

materials could increase the water-resistance properties. He was the first person to control the formation of hydraulic lime. He used a mortar prepared from a hydraulic lime mixed with pozzolan from Italy to build the Lighthouse, which was to last 126 years.

Portland cement (PC) concrete is the most popular and widely used building material, due to the availability of the basic raw materials all over the world, and its ease of use in preparing and fabricating all sorts of shapes. The applications of concrete in the realms of infrastructure, habitation, and transportation have greatly promoted the development of civilization, economic progress, stability, and quality of life. Nowadays, with the occurrence of high-performance concrete (HPC), the durability and strength of concrete have been improved greatly. However, due to the restriction of the manufacturing process and the raw materials, some inherent disadvantages of Portland cement are still difficult to overcome. There are two major drawbacks with respect to sustainability: (1) About 1.5 tons of raw materials is needed in the production of every ton of PC, while, at the same time, about 1 ton of carbon dioxide (CO_2) is released into the environment during the production. The world's cement production has increased from 1.4 billion tons in 1995 to almost 3 billion tons by the year 2009. Therefore, the production of PC is an extremely resource- and energy-intensive process. (2) Concrete made of PC deteriorates when exposed to harsh environments, under either normal or severe conditions. Cracking and corrosion have significant influence on service behavior, design life, and safety.

To overcome these problems, other different cementitious materials have been developed recently. Two of them to be discussed in this chapter are geopolymer and magnesium phosphate cement (MPC). Compared with Portland cement, the properties of these two cements have some advantages to the sustainable development of modern society.

2.2.2 Portland cement

Development of Portland cement can be summarized as follows:

1796	James Parker	England	Patent on a natural hydraulic cement
1813	Vicat	France	Artificial hydraulic lime
1824	Joseph Aspdin	England	Portland cement

Portland cement was developed by Joseph Aspdin in 1824, so named because its color and quality are similar to a kind of limestone, Portland stone (Portland, England).

2.2.2.1 Manufacture of Portland cement

Portland cement is made by blending an appropriate mixture of limestone and clay or shale together, and by heating them to 1450°C in a rotary kiln. Currently, the capability of a rotary kiln can reach 10,000 metric tons daily. Figure 2-8 shows a model production line of the China Hailuo Cement Company.

The sequence of operations is shown in Figure 2-9, in which the preliminary steps are a variety of blending and crushing operations. The raw feed must have a uniform composition and be of fine enough size that reactions among the components can be completed in the kiln. Subsequently, the burned clinker is ground with gypsum to form the familiar gray powder known as Portland cement. The basic raw materials used for manufacturing Portland cement are limestone, clay, and iron ore. The primary reactions during the calcination process are listed as below.

(a) Clay is mainly providing silicates (SiO_2) together with small amount of Al_2O_3 and Fe_2O_3. The decomposition of clay happens at a temperature around 600°C:

$$\text{Clay} \xrightarrow{(600^\circ\text{C})} SiO_2 + Al_2O_3 + Fe_2O_3 + H_2O \tag{2-19}$$

Figure 2-8 A production line of 10,000 metric tons per day (Hai Luo Cement Company, China)

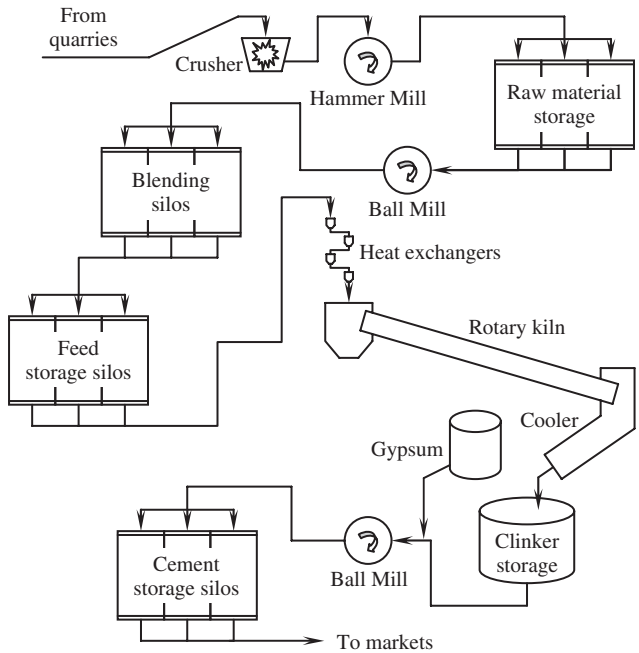

Figure 2-9 Manufacturing process of Portland cement

(b) Limestone ($CaCO_3$) is mainly providing calcium (CaO) and is decomposed at 1000°C:

$$CaCO_3 \xrightarrow{(1000^\circ C)} CaO + CO_2 \tag{2-20}$$

(c) Iron ore and bauxite provide additional aluminum and iron oxide (Fe_2O_3), which help the formation of calcium silicates at low temperature. They are incorporated into row mix.

(d) There are different temperature zones in a rotary kiln. At various temperatures between 1000 and 1450°C, different chemical compounds are formed. The initial formation of C_2S occurs at a temperature of around 1200°C. C_3S is formed around 1400°C.

$$\left.\begin{array}{l}\text{Limestone}\\ \text{Clay}\\ \text{Iron ore, bauxite}\end{array}\right\} \xrightarrow[\text{High temperature}]{(1450^\circ C)} \left\{\begin{array}{l}3CaO \cdot SiO_2\\ 2CaO \cdot SiO_2\\ 3CaO \cdot Al_2O_3\\ 4CaO \cdot Al_2O_3 \cdot Fe_2O_3\end{array}\right. \tag{2-21}$$

(e) The final product from the rotary kiln is called clinker. Pulverizing the clinker into small sizes (<75 μm) with addition of 3–5% gypsum or calcium sulf produces the Portland cement. Gypsum added is to control fast setting caused by $3CaO \cdot Al_2O_3$.

The majority of cement particle sizes are from 2 to 50 μm. Plots of typical particle size distribution data analysis are given in Figure 2-10.

2.2.2.2 Chemical composition

(a) *Abbreviations*: In cement chemistry, the following abbreviations are adopted. Please note that they are not consistent with other types of chemistry, although these notations are also frequently used in ceramic chemistry.

$$\begin{array}{llll} CaO = C & SiO_2 = S & Al_2O_3 = A & Fe_2O_3 = F \\ H_2O = H & SO_3 = \overline{S} & MgO = M & \end{array}$$

Thus, we can write $Ca(OH)_2 = CH$, $3CaO = C_3$, and $2CaO \cdot SiO_2 = C_2S$.

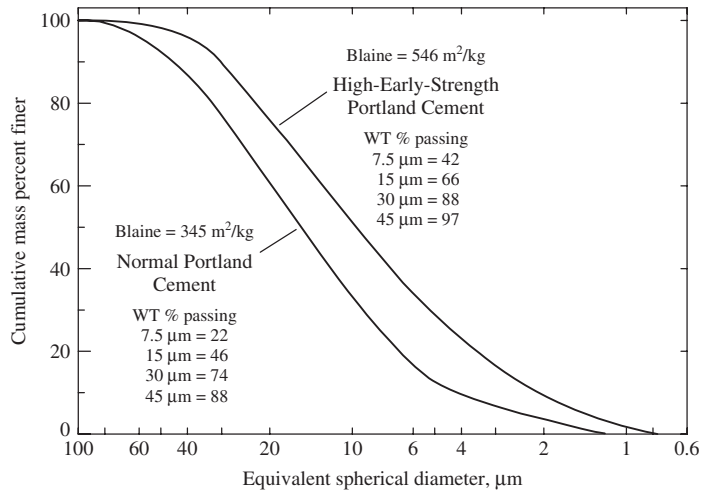

Figure 2-10 Typical particle size distributions of Portland cement

Table 2-4 Major compounds of ordinary Portland cement

Compound	Oxide Composition	Color	Common Name	Weight Percentage
Tricalcium silicate	C_3S	White	Alite	50
Dicalcium silicate	C_2S	White	Belite	25
Tricalcium aluminate	C_3A	white/grey	n/a	12
Tetracalcium aluminoferrite	C_4AF	Black	Ferrite	8

(b) *Major compounds*: The major compounds of ordinary Portland cement are listed in Table 2-4. They are C_3S, C_2S, C_3A, and C_4AF. C_3S is called tricalcium silicate; C_2S, dicalcium silicate; C_3A, tricalcium aluminate; and C_4AF, tetracalcium aluminoferrite. In addition, C_3S the nickname alite; C_2S, belite; and C_4AF, ferrite. It should be indicated that C_3S and C_2S occupy 68 to 75% of Portland cement. Since the primary constituents of Portland cement are calcium silicates, we can define Portland cement as a material that combines CaO and SiO_2 in such a proportion that the resulting calcium silicate will react with water at room temperature and normal pressure.

The typical oxide composition of a general-purpose Portland cement can be found in Table 2-5. From the weight percentage of these oxides, the weight percentage of C_3S, C_2S, C_3A, and C_4AF in Portland cement can be calculated using an equation initially developed by Bogue and adopted by ASTM C150 as follows:

$$C_3S(\%) = 4.071C - 7.600S - 6.718A - 1.450F - 2.852\overline{S}$$

$$C_2S(\%) = 2.867S - 0.754C_3S$$

$$C_3A(\%) = 2.650A - 1.692F$$

$$C_4AF(\%) = 3.043F$$

where C, S, A, F, and $\overline{S}$ are weight percentage of corresponding oxide in a Portland cement such as what listed in Table 2-5.

It should be noted that the above equations are valid only when $A/F \geq 0.64$. Fortunately, most Portland cements satisfy the condition.

Table 2-5 Typical oxide composition of a general-purpose Portland cement

Oxide	Shorthand Notation	Common Name	Weight Percent
CaO	C	lime	64.67
SiO_2	S	silica	21.03
Al_2O_3	A	alumina	6.16
Fe_2O_3	F	ferric oxide	2.58
MgO	M	magnesia	2.62
K_2O	K	alkalis	0.61
Na_2O	N	alkalis	0.34
SO_3	$\overline{S}$	sulfur trioxide	2.03
CO_2	$\overline{C}$	carbon dioxide	—
H_2O	H	water	—

(c) *Minor components of Portland cement*: The most important minor components of cement are gypsum, MgO, and alkali sulfates. Gypsum ($2CaSO_4 \cdot 2H_2O$) is added in the last procedure of grinding the clinker to produce Portland cement. The reason for adding gypsum cement is to avoid the flash setting caused by fast reaction of C_3A, because it can react with C_3A and form a hydration product called ettringite on the surface of C_3A to prevent further reaction of C_3A as a barrier. The normal percentage of gypsum added cement is about 4–5%. Only when gypsum is more than 3% in a Portland cement, can the formation of ettringite be guaranteed. When the percentage of gypsum is between 1 and 3%, both ettringite and monosulfoaluminate will be formed. When the percentage of gypsum is less than 1%, only monosulfoaluminate will be formed.

Alkalies (MgO, Na_2O, and K_2O) can increase the pH value of concrete up to 13.5, which is good for reinforcing steel protection. However, a high alkaline environment can also cause some durability problems, such as alkali aggregate reaction and leaching.

2.2.2.3 Hydration

Hydration of cement is the reaction between cement particles and water, including chemical and physical processes. The properties of fresh concrete, such as setting and hardening, are the direct results of hydration. The properties of hardened concrete are also influenced by the process of hydration. Hence, to understand the properties and behavior of cement and concrete, some knowledge of the chemistry of hydration is necessary.

(a) *Hydrations of pure cement compounds*: The mechanism of hydration of the cement as whole is very complex and has not been fully understood yet. So far, the only approach to studying the hydration of Portland cement is to investigate the reaction mechanism of individual compounds separately. This assumes that the hydration of each compound takes place independently and no interaction occurs. Although this assumption is not valid completely, it helps to understand the chemistry of hydration.

(b) *Calcium silicates*: The hydrations of two calcium silicates are stoichiometrically similar, differing only in the amount of calcium hydroxide formed, the heat released, and the reaction rate:

$$2C_3S + 11H \rightarrow C_3S_2H_8 + 3CH \tag{2-22}$$

$$2C_2S + 9H \rightarrow C_3S_2H_8 + CH \tag{2-23}$$

The principal hydration product is $C_3S_2H_8$, calcium silicate hydrate, or C–S–H (nonstoichiometric). C–S–H occupies about 50% of the structural component in a cement paste and forms directly on the surface of cement particles. In addition, the size of C–S–H is quite small. It is believed that C–S–H is the major strength provider for Portland cement concrete due to its amount and small size. The structure of C–S–H is in the nanometer scale and is not a well-defined compound. The formula $C_3S_2H_8$ is only an approximate description. In an x-ray diffraction (XRD) investigation, C–S–H does not show sharp peaks and has been considered as an amorphous structure. C–S–H is usually called a glue gel binder. Recently, much research has been conducted toward understanding the structure of C–S–H and thus the nature of binding of concrete. The progress is introduced in detail in Chapter 4.

Another product is CH, calcium hydroxide. This product is a good crystalline with a plate shape in most cases. CH is formed in solution by crystallization and occupies about 25% of the structural component of cement paste. CH can bring the pH value to over 12 and it is good for corrosion protection of steel. From a durability of concrete point of view, CH may lead to

leaching due to its solubility, carbonation due its reaction with carbon dioxide, alkali aggregate reaction due to its high pH value, or sulfate attack due to its reaction with sulfate. Hence, in contemporary concrete technology, there has been a trend to reduce amount of CH in concrete as much as possible. However, a minimum amount of CH is needed to keep the high alkali environment in concrete.

One more thing that needs to be mentioned is that both C–S–H and CH are very "gentle" and pass around something blocking their way or stopping their formation, as there is no free space for them to occupy. It should be pointed out that although C_3S and C_2S produce the same hydration products, their reaction rates are very different; C_3S reacts very fast at the early stage, releases more hydration heat, and contributes most to early age strength of concrete. On the other hand, C_2S reacts very slowly, releases less heat, and contributes minimally to early age strength of concrete. C_2S contributes the most to the long-term strength of concrete.

(c) *Tricalcium aluminate and ferrite phase*: The primary initial reaction of C_3A with water in the presence of a plentiful supply of gypsum is

$$C_3A + 3\left(C\overline{S}H_2\right) + 26H \rightarrow C_6A_3H_{32} \tag{2-24}$$

The 6-calcium aluminate trisulfate-32-hydrate, is usually called calcium sulfoaluminate hydrate and more commonly *ettringite*, which is the name of a naturally occurring mineral of the same composition. The nickname of ettingite is AFt. The formation of ettringite is right on the surface of the particles of C_3A. It can slow down the hydration of C_3A because it acts as a diffusion barrier around C_3A, analogous to the behavior of C–S–H during the hydration of the calcium silicates. Thus, it can avoid a C_3A flash setting. Ettringite is a needle-shaped crystal with a large volume expansion. Moreover, ettringite is very aggressive and will make space to grow if there is no free space left. The effect of ettringite on concrete strength can be evaluated in two cases. In case 1, ettringite is formed before the paste has hardened and gained strength due to hydration of C_3S. It will contribute to the early strength development of concrete since the needle-shaped crystals can work as reinforcement for the surrounding C–S–H, and the expansion is not so significant. In case 2, if ettringite is formed after the concrete has hardened and free space has been occupied by other hydration products, it will make its space to grow by breaking the hardened hydration products and hence create cracks and volume instability.

The ettringite is stable only when there is an ample supply of sulfate available and at a temperature lower than 60°C. If all the sulfate is consumed before the C_3A has completely hydrated or the temperature rises to above 60°C, it can be broken down during the hydration of the conversion to monosulfoaluminate:

$$2C_3A + C_6A_3H_{32} + 4H \rightarrow 3C_4A\overline{S}H_{12} \tag{2-25}$$

Monosulfoaluminate is also called tetracalcium aluminate monosulfate-12-hydrate. Its nickname is AFm. When monosulfoaluminate is brought into contact with a new source of sulfate ions, ettringite can be formed again:

$$C_4A\overline{S}H_{12} + 2C\overline{S}H_2 + 16H \rightarrow C_6A\overline{S}_3H_{32} \tag{2-26}$$

If there is no gypsum, C_3A will react with water very quickly:

$$2C_3A + 21H \rightarrow C_4AH_{13} + C_2AH_8 \tag{2-27}$$

The hydrates can be further converted to

$$C_4AH_{13} + C_2AH_8 \rightarrow 2C_3AH_6 + 9H \tag{2-28}$$

The reaction occurs so fast that it causes flash set of concrete. The hydration products of C_4AF are similar to those of C_3A. However, the reaction rate of C_4AF is slower than that of C_3A. When reacting with gypsum, the following equation applies:

$$C_4AF + 3\left(C\overline{S}H_2\right) + 21H \rightarrow C_6(A, F)\overline{S}_3H_{32} + (F, A)H_3 \quad (2\text{-}29)$$

In the equation, the expression $C_6(A, F)\overline{S}_3H_{32}$ indicates that iron oxide and alumina occur interchangeably in the compound. The order of symbols in the brackets implies the order of richness of the corresponding element in the compound. $C_6(A, F)\overline{S}_3H_{32}$ can further react with C_4AF and water:

$$C_4AF + C_6(A, F)\overline{S}_3H_{32} + 7H \rightarrow 3C_4(A, F)\overline{S}H_{12} + (F, A)H_3 \quad (2\text{-}30)$$

(d) *Kinetics and reactivities*: The rate of hydration during the first few days is in the order of $C_3A > C_3S > C_4AF > C_2S$. The rate of hydration can be observed in Figure 2-11. Figure 2-12 shows the strength development of different minerals. It can be seen that C_3S has a high early strength and C_2S develops its strength slowly in the early age but very fast later on. It can be deduced that C_3S contributes the most to early strength and C_2S to long-term strength of Portland cement. On the other hand, the contribution to the strength of Portland cement from C_3A and C_4AF is not significant. Moreover, the strength development and kinetics of different minerals is somehow but not very closely related.

(e) *Calorimetric curve of Portland cement*: In discussing the hydration of individual major compounds of Portland cement, it is assumed that there is no interaction among the reaction of each compound. In fact, this is not entirely true and there are some mutual influences in the reaction of different compounds. For instance, all the hydration products consume CaO and there may be some competition in catching Ca^{2+} from other compounds. In addition, both C_3A and C_4AF compete for sulfate ions and this will cause different reaction rates and change their reactivity. Moreover, C–S–H can incorporate some sulfate, alumina, and iron during the hydration of cement that leads to less calcium sulfoaluminates in the hydration of cement than for pure compounds. Hence, the hydration of Portland cement is far from being fully understood and more research is needed.

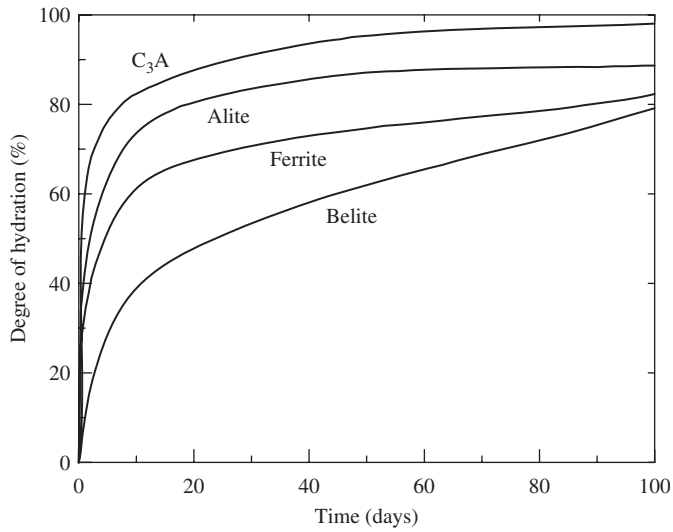

Figure 2-11 Hydration process of primary constituents of Portland cement

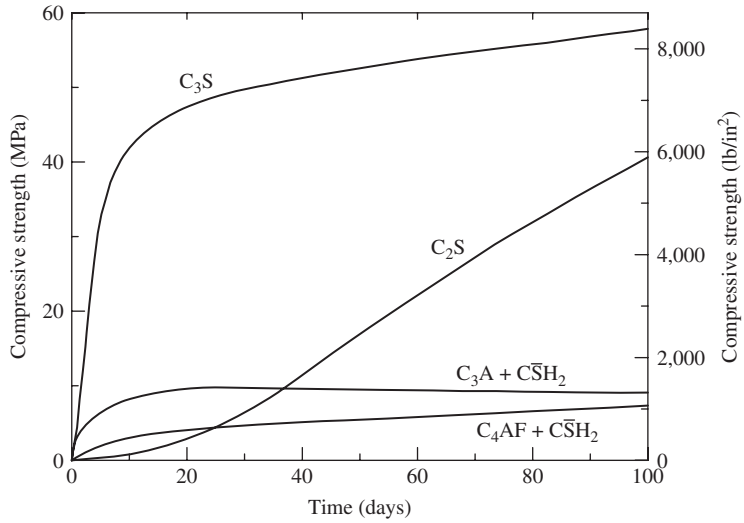

Figure 2-12 Strength development of primary constituents of Portland cement

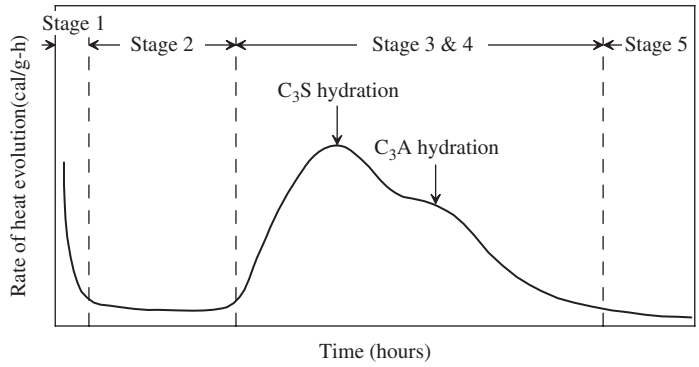

Figure 2-13 A typical calorimetric curve of Portland cement

To study the dynamics of hydration of Portland cement, heat release rate measurement is frequently adopted because the process is exothermal. A typical calorimetric curve of Portland cement is shown in Figure 2-13. Several characteristic points can be observed in the figure. The curve decreases initially and then keeps flat for a while after reaching the lowest value of heat evolution rate. Then it goes up in a very steep manner. After the first crest is reached, the curve goes down and rises up again to form the second peak. After that the curve decreases gradually. The two peaks in the curve represent the dominant effect of C_3S or C_3A correspondingly and their order of occurrence can be reversed.

Based on the characteristic points on the curve, the hydration process of Portland cement can be easily distinguished in five stages; dissolution, dormant, acceleration, deceleration, and steady state. It should be pointed out that the curve of heat evolution of Portland cement is very similar to that of C_3S as that C_3S has a dominant effect in cement. Thus, the five stages traditionally defined in cement chemistry can be explained by using the reaction process of C_3S, as detailed in Table 2-6.

Table 2-6 Kinetics of reaction, chemical processes, and relevance to concrete of the different reaction stages of cement

Reaction Stage	Kinetics of Reaction	Chemical Processes	Relevance to Concrete
1. Initial hydrolysis	Chemical control; rapid	Initial hydrolysis; dissolution of ions	n/a
2. Induction period	Nucleation control; slow	Continued dissolution of ions	Determines initial set
3. Acceleration	Chemical control; rapid	Initial formation of hydration products	Determines final set and rate of initial hardening
4. Deceleration	Chemical and diffusion control; slow	Continued formation of hydration products	Determines rate of early strength gain
5. Steady state	Diffusion control; slow	Slow formation of hydration products	Determines rate of later strength gain

On first contact with water, calcium ions and hydroxide ions are rapidly released from the surface of each C_3S grain; the pH values rises to over 12 within a few minutes. This hydrolysis slows down quickly but continues throughout the induction period. The induction (dormant) period is caused by the need to achieve a certain concentration of ions in solution, before crystal nuclei form, from which the hydration products grow. At the end of the dormant period, CH starts to crystallize from the solution with the concomitant formation of C–S–H, and the reaction of C_3S again proceeds rapidly (the third stage, acceleration, begins). CH crystallizes from the solution, while C–S–H develops on the surface of C_3S and forms a coating covering the grain. When the first peak of the rate of heat evolution is reached, the deceleration stage is started. As hydration continues, the thickness of the hydrate layer increases and forms a barrier through which water must flow to reach the unhydrated C_3S and through which ions must diffuse to reach the growing crystals. Eventually, movement through the C–S–H layer determines the rate of reaction, and hydration becomes diffusion controlled and moves into the 5th stage, the steady-state stage.

(f) *Setting and hydration*: Traditionally, it is believed that the initial set of cement corresponds closely to the end of the induction period, 2–4 h after mixing. The initial set indicates the beginning of gel formation. It is controlled primarily by the rate of hydration of C_3S. The final set occurs 5–10 h after mixing, which indicates that sufficient hydration products are formed and the cement paste is ready to carry some external load.

It should be noted that the initial and the final set have a physical importance. However, there is no fundamental change in the hydration process for these two different sets. The hydration process of fresh cement paste is schematically illustrated in Figure 2-14.

The rate of early hardening, which means a gain in strength, is primarily determined by the hydration of C_3S, and the strength gain is roughly proportional to the area under the heat peak in the calorimetric curves of Portland cement. The strength development is mainly derived from the hydration of silicates.

2.2.2.4 New understanding of the dynamics of cement hydration

Cement hydration is a complex physical–chemical process. During the process, a cement–water mixture is changed from a fluid state to a porous solid state. An adequate understanding of the mechanism of cement hydration is necessary for a full appreciation of cement concrete properties.

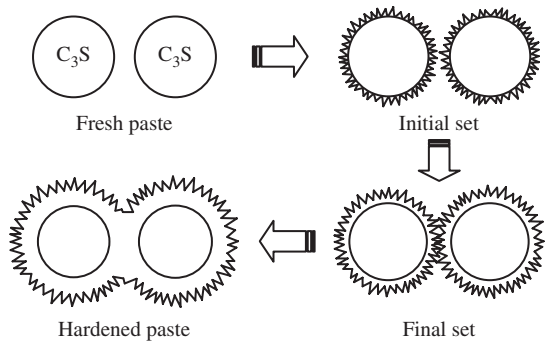

Figure 2-14 Setting of fresh cement paste

The cement hydration process was traditionally studied using the calorimetric method. The hydration stages were identified by heat liberation measurement and the hydration mechanism was explained based on heat evolution. Some limitations (Gartner et al., 2002) were pointed out, such as that the liberated heat content was simply proportional neither to the degree of cement hydration nor to the development of the physical properties. This method provides only an approximation of the understanding of cement hydration and leaves space for cement scientists and engineers to explore more accurate ways.

Chemically, cement hydration involves ion dissolution and the formation of new chemical compounds. Physically, cement hydration involves microstructure formation and a porosity decrease process. When water is added into cement, the soluble ions in the cement dissolve into water. The ions in the pore solution are conductive and can form an electrical current under a certain electrical field. The conductivity of a cement mix depends mainly on the concentration of the ion solution and microstructure, especially the porosity and pore connectivity of the cement paste. Therefore, the electrical conductivity or resistivity of a cement mixture can be used to interpret the cement hydration process.

Taylor et al. (1974), Christensen et al. (1994), Tashiro et al. (1994), McCarter et al. (1981, 2003) and Gu et al. (1985) observed the electrical responses of the cementitious hydration systems using alternating current impedance spectroscopy. However, since the experiments were carried out with electrodes, the accuracy and consistency of the test results were largely affected by contact problems, such as the interface gap between the electrodes and the shrunken cement paste mixes.

Recently, the dynamics of the cement hydration process have been studied with an advanced monitoring technique, noncontact electrical resistivity measurement (Li and Li, 2003, Li et al., 2003, and Wei and Li, 2005), as shown in Figure 2-15. It was realized long ago that resistivity of cement paste is a fingerprint of its hydration. However, the inaccurate nature of resistivity measurement due to the contact of electrodes in fresh concrete made it difficult to reach any useful conclusion. The newly developed technique adopts a transformer principle and eliminates electrodes in the resistivity measurement; thus, it completely eliminates the contact problems and provides more reliable results. For the purpose of obtaining a clear understanding of the relationship between electrical resistivity development and the hydration process, microstructure analysis has been conducted and the results are correlated to each stage of the hydration process.

A typical electrical resistivity development curve with time ($\rho(t) - t$) and its differential curve ($d\rho(t)/dt - t$), which represents the rate of resistivity development, are shown in Figure 2-16. The minimum point M and the level point L, which is at the end of a relatively flat region after point M, are marked on the curve of $\rho(t) - t$. Peak points $P1$ and $P2$ are marked on

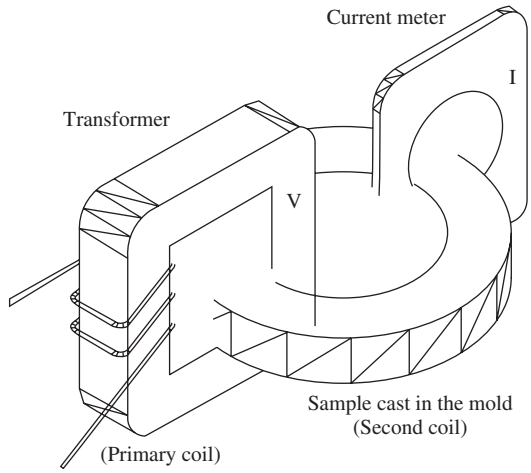

Figure 2-15 Electrical resistivity measurement setup

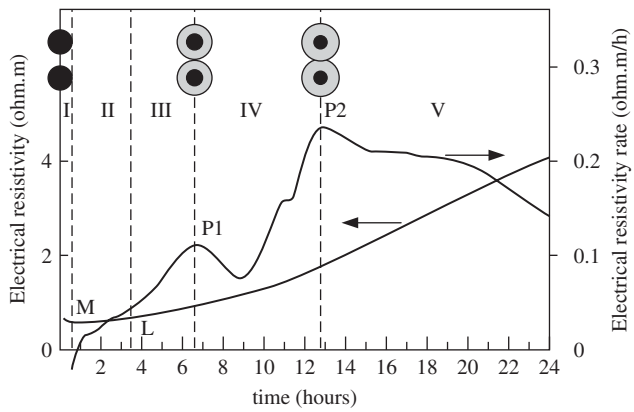

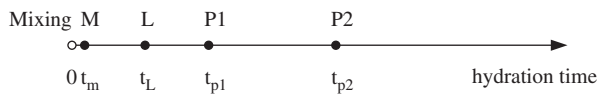

Electrical resistivity response				Setting time (ASTM C191)	
t_m	t_L	t_{p1}	t_{p2}	initial t_{ini}	final t_{fin}
0.73h	3.5h	6.7h	12.8h	3.75h	6.28h

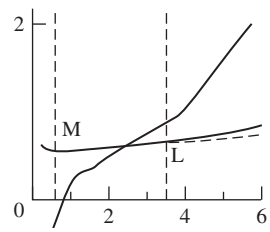

Figure 2-16 Electrical resistivity development and the rate in resistivity of the cement paste during the first 24 h

the curve of $d\rho(t)/dt - t$. The times at which the characteristic points occurred and the paste setting time are listed in the table in Figure 2-16. According to the characteristic points, the hydration process is divided into five stages: dissolution, dynamic balance, setting, hardening, and hardening rate deceleration stage.

To investigate the cement hydration process and understand what happens at each characteristic point on the resistivity and its differential curves, microstructural investigations have been conducted on the samples corresponding to the characteristic point occurrences using scanning electron microscopy (SEM), XRD, differential thermal analysis (DTA), and Fourier transform infrared spectroscopy (FTIR). The results are shown in Figures 2-17, 2-18, and 2-19, respectively.

The XRD patterns in Figure 2-17 show the presence of crystalline substances in anhydrous cement and in the hydrated samples at various ages. At a very early hydration age, the ettringite (AFt) phase starts to form with consumption of sulf, which is detected in the sample at 0.73 h. The intensity of the ettringite peaks decreases and monosulf (AFm) appears, as shown in the hydrated sample for 12.8 h in comparison with that in the 6.7 h sample. The amorphous hydrates of C–S–H cannot be detected by the XRD technique. The relative density of the peaks of the crystal calcium hydroxide (CH) become significant with time due to the increase of CH content in the hydrated samples.

The DTA has been performed for characterization of the hydration products and the quantification of calcium hydroxide in the samples, as shown in Figure 2-18. The existence of four endothermic peaks is shown in the detected temperature range. Peak 1 and peak 2, located at 85 and 128°C, mainly characterize gypsum. The shift of the first peak from 85°C to around 92°C and the reduced intensity of the second peak with hydration indicate that gypsum is consumed and the AFt formation is at the expense of the gypsum peaks. The third peak, observed at about 165°C, represents the decomposition of AFm in the samples hydrated for 12.8 h and 24 h. The fourth peak, at 465–470°C, is due to the CH. The shifts of the CH peaks to the right with age increase show that CH crystallines become denser and larger, and increasing temperature is needed for the decomposition of the CH crystalline. The index of the formed CH content, estimated by determining the endothermic area of the CH peaks, as an indication of the hydration product contents, is marked in Figure 2-18.

The FTIR spectra of the samples at various ages, as shown in Figure 2-19, provide information on chemical bonding. Calcium hydroxide gives a peak at 3643 cm^{-1}; ettrengite has a strong peak at 3422 cm^{-1} and a weaker one at 3545 cm^{-1}, marked A in Figure 2-19; and monosulfate has bands at 3260, 3333, 3402, 3458, and 3527 cm^{-1}, which are separated from a broad band 3200–3600 cm^{-1}, and the broad band centered at 3402 cm^{-1}, marked in Figure 2-19.

Bands $\nu 3$ (SiO_4) and $\nu 4$ (SiO_4) in the anhydrous cement are located at 924 and 523 cm^{-1}. The hydration of the silicate phases causes a shift in band $\nu 3$ (SiO_4) from 924 to 978 cm^{-1} over 24 h. There is an obvious shift occurring in band $\nu 3$ (SiO_4) from 6.7 to 12.8 h, corresponding to new Si–O bonding formation during the period. The shift is likewise observed in band $\nu 4$ (SiO_4), from a wave number of 523 cm^{-1} in the anhydrous cement to a lower wave number 518 cm^{-1} in the hydrated sample at 0.73 h, characterizing C_3S initial hydration.

Microstructure investigations can help to understand the relationship between electrical resistivity development and the hydration process. The correlation of the microstructure analysis to the hydration stages is respectively described as follows.

(I) *Dissolution stage*: From the start of mixing to point M (0.73 h), the resistivity $\rho(t)$ of the mixture deceases. When cement is mixed with water, the mobile ions in the cement, such as potassium (K^+), sodium (Na^+), calcium (Ca^{2+}), hydroxyl ions (OH^-), and sulfate ($SO_4{}^{2-}$), dissolve into the water and form an electrolytical solution. The dissolving process of the ions causes the resistivity to decrease in the hydration system.

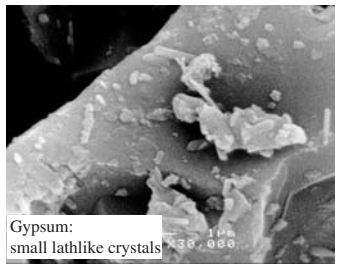

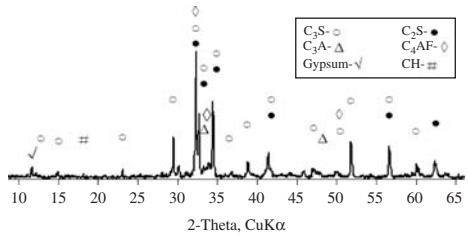

(a) t = 0, anhydrous cement

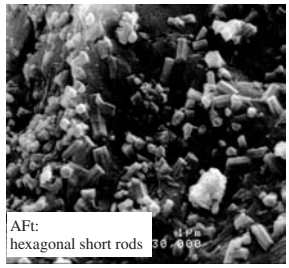

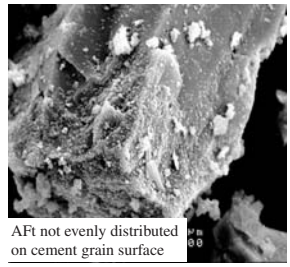

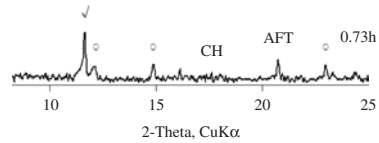

(b) t = 0.73h (at point M), C_3A rapid reaction

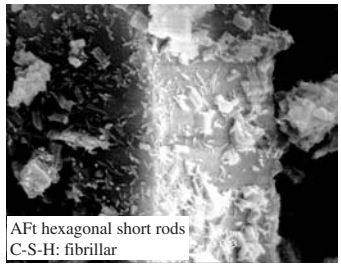

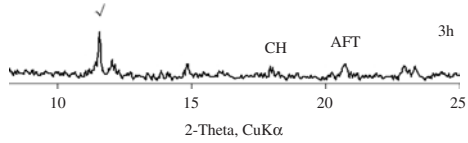

(c) t = 3h (close to point L)

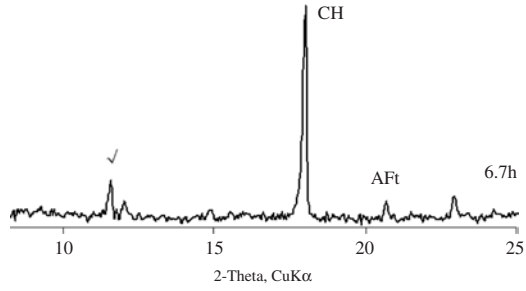

(d) t = 6.7h (at point P1), close to final setting

Figure 2-17 Cement and hydrated pastes at the ages of 0.73, 3, 6.7, 12.8, and 24 h from SEM and XRD

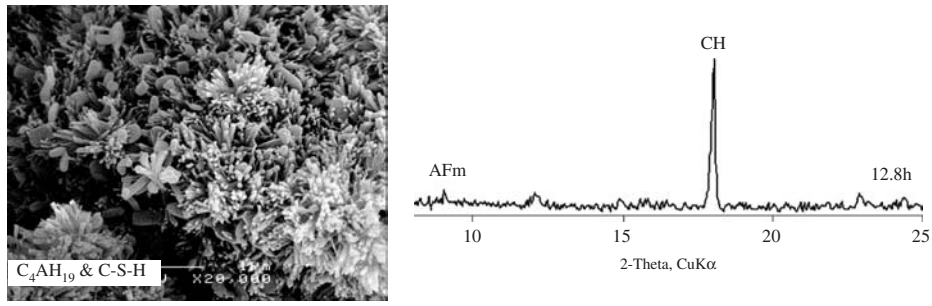

(e) t = 12.8h (at point P2), AFt transfers to AFm

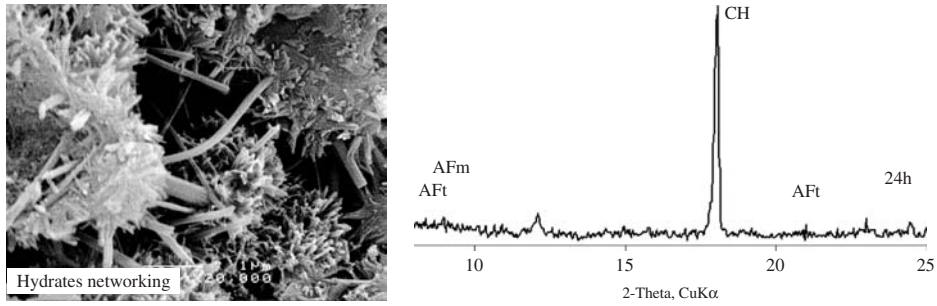

(f) t = 24h

Figure 2-17 (*continued*)

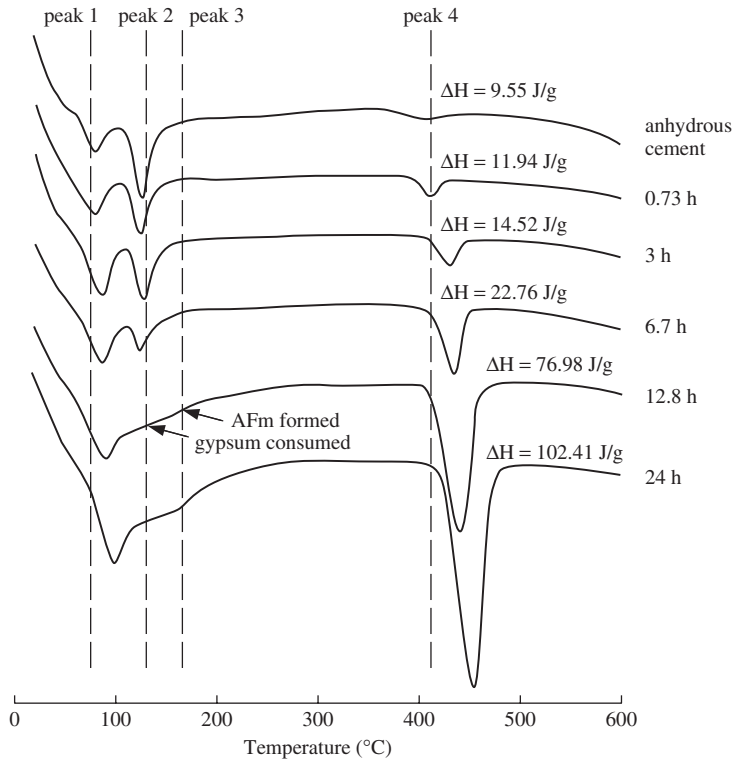

Figure 2-18 DTA results of cement and hydrated pastes at different ages

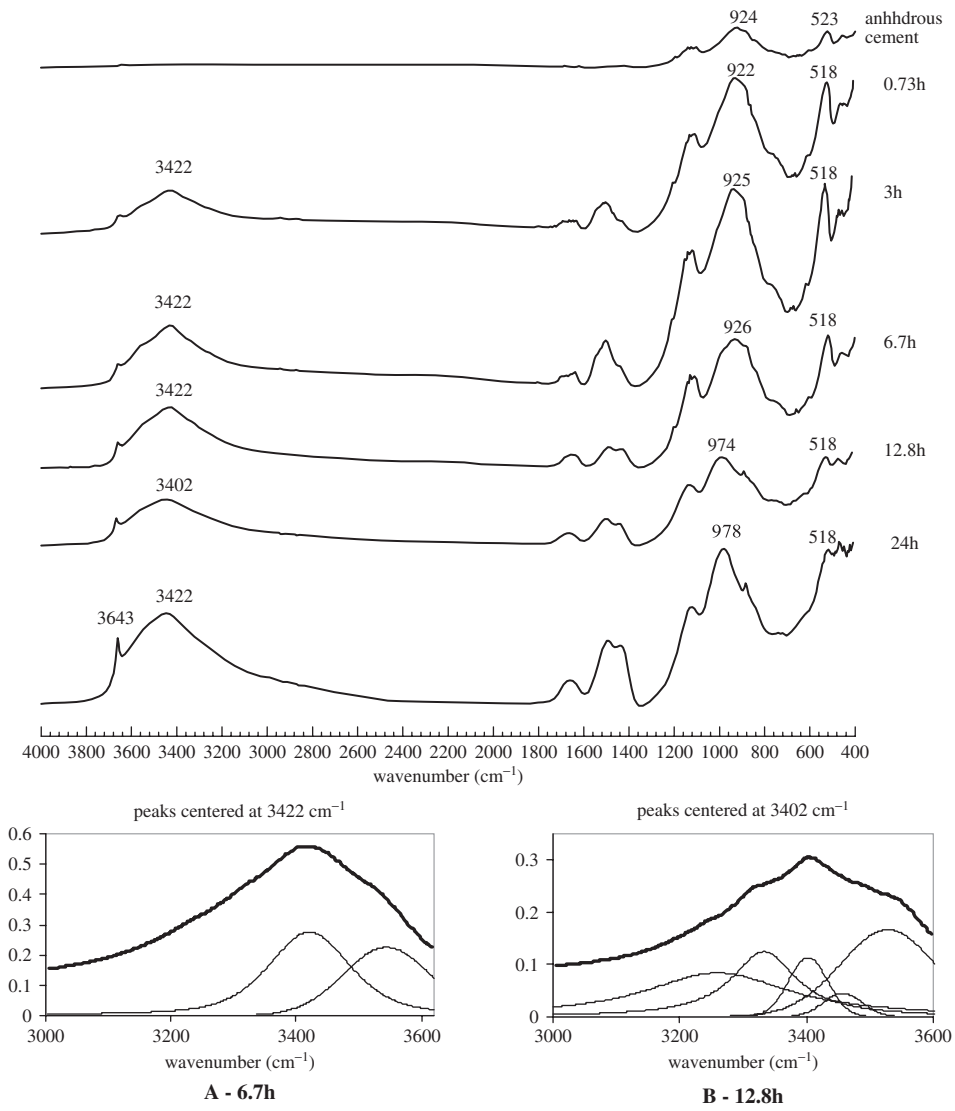

Figure 2-19 FTIR spectra of anhydrous cement and hydrated samples at different ages

An immediate increase in resistivity is observed right after point *M*, and it is inferred that some hydration products have been formed. This point has been verified by SEM, XRD, DTA, and FTIR results.

C_3A is the most active chemical compound in cement, and it reacts with sulfate ions in the solution dissolved from the gypsum. As shown in Figure 2-17a, only raw materials appear in the SEM photo at $t = 0$. The hydration product, ettringite crystal, as short rods, is formed directly on the surface of the cement grains, as can be observed in the SEM picture in Figure 2-17b, which corresponds to the time of the *M* point at $t = 0.73$ h. The picture with a magnification of 5000 shows that the AFt crystals are not evenly distributed on the cement surface; one possibility is that the AFt forms just on the surface C_3A.

At same time, a supersaturation point of Ca^{2+} is reached, and the CH precipitates from the solution, as detected by DTA technique in the hydrated sample for 0.73 h, which is shown in Figure 2-18. The DTA results show that the index of CH (peak 4) content in the hydrated sample for 0.73 h ($\Delta H = 11.94$ J/g) is larger than that of the CH formed from free lime by chemisorbed water in the anhydrous cement ($\Delta H = 9.55$ J/g) during storage, indicating that new CH is formed at that moment.

The shift of the band $\nu 4$ SiO_4 over 0.73 h indicates a C_3S hydration occurrence. It has been reported that a gelatinous layer on the surface of the cement was observed in an undried specimen soon after mixing by using an environmental cell, and identified as an amorphous colloidal product (Ménétrier et al., 1979; Jennings and Pratt, 1980).

Therefore, during this period, the resistivity decrease implies that the process is dominated by the ion dissolution and is identified as the dissolution stage until the M point. The formation of hydration products AFt, a gelatinous substance, and CH in the solution leads to the resistivity increase from point M and signals the end of the dissolution stage.

(II) *Dynamic balance stage*: From point M (0.73 h) to point L (3.5 h), the electrical resistivity slightly increases, by approximately 0.03 Ωm from point M to point L. Point L is the transition point from a linear to a curved shape. In this stage, the hydration products continue to form and break the balance condition, then ions continue to dissolve to recover to the saturation point. Thus, a competitive balance between the ion dissolution and CH, and other hydrates precipitation is dynamically kept. This stage is identified as a dynamic balance stage.

The C–S–H formation can be observed in the dried sample as small acicular shapes (diamond type I, fibrillar morphology) among AFt rods in the sample hydrated at $t = 3$ h, from the SEM picture shown in Figure 2-17c. The DTA results show that the CH content index ΔH increases from 11.94 to 14.52 J/g, and the FTIR shows that the $\nu 3$ bands (SiO_4) have a peak shift from 922 to 925, which confirms C–S–H formation during this period. During this stage, the hydration products are increasing to reach a point at which they start to contact each other at the end of the stage. The mix maintains its fluidity in this stage due to the hydration products not being joined together.

(III) *Setting stage*: From the end of the dynamic balance stage, the hydration products start to join together. Concrete starts to lose its plastic behavior and proceeds to the setting period. As can be seen from Figure 2-16, correspondingly, from point L (3.5 h) to point $P1$ (6.7 h), the resistivity increases at a fast rate, indicating a rapid change in the microstructure during this period. It can be seen in the sample hydrated for 6.7 h, as shown in Figure 2-17d, that a great amount of C–S–H is formed in the bundles, compared with 3 h, and the cement particles are surrounded by the C–S–H bundles. The solid phase in the hydration system is closely connected, resulting in a percolation of the solid phase. The initial setting time and the final setting time of the paste are 3.75 and 6.28 h, respectively, obtained by a Vicat needle penetration. The initial setting time is close to the end of the dynamic balance period, and the final setting time is close to the time point of $P1$. Thus, this period is identified as the setting stage. The XRD result at 6.7 h shows a significant increase of the CH peak intensity.

The setting of cement paste appears to be a consequence of C_3S hydration and the formation of sufficient C–S–H and CH hydrates. The C_3S hydration dominates the setting period and the C–S–H formations lead to a normal cement paste set.

(IV) *Hardening stage*: From point $P1$ (6.7 h) to point $P2$ (12.8 h), the resistivity continuously increases at a reduced rate and then the rate increases again. When the hydration proceeds to 12.8 h, gypsum is significantly consumed, the AFt peak disappears, and AFm appears in the XRD pattern in Figure 2-17e. This indicates the transformation of phase AFt to phase AFm

during the period of 6.7–12.8 h. When there is sufficient SO_4^{2-} in the pore solution, the ettringite forms and remains stable. After SO_4^{2-} is consumed, the ettringite is transformed into monosulfate (AFm). The DTA results at 6.7 and 12.8 h, as shown in Figure 2-18, confirm the phase transformation occurrence by the disappearance of the gypsum peak (peak 2) and the appearance of the AFm peak (peak 3) at 12.8 h. Additionally, the FTIR pattern, as shown in Figure 2-19, from 6.7 to 12.8 h, and the shift of the band SO_4^{2-} from wave number of 3422 to 3402 support the observation.

The transformation of AFt to AFm (El-Enein Abo et al., 1995) leads to an increasing trend in ion concentration due to the releasing of SO_4^{2-} and Ca^{2+}, and a decreasing trend in the solid volume fraction due to phase AFm possessing a higher density than phase AFt, while the reaction in Equation 2-26 (Hewlett, 1998) leads to the latter effect only. No matter which way it takes place, the consequence is that there is a decreasing trend in resistivity. However, the C_3S hydration continuously progresses and the formation of hydrates C–S–H largely increases the solid phase in the hydration system, which compensates the decreasing resistivity trend caused by the phase transformation. The phase transformation slows down the rate of resistivity development, but it does not change the increasing trend of the resistivity. This corresponds to the resistivity increase at a lowered rate ($d\rho(t)/dt$). When the balance between the phase transformation and the AFt formation process, by releasing and consuming ions Ca^{2+} and SO_4^{2-}, is achieved, the factors leading to the $d\rho(t)/dt$ decrease, become minor, or disappear, and eventually a larger increase in C–S–H and the other hydrate contents dominates the resistivity development, and the rate ($d\rho(t)/dt$) increases again.

When there is insufficient gypsum, there is also a trend of forming hexagonal plate C_4AH_{19}, as shown in Figure 2-17e (Hewlett, 1998), which belongs to the broad group of AFm. This process leads to a similar effect on electrical resistivity development as the formation of phase AFm. The SEM picture shows that C–S–H becomes denser at 12.8 h than at 6.7 h. The FTIR spectra of the samples at 6.7 and 12.8 h show new C–S–H hydrate formation, as described earlier. With the thickness of hydration products increasing, the solution in the pores must go through the thick layer of the products for further hydration and the rate of the chemical reaction then decreases, which corresponds to a decreased rate $d\rho(t)/dt - t$ from point $P2$.

(V) *Hardening rate deceleration stage*: After point $P2$ (from 12.8 h onward), the resistivity increases at a decreasing rate. The decreasing rate $d\rho(t)/dt$ describes slowdown in the chemical reaction rate, and the process is controlled by ion diffusion, with the increase of hydrate thickness on the cement particle surface (Mindess et al., 2003).

When hydration proceeds up to the age 24 h, shown in Figure 2-17f, the C–S–H bundles and long rods of AFt intersect each other to form solid networking for strength gain. Meanwhile, the free water space decreases, porosity decreases, and tortuosity increases for conduction paths. Hydration product contents increase with hydration time and can also be represented by the increase in CH hydrate content as the endothermic heat of CH in Figure 2-18.

The new hydration process stages are summarized in Table 2-7. From a macro point of view, fresh concrete changes from a fluid to a solid state. From the micro point of view, a series of physical and chemical reactions are occurring and the consequences lead to microstructure formation. Microstructure formation and concrete property time dependence are essentially correlated. Electrical resistivity can dynamically record the microstructure change process and is related to the concrete properties. Therefore, the electrical resistivity response $\rho(t)$ can provide an indication of setting behavior and strength development as a nondestructive test method.

Table 2-7 New understanding of the stages of hydration process

Hydration Stage	Kinetics of Hydration	Main Chemical Phenomena	Chemical Reaction
I. Dissolution (mixing to M)	Ion dissolution dominating	Initial rapid chemical reaction of C_3A	$C_3A + 3\left(C\overline{S}H_2\right) + 26H \rightarrow C_6A\overline{S}_3H_{32}$
II. Dynamic balance (M to L)	A competition process of dissolution and precipitation	CH nucleation	$Ca^{2+} + OH^- \rightarrow Ca(OH)_2$
III. Setting (L to $P1$)	The formation of hydration product C–S–H dominating	Chemical reaction control of C_3S	$C_3S + 11H \rightarrow C_3S_2H_8 + 3CH$
IV. Hardening ($P1$ to $P2$)	Continuous formation of hydration products	C_3S hydration; phase transfer from Aft to AFm	$C_3S + 11H \rightarrow C_3S_2H_8 + 3CH$ $2C_2S + 9H \rightarrow C_3S_2H_8 + CH$ $C_6A\overline{S}_3H_{32} \rightarrow C_4A\overline{S}H_{12} + 2CaSO_4$ $C_6A\overline{S}_3H_{32} + 2C_3A + 4H \rightarrow 3C_4A\overline{S}H_{12}$
V. Hardening deceleration ($P2$ onward)	Chemical reaction slows down; diffusion control	The second reaction of C_3A, C_3S and other components	$C_3A + 3\left(C\overline{S}H_2\right) + 26H \rightarrow C_6A\overline{S}_3H_{32}$ $C_3S + 11H \rightarrow C_3S_2H_8 + 3CH$ $2C_2S + 9H \rightarrow C_3S_2H_8 + CH$

2.2.2.5 Types of Portland cements

According to the ASTM standard, there are five basic types of Portland cement:

Type I	regular cement, general use.
Type II	moderate sulfate resistance, moderate heat of hydration
Type III	increase C_3S, high early strength
Type IV	low heat
Type V	high sulfate resistance

In BSI, four basic Portland cements are standardized: ordinary Portland cement (OPC), rapid-hardening Portland cement (RHPC), low-heat Portland cement (LHPC), and sulfate-resistant Portland cement (SRPC). OPC is equivalent to type I in ASTM, and RHPC, type III; LHPC, type IV; and SRPC, type V. There is no Portland cement similar to type II in BSI.

The typical chemical compositions of five types of Portland cement in ASTM are given in Table 2-8. Type I is usually used as a reference, which contains 50% C_3S, 25% C_2S, 12% C_3A, 8% C_4AF, and 5% gypsum. Compared to type I, type III has more C_3S (60%) and less C_2S (15%). Moreover, type III has a larger fineness number than type I. As a result, the early strength of type III at 1 day is doubled as compared to that of type I. Meanwhile, the heat released by type III increases to 500 J/g (type I is 330 J/g). On the other hand, type IV has less C_3S (25%) and more C_2S (50%). Hence, the early strength of type IV at 1 day is only half of that of type I. However, the heat released by type IV greatly decreases to 210 J/g, and thus is called-low heat Portland cement. As for type V, its sum of C_3A and C_4AF is only 14% and much less than the 20% of type I. Since these two compounds readily react with sulfate, the lower content gives

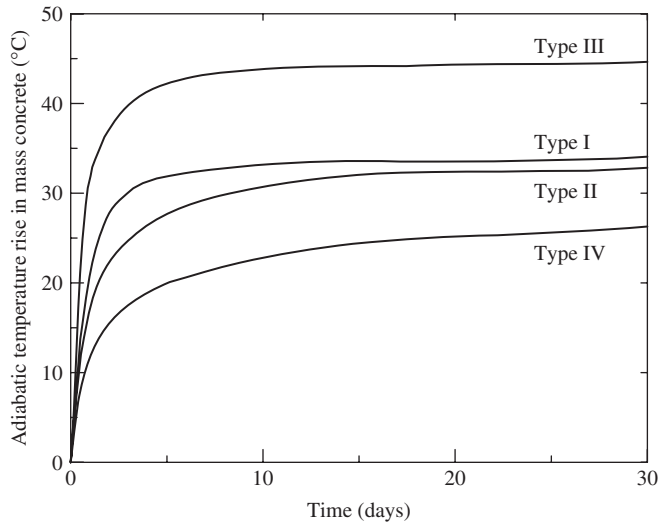

Figure 2-20 Adiabatic temperature rise in mass concretes with different types of cement

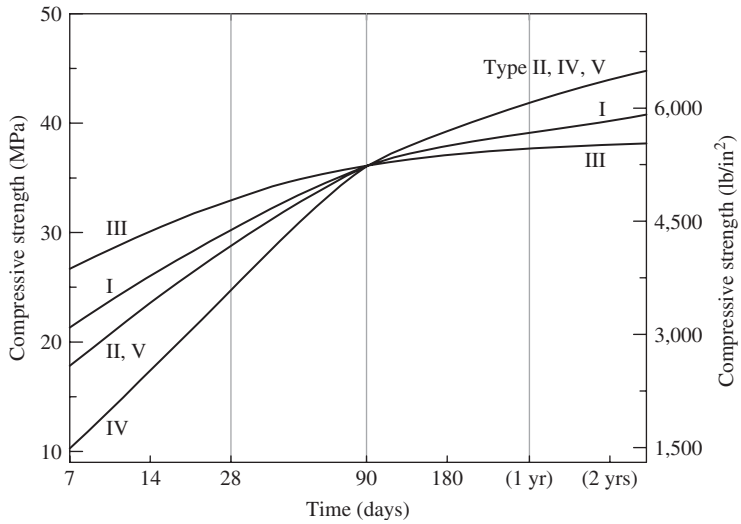

Figure 2-21 Strength development of cement pastes with different types of cement

it less opportunity to be attacked by sulfate ions. In addition, Figures 2-20 and 2-21 show the strength and temperature rise for the different types of cement, which are consistent with the information in Table 2-8.

From the information provided in Table 2-8, we can evaluate the behavior of each type of cement. The various behaviors provide the basic justification in selecting cement for engineering practice. For instance, for massive concrete structures, hydration heat is a big consideration

Table 2-8 Chemical compositions and physical properties of different Portland cements

Chemical Compositions and Physical Properties	Portland Cement Type				
	I	II	III	IV	V
C_3S	50	45	60	25	40
C_2S	25	30	15	50	40
C_3A	12	7	10	5	4
C_4AF	8	12	8	12	10
CSH_2	5	5	5	4	4
Fineness (Blaine, m^2/kg)	350	350	450	300	350
Compressive strength (1 day, MPa [psi])	7 [1000]	6 [900]	14 [2000]	3 [450]	6 [900]
Heat of hydration (7 days, J/g)	330	250	500	210	250

because too much heat will cause a larger temperature gradient, thermal stress, and cracking. Hence, type IV cement should be the first candidate and type III should not be used. For a marine structure, high sulfate resistance and lower ettringite are needed; thus, type V should be selected. If high early strength is needed, type III will be the best choice. Generally, type I is the most popular cement used in civil engineering.

2.2.2.6 The role of water

Of course, water is necessary for the hydration of cement. However, the water added in the mix is usually much higher than what the chemical reaction needs due to the fluidity requirement of concrete for placing. Thus, we can distinguish the three kinds of water in cement paste according to their roles: chemically reacted water, absorbed water, and free water. The chemically reacted water or chemically bonded water is the water that reacts with C, S, A, F, and $\overline{S}$ to form a hydration products such as C–S–H, CH, and AFt. This type of water is difficult to remove from cement paste and a complete decomposition happens at a temperature about 900°C. Absorbed water is the water molecules inside the layers of C–S–H gel. The loss of absorbed water causes shrinkage, and the movement or migration of absorbed water under a constant load affects the creep. Free water is the water outside the C–S–H gel. It behaves as bulk water and creates capillary pores when evaporated, and can influence the strength and permeability of concrete.

Porosity is a major component of the microstructure that is mainly caused by loss of water. The size of the capillary pores formed due to the loss of free water is in the range of 10 nm to 10 μm. The size of the gel pores involved in absorbed water is in the range of 0.5 to 10 nm. A knowledge of porosity is very useful since porosity has such a strong influence on strength and durability. According to experiments, the gel porosity for all normally hydrated cements is a constant, with a value of 0.26. The total volume of the hydration products (cement gel) is given by

$$V_g = 0.68\alpha \text{ cm}^3/\text{g of original cement} \tag{2-31}$$

where α represents the degree of hydration. The capillary porosity can then be calculated by

$$P_c = \frac{w}{c} - 0.36\alpha \text{ cm}^3/\text{g of original cement} \tag{2-32}$$

where w is the original weight of water, c is the weight of cement, and w/c is the water to cement ratio. It can be seen that with an increase of w/c, the capillary pores increase. The gel/space ratio (X) is defined as

$$X = \frac{\text{volume of gel (including gel pores)}}{\text{volume of gel} + \text{volume of capillary pores}} = \frac{0.68\alpha}{0.32\alpha + w/c} \tag{2-33}$$

The gel/space ratio reflects the percentage of solid materials in a cement paste. The higher the ratio, the more solid the materials and hence the higher the compressive strength. It can be seen from Equation 2-33 that the gel/space ratio is inversely proportional to the w/c. It can be deduced that a higher w/c leads to a low compressive strength of cement paste or concrete.

The minimum w/c ratio for complete hydration is usually assumed to be 0.36 to 0.42. It should be noted that complete hydration never happens and that residual anhydrate cement is beneficial for attaining a high ultimate strength. The space requirements for the cement gel are less than the requirements of water plus cement particles so that when the available water is used up, the cement paste will self-desiccate.

2.2.2.7 Basic tests of Portland cement

Portland cement concrete is the most widely used material in the world. The quality of Portland cement plays an important role in assuring the quality of construction and hence requires strict quality control. In this section, the basic tests for checking the quality of Portland cement are introduced.

(a) *Fineness (= surface area/weight)*: The fineness of Portland cement is an important quality index. It represents the average size of the cement grains. The fineness controls the rate and completeness of hydration due to the exposure surface of cement particles to the water. The finer the cement particles, the more rapid the reaction, the higher the rate of heat evolution, and the higher the early strength. However, finer cement particles can lead to high hydration heat, high possibility of early age cracking, and possible reduced durability. The fineness of Portland cement can be measured by different methods. One is the Blaine air permeation method defined in ASTM C204. In this method, cement particles are placed on a porous bed and then a given volume of fluid (air) is passed through the bed at a steady diminishing rate. After all the air is passed, the time (t) for the process is recorded. The specific surface of the cement can be calculated using

$$S = K\sqrt{t} \tag{2-34}$$

where K is a constant. In practice, S (or K) can be determined by comparing the sample to the known surface area issued by the U.S. National Institute of Standards and Technology. Examples of surface measurement are the surface area and pore size analyzer, which utilizes the adsorption of nitrogen on the particle surface. The ultimate sensitivity of the equipment is sufficient to detect less than 0.001 cm^3 of desorbed nitrogen from 30% N_2/He mixture. Such equipment is shown in Figure 2-22.

Another method to determine the surface area of cement particles is the Wagner turbidimeter method. In this method, cement particles are placed in a tall glass container that is filled with kerosene and then parallel rays of lights are passed through the container onto a photoelectric cell. The cross-sectional area of the particles intersecting the beam can be determined by measuring the light intensity. The radius of the particles, assuming spheres, can be obtained as

$$a = \sqrt{\frac{9V\eta}{2g(D_1 - D_2)}} \tag{2-35}$$

Figure 2-22 BET surface area analyzer

where V is the velocity of the cement particle falling in the viscous medium (kerosene), η is the viscosity coefficient, g is the acceleration of gravity, D_1 is the density of the particles, and D_2 is the viscous medium. A similar instrument is the particle size analyzer, which uses a laser beam as the measurement light and has a revolution of 0.04–2000 μm, as shown in Figure 2-23.

There is also a simple method to determine the fineness through sieving (ASTM C184-94). This method includes the following steps: Place a 50-g sample of cement on a clean and dry sieve having a hole size of 0.15 mm with the pan attached to it. While holding the sieve and the uncovered pan in both hands, sieve with a gentle wrist motion until most of the fine materials have passed through and the residue looks fairly clean. Place the cover on the sieve and remove the pan. Now, holding them firmly in one hand, gently tap the side of the sieve. The dust adhering to the sieve will be dislodged and the underside of the sieve may now be swept clean. Empty the pan and thoroughly wipe it out with a cloth or napkin. Replace the sieve in the pan and carefully remove the cover. Return any coarse material in the cover caught during tapping of the sieve. Continue the sieving as described earlier, without the cover, depending on the condition of cement. Continuously rotate the sieve along with gentle wrist motion, taking care not to spill any cement. Do this for about 9 min. Replace the cover and clean, following the same procedure as described earlier. If the cement is in a proper condition, there should now be no appreciable dust remaining in the residue or adhering to the sieve and the pan. Hold the sieve in one hand, with the pan and the cover attached, in a slightly inclined position and move it backward and forward in the plane of inclination. At the same time, gently strike the

Figure 2-23 Particle size analyzer

side about 150 times per minute against the palm of the other hand on the upstroke. Perform the sieving over a sheet of white paper. Return any material escaping from the sieve or pan and collecting on the paper. The fineness of cement can then be calculated as

$$F = 100 - (R_t/W) \times 100 \tag{2-36}$$

where F = fineness of cement expressed as the percentage passing through the 0.15-mm sieve, R_t = weight remaining in the 0.15-mm sieve, and W = total weight of the sample in grams.

(b) *Normal consistency test*: This test is undertaken to determine the water requirement for the desired cement paste plasticity state required by the setting and soundness test for Portland cement. The normal consistency test is regulated in ASTM C187. The procedures are listed below:

- Secure 300 g of cement.
- Mix cement with measured quantity of clean water.
- Mould the cement paste into the shape of a ball. With gloved hands, toss the ball six times through a free path of about six inches from one hand to the other.
- Press the ball into the larger end of a Vicat ring and completely fill the ring with paste.
- Remove excessive paste without compressing samples and locate the ring under the plunger of the Vicat apparatus.
- Place the plunger with a needle of 10-mm diameter under a load of 300 g in contact with the top of the paste and lock. Set the indicator on the scale to zero.
- Release the plunger and record the settlement of the plunger in mm after 30 sec.
- Repeat the process with the trial paste with varying percentages of water until normal consistency is observed, i.e., when a Vicat plunger penetrates 10 ± 1 mm in 30 sec.

The w/c for a normal consistency of Portland cement is 0.24 to 0.33.

(c) *Time of setting*: This test is undertaken to determine the time required for the cement paste to harden. The initial set cannot be too early due to the requirements of mixing, conveying, placing, and casting. Final setting cannot be too late owing to the requirement of strength development.

Time of setting is measured by the Vicat apparatus with a 1-mm-diameter needle. The initial setting time is defined as the time at which the needle penetrates 25 mm into the cement paste. The final setting time is the time at which the needle does not sink visibly into the cement paste.

(d) *Soundness*: Unsoundness in cement paste results from excessive volume change after setting. Unsoundness in cement is caused by the slow hydration of MgO or free lime. The reactions are

$$MgO + H_2O \rightarrow Mg(OH)_2 \tag{2-37}$$

$$\text{and} \quad CaO + H_2O \rightarrow Ca(OH)_2 \tag{2-38}$$

Another factor that can cause unsoundness is the later formation of ettringite. Since these reactions are very slow processes, taking several months and even years to finish, and their hydration products are very aggressive, their crystal growth pressure will crack and damage the already hardened cement paste and concrete. The soundness of the cement must be tested by an accelerated method due to the slow process. One test is called the Le Chatelier test (BS 4550), and is used to measure the potential for the volumetric change of the cement paste. The Le Chatelier test is used mainly for free lime detection. The main procedures are as follows:

- Fill the cylinder-shaped container with cement paste of normal consistency as shown in Figure 2-24.
- Cover the container with glass plates.
- Immerse in water (20°C) and measure the distance of the indicator at the top of the apparatus.
- Boil the specimen for 1 h and measure the distance again after cooling.
- Expansion should less than 10 mm for acceptable cement quality.

Another method is the autoclave expansion test (ASTM C151), which uses an autoclave to increase the temperature to accelerate the process. The procedures are as follows: Mold a cement paste with normal consistency into a container and cure normally for 14 h. Then remove from the mold, measure the size of the specimen, and place the specimen into autoclave. Raise the temperature in the autoclave so that the stem pressure inside can reach 2 MPa in 45 to 75 min. Maintain the pressure of 2 MPa for 3 h. Cool the autoclave down so that the pressure is released in 1.5 h. Cool the specimen in water to 23°C in 15 min. After another 15 min, measure the size of the specimen again; the expansion must be less than 0.80% to be acceptable. Autoclave testing can test both excess free lime and excess MgO.

(e) *Strength*: The strength of cement is measured on mortar specimens made of cement and standard sand (silica). Compression testing is carried out on a 50-mm cube with an S/C ratio of 2.75:1 and w/c ratio of 0.485, for Portland cements. The specimens are tested wet, using a loading rate that can let the specimen fail in 20 to 80 sec. A direct tensile test is carried out on a specimen shaped like a dog's bone, and the load is applied through specifically designed grips. Flexural strength is measured on a $40 \times 40 \times 160$-mm prism beam test under a center-point bending.

(f) *Heat of hydration test* (BS 4550: Part 3: Section 3.8 and ASTM C186): Hydration is a heat-release process. The heat of hydration is usually defined as the amount of heat released during the setting and hardening at a given temperature, measured in J/g. The experiment is

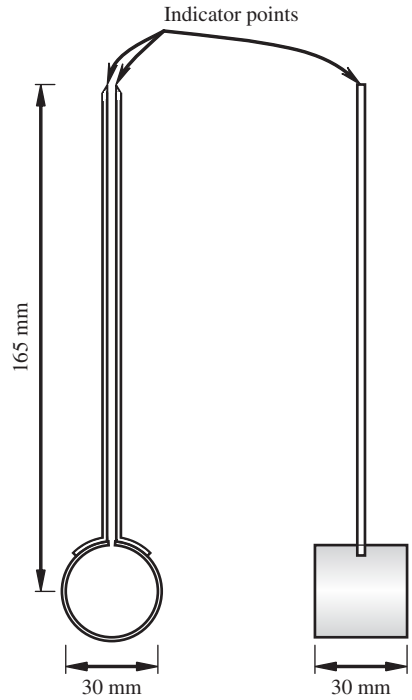

Figure 2-24 Le Chatelier test apparatus

called the heat of solution method. Basically, the heat of solution of dry cement is compared to the heats of solution of separate portions of the cement that have been partially hydrated for 7 and 28 days. The heat of hydration is then the difference between the heats of solution of the dry and partially hydrated cements for the appropriate hydration period. Useful information is the accumulated percentage of the heat release. It is verified by experiments that the heat release is 50% for 1–3 days, 75% for 7 days, 83–91% for 6 months.

The hydration heat can raise the temperature in concrete to 50–60°C and thus cause microcracks. The hydration heat should be taken care of in massive concrete constructions.

(g) *Other experiments, including sulfate expansion and mortar air content*: These tests are more meaningful for concrete and hence we discuss them in Chapter 5 in detail. Cement S.G. and U.W. The S.G. for most types of cements is 3.15, and the U.W. about 1000–1600 kg/m^3.

2.2.3 Geopolymers

2.2.3.1 Advantages and applications of geopolymers

Compared with ordinary Portland cement, newly developed inorganic binder geopolymers possess the following characteristics.

Abundant raw material resources: Any pozzolanic compound or source of silicates or aluminosilcates that is readily dissolved in alkaline solution will suffice as a source for the production of a geopolymer.

Energy saving and environment protection: Geopolymers do not require large energy consumption. A great amount of CO_2 is emitted during the production of Portland cement, which is one of the main reasons for global warming. Studies have shown that one ton of carbon dioxide gas is released into the atmosphere for every ton of Portland cement made anywhere in the world. In contrast, geopolymer cement is manufactured in a different way from Portland cement. It does not require extremely high-temperature treatment of the limestone. Only low-temperature processing of naturally occurring or direct man-made alumino-silicates (kaoline or fly ash) provides suitable geopolymeric raw materials. This leads to a significant reduction in energy consumption and CO_2 emission. Thermal processing of natural alumino-silicates at relative low temperature (600 to 800°C) provides suitable geopolymeric raw materials, resulting in much less energy consumption than for Portland cement. In addition, only a small amount of CO_2 is emitted. It was reported by Davidovits (1994b) that about 60% less energy is required, and 80–90% less CO_2 is generated for the production of geopolymers than for Portland cement. Thus the development and application of geopolymer cement is of great significance in environmental protection.

Simple preparation technique: Geopolymers can be synthesized simply by mixing alumino-silicate-reactive materials and strongly alkaline solutions, then curing at room temperature. In a short period, reasonable strength will be gained. This is very similar to the preparation of Portland cement concrete.

Good volume stability: Geopolymers have 80% lower shrinkage than Portland cement.

Reasonable strength gain in a short time: Geopolymers can obtain 70% of the final compressive strength in the first 4 hrs of setting.

High fire resistance and low thermal conductivity: Geopolymer cement possesses excellent high temperature resistance up to 1200°C and can endure 50-kW/m^2 fire exposure without sudden property degradation. In addition, no smoke is released after the extended heat flux. The heat conductivity of geopolymers varies from 0.24 to 0.3 w/m-k, and compares well with that of lightweight refractory bricks (0.3 to 0.438 w/m-k).

Geopolymers are an abundant raw resource, and have low CO_2 emission, less energy consumption, low production cost, high early strength, and fast setting. These properties make geopolymers suitable for applications in many fields of industry, such as civil engineering, automotive and aerospace industries, nonferrous foundries and metallurgical industries, plastics industries, waste management, art and decoration, and retrofitting of buildings. Several areas of application are described below.

(a) *Toxic waste treatment*: Immobilization of toxic waste may be one of the major areas where geopolymers can impact significantly on the status quo. The molecular structure of a geopolymer is similar to that of zeolites or feldspathoids, which are known for their excellent abilities to adsorb and solidify toxic chemical wastes, such as heavy metal ions and nuclear residues. It is the structures that make a geopolymer a strong candidate for immobilizing hazardous elemental wastes. Hazardous elements that present in waste materials mixed with geopolymer compounds are tightly locked into the 3-D network of the geopolymer bulk matrix.

(b) *Civil engineering*: Geopolymer binders behave similarly to Portland cement, and can set and harden at room temperature, and gain reasonable strength in a short period of time. Some geopolymer binders have been tested and proven to be successful in construction, transportation, and infrastructure applications. They yield synthetic mineral products with properties such as high mechanical performance, hard surface (Davidovits 1994a; Lyon

et al., 1997), thermal stability, and high acid resistance. Any current building component, such as bricks, ceramic tiles, and cement, could be replaced by geopolymers.

(c) *Automotive and aerospace*: The merits of high-temperature resistance allow geopolymers to have great advantages in the automotive and aerospace industries. At present, some geopolymer products are being used in aircraft to avoid cabin fires in aircraft accidents.

2.2.3.2 Development of geopolymers

Since French scientist Davidovits invented geopolymer materials in 1978 (Davidovits, 1993), great interest in the development of geopolymers has been voiced around the world. More than 28 international scientific institutions and companies have presented updated research and published their results. These works mainly focus on the following aspects.

(a) *Solidification of toxic waste and nuclear residues*: Davidovits et al. (1994c) first began to investigate the possibilities of heavy metal immobilization by commercial geopolymeric products in the early 1990s. The leachate results for geopolymerization on various mine tailings showed that over 90% of heavy metal ions included in the tailings can be tightly solidified in a 3D geopolymer framework. In the middle of the 1990s, Van Jaarsveld and Van Deventer et al. (Davidovits et al., 1990; Van Jaarsveld and Van Deventer, 1997, 1999; Van Jaarsveld et al., 1998) also set out to study the solidification effectiveness of geopolymers manufactured from fly ash. The bond mechanism between heavy metal ions and the geopolymer matrix is also simply explained on the basis of the XRD, infrared spectroscopy and magic-angle spinning nuclear magnetic resonance and leaching results. Recently, the European research project GEOCISTEM (Van Jaarsveld et al., 1999) successfully tested geopolymerization technology in the context of the East German mining and milling remediation project, carried out by WISMUT. Another research project into the solidification of radioactive residues was jointly carried out by Cordi-Geopolymer and Comrie Consulting Ltd., (European, 1997).

(b) *Fire resistance*: Recently the Federal Aviation Administration (FAA), USA, and the Geopolymer Institute of Cordi-Geopolymere SA, France (Comrie, 1988), have jointly initiated a research program to develop low-cost, environmentally friendly, fire-resistant matrix materials for use in aircraft composites and cabin interior applications. The flammability requirement for new materials is that they withstand a 50-kW/m^2 incident heat flux characteristic from a fully developed aviation fuel fire penetrating a cabin opening, without propagating the fire into the cabin compartment. The goal of the program is to eliminate cabin fire as a cause of death in aircraft accidents. As with this program, the fire-resistance properties of geopolymers reinforced by various types of fiber, such as carbon fiber, glass fiber, and SiC fiber, were tested and the fireproof mechanics were also analyzed. In addition, comparisons were made among geopolymer composites and carbon-reinforced polyesters, vinyl, epoxy, bismaleinide, cyanate ester, polyimide, phenolic, and engineering thermoplastic laminates. The test results showed that these organic large molecular polymers ignited readily and released appreciable heat and smoke, while carbon-fiber-reinforced geopolymer composites did not ignite, burn, or release any smoke even after extended heat flux exposure. On the basis of these fireproof studies, some nonflammable geopolymer composites for aircraft cabin and cargo interiors were produced on November 18, 1998, in Atlantic City, NJ, USA.

(c) *Archeological research*: In the 1970s, Davidovits proposed a controversial theory documented in a book by Lyon, (1994) and has since gained widespread support and acceptance. He postulated that the great pyramids of Egypt were not built by natural stones, but that the blocks were cast in place and allowed to set, creating an artificial zeolitic rock with geopolymerization technology. He collected a great amount of evidence from ancient Egyptian literature and samples in sites to confirm his geopolymerization theory. From then on, many experts began to focus their concerns on geopolymer studies. Some related papers (Davidovits, 1987; Morris, 1991; Campbell and Folk, 1991; Folk and Campbell, 1992; Mckinney, 1993) and patents were also published.

2.2.3.3 Reaction mechanism of geopolymers

Many studies on the formation mechanism have been made since the invention of geopolymers, but only one formation mechanism was proposed by Davidovtis. He believed that geopolymer synthesis consists of three steps—dissolution of alumino-silicate under a strong alkali solution, reorientation of the free ion clusters, and polycondenzation—but that each step includes many pathways. The dissolution step, for example, includes 8 pathways according to thermodynamics. Different pathways can create different ion clusters that directly determine the final properties of a geopolymer. Thus, it is important to understand the actual pathway for producing a geopolymer in order to gain insights into the mechanism of geopolymerization. However, until now, these studies have not been carried out. Because the forming rate of a geopolymer is very rapid, these three steps take place almost at the same time, which make the kinetics of the three steps interdependent. Thus it is impossible to separate these steps in experimental studies, which leads to the use of molecular simulation to solve these problems.

In the studies, two 6-membered-ring molecular structural models, to represent the chemical structure of metakaolinite (main raw material for synthesizing geopolymer), were established to quantitatively analyze the formation process of a geopolymer, as shown in Figure 2-25. Based on these two 6-membered ring models, all possible dissolution pathways of metakaoline under a strongly alkali environment were numerically simulated using quantum mechanics, quantum chemistry, computation chemistry, and thermodynamics theories. All possible pathways, Equations 2-39 to 2-46, involved in the formation process of the geopolymer were analyzed,

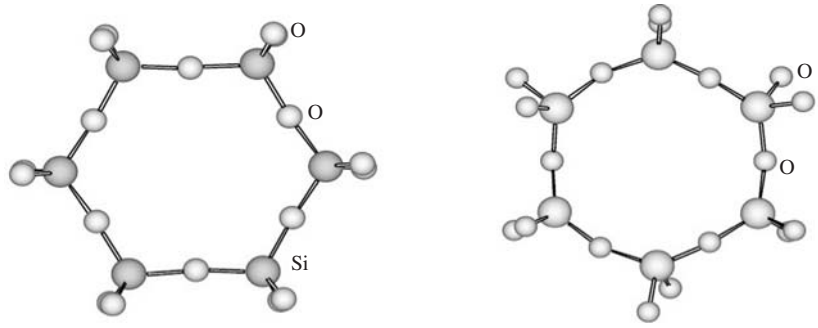

(a) 6-member ring structure cluster of SiO_4 tetrahedron

(b) 6-member ring structure cluster of AlO_4 tetrahedron

Figure 2-25 Molecular structure representing model of metakaolinite

Table 2-9 Reaction heats of single 6-member ring structure models under strongly alkaline solution

(a) Single 6-member ring of SiO_4 tetrahedral

Molecular Structural Unit	Formation Enthalpy	Reaction Enthalpy (kJ/mol)			
		ΔE1	ΔE2	ΔE3	ΔE4
$(Si(OH)_2O)_6$	−1491.45				
$(OH)_3Si–(Si(OH)_2O)_3–Si(OH)_3$	−1294.65				
$(OH)_3Si–(Si(OH)_2O)_3–Si(OH)_2–ONa$	−1385.43				
$(OH)_3Si–(Si(OH)_2O)_3–Si(OH)_2–OK$	−1370.88				
$HO–Si{\equiv}(ONa)_3$	−500.94	−5.49	12.12	−36.23	−19.23
$HO–Si{\equiv}(OK)_3$	−437.85				
NaOH	−119.30				
KOH	−104.14				
H_2O	−59.25				

(b) Single 6-member ring of AlO_4 tetrahedral

Molecular Structural Unit	Formation Enthalpy	Reaction Enthalpy (kJ/mol)			
		ΔE5	ΔE6	ΔE7	ΔE8
$(Al^-(OH)_2O)_6$	−619.67				
$(OH)_3Al^-–(Al^-(OH)_2O)_3–Al^-(OH)_3$	−776.45				
$(OH)_3Al^-–(Al^-(OH)_2O)_3–Al^-(OH)_2–ONa$	−839.39				
$(OH)_3Al^-–(Al^-(OH)_2O)_3–Al^-(OH)_2–OK$	−810.59				
$HO–Al^-{\equiv}(ONa)_3$	−441.66	−299.80	−245.79	−302.69	−235.03
$HO–Al^-{\equiv}(OK)_3$	−342.17				
NaOH	−119.30				
KOH	−104.14				
H_2O	−59.25				

and the enthalpies of each possible pathway were also calculated, as listed in Table 2-9. As a result, the optimum theoretical pathways in the geopolymerization process were determined.

$$(Si(OH)_2O)_6 + 3NaOH \rightarrow (OH)_3Si–(Si(OH)_2O)_3–Si(OH)_3 + HO–Si{\equiv}(ONa)_3 + H_2O \ \Delta E1 \quad (2\text{-}39)$$

$$(Si(OH)_2O)_6 + 3KOH \rightarrow (OH)3Si–(Si(OH)_2O)_3–Si(OH)_3 + HO–Si{\equiv}(OK)_3 + H_2O \ \Delta E2 \quad (2\text{-}40)$$

$$(Si(OH)_2O)_6 + 4NaOH \rightarrow (OH)_3Si–(Si(OH)_2O)_3–Si(OH)_2–ONa + HO–Si{\equiv}(ONa)_3 + 2H_2O \ \Delta E3 \quad (2\text{-}41)$$

$$(Si(OH)_2O)_6 + 4KOH \rightarrow (OH)_3Si–(Si(OH)_2O)_3–Si(OH)_2–OK + HO–Si{\equiv}(OK)_3 + 2H_2O \ \Delta E4 \quad (2\text{-}42)$$

$$(Al^-(OH)_2O)_6 + 3NaOH \rightarrow (OH)_3Al^-–(Al^-(OH)_2O)_3–Al^-(OH)_3 + HO–Al^-{\equiv}(ONa)_3 + H_2O \ \Delta E5 \quad (2\text{-}43)$$

$$Al^{-}(OH)_2O)_6 + 3KOH \rightarrow$$
$$(OH)_3Al^{-} - (Al^{-}(OH)2O)_3 - Al^{-}(OH)_3 + HO - Al^{-}{\equiv}(OK)_3 + H_2O\ \Delta E6 \quad (2\text{-}44)$$
$$Al^{-}(OH)_2O)_6 + 4NaOH \rightarrow$$
$$(OH)_3Al^{-}{-}(Al^{-}(OH)_2O)_3{-}Al^{-}(OH)_2{-}ONa + HO{-}Al^{-}{\equiv}(ONa)_3 + 2H_2O\ \Delta E7 \quad (2\text{-}45)$$
$$(Al^{-}(OH)_2O)_6 + 4KOH \rightarrow$$
$$(OH)_3Al^{-}{-}(Al^{-}(OH)_2O)_3{-}Al^{-}(OH)_2{-}OK + HO{-}Al^{-}{\equiv}(OK)_3 + 2H_2O\ \Delta E8 \quad (2\text{-}46)$$

2.2.3.4 Microstructure characterization

The structural characteristics of the products directly determine the final mechanical and durability properties. The case is also true for geopolymers. Many researchers have investigated the microstructure using different advanced techniques. Because a geopolymer is a type of amorphous 3D material with complex composition, it is very difficult to quantitatively measure the exact arrangement and chemical atmosphere of different atoms in geopolymers. If we want to solve this difficulty, we have to turn to statistical theories for establishing its molecular model. Unfortunately, until now, these studies have not yet been done. Therefore, the structural nature of geopolymers is not understood thoroughly.

The relationship between geopolymers and the corresponding zeolites has been investigated and the intertransformation between geopolymers and zeolites can be realized under specified conditions. On the basis of these results, the microstructure of geopolymers can be clearly characterized: a geopolymer is an amorphous 3D alumino-silicate material, which is composed of AlO_4 and SiO_4 tetrahedral lined alternatively by sharing all oxygen atoms. Positive ions (Na^+, K^+) are present in the framework cavities to balance the negative charge in a fourfold coordination. In addition, 3D statistical models of geopolymers, as shown in Figure 2-26, were simulated according to the decomposition results of MAS-NMR spectra.

2.2.4 Magnesium phosphoric cement (MPC)

2.2.4.1 Advantages and applications of MPC

MPC concrete is a type of artificial stone made from an acid–base reaction of magnesia and phosphates. They possess some properties that Portland cements do not possess according to the previous studies. Therefore, they can be utilized in fields in which Portland cements are not suitable (Kingery, 1950; Yoshizake et al., 1989; Seehra et al., 1993; Yang et al., 2002; Singh et al., 1997; Wagh et al., 1999). The applications of MPCs include the following.

(a) Due to its rapid setting and high early strength, MPC has been utilized in rapid repair of concrete structures, such as highways, airport runways, and bridge decks, for many years. It can save a lot of idle time and cost caused by the long disrupting period of other materials. If the interruption period is too long for a busy highway, airport runway, or bridge, etc., it will cause losses of millions of dollars. By using MPC materials, the interrupt time for transportation can be greatly shortened. Therefore, valuable time and resources can be saved.

(b) MPC can be incorporated with nontoxic industrial waste, such as class F fly ash (FA) and be converted into useful construction materials. The addition of FA in MPC can be over 40% by mass of MPC, about two times that of PC. In addition, MPC can combine with the FA that is not suitable in PC because of its high carbon content and other impurities. Besides FA, acid blast furnace slag, red mud (the residue of the aluminum industry), and

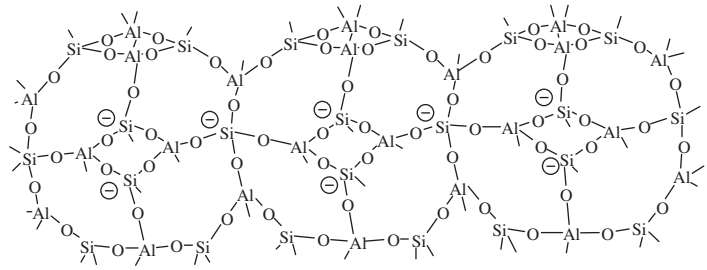

(a) Statistical structure model of K-PS geopolymer: the Si ions with a symbol of ⊕ corresponding for $Si^4(2Al)$, ⊖ for $Si^4(4Al)$, • for $Si^4(4Si)$

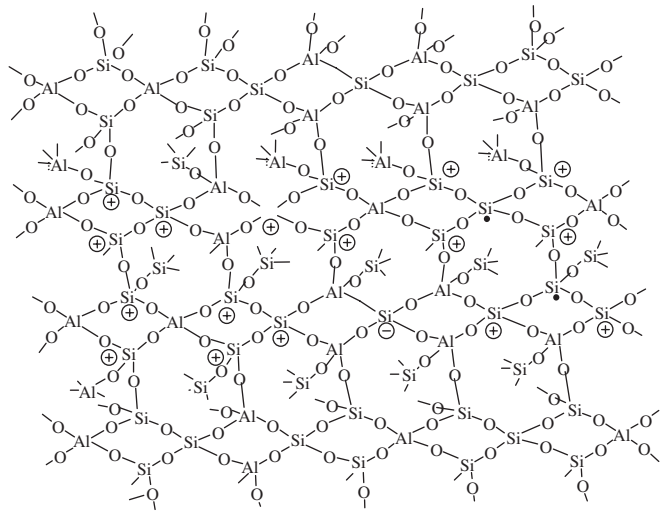

(b) Statistical structure model of K-PSDS geopolymer

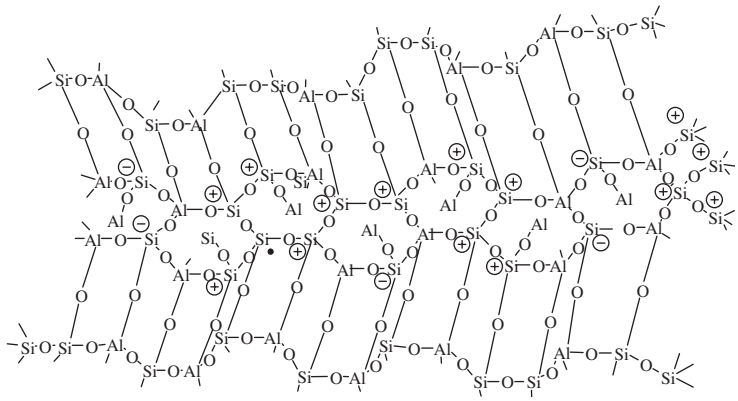

(c) Statistical structure model of K-PSS geopolymer

Figure 2-26 Statistical structure models of K-PSS geopolymer

even tails in gold mines can also be utilized in MPC in large amounts. These wastes are difficult to use in PC concrete in appreciable amounts.

(c) Due to the high alkali environment of PC (pH over 12.5), when they are used with fiber reinforcement, some components such as natural fibers, notably lignin, and hemicelluose will be susceptible to degradation. However, the lower alkalinity of MPC matrices (pH value 10 to 11) makes them potentially better suited to fiber reinforcement obtained from vegetation. Furthermore, the sugar in some natural fibers, such as sugarcane and cornstalks, can prohibit the setting of PC, which weakens the bonding between the Portland cement and the fiber. The set of MPC is not influenced by sugar.

(d) MPC can be used in the management and stabilization of toxic and radioactive wastes, including solids and liquids. The waste can be micro- and /or macroencapsulated and chemically bonded by MPC to form a strong, dense, and durable matrix that stores the hazardous and radioactive contaminants as insoluble phosphates, and microencapsulates insoluble radioactive components. The waste forms are not only stable in groundwater environments, but are also nonignitable and hence safe for storage and transportation.

(e) MPCs are very suitable for repairing deteriorated concrete pavements in cold regions. MPC can develop strength at low temperature due to its exothermic hydration and low water-to-binder ratio. At the same time, MPCs possess a higher deicer scaling property than Portland cement.

(f) The raw material of MPC is hard burnt magnesia, and is, in fact, a refractory material. Therefore, MPC can be designed to be fireproof and/or as a cold setting refractory, according to practical need.

2.2.4.2 Development of MPC

Phosphate bonding has been known for about a century, since the advent of dental cement formulations. In the refractory industry, the properties of cold-setting and heat-setting compositions were used as chemically bonded refractory material. According to the comprehensive studies of Kingery in 1950, phosphate bonding can be classified as (1) zinc–phosphate bonding; (2) silicate–phosphoric acid bonding; (3) oxide–phosphoric acid bonding; (4) acid phosphate bonding; and (5) metaphosphate–polyphosphate bonding (Kingery, 1950). The oxides, such as magnesium, aluminum, and zirconium, will react with phosphoric acid or acid phosphate at room temperature, forming a coherent mass, which sets quickly and gives high early strength. The hydration system, based on magnesia and ammonia phosphate (Kingery, 1950; Yoshizake et al., 1989; Seehra et al., 1993; Yang et al., 2002; Singh et al., 1997; Wagh et al., 1999) drew the most attention in the past.

From the 1970s, many patents using the reaction of magnesia and acid ammonia phosphate had been granted for rapid repair of concrete. The variation in patents arises from the use of different raw materials, inert materials to reduce cost, and retarders to control the reaction rate. Most claims are supported by a few examples cited in the patents without systematic scientific approach. From the middle of the 1980s, systematic studies on magnesia and ammonia phosphates were made by researchers (Yoshizake et al., 1989; Seehra et al., 1993; Yang et al., 2002). The hydration products, setting process, and strength development were the main thrusts of these investigations. Only a very few papers focused on the durability of the system (Yoshizake et al., 1989; Seehra et al., 1993; Yang et al., 2002). By the mid-1990s, it was found that MPC can be incorporated with industrial waste, producing solid to bond toxic waste (Singh et al., 1997; Wagh et al., 1999; Davidovits 1993). Therefore, MPC became a leading candidate for sustainable development. The environmental benefits arise from two aspects: (1) the nontoxic industrial

waste can be recycled to useful building materials, and (2) many toxic and radioactive wastes are difficult to treat with traditional processes, but can be easily treated by MPC. This function ensures more promising uses of MPC in the future, especially for the sustainable development of modern society.

Concerning the durability of MPCs, research that has been done by other investigators mainly includes superior durability topics, such as freezing–thawing and scaling resistance, protection of steel from corrosion, better bonding properties with waste organic materials, the transfer of noncontaminated industrial wastes into useful construction materials, and the stabilization of toxic or radioactive wastes.

The deterioration of concrete pavements is mainly caused by frost action in cold regions, and is severely amplified by the use of deicer chemicals. The repair material must possess high frost/deicer resistance, and MPC has very high deicer–frost resistance (Yoshizake et al., 1989; Yang et al., 2002). Scaling does not occur on the surfaces of MPC materials until after 40 freeze–thaw cycles. The regime of freeze–thaw cycling was achieved with a cooling rate of about 0.5°C/min, freezing for 4 h at -20 ± 2°C and then thawing for 4 h at 20 ± 5°C. A 3% NaCl solution was used as the deicer solution. The studies showed that the freezing/thawing resistance of MPCs was basically equal to the well-air-entrained PC concrete in general.

Steel corrosion in PC concrete is a serious problem, and MPC is an inhibitor of steel corrosion, forming an iron phosphate film at the surface of the steel. The pH of hardened MPC mortar is 10 to 11, and this may contribute a little to the inhibition of reinforcing steel corrosion. In addition, the ratio of permeability of MPC to PC concrete is 47.3%, or more than double the resistance to permeation (Yoshizake et al., 1989). Abrasion resistance testing has shown that MPC mortar possesses approximately double the abrasion resistance compared with slab-on-grade floor concrete, and nearly equal that of pavement concrete (Yoshizake et al., 1989; Seehra et al., 1993). With respect to chemical corrosion resistance, in the case of continuous immersion of specimens in sulfate solutions and potable water, results indicate that MPC mortar patches will remain durable under sulfate and moist conditions.

A wide range of waste particle sizes can be utilized when producing structural products using MPC. Styrofoam materials are candidates for optimal results. Styrofoam articles can be completely coated with a thin, impermeable layer of MPC. The uniform coating of the styrofoam particles not only provides structural stability but also confers resistance to fire, chemical attack, humidity, and other weathering conditions. The styrofoam insulation material provides superior R values. Furthermore, wood waste (suitable size range from 1 to 5 mm long, 1 mm thick, and 2 to 3 mm wide) can be bonded with MPC to produce chipboard having good flexural strength. For example, samples containing 50 wt% of wood and 50 wt% of binder achieve approximately 10.4 MPa in flexural strength. Samples containing 60 and 70 wt% of wood exhibit flexural strength of 2.8 and 2.1 MPa, respectively. Once the wood and binder are thoroughly mixed, the samples are subjected to pressurized molding to the order of approximately 18.3 MPa, for approximately 30 to 90 min.

With the progress of modern civilization, living conditions have been greatly improved; at the same time, however, a large amount of industrial waste (including toxic and nontoxic) has been produced. MPC can bind lots of nontoxic industrial waste to useful construction materials. If the wastes are toxic, MPC can solidify and stabilize them. It is important to recycle or stabilize waste, especially when natural resources are becoming more and more scarce. The waste is in various forms, such as aqueous liquids, inorganic sludge, particles, heterogeneous debris, soils, and organic liquids. However, only a few parts of the total waste can be recycled, such as fly ash and red mud, which can be blended with Portland cement. Most of the wastes need to be solidified and stabilized. Because of the diverse nature of the physical and chemical composition of these

wastes, no single solidification technology can be used to successfully treat and dispose of them. For example, the low-level wastes contain both hazardous chemical and low-level radioactive species (Singh et al., 1997). To stabilize them requires that the two kinds of contaminants be immobilized effectively. Generally, the contaminants are volatile compounds and hence cannot be treated effectively by high-temperature processes.

In a conventional verification or plasma hearth process, such contaminants may be captured in secondary waste streams or off-gas particulates that need further low-temperature treatment for stabilization. Also, some of these waste streams may contain pyrophorics that will ignite spontaneously during thermal treatment and thus cause hot spots that may require an expensive control system and equipment with demanding structural integrity. Therefore, there is a critical need for a low-temperature treatment and stabilization technology that will effectively treat the secondary wastes generated by high-temperature treatment processes and wastes that are not amenable to thermal treatment. Now those wastes can be successfully solidified by magnesia phosphate cement or chemically bonded phosphate ceramics (CBPC) (Singh et al., 1997). Other forms of waste, such as ash, liquid, sludge, and salts can be also solidified by MPC.

MPC is extremely insoluble in groundwater which will protect groundwater from contamination by the contained waste. Long-term leaching tests conducted on magnesium phosphate systems have shown that these phosphates are insoluble in water and brine. The radiation stability of MPC is excellent (Wagh et al., 1999). No changes in the mechanical integrity of the materials were detected even after gamma irradiation to a cumulative dosage of 10^8 rads.

2.2.5 Magnesium oxychloride cement

Magnesium oxychloride cement (MOC), also known as Sorel cement (Sorel, 1867), is a type of nonhydraulic cement. It is formed by mixing powdered magnesium oxide (MgO) with a concentrated solution of magnesium chloride ($MgCl_2$). Magnesium oxychloride cement has many superior properties as compared to ordinary Portland cement (Bensted and Barnes, 2002). It has high fire resistance, low thermal conductivity, and good resistance to abrasion, and is unaffected by oil, grease, and paint. It also has high early strength and is suitable for use with all kinds of aggregates in large quantities, including gravel, sand, marble flour, asbestos, wood particles, and expanded clays. The lower alkalinity of magnesium oxychloride (pH of 10–11), compared to the higher alkalinity of ordinary cement (pH of 12–13), makes it suitable for use with glass fiber by eliminating aging problems.

Magnesium oxychloride cement has drawn much research interest due to the ever-increasing awareness of the need for environmental protection (Li et al., 2003b). One of the important issues is to recycle waste wood in light of producing cement-based wood composites. However, lignin compounds and some other adverse chemicals contained in wood significantly retard the hydration of ordinary Portland cement. To solve the problem, magnesium oxychloride cement provides an excellent substitute for the binder (Odler, 2000). Some other major commercial applications of magnesium oxychloride cement are industrial flooring, fire protection, and grinding wheels. Due to its resemblance to marble, it is also used for rendering wall insulation panels, stuccos with revealed aggregates, and decorative purposes (de Henau and Dupas, 1976).

Magnesium oxide, or calcined magnesia, is normally obtained by calcinations of magnesite ($MgCO_3$) at a temperature of around 750°C. The quality or reactivity of the formed magnesium oxide powder is largely affected by its thermal history (calcination temperature and duration) and particle size (Haper 1967; Sorrel and Armstrong 1976; Matkovic et al., 1977). This in turn influences both the reaction rate and the properties of the reacted products of magnesium oxychloride cement. The setting and hardening of the magnesium oxychloride cement takes place in a through-solution reaction (Urwongse and Sorrell, 1980). The four main reaction phases in the

ternary MOC system are $2Mg(OH)_2 \cdot MgCl_2 \cdot 4H_2O$ (phase 2), $3Mg(OH)_2 \cdot MgCl_2 \cdot 8H_2O$ (phase 3), $5Mg(OH)_2 \cdot MgCl_2 \cdot 8H_2O$ (phase 5), and $9Mg(OH)_2 \cdot MgCl_2 \cdot 5H_2O$ (phase 9). Of these, phases 3 and 5 may exist at ambient temperature, whereas phases 2 and 9 are stable only at temperatures above 100°C (Cole and Demediuk, 1955). Another possible reaction product with a suitable reaction environment is magnesium hydroxide or brucite, $Mg(OH)_2$.

Therefore, optimum formation of phase 5 crystals in the hydrated MOC cement is desirable, as it is widely reported that the crystals provide the best mechanical properties. The formation mechanism of the four magnesium oxychloride phases has sparked vigorous discussion (Bilinski, et al., 1984; Menetrier-Sorrentino et al., 1986; Deng and Zhang 1999). Theoretically speaking, phase 5 can be obtained from a molar ratio of $MgO/MgCl_2$ of 5 along with the water required by the stoichiometry. The mechanical strength developed largely depends on the MOC phases produced and consequently on the appropriate proportions of the starting materials. Nevertheless, the correct or theoretical proportions of the starting materials alone are not sufficient to ensure the formation of phase 5 crystals, since the reactivity of MgO can have an influence.

For normal practice, it is believed that the chemical reactions in the system of $MgO–MgCl_2–H_2O$ are not complete and many unreacted MgO particles are expected to be left in the final reaction products. While unreacted MgO particles can be treated as a filler, surplus chloride ions are troublesome, as they cause corrosion problems (Maravelaki-Kalaitzaki and Moraitou, 1999) when they are involved in reinforcing steels. Besides, a higher water content is usually required as a lubricant for the required workability of a mixture. Therefore, excess magnesium oxide and water are suggested to be used in producing magnesium oxychloride cement to ensure the formation of phase 5, while keeping the free chloride ions to a minimum. From the practical point of view, the optimal molar ratios between different components of the ternary system $MgO–MgCl_2–H_2O$ would be the most important thing to know before further formulation for commercial products with various additives and fillers (Ji, 2001; Deng, 2003).

2.3 ADMIXTURES

Historically, an admixture is almost as old as concrete itself. The Romans used animal fat, milk, and blood to improve their concrete properties. Although these were added to improve workability, blood was a very effective air-entraining agent and might well have improved Roman concrete durability. In more recent times, calcium chloride was often used to accelerate the hydration of cement. The systematic study of admixtures began with the introduction of air-entraining agents in the 1930s, when it was accidentally found that cement ground with beef tallow (grinding aid) had more resistance to freezing and thawing than a cement ground without beef tallow. Nowadays, as we mentioned earlier, admixtures are important and necessary components for modern concrete technology. The concrete properties, both in fresh and hardened states, can be modified or improved by admixtures. The benefits of admixtures to concrete are listed in Table 2-10. Today, almost all the contemporary concretes contain one or more admixtures. It is thus important for civil engineers to be familiar with commonly used admixtures.

2.3.1 Definition and classifications

An admixture is defined as a material other than water, aggregates, cement, and reinforcing fibers that is used in concrete as an ingredient, and added to the batch immediately before or during mixing. Admixtures can be roughly divided into the following groups.

(a) *Air-entraining agents (ASTM C260)*: This kind of admixture is used to improve the frost resistance of concrete.

Table 2-10 Beneficial effects of different kinds of admixtures on concrete properties

Concrete Property	Admixture Type	Category of Admixture
Workability	Water reducers	Chemical
	Air-entraining agents	Air entraining
	Inert mineral powder	Mineral
	Pozzolans	Mineral
	Polymer latexes	Miscellaneous
Set control	Set accelerators	Chemical
	Set retarders	Chemical
Strength	Pozzolans	Mineral
	Polymer latexes	Miscellaneous
Durability	Air-entraining agents	Air entraining
	Pozzolans	Mineral
	Water reducers	Chemical
	Corrosion inhibitors	Miscellaneous
	Shrinkage reducer	Miscellaneous
Special concrete	Polymer latexes	Miscellaneous
	Silica fume	Mineral
	Expansive admixtures	Miscellaneous
	Color pigments	Miscellaneous
	Gas-forming admixtures	Miscellaneous

(b) *Chemical admixtures (ASTM C494 and BS 5075)*: A chemical admixture is any chemical additive to the concrete mixture that enhances the properties of concrete in the fresh or hardened state. The general-purpose chemicals include those that reduce the water demand for a given workability (called *water reducers*), and those chemicals that control the setting time and strength gain rate of concrete (called *accelerators* and *retarders*). Apart from these chemicals, there are others for special purposes—viscosity-modifying agents, shrinkage-reducing chemicals, and alkali–silica reaction-mitigating admixtures.

(c) *Mineral admixtures*: This kind of admixture consists of finely divided solids added to concrete to improve its workability, durability, and strength. Slag and pozzolans are important categories of mineral admixtures.

(d) *Miscellaneous admixtures* include all those materials that do not come under the above-mentioned categories, such as latexes, corrosion inhibitors, and expansive admixtures.

2.3.2 Chemical admixtures

This class of admixtures encompasses the total spectrum of soluble chemicals that are added to concrete for the purpose of modifying setting times and reducing the water requirements of concrete mixes. Figure 2-27 shows some typical chemical admixtures in the liquid form.

2.3.2.1 Water-reducing admixture

Water-reducing admixtures are used to reduce the water content of a concrete mixture while maintaining a given constant workability. Application of a water-reducing admixture can achieve different purposes. The resultant effect of reduced water content is increased strength and

Figure 2-27 Commonly used admixtures: (a) corrosion inhibitor; (b) set-retarding admixture; (c) air entraining agent; and (d) high-range water-reducing admixture (superplasticizer).

durability of concrete. However, water reducers may also be employed to "plasticize" the concrete, i.e., to make concrete flowable. In this case, the water content (or water-to-cement ratio) is held constant, and the addition of the admixtures makes the concrete flow better, while the compressive strength (which is a function of the water-to-cement ratio) is not affected. Another use of water reducers is to lower the amount of cement (since water is proportionately reduced) without affecting strength and workability. This makes the concrete cheaper and more environmentally friendly, as less cement is consumed.

Water reducers are classified broadly into two categories: (1) normal and (2) high range. The normal water reducers are also called *plasticizers*, while the high-range water reducers are called *superplasticizers*. While the normal water reducers can reduce the water demand by 5–10%, the high-range water reducers can cause a reduction of 15–40%. Lignosulfonate salts of sodium and calcium are an example of normal water reducers. Lignosulfonates are derived from neutralization, precipitation, and fermentation processes of the waste liquor obtained during production of paper-making pulp from wood. Sulfonated naphthalene formaldehyde (SNF) and polycarboxylic ether (PCE) are examples of the high-range water reducers. SNF is produced from naphthalene by oleum or SO_3 sulfonation; subsequent reaction with formaldehyde leads to polymerization and the sulfonic acid is neutralized with sodium hydroxide or lime. Polycarboxylic ether is manufactured by a polymerization process in which a free radical mechanism with peroxide initiators is used.

Lignosulfonates are generally regarded as 1st-generation water reducers, while the sulfonated naphthalene formaldehyde condensates are 2nd-generation water reducers and polycarboxylic ether is a 3rd-generation water reducer. The introduction of polycarboxylate dispersants into the concrete industry in the last decade has made it possible to develop water-reducer molecules in specific and tailored ways to influence the performance of the material. This is a tremendous technological advancement for the concrete industry as it enables the use of molecules developed for the sole purpose of dispersing Portland cement, whereas previous dispersants were mainly by-products of other industries. Polycarboxylates are classified as *comb* polymers. The name itself implies much about the structure of these molecules in that they consist of a backbone with pendant side chains, much like the teeth of a comb, as shown in

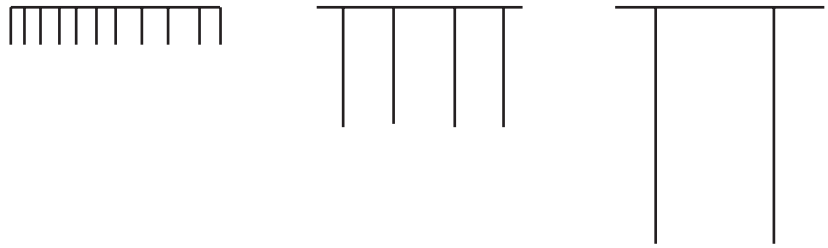

Figure 2-28 Structure of PCE

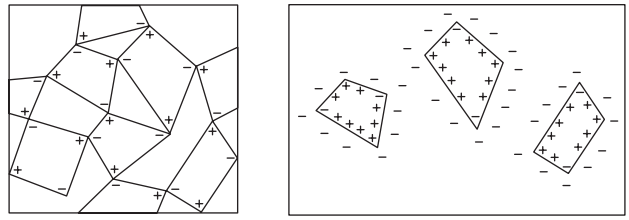

Figure 2-29 Mechanism of water-reducing admixture

Figure 2-28. For these molecules to be effective as dispersants, they must be attracted to the surface of a cement particle. The backbone of the polycarboxylate molecules typically serves two functions: as the location of binding sites (to the surface of the cement particle) and to provide anchoring sites for the side chains of the molecule. The pendant side chains serve as a steric, or physical, impediment to reagglomeration of the dispersed cement grains.

The mechanism of water reduction is different for different water reducers. Lignosulfonates (normal and sugar-refined), and SNF-based water reducers work on the mechanism of lowering zeta potential, which leads to electrostatic repulsion to separate cement particles from flocculation, thus releasing the entrapped water by cement particle clusters, as shown in Figure 2-29. Polycarboxylic ether-based water reducers are polymers with backbone and side chains. The backbone gets adsorbed on the surface of the cement grains, and the side chains cause dispersion of cement grains by steric hindrance (Uchikawa et al., 1997). This phenomenon relates to the separation of the admixture molecules from each other due to the bulky side chains, demonstrated in Figure 2-30. Steric hindrance is a more effective mechanism than electrostatic repulsion. The side chains, primarily of polyethylene oxide extending on the surface of cement particles, migrate in water and the cement particles are dispersed by the steric hindrance of the side chains.

Water-reducing chemicals are generally supplied in two types: powder and liquid. In a liquid form, the active solids content in the liquid is in the range of 30–40%. The dosages of water reducer for the liquid form can refer to either the solid content or liquid mass and is expressed as weight percentage of the binder. However, referring to solid content is preferred because it is consistent to the dosage of water reducer in powder form and it is more scientific since, the reducer in liquid form has a different amount of solid content. For example, if a concrete mix utilizes 350 kg cement and 100 kg fly ash as well as 1% of water reducer in 1 m^3 concrete, the solid content of water reducer used should be $0.01 \times (350 + 100) = 4.5$ kg. If a liquid form of water reducer is used and there is 30% solid in the liquid, the amount of liquid

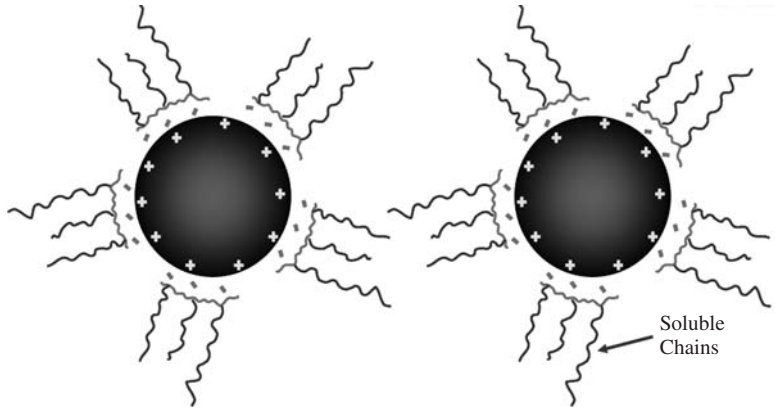

Figure 2-30 Steric effect of PCE

is 4.5/0.3 = 15 kg. Thus, the additional water added into concrete mix is 10.5 kg, that has to be deducted from the free mixing water.

Superplasticizers (SPs) are used mainly for two main purposes: (1) to produce high-strength concrete at a w/c ratio in a range of 0.23–0.3; and (2) to create "flowing" concrete with high slump flow in the range of 500 to 600 mm, the self-compacting concrete. Another benefit is that a lower w/c ratio would lead to better durability and lower creep and shrinkage. The major drawbacks of superplasticizers are that they (1) retard setting (especially in large amounts), (2) cause more bleeding; and (3) entrain too much air.

The most common problem in the application of water reducers in concrete is incompatibility, which refers to the abnormal behavior of a concrete due to the superplasticizer used. Common problems include flash setting, delayed setting, rapid slump loss, and improper early-age strength development. These issues in turn affect the hardened properties of concrete, primarily strength and durability. Compatibility between cements and superplasticizers is affected by many factors, including cement composition, admixture type and dosage, and concrete mixture proportions.

The C_3A content or, more specifically, the C_3A to SO_3 ratio has a profound effect on the compatibility between cement and SPs. When the C_3A content of cement is high and the sulfate availability is low, superplasticized concretes experience high rates of slump loss. When there is less C_3A available, higher amounts of SPs tend to adsorb on C_3S and C_2S, resulting in a reduction in the rate of strength development.

SP molecules with sulfonate functional groups have an affinity for the positively charged aluminates. They compete with the sulfate released from gypsum for the aluminate reaction sites (Ramachandran, 2002; Jolicoeur et al., 1994). When the solubility of the calcium sulfate is low, the SP molecules tend to get adsorbed first on the aluminate compounds, thus preventing the normal setting reaction. It must be also noted that the solubility of sulfates would decrease in the presence of SPs with sulfonate functional groups, thus affecting the normal setting process of the cement. To avoid such problems, cements usually contain sufficient amounts of quickly soluble alkali sulfates.

The type and dosage of admixture have major effects on the cement–admixture compatibility issues. Primarily, SPs cause the slowing down of the dissolution of Ca^{2+} and inhibit ettringite crystallization (Prince et al., 2002). The adsorption of the admixture on the surface of cement particles leads to a reduction of the chemical in solution. Thus, when adsorption levels are higher, more admixture is required to obtain a given fluidity. The surface adsorption of the

admixture increases with the molecular weight of the polymer, and the presence of calcium ions promotes this adsorption. In the case of the lignosulfonates (Rixom and Mailvaganam, 1999), the presence of low-molecular-weight ingredients causes excessive air entrainment and leads to loss of strength. In addition, the high sugar content of these admixtures could cause unnecessary retardation, especially at high dosages. SNF-based admixtures are most prone to rapid loss of workability, particularly at low water-to-cement ratios, which are the norm for most special concretes today. Another common problem with SNF admixtures is excessive retardation, which may be caused because of the blending of these chemicals with lignosulfonates in commercial formulations. Similar to lignosulfonates, the presence of moderate- to high-molecular-weight chain fractions leads to a better performance for SNF admixtures. The low-molecular-weight fractions cause excessive retardation by covering reactive sites on the cement surface and inhibiting reactions.

The factors influencing compatibility between SP and cement are broad and the mechanism is very complicated. For construction practice, a simple method is needed for quick selection of the proper SP as well as its dosage for concrete proportion. Traditionally, there are many methods to evaluate SP from a rheological point of view, such as the flow-table method of ASTM C230-90, the mini-slump cone test (Kantro, 1981), and the Marsh cone test (Aitcin et al., 1994). However, these methods cannot provide information on the effect of SP on setting and strength development of the concrete. Recently, a new method has been proposed for selection of SP using noncontact resistivity measurement (Xiao et al., 2007). Typical resistivity curves and the differential curves of the cement pastes with or without SPs are shown in Figure 2-31.

The figure shows that for the same SP, the paste with the larger dosage demonstrated a longer flat region, which implies a more effective retarding influence and slow strength development. With a suitable dosage, such as 0.4% for SP1 and 0.15% for SP2, the resistivity of corresponding pastes increases quickly after the dynamic balance period and exceeds the one

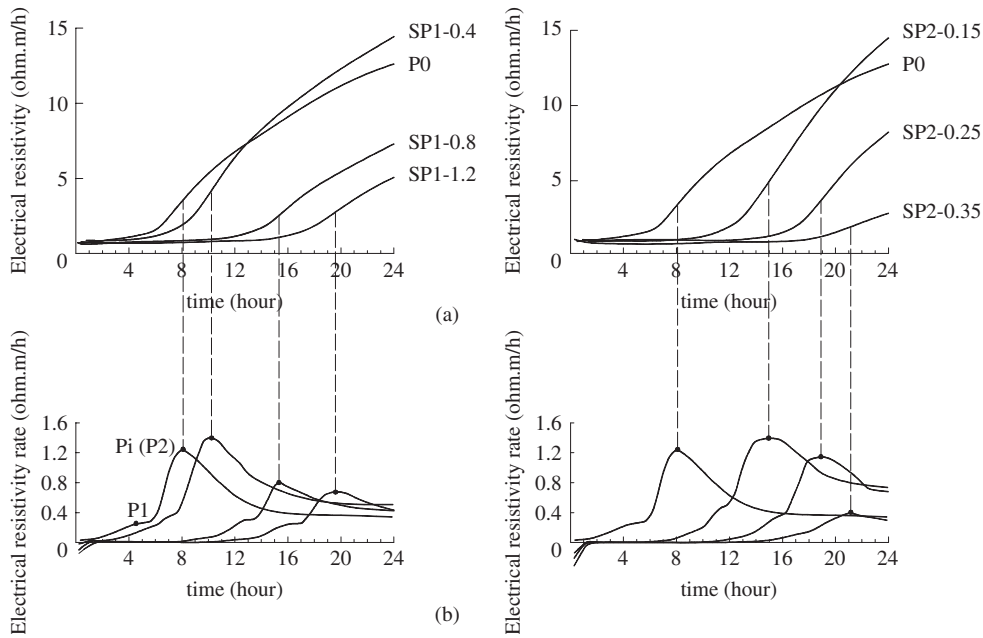

Figure 2-31 Typical resistivity curves and their differential curves

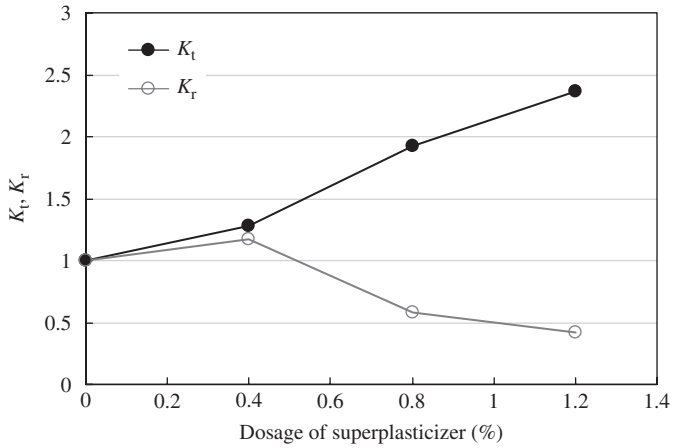

Figure 2-32 Typical plot of K_t and K_r

of the reference paste without SP addition. In this method, two parameters are proposed for selecting SPs:

$$K_t = \frac{t_{i,SP}}{t_{i,P0}} \tag{2-47}$$

where $t_{i,SP}$ is the inflection point time for a specimen with SP, and $t_{i,P0}$ is the inflection point time for the reference specimen without SP.

$$K_r = \frac{\rho_{24,SP}}{\rho_{24,P0}} \tag{2-48}$$

where $\rho_{24,SP}$ is the value of resistivity for a specimen with SP at 24 h, and $\rho_{24,P0}$ is the value of resistivity for reference specimen without SP at 24 h.

A typical plot of K_t and K_r is shown in Figure 2-32. Since both $t_{i,SP}$ and $t_{i,P0}$ are related to the setting time of the cement paste, the parameter K_t is in fact, reflecting the change of the setting time for the specimen with SP. If K_t is smaller than 1, it implies an accelerated setting due to addition of SP. If K_t is great than one, it means a retarded setting due to the addition of SP. Hence, a value of K_t close to 1 is preferred. On the other hand, both $\rho_{24,SP}$ and $\rho_{24,P0}$are related to the microstructure development, especially the porosity. A higher ρ_{24} value implies smaller porosity and hence a higher compressive strength. If K_r is smaller than 1, it implies a slow strength development and a lower compressive strength at 1 day due to the addition of SP. If K_r is great than one, it means a fast strength development and a higher compressive strength at 1 day that implies the addition of SP benefits the strength development. From Figure 2-32, it can be seen that for this type of SP the optimum dosage is 0.4%.

2.3.2.2 Shrinkage-reducing admixture

Shrinkage-reducing admixtures (SRA) provide a significant technical approach to reduce the drying shrinkage of concrete. SRA was invented in 1982, and Goto et al. (1985) applied for their patent in 1985. Subsequently, many researchers performed detailed studies on SRA. SRA is a liquid organic compound consisting of a blend of propylene glycol derivatives. Some literature has indicated that SRA can reduce long-term drying shrinkage by 50%, and there is a significant

improvement in restrained shrinkage performance. Even for concrete with proper curing at which the drying shrinkage would reduce to minimum, there is still a substantial reduction in drying shrinkage due to effect of SRA (Berke, et al., 1999). The main mechanism of SRA in reducing drying shrinkage of concrete is that the SRA lowers the surface tension of the pore solution and subsequently reduces the stresses in the pore solution that are directly proportional to the surface tension. With the reduction of the driving stress, the drying shrinkage can be reduced. However, in additional to reducing the surface tension, SRA also influences the dynamic process of cement hydration, as studied by He et al. (2006).

2.3.2.3 Setting-control admixture

Setting-control admixtures are used to either extend or shorten the plastic stage of concrete to meet the special requirements of the construction of concrete structures. If the admixture is used to extend the plastic period, it is called a retarder. If the admixture is used to shorten the plastic period, it is called an accelerator.

(a) *Mechanism*: The setting phenomenon of Portland cement paste signals the end of the plastic stage of concrete. It is a result of the progressive crystallization of the hydration products. Thus, to change the length of the plastic period equally means to change the setting rate. To influence the rate of setting, one has to change the rate of the crystallization. One way to do it is to add certain soluble chemicals to the cement–water system to influence the ion dissolution rate.

To understand the mechanism of acceleration or retardation, it is helpful to consider a hydrating Portland cement paste as being composed of certain anions (silicate and aluminate) and cations (calcium), the solubility of each being dependent of the type and concentration of the acid and base ions present in the solution. Usually, the setting will be speeded up when the dissolution rates of cations and anions are higher. On the other hand, the setting will be slowed down when the dissolution rates of cations and anions are lower. Thus, an accelerating admixture must promote the dissolution of cations (calcium ions) and anions from the cement, especially the silicate ions, which have the lowest dissolving rate, during the early hydration period. On the other hand, a retarding admixture must impede the dissolution of cations (calcium ions) and anions from the cement, especially the anions, which have the highest dissolving rate during the early hydration period (e.g., aluminate ions).

It should be noted that most chemical admixtures used for setting control purposes have both complementary and opposing effects. For instance, the presence of monovalent cations in solution (i.e., K^+ or Na^+) reduces the solubility of Ca^{2+} ions but promotes the solubility of silicate and aluminate ions. Also, the presence of certain monovalent anions, such as Cl^- or $NO_3{}^-$, reduces the solubility of silicates and aluminates but tends to promote the solubility of calcium ions. Moreover, the effects of promotion and reduction are a function of concentrations or dosage of these chemicals. For example, for a small dosage of the monovalent cations in solution (i.e., K^+ or Na^+), the dominant effect is in reducing the solubility of Ca^{2+} ions and thus acting as a retarder. For a large dosage, the dominant effect is promoting the silicate and aluminate ions and thus acting as an accelerator. The monovalent anions, such as Cl^- or $NO_3{}^-$, have the same phenomena.

There is also a monotonic retarding agent, which works with a different mechanism. These kinds of retarders reduce the solubility of the anhydrous constituents from cement by forming insoluble and impermeable products around the particles, or delaying the bond formation among hydration products. Once insoluble and dense coatings are formed around the cement grains, further hydration slows down considerably. Sugar and carbonated beverages belong to this category. There is some usage of sugar to retard the concrete inside the drum of transporting truck

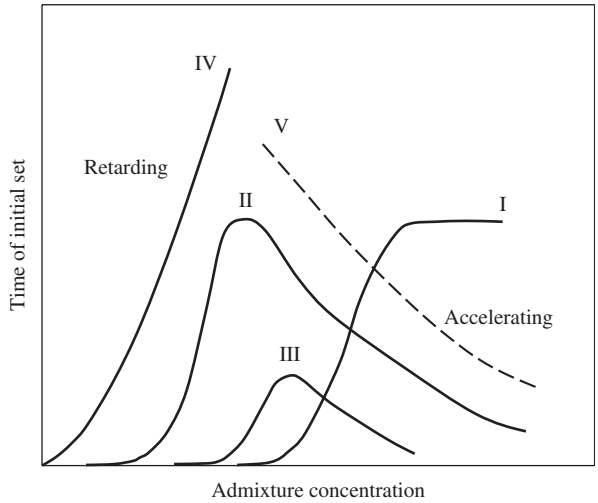

Figure 2-33 Different types of setting-control admixtures

when it has a problem in traffic or operation. Figure 2-33 demonstrates the different types of setting control admixtures: monotonic retarding admixture, monotonic accelerating admixture, and dual-role setting control admixture. It can be seen from the figure that the function of a dual-role setting admixture largely depends on its concentration.

(b) *Applications*: The major applications for setting-control admixtures are as follows.

(i) *Retarding admixtures*: Mainly used (1) to offset fast setting caused by ambient temperature, particularly in hot weather; (2) as a setting control of large structural units to keep concrete workable throughout the entire placing period; (3) to meet the requirement of long transportation time from the concrete plant to the construction site. For example, for the construction of a pier for a bridge built up in the ocean, the concrete has to be transported by ferry from land to the site. In this case, 5 to 6 h or even longer may be required.

(ii) *Accelerators*: Accelerators have been widely used in civil engineering. The applications include plugging leaks in swimming pools, water tanks, and pipelines; emergency repairs for highways, bridges, airport runways, and tunnels; and winter construction in cold regions. Soluble inorganic salts, such as calcium chloride, are by far the best-known and most widely used accelerators. A side effect of using chloride, however, is that it induces corrosion of the reinforcement in concrete structures.

2.3.3 Air-entraining admixtures

Air-entraining admixtures entrain air in the concrete. An air-entraining admixture contains surface-active agents that have two poles: one is hydrophobic and the other hydrophilic. The agents are concentrated at the air–water interface, the hydrophilic side with water and the hydrophobic side with air (see Figure 2-34). The surface tension is lowered so that bubbles can form more readily and then stabilize once they are formed. Commonly, carboxylic acid or sulfonic acid groups are used as to achieve the hydrophilicity, while aliphatic or aromatic hydrocarbons are used for hydrophobility. In summary, the entrained air is produced by admixtures that cause the mixing water to foam, and the foam is locked into the paste during hardening.

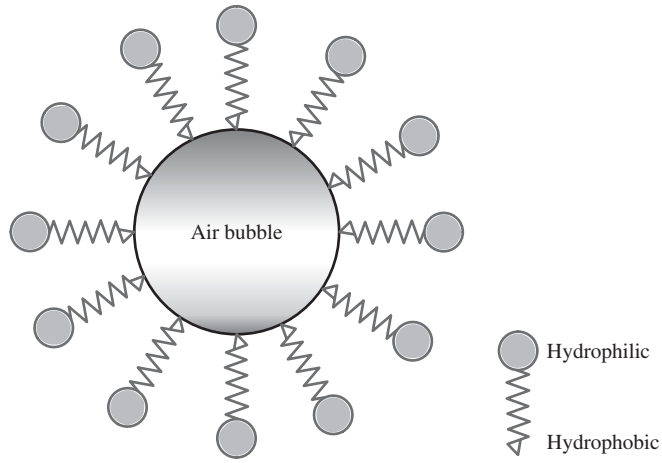

Figure 2-34 Mechanism of air entraining

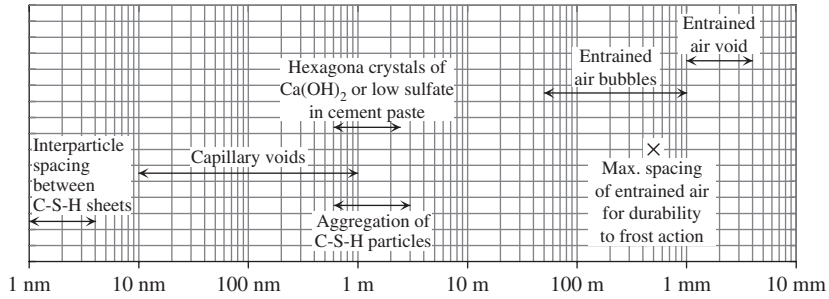

Figure 2-35 Size distribution of solids and pores in hydrated cement paste

Entrained air voids are different from entrapped air voids. Entrained air voids are formed on purpose, while an entrapped air void is formed by chance when the air gets into the fresh concrete during mixing. Entrapped air voids may be as large as 3 mm; entrained air voids usually range from 50 to 200 μm. The size distribution of the solids and pores in a hydrated cement paste is given in Figure 2-35.

Various advantages can be obtained by adding air-entraining admixtures into concrete. First, the workability of concrete can be improved because air bubbles act as lubricants in a fresh concrete. Subsequently, the water amount can be reduced for a targeted workability. Second, the ductility of concrete can be improved, since the air bubbles generated by the air-entraining agent provide more room for deformation to occur. Third, the permeability of concrete can be improved due to the effect of air-entraining agent in enclosing the air bubbles. Fourth, the impact resistance of concrete, can be improved as the air bubbles provide more deformation. Finally and most importantly, the durability, especially the ability to resist freezing and thawing of concrete, can be significantly improved by adding an air-entraining agent. This is because, in addition to the improved permeability, the small air bubbles in concrete provide spaces to release the pressure generated during the ice formation in the freezing process, which can prevent concrete from cracking and damage.

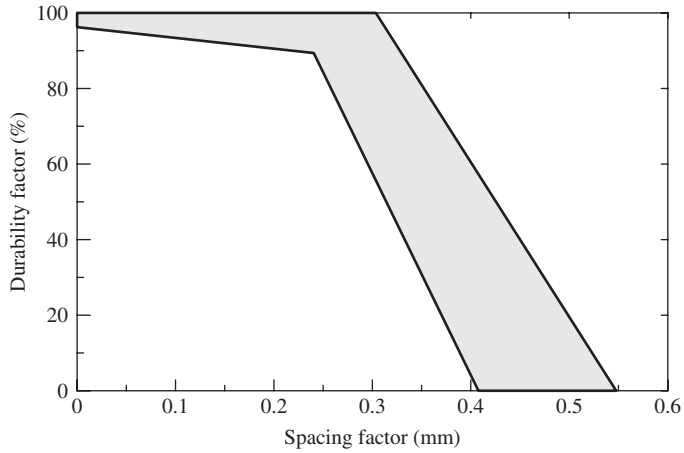

Figure 2-36 Effects of spacing factor on durability factor

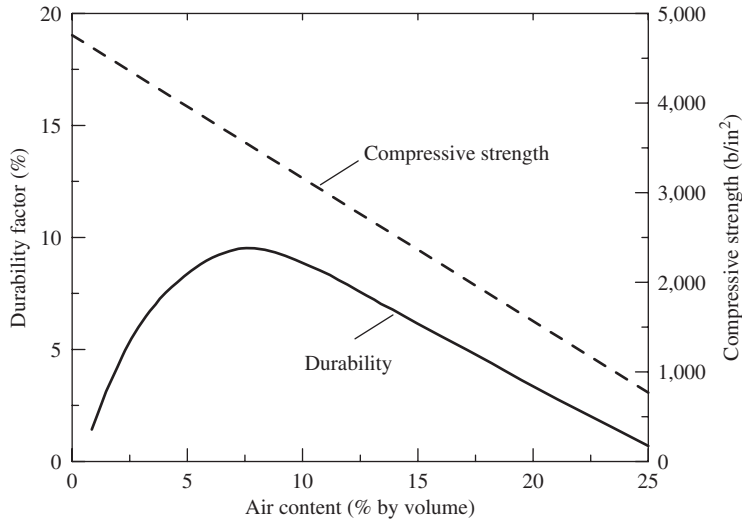

Figure 2-37 Effects of air content on durability factor and compressive strength

The spacing among the air bubbles also plays an important role in determining durability. As shown in Figure 2-36, the smaller the spacing factor (which is defined as the average distance from any point in the paste to the edge of a nearest entrained air bubble), the more durable the concrete. For the case of a spacing factor greater than 0.3 mm, the air entrained has a small or negligible effect on durability. Although the entrained air bubbles can decrease the capillary porosity due to the pore enclosing effect and the ability for increasing the workability of the entrained air, generally, a strength loss of 10–20% can be anticipated for most air-entrained concrete, as shown in Figure 2-37.

The volume of air required to give optimum durability has been found to be about 4–8% by volume of concrete, as observed from the above figures. The actual fraction depends on the maximum size of aggregate: the larger the aggregate size, the lower requirement for air content.

This is because more paste is required to provide similar workability for concrete with a smaller size of coarse aggregate due to the surface coating requirement.

The formula used to calculate the gel space ratio has to be modified if entrained air in cement paste is considered:

$$X = \frac{\text{volume of gel (including gel pores)}}{\text{volume of gel} + \text{volume of capillary pores} + \text{entrained air}} = \frac{0.68a}{0.32a + w/c + \text{entrained air}} \tag{2-49}$$

The percentage of the entrained air is based on the volume of concrete, and not the volume of cement paste.

2.3.4 Mineral admixtures

Mineral admixtures are finely divided siliceous materials that are added to concrete during mixing in relatively large amounts. Industrial by-products are the primary source of mineral admixtures. In Europe, mineral admixtures are normally called additions. Many researchers also call them supplementary cementing materials (SCM). A traditional concrete has four components: cement, water, fine aggregates, and coarse aggregates. However, a contemporary concrete contains 2 extra components: chemical admixture and SCM. Hence, some researchers also call SCM the 6th component of concrete. Figure 2-38 shows four commonly used mineral admixtures: silica fume, slag, fly ash, and metakaoline.

2.3.4.1 Silica fume

Silica fume is a by-product of induction arc furnaces in the silicon metal and ferrosilicon alloy industries. Reduction of quartz to silicon at temperatures up to 2000°C produces SiO_2 vapors, which oxidize and condense in the low-temperature zone to very fine spherical particles consisting of noncrystalline silica. Hence, silica fume is also called condensed silica fume or microsilica. The material is collected by filtering the outgoing gases in bag filters. The typical size distributions of silica fume, ordinary Portland cement, and fly ash are compared in Figure 2-39.

More accurately, the size distribution of a typical silica fume product is provided as 20% below 0.05 μm, 70% below 0.10 μm, 95% below 0.20 μm, and 99% below 0.50 μm. As most of the silica fume particles are less than 100 nm, they can be treated as nanoparticles. Typical chemical compositions of a silica fume are shown in Table 2-11. It can be seen that silica dominates (>92%) in the material.

Microsilica has a surface area around 20 m^2/g and an average bulk density of 586 kg/m^3. Compared with normal Portland cement and typical fly ashes, silica fume sizes are two orders of

Figure 2-38 Examples of mineral admixtures

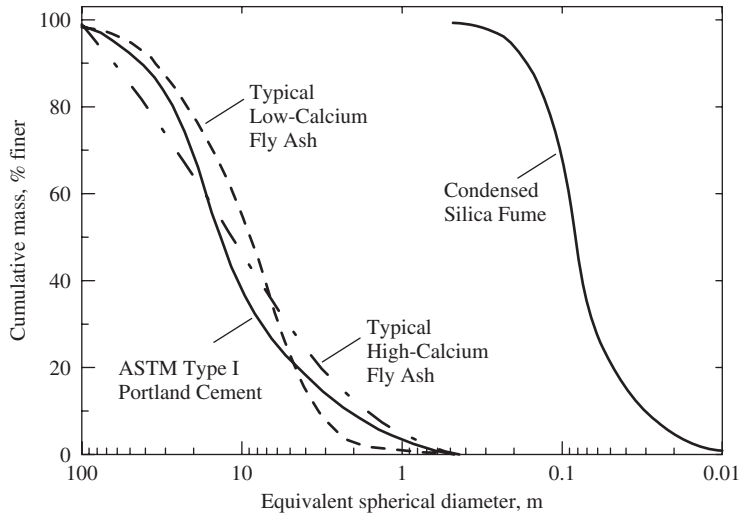

Figure 2-39 Size distribution of typical Portland cement, fly ash, and silica fume

Table 2-11 Typical chemical compositions of silica fume

Chemical Compositions	Typical Contents by Weight (%)	Standard Deviation	Minimum (%)	Maximum (%)
SiO_2	92.9	0.60	92.0	94.0
Al_2O_3	0.69	0.10	0.52	0.86
Fe_2O_3	1.25	0.46	0.74	2.39
CaO	0.40	0.09	0.28	0.74
MgO	1.73	0.31	1.23	2.24
K_2O	1.19	0.15	1.00	1.53
Na_2O	0.43	0.03	0.37	0.49
C	0.88	0.19	0.01	0.03
Cl	0.02	0.01	0.01	0.03
S	0.20	—	0.10	0.30
P	0.07	—	0.03	0.12
LOI	1.18	0.26	0.79	0.73
Moisture	0.30	0.09	0.09	0.50

magnitude finer. Thus, the material is highly pozzolanic. However, it creates handling problems and increases the water requirement in concrete appreciably, unless superplasticizer is used.

Silica fume is supplied in two forms, powder and slurry. The slurry of silica fume is adopted to avoid possible health issues caused by breathing in the fine particles of silica fume when people work with it. Before the mid-1970s, silica fume was discharged into the atmosphere. Environmental concerns necessitated the collection and landfilling of silica fume, and it has been applied in concrete production since the 1980s and has now become a valuable material for high-performance concrete. The normal percentage of silica fume used to replace Portland cement is from 5 to 15%. Silica fume benefits concrete properties in two ways: particle packing and pozzolanic reaction. Since the size of silica fume is two magnitudes of order smaller than that

of Portland cement, it can easily fill in the space between cement particles. Subsequently, a denser concrete microstructure can be achieved and a high compressive strength can be reached. Pozzolanic reaction is defined as

$$\text{pozzolan} + \text{calcium hydroxide} + \text{water} = \text{calcium silicate hydrate (secondary)} \quad (2\text{-}50)$$

Silica fume is a very active pozzolan material and readily reacts with CH and water to form secondary C–S–H. Through pozzolanic reaction, silica fume can consume a large amount of CH, and generated C–S–H also fills the capillary voids. The process can further reduce the porosity and permeability in concrete as well as the possibility of chemical reaction of CH with other ions to form harmful products. Thus, the durability of concrete can be greatly enhanced. Li et al. (1999a and 1999b) have shown that silica fume can greatly enhance the resistance of high-performance concrete to alkali aggregate reaction and chloride diffusion. Nowadays, silica fume is widely used in producing high-performance and ultrahigh-performance concrete worldwide.

2.3.4.2 Metakaolin

High-reactivity metakaolin (MK) is one of the recently developed supplementary cementing materials for high-performance concrete. It is produced by calcining purified kaolinite clay in a specific temperature range (650 to 800°C) to drive off the chemically bound water in the interstices of kaolin and destroy the crystalline structure, which effectively converts the material to the MK phase, an amorphous aluminosilicate. Unlike industrial by-products, such as silica fume (SF), fly ash, and blast-furnace slag, MK is carefully refined to lighten its color, remove inert impurities, and control its particle size. This well-controlled process results in a highly reactive white powder that is consistent in appearance and performance. The particle size of MK is generally less than 2 μm, which is significantly smaller than cement particles, though not as fine as SF, see Figure 2-40. It is typically incorporated into concrete to replace 5–20 % of cement by mass.

The typical chemical composition of MK is shown in Table 2-12. It can be seen that silicon dioxide and aluminum oxide are the two main components in MK and little CaO exists in MK. Similar to silica fume, metakaolin improves concrete performance by the packing effect and by reacting with calcium hydroxide to form secondary C–S–H. However, MK was found to improve concrete properties while offering good workability. Concrete modified by MK requires less

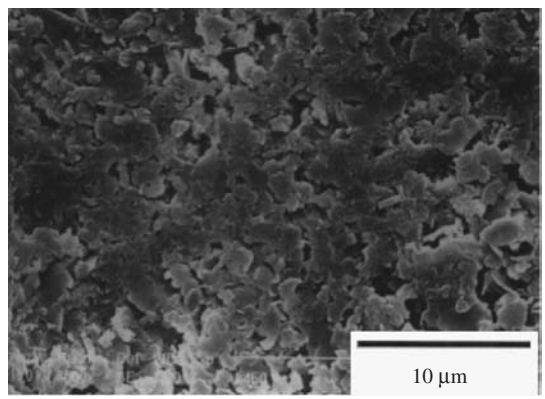

Figure 2-40 SEM photo of MK

Table 2-12 Chemical composition of MK (%)

SiO_2	Al_2O_3	Fe_2O_3	CaO	LOI
51.34	41.95	0.52	0.34	0.72

water-reducing admixture than that modified by SF to achieve a comparable fluidity (Caldarone et al., 1994). It has also been demonstrated that MK is particularly effective in reducing the rate of diffusion of sodium and chloride ions. The diffusion coefficient can be reduced by about 50% when 8% MK is added into the concrete mixture (Thomas et al., 1997). Ding and Li (2002) systematically studied the effect of MK and SF on the workability, strength, shrinkage, and resistance to chloride penetration of concrete. They found that MK and SF had similar functions in improving strength of concrete, reducing free drying shrinkage, and chloride diffusion rate. In addition, because of its white color, high-reactivity MK does not darken concrete as SF typically does (the white-colored SF is very limited in tonnage), which makes it suitable for color matching and other architectural applications. The cost of MK is now much lower than that of SF, which gives MK a bigger potential for application in concrete structures.

2.3.4.3 Fly ash

Fly ash (pulverized fuel ash) is a by-product of an electricity-generating plant using coal as fuel. During combustion of powdered coal in modern power plants, as coal passes through the high-temperature zone in the furnace, the volatile matter and carbon are burned off, whereas most of the mineral impurities, such as clays, quartz, and feldspar, will melt at the high temperature. The fused matter is quickly transported to lower-temperature zones, where it solidifies as spherical particles of glass. Some of the mineral matter agglomerates, forming bottom ash, but most of it flies out with the flue gas stream and thus is called fly ash. This ash is subsequently removed from the gas by electrostatic precipitators.

Fly ash can be divided into two categories according to type of coal burned (ASTM C618): class F fly ash is obtained by burning anthracite or bituminous coal and class C by burning lignite or sub-bituminous coal. The chemical compositions of class F and class C are listed in Table 2-13. It can be seen from the table that class F contains less than 10% CaO and class C 15 to 30% of CaO. Thus, sometimes class F is called low-calcium fly ash and class C is called high-calcium

Table 2-13 Chemical composition of fly ashes (%)

Oxide	Class F	Class C
SiO_2	49.1	53.79
Al_2O_3	16.25	15.42
Fe_2O_3	22.31	5
TiO_2	1.09	1.68
CaO	4.48	18
MgO	1	3.4
Na_2O	0.05	0.5
K_2O	1.42	0.5
SO_3	0.73	1.44
LOI	2.55	0.8

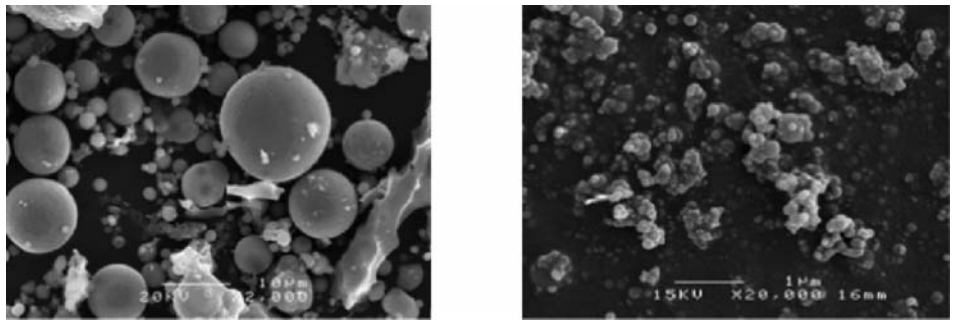

(a) Fly ash (b) Silica fume

Figure 2-41 Morphology of fly ash and silica fume

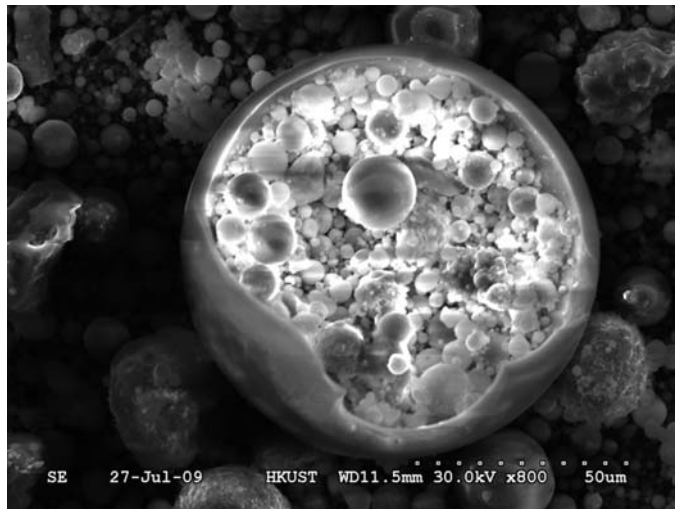

Figure 2-42 Fly ash particle having plerospheres

fly ash. Usually, high-calcium fly ash is more reactive because it contains most of the calcium in the form of reactive crystalline compounds, such as C_3A and CS.

The morphology of fly ash is compared with that of silica fume in Figure 2-41. It shows that most of the particles in fly ash occur as solid spheres of glass, but sometimes a small number of hollow spheres, called cenospheres (completely empty) and plerospheres (packed with numerous small spheres), are present, see Figure 2-42. The size distributions of fly ash are slightly smaller than those of Portland cement with more than 50% under 20 μm.

Fly ash can be used to produce a so-called blended cement. In this case, fly ash is milled with clinker and gypsum in the last procedure in cement production. Fly ash can also be used to produce modified concrete by adding it during the mixing process. Research carried out in past 40 years or so shows that the incorporation of fly ash into concrete has certain advantages and some disadvantages. Incorporation of fly ash into concrete can improve the workability due to the spherical shape and glassy surface of fly ash particles. By replacing cement with fly ash, the cost of concrete can be reduced, since fly ash costs low than cement. Because fly ash is an industrial

by product, it lowers the energy demand in producing concrete. In addition, incorporating fly ash into concrete can reduce the hydration heat of fresh concrete and is good for mass concrete structures.

The disadvantages of fly ash concrete are low early age strength and longer initial setting time due to the low reactivity of fly ash. Much research has been carried out to improve the reactivity by chemically activating (Xie and Xi, 2000). One method is to add an alkali activator such as 1 or 2% NaOH or KOH into concrete mix. Another is to use lime to mix with fly ash for a few days before incorporating the fly ash into the concrete mix. Recently, some studies using a mechanical method to wet grind or mill fly ash to "activate" its reactivity have been conducted and some promising results have been obtained (Blanco et al., 2005). The normal replacement of cement by fly ash is around 25 to 30% by weight. However, in high-volume fly ash concrete, fly ash content up to 60% is reached (Langley et al., 1989).

2.3.4.4 Slag

Slag is a by-product of iron or steel production. For iron production, blast furnaces are used and for steel production, either a basic oxygen furnace or an electrical furnace. The slag produced in iron production is different from that from steel production. Currently, the slag used in the concrete industry is mainly the slag from iron production, and its full name is ground, granulated blast furnace slag or GGBS.

In the production of cast iron or pig iron, the liquid slag is usually quenched from a high temperature to ambient temperature rapidly by either water or a combination of air and water. Due to the very fast process, most of the lime, magnesia, silica, and alumina in slag are held in a noncrystalline or glassy state. The water-quenched product is called granulated slag due to the sand-size particles, while the slag quenched by air and a limited amount of water, which is in the form of pellets, is called palletized slag. Normally, the former contains more glass; however, when ground to powder with a fineness of 400 to 700 m^2/kg Blaine, both products can develop satisfactory cementitious properties. Figure 2-43 shows the slag particles observed with SEM. The production and use of ground, granulated blast-furnace slag has a long history of more than

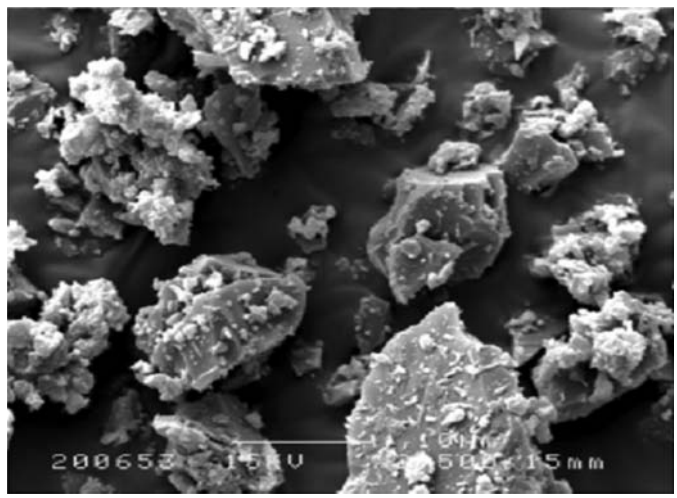

Figure 2-43 SEM photo of slag particles

Table 2-14 Chemical composition of slag (%)

CaO	SiO_2	Al_2O_3	Fe_2O_3	MgO	SO_3	K_2O	Na_2O	LOI
30–45	~30	10–15	1–2	<6	<6	0.4–1.5	0.05–0.5	0.2–1

100 years. The typical chemical composition of slag is shown in Table 2-14. It can be seen from the table that CaO and SiO_2 are the two main components, and the CaO content in slag is quite close to that of high-calcium fly ash.

Ground granulated blast-furnace slag and high-calcium fly ashes are similar in mineralogical character and reactivity. Besides a similar content of CaO, both are essentially noncrystalline, and their high-calcium glassy phases have a similar order of reactivity. Compared to low-calcium fly ash, which usually does not make any significant contribution to the strength of Portland cement concrete until after about 4 weeks of hydration, the strength contribution by high-calcium fly ash or granulated blast-furnace slag may become apparent as early as 7 days after hydration. Although the particle size characteristics, composition of glass, and glass content are the primary factors determining the activity of fly ashes and slag, the reactivity of the glass itself varies with the thermal history of the material. Glass chilled from a higher temperature and at a faster rate will have a more disordered structure and will therefore be more reactive.

Slag particles of less than 10 μm contribute to early strengths in concrete up to 28 days; particles of 10 to 45 μm contribute to later strengths, but particles coarser than 45 μm are difficult to hydrate. Since the slag obtained after granulation is very coarse and moist, it is dried and pulverized to a particle size mostly under 45 μm, which corresponds to approximately a 500-m^2/kg Blaine surface area.

Similar to fly ash, slag can also be used in both cement and concrete production. In cement production, slag can be milled with clinker and gypsum to produce Portland–slag blended cement. In concrete production, up to 50% of cement can be replaced by slag. In slag-modified concrete, the products of slag hydration form a mixture of C–S–H and AFm. The C–S–H formed through slag has a lower C/S ratio, as expected. Slag-modified concrete shows an improved slump retention as well as both early and long-term strength (Yao et al., 1998). However, reactivities can vary from slag to slag even if they have similar composition. Experimental verification is necessary to identify the reactivity of specific types of slag in practice.

2.3.4.5 Benefits of using mineral admixtures in concrete

For modern or advanced concrete technology, various mineral admixtures have been widely used in concrete construction. The purposes in using these mineral admixtures in concrete are to gain economic benefits, protect the environment, improve the workability of fresh concrete, enhance strength, and especially the durability of hardened concrete, and decrease hydration heat. The benefits of using various mineral admixtures in modern concrete construction are shown in Tables 2-15 and 2-16.

2.4 WATER

Water is an important ingredient of concrete, and a properly designed concrete mixture, typically with 15 to 25% water by volume, will possess the desired workability for fresh concrete and the required durability and strength for hardened concrete. The roles of water have been discussed

Table 2-15 Benefits of using mineral admixtures in fresh concrete

Mineral Admixtures	Usual Dosage[a] (%)	Economic Benefits	Protecting Environment	Workability of Fresh Concrete		
				Increasing Fluidity	Increasing Cohesiveness	Decreasing Segregation
PFA or FA	10–40	✓	✓	✓	✓	✓
BFS or slag	20–60	✓	✓	✓	✓	✓
Silica fume	5–15		✓		✓	✓
Other pozzolans	10–30	✓	✓			✓

[a]Replacement of Portland cement

Table 2-16 Benefits of using mineral admixtures in hardened concrete

Mineral Admixtures	Usual Dosage[a] (%)	Increasing Strengths	Decreasing Heat	Decreasing Cracking	Impermeability	Anti-chemical Attack[d]
PFA or FA	10–40	✓[b]	✓	✓	✓	✓
BFS or slag	20–60	✓[c]	✓		✓	✓
Silica fume	5–15	✓[c]		✓	✓	✓
Other pozzolans	10–30	✓[b]	✓	✓	✓	✓

[a]Replacement of Portland cement.
[b]Increasing strength at long term age.
[c]Increasing strength at early age and long term age, especially using silica fume.
[d]Anti-chemical attack may involve salt scaling, sulfates or seawater attack, resistance to alkali–aggregate reaction (AAR), resistance to corrosion of rebar, and so on.

earlier and are known as hydration and workability. The total amount of water in concrete and the water-to-cement ratio may be the most critical factors in the production of good-quality concrete. Too much water reduces concrete strength, while too little makes the concrete unworkable. Because concrete must be both strong and workable, a careful selection of the cement-to-water ratio and total amount of water are required when making concrete (Popovics, 1992).

2.4.1 Mixing water

Water can exist in a solid form as ice, a liquid form as water, or a gaseous form as vapor. Mixing water is the free water encountered in freshly mixed concrete. It has three main functions: (1) it reacts with the cement powder, thus producing hydration products; (2) it acts as a lubricant, contributing to the workability of the fresh mixture; and (3) it secures the necessary space in the paste for the development of hydration products. The amount of water added for adequate workability is always greater than that needed for complete hydration of the cement in practice.

Unlike other raw materials, the raw water supply varies significantly in quality, both from one geographical region to another and from season to season. Water derived from an upland surface source, for instance, usually has a low content of dissolved solids and is relatively soft, but has a high concentration of organic contamination, much of it colloidal. By contrast, water from an underground source generally has a high content of dissolved solids and a high hardness level but a low organic content. Seasonal variations in water quality are most apparent in surface waters. During the autumn and winter months, dead leaves and decaying plants release large

quantities of organic matter into streams, lakes, and reservoirs. As a result, the degree of organic contamination in surface waters reaches a peak in spring, and falls to a minimum in summer. Excessive impurities in mixing water not only may affect setting time and concrete strength, but also may cause efflorescence, staining, corrosion of reinforcement, volume instability, and reduced durability.

There is a simple rule concerning the acceptability of mixing water: if water is potable, that is, fit for human consumption, with the exception of certain mineral waters and water containing sugar, it is also suitable for concrete making. In other words, if water does not have any particular taste, odor, or color, and does not fizz or foam when shaken, then there is no reason to assume that such water will hurt the concrete when used properly as mixing water. Some water unsuitable for drinking is still satisfactory for concrete making.

2.4.2 Impurities in water

The unique ability of water in dissolving, to some extent, virtually every chemical compound and supporting practically every form of life means that raw water supplies contain many contaminants. Water impurities can be either dissolved in the water or present in the form of suspensions. Water should be avoided if it contains large quantities of suspended solids, excessive amounts of dissolved solids, or appreciable amounts of organic materials. The major categories of impurities found in raw water include (1) suspended solids; (2) dissolved solids, and (3) dissolved organic material.

Suspended solids in water include silt, clay, pipe work debris, organic matter, and colloids. Usually up to about 2000 ppm of suspended clay or silt can be tolerated (Mindess et al., 2003). Higher amounts may increase water demand, increase drying shrinkage, or cause efflorescence. Muddy water should be allowed to clear in settling basins before use. Colloidal particles, either organic or inorganic, are not truly in solution or suspension and give rise to haze or turbidity in the water. The degree of colloidal contamination can be determined by a fouling index test or by turbidimetry. In the fouling index, raw water is passed through a standard filter and the rate of blockage is measured. The greater the rate of blockage, the greater the amount of colloidal contamination. The turbidimetric method determines the total suspended solids content of the raw water by passing a beam of light through the water and measuring the proportion of light scattered from the suspended particles. Since the mix water quickly becomes a highly alkaline solution, organic materials may dissolve during mixing and subsequently retard setting and strength development by interfering with cement hydration. Organic impurities may also entrain excessive amounts of air, thereby reducing strength, or, conversely, they may interfere with the action of air-entraining agents.

Total dissolved solids (TDS) are the residue in ppm obtained by the traditional method of evaporating a water sample to dryness and heating at 180°C. This residue includes colloids, nonvolatile organic compounds and salts that are stable at this temperature. It can be measured directly or estimated by multiplying the conductivity of the water in μS/cm at 25°C by 0.7. Water containing less than 2000 ppm of dissolved solids can in most instances be used safely, although this depends on the nature of the dissolved material. As little as 100 ppm of sodium sulfide may cause problems. At the other extreme, seawater, which contains about 34,000 ppm (3.4%) of dissolved salts, can be used to make satisfactory concrete if certain precautions are taken. Indeed, soluble salts may be added deliberately as admixtures, the most common example being $CaCl_2$, which is used as an accelerating agent. Soluble carbonates and bicarbonates can promote rapid setting; large quantities of carbonates and sulfates may cause a reduction in 28-day strength or long-term strength. Some soluble inorganic salts may retard the setting and hardening of concrete. Salts of zinc, copper, lead, and, to a lesser extent, manganese and tin fall into this

category, as well as phosphates, arsenates, and borates. Soluble inorganic salts of up to 500 ppm can generally be tolerated in mixing water. Acidic waters can be used in concrete making; the pH of the water may be as low as 3.0, at which level there are more problems surrounding the handling of the water than will occur in the concrete. Organic acids may affect the setting and hardening of concrete. Alkaline waters, containing sodium or potassium hydroxide, may cause quick setting and low strengths at concentrations above 500 ppm.

Organic impurities in water usually arise from the decay of vegetable matter, principally humic and fulvic acids, and from farming, paper making, and domestic and industrial waste. These include detergents, fats, oils, solvents, and residues from pesticides and herbicides. In addition, water-borne organics may include compounds leached from pipe lines, tanks, and purification media. A water purification system can also be a source of impurities and so must be designed not only to remove contaminants from the feed water, but also to prevent additional recontamination from the system itself. Colored natural water generally indicates the presence of dissolved organic material, mostly tannic and humic acids, which may retard the hydration of cements. Many organic compounds that occur in industrial wastes may also severely affect the hydration of cement or entrain excessive amounts of air. Wastes from the pulp and paper industries, the tanning industries, and food-processing industries have been used as a source of chemicals for the formulation of set-retarding or air-entraining admixtures. Thus, untreated industrial wastewaters should be used with caution, but if they have passed through a sewage treatment process, the organic matter will be reduced to safe levels. The degree of organic contamination can be measured by the oxygen-absorption (OA) test using potassium permanganate solution or the chemical oxygen demand (COD) test. Increasingly, however, total organic carbon (TOC) analyzers are being used because of the ease of interpretation of the results and their sensitivity in detecting low levels of organic compounds in water samples.

Oxygen and carbon dioxide are the two gases most commonly found in natural waters. Carbon dioxide behaves as a weak anion and is removed by strong exchange resins. Dissolved oxygen can also be removed by degassing or by anion exchange resins in the sulfite form, and the level of dissolved oxygen in the feed water can be monitored with oxygen-specific electrodes.

2.4.3 Water for curing and washing

The requirements for curing water are less stringent than those discussed above, mainly because curing water is in contact with the concrete for only a relatively short time. Such water may contain more inorganic and organic materials, sulfuric anhydride, acids, chlorides, and so on, than an acceptable mixing water, especially when slight discoloration of the concrete surface is not objectionable. Nevertheless, the permissible amounts of the impurities are still restricted. In cases of any doubt, water samples should be sent to a laboratory for testing and recommendations. Water for washing aggregates should not contain materials in quantities large enough to produce harmful films or coatings on the surface of aggregate particles. Essentially the same requirement holds when the water is used for cleaning concrete mixers and other concreting equipment. Chemical limitations for the impurities in wash water are specified in ASTM C94.

DISCUSSION TOPICS

How are aggregates classified?

Give some examples of aggregates.

Why is the gradation of aggregate important?

What are the important physical properties of aggregates?

Why can the moisture content influence concrete properties?
What are the differences between organic and inorganic binders?
What are the differences between hydraulic and nonhydraulic cement?
What are main chemical components of Portland cement?
What are main hydration products of Portland cement? State their functions in concrete.
How many stages are there in Portland cement hydration?
What happened chemically during each stage of cement hydration?
What are the differences among five types of Portland cement? Give some suitable applications for each type of cement in practice.
What are the main advantages of a geopolymer? What are its main applications?
What are the main advantages of MPC? What are its main applications?
What are the main advantages of MOC? What are its main applications?
How admixtures are classified?
Why does modern concrete technology stress the importance of admixtures?
What is the mechanism for water reducers, air entraining agents, and setting control admixtures?
Compare the chemical composition for four main mineral admixtures.
What are major influences of fly ash on concrete's properties?
What are the main functions of silica fume?
What is the common reaction of mineral admixture in concrete?

PROBLEMS

1. A sample of sand weighs 490 g in stock and 475 g in OD condition, respectively. If absorption capability of the sand is 1.1%, calculate MC(SSD) for the sand.

2. The sieve results of a batch of aggregate are as follows: retained on 1.5" sieve: 0.3 kg; retained on 1" sieve: 1.2 kg; retained on 0.75" sieve: 7.6 kg; retained on 0.5" sieve: 6.2 kg; retained on 3/8" sieve: 4.2 kg; retained on No. 4 sieve: 0.8 kg; retained on No. 8 sieve: 0.1 kg. Calculate the fineness modulus for the aggregate. Is it coarse or fine aggregate?

3. A 1000g sample of coarse aggregate in the SSD condition in air weighed 633g when immersed in water. Calculate the BSG of the aggregate.
If some sample from same batch of aggregate after being exposed to air dry condition for some time weighed 978 g in air and weighed 630 g after they immersed in water for 2 hours, calculate the moisture content, MC(SSD), of the air dried aggregate at that time.

4. A mixture of 1800 g of gravel with an absorption of 1.3% and 1200 g of sand with a surface moisture of 2.51% was added into a concrete mix. Compute the adjustment of water that must be made to maintain a constant w/c ratio.

5. Demonstrate that the specific gravity of a blend of n aggregates with specific gravities of SG_1, SG_2, ..., SGn can be given by:

(a) $SG = SG_1\ P_1 + SG_2\ P_2 + \ldots + SG_n\ P_n$ if P_1, P_2, ..., P_n are the volume fractions of each of the n aggregates

(b)

$$SG = \frac{1}{\frac{p_1}{SG_1} + \frac{P_2}{SG_2} + \bullet\bullet\bullet + \frac{P_n}{SG_n}}$$

If P_1, P_2, ..., P_n are the weight fractions of each of the n aggregates.

6. The material ratio for concrete mix is 1:1.5:2 (C:Sand:Coarse Aggregate by weight). The BSG for cement is 3.15, for sand is 2.5 and for coarse aggregate is 2.7. Air content is 4.8%. The gel/space ratio is 0.72. Calculate the water cement ratio for α=0.8?
7. If one ton Portland cement contains 620kg CaO, how much CO_2 is produced during cement production due to decomposition of limestone?

REFERENCES

Aitcin, P., Jolicoeur, C., and MacGregor, J. (1994) "A look at certain characteristics of superplasticizer and their use in the industry," *Concrete International*, **16** 45–52.

American Society for Testing and Materials, ASTM C230-90, Standard Specification for flow table for use in tests of hydraulic cement.

Bensted, J. and Barnes, P. (2002) *Structure and Performance of Cements*, 2nd ed., London: Spon Press.

Berke, N.S., Dallaire, M.P., and Hicks, M.C. (1999) "New development in shrinkage-reducing admixtures," ACI SP-173-48, Hormington Hills, MI: American Concrete Institute, pp. 973–998.

Bilinski, H., Matkovic, B., Mazuravic, C., and Zunic, T.A. (1984) "The formation of magnesium oxychloride phases in the system of MgO–$MgCl_2$–H_2O and NaOH–$MgCl_2$–H_2O," *Journal of the American Ceramic Society*, **67** 266–269.

Blanco, F., Garcia, M.P., and Ayala, J. (2005) "Variation in fly ash properties with milling and acid leaching", *Fuel*, **84**(1) 89–96.

Caldarone, M.A, Gruber, K.A., and Burg, R.G. (1994) "High-reactivity metakaolin: a new generation mineral admixture," *Concrete International*, **16**(11) 37–40.

Campbell, D.H. and Folk, R.L. (1991) "The ancient pyramids—concrete or rock," *Concrete International: Design & Construction*, **13**(8) 28–39.

Chandra, S, and Bjornstrom, J. (2002) "Influence of cement and superplasticizer type and dosage on the fluidity of cement mortars," *Cement and Concrete Research*, **32**, 1613–1619.

Christensen, B.J., Coverdale, R. T., Olson, R. A., Ford, S.J., Garboczi, E. J., Jennings, H. M., and Mason, T. O. (1994) "Impedance spectroscopy of hydrating cement-based materials: measurement, interpretation, and application," *Journal of the American Ceramic Society*, **77**(11) 2789–2804.

Cole, W. F. and Demediuk, T. (1955) "X-ray, thermal and dehydration studies on magnesium oxychloride," *Australian Journal of Chemistry*, **8**, 234–237.

Comrie Consulting Ltd. (1988) Comrie Preliminary Examination of the Potential of Geopolymers for Use in MineTailings Management, D. Comrie Consulting Ltd., Mississauga, Ontario, Canada.

Davidovits, J. (1987) "Ancient and modern concretes: what is the real difference?" *Concrete International: Design & Construction*, **9**(12) 23–35.

Davidovits, J. (1993) "Geopolymer cement to minimize carbon-dioxide greenhouse warming," *Ceramic Transactions*, **37**, 165–182.

Davidovits, J. (1994a) "Recent progresses in concretes for nuclear waste and uranium waste containment," *Concrete International*, **16**(12) 53–58.

Davidovits, J. (1994b) "Properties of geopolymer cements," Alkaline Cements and Concretes, Kiev Ukraine, page 9.

Davidovits, J. (1994c). "Geopolymers: inorganic polymeric new material", *Journal of Materials Education*, **16**, 91–139.

Davidovits, J., Comrie, D. C., Paterson, J. H., and Ritcey, D. J. (1990) "Geopolymeric concretes for environmental protection," *Concrete International: Design & Construction*, **12**(7) 30–40.

de Henau, P. and Dupas, M. (1976) "Study of the alternation in acropolis monuments," *Proceedings of Second International Symposium on the Deterioration of Building Stone, Athens*, pp. 319–325.

Deng, D. (2003) "The mechanism for soluble phosphates to improve the water resistance of magnesium oxychloride cement," *Cement and Concrete Research*, **33**, 1311–1317.

Deng, D. and Zhang, C. (1999) "The formation mechanism of the hydrate phases in magnesium oxychloride cement," *Cement and Concrete Research*, **29**, 1365–1371.

Ding, J. and Li, Z. (2002) "Effects of metakaolin and silica fume on properties of concrete," *ACI Materials Journal*, **99**(4) 393–398.

EL-Enein, Abo S. A, Kotkata, M. F., and Hannan, G. B. (1995) "Electrical resistivity of concrete containing silica fume," *Cement and Concrete Research*, **25**(8) 1615–1620.

European R&D project BRITE-EURAM BE-7355-93 (1997) Cost-effective geopolymeric cement for innocuous stabilization of toxic elements (GEOCISTEM). final report, April 1997.

Folk, R. L. and Campbell D. H. (1992) "Are the pyramids built of poured concrete blocks?" *Journal of Geological Education*, **40**, 25–34.

Gartner, E. M., Young, E. M., Damidot, D. A., & Jawed, I. (2002) "Hydration of Portland cement." In: Bensted J. and Barnes P., eds., *Structure and performance of cements*, London: Spon Press, pp. 83–84.

Goto, et al. (1985) United States Patent Number 4547223, Oct. 15.

Gu, P., Xie, P. and Fu, Y. (1985) "Microstructural characterization of cementitious materials: conductivity and impedance methods," In Skalny J. and Mindess S., eds., *Materials science of concrete IV* . Cincinnati, OH: American Ceramics Society, pp. 94–124.

Haper, F. C. (1967) "Effect of calcinations temperature on the properties of magnesium oxides for use in magnesium oxychloride cements," *Journal of Applied Chemistry*, **17**, 5–10.

He, Z., Li., Z., Chen, M. and Liang, W. (2006) "Properties of shrinkage-reducing admixture-modified pastes and mortar," *Materials and Structures RILEM* , **39**(4) 445–453.

Hewlett, P. C. (1998) *Lea's chemistry of cement and concrete*, 4th ed., London, Arnold.

Jennings, H. M. and Pratt, P. L. (1980) "On the reactions leading to calcium silicate hydrate, calcium hydroxide and ettingite during the hydration of cement," *Proceedings of the 7th international congress on the chemistry of cement*, Vol. II. Paris: Editions Septima, pp. 141–146.

Ji, Y. (2001) "Study of the new type of light magnesium cement foamed material," Materials Letters, **50**, 28–31.

Jolicoeur, C., Nkinamubanzi, P. C., Simard, M. A., and Piotte, M. (1994) "Progress in understanding the functional properties of superplasticizer in fresh concrete," ACI SP-148, pp. 63–88.

Kantro, D. (1981) "Influence of water-reducing admixtures on properties of cement paste—a miniature slump test," *Research and Development Bulietin*, RD079.01T, Portlan Cement Association.

Kingery, W. D. (1950) "Fundamental study of phosphate bonding in refractories (I): Literature review," *Journal of the American Ceramic Society*, **33**(8) 239–250.

Langley, W., Carette, G. and Malhotra, V. (1989) "Structural concrete incorporating high volume of class F fly ash," *ACI Materials Journal*, **86**(5) 507–514.

Li, Z., and Li, W. (2003) "Contactless, transformer-based measurement of the resistivity of materials," United States Patent 6639401.

Li, Z., Mu, B., and Peng, J. (1999a) "The combined influence of chemical and mineral admixtures upon the alkali-silica reaction," *Magazine of Concrete Research*, **51**(3) 163–169.

Li, Z., Peng, J, and Ma, B. (1999b) "Investigation of chloride diffusion for high-performance concrete containing fly ash, microsilica, and chemical admixtures," *ACI Materials Journal*, **96**(3) 391–396.

Li, Z., Ding, Z., and Zhang, Y. (2003a) "Development of sustainable cementitious materials," *Proceedings of the international workshop on sustainable development and concrete technology*, pp. 55–76.

Li, Z., Wei, X., and Li, W. (2003b) "Preliminary interpretation of Portland cement hydration process using resistivity measurements," *ACI Material Journal*, **100**(3) 253–257.

Lyon, R. E. (1994) Technical Report DOT/FAA/CT-94/60.

Lyon, R. E., Foden, A., Balaguru, P. N., Davidovits, M., and Davidovits, J. (1997) "Fire resistant aluminosilicate composites," *Journal Fire and Materials*, **21**(1), 67–73.

Maravelaki-Kalaitzaki, P. and Moraitou, G. (1999) "Sorel's cement mortars decay susceptibility and effect on pentelic marble," *Cement and Concrete Research*, **29**, 1929–1935.

Matkovic, B. et al. (1977) "Reaction products in magnesium oxychloride cement pastes system $MgO–MgCl_2–H_2O$," *Journal of the American Ceramic Society*, **60**, 504–507.

McCarter, W. J., Whittington, H. W., and Forde, M. C. (1981) "The conduction of electricity through concrete," *Magazine of Concrete and Research*, **33**(114), 48–60.

McCarter, W. J., Chrisp, T. M., Starrs, G., and Blewett, J. (2003) "Characterization and monitoring of cement-based systems using intrin0sic electrical property measurements," *Cement and Concrete Research*, **33**(2) 197–206.

Mckinney, R. G. (1993) "Comments on the work of Harrell and Penrod," *Journal of Geological Education*, **41**, 369.

Ménétrier, D., Jawed, I., Sun, T. S., and Skalny, J. (1979) "ESCA and SEM studies on early C_3S hydration," *Cement and Concrete Research*, **19**(4) 473–482.

Menetrier-Sorrentino, D., Barret, P., and Saquat, S. (1986) "Investigation in the system $MgO–MgCl_2–H_2O$ and hydration of Sorel cement," *Proceedings of the 8th ICCC, Rio de Janeiro*, **4**, 339–343.

Mindess, S., Young, J. F., and Darwin, D. (2003) *Concrete*, 2nd ed,, Upper Saddle River, NJ: Prentice Hall.

Morris, M. (1991) "The cast-in-place theory of pyramid construction," *Concrete International: Design & Construction*, **13**(8) 39–44.

Neville, A. M. and Brooks, J. J. (1990) *Concrete technology*, Essex, UK: Longman Group.

Odler, J. (2000) *Special inorganic cements*, London: E & FN Spon.

Penttala V. (1997) "Concrete and sustainable development," *ACI Materials Journal*, **94**(5) 409–416.

Popovics, S. (1992). *Concrete materials: properties, specifications, and testing*, Park Ridge, NJ: Noyes Publications.

Prince, W., Edwards-Lajnef, M., and Aitcin, P. C. (2002) "Interaction between ettringite and polynapthalene sulfonate superplasticizer in cementitious paste," *Cement and Concrete Research*, **32**(1) 79–85.

Ramachandran, V. S. (2002) Concrete admixtures handbook, New Delhi: Standard Publishers.

Rixom, R. and Mailvaganam, N. (1999) Chemical Admixtures for concrete, E & FN Spon, London.

Seehra, S. S., Gupta, S., and Kumar, S. (1993) "Rapid setting magnesium phosphate cement for quick repair of concrete pavements—characterization and durability aspects," *Cement and Concrete Research*, **23**(2) 254–266.

Singh, D., Wagh, A., Cunnane, J., and Mayberry, J. (1997) "Chemically bonded phosphate ceramics for low-level mixed-waste stabilization," *Journal of Environmental Science and Health*, A**32**(2) 527–541.

Sorel, S. (1867) "On a new magnesium cement," *Compes Rendus, Hebdomadaires des Seances de l'Academie des Sciences*, **65**, 102–104.

Sorrel, C. A. and Armstrong, C. R. (1976) "Reactions and equilibria in magnesium oxychloride cements," *Journal of the American Ceramic Society*, **59**, 51–59.

Tashiro, C., Ikeda, K., and Inome, Y. (1994) "Evaluation of pozzolanic activity by the electric resistance measurement method," *Cement and Concrete Research*, **24**(6) 1133–1139.

Taylor H. F. W. (1997) *Cement chemistry*, 2nd ed., London: Telford.

Taylor, M. A. and Arulanadan, K. (1974) "Relationships between electrical and physical properties of cement pastes," *Cement and Concrete* Research, **4**(6), 881–897.

Thomas, M. D. A., Gruber, K. A., and Hooton R. D. (1997) "The use of high-reactivity metakaolin in high-performance concrete," in Azizinamini, A. Darwin, D., and French, C., eds., *High Strength Concrete, Proceedings of the First International Conference*, Kona, HI: ASCE, 517–530.

Uchikawa, H., Hanehara, S., and Sawaki, D. (1997) "The role of steric repulsive force in the dispersion of cement particles in fresh paste prepared with organic admixture," *Cement and Concrete Research*, **27**, 37–50.

Urwongse, L. and Sorrell, C. A. (1980) "The system MgO–MgCl2–H2O at 23°C," *Journal of the American Ceramic Society*, **63**, 501–504.

Van Jaarsveld, J. G. S. and van Deventer, J. S. J. (1997) "The potential use of geopolymeric materials to immobilize toxic metals: Part I. Theory and applications," *Minerals Engineering*, **10**(7), 659–669.

Van Jaarsveld, J. G. S. and van Deventer, J. S. J. (1999a). "The effect of metal contaminants on the formation and properties of waste-based geopolymers," *Cement and Concrete Research*, **29**(12), 1189–1200.

Van Jaarsveld, J. G. S., van Deventer, J. S. J., and Lorenzen, L. (1998) "Factors affecting the immobilization of metals in geopolymerized fly ash," *Metallurgical and Materials Transactions B*, **29**B(1), 283–291.

Van Jaarsveld, J. G. S., van Deventer, J. S. J. and Schwartzman, A. (1999b) "The potential use of geopolymeric materials to immobilize toxic metals: Part II. Material and leaching characteristics," *Minerals* Engineering, **12**(1), 75–91.

Waddall, J. J. and Dobrowolski, J. A. (1993) Concrete construction handbook, 3rd ed., York: McGraw-Hill.

Wagh, A., Strain, R., Jeong, S., Reed, D., Krouse T., and Singh, D. (1999) "Stabilization of rocky flats Pu-contaminated ash within chemically bonded phosphate ceramics," *Journal of Nuclear Materials*, **265**(3), 295–307.

Wei, X. and Li, Z. (2005) "Study on hydration of Portland cement with fly ash using electrical measurement," Materials and Structures, **38**(277), 411–417.

Xiao, L., Li, Z. and Wei, X. (2007) "Selection of superplasticizer in concrete mix design by measuring the early electrical resistivities of pastes," *Cement Concrete and Composites*, **29**, 350–356.

Xie, Z. H. and Xi, Y.P. (2000) "Hardening mechanism of an activated class F fly ash", *Cement and Concrete Research*, **31**, 1245–1249.

Yang, Q. B., Zhang, S. Q and Wu, X. L. (2002) "Deicer-scaling resistance of phosphate cement-based binder for rapid repair of concrete," *Cement and Concrete Research*, **32**(1), 165–168.

Yao, W., Li, Z., and Wu, K. R. (1998) "Effects of slag upon the flowability and mechanical properties of high strength concrete," *Proceedings of sixth CANMET/ACI international conference on fly ash, silica fume, slag and natural pozzolans in concrete*, Bangkok, Thailand, pp. 413–424.

Yoshizake, Y., Ikeda, K., Yoshida, S. and Yoshizumi, A. (1989) "Physicochemical study of magnesium-phosphate cement," *Proceedings of the MRS International Meeting on Advanced Materials*, **13**, 27–38.

CHAPTER 3

FRESH CONCRETE

Fresh concrete is defined as a fully mixed concrete in a rheological state that has not lost its plasticity. The fresh concrete stage covers the cement hydration stages I and II. The plastic state of fresh concrete provides a time period for transportation, placing, compaction, and surface finishing. The properties of fresh concrete have a large influence on construction speed and decision making.

3.1 WORKABILITY OF FRESH CONCRETE

Having discussed the constituents of concrete, we can now examine the properties of freshly mixed concrete. The properties of fresh concrete affect the choices of handling, consolidation, and construction sequence. They may also affect the properties of the hardened concrete. The properties of fresh concrete are short-term requirements in nature, and should satisfy the following requirements:

1. It must be easily mixed and transported.
2. It must be uniform throughout a given batch, and between batches.
3. It must keep its fluidity during the transportation period.
4. It should have flow properties such that it is capable of completely filling the forms.
5. It must have the ability to be fully compacted without segregation.
6. It must set in a reasonable period of time.
7. It must be capable of being finished properly, either against the forms or by means of troweling or other surface treatment.

Compaction plays an important role in ensuring the long-term properties of the hardened concrete, as proper compaction is vital in removing air from concrete and in achieving a dense concrete structure. Subsequently, the compressive strength of concrete can increase with an increase in the density. Traditionally, compaction is carried out using a vibrator. Nowadays, the newly developed self-compacting concrete can reach a dense structure by its self-weight without any vibration.

3.1.1 Definition of workability

Workability of concrete is defined in ASTM C125 as the property determining the effort required to manipulate a freshly mixed quantity of concrete with minimum loss of homogeneity (uniform). The term manipulate includes the early-age operations of placing, compacting, and finishing. Mindess et al. (2003) defined the workability of fresh concrete as "the amount of mechanical work, or energy, required to produce full compaction of the concrete without segregation."

The effort required to place a concrete mixture is determined largely by the overall work needed to initiate and maintain flow, which depends on the rheological properties of the cement

paste and the internal friction between the aggregate particles, on the one hand, and the external friction between the concrete and the surface of framework, on the other hand. Workability of fresh concrete consists of two aspects: consistency and cohesiveness. Consistency describes how easily fresh concrete flows, while cohesiveness describes the ability of fresh concrete to hold all the ingredients together uniformly. Traditionally, consistency can be measured by a slump-cone test, the compaction factor, or a ball penetration compaction factor test as a simple index for fluidity of fresh concrete. Cohesiveness can be characterized by a Vebe test as an index of both the water-holding capacity (the opposite of bleeding) and the coarse-aggregate-holding capacity (the opposite of segregation) of a plastic concrete mixture. The flowability of fresh concrete influences the effort required to compact concrete. The easier the flow, the less work is needed for compaction. A liquid-like self-compacting concrete can completely eliminate the need for compaction. However, such a concrete has to be cohesive enough to hold all the constituents, especially the coarse aggregates in a uniform distribution during the process of placing.

Workability is not a fundamental property of concrete; to be meaningful it must be related to the type of construction and methods of placing, compacting, and finishing. Concrete that can be readily placed in a massive foundation without segregation would be entirely unworkable in a thin structural member. Concrete that is judged to be workable when high-frequency vibrators are available for consolidation, would be unworkable if hand tamping were used.

The significance of workability in concrete technology is obvious. It is one of the key properties that must be satisfied. Regardless of the sophistication of the mix design procedures used and other considerations, such as cost, a concrete mixture that cannot be placed easily or compacted fully is not likely to yield the expected strength and durability characteristics.

3.1.2 Measurement of workability

Unfortunately, there is no universally accepted test method that can directly measure the workability as defined earlier. The difficulty in measuring the mechanical work defined in terms of workability, the composite nature of the fresh concrete, and the dependence of the workability on the type and method of construction makes it impossible to develop a well-accepted test method to measure workability. The most widely used test, which mainly measures the consistency of concrete, is called the slump test. For the same purpose, the second test in order of importance is the Vebe test, which is more meaningful for mixtures with low consistency. The third test is the compacting factor test, which attempts to evaluate the compactability characteristic of a concrete mixture. The fourth test method is the ball penetration test that is somewhat related to the mechanical work.

3.1.2.1 Slump test

The equipment for the slump test is indeed very simple. It consists of a tamping rod and a truncated cone, 300 mm in height, 100 mm in diameter at the top, and 200 mm in diameter at the bottom, see Figure 3-1. To conduct a slump test, first moisten the slump test mold and place it on a flat, nonabsorbent, moist, and rigid surface. Then hold it firmly to the ground by foot supports. Next, fill 1/3 of the mold with the fresh concrete and rod it 25 times uniformly over the cross section. Likewise fill 2/3 of the mold and rod the layer 25 times, then fill the mold completely and rod it 25 times. If the concrete settles below the top of the mold, add more. Strike off any excessive concrete. Remove the mold immediately in one move. Measure and record the slump as the vertical distance from the top of the mold to average concrete level. The sequence of a slump test is shown in Figure 3-2.

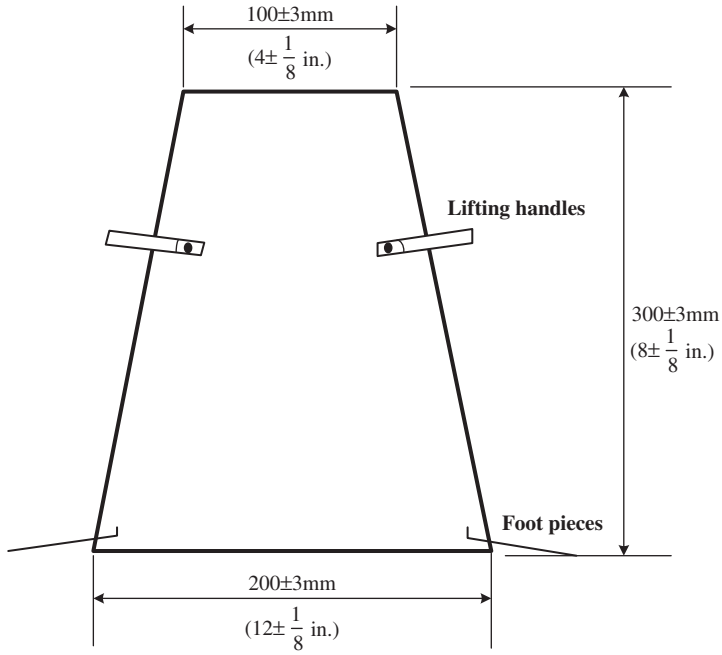

Figure 3-1 Truncated cone for the slump test

a b c

Figure 3-2 Sequence of slump test

If slumping occurs evenly all around, it is regarded as a true slump. If one-half of the cone slides down along an inclined plane, it is regarded as shear slump. Shear slump is caused by insufficient cohesiveness and the concrete proportions should be adjusted. Mixes of very stiff consistency have zero slump, so that in the rather dry range no slump can be detected between mixes of different workability. There is no problem with rich mixes, their slumps are sensitive to variations in workability; however, in a lean mix with a tendency to harshness, a true slump can be easily changed to the shear type, or even collapse with a nonuniform distribution of aggregates, especially coarse aggregates, and widely different values of slump can be obtained in different samples from the same mix. Thus, the slump test is unreliable for lean mixes.

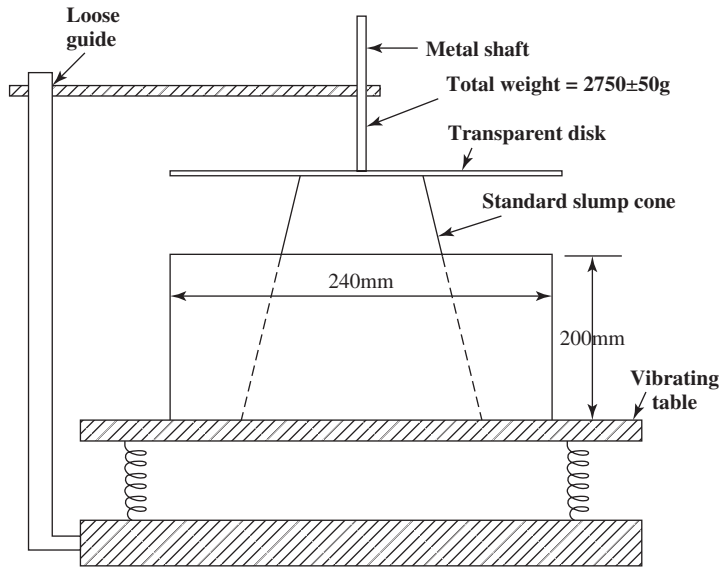

Figure 3-3 Vebe test setup

3.1.2.2 Vebe test

The test equipment, which was developed by Swedish engineer V. Bahrner, is shown in Figure 3-3. It consists of a vibrating table, a cylindrical pan, a slump cone, and a glass or plastic disk attached to a free-moving rod, which serves as a reference endpoint. The cone is placed in the pan. After it is filled with concrete and any excessive concrete is struck off, the cone is removed. Then, the disk is brought into a position on top of the concrete cone, and the vibrating table is set in motion. The time required for the concrete cone to shorten and change from the conical to a cylindrical shape, until the disk on the top is completely covered with concrete, is the index of workability and is reported as the number of Vebe seconds.

The Vebe test is a good laboratory test, particularly for very dry mixes. This is in contrast to the compacting factor test where error may be introduced by the tendency of some dry mixes to stick in the hoppers. The Vebe test also has the additional advantage that the treatment of concrete during the test is comparatively closely related to the method of placing in practice. Moreover, the cohesiveness of concrete can be easily distinguished by Vebe test through the observation of distribution of the coarse aggregate after vibration.

3.1.2.3 Compaction factor

Figure 3-4 shows the compaction factor test apparatus. It consists of two hoppers and one cylindrical mold stacked in three levels. To perform an experiment, the upper hopper is first fully filled with fresh concrete. Then the hinged door is slid open and hence the concrete will fall into the lower hopper by gravity. Next, the hinged door of the power hopper is slid open and the concrete free falls into the 150 × 300 mm cylindrical mold. After the excessive concrete is struck off on the top of the mold, the weight of the cylinder is measured and noted as M_p, representing a partially compacted cylinder mass. Another cylinder is made with same concrete by three layers with 25 times rodding on each layer and striking off any excessive concrete.

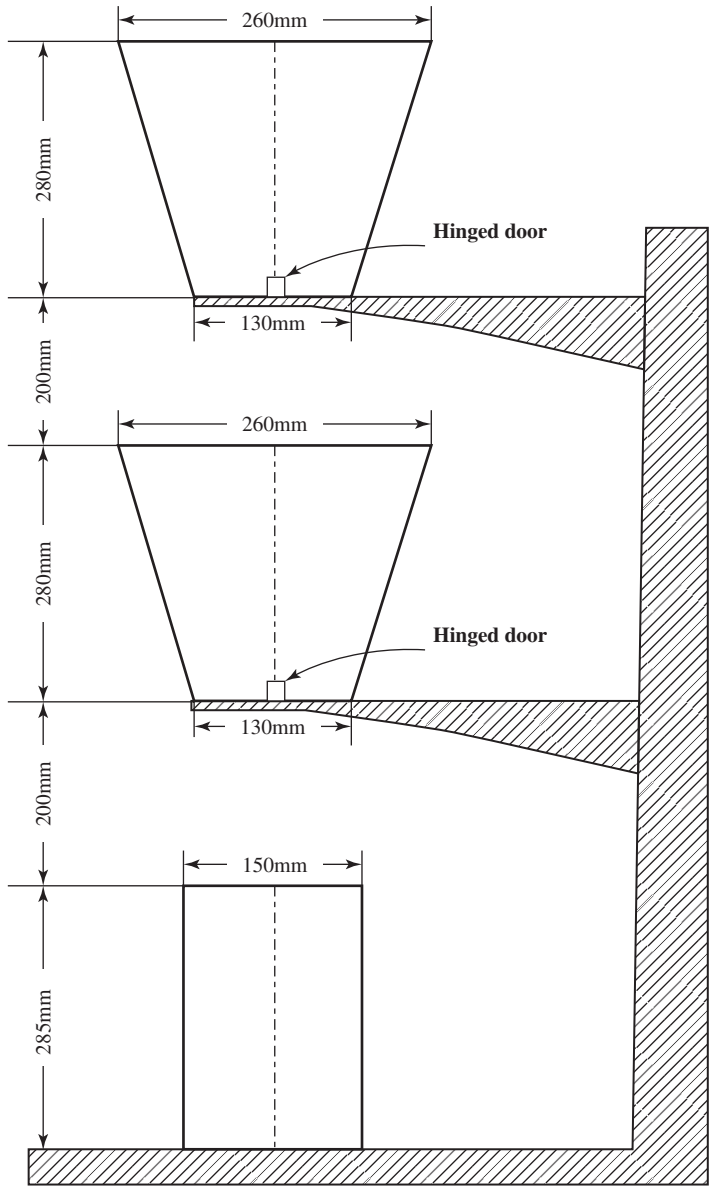

Figure 3-4 Compaction factor test apparatus

The weight of the cylinder is measured as M_f, representing the fully compacted cylinder mass. The compaction factor is defined as

$$\text{compaction factor} = \frac{M_p}{M_f} \tag{3-1}$$

Usually, the range of compaction factor is from 0.78 to 0.95 and concrete with high fluidity has a higher compaction factor.

3.1.2.4 Ball penetration test

ASTM C360 covers the Kelly ball penetration test. The test setup is shown in Figure 3-5. A 152-mm-diameter hemisphere hammer of weight 13.6 kg is connected to a handle with a ruler. The hammer is fixed on a box container through a pin. When taking measurements, the box is placed on the top of the concrete to be tested with the surface of the hammer touching the concrete. When the pin is removed, the hammer will sink into the fresh concrete by its own weight. The depth of the hammer penetration can be read from the ruler and is used as an index of workability. A concrete with higher consistency leads to a deeper ball penetration. Since the measurement is related to the work done by the hammer penetration, ball penetration

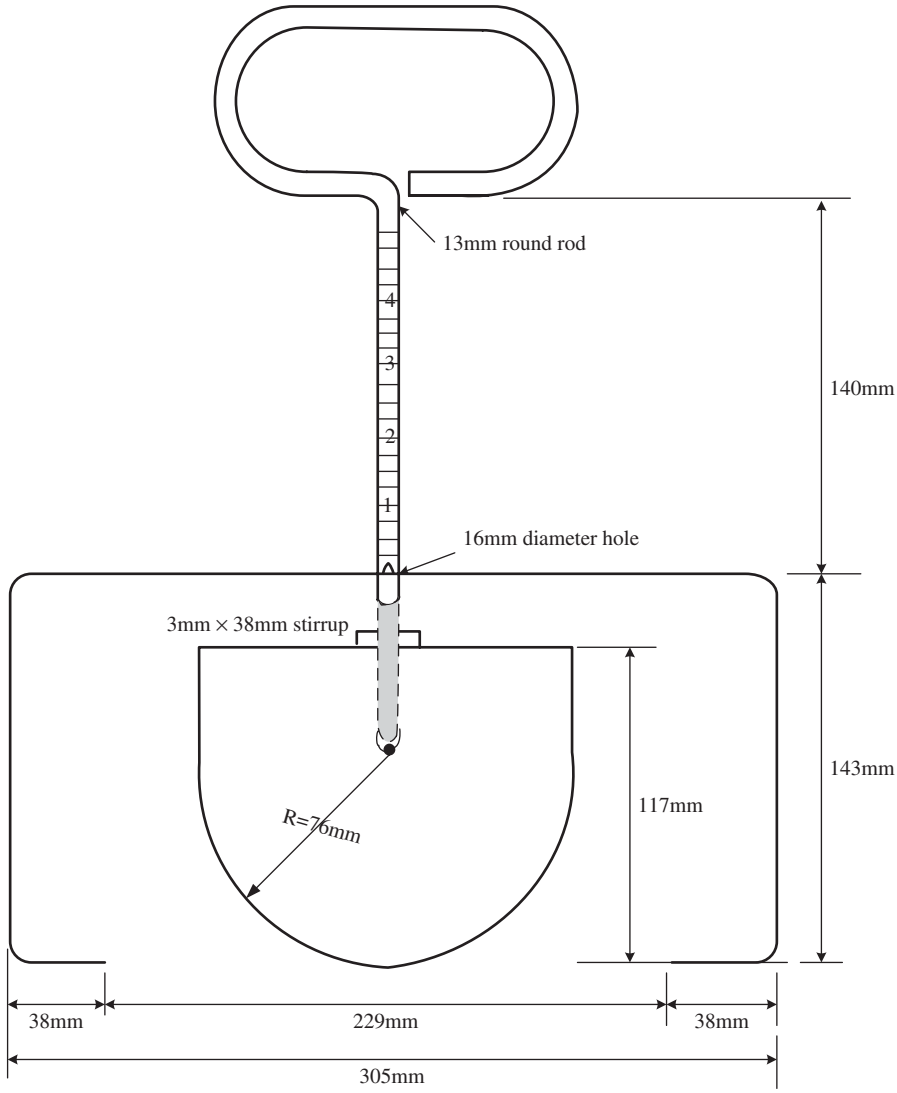

Figure 3-5 Ball penetration test setup

measurement is close to the definition of workability given by Mindess et al. (2003). The penetration test is usually very quick and can be done on site, right in the formwork, provided it is wide enough. The ratio of slump value to penetration depth is from 1.3 to 2.0.

3.1.3 Factors affecting workability

The workability of concrete contains two aspects, consistency and cohesiveness. Due to the different requirements and characteristics of the two aspects, the influence of a factor on workability may be opposite. In general, through the influence on consistency and/or cohesiveness, the water content, the cement content, the aggregate grading, and other physical characteristics, and admixtures can affect the workability of concrete mixtures.

3.1.3.1 Water content

Water content is regarded as the most important factor influencing the workability of concrete. After adding water to a concrete mix, the water is absorbed on the surface of the particles of the cement and aggregates. Additional water fills the spaces among the particles and "lubricates" the particles by a water film. Decreasing the water content will result in a low fluidity. If the water content is too small, the concrete will become too dry to mix and place. Increasing the amount of water will increase the amount of water for lubrication and hence improve the fluidity and make it easy to be compacted. However, too much water will reduce cohesiveness. This not only leads to segregation and bleeding, but also reduces the concrete strength. The water content in a concrete is determined by w/c or w/b and cement or binder content.

3.1.3.2 Cement content

Cement content influences the workability of concrete in two ways. First, for given w/c ratio, the larger the cement content, the higher the total water amount in the concrete; hence, the consistency of concrete will be enhanced. Second, cement paste itself plays the roles of coating, filling, and lubrication for aggregate particles. In normal concrete, a considerably low cement content tends to produce a harsh mixture, with poor consistency and, subsequently, poor finishability. High cement content implies that more lubricant is available for consistency improvement. Finally, with an increase of the cement content at a low w/c ratio, both consistency and cohesiveness can be improved. Under the same w/c ratio, the higher the cement content, the better the workability.

Increasing the fineness of the cement particles will decrease the fluidity of the concrete at a given w/c ratio, but will increase the cohesiveness. Concretes containing a very high proportion of cement or very fine cement show excellent cohesiveness but tend to be sticky.

3.1.3.3 Aggregate characteristics

Aggregates can influence the workability of concrete through their need for surface coating and their friction and mobility during mixing, placing, and compaction. Maximum aggregate size, aggregate/cement ratio, fine aggregate/coarse aggregate ratio, and aggregate shape and texture are four aspects influencing the workability of concrete.

The particle size of coarse aggregates influences the paste requirement for coating through the surface area. The larger aggregates have smaller surface area than smaller aggregates with the same volume. Subsequently, the amount of the paste available for lubrication is increased for concrete with large aggregates, and consistency is improved. Hence, for a given w/c ratio, as the maximum size of aggregate increases, the fluidity increases. Moreover, very fine sands or

angular sands will require more paste for a given consistency; alternatively, they will produce harsh and unworkable mixtures at water contents that might have been adequate with coarser or well-rounded particles. In general, to get a similar consistency of concrete, more water is needed when crushed sand is used instead of natural sands.

The aggregate/cement ratio influences the paste requirement. A higher aggregate/cement ratio implies more aggregates and less cement paste. Thus, the concrete consistency decreases with aggregate/cement ratio increase due to less cement paste being available for lubrication.

Fine aggregate/coarse aggregate ratio also affects the cement paste requirement. With an increase of the fine aggregate/coarse aggregate ratio, concrete contains more fine aggregates and less coarse aggregates. Thus, the total surface area of the aggregates increases, which leads to a higher demand on the cement paste for surface coating. As a result, the consistency of concrete decreases and the cohesiveness improves. Increasing the fine aggregate/coarse aggregate ratio is the most effective measure to increase the cohesiveness of concrete.

The shape and texture of aggregate particles can affect the workability of concrete through the influence on paste requirement, particle moving friction, and moving ability. Cubical, irregular, granular, and rough aggregates require more coating cement paste and have higher friction than spherical, glassy, and smooth aggregates. As a general rule, the more spherical the particles, the more workable is the concrete.

3.1.3.4 Admixtures

Both chemical and mineral admixtures can influence the workability of concrete. Their effects have been discussed in Chapter 2. For instance, an air-entraining agent increases the paste volume and improves the consistency of concrete for a given water content through the entrained air. The entrained air also increases cohesiveness by reducing bleeding and segregation. Improvement in consistency and cohesiveness by air entrainment is more pronounced in harsh and unworkable mixtures, such as in mass concrete, which has low cement content. Water-reducing admixtures can improve the fluidity of concrete due to the dispersing effect on cement particles and the releasing of entrapped water by cement clusters. Similarly, when the water content of concrete mixtures is held constant, the addition of water-reducing admixtures (plasticizer) will increase the consistency.

Different mineral admixtures have different effects on workability, although they all tend to improve the cohesiveness of concrete. Fly ash, when used as a partial replacement for cement, generally increases the consistency at a given water content due to the spherical shape and glassy surface. When silica fume is used to replace part of the cement, it tends to reduce the amount of water used for lubrication, due to its very large surface area and hence the need for a water film coating.

3.1.3.5 Temperature and time

Freshly mixed concrete stiffens with time due to evaporation of the mixing water, particularly when the concrete is directly exposed to sun or wind, absorption by the aggregate, and consumption in the formation of hydration products. The stiffening of concrete is effectively measured by a loss of workability with time, known as slump loss, which varies with richness of the mix, type of cement, temperature of the concrete, and initial workability. A high temperature reduces the workability and increases the slump loss because the hydration rate is higher and the loss of water is faster at a higher temperature. In practice, when the ambient conditions are unusual, it is best to perform actual site tests to determine the workability of the mix.

3.1.4 Segregation and bleeding

3.1.4.1 Segregation

In discussing the workability of concrete, it has been pointed out that cohesiveness is an important characteristic of the workability. A proper cohesiveness can ensure concrete to hold all the ingredients in a homogeneous way without any concentration of a single component, and even after the full compaction is achieved. An obvious separation of different constituents in concrete is called segregation, as shown in Figure 3-6. Thus, segregation can be defined as concentration of individual constituents of a heterogeneous (nonuniform) mixture so that their distribution is no longer uniform. In the case of concrete, it is the differences in the size and weight of particles (and sometimes in the specific gravity of the mix constituents) that are the primary causes of segregation, but the extent can be controlled by the concrete proportion, choice of suitable grading, and care in handling.

3.1.4.2 Bleeding

Bleeding is a form of local concentration of water in some special positions in concrete, usually the bottom of the coarse aggregates, the bottom of the reinforcement, and the top surface of the concrete member, as shown in Figure 3-7. During placing and compaction, some of water in

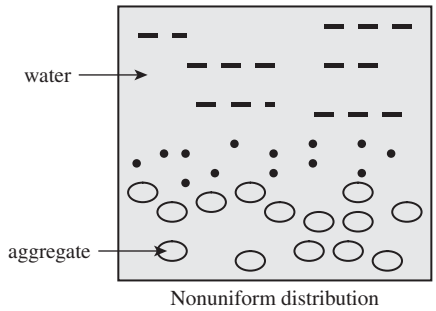

Figure 3-6 Segregation of concrete mixture

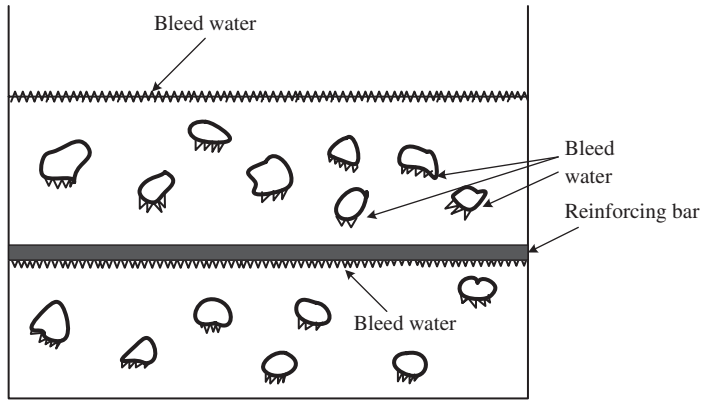

Figure 3-7 Bleeding phenomenon

the mix tends to rise to the surface of freshly placed concrete. This is caused by the inability of the solid constituents of the mix to hold all the mixing water when they settle downward due to the lighter density of water. Bleeding can be expressed quantitatively as the total settlement (reduction in height) per unit height of concrete, and bleeding capacity as the amount (in volume or weight) of water that rises to the surface of freshly placed concrete.

As a result of bleeding, an interface between aggregates and bulk cement paste is formed, and the top of every lift (layer of concrete placed) may become too wet. If the water is trapped by the superimposed concrete, a porous and weak layer of nondurable concrete may result. If the bleeding water is remixed during the finishing process of the surface, a weak wearing surface can be formed. This can be avoided by delaying the finishing operations until the bleeding water has evaporated, and also by the use of wood floats and avoidance of overworking the surface. On the other hand, if evaporation of water from the surface of the concrete is faster than the bleeding rate, plastic shrinkage cracking may be generated.

3.1.5 Slump loss

Slump loss can be defined as the loss of consistency in fresh concrete with elapsed time. Slump loss is a normal phenomenon in all concretes because it results from gradual stiffening and setting of hydrated cement paste, which is associated with the formation of hydration products such as ettringite and calcium silicate hydrate. Slump loss occurs when the free water from a concrete mixture is removed by hydration reactions, by absorption on the surface of hydration products, and by evaporation. Slump loss should be controlled to an acceptable value, especially for concrete transported with a long delivery time, to ensure that it is still placeable and compactable when shipped to the construction site. Slump loss can be minimized by using a setting retarder.

3.1.6 Setting of concrete

3.1.6.1 Definition

Setting of concrete is distinguished as the initial and final setting of cement paste. The initial setting is defined as the loss of plasticity or the onset of rigidity (stiffening or consolidating) in fresh concrete. The final setting is defined as the onset point of strength. It is different from hardening, which describes the development of useful and measurable strength. Setting precedes hardening, although both are controlled by the continuing hydration of the cement. The measurement of the setting time for concrete is very different from that of cement paste. For cement paste, it uses the samples made of the water amount needed for consistency. For concrete, it uses the sieved mortar from a concrete with different water/cement or water/binder ratios. Moreover, for cement paste, it measures the penetration depth of the Vicat needle, 1 mm in diameter, under a constant weight. For concrete, it measures the resistance of the mortar to a rod under an action of the load. A setup for concrete setting time measurement is shown in Figure 3-8.

It can be seen from Figure 3-8 that the container is full with the sieved mortar from a concrete. A steel rod is fixed on a load cell. The rod and load cell can be moved downward and penetrate into the mortar. The resistance of the rod encountered during the penetration process can be measured by a load cell and displayed on a meter. ASTM C 403 (1995) defines two points as the initial setting time and the final setting time, corresponding approximately to the point at which the concrete will no longer be plastic during vibration, and a concrete strength gain of about 0.7 MPa. Initial setting and final setting of concrete are determined by the times at which the penetration resistance reaches 3.5 and 27.6 MPa, when a designated rod penetrates 25.4 mm into the mortar, sieved from the fresh concrete.

Figure 3-8 Measurement setup of concrete mixture setting time

3.1.6.2 Abnormal setting

(a) *False setting*: If a concrete stiffens rapidly in a short time right after water is added and restores its fluidity by remixing and sets normally, it is called false setting. The main reason causing the false setting is crystallization of gypsum. In the last procedure in the process of cement production, gypsum is milled with a clinker by intergrounding. During grinding, due to clinkers that may be still very hot and heat generated by friction, the temperature can rise to about 120°C, thus causing the reaction

$$C\overline{S}H_2 \xrightarrow{120^\circ C} C\overline{S}H_{1/2} \tag{3-2}$$

$C\overline{S}H_{1/2}$ is called half-water gypsum or plaster. During mixing, when water is added, the plaster will rehydrate back to two-water gypsum, form a crystalline matrix quickly, and make the concrete stiffen. However, due to the small amount of plaster in the mix, very little strength will actually develop and the fluidity can be easily restored by further mixing to break the plaster set. Hence, it is not real setting, but false setting.

(b) *Flash setting*: Flash setting is caused by the formation of large quantities of monosulfoaluminate or other calcium aluminate hydrates due to quick reactivities of C_3A, without the presence of gypsum. This is a rapid set and thus is a more severe condition than

false setting. However, as mentioned before, flash setting has been largely eliminated by the addition of 3 to 5% gypsum to the cement, which can react with C_3A and water to form AFt as a barrier layer of C_3A to prevent further reaction of C_3A, as discussed in Chapter 2.

3.1.6.3 New method for determining concrete setting time

Concrete setting time is a crucial parameter for construction progress and concrete quality control. When the setting time is known, the times of mixing, transporting, casting, and finishing can be regulated and the effectiveness of various set-controlling admixtures can be decided. In addition, the setting time also influences the time of demolding. As discussed earlier, the initial and final setting times of concrete are measured by a penetration method that has been standardized in ASTM C 403 (1995). This method utilizes a sieved mortar for penetration testing. However, it is hard work to obtain the mortar fraction through a 4.75-mm sieve from fresh concrete, especially for concretes with poor fluidity. Additionally, for concrete with the incorporation of a retarder, it probably takes an operator more than ten hours to finish the test, at regular intervals. Moreover, the test results can be largely affected by the skill of the operators. For these reasons, there have been some attempts to use alternative techniques, such as the impact-echo method (Pessiki and Carino, 1988) and ultrasonic measurement (Subramaniam et al., 2005; Lee et al., 2004; Voigt et al., 2005) to determine the setting time for concretes. The impact-echo method defines the setting time of concrete as when the wave velocity begins to increase. However, it is hard to impact on early-age concrete and is thus not practical. The ultrasonic method is based on generation, transmission, and reflection of mechanical waves in concrete. Preliminary studies have shown good correlation between the measured wave reflection factor and the hydration process.

Recently, the noncontacting electrical resistivity method has been used to determine the setting time of concrete based on the characteristic points on the resistivity measurement curve of concrete (Li et al., 2007). The electrical resistivity of concrete is measured by a noncontacting electrical resistivity apparatus, which is introduced in detail in Chapter 8. The transformer principle was adopted in this apparatus. Three typical examples of the bulk electrical resistivity development with time (ρ–t) for plain concrete, concrete containing superplasticizers, and concrete with a higher water cement ratio are plotted in Figure 3-9. Figure 3-9a shows ρ change with time up to 400 min and the characteristic point at the minimum resistivity, P_m, is marked as solid dots on the curves. Figure 3-9b shows the ρ change up to 1440 min on a logarithmic scale and the second critical point P_t, is identified on the curves.

These two characteristic points have been utilized to relate to the setting times of the concrete measured by the penetration method. The relationships (Equations 3-3 and 3-4) have been developed using regression methods:

$$t_t = 1.8807t_m + 0.4429t_t \ (R^2 = 0.8950) \tag{3-3}$$

$$t_f = 0.9202t_t + 0.2129 \ (R^2 = 0.9895) \tag{3-4}$$

Equation 3-3 is for initial setting time and Equation 3-4 for final setting time. Figure 3-10 shows the comparison of the predicted initial and final setting using Equations 3-3 and 3-4 and that measured using the penetration test. Good agreement is found, as shown in the figure. This proves that it is possible to use the electrical resistivity measurement method to judge the setting time of concrete, especially the final setting time. Figure 3-10 plots the measured and calculated setting times and a good correlation can be observed.

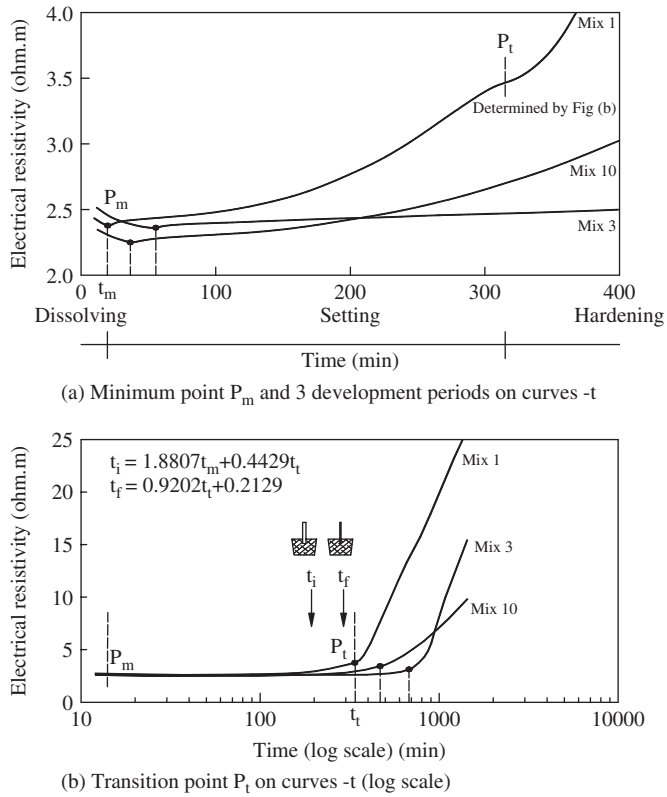

Figure 3-9 The electrical resistivity response of concretes

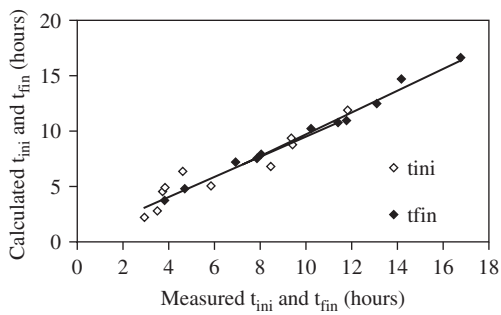

Figure 3-10 Correlation of measured and calculated setting times

The electrical resistivity method (ERM) provides practical advantages over the conventional penetration resistance method because it can continuously measure the data immediately after mixing and can be conducted directly on concrete rather than on sieved mortar. ERM needs only about 0.0016 m^3 of fresh concrete, but the penetration method needs at least 0.01 m^3 of mortar sieved from fresh concrete. ERM is a practical method to assess the setting time and strength development trend, and gives the in situ information to determine the demolding time.

3.2 MIX DESIGN

The mix design of concrete is the process of deciding what type of raw material and how much of each raw material needs to be selected to make concrete that can meet prerequisites such as strength, durability, and workability. The required properties of hardened concrete are specified by the designer of the structure and the properties of fresh concrete are governed by the type of construction and by the techniques of placing and transporting. These two sets of requirements are the main factors that determine the composition of the mix, also taking account of the construction experience on site. Mix design can, therefore, be defined as the processes of selecting suitable ingredients and determining their relative quantities, with the purpose of producing an economical concrete that has certain minimum properties, notably workability, strength, and durability. It should be pointed out that the mix design of concrete is frequently done by trial and error. Hence, mix design of concrete is an art, not a science. This means that the mix design of concrete in the strict sense is not possible: the materials used vary in a number of respects and their properties cannot be assessed truly quantitatively, so that we are really making no more than an intelligent guess at the optimum combinations of the ingredients on the basis of relationships established in the earlier sections. It is not surprising, therefore, that to obtain a satisfactory mix, we must check the estimated proportions of the mix by making trial mixes and, if necessary, make appropriate adjustments to the proportions until a satisfactory mix has been obtained (Neville and Brooks, 1994).

3.2.1 Principal requirements for concrete

The main purpose of the mix design is to obtain a product that will perform according to predetermined requirements. These requirements include the following concrete properties.

(a) *Quality (strength and durability)*: Strength and permeability of hydrated cement paste are mutually related through the capillary porosity that is controlled by w/c ratio and degree of hydration. Since durability of concrete is controlled mainly by its permeability, there is a relationship between strength and durability. Consequently, routine mix design usually focuses on strength and workability only. When the concrete is exposed to special environmental conditions, provisions on durability (e.g., limit on w/c ratio, minimum cement content, minimum cover to steel reinforcement) will also be considered.

(b) *Workability*: As mentioned earlier, workability is a complicated concept for fresh concrete and embodies various properties, including consistency and cohesiveness. There is still not a single test method that can fully reflect workability. Since the slump represents the ease with which the concrete mixture will flow during placement, and the slump test is simple and quantitative, most mix design procedures rely on slump as a crude index of workability. Sometimes, the Vebe time may be employed.

(c) *Economy*: Among all the constituents of the concrete, the admixture has the highest unit cost, followed by cement. The cost of aggregates is about one-tenth that of cement. Admixtures are often used in small amounts, or they are required to achieve certain properties. To minimize the cost of concrete, the key consideration is the cement cost. Therefore, all possible steps should be taken to reduce the cement content of a concrete mixture without sacrificing the desirable properties, such as strength and durability. The scope for cost reduction can be enlarged further by replacing a part of the Portland cement with cheaper materials, such as fly ash or ground blast-furnace slag.

As mentioned earlier, under normal conditions, it is sufficient to consider workability and strength for concrete design. For special conditions, additional considerations on dimensional stability and durability have to be taken into account.

3.2.2 Weight method and absolute volume method

There are two approaches for concrete mix design; the weight method and the absolute volume method. In the weight method, the unit weight of fresh concrete is known from previous experience for the commonly used raw materials and is used to calculate the weight of the last unknown component of concrete, usually the sand. If the unit weight of fresh concrete (wet concrete) is known, we have

$$W_{\text{wet concrete}} = W_{\text{cement}} + W_{\text{water}} + W_{\text{aggregate}} + W_{\text{sand}} + W_{\text{admixtures}} \tag{3-5}$$

If the weights of cement, water, coarse aggregate, and admixtures have been determined, then the weight of sand can be obtained from above equation. The unit weight of wet concrete usually ranges from 2300 to 2400 kg/m^3.

In the absolute volume method, the total volume ($1\,\text{m}^3$) is equal to the sum of volume of each ingredient (i.e., water, air, cement, and coarse aggregate). Thus, we have

$$\frac{W_{\text{cement}}}{\rho_{\text{cement}}} + \frac{W_{\text{water}}}{\rho_{\text{water}}} + \frac{W_{\text{aggregate}}}{\rho_{\text{aggregate}}} + \frac{W_{\text{sand}}}{\rho_{\text{sand}}} + \frac{W_{\text{admixture}}}{\rho_{\text{admixture}}} + \text{volume\%(air)} = 1 \tag{3-6}$$

Again, when the weights of cement, water, coarse aggregate, and admixture have been determined, their corresponding volumes can be calculated, with their densities known. With the volume of air determined during concrete mix design, the volume of sand (usually the last unknown component) can be calculated using the above equation. Since the weight of each ingredient is easier to measure than the volume, the design proportion of concrete is usually expressed as a weight ratio. Hence, the proportion obtained in the volume method has to be converted to weight units by multiplying the volume with the density of the material.

3.2.3 Factors to be considered

In the previous sections, the various factors that influence the properties of concrete have been discussed in detail. In this section, the technical and economic factors that need to be considered in concrete mix design are addressed. As always, the projected strength of concrete has to be considered first. The projected strength is usually specified by the structural designer. Normally, the strength at 28 days is used as the design index for structural purposes, but other considerations may dictate the strength at other ages, e.g., formwork demolding time. By adopting quality-control techniques, the variability of strength can be minimized so that the projected strength can be achieved. Nowadays, most concrete is supplied by commercial concrete operators. In these designed mixes, specifications for a range of properties must be satisfied. These properties include the maximum water/cement ratio, minimum cement content, projected strength, projected workability, maximum size of aggregate, and air content.

3.2.3.1 Water/cement ratio

Although the w/c ratio can be estimated from Abram's law, based on projected strength of concrete, in concrete design, the w/c ratio required to produce a given mean compressive strength is usually determined from previously established relations for mixes made from similar ingredients, or by carrying out tests using trial mixes made with the actual ingredients to be used in

Table 3-1 Relation between *w/c* and average compressive strength of concrete, according to ACI 211.1-81

Average Compressive Strength at 28 Days[a] (MPa)	Effective Water/Cement Ratio (by Mass)	
	Non-Air-Entrained Concrete	Air-Entrained Concrete
45	0.38	—
40	0.43	—
35	0.48	0.40
30	0.55	0.48
25	0.62	0.53
20	0.70	0.61
15	0.80	0.71

[a]Measured on standard cylinder. The values given are for a maximum size of aggregate of 20 to 25 mm, for concrete containing not more than the percentage of air shown in Table 3-8, and for ordinary Portland (type I) cement.

Table 3-2 Relation between *w/c* and specified compressive strength of concrete according to ACI 318-83

Specific Compressive Strength at 28 Days[a] (MPa)	Absolute Water/Cement Ratio (by Mass)	
	Non-Air-Entrained Concrete	Air-Entrained Concrete
30	0.40	—
25	0.50	0.39
20	0.60	0.49
17	0.66	0.54

[a]Measured on standard cylinder. Applicable for cements: ordinary Portland (types I & IA), modified Portland (types II & IIA) cement, rapid-hardening Portland (types III & IIIA), sulfate-resisting Portland (type V); also Portland blast furnace (types IS, IS-A) and Portland pozzolan (types IP, P, I(PM), IP-A), including moderate sulfate-resisting cement (MS).
Note: The use of admixtures, other than air-entraining, or of low-density aggregate is not permitted. The values of absolute water/cement ratio are conservative and include any water absorbed by the aggregates. Hence, with most materials, the water/cement ratio will provide average strengths that are greater than the specified strength.

the construction, including admixtures. These relations can be summarized into tables or graphs. Tables 3-1 and 3-2 are two examples. They may be used to estimate the approximate *w/c* ratio for the cements listed for each set of values as a starting point.

It is important that the *w/c* ratio selected on the basis of strength is also satisfactory for the durability requirements. Moreover, this *w/c* ratio for durability should be established prior to the commencement of the structural design because, if it is lower than necessary from structural considerations, the advantage of the use of a higher strength of concrete can be taken in the design calculations.

When supplementary cementitious materials are used in concrete, the water/binder ratio by mass has to be considered. With supplementary cementitious materials, the ACI 211.1-81 approach treats the water/binder ratio as equivalent to the *w/c* ratio of a Portland cement mix. With the mass method, water/binder ratio is equal to the *w/c* ratio of the Portland-cement-only mix. In the absolute volume method, however, because supplementary cementitious materials usually have a lower specific gravity than Portland cement does, the volume replaced by the supplementary cementitious materials is greater than that of Portland cement. With the volume

method, the mass of the cementitious material is smaller than that of the cement in the Portland-cement-only mix so that the water/cementitious material ratio is greater than in the Portland-cement-only mix. Whichever approach is used, a partial replacement of cement by pozzolan generally reduces the strength at an early age. For this reason, the ACI 211.1-81 mix design is used mainly for mass concrete, in which the reduction of the heat of hydration is of paramount importance and the early strength is of lesser significance.

3.2.3.2 Durability

Severe exposure conditions require a stringent control of the w/c ratio because it is the fundamental factor determining the permeability and diffusivity of the cement paste and, to a large extent, of the resulting concrete. In addition, adequate cover to embedded reinforcing steel is essential. However, the w/c ratio can be assessed indirectly through the workability of the mix, the cement content, and strength. If the w/c ratio is determined due to durability requirements, the cement content can be reduced by the use of a larger-size aggregate.

The requirements on the water/binder ratio and the minimum cover thickness for reinforced concrete by ACI 318-83 are given in Tables 3-3 and 3-4. It must be remembered that air entrainment is essential under conditions of freezing and thawing or exposure to deicing salts (see the Table 3-5), although entrained air does not protect concrete containing coarse aggregate that undergoes disruptive volume changes when frozen in a saturated condition.

3.2.3.3 Workability

As discussed earlier, the workability of concrete consists of two aspects, flowability and cohesiveness. Two factors have to be taken into consideration when determining the workability. One is the geometry of the member to be cast, including size of cross section and the amount and spacing of reinforcement. The other is the compaction method, including the equipment for compacting and duration of consolidation.

Table 3-3 Requirements of ACI 318-83 for water/cement ratio and strength for special exposure conditions

Exposure Condition	Maximum Water/Cement Ratio, Normal-Density Aggregate Concrete	Minimum Design Strength in MPa, Low-Density Aggregate Concrete
Concrete intended to be watertight		
Exposed to fresh water	0.50	25
Exposed to brackish or seawater	0.45	30
Concrete exposed to freezing and thawing in a moist condition		
Curbs gutters, guardrails, or thin sections	0.45	30
Other elements	0.50	25
In presence of deicing chemicals	0.45	30
For corrosion protection of reinforced concrete exposed to deicing salts, brackish water, seawater, or spray from these sources	0.40[a]	33[a]

[a]If minimum cover required in Table 3-4 is increased by 10 mm, water/cement ratio may be increased to 0.45 for normal density concrete or design strength reduced to 30 MPa for low-density concrete.

Table 3-4 Requirements of ACI 318-83 for minimum cover for protection of reinforcement

Exposure Condition	Minimum Cover in mm		
	Reinforced Concrete Cast in Suit	Precast Concrete	Prestressed Concrete
Concrete cast against, or permeability exposed to, earth	70	—	70
Concrete exposed to earth or weather			
Wall panels	40–50	20–40	30
Slabs and joists	40–50	—	30
Other members	40–50	30–50	40
Concrete not exposed to weather or in contact with earth			
Slabs, walls, joists	20–40	15–30	20
Beams, columns	40	10–40	20–40
Shells, folded plate members	15–20	10–15	10
Nonprestressed reinforcement	—	—	20
Concrete exposed to deicing slats, brackish water, seawater, or spray from these sources			
Walls and slabs	50	40	—
Other members	60	50	—

Note: Ranges of cover quoted depend on the size of steel used.

Table 3-5 Recomended air content of concretes containing aggregates of different maximum size, according to ACI 201.2R-77 (reaffirmed 1982)

Maximum Size of Aggregate (mm)	Recommended Total Air Content of Concrete (%) for Level of Exposure	
	Moderate[a]	Severe[b]
10	6.0	7.5
12.5	5.5	7.0
20	5.0	6.0
25	4.5	6.0
40	4.5	5.5
50	4.0	5.0
70	3.5	4.5
150	3.0	4.0

[a]Cold climate where concrete will be occasionally exposed to moisture prior to freezing, and where no deicing salts are used, e.g., exterior walls, beams, slabs not in concrete with soil.
[b]Outdoor exposure in cold climate where concrete will be in almost continuous contact with moisture prior to freezing or where deicing salts are used, e.g., bridge decks, pavements, sidewalls, and water tanks.

It is clear that when the cross section of the member to be cast is narrow and complicated in shape, the concrete must have a high fluidity so that full compaction can be achieved. The same applies when the member is heavily reinforced with steel bars that make placing and compaction difficult. Moreover, it is important to choose proper compacting equipment, such as a plate-type vibrator or a sticker-type vibrator, and a compaction duration to ensure that concrete can be fully

Table 3-6 Workability, slump, and compacting factor of concretes with 19 or 38 mm maximum size of aggregate

Degree of Workability	Slump (mm)	Slump (in.)	Compacting Factor	Use for which Concrete is Suitable
Very low	0–25	0–1	0.78	Roads vibrated by power-operated machines. At the more workable end of this group, concrete may be compacted in certain cases with hand-operated machines.
Low	25–50	1–2	0.85	Roads vibrated by hand-operated machines. At the more workable end of this group, concrete may be manually compacted in roads using aggregate of rounded or irregular shape. Mass concrete foundations without vibrated or lightly reinforced sections with vibration.
Medium	25–100	2–4	0.92	At the less workable end of this group, manually compacted flat slabs using crushed aggregate. Normal reinforced concrete manually compacted and heavily reinforced sections with vibration.
High	100–175	4–7	0.95	For sections with congested reinforcement. Not normally suitable for vibration.

Source. Building Research Establishment, Crown copyright.

Table 3-7 Recommended values of slump for various types of construction as given by ACI 211.1-81

Type of Construction	Range of Slump[a] (mm)	Range of Slump[a] (in.)
Reinforced foundation walls and footings	20–80	1–3
Plain footings, caissons and substructure walls	20–80	1–3
Beams and reinforced walls	20–100	1–4
Building columns	20–100	1–4
Pavements and slabs	20–80	1–3
Mass concrete	20–80	1–2

[a]The upper limit of slump may be increased by 20 mm for compaction by hand.

compacted during the entire progress of construction. A guide to workability for different types of construction is given in Tables 3-6 and 3-7.

After choosing the workability, the water content of the mix (mass of water per unit volume of concrete) can be estimated by considering the workability requirement. ACI 211.1-81 gives the water content for various maximum sizes of aggregate and slump value (as an index of workability), with and without air entrainment (see Table 3-8). The values apply for well-shaped coarse aggregates and, although the water requirement is influenced by the texture and shape of the aggregate, the values given are sufficiently accurate for a first estimate.

Table 3-8 Approximate requirement for mixing water and air content for different workabilities and nominal maximum sizes of aggregates according to ACI 211.1-81

Workability or Air Content	Water Content (kg/m^3) of Concrete for Indicated Maximum Aggregate Size in mm							
	10	12.5	20	25	40	50	70	150
	Non-air-entrained concrete							
Slump								
30–50 mm	205	200	185	180	160	155	145	125
80–100 mm	225	215	200	195	175	170	160	140
150–180 mm	240	230	210	205	185	180	170	—
Approximate entrapped air content (%)	3	2.5	2	1.5	1	0.5	0.3	0.2
	Air-entrained concrete							
Slump								
30–50 mm	180	175	165	160	145	140	135	120
80–100 mm	200	190	180	175	160	155	150	135
150–180 mm	215	205	190	185	170	165	160	—
Recommended average total air content (%)								
Mild exposure	4.5	4.0	3.5	3.0	2.5	2.0	1.5[a]	1.0[a]
Moderate exposure	6.0	5.5	5.0	4.5	4.5	4.0	3.5[a]	3.0[a]
Extreme exposure[b]	7.5	7.0	6.0	6.0	5.5	5.0	4.5[a]	4.0[a]

[a]For concrete containing large aggregate which will be wet-screened over a 40-mm sieve prior to testing of air content, the percentage of air expected in the material smaller than 40 mm should be as tabulated in the 40-mm column. However, initial proportioning calculations should be based on the air content as a percentage of the whole mix.
[b]These values are based on the criterion that a 9% air content is needed in the mortar of concrete.
Notes.Slump values for concrete containing aggregate larger than 40 mm are based on slump test made after removal of particles larger than 40 mm by wet screening. Water contents for nominal maximum size of aggregate of 70 and 150 mm are average values for reasonably well-shaped coarse aggregates, well graded from coarse to fine.

3.2.3.4 Cement type and content

The properties of the different types of cement were discussed in Chapter 2. The choice of the types of cement depends on the required hydration rate and strength development, the likelihood of chemical attack, and thermal considerations. Although all have been discussed earlier, it is worth reiterating the need for a cement with a high rate of heat of hydration developed for cold-weather concreting, and with a low rate of heat of hydration for mass concreting, as well as for concreting in hot weather. In the latter case, it may be necessary to use a lower w/c ratio to ensure a satisfactory strength at early ages.

Because cement is more expensive than aggregate, it is desirable to reduce the cement content as much as possible, provided it can satisfy the strength, durability, and workability requirements. Moreover, low to moderate cement content confers the technical advantage of a lower hydration heat as well as cracking potential in the case of mass concrete, where the heat of hydration needs to be controlled, and in the case of structural concrete where shrinkage cracks should be minimized.

In technical terms, the cement content is obtained from the water/binder ratio and the mixing water requirement from the workability requirement. However, the cement content has to meet the minimum requirement by specification from the durability considerations.

3.2.3.5 Major aggregate properties and aggregate content

Many parameters have to be determined in choosing an aggregate. Usually, the maximum size of aggregate is determined first, as it has a significant influence on concrete properties. In reinforced concrete, the maximum size of an aggregate is governed by the geometry of the member and the spacing of the reinforcement. Generally, the maximum aggregate size has to be smaller than 1/4 to 1/5 of the smallest size of the cross section of a member and 3/4 of the net spacing distance of reinforcement. With this proviso, it is generally considered desirable to use as large a maximum size of aggregate as possible. However, the improvement in the properties of concrete with an increase in the size of aggregate does not extend beyond about 40 mm. For high-strength concrete, the maximum aggregate size is limited to 20 mm. For mass concrete utilized in dam construction, the maximum aggregate size can be as large as a few hundred millimeters.

The choice of the maximum size of aggregate may also be governed by the availability of material and by its cost. For instance, when various sizes are screened from a pit it is generally preferable not to reject the largest size, provided this is acceptable on technical grounds.

Another important parameter of an aggregate is its grading. In all cases, dense-graded or well-graded aggregate is preferred, and uniformity has to be achieved. In the case of a coarse aggregate, uniformity can be obtained relatively easier by the use of separate stockpiles for each size fraction. For mass concrete with a maximum size of aggregate larger than 40 mm, ACI 211.1-81 recommends a combination of coarse aggregate fractions to give maximum density and minimum voids. In the case of fine aggregate, however, considerable care is required in maintaining the uniformity of grading of fine aggregate as the sand is usually obtained from river beds directly and can vary from place to place. This is especially important when the water content of the mix is controlled by the mixer operator on the basis of a constant workability: a sudden change toward finer grading requires additional water for the workability to be preserved, and this means a lower strength of the batch concerned. An excess of fine aggregate may also make full compaction impossible and thus lead to a drop in strength.

Table 3-9 gives the idealized combined grading for the 150 and 75 mm nominal maximum sizes of the aggregate. To demonstrate the proportioning of fractions of crushed coarse aggregate so as to obtain the ideal combined grading of the first column of Table 3-9, consider four size fractions: 150 to 75 mm, 75 to 37.5 mm, 37.5 to 19 mm, and 19 to 4.76 mm. The gradings of these fractions are given in Table 3-10. In concrete mix design, the aggregate content has to be

Table 3-9 ''Ideal'' combined grading for coarse aggregate of nominal maximum size of 150 and 75 mm

	Cumulative Percentage Passing for Nominal Size of Aggregate in mm			
	150 mm		75 mm	
Sieve Size (mm)	Crushed	Rounded	Crushed	Rounded
150	100	100	—	—
125	85	89	—	—
100	70	78	—	—
75	55	64	100	100
50	38	49	69	75
37.5	28	39	52	61
25	19	28	34	44
19	13	21	25	33
9.5	5	9	9	14

Table 3-10 Example of grading of individual coarse aggregate fractions to be combined into an ''ideal'' grading for mass concrete

Sieve Size (mm)	Cumulative Percentage Passing for Fraction (%)			
	150–75 mm	75–37.5 mm	37.5–19 mm	19–4.76 mm
175	100	—	—	—
150	98	—	—	—
100	30	100	—	—
75	10	92	—	—
50	2	30	100	—
37.5	0	6	94	—
25	0	4	36	100
19	0	0	4	92
9.5	0	0	2	30
4.76	0	0	0	2

Table 3-11 Dry bulk volume of coarse aggregate per unit volume of concrete as given by ACI 211.1-81

Maximum Size of Aggregate (mm)	Dry Bulk Volume of Rodded Coarse Aggregate Per Unit Volume of Concrete for Different Fineness Modulus of Sand			
	2.40	2.60	2.80	3.00
10	0.50	0.48	0.46	0.44
12.5	0.59	0.57	0.55	0.53
20	0.66	0.64	0.62	0.60
25	0.71	0.69	0.67	0.65
40	0.75	0.73	0.71	0.69
50	0.78	0.76	0.74	0.72
70	0.82	0.80	0.78	0.76
150	0.87	0.85	0.83	0.81

Note. The values will produce a mix with a workability suitable for reinforced concrete construction. For less workable concrete, e.g., that used in road construction, the values may be increased by about 10%. For more workable concrete, such as may be required for placing by pumping, the values may be reduced by up to 10%.

determined carefully. As the aggregate occupies 65 to 75% of the total volume of concrete, it plays an important role in determining the concrete properties and cost.

The parameters for aggregate content in a concrete mix design that need to be decided include the total aggregate-to-binder ratio and the fine aggregate-to-coarse aggregate ratio. Table 3-11 provides the dry bulk volume of coarse aggregate per unit volume of concrete, which is expressed as a function of both fineness modules of the fine aggregate and the maximum size of aggregate. The mass of the coarse aggregate can then be calculated from the product of the dry bulk volume and the density (or unit weight) of the dry coarse aggregate.

The fine aggregate content per unit volume of concrete can be then estimated using either the mass method or the volume method. In the former, the sum of the masses of cement, coarse aggregate, and water is subtracted from the mass of a unit volume of concrete, which is often known from previous experience with the given materials. However, in the absence of such information, Table 3-12 can be used as a first estimate; adjustment is made after trial mixes.

Table 3-12 First estimate of density (unit weight) of fresh concrete as given by ACI 211.1-81

Maximum Size of Aggregate (mm)	First Estimate of Density (Unit Weight) of Fresh Concrete (kg/m^3)	
	Non-Air Entrained	Air Entrained
10	2285	2190
12.5	2315	2235
20	2355	2280
25	2375	2315
40	2420	2355
50	2445	2375
70	2465	2400
150	2505	2435

A more precise estimate can obtained from the following equation:

$$\rho = 10\gamma_a\,(100 - A) + C\left(1 - \frac{\gamma_a}{\gamma}\right) - W\,(\gamma_a - 1)\,\left(\text{kg/m}^3\right) \tag{3-7}$$

where

ρ = density (unit weight) of fresh concrete, kg/m^3
γ_a = weighted average bulk specific gravity (SSD) of combined fine and coarse aggregate; clearly, this needs to be determined from tests
A = air content, %
C = cement content, kg/m^3
γ = specific gravity of cement (generally 3.10 for Portland cement)
W = mixing water requirement, kg/m^3

The volume method is an exact procedure for calculating the required amount of fine aggregate. Here, the mass of fine aggregate, A_f, is given by

$$A_f = \gamma_f\left[1000 - \left(W + \frac{C}{\lambda} + \frac{A_c}{\gamma_c} + 10A\right)\right]\ (\text{kg/m}^3) \tag{3-8}$$

where

A_c = coarse aggregate content, kg/m^3
γ_f = bulk specific gravity (SSD) of fine aggregate
γ_c = bulk specific gravity (SSD) of coarse aggregate

3.3 PROCEDURES FOR CONCRETE MIX DESIGN

There are many different methods for designing the concrete mix, for example, the ACI method and the UK method. However, there are no fundamental differences among these methods. Thus, it is sufficient to introduce one method. Here, the method proposed by American Institute of Concrete (ACI 211.1-81) is introduced.

Before starting concrete mix design, basic information on raw materials and background data should be collected, including

(a) Sieve analysis results and fineness modulus of fine and coarse aggregate
(b) Dry-rodded density (unit weight) of coarse aggregate

(c) Bulk specific gravity of each raw material
(d) Absorption capacity or moisture content of the aggregates
(e) Variation of the approximate mixing water requirement with slump, air content, and grading of the available aggregates
(f) Relationships between strength and water/cement ratio for available combinations of cement and aggregate
(g) Job specifications, if any, e.g., maximum water/cement ratio, minimum air content, minimum slump, maximum size of aggregate, and strength at early ages (normally, 28-day compressive strength is specified)

Regardless of whether the concrete characteristics are prescribed by the specifications or left to the mix designer, the batch weights in per kilograms cubic meter of concrete can be computed in the following sequence:

Step 1: *Choice of slump.* If the slump value is not specified, an appropriate value for the particular work can be selected from Table 3-7 according to the type of structure to be built.

Step 2: *Choice of maximum size of aggregate.* For the same volume of coarse aggregate, using a large maximum size of well-graded aggregate will produce less void space than using a smaller size, and this will have the effect of reducing the mortar requirement in a unit volume of concrete. Generally, the largest size of coarse aggregate economically available should be selected as long as it can meet the general requirement mentioned earlier. In no event should the maximum size exceed one-fifth of the narrowest dimensions between the size of the forms, one-third the depth of slabs, or three-fourths of the minimum clear spacing between reinforcing bars.

Step 3: *Estimation of mixing water and the air content*. The quantity of water per unit volume of concrete required for a given slump value depends on the maximum particle size, shape, and grading of the aggregates, as well as on the amount of entrained air. If data based on experience with the given aggregates are not available, assuming normally shaped and well-graded particles, an estimate of the mixing water, with or without air entrainment, can be obtained from Table 3-8 for the purpose of deriving the trial batches.

Step 4: *Selection of water/cement ratio.* Since different aggregates and cements generally produce different strengths at the same w/c, it is highly desirable to develop the relationship between strength and w/c for the materials actually to be used. In the absence of such data, approximate and relatively conservative values for the concretes made with type I Portland cement can be selected from Table 3-1. Since the selected w/c must satisfy both the strength and the durability criteria, the values of w/c (w/b) should conform to the values in Table 3-3.

Step 5: *Calculation of cement content*. The required cement content is equal to the mixing water content obtained in step 3 divided by the w/c determined in step 4.

Step 6: *Estimation of coarse aggregate content*. To reduce the cost of concrete, aggregates should be used as much as possible. Statistics on a large number of tests have shown that for properly graded materials, the finer the sand and the larger the size of the particles in a coarse aggregate, the more the volume of coarse aggregate that can be used to produce a concrete mixture with satisfactory workability. It can be seen from Table 3-11 that, for a suitable degree of workability, the volume of coarse aggregate in

a unit volume of concrete depends only on its maximum size and fineness modulus of the fine aggregate. It is assumed that differences in the amount of mortar required for workability with different aggregates, due to differences in particle shape and grading, are compensated for automatically by differences in dry-rodded void content.

Step 7: *Estimation of fine aggregate content*. At the completion of step 6, all the ingredients of the concrete have been estimated except the fine aggregate. The amount of fine aggregate can be determined by either the *weight* method or *volume* method.

According to the weight method, if the unit weight of the wet fresh concrete is known from previous experience, then the required weight of fine aggregate is simply the difference between the unit weight of concrete and the total weight of water, cement, and coarse aggregate. In the absence of a reliable estimate of the unit weight of concrete, Table 3-12 can be used to as a guide to choose the unit weight of fresh concrete. Experience shows that even a rough estimate of the unit weight is adequate for the purpose of producing trial concrete.

$$U_m = 10G_a(100 - \overline{A}) + C_m\left(1 - \frac{G_a}{G_c}\right) - W_m(G_a - 1)\ \text{kg/m}^3 \tag{3-9}$$

where U_m is the weight of fresh concrete, kg/m^3; G_a is the weighted average bulk specific gravity (SSD) of combined fine aggregate and coarse aggregate, assuming reasonable weight proportions; G_c is the specific gravity of cement; $\overline{A}$ is the air content, %; W_m is the mixing water content, kg/m^3; C_m is the cement content, kg/m^3.

In the absolute volume method, the total volume displaced by the known ingredients (i.e., water, air, cement, and coarse aggregate) is subtracted from the unit volume of concrete to obtain the required volume of fine aggregate. This in turn is converted to weight units by multiplying by the density of fine aggregates.

Step 8: *Adjustment of amount of free water*. The mix proportions determined by steps 1 to 7 assume that aggregates are in SSD condition. Generally, however, the stock aggregates are not in a balanced condition, i.e., the SSD condition. They are either in an air dry or wet condition that will either absorb mixing water or given up extra water to the mix during mixing process. Moreover, when admixtures in liquid form are used, extra water will be supplied. If water related to these sources is not taken into account for the adjustment of mixing water, the actual *w/c* of the trial mix will be inaccurate. Hence, the moisture content of aggregates and the extra water in liquid admixtures has to be carefully calculated and the amount of mixing water should be adjusted. The procedures will be demonstrated in the sample computations.

Step 9: *Trial mixes*. Due to so many assumptions underlying the foregoing theoretical calculations, the mix proportions for the actual concrete have to be checked and adjusted by means of laboratory trials consisting of small batches (e.g., 0.02 m^3 or 50 kg of concrete). Fresh concrete should be tested for slump, cohesiveness, finishing properties, and air content, as well as for unit weight. The specimens of hardened concrete cured under standard conditions should be tested for strength at specified ages. If any property cannot meet the design requirement, adjustments to the mix proportions have to be conducted. For example, lack of cohesiveness can be corrected by increasing the fine aggregate content at the expense of the coarse aggregate content. The rules of thumb for other adjustments are as follows:

(a) If the correct slump is not achieved, the estimated water content is increased (or decreased) by 6 kg/m^3 for every 25 mm increase (or decrease) in slump.

(b) If the desired air content is not achieved, the dosage of the air-entraining admixture should be adjusted to produce the specified air content. The water content is then increased (or decreased) by 3 kg/m^3 for each 1% decrease (or increase) in air content.

(c) If the estimated density (unit weight) of fresh concrete by the mass method is not achieved and is of importance, the mix proportions should be adjusted, with allowance being made for a change in air content.

(d) If the projected strength cannot be met, w/b should be reduced at a rate of 0.05 for every 5 MPa.

Step 10: *Mix proportion adjustments*. After several trials, when a mixture satisfying the desired criteria of workability and strength is obtained, the mix proportions of the laboratory-size trial batch can be fixed and scaled up for producing large amounts of field batches.

Examples

Example I Concrete mix design

Concrete is required for a column that will be moderately exposed to freezing and thawing. The cross section of the column is 300 × 300 mm. The smallest spacing between reinforcing steel is 30 mm. The specified compressive strength of concrete at 28 days is 40 MPa with a slump of 80 to 100 mm. The properties of materials are as follows:

(a) Cement used is type I Portland cement with a specific gravity of 3.15.

(b) The available coarse aggregate has a maximum size of 20 mm, a dry-rodded unit weight of 1600 kg/m^3, a bulk specific gravity (SSD) of 2.68, absorption capacity of 0.5%, and moisture content (OD) of 0.25%.

(c) The fine aggregate has a bulk specific gravity (SSD) of 2.65, absorption capacity of 1.3%, a moisture content (SSD) of 3%, and a fineness modulus of 2.60. The aggregates conform to the ASTM C33-84 requirements for grading.

With the given information, the mix design will be carried through in detail, using the sequence of steps outlined.

Step 1: *Choice of slump*. The slump is given and consistent with Table 3-7.

Step 2: *Maximum aggregate size*. The maximum aggregate size is 20 mm, which meets the limitations of 1/5 of the minimum dimension between forms and 3/4 of the minimum clear space.

Step 3: *Estimation of mixing water and air content*. The concrete will be exposed to freezing and thawing; therefore, it must be air entrained. From Table 3-8, the recommended mixing water amount is 180 kg/m^3, and the air content recommended for moderate exposure is 5.0%.

Step 4: *Water/cement ratio (w/c)*. According to both Table 3-1 and Table 3-3, the estimate of the required w/c ratio to give a 28-day compressive strength of 40 MPa is 0.35.

Step 5: *Calculation of cement content*. Based on the steps 3 and 4, the required cement content is $180/0.35 = 514$ kg/m^3.

Step 6: *Estimation of coarse aggregate content*. From Table 3-11, for fineness modulus of the fine aggregate of 2.60, the volume of dry-rodded coarse aggregate per unit volume of concrete is 0.64. Therefore, there will be 0.64 m^3 coarse aggregate in per volume

concrete. And, the OD weight of the coarse aggregate is $0.64 \times 1600 = 1.024$ kg. The SSD weight is $1024 \times 1.005 = 1029$ kg.

Step 7: *Estimation of fine aggregate content*. The fine aggregate content can estimated by either the weight method or the volume method.

(a) *Weight method*. From Table 3-12, the estimated concrete weight is 2280 kg/m^3. Although for a first trial it is not generally necessary to use the more exact calculation based on Equation 3-9, this value will be used here:

$$U_m = (10)(2.67)(100 - 5) + 514(1 - 2.67/3.15) - 180(2.67 - 1)$$
$$= 2314 \text{ kg/m}^3$$

Based on the already determined weights of water, cement, and coarse aggregate, the SSD weight of the fine aggregate is $2314 - 180 - 514 - 1,029 = 591$ kg.

(b) *Volume method*. Based on the known weights and specific gravity of water, cement, and coarse aggregate, the air volume, the volumes per m^3 occupied by the different constituents can be obtained as follows:

Water: $\dfrac{180}{1000} = 0.180 \text{ m}^3$

Cement: $\dfrac{514}{1000 \times 3.15} = 0.163 \text{ m}^3$

Coarse aggregate (SSD): $\dfrac{1029}{1000 \times 2.68} = 0.384 \text{ m}^3$;

Air: 0.05 m^3;

Therefore, the fine aggregate must occupy a volume of $1 - (0.180 + 0.163 + 0.384 + 0.05) = 0.223$ m^3. The required SSD weight of the fine aggregate is $0.223 \times 2.65 \times 1000 = 591$ kg.

Step 8: *Adjustment for moisture in the aggregate*. Since the aggregates will be neither SSD nor OD in the field, it is necessary to adjust the aggregate weights for the amount of water contained in the aggregate. Since absorbed water does not become part of the mix water, only surface water needs to be considered. For the given moisture contents, the adjusted aggregate weights become

Coarse aggregate (stock): From

$$W(\text{stock}) = W(\text{OD})[1 + \text{MC}(\text{OD})]$$

Get: $W(\text{stock}) = 1024 \times 1.0025 = 1026$ kg

The extra water needed for coarse aggregate absorption is

W(SSD) − W(stock) = 1029 − 1026 = 3 kg

Fine aggregate (stock): $591 \times 1.03 = 609$ kg/m^3

Extra water provided by fine aggregate: $609 - 591 = 18$ kg

The mixing water is then: $180 + 3 - 18 = 165$ kg.

Thus, the estimated batch weights per m^3 are as follows: water, 165 kg; cement, 514 kg; coarse aggregate, 1026 kg; fine aggregate, 609 kg; total, 2314 kg.

Step 9: *Trial mixes*. Trial mixes should be carried out using the proportions calculated. The properties of the concrete in the trial mix must be compared with the desired properties, and the mix design must be corrected as described.

Example II Raw material calculation for a given concrete mix ratio

A concrete mix has a proportion of 1:0.4:1.8:2.5 (P:W:S:A). In the powder content, 90% percent is Portland cement and 10% is solid silica fume (SF). The concrete also uses 0.25% retarder and 1.5% superplasticizer. The absorption for sand is 1.2% and for aggregate is 0.9%. The MC (OD) is 2.5% for sand and 0.4% for coarse aggregate. The solid content is 35% in retarder and 40% in superplasticizer. The SF used is a slurry with 50% of water. To cast 5 beams ($100 \times 100 \times 500$ mm) and 18 cylinders (100×200 mm), how much of each individual ingredient should be used (consider 5% extra amount)?

Solution

1. The total volume of concrete specimen is

$$5 \times 0.1 \times 0.1 \times 0.5 + 18 \times 3.14159 \times (0.1/2)^2 \times 0.2 = 0.053274 \text{ m}^3$$

2. The total weight is (assuming the unit weight of concrete is 2400 kg/m^3)

$$2400 \times 0.053274 \times (1 + 0.05) = 134.2492 \text{ kg}$$

(Note that P:W:S:A refers to the SSD states)

3. The weight of cement and SF is

$$W_{C+SF} = 134.2492/(1 + 0.4 + 1.8 + 2.5 + 0.0025 + 0.015) = 23.480 \text{ kg}$$
$$W_C = 23.48 \times 0.9 = 21.132 \text{ kg}$$

4. For sand

$$W_{SSD} = 1.8 \times 23.480 = 42.265 \text{ kg}$$
$$\text{Absorption capability (AB)} = (W_{SSD} - W_{OD})/W_{OD}$$
$$\text{MC(OD)} = (W_{stock} - W_{OD})/W_{OD}$$
$$\text{So } W_{stock}/W_{SSD} = (1 + \text{MC(OD)})/(1 + \text{AB})$$
$$\text{Thus, } W_{stock} = (1 + 0.025)/(1 + 0.012) \times 42.265 = 42.808 \text{ kg}$$
$$\text{Water provided by sand} = 42.808 - 42.265 = 0.543 \text{ kg}$$

5. For aggregate

$$W_{SSD} = 2.5 \times 23.48 = 58.701 \text{ kg}$$
$$W_{stock} = (1 + 0.004)/(1 + 0.009) \times 58.701 = 58.410 \text{ kg}$$
$$\text{Water required by aggregate} = 58.410 - 58.701 = -0.291 \text{ kg}$$

6. For retarder

$$W_{\text{solid}} = 0.0025 \times 23.48 = 0.059\,\text{kg}$$
$$W_{\text{solution}} = 0.059/0.035 = 0.168\,\text{kg}$$
$$\text{Water provided by retarder solution} = 0.168 - 0.059 = 0.109\ \text{kg}$$

7. For superplasticizer

$$W_{\text{solid}} = 0.015 \times 23.48 = 0.352\,\text{kg}$$
$$W_{\text{solution}} = 0.352/0.4 = 0.881\,\text{kg}$$
$$\text{Water provided by superplasticizer solution} = 0.881 - 0.352 = 0.528\ \text{kg}$$

8. For SF

$$W_{\text{solid}} = 0.1 \times 23.48 = 2.348\,\text{kg}$$
$$W_{\text{solution}} = 2.348/0.5 = 4.696\ \text{g}$$
$$\text{Water provided by superplasticizer solution} = 4.696 - 2.348 = 2.348\ \text{kg}$$

9. For water

$$\text{Water} = 0.4 \times 23.48 - (0.543 - 0.291 + 0.109 + 0.528 + 2.348) = 6.155\ \text{kg}$$

This example provides the method that can be used to make adjustments to the mixing water in practice.

3.4 MANUFACTURE OF CONCRETE

Nowadays, concretes are usually produced in two ways: manufactured in a commercial concrete plant, and produced on the construction site. Over the last few decades, ready-mixed concrete has developed very fast. The advantages of ready-mixed concrete are as follows: (1) it provides concrete with better quality due to specialized operation; (2) mass production; (3) elimination of storage space for basic materials at site; (4) basic materials can be fully utilized; (5) it reduces the labor requirement; (6) it reduces noise and dust pollution on the construction site; and (7) it reduces the production cost of concrete. ASTM C94 / C94 M-09a (Standard Specification for Ready-mixed Concrete) specifies the requirements for quality control of ready-mixed concrete manufactured and delivered to a purchaser in a freshly mixed and unhardened state. Mixers will be stationary mixers or truck mixers. Except as otherwise specifically permitted, cement, aggregate, and admixtures are measured by mass. Figure 3-11 shows a modern ready-mixed concrete plant. The green pipes in the figure are silo containers for raw materials. The truck position is the location of the mixed concrete discharge. Nowadays, stationary mixers are usually used to produce wet concretes and are referred to as wet processing. A dry process just discharges all the raw materials into a truck mixer and the mixing is finished in the truck on the way to the site. The mixing capacity of a stationary type of drum mixer reaches 9 m^3. The pan mixer (see Figure 3-12) is usually utilized at the construction site, precast concrete plant, and laboratories. Mostly, it is for small amounts of concrete, as compared to a ready-mix concrete plant.

Figure 3-11 Ready-mix concrete plant

Figure 3-12 Small pan mixer

3.5 DELIVERY OF CONCRETE

The delivery of fresh concrete from the concrete plant to the construction site is usually done by agitators, either truck mixers or truck agitators. The truck is equipped with a rotating drum for agitation, shown in Figure 3-13. The truck mixer receives raw materials from the plant and completely mixes them into workable fresh concrete on the way to the construction site. The

Figure 3-13 Delivery of concrete by truck

Figure 3-14 Delivery of concrete to an ocean construction site using a ferry (photo provided by Ove Arup, HK)

advantage of truck mixing is that the water can be stored separately and added into the solid materials for mixing according the time of shipping, to avoid slump loss. If the construction site is offshore, a ferry is used to carry a large number of trucks from land to the site (see Figure 3-14). In this case, due to a long shipping period, special care has to be paid to the slump loss. Usually, retarding admixtures have to be used to keep concrete workable for a period of 5 to 6 h, and an

initial setting time of 7 to 8 h. In this case, A truck mixer has priority to be selected, if available. A truck mixer has to meet the requirements of environmentally friendly production nowadays.

3.6 CONCRETE PLACING

Placing concrete is a construction process that can be divided into four operations: site preparation to receive the concrete, conveying and placing the concrete into the forms, compacting concrete, and taking care of the concrete after it has been compacted. Concrete should be placed as close to its final position as possible. To minimize segregation, it should not be moved over too long a distance. After concrete is placed in the formwork, it has to be compacted to remove entrapped air. Compaction can be carried out by hand rodding or tamping, or by the use of mechanical vibrators. In this section, the focus is on preparation, conveying, placing, and compacting.

3.6.1 Site preparation

Before ordering and receiving concrete from commercial concrete plants, the construction site has to be prepared carefully. Site preparations include processing steel reinforcement, setting up formwork, and arranging the handling equipment for concrete. Different structures have different preparations.

(a) *Foundations*: Preparation for foundations to receive concrete is complicated due to the large area and excavation involved. Excavation for foundations should extend into sound, undisturbed soil or rock. If a large hole is encountered during excavation, the hole must be backfilled with the material selected having similar stiffness with the surrounding soil to avoid uneven settlement of the foundation. Rock surfaces should be clean and sound. If free water is present, it should be blown out with air jets or removed by other methods. In some cases it may be necessary to provide a sump (outside the form area) into which the water drains, for removal by means of a pump.

Foundations should be free of frost and ice when concrete is placed in winter. During the dry seasons, the earth should be moist but not muddy. Steel shells for cast-in-place piles and shafts for caissons should be inspected to ensure that the way is not blocked.

(b) *Construction joints*: For a structural member with large areas or volumes or big heights, it is impossible to cast the whole member at one time. The limitations of concrete supply, construction processes, and time make concrete casting stop at some point, leaving a construction joint to separate the currently cast concrete to the later resumed casting. A construction joint may be horizontal or vertical, depending on the type of structural member and construction process. Locations of construction joints have to be planned carefully according to the structural member size, the amount of concrete that can be provided during the period, the coefficient of thermal expansion, the construction planning, the moment and shear force distribution in the structural member, and the shrinkage properties of concrete. The joint should be made in a plane normal to the main reinforcing bars and in a region with minimum shear force. Construction joints must be made and located so as not to impair the strength of the structure. Where a joint is to be made, the surface of the concrete must be cleaned and laitance removed. Immediately before new concrete is placed, all construction joints must be wetted and standing water removed (ACI 318 Section 6.4). Reinforcing steel is normally continuous across a construction joint to keep the concrete structure unified as whole.

(c) *Formworks*: Before casting concrete, a formwork has to be built. The formwork is a temporary mold into which concrete is poured. The formwork supports the dead load of fresh

Figure 3-15 Framework for transfer block of a tall building (photo provided by Peter Allen)

concrete and some construction load until the concrete hardens and can carry the load itself. The formwork can be built with steel plate or timber board. Formworks should be clean, tight, and strong enough to carry the wet concrete and resist the pressure generated by the liquid concrete. The formwork lining should be coated with appropriate oil or parting compound to aid in demolding. Wood forms should be moistened with water before concrete pouring to avoid their absorbing water from the concrete. Figure 3-15 shows a formwork for construction of a transfer block of a tall building. Also shown in the figure is the falsework. Falsework is a type of temporary structure used in construction to support spanning or arched structures by holding the component in place until its construction is sufficiently advanced to support itself. Falsework usually includes temporary support structures for formwork, and scaffolding to give workers access to the structure being constructed.

In placing concrete in high, thin walls or similar structural units, it is common practice to provide ports or windows in the forms. If possible, these windows should be made on a surface that will not be exposed to view in the finished structure, such as the back side of a wing wall on a highway structure. When the level of the fresh concrete within the structure approaches the window, the hole should be closed as tightly and neatly as possible. Because of the danger of segregation resulting from a high-velocity stream of concrete entering the form at an angle, and because of the surface blemishes usually resulting in the area where the hole was closed, it is best to avoid using these ports, if at all possible, or to provide a collecting hopper outside the opening.

Permanent formwork is a part of a concrete structure that can be used to hold the fresh concrete, mold it to the required dimensions and remain in place for the life of the structure. The steel tube-reinforced concrete utilizes steel tubing as permanent formwork. The use of permanent formwork can reduce the number of skilled form workers on a construction site, speed up the construction process, improve curing and reduce shrinkage, reduce construction costs, and improve safety by reducing hazards during construction. It also reduces construction waste generation during construction.

(d) *Reinforcing steel*: After the formwork is built up, a reinforcing steel cage has to be put into the formwork before concrete casting. The main reinforcing steel bars should be held by steel stirrups in the right position. The reinforcing steel should be free of dirt, paint, oil, grease or other foreign substances. The rust should be removed by wire brushing. During the placing and compacting, all reinforcing steel should be held accurately in the right position. Distances from the forms should be maintained by means of chairs, ties, or hangers. The reinforcing steel cage should also be strong enough to carry the construction load. Figure 3-16 shows the reinforcing steel framework before concrete casting.

(e) *Embedded items*: Many concrete structures have objects and fixtures embedded, including manholes, anchor bolts, pipes, instruments for health monitoring, and tubes for holding prestress tendons. Most of them have to be fixed in place prior to concrete placement by attaching them to the formwork or the reinforcing steel. Adjustments to the steel location to accommodate these items should be made only when the load-carrying ability is not affected.

3.6.2 Conveying concrete

After the formwork, the steel work, and embedded items are ready, a final inspection should be conducted to make sure that the plant and equipment are ready to go. The correct amount of concrete should be ordered and the ready-mix supplier prepared to furnish concrete at the required rate. Transporting equipment, such as pumps, cranes, batch trucks, buckets, conveyors, and helicopters, should be capable of handling the concrete at the required rate. Curing materials should be available.

The methods of placing fresh concrete include direct discharge from a mixer into the forms, crane and buckets, pumps, conveyors, buggies, wheelbarrows, pneumatic placers, small railcars, or a combination of two or more of these methods. Helicopters have been employed for transporting equipment and concrete buckets into especially isolated or difficult sites.

The method used depends on the size of the job, adequacy of space, and availability of equipment. The displacing concrete should be as close as possible to the actual site. Direct discharge is a method of pouring concrete from a transport truck directly into the forms or on the subgrade. Extra lengths of chute on the truck can provide a placing radius of about 5 m from the truck.

For a concrete placing to a lower level, such as a foundation, some sort of chuting arrangement for moving concrete is needed. Chutes should be of rounded cross section, made of metal or lined with metal, smooth to prevent the concrete from friction and sticking, and of the proper slope for the concrete to slide fast enough to keep the chute clean. As long as there is no segregation or separation, any reasonable slope can be tolerated. A slope of about 1:3 is good for application without segregation. See Figure 3-17.

Buckets are excellent means of conveying concrete. The capacity range is from less than 1 m^3 for structural use to 10 m^3 for mass concrete. Buckets can be handled by cranes, derricks, trucks, rail cars, helicopters, or cableways. Moving by cranes is the usual method of handling buckets in building construction. Care should be taken to avoid shaking and jarring the concrete, as this causes segregation, especially for relatively high-slump concrete. Figure 3-18 shows concrete being unloaded using a bucket.

Concrete is also frequently moved by belt conveyor, wheelbarrows, and buggies. Belts can move concrete long distances horizontally and, to some extent, vertically. Pneumatic-tired wheelbarrows can be used for moving small amounts of concrete for short distances. About 60 m is the maximum horizontal distance for a wheelbarrow. One person with a wheelbarrow can move a maximum of about 1.2 m^3 of concrete per hour. Hand-operated carts can carry about

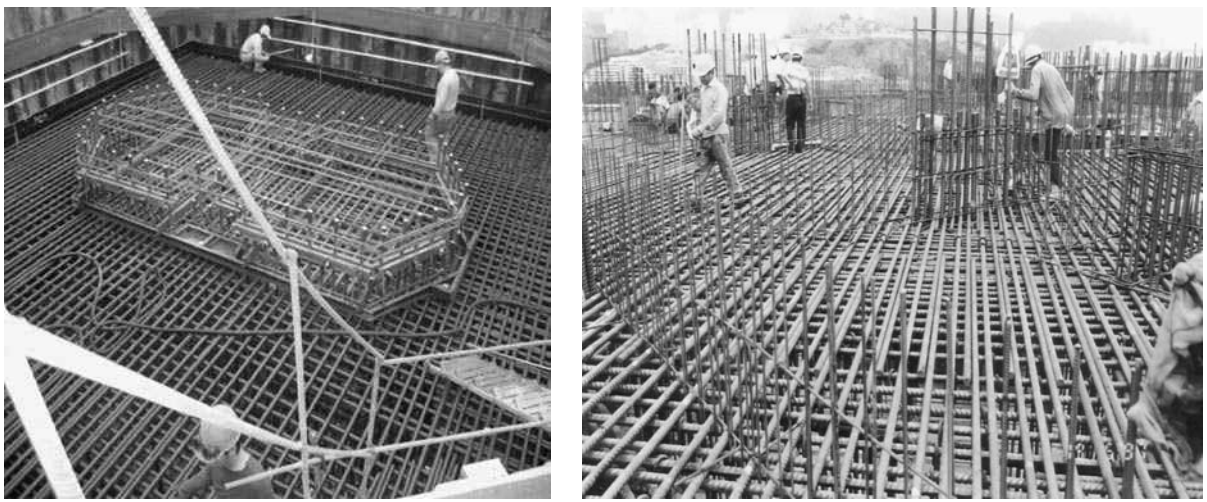

Figure 3-16 Reinforcing steel framework (photo provided by Mr. Peter Allen)

Figure 3-17 Concrete is conveyed into a large foundation construction through chutes (photo provided by Mr. Allen)

Figure 3-18 Unloading concrete (photo provided by Ove Arup, HK)

Figure 3-19 Wheelbarrow used on construction site

0.12 or 0.2 m^3 each, with a maximum haul of about 60 m. A power-driven cart has a capacity of up to 1.2 m^3 and can move a maximum of 17 m^3 of concrete per hour on a moderate length of haul. Maximum haul should not exceed 300 m. Figure 3-19 shows a small wheelbarrow used on a construction site.

Pumping is another effective method to move concrete to the formwork, see Figure 3-20. Pumped concrete is conveyed under pressure through a rigid pipe or flexible hose. With the development of self-compacting concrete, pumping has become more and more popular in the construction of tall buildings, bridge towers, and tunnels. Nowadays, with the help of special high-pressure pumps, concrete can be pumped a distance as far as 1400 m horizontally or as high as 420 m vertically.

The total pressure needed to pump concrete to a height of H can be estimated from the following equation:

$$P_t = \Delta P_f(L + H) + \rho g H + P_l \tag{3-10}$$

where P_t is the total pressure needed, MPa ; ΔP_f is the pressure loss due to friction of the wall of the pipe, MPa/m; L is the total horizontal distance; H is the total vertical distance; ρ is the density of concrete, kg/m^3; g is gravity acceleration, m/s^2; and P_l is pressure loss due to local effects, such as the bending tube, MPa. Once P_t is obtained, the capacity of the pump can be decided and equipment selected.

3.6.3 Depositing concrete in forms

Once all the preparation work and equipment are ready, depositing concrete into the formwork can be started. A basic rule is that concrete should be deposited as close as possible to its final location, especially for vertical dropping. As long as the concrete is deposited near its final position without undue segregation, any method is acceptable. If possible, concrete should fall

Figure 3-20 Pumping of fiber-reinforced concrete to a height of 306 m at Su-Tong Bridge, Suzhou, China (photo provided by Jinyang Jiang)

Figure 3-21 Drop chute-guided concrete fall

vertically. In most cases, free fall should be limited to 0.9 to 1.5 m to avoid aggregate bouncing off from faces and striking the reinforcing steel, which may increase segregation. However, when the formwork is open and the concrete drop is unobstructed, free fall to a depth of 45 m has proven successful without segregation (Mindess et al., 2003). Usually, a drop chute or pipe is used to guide or protect the concrete during its fall, as shown in Figure 3-21.

For concrete deposited in the formwork of walls, footings, beams, and shear walls, concrete should be placed from the ends or corners toward the center, in horizontal layers not exceeding about 450 mm in depth. Mass concrete in dams and foundations is usually placed in lifts of 1.5 or 2.5 m depth, each lift consisting of several layers. To avoid cold joints, these layers are carried across the form in a series of steps. For a rock foundation, a layer of mortar with a thickness of 12 mm should be placed before depositing the first layer of concrete. The compatibility between the mortar and concrete should be taken into consideration. Subsequent layers, continuing to the full height of the structure, should be placed and consolidated before the underlying layer has hardened.

For slope placing and consolidation, the work should be started from the bottom, allowing gravity to aid, rather than to hinder consolidation. The concrete should be constrained to fall vertically onto the slope. A strict watch should always be kept for segregation during placement, and action should be taken to correct problems as soon as they arise.

A number of occasions present unique problems in handling, placing, and consolidating concrete. Among these are slip forms, underwater placing, and preplaced aggregate concrete.

3.6.4 Compacting and finishing

After depositing concrete into formworks, it should be compacted right away. The purpose of compacting is to remove the air entrapped during concrete placement and to consolidate plastic concrete into all the spaces in the formworks, including the corners and the gaps in the reinforcing steels. Compacting can make concrete denser and stiffer and thus have a good compressive strength and low permeability. Without proper compacting, high-quality concrete cannot be achieved. Many years ago, consolidation was accomplished by laborers wielding a variety of spades, tampers, and similar tools. Now, nearly all concrete is consolidated with high-frequency vibrators. At a construction site, two vibrators are frequently used, an internal and an external vibrator. An internal vibrator consists of a poker, housing an eccentric shaft driven through a flexible drive from a mortar. The poker can be immersed in concrete and vibrates in a harmonic way, exerting pressure to the surrounding concrete. The poker vibrator ranges in size from 20 to 150 mm diameter, with head lengths from 250 to 750 mm. Pokers can generate vibration with a frequency ranging from 70 to 200 Hz, and acceleration from 0.7 to 4 m/s^2 at speeds of 5500 to 15,000 vpm (vibrations per minute). The vibration can produce a noise with a level up to 90 dB, and, obviously, poker vibration is not good for people's health. Self-compacting concrete can completely eliminate the vibration and hence is environmentally friendly. Figure 3-22 shows the vibration process of an internal vibrator.

The external vibrator usually has a flat metal base like a plate, including the surface, and pan or screed vibrators. The mortar on the top of the plate can generate vibration on the plate. It can be placed on the surface of the fresh concrete and is usually suitable for slab and floor member compacting. Slabs up to 200 mm thick can be consolidated adequately. Thicker slabs require additional internal vibration. In addition to consolidating the concrete in the slab, the unit strikes off the surface and prepares it for final finishing. Another type of external vibrator is the form vibrator. Form vibrators are attached to the exterior of the mold or form. They are used in locations where it is difficult to use internal vibrators, such as in tunnel linings or heavily congested forms. They are also used for making pipes, masonry units, and many other types of precast concrete. Pneumatically driven units develop vibration by the rotation of an eccentric weight. The speed can be varied by changing the volume of air supplied. When the surface of the concrete takes on a flattened glistening appearance, the rise of entrapped air bubbles ceases, the coarse aggregate blends into the surface but does not disappear, and vibration can be stopped.

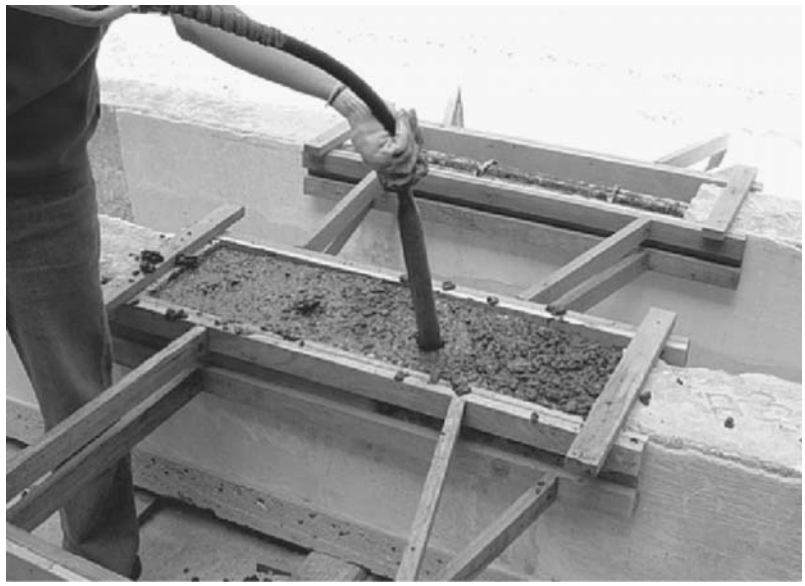

Figure 3-22 Internal vibration

Overvibration sometimes occurs. If so, the coarse aggregate will have sunk below the surface, and the surface may have a frothy appearance. In this case, the slump should first be reduced, and the amount of vibration then has to be adjusted.

A simple finishing on the fresh concrete is usually done by trowel just before initial setting. The purpose of finishing is to make a smooth surface on the concrete member and to achieve a denser, compact, and properly graded surface layer to prevent water evaporation and increase wear resistance. Proper finishing of good-quality concrete can minimize the maintenance cost of a structural member. In addition to simple finishing, many special techniques have been developed to achieve a decoration effect, as shown in Figure 3-23.

3.6.5 Curing

For concrete to develop strength, the chemical reactions need to proceed continuously. Curing refers to procedures for maintaining a proper environment in fresh concrete for the hydration reactions to proceed. Curing is a simple procedure, and is frequently ignored. However, it is most important in producing a strong, durable, and watertight concrete. In concrete curing, the critical thing is to keep a sufficiently moist condition for the concrete, so that the hydration will not stop. Moist curing is provided by water spraying, ponding, or covering the concrete surface with wet sand, plastic sheets, burlap, or mats. Curing compounds, which can be sprayed onto the concrete surface to form a thin continuous sheet, are also commonly used, especially for vertical surfaces such walls and columns. Loss of water to the surrounding areas should be minimized. If concrete is cast on a soil subgrade, the subgrade should be wetted to prevent water absorption. In exposed areas (such as a slope), windbreaks and sunshades are often built to reduce water evaporation. For Portland cement concrete, a minimum period of 7 days of moist curing is generally recommended.

Under normal curing (at room temperature), it takes 1 week for concrete to reach about 70% of its long-term strength. Strength development can be accelerated with a higher curing

Figure 3-23 Decoration effect of concrete

temperature. In the fabrication of precast concrete components, steam curing is often employed, and the 7-day strength under normal curing can be achieved in 1 day. The mold can then be reused, leading to a more rapid turnover. If curing is carried out at a higher temperature, the hydration products form faster, but they do not form uniformly. As a result, the long-term strength is reduced. This is a worry when casting in hot weather. The concrete may need to be cooled down by the use of chilled water or crushed ice. In large concrete structures, cooling of the interior (e.g., by circulation of water in embedded pipes) is important, not only to prevent the reduction of concrete strength, but also to avoid thermal cracking as a result of nonuniform heating/cooling of the structure.

If fresh concrete is not properly cured, surface water evaporation is fast and the internal water has almost no change. Plastic shrinkage may occur if the rate of water loss (due to evaporation) exceeds the rate of bleeding. Shrinkage is the reduction in volume due to the loss of water. Such early shrinkage occurs when concrete is still at the plastic state (not completely stiffened), especially internal concrete, and thus it is called plastic shrinkage. The small amount of volume reduction due plastic shrinkage is accompanied by the downward movement of the surface layer material. If this downward movement is restrained, by steel reinforcements or large aggregates, cracks will form as long as the low concrete strength is exceeded. Plastic shrinkage cracks often run perpendicular to the concrete surface, above the steel reinforcements. A typical plastic shrinkage crack is shown in Figure 3-24. The presence of plastic shrinkage cracks can affect the durability of the structure, as they allow corrosive agents to easily reach the steel. If care is taken to cover the concrete surface and reduce other water loss (such as absorption by formwork or subgrade), plastic shrinkage cracking can be avoided. If noticed at an early stage, it can be removed by revibration.

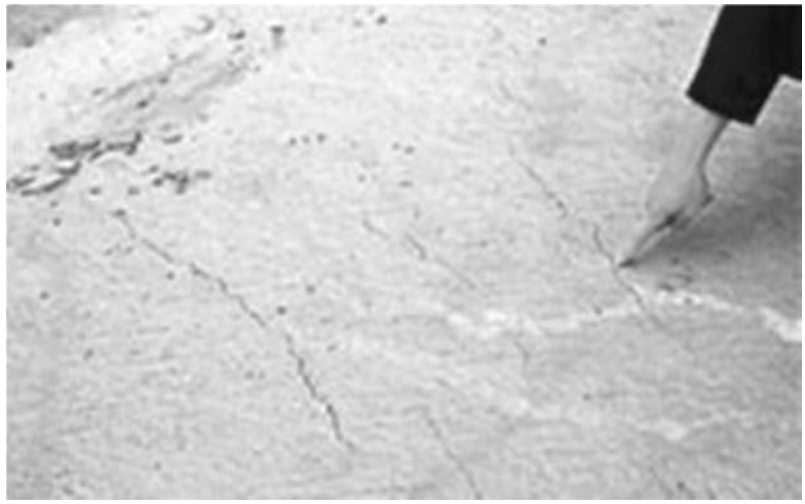

Figure 3-24 Plastic shrinkage crack

3.7 EARLY-AGE PROPERTIES OF CONCRETE

For concrete at an age less than 7 days, cement paste in the concrete undergoes a fast hydration process. Thus, both the mechanical properties and the pore size distribution of the concrete are different from that of mature concrete. The mechanical properties of concrete at early ages play an important role in determining construction speed and quality, especially for high-rise buildings and nuclear power plants. Better understanding of the mechanical properties of concrete at early ages is essential for engineers to make a right decision in the construction stage on issues such as construction planning. Lew and Reichard (1978) studied the compressive strength, splitting strength, and bond strength for concrete at early stages. They obtained relationships between compressive strength, secant modulus, splitting strength under different temperatures, and degree of hydration. Gardner (1990) studied the property development of young concrete with the incorporation of fly ash and proposed some empirical formulas. In recent years, several studies and conferences have been devoted to the various research for concrete at early ages, including the monitoring of determination of modulus of young concrete with the nondestructive method Jin and Li (2001). Jin and Li, (2000) made tensile strength measurements of young concrete, and determined the differences in mechanical properties for normal and high-strength concretes (Jin et al., 2005).

It has been found that the properties of concrete at early ages are very different from those of mature concretes. Here, a complete stress–strain curve is used as an example for illustration. A complete stress–strain curve represents the comprehensive behavior of concrete under an external force. Many properties can be obtained from the stress–strain curve, such as modulus of elasticity, an important parameter. Curves at ages of 18 h and 1, 2, 3, 7, and 28 days are plotted in Figure 3-25 for NSC and Figure 3-26 for HSC.

In Figures 3-25 and 3-26, there are significant differences in the shape of the compressive stress–strain response at various ages. The slope of the ascending part of the stress–strain curve becomes steeper for the concrete after 7 days for NSC, and after 2 days for HSC, and so does the slope of the descending part. As the compressive strength increases, both the ascending and descending portions of the compressive stress–strain curves become steeper and more linear,

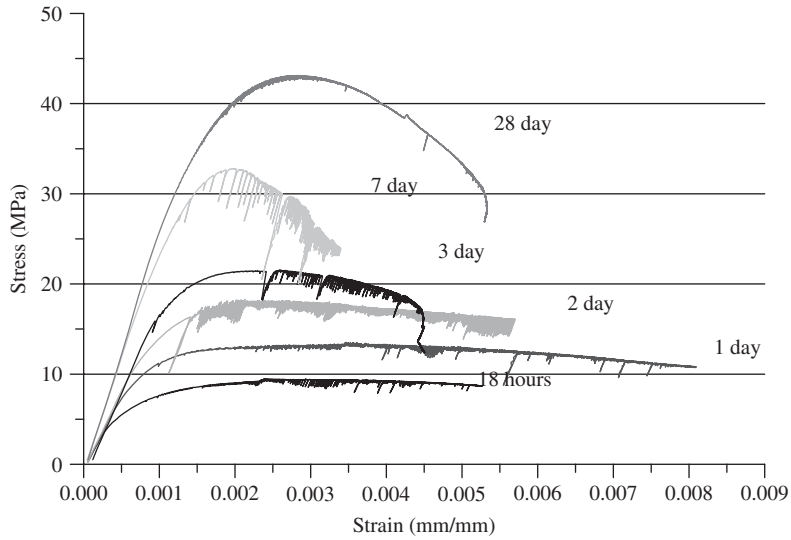

Figure 3-25 Complete stress–strain curves of NSC

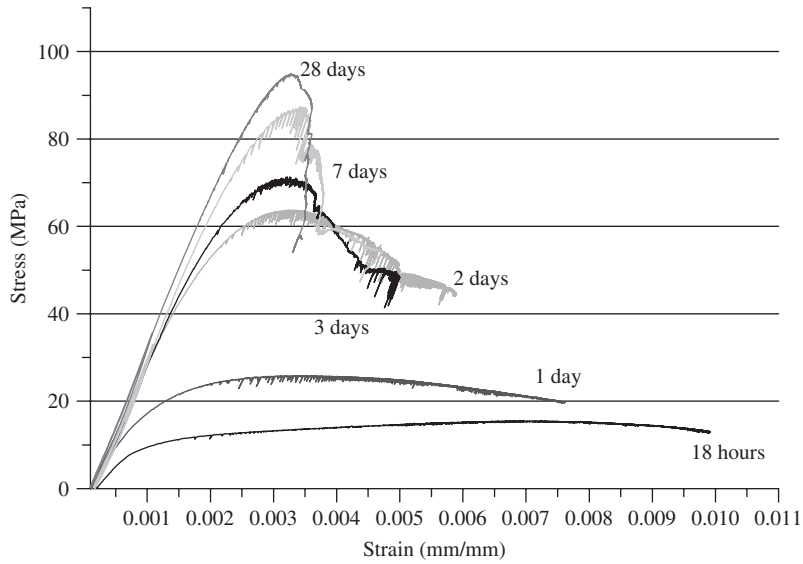

Figure 3-26 Complete stress–strain curves for HSC

which implies that the concrete becomes more brittle as the age increases. Noises can be observed in the later part of curves, which indicate the initiation and propagation of cracks.

It can be seen that the elastic modulus of concrete increases with age. To be quantified, according to ASTM C469-94, the secant modulus at a point with 40% of the maximum stress was used to compare the difference of static elastic modulus at various ages. The values are listed in the Table 3-13.

The remarkable difference between the curves of young concrete and those of mature concrete implies their diversity in mechanical properties. More ductile behavior can be observed

Table 3-13 E modulus of concrete

Age	18 H	1 Day	2 Days	3 Days	7 Days	28 Days
NSC	12.95	14.92	16.12	15.96	24.04	25.47
HSC	10.53	18.88	22.39	28.24	30.02	33.05

for concrete at early age, compared to a mature concrete's brittleness, due to its viscous characteristics. From the test results for compressive strength, it was found that there was an initial retardation of hydration exhibited for HSC as a result of high dosage of superplasticizer in the mixes. As shown in Table 3-13, after this retardation period, HSC has a higher rate of elastic modulus gain than NSC. Obviously, deducting the influence of the retardation, HSC has higher elastic modulus than NSC.

DISCUSSION TOPICS

Can you describe the terms of workability, consistency, cohesiveness, segregation, and bleeding of freshly concrete?

What are the methods to evaluate the workability of fresh concrete? What are their suitability and limitations?

Discuss the factors affecting consistency of concrete.

Discuss the factors affecting cohesion of concrete.

Why does workability decrease with time?

Discuss the role of water in fresh concrete.

What is the purpose of consolidation in concrete construction?

List some methods of curing.

Discuss the effects of curing in ensuring concrete quality.

Discuss the measures that can improve the cohesiveness of concrete.

Discuss the measures that can reduce the bleeding of concrete.

What is relationship between cohesiveness and segregation?

What is the significance of bleeding in forming microstructure?

Generally, how many common methods are used in a mix design of concrete?

What type of moisture condition in aggregate is assumed in a mix design of concrete?

What is difference between w/c and w/b?

How is the durability issue considered in a mix design of concrete?

Do you need to justify the moisture content of aggregates? How?

What is the purpose of trial mixes in a mix design of concrete?

What are the main difference in early age properties between HSC and NSC?

PROBLEMS

1. Use the American method to design a concrete mix that is required to have a specified mean strength of 30 MPa at 28 days. The presence of reinforcement requires a slump of 75 mm and a maximum size of aggregate of 10 mm. The aggregates are of normal weight, and gradings conform to the appropriate

standard with a fineness modulus of 2.8. (Assume that absorption is 0.7% and moisture condition of the aggregates is SSD; the bulk density of coarse aggregate is 1600 kg/m^3; and there will be extreme exposure condition to freeze-thawing.)

2. Use the American method to design a concrete mix that is required to have a specified mean strength of 25 MPa at 28 days. The presence of reinforcement requires a slump of 30–50 mm and a maximum size of aggregate of 40 mm. The aggregates are of normal weight and gradings conform to the appropriate standard with a fineness modulus of 2.8. (Assume there is negligible absorption and moisture content; a dry-rodded bulk density (unit weight) of coarse aggregate is 1550 kg/m^3, and there is a bulk specific gravity (SSD) of 2.70; the fine aggregate has a bulk specific gravity (SSD) of 2.65; and the concrete will be in extreme exposure conditions.)
3. In this problem, we assume that the strength of concrete strictly follows Abram's law as follows:

$$f_c = \frac{14{,}000}{4^{1.5(w/c)}}$$

where, f_c is compressive strength in a dimension of psi (i.e., lb/in^2).
For a concrete mixing with a projected strength of 5000 psi, what value of w/c ratio should be used? If the moisture content of sand (SSD) used for the mixture is 3.5% and amount of cement and sand (SSD) used for this mixture are 814 and 1950 lb, respectively, calculate the actual amount of water and sand (stock) that could guarantee the projected strength of the concrete.

4. A concrete mix with a proportion of 1:0.4:1.8:2.5 (B:W:S:A by weight) of 100 kg is prepared. The binder contains 90% Portland cement and 10% silica fume. The silica fume is in a form of slurry with 50% water. The concrete also uses 0.35% retarder and 1.5% superplasticizer. The solid content in the retarder is 35% and in the superplasticizer is 40%. How much water will be brought to concrete by the admixtures?
5. The material ratio for concrete mix is 1:1.5:2 (C:sand:coarse aggregate by weight). The BSG is 3.15 for cement, 2.5 for sand, 2.7 and for coarse aggregate. Air content is 4.8%. The gel/space ratio is 0.72. Calculate the water/cement ratio ($a = 0.8$) ?

REFERENCES

ASTM (1995). "Standard test method for time of setting of concrete mixtures by penetration resistance," C-403, Philadelphia.

Gardner, N. J. (1990) "Effect of temperature on the early-age properties of type I, type III, and type I/fly ash concretes," *ACI Materials Journal* (American Concrete Institute), 87 (1), 68–78.

Jin, X. and Li, Z. (2000) "Investigation on mechanical properties of young concrete," *Materials and Structures, RELIM*, 33, 627–633.

Jin, X. and Li, Z. (2001) "Dynamic property determination for early-age concrete," *ACI Materials Journal*, 98 (5), 365–370.

Jin, X., Shen, Y., and Li, Z. (2005) "Behavior of high-and normal-strength concrete at early ages," *Magazine of Concrete Research*, 57 (6), 339–345.

Lee, H. K., Lee, K. M., Kim, Y. H., Yim, H., and Bae, D. B. (2004) "Ultrasonic in-situ monitoring of setting process of high-performance concrete," *Cement and Concrete Research*, 34 (4), 631–640.

Lew, H. S. and Reichard, T. W. (1978) "Mechanical properties of concrete at early ages," *Journal of the American Concrete Institute*, 75 (10), 533–542.

Li, Z., Xiao, L., and Wei, X. (2007) "Determination of concrete setting time using electrical resistivity measurement," *Materials in Civil Engineering, ASCE*, 19 (5), 423–427.

Mindess, S., Toung, J. F., and Darwin, D. (2003) *Concrete*, 2nd ed., Upper Saddle River, NJ; USA, *Pearson Education*.

Neville, A. M. and Brooks, J. J. (1994) *Concrete Technology*, Longman.

Pessiki, S. P., and Carino, N. J. (1988) "Setting time and strength of concrete using the impact-echo method," *ACI Material Journal*, 85, 389–399.

Subramaniam, K. V., Lee, J., and Christensen, B. J. (2005) "Monitoring the setting behavior of cementitious materials using one-sided ultrasonic measurement," *Cement and Concrete Research* 35 (5), 850–857.

Voigt, T., Ye, G., Sun, Z., Shah, S.P., and Van Breugel, K. (2005) "Early age microstructure of Portland cement mortar investigated by ultrasonic shear waves and numerical simulation," *Cement and Concrete Research*, 35 (5), 858–866.

CHAPTER 4

STRUCTURE OF CONCRETE

4.1 INTRODUCTION

The type, amount, size, shape, and distribution of different phases present in concrete constitute its structure. The structure is multiscale in nature, ranging from nanometer scale, to micrometer scale, to millimeter scale. The elements of the structure above the millimeter scale can readily be seen by the naked eye, whereas the elements under the millimeter scale usually have to be resolved with the help of microscopes, scanning electron microscopy (SEM), transmit electron microscopy (TEM), and atomic force microscopy (AFM). The traditional term *macrostructure* is generally used for the gross structure, visible to the human eye. The limit of resolution of the unaided human eye is approximately one-fifth of a millimeter (200 μm). The traditional term *microstructure* is used for the microscopically magnified portion of a macrostructure. The magnification capability of modern electron optical microscopes is of the order of 10^5 to 10^6 times; thus, the application of transmission and scanning electron optical microscopy techniques has made it possible to resolve the structure of materials to a fraction of micrometer. Nowadays, the fast development of advanced experimental tools such as the transmission electron microscope, high-resolution magic-angle nuclear magnetic resonance spectroscopy, and the atomic force microscope has made it possible to observe the microstructure of the hydration products of concrete at the nanometer scale. To make the statement on the structure of concrete more accurate, in this book, the terms nanometer-scale structure and micrometer-scale structure are used to describe the structure of concrete.

Progress in the field of materials has resulted primarily in the recognition of the principle that the properties of a material originate from its internal structure. In other words, the properties can possibly be modified or improved by making suitable changes in the material structure. Although concrete is the most widely used structural material, its heterogeneous and highly complex structure is not fully understood yet. Knowledge on structure–property relationships in concrete is essential before we discuss the factors influencing the important engineering properties of concrete, such as strength, elasticity, shrinkage, creep, cracking, and durability. The highly heterogeneous and dynamic nature of the structure of concrete are the primary reasons why the theoretical structure–property relationship models, generally so helpful for predicting the behavior of engineering materials, are of little use in the case of concrete. A broad knowledge of the important features of the structure of individual components of concrete is nevertheless essential for the understanding and controlling of the properties of such a composite material.

Understanding the behavior of cement-based systems, including traditional concrete, requires that one first understand its structure, especially its structure in the nanometer and micrometer scales. Concrete and other cement-based materials are typically complex in structure and require investigation at several different levels of magnification to develop an appreciation of pertinent details. The objectives of this chapter are to understand the multiscale nature of

concrete, to develop an appreciation of the structure of ordinary Portland cement concrete, and to outline an approach to *microstructural engineering*—methods of modifying the structure.

4.2 STRUCTURAL LEVELS

Concrete is a typical multiscale material. Its structure cannot be approached at a single level of scale, but rather requires examination and documentation over a very large range of magnifications. According to Diamond (1993), the structure of a concrete can be examined at five levels: visual, petrographic, intermediate scanning electron microscopy (SEM), high magnification of SEM, and the nanometer level, as shown in Table 4-1. Each level of the structure corresponds to a certain range of the length scale.

The visual level is in the millimeter scale. In this level, aggregates and hardened cement paste can be observed from examination of a cross section of the concrete with the naked eye. As an example, let us take a look at Figure 4-1. Two phases that can easily be distinguished in the figure are the aggregate particles of varying size and shape, as well as the binding medium, composed of an incoherent mass of hydrated cement paste. Details of the size and shape of coarse aggregate are visible. The mineralogy details of the coarse aggregate can be observed and interpreted by an experienced petrographer. At the millimeter scale or visual level, therefore, concrete may be considered to be a two-phase material, consisting of coarse aggregate particles dispersed in a matrix of the cement paste. No details of the hydrated cement paste can be viewed.

The petrographic level falls in the scale of 10^{-5} to 10^{-3} m, which can be made visible in stereooptical and petrographic microscopes. Optical microscopy is more usefully applied to either plane polished surfaces or specially ground petrographic thin sections, typically 25 to 30 μm, and transparent to light. With special techniques, large-area thin sections of 150 × 100 mm can be produced. Such sections are often produced by a process that includes impregnation of the empty spaces, such as cracks, air voids, and empty capillary pores, by a fluorescent dye dissolved in low-viscosity epoxy resin. When such specimens are examined in petrographic microscopes equipped for fluorescent light examination, the details of crack patterns and the degree of local inhomogeneity can be revealed. Figure 4-2 shows an area of a concrete examined by SEM at a

Table 4-1 Levels of microstructure

Level	Optimal Magnification Range	Usual Method of Observation	Structures to be Revealed
Visual	1×–10×	Unaided eye or hand lens	Details of coarse aggregate and air voids
Petrographic	25×–250×	Optical microscope	Fine aggregates, air voids, some paste details, and some cracks
Intermediate SEM	250×–2000×	SEM backscatter mode on plane polished surfaces	Arrangement and juxtaposition of cement paste particles, sand, capillary voids
High-magnification SEM	2000×–20,000×	SEM secondary electron mode on fractured surfaces	Details of the internal structure of individual cement particles and masses
Nanostructure	1,000,000×	AFM, TEM	Some details of C–S–H

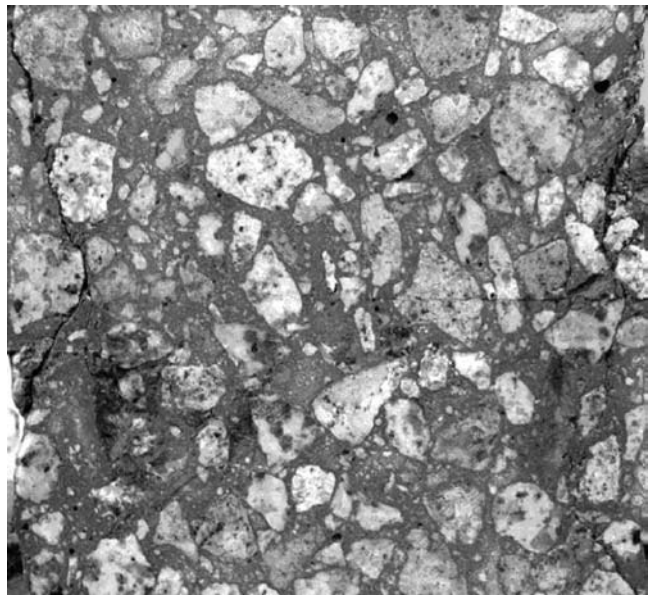

Figure 4-1 Visual level of a concrete's structure (mm scale)

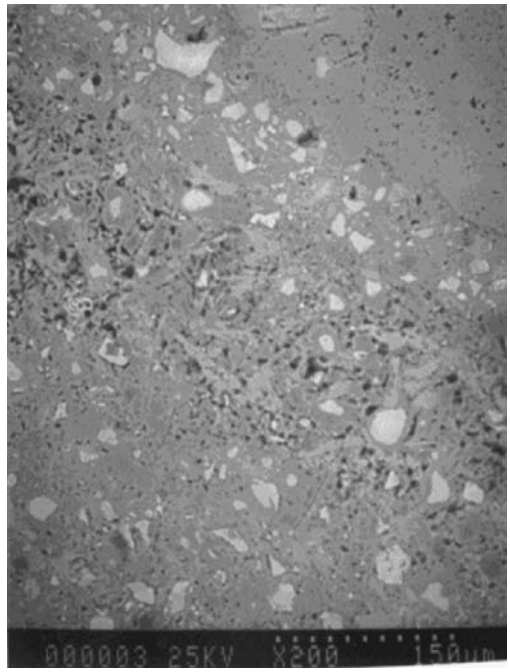

Figure 4-2 Structure of concrete at petrographic level (the white spots are unhydrated cement particles; the black ones are air voids)

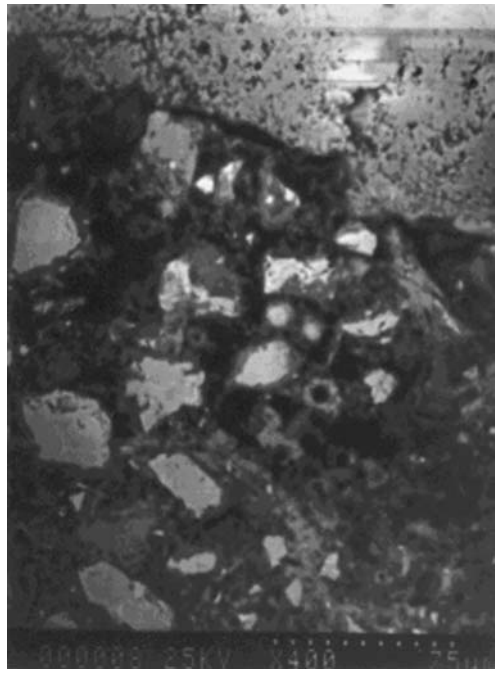

Figure 4-3 Structure of concrete at the intermediate SEM level

magnification of 200×. From the figure, the lower grade of fine aggregates, such as finer sand of size of the order of tens of micrometers, entrapped air voids, and unhydrated cement particles can be observed.

The corresponding length scale for the intermediate level is 10^{-5} m. The technique used for examination in this level is backscatter electron detector scanning microscopy. It is capable of providing reasonably high resolution and at same time being sensitive to small differences in electron scattering power. In a usual procedure, the specimen is dried and potted in a low-viscosity epoxy preparation, which is then sliced with a diamond saw to get a plane surface. The slice is polished before the SEM test. Figure 4-3 is such an SEM backscattered photo taken at a magnification of 400×. Different gray levels in the figure are due to different electron backscatter coefficients of different chemical compositions. The brightest ones are unhydrated cement particles and the darkest areas are pores. From the figure, the arrangement and juxtaposition of cement particles, capillary voids, and unhydrated cement particles, and the interface between coarse aggregates and matrix can be clearly observed. Moreover, the tiny crack on the surface of the coarse aggregate in the top of the photo is readily apparent. Basically, there is no significant difference between the petrographic and intermediate level, and the low end of the intermediate level overlaps the high end of the range available to the petrographic level.

The high-magnification SEM level corresponds to the micrometer scale. The structure of concrete at this level is basically examined in an SEM using a secondary electron detector. The mechanism of contact formation of the secondary image depends primarily on differences in elevation and the local position of the hydrated cement rather than on differences in backscattering ability associated with different elemental composition. Thus, the fracture surface has to be used in the secondary mode of an SEM. Figure 4-4 is a typical photo of a secondary mode taken at a magnification of 10,000×. From the figure, the aggregation of C–S–H, the plate-shaped CH,

and the needle-shaped AFt can be clearly distinguished. In this level, the structure of individual cement particles, the details of different hydration products, and the lower grade of the capillary pores can be observed. From Figure 4-4, it can be seen that the structure is neither homogeneously distributed, nor are the products themselves homogeneous. For instance, in some areas more solid hydrated products appear while other areas are highly porous. For a well-hydrated cement paste, the inhomogeneous distribution of solids and voids may be improved. Figure 4-5

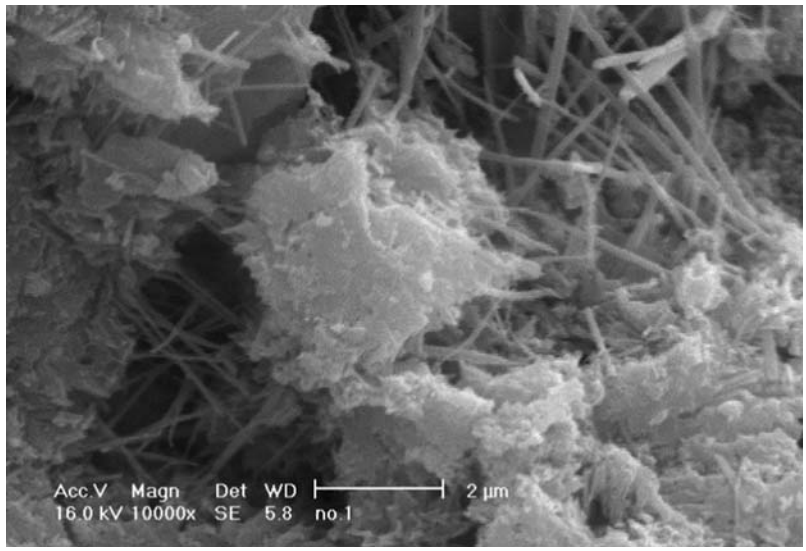

Figure 4-4 Structure of concrete at a high-magnification SEM level

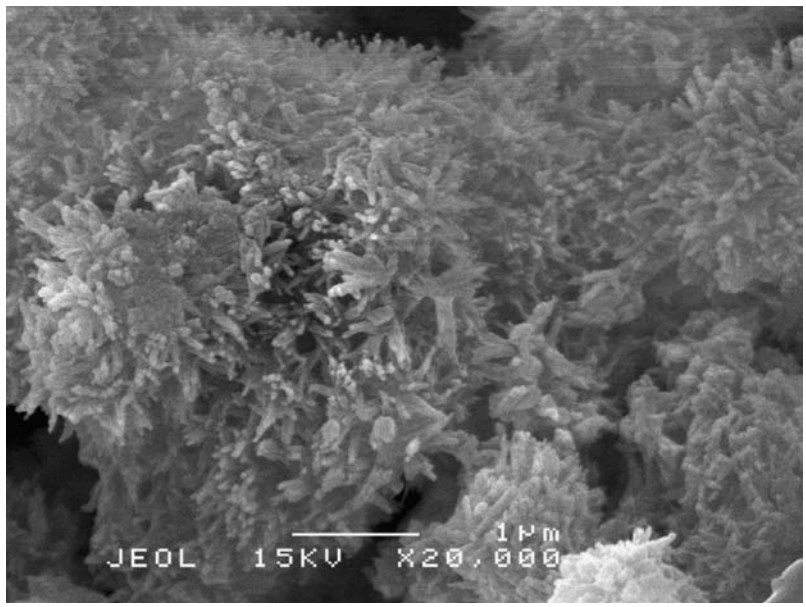

Figure 4-5 Morphology of C–S–H

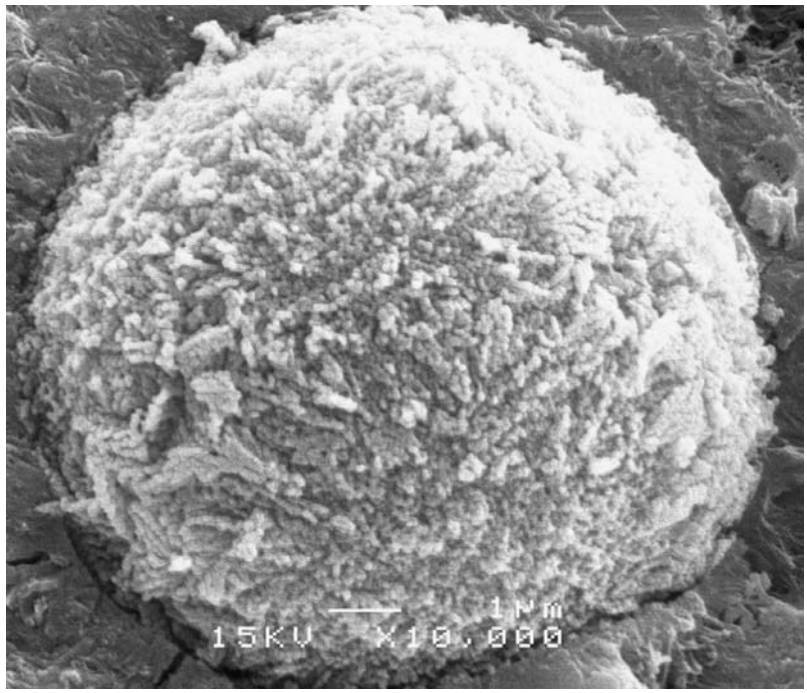

Figure 4-6 Reacted fly ash particle in concrete

shows an SEM photo of the secondary mode taken at a magnification of 20,000×. The morphology of C–S–H can be clearly observed. Figure 4-6 shows a fly ash particle in cement paste. It can be seen that the secondary hydration products are formed on the surface of the fly ash particle. Very fine cracks, about 0.1 micrometer wide, can be seen clearly in surrounding fly ash particles. The ultimate structure of hydrated cement at the nanometer scale is that of calcium silicate hydrate (C–S–H), which is considered to be responsible for the strength of Portland cement concrete. Understanding the structure of C–S–H plays an important role in revealing the concrete strength nature. However, knowledge in this aspect is limited.

Due to the availability of advanced measurement equipment in the nanometer scale, such as atomic force microscopy, nuclear magnetic resonance, and transmission scanning microscopy, as well as powerful computers with powerful software, it is now possible to characterize or simulate some features of C–S–H. Figure 4-7 is a photo of C–S–H taken by AFM. Some aggregation of C–S–H, in an egg shape with a size of 30 to 50 nanometers, can be clearly seen. There exists a clear boundary among the egg-shaped grains and a strong trend in orientation can also be observed. Because C–S–H plays an important role in determining concrete properties, it has recently become a hot topic in concrete research. The following section discusses the modeling of C–S–H structure in detail.

4.3 STRUCTURE OF CONCRETE IN NANOMETER SCALE: C–S–H STRUCTURE

The structure of calcium silicate hydrate (C–S–H) gel is considered at the nanometer scale. Since C–S–H is the most important hydration product in cement-based materials—it takes up

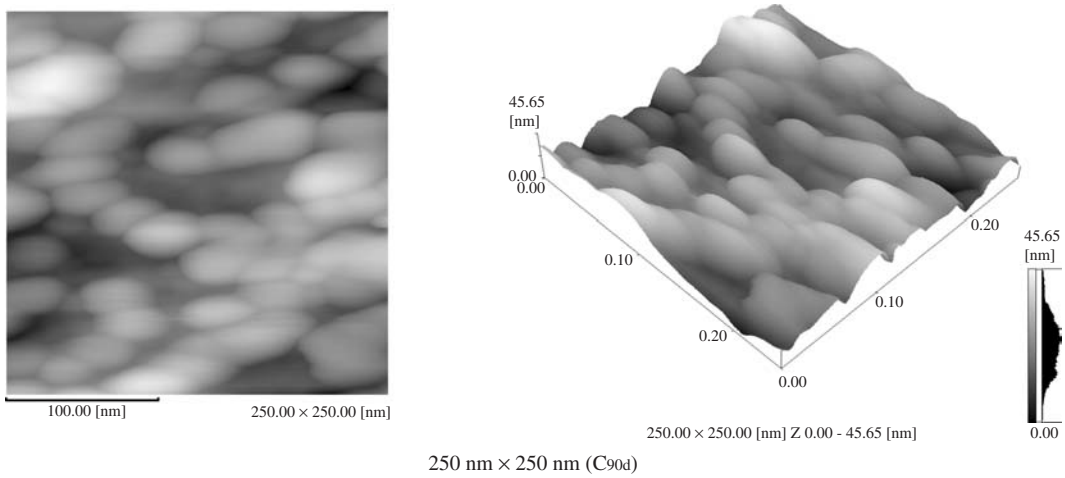

Figure 4-7 AFM photo of C–S–H at nanometer scale

approximately 50–70% of the fully hydrated cement paste and makes dominant contributions to the mechanical properties of the cement-based material—understanding its structure is critical in revealing concrete properties. Unfortunately, with decades of research and development, even in terms of modern advanced technology, the nature of C–S–H gel is still obscure. This is because of not only the intrinsic difficulty in the characterization of the amorphous structure within a single paste and the Ca/Si ratio probably varying from one area to another, but also the complex composition and reaction in the materials, especially when some additives are utilized. To construct a C–S–H phase model, the following aspects should be considered first.

4.3.1 Three aspects of a C–S–H model

(a) *Chemical composition*: A model for the C–S–H structure must be compatible with the widely observed compositional variations, which are contemporarily considered as the most important factors that need to be satisfied. In fact, in recent studies, the models established all start from or concentrate on the chemical composition approach. The Ca/Si ratio in hardened C_3S pastes or pure Portland cements generally has a range of values from 0.7 to 2.3, and a mean value of 1.7 has been experimentally confirmed. Recently a C–S–H composition formula of $(CaO)_{1.7}(SiO_2)(H_2O)_{1.8}$ with density of 2604 kg/m^3 was obtained (Allen et al., 2007) by small-angle x-ray and neutron scattering (SAXS and SANS) methods. It may be used as a starting point to construct a C–S–H model.

(b) *Silicate anion structure*: The basic unit of all the silicates is the SiO_4 tetrahedron. Different numbers of silicate units can form various silicate structures, as shown in Figure 4-8. It can be seen from the figure that each silicate can coordinate with different numbers of silicate units, which is the base for the characterization of the C–S–H structure by ^{29}Si magic-angle spinning nuclear magnetic resonance (MAS-NMR). The Q_n factor ($n = 0, 1, 2, 3, \ldots$) is used to represent the fractional chemical shift of a silicon atom bound to n bridging oxygen (n, the coordinate number of a specific silicate unit with other silicate units; 0, single silicate; 1, dimer or end of chains; 2, middle of silicate chains). The silicate anion structure of the C–S–H phase formed in the hydration of Portland cement has been studied most extensively by ^{29}Si MAS-NMR or trimethylsililation techniques with some of the results described below.

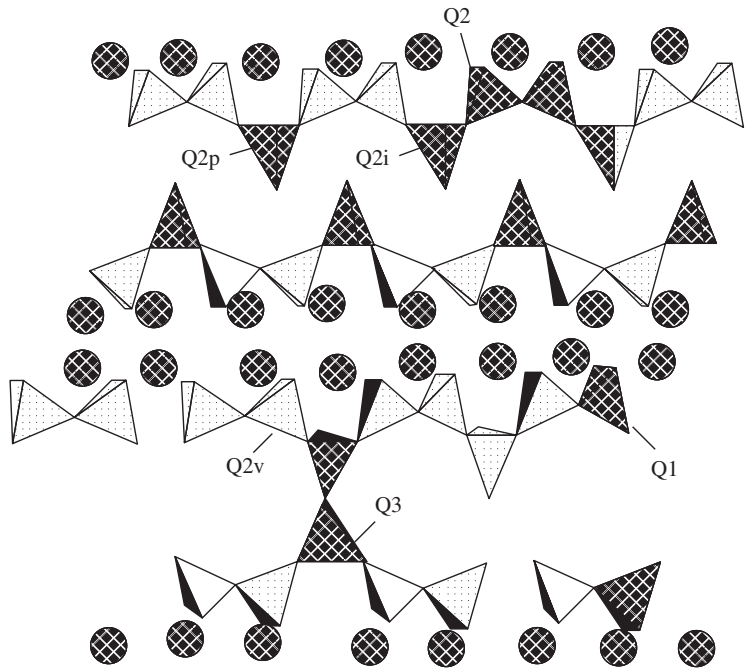

Figure 4-8 Different types of silicate formation

In ^{29}Si MAS-NMR, Q_1 and Q_2 predominate. The ratio of Q_1/Q_2 declines with the hydration progress, indicating that the lengths of silica chains are prolonged at the expense of a decrease of the dimers and an increase of the polymers. However, it has been established that the dimer is the most predominant of all silicate species and the linear pentamer the second most abundant, followed by the octamer, which shows a sequence of silicate chain lengths of $(3n - 1)$. Therefore, for the establishment of the C–S–H gel model, it should account for such a sequence of chain length $(2, 5, 8, \ldots, 3n - 1$, where n is an integer). According to Richardson and Groves (1992), the mean chain length of silicate chains should also be less than 5. If the dimer and pentamer are mainly utilized in the model, this requirement can be achieved automatically.

The Q_3 and Q_4 units cannot form in the hydrated material or in the course of hydration, but they may form in a reaction of the C–S–H phase with CO_2 from the atmosphere. For the Q_0 unit, its fraction steadily declines with the consumption of nonhydrated C_3S, but it may still exist in the late stage of hydration. It has been observed from experiments that in C–S–H, Q_0 is about 13%, Q_1 50%, and Q_2 33%.

(c) *Morphology*: The C–S–H phase in a mature concrete is not evenly distributed and may exist in a variety of morphologies, such as in the form of fibers, flakes, honeycombs, tightly packed grains, or a seemingly featureless dense material. However, at high resolution it becomes apparent that all these C–S–H types have similar underlying foil morphology and therefore probably contain only one type of C–S–H at the nanometer level. The morphologies of the C–S–H formed within the boundaries of the original anhydrous grains (called *inner product*) and in the space originally filled with water (called *outer product*) are different, as is shown in Figure 4-9. The inside is dense with a structure similar to fine foil morphology, while the outside is less dense and more like a fibrillar structure.

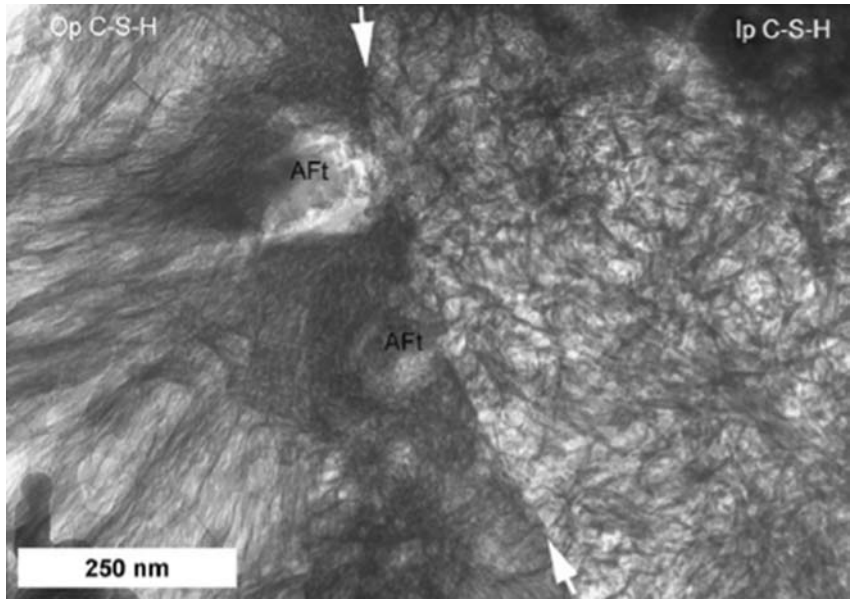

Figure 4-9 TEM of inner product and outer product of C–S–H

4.3.2 Common C–S–H models

With more than half a century's development, a large number of C–S–H gel models have been proposed to describe the relative nanostructure. Richardson has systematically summarized C–S–H models (2008). Tobermorite is one of the earliest models proposed by Taylor and Howison (1956). A tobermorite phase can be classified as tobermorite 14 Å (angstrom), tobermorite 11 Å, and tobermorite 9 Å, according to their basal spacing. The main difference between these models is the hydration degree, with the order of hydration degree in the order of 14 Å > 11 Å > 9 Å. Its ideal chemical composition is $[Ca_4(Si_3O_9H)_2]Ca \cdot 8H_2O$, according to Taylor (1997). But in other references (Bonaccorisi et al., 2005; Richardson, 2008), some differences exist on the amount of water, e.g., $Ca_5Si_6O_{16}(OH)_2 \cdot 7H_2O$ and $[Ca_4(Si_6O_{16}(OH)_2]Ca \cdot 4H_2O$, indicating the difference in regard to understanding the hydration degree. The widely accepted framework of tobermorite 14 Å can be briefly summarized as follows:

(a) The structure of tobermorite 14 Å is basically a layered structure.

(b) The central part is a Ca–O sheet (with an empirical formula: CaO_2, though the chemical aspect CaO should always be CaO, which implies that the oxygen in CaO_2 also includes that of the silicate tetrahedron part).

(c) Silicate chains envelope the Ca–O sheet on both sides, with the characteristics mentioned later.

(d) Between individual layers, Ca^{2+} and H_2O are filled into the space to balance the charges and determine the layer distance, respectively.

A typical sketch of the structure of tobermorite 14 Å is shown in Figure 4-10. In the chemical formula, this 14 Å tobermorite structure can be determined as shown in Figure 4-11, which is much easier to understand in regard to composition aspects, but is obscure on the stereo

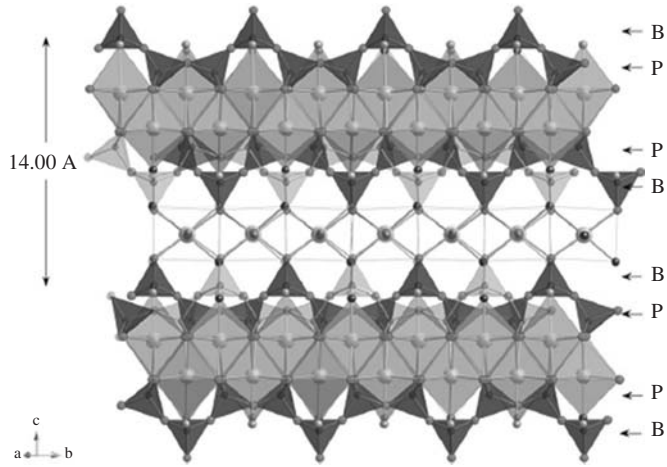

Figure 4-10 The structure of 14 Å tobermorite (Bonaccorsi et al., 2005) B-bridging layer P-paired layer

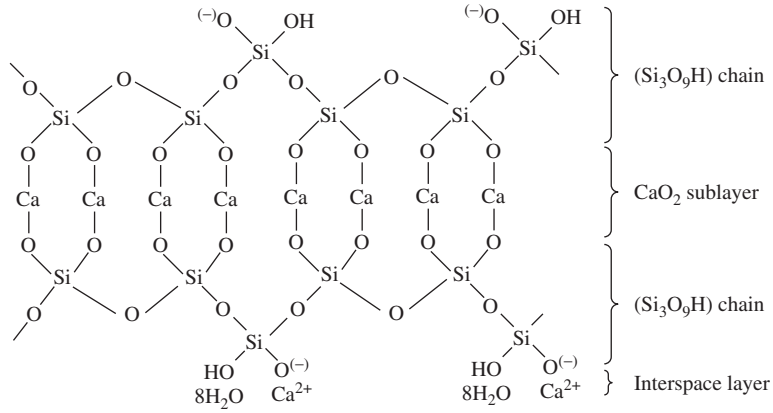

Figure 4-11 Chemical formula of 14 Å tobermorite

structure and water molecules. The subcell chemical composition is $[Ca_4Si_6O_{16}(OH)_2]^{2-}$. In the tobermorite structure, in most cases, the bridging tetrahetra can be removed to increase the Ca/Si ratio, which also agrees with experimental results to some extent.

The Jennite phase is another popular model used to represent the structure of C–S–H. It has the chemical composition of $Ca_9Si_6O_{18}(OH)_6 \cdot 8H_2O$, which has a much higher Ca/Si ratio of 1.5 than that of tobermorite. The Ca/Si ratio in jennite is closer to the experimentally confirmed value of 1.7 in the C–S–H gel, but its full structure is not well determined due to the poor quality of available crystals. Some information about its structure has been proposed by different researchers, based on jaffeite or metajennite, which are related to the structure of jennite. Until now, the most useful structure for the jennite model was proposed by Bonaccorsi et al. in 2004, which agreed well with some experimental results. Basically, jennite is built up by the combination of three modules:

1. Edge-sharing calcium octahedrals
2. "Dreierkette" form of silicate chains
3. Additional calcium octahedrals in special positions on the inversion center to connect different layers

According to Richardson and Groves (1992), a jennite model can be built up from jaffeite with the following procedures:

1. Identify the "tilleyite ribbon" in jaffeite.
2. Remove the ribbon.
3. Insert bridging silicate to form metajennite.
4. Add Ca^{2+} ions and water molecules to form jennite.

In this structure, distinct characteristics about Ca–O layers can be easily found. In some Ca octahedrals, all the vertices of the octahedrals are shared with tetrahedral or interlayer calcium (see Figure 4-12), while some on both sides of the layers are thoroughly free to combine with water.

The distinct difference between jennite and tobermorite is that in a perfect jennite structure only Ca–OH bonds are present, while in a perfect tobermorite structure only Si–OH bonds are present. Taylor (1997) made a hypothesis that in the C–S–H model most of the layers were of structurally imperfect jennite and a smaller proportion was related to tobermorite. It implies that the C–S–H model is a combination of tobermorite and jennite. This model is later called the T/J model. The general formula of C–S–H can be expressed as:

$$Ca_x H_{(6n-2x)} Si_{(3n-1)} O_{(9n-2)} \cdot z\,Ca\,(OH)_2 \cdot m H_2O \tag{4-1}$$

where $Si_{(3n-1)}O_{(9n-2)}$ is an average silicate anion, Ca_x the necessary charge to the balance, not distinguished from those in the interlayers, $H_{(6n-2x)}$ the hydrogen atoms that are directly attached to silicate anions, which are gained by the charge balance and obtained by the following formula:

$$2(9n-2) - 2x - 4(3n-1) = 6n - 2x \tag{4-2}$$

while $z\,Ca(OH)_2$ is the number of $Ca(OH)_2$ units (without considering the structure) with $z = 2n$ $(n = 0, 1, 2, \ldots)$, and $m H_2O$ the number of water molecules bound, but not present, as hydroxyl groups.

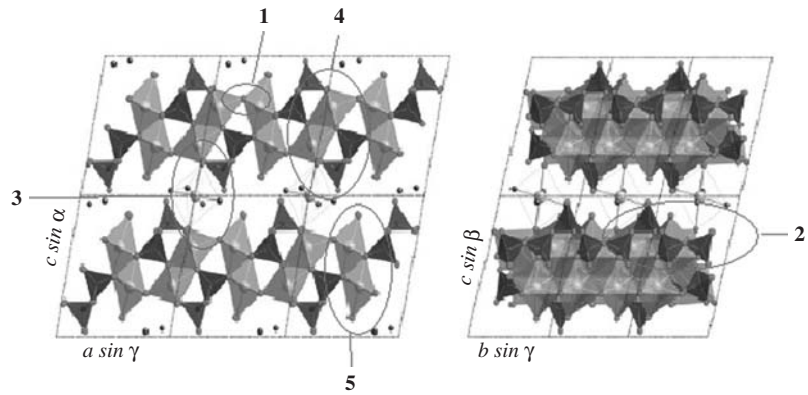

Figure 4-12 Jennite structure on projection from [010] and [100] (Bonaccorsi et al., 2004)

By combining the general formula with ^{29}Si NMR measurement, information about the structure can be obtained.

^{17}O NMR spectroscopy and ^{29}Si NMR have demonstrated the existence of the Ca–OH group and Si–OH groups, no matter whether with high Ca/Si ratios or low ones. When Ca/Si < 1.3, the Si–OH group is necessary and dominant, while when Ca/Si > 1.3, the Ca–OH group is necessary and dominant, which is consistent with the jennite structure proposed by Taylor. This point can also be explained by the charge-balance assumption and is consistent with the degree of protonation proposed by Richardson. The charge balance calculation is based on the assumption that the nonbridging oxygen (NBO) is preferentially balanced by Ca^{2+}. Therefore, to maintain the electrical neutrality, the following equation has to be satisfied:

$$2C/S - \mathrm{NBO} = 0 \text{ (here NBO represents NBO per tetrahedron)} \tag{4-3}$$

For the case of $2C/S - \mathrm{NBO} < 0$ (*low Ca/Si ratio case*), Ca^{2+} is not sufficient and the residual NBO must be neutralized by the formation of Si–OH; therefore, Si–OH linkage is essential. For the case of $2C/S - \mathrm{NBO} > 0$ (*high Ca/Si ratio case*), Ca^{2+} is surplus and extra Ca^{2+} must receive charge-balance from the formation of Ca–OH; therefore, the Ca–OH linkage is essential. Consequently, the process can be expressed as

$$\mathrm{NBO(Si{-}O{-}Ca)} + \mathrm{H_2O} \rightarrow \mathrm{Ca{-}OH} + \mathrm{Si{-}OH} \tag{4-4}$$

Based on surface chemistry, the interlayers are of electrical neutrality, while the surface can be charged and the thermodynamics analyzed. It is proposed that no matter how C–S–H is synthesized, as long as the equilibrium state is the same, the structure of C–S–H should be the same. Based on some equilibrium constants, the structure of C–S–H can be obtained. Models proposed here are structurally descriptive. Concerning the bulk phase, the structural unit of C–S–H is proposed as follows.

Low Ca/Si ratio case

Mainlayer: dimeric, charged balance by Ca^{2+} and proton–$Ca_2H_2Si_2O_7$

Two successive dimerics bridged by tetrahedra: $Ca_2H_2Si_2O_7(SiO_2)_x, (x = 1)$

Silanol partially ionized, balanced by Ca (interlayer): $Ca_2H_{2-p}Si_2O_7(SiO_2)_xCa_{p/2}$ or $Ca_2H_{2-p}Si_2O_7(SiO_2)_x(CaOH)_{2/p}$

Missing bridging tetrahedra by $Ca(OH)_2$: $Ca_2H_{2-p}Si_2O_7(SiO_2)_xCa_{p/2}\ (Ca(OH)_2)_y$

When the bridging tetrahedra is missing, some Si change should occur, which is not shown in the last formula, and thus is questionable. In the whole process, there is no concern about water, and the process is therefore not well-rounded.

High Ca/Si ratio case

Steps are the same as those for the low Ca/Si ration, except is the last step:

The missing silicate bridging tetrahedra is replaced by $Ca(OH)_2$—tobermorite-like

Or the nonbridging tetrahedron is replaced by $2OH^-$—jennite like.

Richardson (2008) classified mainly two categories of C–S–H chemistry: T/J and T/CH composition. For the T/J composition, C–S–H is an assembly of tobermorite regions followed by jennite domains, or, briefly speaking, a mixture of tobermorite and jennite, which is widely known. For the T/CH composition, C–S–H is a kind of tobermorite layer sandwiched between

calcium hydroxide, or it is based on the structure of $Ca(OH)_2$ to some extent. This kind of structure, according to the literature, was the one studied most, dating back to the 1960s. It did not consider the detailed structural characteristics, but some stoichiometry or compositional ones.

The strongest evidence of this model is the chemical extraction experiment showing that significant larger amounts of CH can be extracted from the C–S–H gel than that inferred by XRD. Therefore, the CH is regarded being incorporated into the nearly amorphous gel phase (Viehland et al., 1996). If this assumption makes sense, there should be an explicit signal for CH when doing analysis; however, this is not the case for most experimental results when studying common cement-based materials. But, as is mentioned by Richardson, the T/CH model is more appropriate for the KOH-activated metakaolin Portland cement due to the observation that CH is always present in selected area electron diffraction (SAED).

Recently, a realistic model of C–S–H has been proposed by Roland et al. (2009) through molecular simulation. The model has been compared with experimental results, showing acceptable agreement. The model is based on the structure of 11 Å tobermorite with the starting Ca/Si ratio of 1. This structure is quite analogous to that of 14 Å tobermorite, having a difference in the distance. However, in this model, it is assumed that no OH group is present, which might not be the case for real C–S–H. The procedures to build up the model are as follows.

Step 1: Remove all the water molecules in the tobermorite structure.

Step 2: Remove the SiO_2 neutral group according to the ^{29}Si NMR results to raise the Ca/Si ratio to 1.65, which is the case of missing tetrahedra in the previous mentioned models. This value is close to the mean value of 1.7 (NMR : $Q_0 = 13\%, Q_1 = 67\%, Q_2 = 20\%$, no Q_3 and Q_4, dimers are predominant ones, monomers are present but not that much).

Step 3: Optimize the remaining structure by 0 K energy minimization and relax the whole cell by the core–shell potential model, obtaining a significant distortion of the layer structure.

Step 4: Simulate water adsorption by the Grand Canonical Monte Carlo simulation.

Step 5: Further relax the whole cell under constant pressure and temperature with the interlayer spacing of 11.9 Å and density 2.45 g/cm^3, which is to some extent different from 2.6 g/cm^3 (before this step, the obtained density is shown to be 2.56 g/cm^3, which is much closer).

The unique observation in this model is the distribution of water molecules. In previous studies, water molecules have been considered to be located in the interlayers. However, in this simulation, the water lies not only in the interlayer regions, but also around the silica monomers, which emphasizes the water function in the mechanical properties. Besides, in the optimization of the structure in step 3, a clear distortion structure can be observed. When compared with experimental results, the C–S–H structure can be described as a glass for a short distance range while retained as a layered crystal feature for a long distance range. Here short range and long range refer to intra- and interlayer spacing, respectively.

4.4 TRANSITION ZONE IN CONCRETE

In the presence of an aggregate, the structure of the hydrated cement paste in the vicinity of large aggregate particles is usually different from the structure of the bulk paste or mortar in the system. This forms an individual phase different from the aggregate and bulk hardened matrix in concrete. In fact, many aspects of concrete behavior under stress can be explained only when the cement paste–aggregate interface is treated as an individual phase (third phase) of the concrete structure. Thus, the third phase makes unique features to the concrete structure.

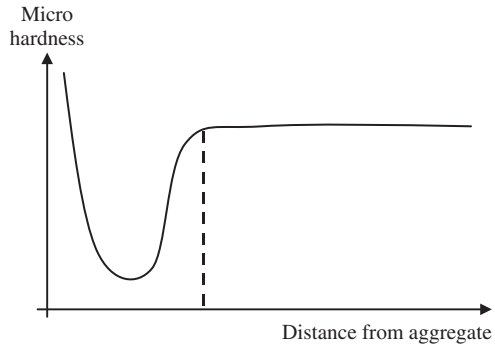

Figure 4-13 Micro hardness distribution

Two methods have been used to identify the existence of the third phase. The first method is micro-indentation, which is a method used to detect the hardness of a material. A typical curve of the variation of hardness along a line in the radial direction from the edge of an aggregate is shown in Figure 4-13. It can be seen from the figure that an obvious valley appears adjacent to the aggregate, which demonstrates that a relative soft belt exists between the aggregate and the bulk matrix. The second method used to identify the third phase is direct observation of an SEM photo, as shown in Figure 4-3. It can be clearly seen that more dark areas appear in the adjacent region to the aggregate. Since the SEM photo was taken in the backscatter mode, the brightness of the photo is related to the amount of the reflected electrons from the surface examined. The dark area means that less or no electrons are reflected and implies that they are pores on the surface.

The third phase is called the transition zone or interfacial zone in concrete technology, which represents the interfacial region between the coarse aggregate particles and the bulk hydrated cement paste. Existing as a thin shell, typically 10 to 50 μm thick around the large aggregate, the transition zone is generally weaker than either of the two other phases of concrete. The transition zone exercises a far greater influence on the mechanical behavior of concrete than is reflected by its volume fraction. It should be pointed out that each of the three phases is multiphase in nature. For instance, each aggregate particle may contain several materials, in addition to microcracks and voids. Similarly, both the bulk hydrated cement paste and the transition zone generally contain a heterogeneous distribution of different types and amounts of solid phases, pores, and microcracks, which are described below. Moreover, it should be noted that unlike other engineering materials, the structure of concrete does not remain stable (i.e., it is not an intrinsic characteristic of the material). This is because two components of the structure—the hydrated cement paste and the transition zone—are subject to change with time, environmental humidity, and temperature.

4.4.1 Significance of the transition zone

The volume fraction of the transition zone in concrete is usually only a few percent, but its influence on concrete properties is far more than such a percentage. It is a fact that many concrete macroscopic properties are sourced in the transition zone. The following examples can support this statement.

(a) As shown in Figure 4-14, when tested separately in uniaxial compression, under the same loading level, the aggregate and hardened cement paste (HCP) can remain elastic, whereas

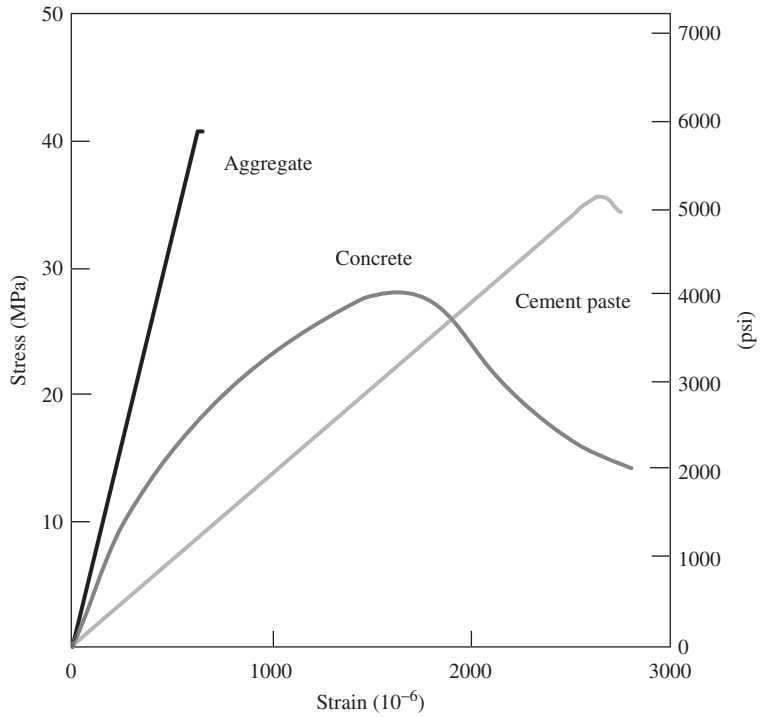

Figure 4-14 Stress–strain behavior of aggregate, concrete, and HCP

Table 4-2 Permeability coefficients of different materials

Type	Permeability Coefficient
HCP	6×10^{-12} cm/sec
Aggregate	$1–10 \times 10^{-12}$ cm/sec
Concrete	$100–300 \times 10^{-12}$ cm/sec

concrete itself shows inelastic behavior. The factor responsible for such behavior is the transition zone. Because the transition zone is porous and thus can deform more, its existence will generate higher deformation under the same load than both aggregate and HCP do.

(b) Table 4-2 shows the permeability coefficient of the aggregate, HCP, and concrete. It can be easily seen that the permeability of a concrete containing the same aggregate and HCP is the highest, and is an order of magnitude higher than the permeability of the corresponding components. The higher permeability coefficient of concrete can be attributed to its transition zone. Since the transition zone is more porous than the aggregate and bulk HCP, water can more easily flow through transition zone, which results in a high permeability.

(c) It has been discovered that at a given cement content, water/cement ratio, and age of hydration, both HCP and cement mortar are always stronger than the corresponding concrete. Also, the strength of concrete goes down as the coarse aggregate size is increased. Again, the porous nature of the transition zone in concrete is responsible for the reduction

of compressive strength as compared to the corresponding HCP and mortar, as shown in Figure 4-14.

In addition to the examples above, the existence of the transition zone in concrete can be used to explain why concrete is brittle in tension but relatively tough in compression? Why is the compressive strength of a concrete higher than its tensile strength by an order of magnitude?

It can be concluded that although the transition zone is composed of the same elements as the hydrated cement paste, the structure and properties of the transition zone are different from the bulk hydrated cement paste, and its influence on concrete properties is significant. Therefore, it should be treated as a separate phase of the concrete structure.

4.4.2 Structure of the transition zone

It is not easy to interpret the structure of the transition zone in concrete, even with advanced equipment. The structural characteristics of the transition zone in concrete described here are based on the work of Maso (1980), following the sequence of the development from the time the concrete is placed. In freshly compacted concrete, water films try to form around the large aggregate particles due to hydrophilic behavior. This leads to a higher water/cement ratio closer to the larger aggregates (i.e., in the bulk matrix). Due to the relatively large amount of water, there are fewer cement particles surrounding the aggregates. With the process of hydration, calcium and hydroxyl ions produced by the dissolution of calcium silicate crystallize when a critical saturation is reached and form calcium hydroxide [$Ca(OH)_2$] in the adjacent region of aggregate as in the bulk paste. Owing to the high solution content, the crystalline product of CH in the vicinity of the coarse aggregate can grow to relatively large crystals. Meanwhile, more water evaporation occurs, which forms a more porous framework than in the bulk cement paste or mortar matrix. The platelike calcium hydroxide crystals tend to form in oriented layers. Moreover, with the progress of hydration, poorly crystalline C–S–H and a second generation of smaller crystals of ettringite and calcium hydroxide start to fill the empty space that exists between the framework created by the large ettringite and the calcium hydroxide crystals. This helps to improve the density and hence the strength of the transition zone. A diagrammatic representation of transition zone in concrete is shown in Figure 4-15.

4.4.3 Influence of the transition zone on properties of concrete

The transition zone is generally considered the weakest link of the concrete chain. It has a strength-limiting effect in concrete. Because of the presence of the transition zone, concrete fails at a considerably lower stress level than either of the two main components, as demonstrated in Figure 4-14. Since it does not require high energy levels to extend the cracks already existing in the transition zone, even at 40 to 70% of the ultimate strength, higher incremental strains are obtained per unit of applied stress. This explains the phenomenon that the components of concrete (i.e., aggregate and hydrated cement paste or mortar) usually remain elastic until fracture in a uniaxial compression test, whereas concrete itself shows inelastic behavior (Mehta and Monteiro, 2006).

At stress levels higher than about 70% of the ultimate strength, the stress concentrations at large voids in the mortar matrix become large enough to initiate strain localization there. With increasing stress, the matrix cracks gradually spread in the localization zone and join the cracks originating from the transition zone. The crack system then becomes continuous and the material ruptures. Because the crack direction is usually parallel to the compressive load, if the loading platen has little constraint on the concrete specimen, considerable energy is needed for the

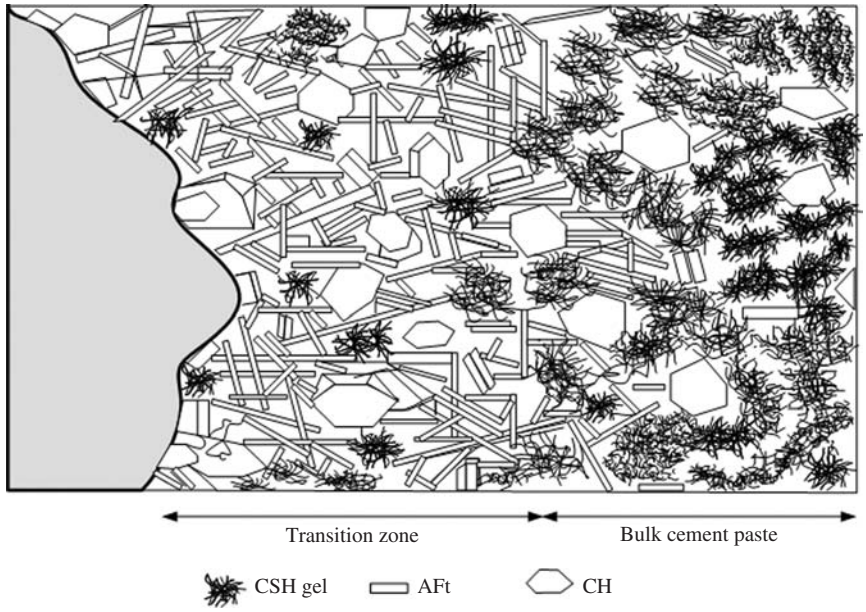

Figure 4-15 Interfacial zone of concrete

formation and extension of matrix cracks under a compressive load. On the other hand, under tensile loading, cracks propagate rapidly and at a much lower stress levels. This is why concrete fails in a brittle manner in tension but is relatively tough in compression, and is also the reason why the tensile strength is much lower than the compressive strength of a concrete.

The structure of the transition zone, especially the volume of voids and microcracks present, has a great influence on the stiffness or the elastic modulus of concrete. In a composite material, the transition zone serves as a bridge between the two components: the bulk matrix and the coarse aggregate particles. Even when the individual components are of high stiffness, the stiffness of the composite may be low because of the broken bridge (i.e., voids and microcracks in the transition zone) that hinder stress transfer, as well as larger deformation occurrences due to the porous nature of the interface.

The characteristics of the transition zone also influence the durability of concrete. Prestressed and reinforced concrete elements often fail due to corrosion of the embedded steel. The rate of steel corrosion is greatly influenced by the permeability of concrete. The existence of relatively large numbers of pores and microcracks in the transition zone at the interface with steel and coarse aggregate make concrete more permeable than the corresponding hydrated cement paste or mortar. Subsequently, oxygen and moisture can penetrate into concrete more easily and lead to corrosion of the steel in the concrete.

4.5 MICROSTRUCTURAL ENGINEERING

4.5.1 Overview

A number of aspects of the structure in the nanometer and micrometer scales of cement-based materials are linked to the built-in characteristics of Portland cement. Only limited variation in

aspects of cements, such as particle size distribution, relative proportions of the different cement components, and the content and type of gypsum interground with the clinker, are commercially feasible. On the other hand, it is feasible and common to modify various characteristics of the final hydration product by incorporating chemical admixtures, pozzolans, or supplementary cementing components during the mixing process of concretes to improve their properties and performance. Some of these modifications act primarily as processing aids without appreciably changing the internal structure of the final product; most, however, result in definite changes, usually for the better. The changes in structure may be physical, such as an increase in density and reduction in porosity, or chemical, such as producing new reaction products and consumption of some nonuseful hydration products. Such changes can be documented with proper advanced instrumentation on a microscopic scale. Initially, improved performance characteristics of the microstructure were "accidentally" achieved in the course of introducing admixtures or additives into concrete to modify its macroscopic properties. Later on, such actions were adopted for deliberating influencing the structural development of concrete in the nanometer or micrometer scales to produce desired and measurable changes.

Developing microstructural systems with defined and prerequisite properties for concrete is called *microstructural engineering.* The term "engineering" here, as elsewhere, first requires carefully designed actions with clear objectives in producing a better material. Second, it needs a proper measurement system to measure the changes in the structure as feedback to be used to deliberately improve previous actions; hence, stronger, less permeable, and more durable cement-based materials can be finally produced. In simple terms, microstructural engineering deals with how to modify the old microstructure to produce a controlled, engineered microstructure with superior characteristics. It was Diamond and Bonen who proposed this wonderful concept (1993).

Naturally, the first approach in microstructural engineering is to reduce the w/c ratio, as a lower w/c ratio can lead to a denser microstructure and subsequently to better mechanical behavior. However, the amount of water that can be reduced depends on many factors, such as aggregate characteristics, mixing techniques, cement properties, and the compacting method. As a result, only a limited amount of such reduction is feasible due to the requirement of workability. If water is reduced too much, without other measures, the mix will become too dry to be properly mixed, placed and compacted. Thus, other measures have to be developed to achieve the objective. Usually these measures consist of the action of chemical and mineral admixtures.

4.5.2 Superplasticizer and dispersion in cement systems

Adding water to normal cement produces a flocculated system. To see the effect of individual flocs, a plain cement paste can be produced at a normal w/c ratio, and then diluted with additional water by a factor of ten or above. This produces a suspension in which individual flocs can be seen as they settle rapidly in the graduated cylinder provided. The bed deposited on the bottom of the cylinder will be open-textured, porous, and not visibly size-sorted.

If a sufficient dose of a commercial superplasticizer is added to another cement paste, otherwise identical with the first one, after dilution, it will be seen that no flocs are evident, and the cement grains settle individually. Since the cement grains are much smaller than the flocs, the sedimentation will take much longer. Examination of the bed deposited at the bottom of the cylinder will show dense packing and size stratification, with the largest cement grains on the bottom (Diamond, 1993). Figure 4-16 shows the effect of the superplasticizer in separating the cement particles. Efforts to delineate the boundaries of individual flocs in fresh cement paste, without diluting them, have been universally unsuccessful. The fresh paste at normal w/c ratios has to be treated as a single large, flocculated mass.

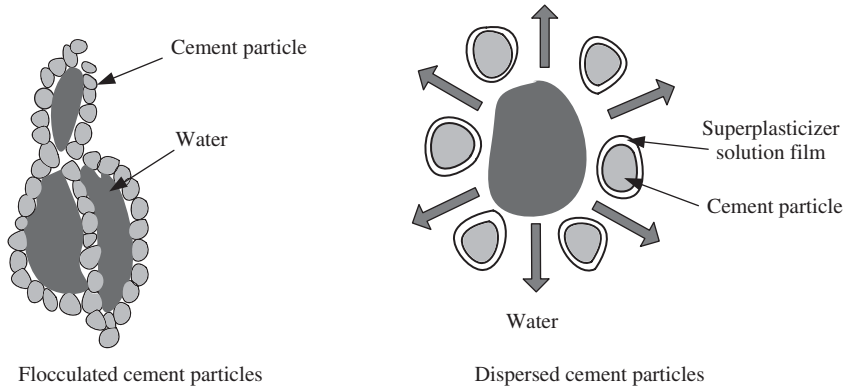

Figure 4-16 Flocculated cement and dispersed cement

The physical chemistry behind the flocculated condition has been well established. Cement grains develop only modest diffuse double layers in the mix water. The mix water in conventional concretes, in fact, rapidly becomes a high ionic strength solution due to dissolution of alkali, sulfate, and free lime from the clinker, and of gypsum. In this high ionic strength solution, attractive van der Waals forces vastly exceed any double-layer repulsive forces that may be developed, and the cement grains attract each other. At points of contact they tend to stick together. A significant shearing force exceeding the yield strength must be applied to get the mass to flow, either in a rheological measurement or in practice.

Superplasticizers work primarily by separating cement particles either through imparting a strong negative charge to the surface of the cement particles or in adsorbing the surfaces of cement particles. At a sufficient superplasticizer dosage, the electrostatic repulsive forces between particles due to negative charge overwhelm the attractive forces, and the cement grains try to separate from each other to the extent possible in the dense suspension. Not much separation is possible at practical w/c ratios, but the particles slip past each other easily and do not tend to stick to each other at points of contact. As a result, fully dispersed cement does not show yield strength, but acts as a Newtonian fluid when examined by the rheological measurement techniques.

With normal dosages of superplasticizer, concrete with same workability can be mixed and consolidated at lower w/c ratio. Thus, the strength of the concrete is improved due to the reduction of the amount of water used, as compared to the concrete mixed using a normal amount of water without superplasticizer. However, for concretes made of same w/c with or without the superplasticizer, the structure of concrete in the nanometer scale and the micrometer scale are the same and so is their strength. The only difference is the workability. In this case, further measures have to be taken to get denser concrete.

4.5.3 Silica fume and particle packing

Cement size varies from 2 to 80 μm, with a mean value of 18 to 20 μm. It appears that cement particles cannot form a dense packing because the water-filled pockets are roughly the same size as the cement particles that exist throughout the mass, as shown in Figure 4-17. It is obvious that an admixture of much finer particles is needed to pack into the water-filled pockets among the cement grains. Silica fume (or *microsilica*) provides such particles. The mean particle size of commercial silica fume is typically less than 0.1 μm, two magnitudes smaller than cement particles. A denser packing may be ensured when microsilica is added to ordinary cement paste.

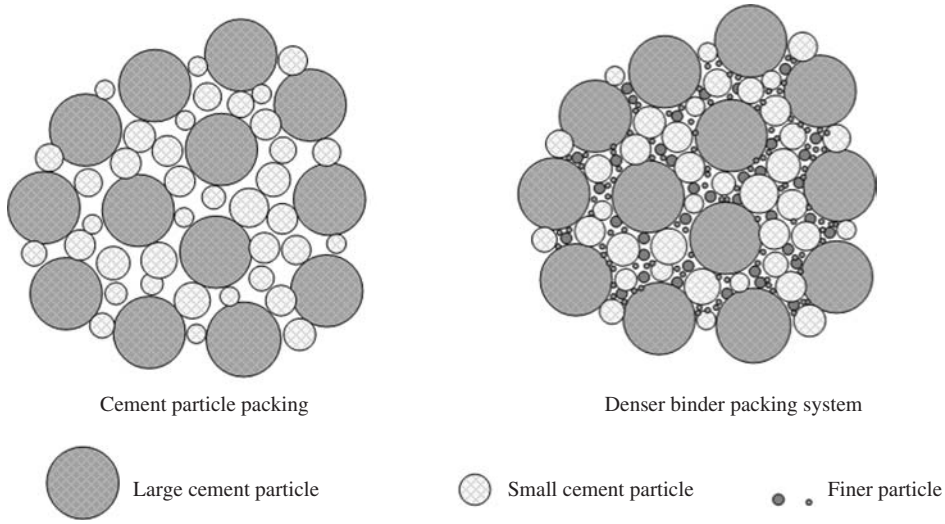

Figure 4-17 Packing systems of cement and binder

However, this happy state of affairs does not usually occur if microsilica is simply added into cement. Early experiments of adding microsilica to concrete in Norway led only to increases in water demand, and little or no improvement in concrete properties. To get the dense particle packing, not only must the fine particles be present, but the system must be effectively deflocculated during the mixing process. Only then can the cement particles move around to incorporate the fine microsilica particles. The fine microsilica particles must themselves be properly dispersed so that they can separate from each other and pack individually between and around the cement grains.

Another requirement for best packing is that the mixing should be more effective than the relatively casual mixing done in ordinary concrete production. High-shear mixers of several kinds have been explored. Proper dispersion and incorporation of fine microsilica particles can thus result in a dense local structure of fresh paste with little water-filled space between grains. When the cement hydrates, the overall structure produced in the groundmass is denser, tighter, and stronger. It is also much more difficult to picture in SEM, because it appears massive and lacks distinctive features. Microsilica is an active and effective pozzolan; that is, it reacts readily with the calcium hydroxide produced by the cement around it to generate additional calcium silica hydrate. Also it somehow stimulates the cement to hydrate faster, and its presence modifies the overall chemistry of the "regular" calcium silicate hydrate produced by the cement. Similar benefits can be obtained if carbon black particles of roughly the same fine size as silica fume and fly ash are introduced into a properly dispersed and mixed concrete. Substituting metakaolin for all or part of the silica fume can produce somewhat the same effects in a heavily superplasticized concrete.

It should be pointed out that if only using silica fume, optimized packing may not be achieved. To reach such a goal, different grades of powders have to be adopted, just like aggregates. Along this line, the mixed use of several mineral admixtures is a good solution. Together with metalkaolin with an average particle size of 2 μm and GGBS of 8 μm, adding silica fume into a cement system can lead to an optimal size distribution and denser packing, as shown in Figure 4-17.

4.5.4 Transition zone improvement

As transition has been identified as a weak link in concrete, it has become customary to ascribe some poor performance characteristics of traditional concrete to the transition zone. From this point of view, microstructural engineering should pay attention to improving the poor structure of the transition zone to enhance the performance of concrete as a whole.

The methodology presented earlier using silica fume to modify the structure of concrete is also effective in improving the structure of the transition zone due to its packing and pozzolanic reaction effect. Bentur and Cohen (1987) prepared two sets of mortar, one was plain mortar and the other silica fume-bearing mortar. Their observation on SEM scans of the interface between the sand grains and the cement paste demonstrated that at least the upper portion of the interface zone of the plain mortar was much more porous than that of the silica fume-modified mortar and obvious CH crystals were visible. In contrast, the silica fume-modified upper interfacial zone was dense and homogeneous, and showed no visible porosity even at a magnification of 200×. Mitsui et al. (1994) have studied the characteristics of the transition zone for different formulations of cement paste and coating methods on coarse aggregate surfaces. Their results also demonstrated that the incorporation of silica fume into cement paste could significantly improve the characteristics of the transition zone and lead to a dense and homogeneous structure. Moreover, together with the surface coating of a slurry of silica fume and cement, the silica fume-modified paste could almost eliminate the transition zone, as shown in Figure 4-18.

The image analysis on the SEM photos of the transition zone of different pastes showed that there were clear distinctions between normal paste and silica fume-modified paste in the porosity distribution along the line from the surface of the aggregate, as shown in Figure 4-19. In addition, since the structure of the transition zone has a significant influence on the bond between

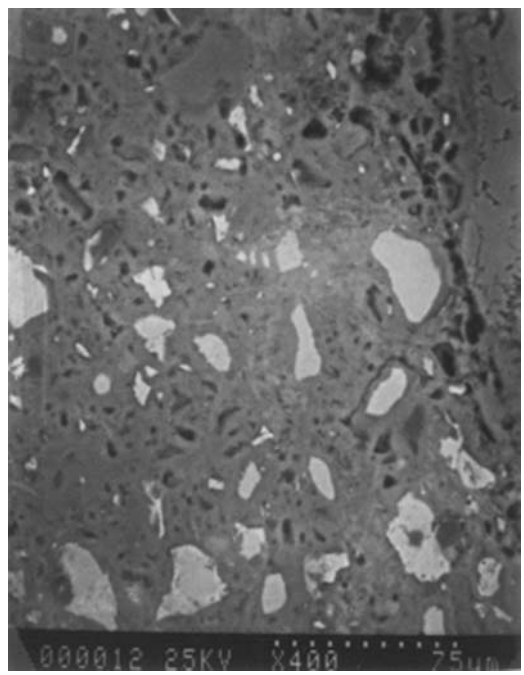

Figure 4-18 Transition zone of high-strength concrete

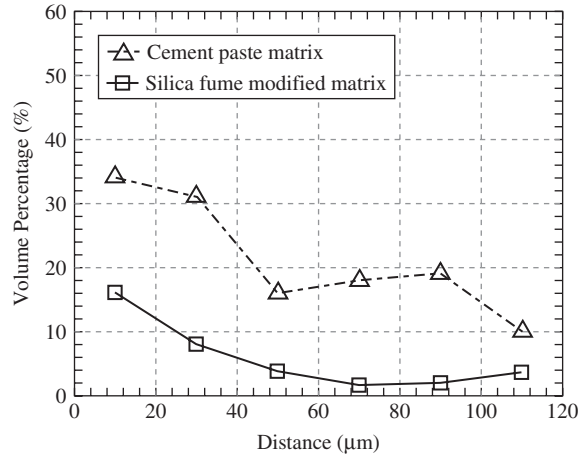

Figure 4-19 Porosity distribution of transition zone for two pastes

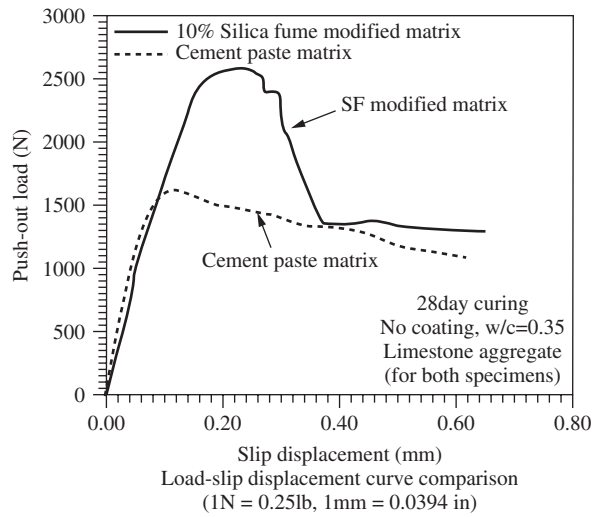

Figure 4-20 Push-out test results for two specimens

the aggregate and paste, different transition zone structures have different bonding properties. Figure 4-20 shows the push-out test results for the two specimens mentioned above.

4.5.5 Effects of polymers in microstructural engineering

It is possible to significantly change the characteristics of hydrated cement systems by incorporating some polymers into the concrete. Mostly, the effect of the incorporated polymer is physical in nature. In latex-modified concrete, the latex forms a film network among the cement hydration products that helps to improve the bonding properties and to reduce permeability. Moreover, with a combination of effects involving the addition of substantial amounts of soluble polymers, significant reduction of water content, and with special mixing and processing techniques,

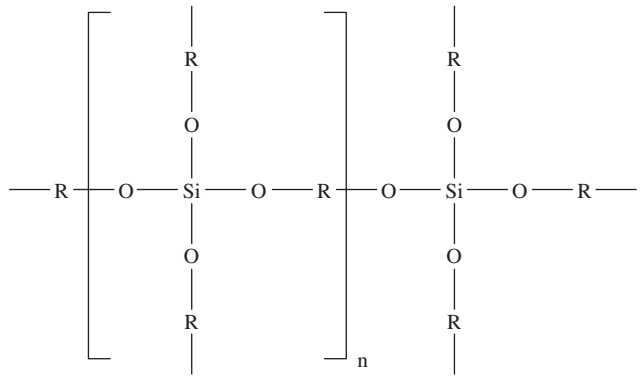

Figure 4-21 Unit for improving toughness of concrete

a special cement system called MDF (macro-defect-free) has been developed. The thin sheet products manufactured by MDF show enormously improved strength levels and enormously modified microstructures. The MDF processing approach works much better with calcium aluminate cement than with Portland cement. In MDF formulation there is only a very small amount of hydration due to very small w/c ratio. To some extent, the system behaves as a filled polymer rather than a cement, but there are significant chemical interactions between the hydrated calcium aluminate products and the polymers. This chemical interaction, combined with the extremely dense microstructure induced by the physical processing, produces a virtually void-free and macro defect-free product that can develop enormous compressive and tensile strengths.

Recently, efforts have been made to develop brand new cement systems by inducing chemical reactions into polymer-modified cement systems (www.nanocem.org). A new mineral organic composite having two poles is being developed to reach this goal. One end can chemically bond with the hydrates of Portland cement, and other end can be polymerized. The hybrid organic–inorganic polymer dispersion is based on the emulsion polymerization of polyacrylate, polyurethane, vinyl acetate, or acrylates and siloxane molecular precursors. Hybrid organic–inorganic particles are functionlized with siloxane molecules $RnSi(OR)4 - n$, where R' can polymerize or copolymerze. Terminal trialkoxysiyl groups undergo hydrolysis bonds with a mineral matrix of concrete (cement or aggregates). The parameters, such as raw material amount, ratio, synthesis procedures, synthesis temperature, and additives, are under study. Figure 4-21 shows a unit that can be used to improve the toughness of concrete designed according to the principles explained earlier. Such mechanisms are still under investigation and a mature technique may need decades to develop.

DISCUSSION TOPICS

How are macrostructures and microstructures in concrete distinguished traditionally?
How is the interface formed?
What are the important characteristics of the interface?
How can the interface be improved?
What is microstructural engineering?
Can you provide a few methods to improve the interface?

Why must learn the structure of concrete?

How can you improve concrete compressive strength from the point of view of microstructure?

Can you eliminate the porous interface in concrete?

How is the microstructure of concrete influenced by a superplasticizer?

Why does modern concrete technology stress the importance of the interface?

Can you list a few common C–S–H structure models?

What do you need to consider if you would like to build up a C–S–H model?

Why is the C–S–H structure important?

REFERENCES

Allen, A. J., Thomas, J. J., and Jennings, H. M. (2007) "Composition and density of nanoscale calcium-silicate-hydrate in cement," *Nature Materials*, 6, 311–316.

Bentur, A. and Cohen, M. D. (1987) "Effect of condensed silica fume on the microstructure of the interfacial zone in Portland cement mortars," *Journal of the American Ceramic Society*, 70(10), 738–743.

Bonaccorsi, E., Merlino, S., and Taylor, H.F.W. (2004) "The crystal structure of jennite, $Ca_9Si_6O_{18}(OH)_6{\cdot}8H_2O$," *Cement and Concrete Research*, 34, 1481–1488.

Bonaccorsi, E. Merlino, S., and Kampf, A. R. (2005) "The crystal structure of tobermorite 14 Å (plombierite), a C–S–H phase," *Journal of the American Ceramic Society*, 88(3), 505–512.

Colombet, P., Grimmer, A.-R., Zanni, H, Sozzani, P. (1998), *Nuclear magnetic resonance spectroscopy of cement-based materials*, Berlin: Springer Verlag.

Diamond, S. (1993), Teaching the materials science, engineering, and field aspects of concrete In. Cohen, ed., Evanston, IL; *Microstructure and microstructural engineering*, NSF, pp. 46–73.

Diamond, S. and Bonen, D. (1993) "Microstructure of hardened cement paste—a new interpretation," *Journal of the J. American Ceramic Society*, 76(7), 2993–2999.

Maso, J.C. (1980) "The bond between aggregates and hydrated cement paste," *Proceedings of the 7th international congress on the chemistry of cement*, Paris: Editions Septima, I, 3–15.

Mehta, K. P. and Monteiro, P.J.M. (2006). *Concrete: microstructure, properties, and materials*, 3rd ed., New York: McGraw-Hill.

Mitsui, K., Li, Z., Lang, D., and Shah, S.P. (1994) "Relationship between microstructure and mechanical properties of the paste–aggregate interface," *ACI Materials Journal*, 91(1), 30–39.

Richardson, G. and Groves, G.W. (1992) "Models for the composition and structure of calcium silicate hydrate (C–S–H) gel in hardened tricalcium silicate paste," *Cement and Concrete Research*, 22, 1001–1010.

Richardson, I.G. (2004) Tobermorite/jennite- and tobermorite/calcium hydroxide-based models for the structure of C–S–H: applicability to hardened pastes of tricalcium silicate, β-dicalcium silicate, Portland cement, and blends of Portland cement with blast-furnace slag, metakaolin, or silica fume. *Cement and Concrete Research*, 34, 1733–1777.

Richardson, I.G. (2008) "The calcium silicate hydrates," *Cement and Concrete Research*, 38, 137–158.

Roland J.M.P., Akihiro, K., Rouzbeh, S., Krystyn, J.V.V., Markus, J. B., Sidney, Y., and Franz-Josef, U. (2009) "A realistic molecular model of cement hydrates," *PNAS Early Edition*.

Taylor, H.F.W. (1997) *Cement chemistry*, 2nd ed., London: Telford, pp. 142–150.

Taylor, H.F.W. and Howison, J. W. (1956) "Relationship between calcium silicates and clay minerals," *Clay Mineral Bulletin*, 31, 98–111.

Viehland, D., Li, J.F., Yuan, L.J., and Xu, Z. (1996) "Mesostructure of calcium silicate hydrate (C–S–H) gels in Portland cement paste: short-range ordering, nanocrystallinity, and local compositional order," *Journal of the American Ceramic Society* 79(7), 1731–1744.

CHAPTER 5

HARDENED CONCRETE

With the development of hydration, concrete will change from a fluid to a plastic state, and finally to a solid hardened state. In the hardened state, concrete is ready to support external loads as a structural material. The most important properties of hardened concrete include various strengths, dimension stability, complete stress–strain relationship, various moduli and Poisson's ratio, and durability.

5.1 STRENGTHS OF HARDENED CONCRETE

5.1.1 Introduction

5.1.1.1 Definitions

To understand the concept of strength, it is necessary to understand what is meant by stress and strain. Nominal stress is defined as the load divided by the original cross-section area. This stress definition can be expressed as

$$[\sigma] = \frac{F}{L^2} \tag{5-1}$$

The dimension used for stress in the SI system is Pa, with the following definition:

$$\text{Pa} = \frac{\text{N}}{\text{m}^2}, \quad \text{MPa} = 10^6 \frac{\text{N}}{\text{m}^2} = \frac{\text{N}}{\text{mm}^2} \tag{5-2}$$

Conventional strain is defined as the change in length per unit original length, and can be expressed as

$$\varepsilon = \frac{\Delta L}{L_0} \tag{5-3}$$

where ΔL is change of the length; and L_0 is original length.

Strength is defined as the ability of a material to resist the stress generated by an external force without failure. For concrete, failure is frequently identified with the appearance of cracks. Since the development of a crack is closely related to the development of deformation, in fact, the real criteria of failure for concrete is the limiting strain rather than the limiting stress. The limiting strain for a concrete is different for different loading conditions and different strength levels. For instance, the limiting strain for concrete under uniaxial tension is 100×10^{-6} to 200×10^{-6}, while for uniaxial compression it is 4×10^{-3} for a concrete with a strength of 14 MPa, and 2×10^{-3} for a concrete with a strength of 70 MPa. For various strengths of concrete, compressive strength is the property generally specified in construction design and quality control. The reasons are as follows:

1. It is relatively easy to measure.
2. It is believed that other properties can be related to the compressive strength and can be deduced from strength data.

Figure 5-1 The universal testing machine

The 28-day compressive strength of concrete, determined by a standard uniaxial compression test, is accepted universally as a general concrete property index for structural design. To measure different strengths of concrete, various tests have to be conducted with a universal testing machine. As shown in Figure 5-1, a universal testing machine usually consists of frames, loading fixture, actuator, loading cell and control unit. The loading process can be controlled either by load or deformation. All the tests have to be carried out using a proper control method.

5.1.1.2 Control methods for strength test

In general, there are two kinds of control methods for strength testing: open-loop or closed-loop control, as shown in Figure 5-2. In open-loop control (OLC), once the prescribed process is set by the controller with the input variables, the process will proceed. The output of the system is not fed back to the controller, and the process depends only on the system input. Hence, there is no chance to correct the process if it deviates from the predetermined directions. Examples of open-loop control include the action of a person throwing a stone to kill a bird or a washing machine washing clothes. In closed-loop control (CLC), the output of the controlled variable is directly monitored by the controller. The current value of the control variable is fed back to the controller and compared with the reference-input signal. The difference between the two signals (i.e., the error) is used to manipulate the control process. Examples of close-loop control include cruise control of a vehicle and firing missiles. In a strength test of a concrete, a universal testing machine is usually used. The variables that can be controlled in such a system are usually the actuator displacement (or stroke) and the applied load (load cell), which are not significantly affected by the behavior of the test specimen, or the deformation of the concrete, which is significantly affected by the behavior of the test specimen. The reference input in testing

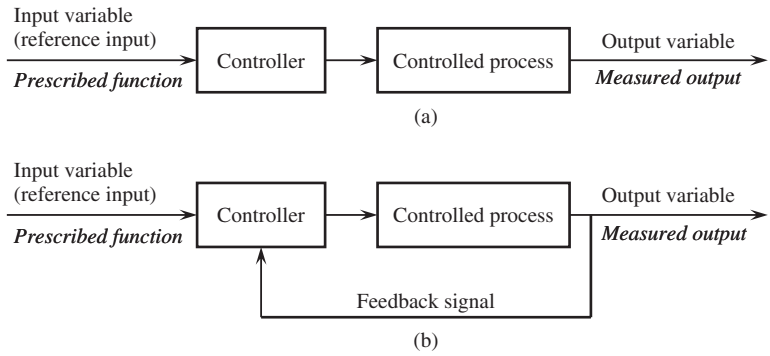

Figure 5-2 Two basic control methods: (a) open-loop control; (b) closed-loop control

machines is provided by a function generator. The feedback signal is normally the measurement of the deformation of a concrete specimen, i.e., the output of a transducer such as extensometer or linear variable differential transformer (LVDT), which is continuously monitored in analog controllers, and sampled at discrete instants in digital controller.

Obviously, the scope of CLC is greater than that of open-loop control, because of the larger number of variables that can be controlled. Even for the same control variable, the CLC system produces a more accurate output than the open-loop system. However, CLC has a few drawbacks. The most important one, other than the higher initial cost, is that the system requires better operator skills because improper use could make the system unstable. There is always a lag between the actual response and the corrective action of the controller, which may result in the loss of control, overcorrection, or undercorrection. Thus, closed-loop controllers have to be properly designed through modeling and analysis.

5.1.1.3 Calibration of transducers

To obtain concrete strength or other properties, the parameters of a specimen such as displacement, strain, crack opening, and force have to be recorded to perform analysis. Various transducers are designed for these purposes. However, most transducers are electronic products that directly measure electrical parameters, such as change of resistance, current, or voltage, which may relate to concrete mechanical properties. Hence, a correlation between electrical variables and mechanical variables is needed for interpreting the experimental results. A process to find such a relationship is called calibration.

The purpose of calibration is to build up a linear relationship between the electrical and mechanical parameters. The procedures of calibration include giving a known output of a mechanical variable, from zero to a full range of the transducer to be calibrated, with a constant increment, adjusting the gain of the electronic transducers to the corresponding reading, and building up a linear relationship between the mechanical variables and the transducer readings. Generally, the full working range of a transducer will be calibrated to an output of 10 volts. The calibration line is used later for interpreting the specimen's mechanical behavior by simply converting the electrical signal into mechanical variables.

The commonly used equipment for calibration includes a standard micrometer for displacement transducers and a standard dead weight for load cells. For example, to calibrate a

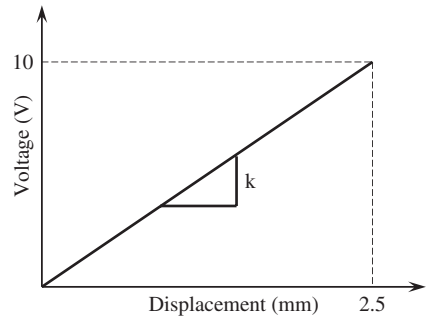

Figure 5-3 Relationship between displacement and voltage

displacement transducer with a full range of 2.5 mm, standard outputs of known displacement values can be provided by a micrometer, as shown in following case:

Displacement (mm):	0.25	0.5	1.25	2.5
Voltage (V):	1	2	5	10

With the displacement of 0.25 mm, the voltage output of transducer is adjusted to 1 volt. Then, 0.5 mm, 2 volts, until full range 2.5 mm, 10 volts. Hence, the relationship between displacement and voltage can be established, as shown in Figure 5-3. During experiments, the reading of the transducer, in voltage, can be easily interpreted into displacement through the equation

$$D = \frac{1}{K}V \tag{5-4}$$

Calibration is an important procedure to ensure accurate measurement of mechanical parameter accuracy.

5.1.2 Compressive strength and corresponding tests

5.1.2.1 Failure mechanism

With a material such as concrete, which contains void spaces of various sizes and shapes in the matrix, and microcracks between the matrix and coarse aggregates or in the matrix, the failure modes under loading are complex and vary with the type of stress. A brief review of the failure modes, however, will be useful in understanding and controlling the factors that influence concrete strength.

In compression, the failure mode is less brittle because considerably more energy is needed to form and to extend cracks in the matrix. It is generally agreed that in a uniaxial compression test on medium- or low-strength concrete, no cracks are initiated in the matrix below about 40–50% of the failure stress. However, at this stage, a stable system of cracks, called shear-bond cracks, already exists in the vicinity of the coarse aggregate. With the increase of the stress level, cracks are initiated in a random manner. Some cracks in the matrix and in the vicinity of the coarse aggregate (shear-bond cracks) eventually join up in a narrow region when the loading

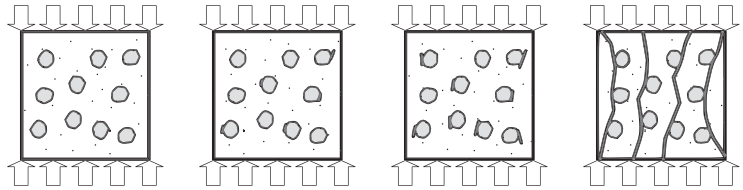

Figure 5-4 Failure process of a concrete under compression: (a) shear-bond crack (load less than 40% ultimate value); (b) load-initiated cracks (load between 40 and 80% ultimate value); (c) crack concentration (load greater than 80% ultimate value); (d) major cracks formed (failure indication)

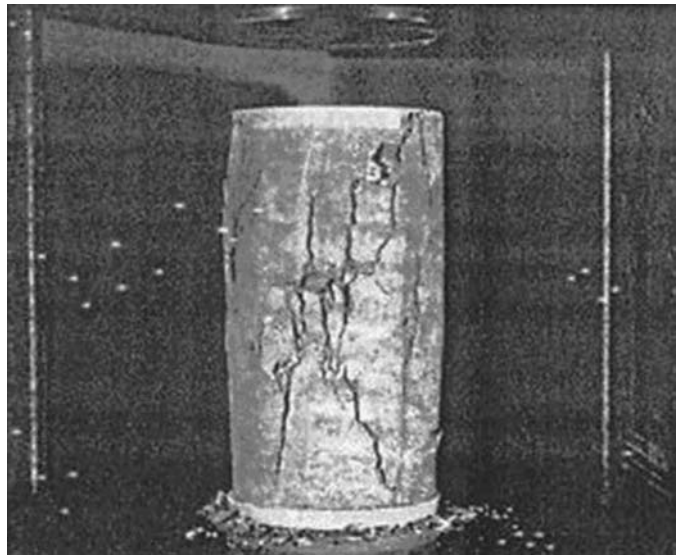

Figure 5-5 Typical failure mode of concrete in compression

reaches about 80% of the ultimate value, while other cracks are closed. Subsequently, major cracks develop in these localized zones in the direction close to the direction of the load, which signals the failure of the compression specimen.

The processes of concrete failure during loading can be also described as shown in Figure 5-4. The development of the vertical cracks causes the expansion of concrete. Final failure is mostly likely splitting (see Figure 5-5), and sometimes failure on the formation of a shear band.

5.1.2.2 Specimen preparation for compression test

There are two types of specimens that can be used for uniaxial compression testing: the cube specimen and the cylinder specimen. The cube specimen method is used in Europe and China, while the cylinder specimen method is used in North America.

(a) *Cube specimen (BS 1881, Part 108: 1993)*: The standard size of the cube specimen is $150 \times 150 \times 150$ mm. It should be prepared by pouring concrete into a cubic mold in three

equal layers, with each layer being stroked 35 times by a hemispherical-tipped steel rod. After demolding, the specimen should be cured at a temperature of $20 \pm 1^{\circ}C$ and a relative humidity of more than 90%. However, a cube of standard size is heavy and sometimes a cube of size $100 \times 100 \times 100$ mm is used instead. To prepare a 100-mm cube, concrete should be poured into the cubic mold in three equal layers, with each layer being stroked 25 times by a steel rod. For a cube specimen, the height to width ratio is 1 and that at least five surfaces are exposure to the mold, which can generate smooth surfaces on the specimen. Hence, a cube specimen can be tested without surface preparation.

(b) *Cylinder specimen (ASTM C470-81)*: The standard cylinder size for compression testing is 150×300 mm. It should be prepared by pouring concrete into the cylindrical mold in three equal layers, with each layer being stroked 25 times by a hemispherical-tipped steel rod. After demolding for 16 to 24 h after casting, the specimen should be cured at a temperature of $23 \pm 1.7^{\circ}C$ and in moist conditions. The cylinder specimen has a length/diameter ratio of 2. Also, the upper surface of the cylinder is never smooth; hence, grinding or capping is needed to level and smooth the compression surface before a test.

5.1.2.3 Factors affecting the measured compressive strength

The compressive strength tests appear to be perfectly straightforward. However, the results obtained can be affected considerably by a number of factors. When interpreting the strength values obtained by standard (although arbitrary) procedures, it is necessary to consider in detail how compressive strength is affected by the test parameters.

(a) *Loading rate*: In general, the lower the rate of the loading, the lower the measured compressive strength. This may be attributed to the fact that deformation generated by loading needs time to develop. The slow rates of loading may allow more subcritical crack growth to occur, thus leading to the formation of larger flaws and hence a smaller apparent load. On the other hand, it may be that slower loading rates allow more creep to occur, which will increase the amount of strain at a given load. When the limiting value of strain is reached, failure will occur. More likely, the observed rate of loading effect is due to a combination of these, and perhaps other factors as well.

So, to make the compression results comparable, a standard load rate has to be followed. For a cylinder specimen, ASTM regulates 0.15–0.34 MPa/sec as the standard loading rate. For a cube specimen, BSI sets 0.2–0.4 MPa/sec as the standard loading rate. In the real situation, the loading rate can be transferred to N/sec by multiplying the area of the specimen under the loading.

(b) *End condition*: The compression test assumes a state of pure uniaxial compression. However, this is not really the case, because of friction between the ends of the specimens and the platens of testing machine that make a contact with them. The frictional force arises due to the fact that, because of the differences in the moduli of elasticity and Poisson's ratio for steel and concrete, the lateral strain in the platens is considerably less than the lateral expansion of the ends of the specimen if they were free to move. Thus, through friction, the platens act to restrain the lateral expansion of the ends of the specimens and to introduce shear stress that is greatest right at the specimen end and gradually dies out at a distance from each end of approximately $(\sqrt{3}/2)d$, where d is the specimen diameter or width. The manifestation of this lateral confining pressure is often the appearance of relatively undamaged cones (or pyramids) of concrete in specimens tested to failure, as shown in Figure 5-6a. Thus, for a standard cylinder with $l/d = 2$, only a small central portion of the cylinder is in true uniaxial compression, the

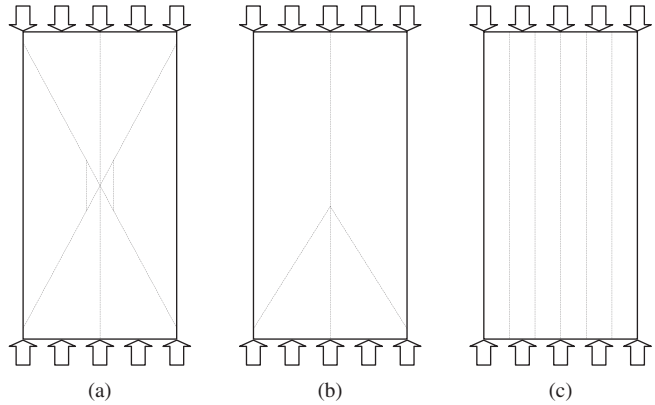

Figure 5-6 Influence of constraint to failure mode of concrete specimen: (a) with constraint on both ends; (b) with constraint in one end; and (c) without constraint

remainder being in a state of triaxial stress. The effect of this type of end restraint is to give an apparently higher strength than the true compressive strength of the specimen. For ordinary concrete, with Poisson's ratio approximately equal to 0.2, lateral tensile strains will occur at fairly low compressive loads, and this could be the cause of failure, as shown in Figure 5-6c. This is probably the natural mode of failure in pure compression. The stresses induced due to the end restraints may cause an apparent conical failure of a specimen, as indicated in Figure 5-6a. Since some end restraints cannot be avoided, it is likely that failure occurs through some combination of factors, as indicated schematically in Figure 5-6b. Tensile cracks may not be able to propagate to the areas of the specimen under lateral confining stress.

As mentioned earlier, due to the height to diameter or width ratio being different for cylinder compression and cube compression specimens, the constraint from the platens of a testing machine to the specimens are different. The friction between the platens and the cube specimen ends confines a much greater portion in the specimen than is the case with the cylindrical specimen, as shown in Figure 5-7. This leads to higher strength values when measured on cubes rather than cylinders. Usually, the ratio between cube strengths and cylinder strengths is commonly assumed to be 1.25 for normal-strength concrete. However, for higher-strength concretes, the ratio will be reduced.

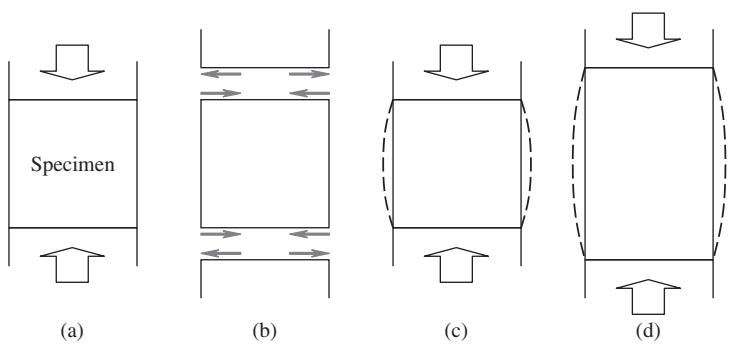

Figure 5-7 Comparison of the end constraints between cube (a, b, c) and cylinder (d) specimens

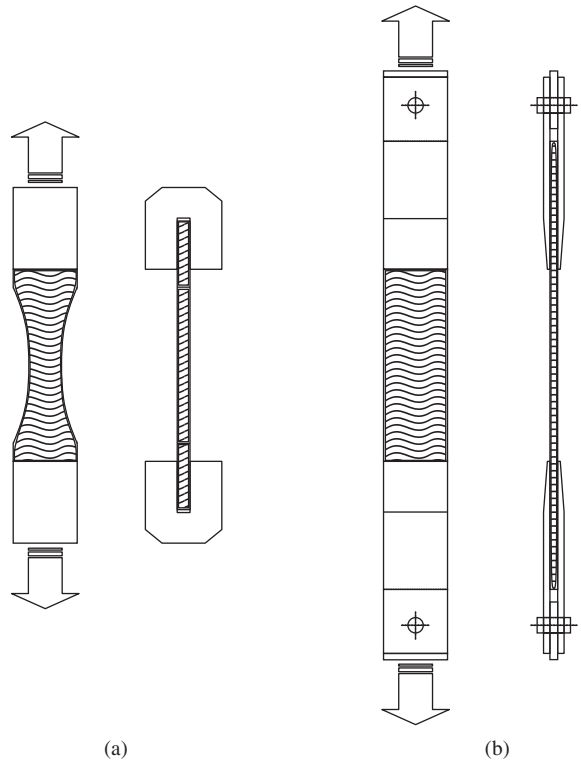

Figure 5-8 Two conventionally used uniaxial tension methods: (a) grips dog bone test; (b) end plate loading method

(c) *Size effect*: The probability of having large deficiencies, such as void and crack, increases with size. Thus, smaller-size specimens will give higher apparent strengths. If nonstandard-size specimens, i.e., a 100-mm cube or 100×200-mm cylinder, are used to measure the compression strength, the test results for small-size specimens need to be modified. Generally speaking, a factor of 0.9 should be used to modify the results of small-size specimens.

5.1.3 Uniaxial tensile strength and corresponding tests

5.1.3.1 Failure mechanism

Uniaxial tension test is more difficult to conduct for three reasons. First, it is difficult to center the loading axis with the mechanical centroid. Second, it is difficult to control the loading process due to the quasi-brittle nature of concrete under tension. Third, the tension process is more sensitive to a sudden change in cross-sectional area, and the specimen-holding devices introduce secondary stress that cannot be ignored. Figure 5-8 shows two conventional test methods for concrete uniaxial tension. One uses a dog-bone-shaped specimen to ensure a smooth transfer of the cross-sectional area and the other utilizes a tapped steel plate glued on the concrete specimen to smoothly transfer the load. In this way, the secondary stresses generated by the holding devices can be minimized.

The processes of failure of a concrete specimen during uniaxial tension can be described as follows: from start of loading to 30% of ultimate value, the response is linear elastic. The

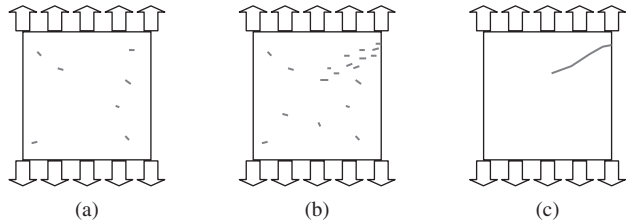

Figure 5-9 Failure process of concrete specimen under tension: (a) random crack development (after 30% peak load is reached); (b) localization of microcracks (after 80% peak load is reached); and (c) major crack formation and propagation

microcracks occur randomly when the loading level is higher than 30% of ultimate load value. The phenomenon of strain localization starts at around 80% of peak load. The microcracks start to concentrate in a narrow region and microcracks in other regions close. The major crack is developed along the localization zone shortly after the peak load is reached and is propagated, signaling the failure of the specimen, as shown in Figure 5-9.

5.1.3.2 Stress concentration factor

The tension strength of concrete is much lower than its compression strength, which can be attributed to the stress concentration generated by the defects in the materials. Stress concentration can be illustrated by a plate with an elliptical hole, as shown in Figure 5-10, where the hole represents the defect. Under a tension load, the distribution of stress in the cross section through the center of the ellipse is not uniform. The highest stress occurs at the edge of the ellipse and can be expressed as

$$\sigma_{\max} = \sigma_0 \left(1 + \frac{2a}{b}\right) = K_t \sigma_0 \tag{5-5}$$

where σ_0 is the remote stress or normalized stress; a is the long radius of the ellipse, and b is the short one; and K_t is the concentration factor. It can be seen that if $a = b, K_t = 3$. K_t depends not only on the geometry of the hole but also on the loading pattern. If the loading is pure shear, K_t can reach 4.

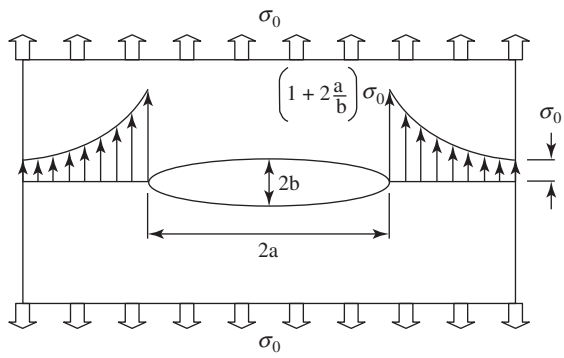

Figure 5-10 Sketch of stress concentration

5.1.3.3 Relationship between compressive strength and tensile strength

It has been pointed out before that other mechanical properties of a concrete can be related to its compressive strength. However, there is no direct proportionality between tensile and compressive strength. As the compressive strength of concrete increases, the tensile strength also increases but at a decreasing rate. In other words, the tensile/compressive strength ratio depends on the general level of the compressive strength; the higher the compressive strength, the lower the ratio. The research work done by Price (1951) showed that the direct (uniaxial) tensile/compressive strength ratio is 10 to 11% for low-strength, 8 to 9% for medium-strength, and 5 to 7% for high-strength concrete.

The relationship between the compressive strength and the tensile/compressive strength ratio seems to be determined by the effect of various factors on the properties of both the matrix and the transition zone in concrete. Not only the curing age but also the characteristics of the concrete mixture, such as water/cement ratio, type of aggregate, and admixtures, affect the tensile/compressive strength ratio to varying degrees. For example, after about 1 month of curing, the tensile strength of concrete is known to increase more slowly than the compressive strength; that is, the tensile/compressive strength ratio decreases with the curing age. At a given curing age, the tensile/compressive strength ratio also decreases with the decrease in water/cement ratio.

The existence of the hole in the plate alters the stress distribution such that the maximum stress along the edge of the hole, σ_{max}, is larger than the normal stress, σ_N. This is called stress concentration. This phenomenon will be discussed in detail in the section on concrete fracture.

5.1.3.4 Indirect tension test (split-cylinder test or Brazilian test)

The indirect tension test is also called the splitting test or Brazilian test. The standard specimen for the splitting test is a 150 × 300-mm cylinder (BS 1881: Part 117:1983, ASTM C496-71). It should be prepared by filling concrete into the mold in three equal layers, with each layer being stroked 35 times by a hemispherical-tipped steel rod. The curing requirement is the same for the compression specimen. The splitting test is carried out by applying compression loads along two axial lines that are diametrically opposite, see Figure 5-11a. The loading rate is 0.02 to 0.04 MPa/sec according to BS, and 0.011 to 0.023 MPa/sec according to ASTM C496-71.

Under such a line load, the stress along the central diameter will be distributed as shown in Figure 5-11b. It can be seen that the stress distribution along the central part of the diameter is under uniform tensile stress, while at the edge there is compressive stress, which is obtained from the elasticity. The expressions of the stresses are

$$\sigma_{com} = \frac{2P}{\pi LD}\left(\frac{D^2}{r(D-r)} - 1\right) \tag{5-6}$$

and

$$\sigma_{ten} = \frac{2P}{\pi LD} \tag{5-7}$$

where P is the applied load, L the cylinder length, D the cylinder diameter, and r the distance from the top of the cylinder.

According to a comparison of the same concrete test results, f_{st} is about 10–15% higher than the direct tensile strength, f_t. In practice, it is difficult to apply a true line load. Usually, a strip of plywood with a width of 25 mm and thickness of 3 mm is used as a bearing to transfer the load from the testing machine to the specimen. It is also allowed to use a cube for a splitting test instead of a cylinder. In this case, the loading is applied to the cube through two hemispherical bars along the center lines of two opposite faces (see Figure 5-12). The formula to obtain the

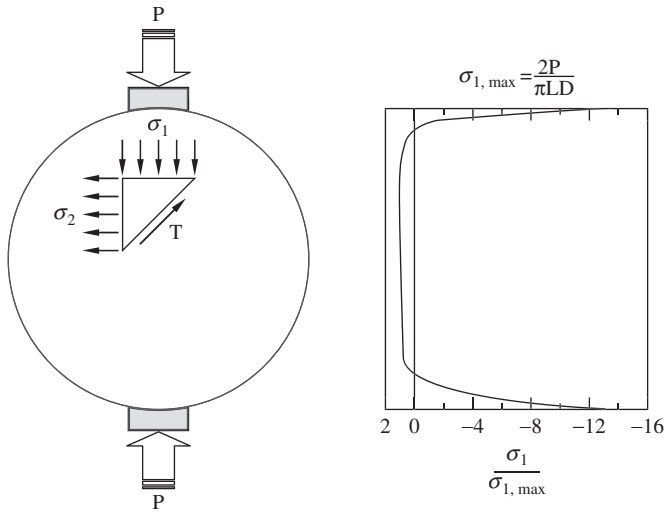

Figure 5-11 Stress distribution of the specimen under the splitting test

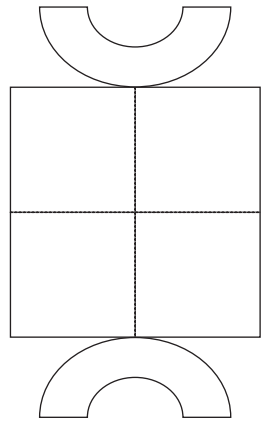

Figure 5-12 Experimental setup of indirect tension test on a cube specimen

indirect tensile strength for the cube specimen is

$$f_{st} = \sigma_{ten} = \frac{2P}{\pi a^2} \tag{5-8}$$

where a is the side length of the cube specimen.

5.1.4 Flexural strength and corresponding tests

Flexural strength is also called the modulus of rupture (MOR). It can be determined by performing a four-point bending test following the procedures of ASTM C78 or BS 1881: Part 118: 1983. The specimen for a flexural strength test is a 150 × 150 × 500-mm beam according to ASTM C78, and a 150 × 150 × 750-mm beam according to BS 1881: Part 118: 1983. BS also

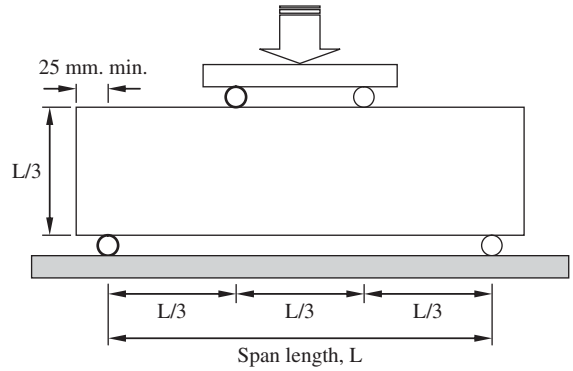

Figure 5-13 Flexural strength test setup for hardened concrete

allows a beam size of $100 \times 100 \times 500$ mm when the maximum size of aggregate is less than 25 mm. The arrangement for the modulus of rupture test is shown in Figure 5-13. According to the mechanics of materials, we know that under the four-point bending, the middle 1/3 portion of the beam is under pure bending. The maximum moment can be calculated by

$$M_{\max} = \frac{p}{2} * \frac{l}{3} = \frac{Pl}{6} \tag{5-9}$$

If fracture takes place inside the middle one-third, beam theory under pure bending can be applied directly and the maximum tension stress can be calculated as

$$f_{\text{bt}} = \frac{M_{\max} y_{\max}}{I} = \frac{\frac{Pl}{6} * \frac{d}{2}}{\frac{bd^3}{12}} = \frac{Pl}{bd^2} \tag{5-10}$$

However, if fracture occurs outside the middle one-third (pure bending zone), the cross section is carrying not only bending moment, but also shear force. According to the elasticity, if the span to height (of the beam) ratio is greater than 5, beam theory under pure bending can be still applied to calculate the normal stress, with an error of less than 1%. However, for the loading setup regulated by ASTM C78 and BS 1881, the span-to-height ratio is only 3. Hence, basically, the formula for calculating normal stress from pure bending cannot be used in this situation. This is why BS suggests discarding such a result. On the other hand, ASTM allows the result of failure outside middle one-third to be used. If an average distance between the failure crack and the nearest support is a, then the MOR can be computed as

$$f_{\text{bt}} = \frac{M_{\max} y_{\max}}{I} = \frac{\frac{Pa}{2} * \frac{d}{2}}{\frac{bd^3}{12}} = \frac{3Pa}{bd^2} \tag{5-11}$$

If, however, failure occurs at a section where $(l/3 - a) > 0.05l$, then the result should be discarded. Although the modulus of rupture is a kind of tensile strength, it is much higher than the results obtained from direct tension because of the support from the inner layers that have not reached their failure criterion.

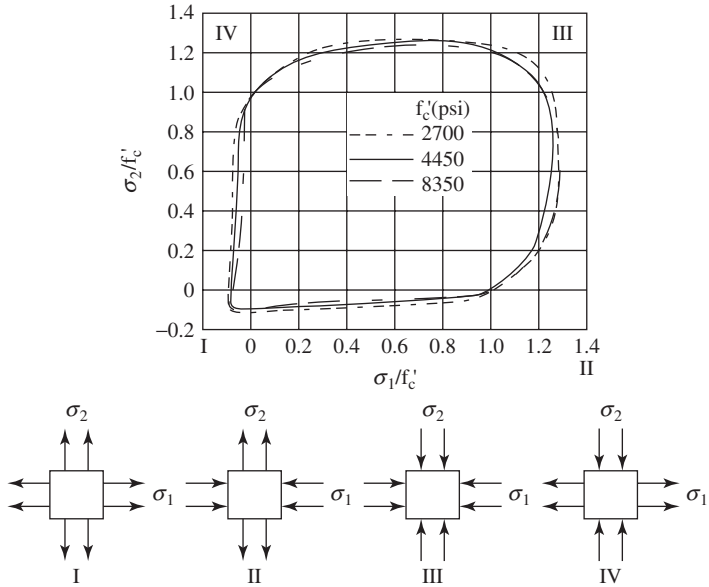

Figure 5-14 Behavior of concrete under biaxial stress

5.1.5 Behavior of concrete under multiaxial stresses

5.1.5.1 Behavior of concrete under biaxial stress

The biaxial test can be carried out using a two-dimensional universal testing machine. The loading parameter in two directions can be selected as the ratio of the applied stress to the ultimate compression strength. The behaviors of three different concretes under different ratios have been plotted in Figure 5-14. It is essential that the level of uniaxial compressive strength of concrete does not affect the shape of the biaxial stress interaction curves. It can be seen that the behavior can be distinguished into four regions. In *region I* both σ_1/f_c and σ_2/f_c are negative, which means that both σ_1 and σ_2 are in tension. For a concrete specimen under biaxial tension, its strength is similar to the strength obtained under uniaxial tension. In *region II* the ratio of σ_1/f_c is positive and σ_2/f_c negative, which means that σ_1 is in compression and σ_2 is in tension. Under biaxial compression–tension, the compressive strength decreases almost linearly. This is because the tensile strain in the transverse direction, generated by compression, is enlarged by an additional tensile force, which speeds up the failure process. In *region III* both σ_1/f_c and σ_2/f_c are positive, which means that both σ_1 and σ_2 are in compression. The test results show that the strength of concrete subjected to biaxial compression is 27% higher than the uniaxial compressive strength. The reason behind the phenomenon is that the tensile strain in the transverse direction, generated by compression, is constrained by the compression force in that direction, which slows down the failure process. It is interesting to note that the increase in strength is not proportional to the stress added in the transverse direction. In *region IV* the ratio of σ_1/f_c is negative and σ_2/f_c is positive, which means that σ_1 is in tension and σ_2 is in compression. The result is similar to that of region II.

The dimensional stability of concrete under biaxial stress has different values, depending on whether the stress states are compressive or tensile. In biaxial compression, the average maximum compressive strain is about 3000 $\mu\varepsilon$ and the average maximum tensile strain varies

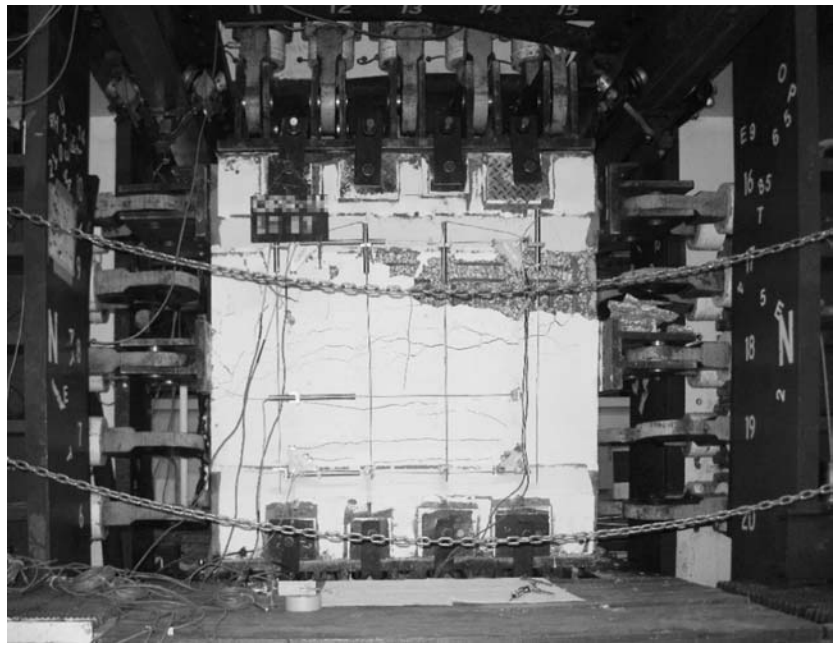

Figure 5-15 Reinforced concrete panel under biaxial stress (University of Houston)

from 200 to 400 $\mu\varepsilon$. In biaxial tension–compression, the magnitude at failure of both the principal compressive and tensile strain decreases as the tensile stress increases. In biaxial tension, the average value of the maximum principal tensile strain is only about 80 $\mu\varepsilon$. It should be pointed out that not only the pure concrete has been tested under biaxial stress conditions, but also reinforced concrete panels. Figure 5-15 shows the setup of such a test at the University of Houston. This universal element tester consists of 40 in-plane jacks of 100 ton each and 20 out-of-plane jacks of 60 ton each, housed in a giant 5 by 5-m steel frame. It was constructed to test full-size concrete panels 1.4 m^2 and up to 0.4 m thick reinforced with steel bars from 10 to 25 mm in diameter. Any self-equilibrium loading condition on the four edges of a test panel can be simulated. The panel can be subjected simultaneously to in-plane tension or compression, in-plane and out-of-plane bending, in-plane and out-of-plane shear, as well as torsion.

5.1.5.2 Behavior of concrete under triaxial stress

Triaxial loading experiments can be conducted in two ways according to a specimen shape. For a cylindrical specimen, the compressive stresses σ_2 and σ_3 can be obtained by subjecting the specimen to hydrostatic pressure in a vessel. To prevent the penetration of the pressure fluid into microcracks and pores of the specimen, the cylindrical specimen has to be sealed in a plastic membrane. For a cubic specimen, the pressure, σ_2 and σ_3, can be added by a flat jack. The compressive stress σ_1 can be added through the hydraulic piston as shown in Figure 5-16. The strength of concrete can be significantly increased under triaxial compression stress because the lateral stress can largely limit the crack development caused by the vertical stress. Roughly, the compressive strength of concrete can be estimated using the following equation:

$$f_{\text{tri-c}} = f_c + Cf_l \tag{5-12}$$

Figure 5-16 Triaxial testing machine at Dalian University of Technology

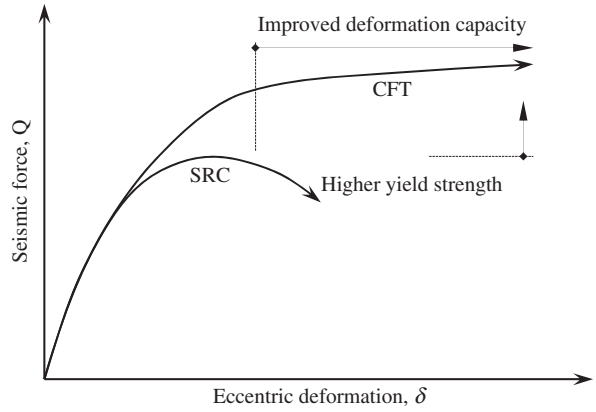

Figure 5-17 Comparison of the loading behaviors

where f_{tri-c} is the compressive strength of concrete under triaxial compressive stress; f_c the compressive strength of concrete under uniaxial compressive stress; f_l the lateral pressure in triaxial stress stage, and C a empirical coefficient ranging from 4.5 to 7, or estimated by

$$C = 2 + \frac{1.5}{\sqrt{f_l/f_c}} \tag{5-13}$$

Not only the strength, but also the dimensional stability can be improved by adding the confining pressure. The ultimate strain in the σ_1 direction can be significantly increased for a tube confined concrete as compared to a structural steel reinforced concrete, as shown in Figure 5-17. The

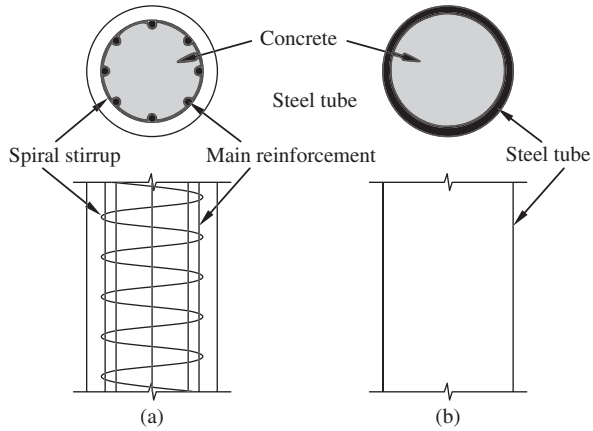

Figure 5-18 Confinement for concrete column in the form of (a) a spiral, and (b) a tube

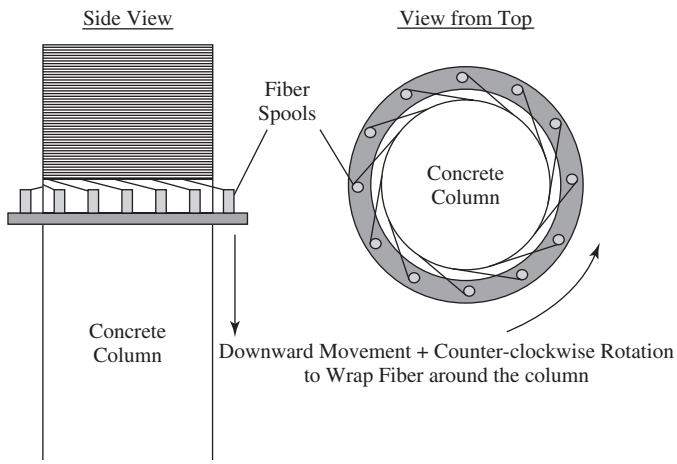

Figure 5-19 Column retrofitting using the confinement concept

philosophy of confinement and triaxial compression has been applied in practice to improve the concrete strength, as well as its ductility. The circular stirrup-reinforced concrete column and tube concrete column are good examples, as shown in Figure 5-18.

The idea of spiral stirrups has been further developed by the Yuntai group in Taiwan. One invention is one-bar confinement, which utilizes a single reinforcement steel to make a stirrups for the entire cross section of a structural member in order to hold all the main reinforcing steel. Another example of Yuntai's invention is a group of circular stirrups to hold the main reinforcing steel and provide confinement to the concrete at different zones.

This concept has also been used in column retrofitting by using filament winding, see Figure 5-19. By applying this technique, a fibrous composite shell surrounding the concrete column tightly can be formed by continuous fiber strands. The shell provides a strong circumferential constraint to the concrete column, and hence significantly increases the loading carrying capacity and ductility of the concrete column. Such a strength effect is especially useful for earthquake design.

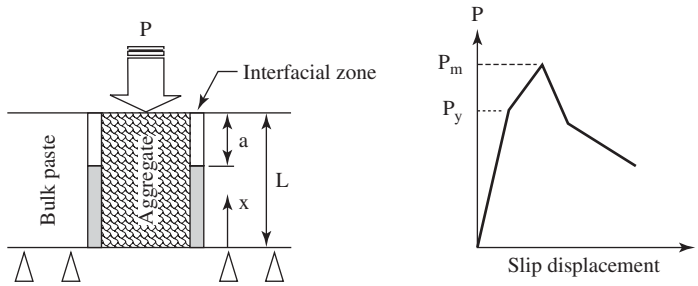

Figure 5-20 Model for the bond between aggregate and matrix

5.1.6 Bond strength

Bond strength is defined as the shear strength between the aggregate, fiber, reinforcing steel, and cement paste. The bond strength plays an important role in determining the properties of concrete, fiber reinforced concrete, and reinforced concrete. There is considerable evidence to indicate that the interface is the weakest region in concrete. In general, bond failure occurs before failure of either the paste or aggregate. Many people have tried to measure the bond properties and have developed many models to interpret the experimental results. Here, the one recently developed by Mitsui et al. (1994) is introduced.

Figure 5-20 represents a schematic of the mathematical model for calculating the interface properties. In the figure, L represents the aggregate embedded length. The aggregate is assumed to be elastic with Young's modulus E_a and cross-sectional area A. The bulk matrix is assumed to be rigid except for the interfacial layer, which is idealized as an elastoplastic shear layer. It is assumed that debonding has occurred over a certain length, a, starting at $x = L$. Treating the boundary layer as a shear lag and assuming that a constant shear stress is acting at the debonded interface, the following equations can be written:

$$q = \begin{cases} kU(x) & 0 < x < L - a \\ q_f & L - a < x < L \end{cases} \tag{5-14}$$

where k is the stiffness per unit length of the interfacial layer for small deformation, q the shear force per unit length acting on the aggregate, q_f is frictional shear force per unit length, and $U(x)$ the aggregate displacement. Denoting the aggregate push-out force as P, the equilibrium equation and the constitutive relationship for the aggregate can be written as

$$\frac{dP}{dx} - q = 0 \tag{5-15}$$

$$\frac{P}{A} = E_a \frac{dU}{dx} \tag{5-16}$$

By introducing Equations 5-14 and 5-16 into Equation 5-15, the following differential equation for U can be obtained:

$$\begin{aligned} U_{,xx} - \omega^2 U &= 0 \qquad 0 < x < (L - a) \\ U_{,xx} - \frac{q_f}{E_a A} &= 0 \qquad (L - a) < x < L \end{aligned} \tag{5-17}$$

in which the subscript comma indicates differentiation. The quantity ω is defined as

$$\omega = \sqrt{\frac{k}{E_a A}} \tag{5-18}$$

Equation 5-17, together with boundary conditions and continuity conditions, constitute a complete set of equations for the determination of $U(x)$. Solving this set of equations, the following closed form expression for the slip displacement at the loading end, U^*, is obtained:

$$U^* = U\ (L) = \frac{P^* - q_f a}{E_a A \omega} \coth\left[\omega(L-a)\right] + \frac{P^* - 0.5 q_f a}{E_a A} a \tag{5-19}$$

The relationship between U and P in the elastic stage can be obtained from the above equation by setting $a = 0$. This leads to a form of

$$\frac{P^*}{U^*} = E_a A \omega \tanh\left[\omega(L)\right] \tag{5-20}$$

The stiffness parameter can be determined from the initial slope of the experimental load–slip displacement curves for a push-out test using the above equation.

Furthermore, it is shown that the relationship between the push-out force and debonding length, a, can be derived from both the shear strength (q_y) criterion (material properties represented by q_y and q_f) and fracture energy (Γ) criterion (material properties represented by Γ and q_f). For the shear strength (q_y) criterion the derivation is obtained from the overall equilibrium of the forces acting on the aggregate. For the fracture energy criterion, a differential equation for P is first derived by applying the energy balance concept, and then the expression for P is obtained by solving the differential equation. The expressions for P take the following forms:

For the shear strength criterion

$$P^* = q_f a + \omega \frac{q_y\ \tanh\left[\omega\,(L-a)\right]}{\omega} \tag{5-21}$$

For the fracture energy criterion

$$P^* = q_f a + \left[\frac{q_f}{2\omega} + \sqrt{\left(\frac{q_f}{2\omega}\right)^2 + 2E_a A p \Gamma}\right] \tanh\left[\omega\,(L-a)\right] \tag{5-22}$$

in which Γ is the specific fracture energy. Note that three material parameters are needed for either model. They are ω, q_y, and q_f or ω, Γ, and q_f. To determine the interfacial yield parameter, $q_y(\tau_y)$, the interfacial frictional forces, $q_f(\tau_f)$, and the specific energy, Γ, one needs to know the length of the debonded crack, a, at the peak load. A method that utilizes the maximum load, P^*_{max}, and the slip displacement corresponding to P^*_{max} is used. The formulas used to calculate τ_f, τ_y, and Γ are Equations 5-23, 5-24, and 5-25, respectively:

$$2\pi R \tau_f = \frac{\omega P^*_{max}}{a\omega + \sinh\left[\omega\,(L-a)\right] \cosh\left[\omega\,(L-a)\right]} \tag{5-23}$$

$$\tau_y = \tau_f\ \cosh^2\left[\omega\,(L-a)\right] \tag{5-24}$$

$$2E_a A \Gamma = \left(\frac{\tau_f}{\omega}\right)^2 \left\{\cosh^4\left[\omega\,(L-a)\right] - \cosh^2\left[\omega\,(L-a)\right]\right\} \tag{5-25}$$

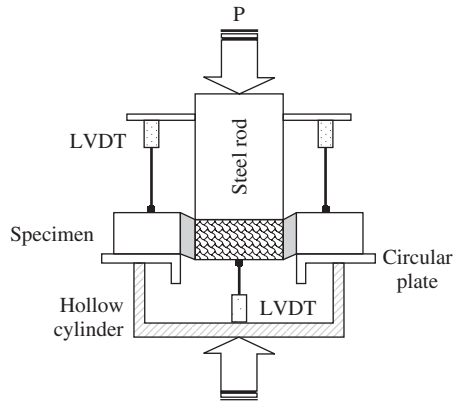

Figure 5-21 Bond strength test setup

Note that an additional equation is needed to determine the debonding length, a:

$$P^*_{\max}\frac{0.5\,(\omega a)^2+\cosh^2\left[\omega\,(L-a)\right]+\omega a\sinh\left[\omega\,(L-a)\right]\cosh\left[\omega\,(L-a)\right]}{\omega a+\sinh\left[\omega\,(L-a)\right]\cosh\left[\omega\,(L-a)\right]}-U^*_{\text{peak}}E_{\text{a}}A\omega=0 \tag{5-26}$$

The procedures are as follows: calculate the debonding length, a, first; then calculate τ_{f}; and, finally, calculate τ_{y}, and Γ. The test setup is shown schematically in Figure 5-21. The specimen is put on a flat, circular plate that is connected with the servo-hydraulic actuator of an material testing system (MTS) machine through a hollow cylinder. The entire specimen fixture can move up with the actuator. A steel rod, which is connected to the load cell, makes contact with the top surface of the aggregate and by resisting the upward movement of the loading fixture pushes the central cylindrical aggregate downward. Two linear variable differential transformers (LVDTs), which are fixed between the circular plate and the rigid wings of the steel rod, are used to measure the slip displacement of the top of the aggregate relative to the surface of the cement matrix annulus. The average output of the LVDTs is used as a feedback signal to control the servo-hydraulic system. The push-out test is performed at a rate of slip displacement of about 1 mm per hour. Slip displacement at the bottom of the aggregate is also measured by another LVDT. Push-out load, slip displacement of aggregate, and stroke of the actuator of MTS are recorded by using a data-acquisition computer.

For a typical push-out test, the four measurements of importance are time, push-out load, average displacement at the top of the aggregate, and slip displacement at the bottom of the aggregate. For a complete analysis of the results, a graph of load vs. top of aggregate displacement and a graph of load, top of aggregate displacement, and bottom of aggregate slip displacement vs. time are produced, as shown in Figure 5-22. Shown in the figure are two curves of slip displacement superimposed over the push-out loading curve as a function of time. The displacement at the top of the aggregate is represented by a linearly increasing line, while the curve of the slip displacement at the bottom of the aggregate is expressed as a broken line, composed of three ascending stages. For measurement of the bottom displacement, the points at which the curve changes its slope signals the transition of the interfacial damage stages. The first portion of the curve represents the elastic deformation of the aggregate–cement interface. The change of the slope, becoming steeper, implies that the deformation rate is increased. This means that the interface becomes less stiff than before, and the elastic bond must have been

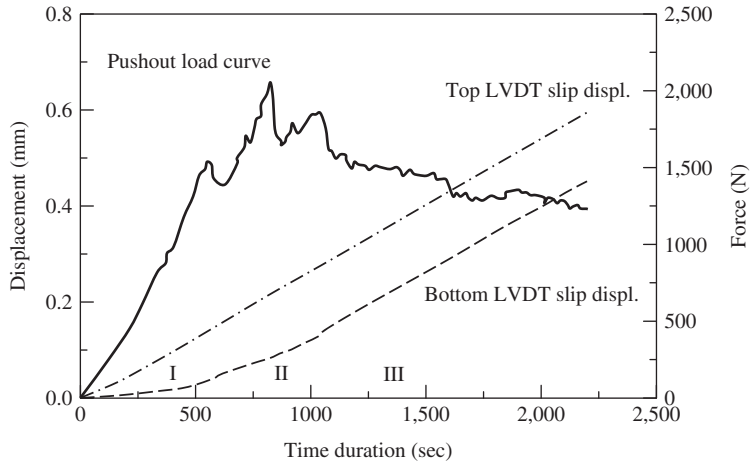

Figure 5-22 Push-out force and displacement as a function of time

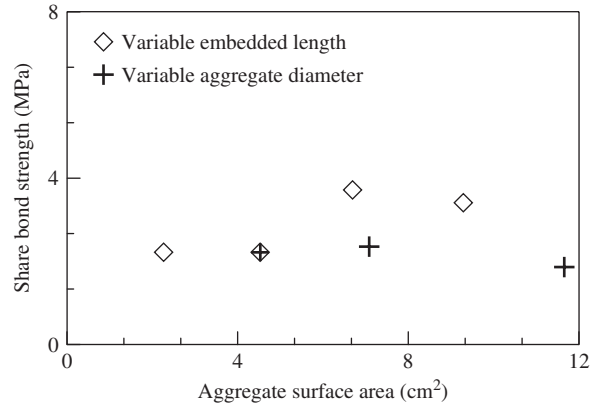

Figure 5-23 Shear strength as a function of surface area

broken. Hence, the end point of the first portion of the curve marks the initial debonding, and the second stage of the curve could be called the partial debonding stage. The point at which the up measured displacement and bottom measured displacement become parallel signals the start of the third stage. The parallelism of the two lines means that the top of the aggregate and the bottom of the aggregate underwent the same amount of displacement. This corresponds to complete debonding. It should be noted that complete debonding of the interface occurs after the peak load has been achieved, as can be seen from the figure, by matching the load curve with the second transition point.

The shear bond strength for specimens with different surface areas is plotted in Figure 5-23. It can be seen that the shear bond strength is of the same order of magnitude as the tensile strength of concrete, with slightly lower values around 2.3 to 4.2 MPa. Except for the push-out test, there are several other methods to measure the different properties of the aggregate–cement interface. They are schematically shown in Figure 5-24.

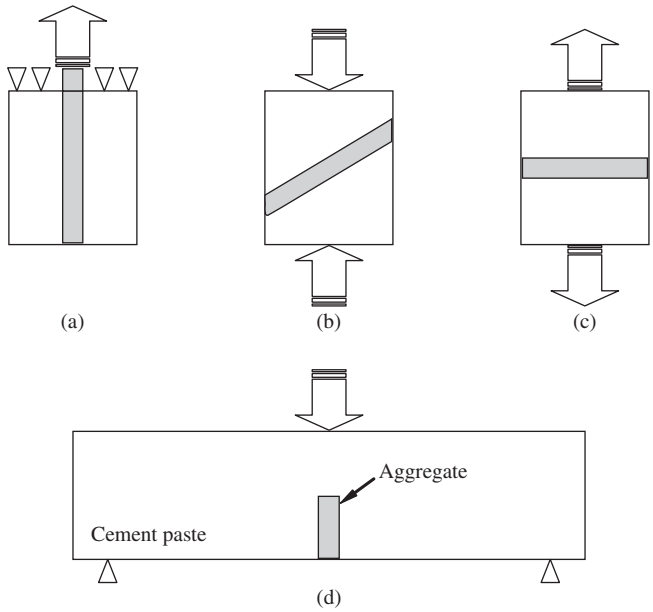

Figure 5-24 Different types of bond test configurations: (a) aggregate pullout test; (b) shear-type test; (c) tension-type test; and (d) bending-type test

5.1.7 Fatigue strength

There are two terms regarding fatigue in concrete technology. One is called static fatigue and the other cyclic fatigue. The static fatigue describes a failure of concrete under a slowly increasing loading rate at a peak values slightly lower than the strength obtained in a test at standard loading rate. It can be explained by the effect of loading rate on the load-carrying capacity of concrete, as discussed earlier. In other words, the phenomenon of a decreasing of load-carrying capacity as a function of the decrease of the loading rate in a wide range is called static fatigue. Under low rates of loading, static fatigue occurs when the stress in concrete exceeds 70–80% of the defined (short-term) strength. This threshold represents the onset of microcrack localization, which leads to macrocrack development and failure. This stress value also initiates unstable creep development, which is discussed later, so sometimes the static fatigue is also called creep rupture. The influence of the loading rate on the load-carrying capability, or the phenomenon of static fatigue, can be clearly seen in Figure 5-25.

The cyclic fatigue can be defined as a failure caused by the repeated application of loads that are not large enough to cause failure in a single application. This implies that some internal progressive permanent structural damage accumulates in the concrete under repeated stress. A typical cyclic loading is shown in Figure 5-26. By referring to the figure, some useful definitions and basic concepts for cyclic loadings can be introduced.

Constant amplitude stressing: cycling between maximum and minimum stress levels that are constant

Stress range, $\Delta\sigma$: the difference between the maximum and the minimum values:

$$\Delta\sigma = \sigma_{\max} - \sigma_{\min} \tag{5-27}$$

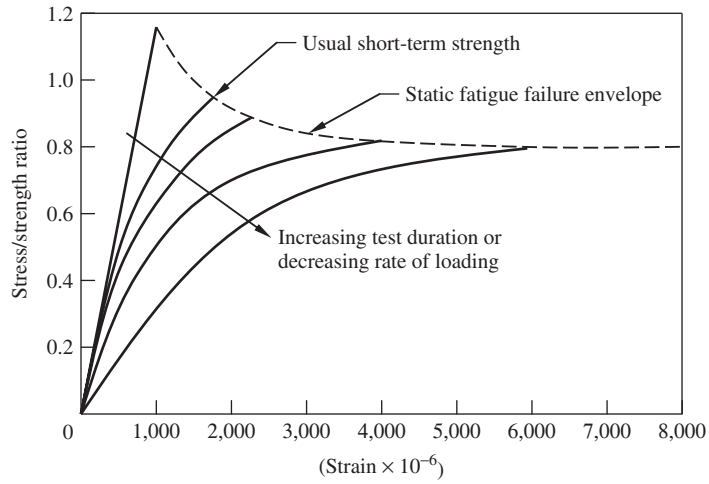

Figure 5-25 Influence of loading rate on load-carrying capability

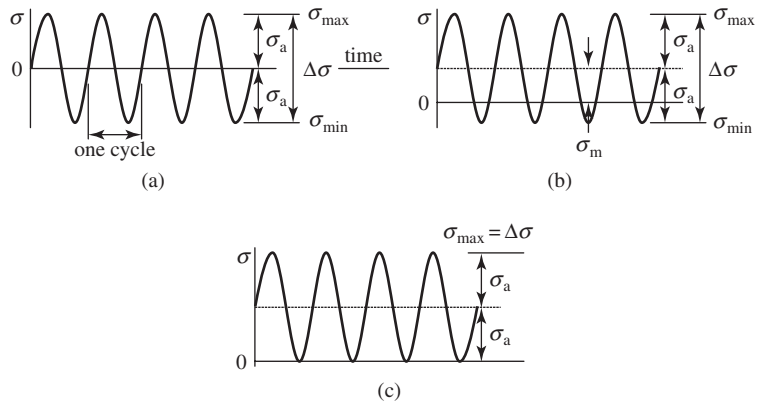

Figure 5-26 Typical cyclic loading patterns

Mean stress, σ_m: the average of the maximum and minimum values:

$$\sigma_{\mathrm{m}} = \frac{\sigma_{\max} + \sigma_{\min}}{2} \tag{5-28}$$

Stress amplitude, σ_a: is half of the stress range:

$$\sigma_{\mathrm{a}} = \frac{\Delta\sigma}{2} = \frac{\sigma_{\max} - \sigma_{\min}}{2} \tag{5-29}$$

Completely reversed stressing: means that the mean stress is equal to zero, with constant amplitude

In cyclic fatigue, the symbol S is usually utilized to represent a nominal or average stress, which has some difference with the true stress at a point σ. The nominal stress distribution is determined from the load or moment using mechanics of materials formulas as a matter

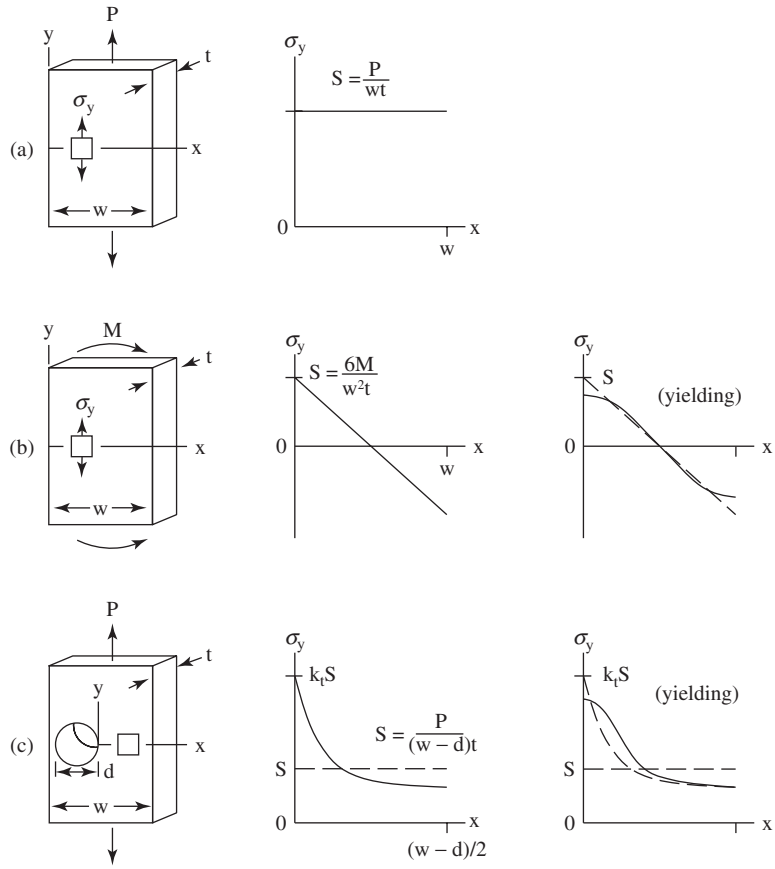

Figure 5-27 Comparisons between S and σ

of convenience, while true stress is determined according to the real materials states (stress concentration, yielding). S is equal to σ only in certain situations, see Figure 5-27.

The fatigue strength of a material is largely influenced by the maximum stress applied, the difference between maximum and minimum stress (stress range), and the number of cycles. The fatigue life of a material is usually plotted as nominal stress versus cyclic number on an *S-N* diagram. To get the *S-N* diagram, fatigue tests have to be conducted. Each test deals with a fixed stress amplitude and mean stress. The test continues until the specimen fails at a cyclic number of N_f. One experimental result will generate one point in the *S-N* diagram. The *S-N* diagram should have sufficient data points to make the empirical analysis meaningful. To make things simple, usually a completely reversed stressing, mean stress equaling to zero with constant amplitude, is adopted first to build up the *S-N* diagram. For the cases of mean stress not equaling to zero, the fatigue life can be estimated by using the *S-N* diagram of completely reversed stress, as stated in the following section.

When sufficient experimental data are obtained from completely reversed stress fatigue tests, an *S-N* diagram can be plotted in linear–linear coordinates, linear–log coordinates, or log–log coordinates. Figure 5-28 shows a linear–log plot of an *S-N* diagram. If *S-N* data are

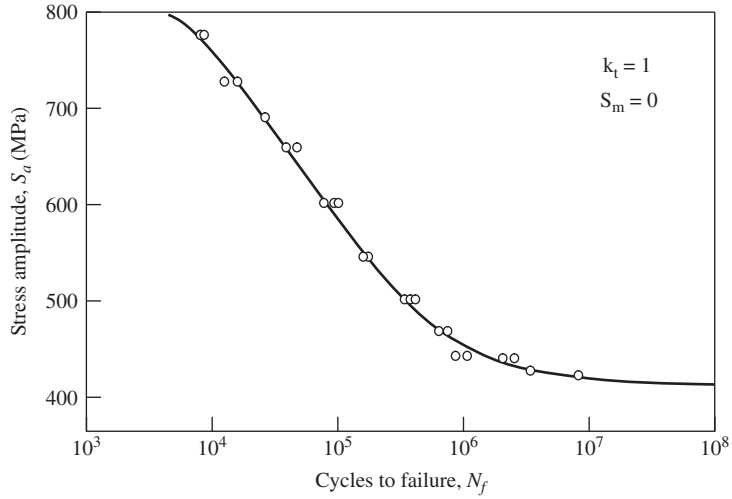

Figure 5-28 An *S-N* diagram

found to be a straight line on a log–log plot, the relationship between stress amplitude and fatigue cycles can be written as

$$\sigma_{\text{ar}} = A(N_{\text{f}})^B \tag{5-30}$$

where σ_{ar} is the stress amplitude for completely reversed stressing ($\sigma_{\text{m}} = 0$) corresponding to N_{f}, A and B are the material constants, and N_{f} is the cycle to failure. For the cases in which $\sigma \neq 0$ the relationship between the stress amplitude and the stress amplitude for completely reversed stressing can be expressed by the empirical modified Goodman law,

$$\sigma_{\text{a}} = \sigma_{\text{ar}} \left(1 - \frac{\sigma_{\text{m}}}{\sigma_{\mu}}\right) \tag{5-31}$$

where σ_{a} is the stress amplitude for $\sigma_{\text{m}} \neq 0$ for a given fatigue life, σ_{ar} the stress amplitude of completely reversed stressing at fatigue failure (N_{f}), σ_{m} the mean stress, and σ_{μ} the static strength of the material. This equation provides a base for estimating the fatigue life for a case in which $\sigma_{\text{m}} \neq 0$ by utilizing the *S-N* diagram for completely reversed stress. The fatigue life of any $(\sigma_{\text{m}}, \sigma_{\text{a}})$ combination can be estimated from the following procedures. First, substitute Equation 5-30 into 5-31:

$$\sigma_{\text{a}} = \left(1 - \frac{\sigma_{\text{m}}}{\sigma_{\mu}}\right) A N_{\text{f}}^B \tag{5-32}$$

This equation reduces to $\sigma_{\text{a}} = AN_{\text{f}}^B$ as it should, if $\sigma_{\text{m}} = 0$. On a log–log plot, Equation 5-32 produces a family of *S-N* curves for different values of mean stress, which are all parallel straight lines. In general, let the *S-N* curve be

$$\sigma_{\text{a}} = \left(1 - \frac{\sigma_{\text{m}}}{\sigma_{\mu}}\right) f(N_{\text{f}}) \tag{5-33}$$

which is a corresponding family of *S-N* curves. From Equation 5-32,

$$N_{\text{f}} = \sqrt[B]{\frac{\sigma_{\text{a}}}{A\left(\sigma_{\mu} - \sigma_{\text{m}}\right)}} \tag{5-34}$$

If more than one amplitude or mean level occurs in a fatigue test, the fatigue life may be estimated by summing the cycle ratios, called the Palmgren-Miner rule:

$$\sum \frac{N_i}{N_{fi}} = 1 \tag{5-35}$$

where N_i is the number of applied cycles under $\Delta\sigma_i$ or σ_{ai}, and N_{fi} is the number of cycles to failure under $\Delta\sigma_i$ or σ_{ai}.

Often, a sequence of variable amplitude loading is repeated a number of times. Under these circumstances, it is convenient to sum cycle ratios over one repetition of the history, and then multiply this by the number of repetitions required for the summation to reach unity.

$$B_f \sum \left(\frac{N_i}{N_{fi}}\right)_{\text{one repetition}} = 1 \tag{5-36}$$

where B_f is the number of repetitions to failure. Another approach for fatigue life prediction involves fracture mechanics concepts. Considering a growing crack that increases its length by an amount Δa due to the application of a number of cycles ΔN. The rate of growth with cycling can be characterized by da/dN.

Assume that the applied loading is cyclic with constant values of the loads P_{max} and P_{min}, and also with constant values of the nominal stresses S_{max} and S_{min}. For fatigue crack growth, it is conventional to use the nominal stresses that are generally defined based on the gross area to avoid the change of stress values with crack length. The primary variable affecting the growth rate of a crack is the range of the stress intensity factor. This is calculated using the stress range ΔS:

$$\Delta K = F \Delta S \sqrt{\pi a} \tag{5-37}$$

The value of F depends only on the geometry and the relative crack length, $\alpha = a/b$, just as if the loading was not cyclic. Since K and S are proportional for a given crack length, the maximum, minimum, and range for K during a loading cycle are given by

$$K_{max} = F S_{max} \sqrt{\pi a} \tag{5-38}$$

$$K_{min} = F S_{min} \sqrt{\pi a} \tag{5-39}$$

$$\Delta K = K_{max} - K_{min} \tag{5-40}$$

For a given material and set of test conditions, the crack growth behavior can be described by the relationship between cyclic crack growth rate da/dN and the stress intensity range K. The empirical curve fitted suggests that the following relationship can be used:

$$\frac{da}{dN} = C(\Delta K)^m \tag{5-41}$$

where C and m are curve-fitting constants (from the log–log plot).

It should be noted that Equation 5-41 is obtained empirically and is valid for an intermediate crack growth rate or the ΔK range. At low growth rates, the curve generally becomes steep and appears to approach a vertical asymptote denoted K_{th}, which is called the fatigue crack growth threshold. This quantity is interpreted as a lower limiting value of K, below which crack growth does not ordinarily occur. At high growth rates, the curve may again become steep. This is due to rapid unstable crack growth just prior to the final failure of the test specimen. The number of cycles to failure during a fatigue test can be calculated using the following equation:

$$N_f = \int_{a_i}^{a_f} \frac{da}{C(\Delta K)^m} \tag{5-42}$$

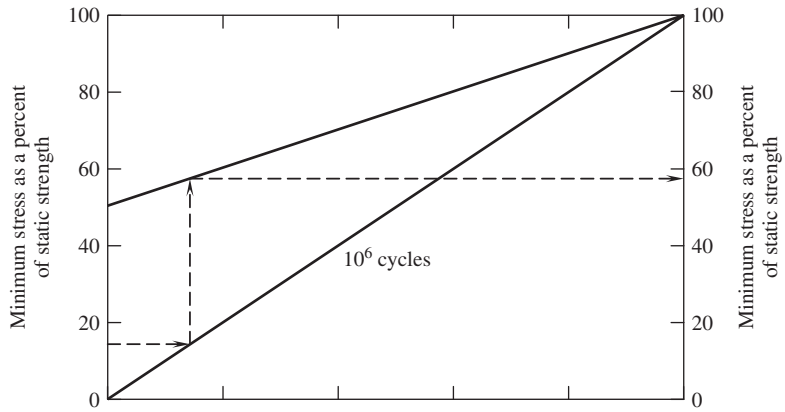

Figure 5-29 A fatigue design diagram (ACI 215R-74)

where a_i is the initial crack size obtained from inspection (if no crack is found, take a_i as the crack detection threshold), and a_f the final crack size obtained from $K_{max}(a_f) = K_c$. By substituting the expressions in Equation 5-42, we can obtain

$$N_{if} = \left[\frac{1 - \left(\frac{a_i}{a_f}\right)^{(m/2-1)}}{C\left(F\Delta S\sqrt{\pi}\right)^m \left(\frac{m}{2} - 1\right)} \right] \frac{1}{a_i^{(m/2-1)}} \tag{5-43}$$

where N_{if} is the cycle number for material failure in fatigue from a crack growing from a_i to a_f, and F is a geometrical function that depends on the loading pattern and the ratio of crack size to specimen size. In concrete design, a simple diagram or formula is usually used for fatigue strength. For this purpose, the Goodman law can be rewritten as

$$\sigma_a = \sigma_{ar}\left(1 - \frac{\sigma_m}{\sigma_\mu}\right) = \frac{\sigma_{max} - \sigma_{min}}{2} \tag{5-44}$$

This equation gives a hint that the fatigue life of a concrete structure can be generally governed by the maximum and minimum stress carried by the concrete. Following this idea, the ACI Committee 215 recommended a simple method for use in design for plain concrete in both tension and compression, as shown in Figure 5-29. This figure allows the determination of the maximum stress that concrete can withstand for 10^6 load cycles, for a known minimum stress. For example, for zero minimum stress, the maximum stress for 10^6 cycles is the value corresponding to the 50% of short-term strength. It provides the maximum stress range. As the minimum stress increases, the stress range reduces, although the maximum stress increases.

5.2 STRESS–STRAIN RELATIONSHIP AND CONSTITUTIVE EQUATIONS

5.2.1 Methods to obtain a stress–strain (deformation) curve

A complete stress–strain curve includes the post-peak response. To obtain a complete stress–strain curve, a proper loading control mechanism is a must. For a uniaxial compression test, the load cell is used to measure the load, and sensors such as strain gauges, extensometers, or LVDTs

are used to measure the deformation. If a very stiff machine is being used, for normal-strength concrete, the stroke control is good enough to obtain the post-peak response. However, for high-strength concrete, the stroke control cannot determine sufficient downward movement as a good feedback signal, and the specimen usually explodes around the peak load. In this case, another control method has to be used to obtain the post-peak behavior. One of the methods is circumferential control by using a roller chain tied on the specimen in a transverse condition, as shown in Figure 5-30. Under uniaxial compression, the circumferential displacement is a monotonic function of the loading process, even in the post-peak response stage. Hence, by using it as feedback in the post-peak response stage, the control is stable and reliable.

For a uniaxial tension test, it is much more difficult to obtain a complete stress–deformation curve. Conventionally, two methods are used to obtain a stable response in the post-peak region for a uniaxial tension test. One is called the loading-sharing method, see Figure 5-31. In this method, an elastic load-sharing system is parallel to the specimen (in the loading direction). In

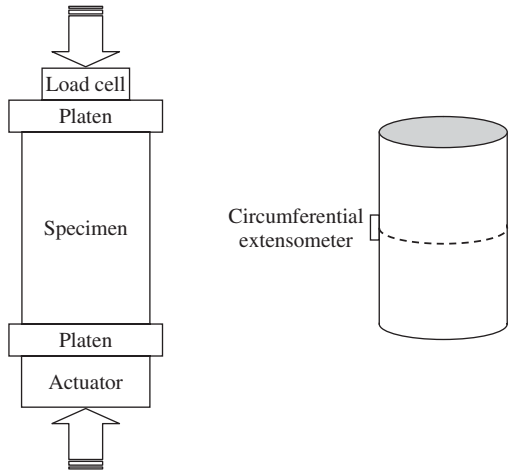

Figure 5-30 Circumferential controlled test setup

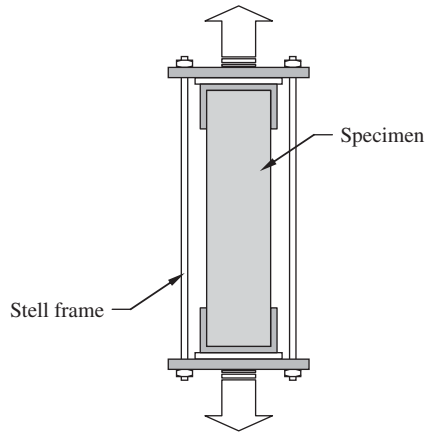

Figure 5-31 Concrete tension test conducted with loading sharing system

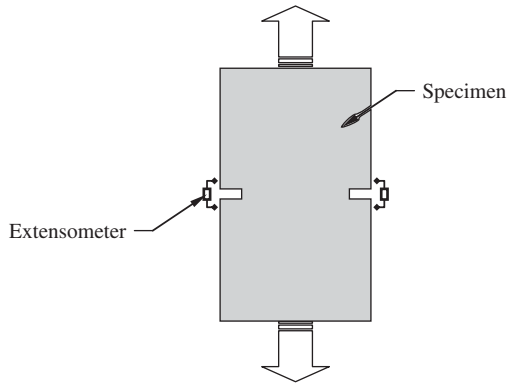

Figure 5-32 Notched specimen used for uniaxial tension test

this way unstable failure near the peak load (resulting from the sudden release of stored elastic energy) is avoided. The load shared by the concrete is obtained by subtracting the contribution of the load-sharing system from the total load, implying subtraction of two relatively large numbers to obtain a small number. Since the load carried by the system is calculated from the strain measured by a strain gage attached to the steel bar, any small error in strain gage measurement can lead to a big error in load calculation. Hence, the major drawback of using parallel load-sharing system is poor accuracy, especially in the post-peak region.

Noting the disadvantages of the parallel load-sharing method, attempts were made to perform tensile tests on a specimen with two edge notches using closed-loop control, see Figure 5-32. Tensile failure of concrete is the result of the opening of a single "major" crack. If the opening of the crack is controlled in a closed-loop manner, gradual failure can be obtained, and instability near the peak load can be avoided. Since the cross section with two edge notches is significantly weaker, a major crack will be forced to form at this position. A pair of displacement sensors is usually used with one on each side of the specimen, to cover the notch, and the average output is used as a feedback control signal. Since the location of the major crack is predetermined by introducing a notch in the specimen, the opening of the notch will always be increasing, and thus a stable control can be obtained. One of the problems associated with a notched specimen is that it forces the major crack to form at a predetermined location. Also, the state of stress in the specimen is not truly uniform. When a notched specimen is used, it is not possible to study the accumulation of damage and strain localization phenomena, which are of great interest in the failure process.

A new method was developed to obtain the complete stress–deformation response of an unnotched concrete specimen, as shown in Figure 5-33. This method employs a digitally controlled closed-loop-testing machine and five control channels: stroke LVDT and four LVDTs mounted on the specimen. The test portion of the specimen was fully spanned by these four LVDTs. The outputs of these control channels and the load cell were monitored during the test by a computer equipped with LabTech's Notebook software. A C-language program was written to enable quick switching of the mode of control from one LVDT to another. The problem of uncertainty in the location of the major crack was tackled by the said LVDT arrangement and the computer program. It was demonstrated that it is always possible to obtain a stable post-peak response provided one ensures that at any time during the test, the feedback used is the LVDT that exhibits, at that time, the largest slope of the response–time curve. An acoustic emission (AE) measurement system of six channels was also used in the experiments. Monitoring of

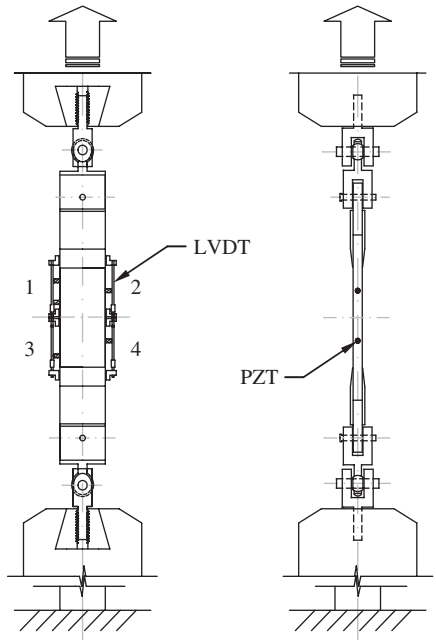

Figure 5-33 Uniaxial tension test setup for unnotched concrete specimen

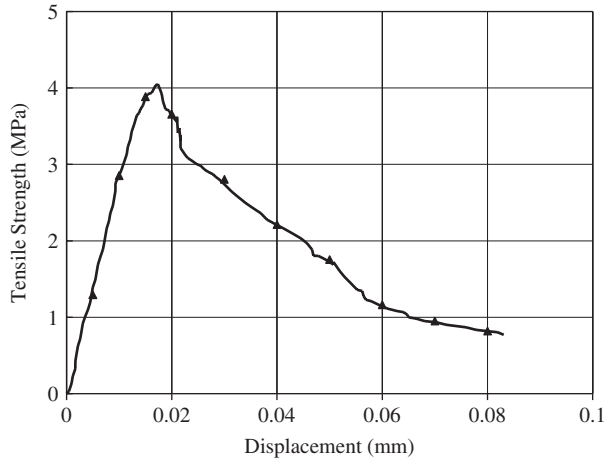

Figure 5-34 The stress–deformation curve of unnotched concrete specimen

signals from the AE transducers provide valuable information, which help in making a decision to switch the control.

For the plain concrete specimen tested, a reliable result was obtained. The stress–deformation curve is shown in Figure 5-34 for the plain concrete specimen. In the figure, "Deformation" refers to displacement measured by the LVDT, which was in control in the post-peak region. The curve can be divided into three parts: the linear elastic part, the nonlinear pre-peak part, and the post-peak part. In the first part, concrete behaves elastically. The linear

elastic part is characterized by uniform deformation and "global" behavior of the material. In the second part, due to the damage (indicated by the occurrence of AE events) in the specimen, the modulus of the material starts to reduce and thus nonlinearly appears in the stress–deformation curves. Since damage does not happen uniformly in the specimen, behavior of the material ceases to be "global."

After the peak load, a major crack develops in the specimen. The behavior of the specimen in this region can be explained with the help of fracture mechanics theory. One of the results from this theory is that the stiffness of a specimen (defined as the ratio of load-to-load-point displacement) decreases as a result of the growth of a crack. In the tests described here, the test machine was issued a command to apply load in such a way that the response of the controlling LVDT increased linearly with time. To do this in the post-peak region, the machine must decrease the load on the specimen to maintain equilibrium. Such reduction in load was explained in earlier hypotheses that the material becomes "soft" in the post-peak region. Today, it is understood that a "softening" response in tension is actually a manifestation of the growth of a single crack.

5.2.2 Modulus of elasticity

The modulus of elasticity can be measured directly from the initial slope of a specially designed stress–strain curve. To get such a curve, the load should be applied gradually, at a rate of 2–3 MPa per second, until the value of the load, P, corresponding to 0.4 of the peak value is reached. Then the load is reduced to near zero at approximately the same rate as it was increased. The above loading/unloading procedure is repeated three times. After finishing three loading cycles, the fourth loading cycle is applied at the aforementioned rate to the value P_0, corresponding approximately to a stress value of 5 MPa. This load is maintained for 30 sec. The deformation (δ_b) is measured from the displacement sensors, and then the load is increased to P, corresponding to 0.4 of the peak value, and maintained for 30 sec (see Figure 5-35). Similarly, the corresponding deformation (δ_a) is recorded from the displacement sensor. After calculating the mean value of the difference ($\delta_a - \delta_b$) of the two deformation readings, the result is denoted as δ_4. Loading is then reduced to the base value of P_0, as the initial load for the 5th loading cycle. Apply the 5th loading cycle as in the above procedure. Record the corresponding deformation and calculate the mean value (δ_5) of the deformation changes recorded by the two gauges. If the difference between δ_4 and δ_5 is not greater than 0.003 mm, take off the gauges and increase the load at the aforementioned rate until the specimen fails, then f_c is recorded. The modulus is calculated with the following equation

$$E_h^s = \frac{P - P_0}{A} \times \frac{l}{\delta_n} \tag{5-45}$$

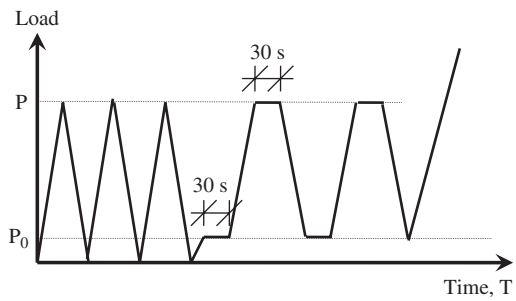

Figure 5-35 Loading time diagram for evaluating the modulus of elasticity of concrete

in which, E_h^s is the modulus of elasticity of concrete in compression, P_0 the load corresponding to a stress level of 5 MPa, P the load corresponding to 0.4 f_c, A the area over which the load is applied, l the measuring length, and δ_n the mean value of the deformation differences in the last loading cycle.

The modulus of elasticity of concrete can also be predicted theoretically using information on the aggregate's modulus and the cement paste's modulus. Here three popular models are introduced.

(a) *Parallel model (or isostrain model)*: In the parallel model, it is assumed that all the aggregates are concentrated in the central part of the concrete, in parallel to the loading direction, as shown in Figure 5-36. For this loading pattern, two conditions have to be satisfied: the deformation must be the same in the matrix, the aggregate, and the concrete, and the total force carried by the concrete must be equal to the force carried by the matrix and by the aggregate. Thus, we have

$$\Delta l_c = \Delta l_m = \Delta l_a \tag{5-46}$$

and

$$P_c = P_m + P_a \tag{5-47}$$

where Δl_c is the length change of the concrete, Δl_m the length change of the matrix, and Δl_a the length change of the aggregate; P_c is the load carried by the concrete, P_m by the matrix, and P_a by the aggregate. Since all the components in the parallel model have same original length, from Equation 5-46, we can derive that

$$\varepsilon_c = \varepsilon_m = \varepsilon_a \tag{5-48}$$

By dividing Equation 5-47 by A_c, the cross-sectional area, on both sides, we can get

$$\frac{P_c}{A_c} = \frac{P_m + P_a}{A_c} = \frac{P_m A_m}{A_m A_c} + \frac{P_a A_a}{A_a A_c} \tag{5-49}$$

Based on the definition of stress and volume fraction ratio, we can get the following equation from the above equation:

$$\sigma_c = \sigma_m V_m + \sigma_a V_a \tag{5-50}$$

where V_m and V_a are volume fraction of the matrix and aggregate, respectively. By dividing Equation 5-48 and applying the relationship between stress and strain, the modulus of elasticity can be expressed as

$$E_c = E_m V_m + E_a V_a \tag{5-51}$$

This formula is also called the rule of mixtures and is widely accepted in composite mechanics.

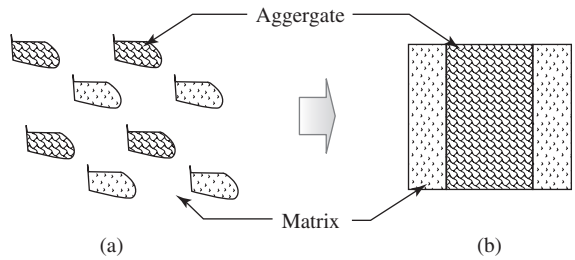

Figure 5-36 The parallel model for estimating the elastic modulus: (a) the discrete system; and (b) the representative volume

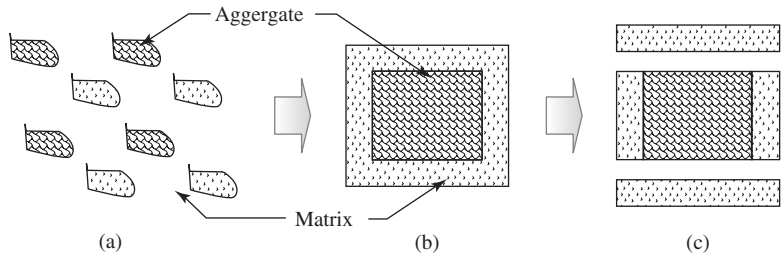

Figure 5-37 The square-in-square model: (a) the discrete system; (b) the representative volume; and (c) the sliced system

(b) *Series model (isostress model)*: In this kind of model, it is assumed that the force in the matrix and aggregate is the same and the deformation change of the concrete equals the sum of the deformation changes in the matrix and aggregate. Starting from

$$P_c = P_m = P_a \tag{5-52}$$

and

$$\Delta l_c = \Delta l_m + \Delta l_a \tag{5-53}$$

we can obtain

$$\frac{1}{E_c} = \frac{v_m}{E_m} + \frac{v_a}{E_a} \tag{5-54}$$

(c) *Square-in-square model*: In this kind of model, the representative volume in concrete is idealized as a square, as shown in Figure 5-37b. If we break the system into 3 slices as shown in Figure 5-37c and consider these three slices to be in series, we can finally obtain the following equation:

$$\frac{1}{E_c} = \frac{1-\sqrt{v_a}}{E_m} + \frac{\sqrt{v_a}}{\left(1-\sqrt{v_a}\right)E_m + \sqrt{v_a}E_a} \tag{5-55}$$

It has been verified by experiments that the results obtained from this equation agree better than lower- and upper-bound equations, i.e., series and parallel model.

Relationship between compressive strength and modulus of elasticity: According to the British Standard for the structural use of concrete (BS 8110: part 2), modulus of elasticity concrete can be related to the cube compressive strength by the expression

$$E_c = 9.1 f_c^{0.33} \tag{5-56}$$

when the density of concrete is 2320 kg/m^3, i.e., for a typical normal-weight concrete. If the density of concrete is between 1400 and 2320 kg/m^3, the expression for Young's modulus is

$$E_c = 1.7\rho^2 f_c^{0.33} \times 10^{-6} \tag{5-57}$$

where ρ is the density of concrete in kg/m^3. According to the ACI Building Code 318-83, the relationship between Young's modulus and compressive strength for normal density concrete is

$$E_c = 4.70 f_c^{0.5} \tag{5-58}$$

where f_c is the cylinder compressive strength. For concrete with density of 1500 to 2500 kg/m^3, the relationship changes to

$$E_c = 43\rho^{1.5} f_c^{0.5} \times 10^{-6} \tag{5-59}$$

It should be noted that in all the above equations, MPa is used for strength and stress, and GPa for Young's modulus.

5.2.3 Constitutive equations

A constitutive equation is a relation between two physical quantities that describes the response of a material or substance to external functions, such as load, temperature, water flow, or ionic transport. In concrete structural analysis, the most popular constitutive equation is the stress–strain relationship that connects applied stress or forces to strain or deformation in concrete. The stress–strain relationship is also called Hooke's law. There are two ways to obtain constitutive equations: the phenomenological method and the upscaling method. The phenomenological method is used to obtain knowledge of constitutive equations through empirical observations of phenomena that are consistent with fundamental theory, but not directly derived from theory. The upscaling method is used to obtain the constitutive equations from the nature of the microstructure of a material and through theoretical derivation based on first principles. For concrete, the constitutive equations are mostly obtained by the phenomenological method, or curve fitting of experimentally obtained stress–strain (deformation) relationships.

As shown in Figure 5-38, a typical stress–strain curve obtained through compressive testing shows several stages: linear elastic, inelastic, and stain-softening or post-peak response (Chen, 1981). Numerous mathematical equations have been developed for the nonlinear constitutive stress–strain relationship of concrete under uniaxial compression. Difficulty arises on how to represent the suspected nature of the deformations of concrete that are generally attributed to the process of progressive microcracking. Moreover, concrete is a highly complex composite and its deformation response is closely related to its composition, as well as its internal microstructure. It is anticipated that a single mathematical equation is not sufficient to represent the expected wide range of constitutive behavior for different grades of concretes. Yip (1998) has derived a general stress–strain equation for a prismatic concrete specimen, having an aspect ratio of 2.5, under uniaxial compression, as

$$\frac{\sigma_c}{\sigma_{c,u}} = \frac{\varepsilon_c}{\varepsilon_{c,u}} e^{\left(1-\frac{\varepsilon_c}{\varepsilon_{c,u}}\right)} \tag{5-60}$$

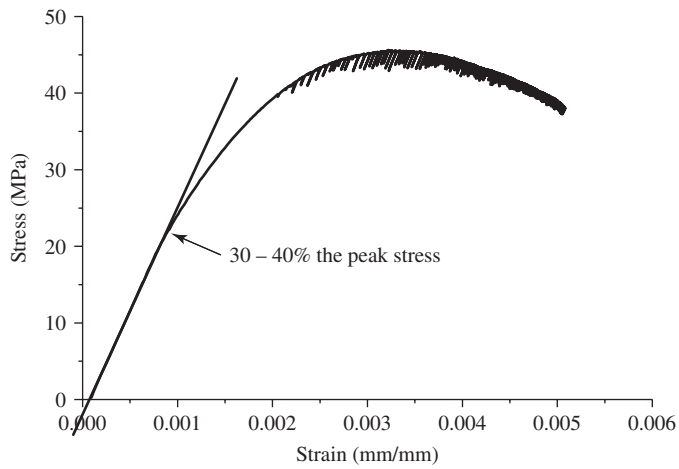

Figure 5-38 A typical stress–strain curve obtained through compressive test

where σ_c is the compressive stress, $\sigma_{c,u}$ the ultimate compressive stress, ε_c the compressive strain, and $\varepsilon_{c,u}$ the strain corresponding to $\sigma_{c,u}$. By using the exponential power series expansion, Equation 5-60 can be rewritten as

$$\sigma_c = \frac{2.7182 E_{c,u}\ \varepsilon_c}{1 + \left(\frac{\varepsilon_c}{\varepsilon_{c,u}}\right) + \frac{1}{2}\left(\frac{\varepsilon_c}{\varepsilon_{c,u}}\right)^2 + \frac{1}{6}\left(\frac{\varepsilon_c}{\varepsilon_{c,u}}\right)^3} \tag{5-61}$$

where $E_{c,u}$ is the modulus of elasticity. It should be pointed out that Equation 5-61 describe not only the ascending branch of the stress–strain curve, but also the descending branch of the curve after the peak stress point. Moreover, the constitutive model presented above is only one typical example in this area. Many other attempts have been made to derive empirical stress–strain equations, including the descending branch, by Wang et al. (1978), Popovics (1973), and Blechman (1992). Recently, with the development of a better understanding of the concrete structure at the nano- and microscales, attempts to develop constitutive relationships from the microstructure using the upscaling method or multiple scaling techniques have been made.

5.3 DIMENSIONAL STABILITY—SHRINKAGE AND CREEP

Dimensional stability is defined as the ability of a material to keep its size, shape, or dimension over a long period. The volumetric change of a dimensionally stable material over a long period of time should be sufficiently small that it will not cause any structural problems. For concrete, shrinkage and creep are the two major phenomena that compromise the dimensional stability problem. Shrinkage and creep are often discussed together because they both originate in the hydrated cement paste within concrete. The aggregate in concrete does not exhibit shrinkage and creep. In addition, shrinkage and creep are caused and influenced by many common factors, such as water content, curing conditions, relative humidity, aggregate proportions, and specimen sizes.

5.3.1 Shrinkage

Several types of shrinkage can occur in a concrete, including thermal shrinkage, plastic shrinkage, autogenous shrinkage, chemical shrinkage, and drying shrinkage. In this section, we focus on plastic, autogenous, and drying shrinkage.

5.3.1.1 Plastic shrinkage

Plastic shrinkage is surface shrinkage that happens at a very early age of concrete (only a few hours after casting) while the concrete underneath is still in the plastic stage. After casting, if the concrete is not properly taken care of with a good curing method, the top surfaces of concrete pours are subjected to evaporation and consequent loss of mix water. The rate of evaporation depends on ambient conditions such as temperature, exposure to sun, wind speed, and relative humidity. The water lost by evaporation on the surface is usually replaced by water rising from the internal regions of the concrete. Once the rate of removal of water from the surface exceeds the rate of immigration of the internal water to the surface, the surface layer's volume starts to show local reductions, or plastic shrinkage. The magnitude of the plastic shrinkage in extreme cases can be as large as 10,000 microstrain (Troxell et al., 1968), and has been shown by L'Hermite (1960) to be over 6000 microstrain for paste and 2000 microstrain for concrete. In a plastic state, no great stress is induced in the concrete and further working of the concrete can generally be applied to eliminate consequential cracks.

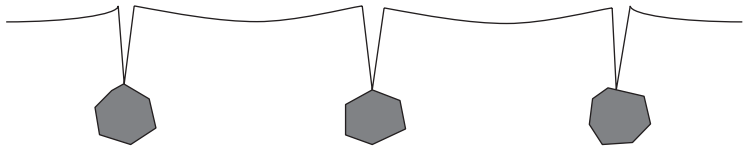

Figure 5-39 Formation of plastic shrinkage crack

Plastic shrinkage usually leads to a downward movement of the solid and heavier ingredients in the surface layer. This downward movement may be resisted by the large size of coarse aggregates or by the top layer of reinforcement. In this case, the surface layer of the concrete above the coarse aggregate or reinforcing bar tends to become draped over the aggregates or bars, and hence creates the cracks, called plastic shrinkage cracks. The process leading to plastic shrinkage cracking is shown diagrammatically in Figure 5-39. Plastic shrinkage cracks are usually of shallow depth, generally 38 to 50 mm, and 300 to 450 mm long, normally perpendicular to the wind, and typically run parallel to one another. These plastic shrinkage cracks provide a path for water and other chemical to reach the steel reinforcement, which can greatly affect the durability of concrete structures, for instance, corrosion is easily generated.

The most effective ways of preventing plastic shrinkage is by sheltering the surface from the wind and sunshine during construction and by covering the concrete surface immediately after finishing, which are all directed toward reducing the rate of evaporation. BS 8110 has recommended minimum periods of curing and protection (see Table 5-1) for fresh concrete to reduce plastic shrinkage. Changes in concrete mix design, and especially the use of air entrainment, may also be helpful in reducing plastic shrinkage. Remedial measures after the cracks have formed usually consist of sealing them against the ingress of water by brushing in cement or low-viscosity polymers (Allen et al., 1993).

5.3.1.2 Autogenous shrinkage

Autogenous shrinkage is defined as the macroscopic volume contraction of concrete at an early age (less than one day after casting) occurring without moisture transfer from the concrete to the surrounding environment. Autogenous shrinkage can be attributed to self-desiccation due to the hydration of cement and is a result of chemical shrinkage. Autogenous shrinkage was first

Table 5-1 Minimum periods of curing and protection

		Minimum Period of Curing and Protection	
		Average Concrete Surface Temperature	
Type of Cement	Ambient Conditions After Casting	5 to 10°C	Above 10°C
Portland cement, SRPC	Average	4 days	3 days
	Poor	6 days	4 days
All except Portland cement and SRPC, and all with GGBS or PFA	Average	6 days	4 days
	Poor	10 days	7 days
All	Good	No special requirements	

Note: SRPC, sulfate-resisting Portland cement; GGBS, ground granulated blastfurnace slag; PFA, pulverized fuel ash.

described in the 1930s by Lyman (1934) as a factor contributing to the total shrinkage. However, in the earlier days, it was noted that autogenous shrinkage occurred only at very low *w*/*c* ratios, far below the practical *w*/*c* range, and did not draw much attention. With the development and applications of advanced admixtures such as superplasticizers, *w*/*c* ratios lower than 0.42 are realized in concrete practice and autogenous shrinkage has become an important issue for contemporary concrete. This issue has been further enlarged by the incorporation of silica fume into concrete mixes.

To better understand the concept of autogenous shrinkage, let us examine the chemical shrinkage first. When cement contacts water, the ions dissolve into solutions from cement and react with water to produce hydrates. The hydration leads to the reduction of the total absolute volume of the cement system. This phenomenon is called chemical shrinkage. It was first discovered by Le Chatelier (1900) in 1900, who described the basic distinction between the apparent and the absolute volume of cement paste. The apparent volume is essentially the external volume of a sample, which contains the spaces occupied by solid, liquid, and gas phases. The absolute volume excludes the space occupied by the gas phase. Chemical shrinkage can be seen from the volume change before and after a complete reaction of C_3S. The stoichiometric equation for fully hydrated C_3S can be expressed as (Damidot, et al., 1990):

$$C_3S + 5.2H \rightarrow C_{1.75}SH_{3.9} + 1.3CH \tag{5-62}$$

By substituting the molecular weight and the densities of all products in the above equation, it can be seen that the hydration of C_3S results in a reduction of absolute volume of the system (Nawa and Horita, 2004):

$$\begin{gathered} C_3S + 5.2H \rightarrow C_{1.75}SH_{3.9} + 1.3CH \\ 72.8\,cm^3 + 93.6\,cm^3 \rightarrow 95.9\,cm^3 + 42.9\,cm^3 \\ 166.4\,cm^3 \rightarrow 138.9\,cm^3 \end{gathered} \tag{5-63}$$

Obviously, there is about a 16.5% reduction in volume after hydration if the reactants follow their stoichiometric proportions. It should be pointed out that autogenous shrinkage and chemical shrinkage have some differences. The relationship between autogenous shrinkage and chemical shrinkage is shown schematically in Figure 5-40. When cement paste is in a plastic stage, the apparent volume change or autogenous shrinkage is essentially same, with reduction of absolute

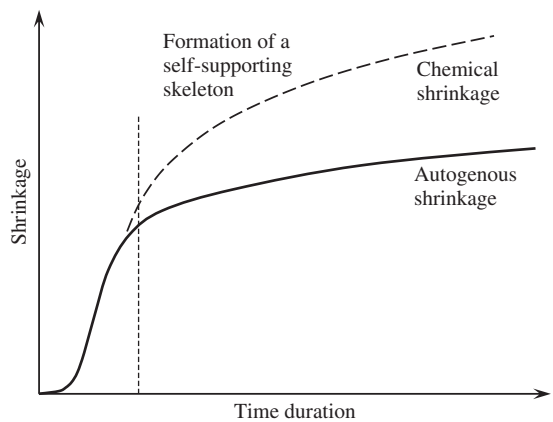

Figure 5-40 Relationship between autogenous shrinkage and chemical shrinkage

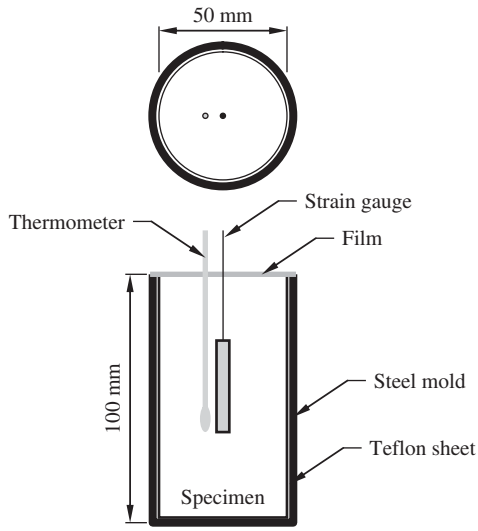

Figure 5-41 Method of measuring autogenous shrinkage of cement paste

volume or chemical shrinkage. When the hydration products percolate to form a structural skeleton, autogenous shrinkage can be restrained by the skeleton and deviates from the theoretical chemical shrinkage.

Many techniques have been developed to measure the autogenous shrinkage. They can be classified in two basically different ways. One is to measure the volume change and other is to measure the change in linear length. The volume change of cement paste can be measured by immersing the specimen in a tight rubber balloon and then measuring the amount of water displaced by the specimen. The linear length change can be measured using a strain gauge embedded in the specimen. During the hydration process, the cement paste deforms and generates internal strain that reflects autogenous shrinkage. Autogenous shrinkage has to be measured without any moisture transferred. Hence, the specimen has to be sealed tightly by materials such as a Teflon sheet or a rubber membrane, as shown in Figure 5-41.

5.3.1.3 Drying shrinkage

As mentioned earlier, to produce workable concrete nearly twice as much of water theoretically needed to hydrate the cement has to be added to the concrete mix if no water-reducing admixture is used for normal concrete. After concrete has been cured and begins to dry, the excessive water that has not reacted with the cement will begin to migrate from the interior of the concrete mass to the surface. As the moisture evaporates, the concrete volume shrinks. The loss of moisture from the concrete varies with distance from the surface. Drying occurs most rapidly near the surface because of the short distance the water must travel to escape, and more slowly from the interior of the concrete because of the increased distance from the surface. The shortening per unit length associated with the reduction in volume due to moisture loss is termed shrinkage. A nearly linear relationship exists between the magnitude of the shrinkage and the water content of the mix for a particular value of relative humidity. If the relative humidity increases, the shrinkage of the concrete drops. When concrete is exposed to 100% relative humidity or is submerged in water, it will actually increase in volume slightly as the gel continues to form because of the ideal conditions for hydration.

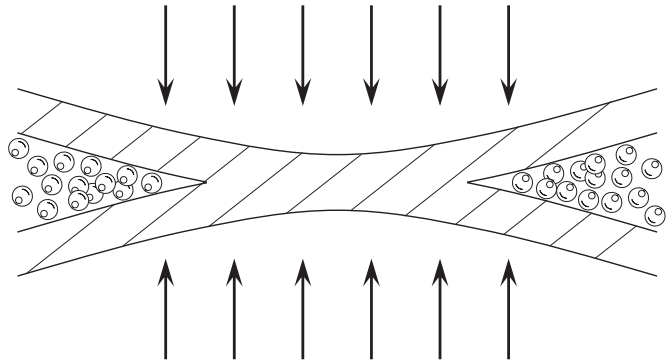

Figure 5-42 Absorbed water film

Three basic mechanisms are responsible for the shrinkage of Portland cement concrete. One is the disjointing pressure that is related to the water absorbed on the surface of C–S–H. Water is absorbed in the layers of C–S–H at all relative humidities, the thickness of the water layer increasing with increasing humidity. At a relative humidity of more than 100%, the surface bounding the narrow spaces can form an absorbed film of water, as shown in Figure 5-42. If the distance between two layers is restricted due to the van der Waals force of attraction, the absorbed water molecules between the C–S–H surfaces may generate a pressure, which leads to an expansion. This pressure is termed disjointing pressure. However, if the relative humidity of the system reduces, the disjointing pressure decreases accordingly and the separated surfaces will be brought closer by the van der Waals force again, leading to the reduction of volume or shrinkage. Disjointing pressure plays an important role in shrinkage when the relative humidity is higher than 75% and has no effect when the RH is lower than 45%.

The second mechanism responsible for the shrinkage is the capillary surface tension effect. With the progress of hydration, the air volume increases and, subsequently, the interface between the air and water increases in a capillary pore. The interface, or meniscus, creates stress, called capillary stress. Capillary tension effects are due to meniscus formation in the capillary pores. This process results in equal hydrostatic compression in the solid phase, which pulls the voids in the C–S–H body closer (Powers, 1965). The capillary surface tension effect can be viewed by considering the Kelvin and the Laplace equations. The Kelvin equation is given as

$$\ln(\mathrm{RH}) = -\frac{2\sigma}{r}\frac{M}{\nu RT}\cos\theta \tag{5-64}$$

$$\text{or} \qquad \frac{2\sigma}{r}\cos\theta = -\frac{\nu RT}{M}\ln(\mathrm{RH}) \tag{5-65}$$

where RH is the relative humidity, σ the surface tension of water in contact with air, M the mass of a mole of water, θ the contact angle of water and solid, r the radius of pore, ν the density of water, R the ideal gas constant, and T the temperature on the Kelvin scale. The Laplace equation can be written as

$$p_c - p_v = \frac{2\sigma}{r}\cos\theta \tag{5-66}$$

$$\text{or} \qquad \Delta p = \frac{2\sigma}{r}\cos\theta \tag{5-67}$$

where p_c is the capillary pressure of water in a pore, p_v is the vapor pressure, and Δp is the suction pressure. By substituting the Kelvin equation into the Laplace equation, we get

$$\Delta p = -\frac{\nu RT}{M} \ln (\text{RH}) = -\frac{\ln (\text{RH})}{K} \tag{5-68}$$

From this equation, it can be seen that suction pressure increases with a decrease in internal humidity. In other words, the reduction of the internal relative humidity will create a larger pressure that leads to the shrinkage of concrete. It cannot exist below about 45% RH, since the disjointing pressure and capillary stress no longer exist, and shrinkage has to be explained by a change of surface energy. As the most strongly adsorbed water (equivalent to one or two molecular layers) is removed, the surface free energy of the solid begins to increase significantly. A liquid droplet is under hydrostatic pressure by virtue of its surface tension (surface energy). This pressure can be described as

$$P_{\text{ave}} = \frac{2\gamma S}{3} \tag{5-69}$$

where P_{ave} is the mean pressure, γ the surface energy in J/m^2, and S the specific surface area of solid in m^2/g. Since S is large in the case of C–S–H (about 400 m^2/g), P_{ave} can be large and causes compression in the solid (Mindess et al., 2003). Shrinkage can create stress inside concrete. Let us take a concrete cylinder as an example. Because the concrete adjacent to the surface of the cylinder dries more rapidly than the interior, shrinkage strains are initially larger near the surface than in the interior. As a result of the differential shrinkage, a set of internal self-balancing forces, i.e., compression in the interior and tension on the outside, is set up. The stresses induced by shrinkage can be explained by imagining that the cylindrical core of a concrete cylinder is separated from its outer shell and that the two sections are then free to shrink independently in proportion to their existing water content. Since deflections must be compatible at the junction between the core and the shell, shear stresses must be created between the core and the shell. If free-body diagrams of the upper half of the cylinder are considered, it is clear that vertical equilibrium requires the shear stresses to induce compression in the core and tension in the shell, see Figure 5-43. The self-balanced shrinkage stress may have some influence on flexural strength and splitting strength measurement. For flexural strength, the existence of a self-balanced stress will reduce a concrete's true bending strength, while splitting testing will increase it. In addition to the self-balancing stresses set up by differential shrinkage, the overall shrinkage creates stresses if members are restrained in the direction in which shrinkage occurs. Tensile cracking due to shrinkage will take place in any structural element restrained by its boundaries, such as a beam–column joint as shown in Figure 5-44. It must be controlled since it

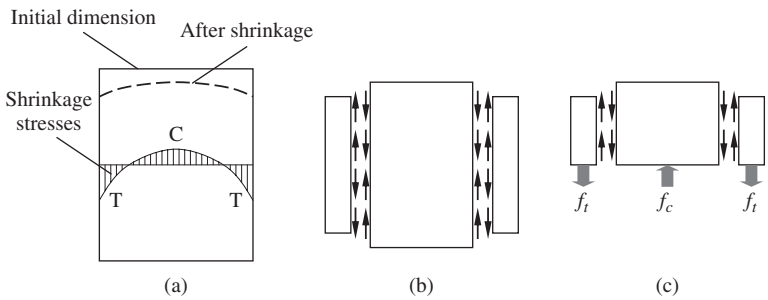

Figure 5-43 Self-balanced stress generated by drying shrinkage

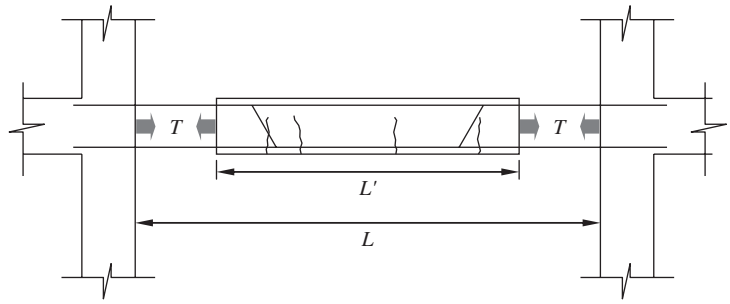

Figure 5-44 Shrinkage crack generated by restraint

permits the passage of water, is detrimental to appearance, reduces shear strength, and exposes the reinforcement to the atmosphere.

The magnitude of the ultimate shrinkage is primarily a function of the initial water content of the concrete and the relative humidity of the surrounding environment. The shrinkage strain, ε_{sh}, is time dependent. Approximately 90% of the ultimate shrinkage occurs during the first year. Both the rates at which shrinkage occurs and the magnitude of the total shrinkage increase as the ratio of the surface to volume increases. This is because the larger the surface area, the more rapidly moisture can evaporate. The value of shrinkage strain for plain concrete members ranges from 0.0004 to 0.0007 for standard conditions. For reinforced concrete members, the shrinkage strain values are between 0.0002 and 0.0003. This means reinforcement is helpful in reducing shrinkage. Free-drying shrinkage can be measured by using a Demac gage on a cylindrical specimen, as shown in Figure 5-45, a prismatic specimen, or a ring-shaped specimen. The specimens for shrinkage tests should be moved into the shrinkage test room after curing to a specified age. The temperature in the room is kept at $27 \pm 2^{\circ}C$ and relative humidity $55 \pm 5\%$. The shrinkage is usually measured at different ages using a Demac gage, such as CT 171M with a maximum displacement measurement of 5 mm.

In addition to the free shrinkage test, constrained shrinkage tests are required to investigate the cracking sensitivity of concrete. There is no standard test to assess cracking due to restrained shrinkage. Recent studies have been performed mainly using three types of specimen: bars, plates, and rings. The bar-type test can provide uniaxial stress development for specimens with large-size aggregates. However, the difficulties of providing a constant restraint and end conditions often make this type of test complicated. Plate-type testing has been used to evaluate both biaxial and plastic shrinkage, and provides a biaxial restraint that depends on geometry and boundary conditions. Ring-type specimens are easily cast and end effects are removed due to closed loop shapes. The ring tests are widely used for restraint shrinkage cracking (Bloom and Bentur, 1995). In such tests, ring-shaped specimens are cast around a rigid inner steel core, as shown in Figure 5-46, to provide a restraint when the specimen has a tendency to shrink. The grade of cracking depends on the restraining conditions and the drying environment. The restraint induces tensile stresses in the concrete ring, which reach a maximal value at the inner surface of the specimen. If the tensile stress developed exceeds the tensile strength of concrete, cracking will be initiated.

Conventional circular ring testing has several disadvantages. Firstly, it is difficult to predict the location of initial cracking due to the equal opportunity of cracking around the circumference of the ring. Secondly, for a steel ring without adequate stiffness, concrete with a higher toughness cannot generate a visible crack, but more invisible fine cracks, which may result in some crisis regarding concrete durability (Burrows, 1998). The low cracking sensitivity (mortar or concrete)

Figure 5-45 Free-drying shrinkage measurement using a Demac gage on a cylinder specimen

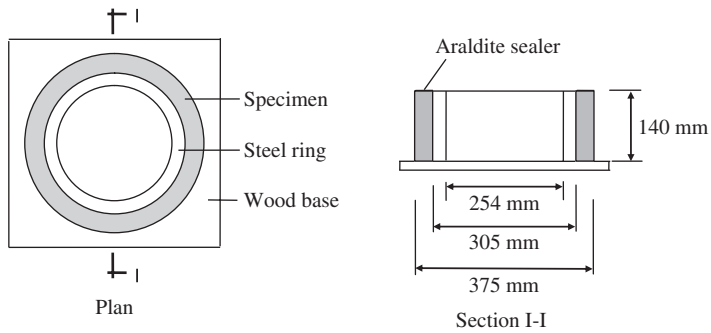

Figure 5-46 Ring-shaped specimen for restrained shrinkage test

is associated with geometry and non-stress intensity effects. In a circular ring-type test, the geometry of the sample does not generate sufficient stress to develop a visible crack at certain locations. The deterioration process in concrete is very complex. Commonly, the deterioration of a concrete will be advanced by early-age cracking. Thus, evaluation of cracking sensitivity of a material is necessary in concrete durability assessment. For the sake of improving the crack propagation rate of mortar or concrete and distinguishing cracking sensitivity of materials in shorter periods, a novel ellipse-type ring for restrained shrinkage test was developed (He et al., 2004). In this setup, the shrinkage diffusive stress development in the direction of the long principal axis is faster than that of the short principal axis, which leads to the crack occurring

Figure 5-47 Elliptical ring test for constrained shrinkage

at a more predictable position. The test apparatus not only can discriminate the extension of mortar or concrete in a short time, but also can lead to an early shrinkage crack. Therefore, the new apparatus is useful to discriminate early-cracking sensitivity of concrete. Moreover, the new method introduced an electrical conduction line along the circumference of the elliptical ring-shaped specimen. Automatic and continuous monitoring on the resistance of the line was able to detect the crack occurrence time exactly, see Figure 5-47.

Since shrinkage cracking can lead to premature deterioration, which shortens the useful life of concrete structures, many attempts have been made to reduce the shrinkage cracking or to control shrinkage. Following this approach, using expansive concrete (shrinkage-compensating concrete) is a good solution. The details regarding this special concrete are provided in Chapter 6. Another method to reduce shrinkage is to use reinforcement. Since reinforcement does not shrink, it can restrain the shrinkage of concrete through the mutual bonding. During the restraining process, compression stress will be developed in the reinforcement steel and tension stress in the concrete. The resultant force of the two are self-balanced. In using reinforcement steel to reduce shrinkage, care has to be taken on the magnitude of the tension stress generated in the concrete to ensure that it does not exceed the tension strength. For this purpose, if the area of the reinforcement steel is fixed, finer steel bars are preferred to thick steel bars. Using fibers to control shrinkage is another popular method. By adding fibers into the concrete, the shrinkage can be reduced due to the restraining effect of the fibers. More importantly, the shrinkage crack width can be controlled due to the bonding between the concrete and fibers. For early age shrinkage crack control, polymer fibers are frequently used. Recently, using a shrinkage reducer, a type of chemical admixture, to control shrinkage has gained more and more attention. The shrinkage-reducing admixture (SRA) was invented in 1982, and Goto et al. (1985) applied for their patent in 1985. Subsequently, many researchers have performed detailed studies on SRA, which is a liquid organic compound consisting of a blend of propylene glycol derivatives. Some literature has indicated that the reduction of free shrinkage can postpone the time to cracking.

Moreover, SRA can reduce the long-term drying shrinkage by 50%, and there is a significant improvement in the restrained shrinkage performance. Even for concrete with proper curing at which the drying shrinkage would reduce to a minimum, there is still a substantial reduction in drying shrinkage due to the effect of SRA (Berke et al., 1999).

5.3.2 Creep

5.3.2.1 Phenomenon of creep

For many materials (e.g., polymers, wood, concrete), the response to stress or strain has a time-dependent component. For example, when a fixed stress is applied, after an instantaneous elastic response, the strain will continue to increase with time. This phenomenon is called creep and is illustrated in Figure 5-48a. Hence, creep is defined as a time-dependent deformation under a constant load. The creep develops in a concrete rapidly at the beginning and gradually decreases with time. Approximately 75% of the ultimate creep in concrete occurs during the first year. The total deformation of a reinforced concrete specimen consists of the instantaneous deformation, shrinkage deformation, and creep. On the other hand, when a fixed strain is applied (e.g., by stretching a member and then fixing its ends), the stress in the member will decrease with time as shown in Figure 5-48b. This phenomenon is called relaxation.

If creep and relaxation are linear (e.g., if the stress is doubled, the strain at a particular time is also doubled), and we can define the following two parameters:

$$\text{Creep compliance: } J(t) = \varepsilon(t)/\sigma \tag{5-70}$$

$$\text{Relaxation modulus: } E_r(t) = \sigma(t)/\varepsilon \tag{5-71}$$

Creep compliance can be obtained from a test with a fixed load applied to a specimen. When $J(t)$ is known, the time-dependent behavior of the material under a arbitrary loading history can be obtained from superposition (see Section 2.3.5).

For materials exhibiting creep behavior, when a stress is applied, the strain will increase with time. If stress is applied at a slower rate (i.e., over a longer period of time), the resulting strain will be more than that due to a stress applied at a rapid rate. Figure 5-49 shows the loading/unloading behavior for three general cases (low, high, and intermediate loading rates). For creeping materials, the loading and unloading curves do not overlap with one another. The area between the two curves (called the hysteresis loop) reflects the energy absorbed by the material over a loading/unloading cycle. This energy absorption varies with loading rate, and is highest at intermediate loading rate.

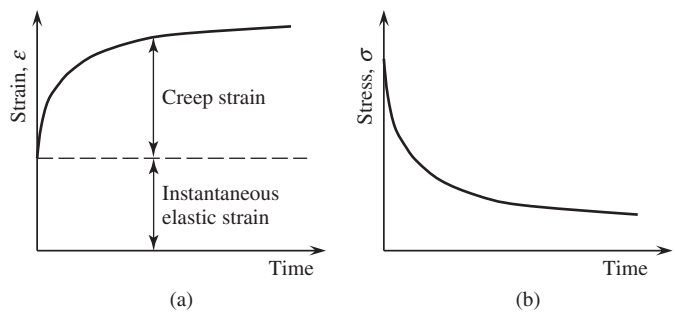

Figure 5-48 The time-dependent behaviors: (a) creep, and (b) relaxation

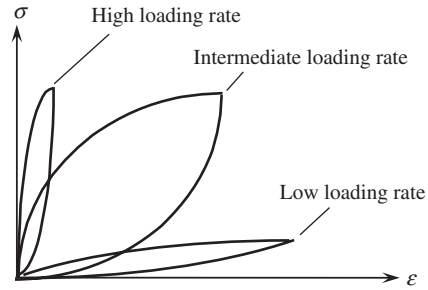

Figure 5-49 Hysteresis behavior under high and low loading rates

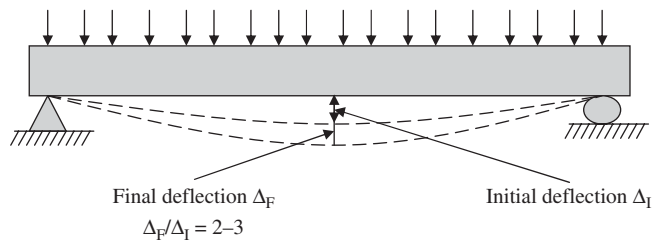

Figure 5-50 The long-term deformation of reinforced concrete beam

5.3.2.2 Influence of creep on reinforced concrete

When a material exhibits time-dependent behavior, it will affect the structural behavior in a number of ways. In a reinforced concrete (RC) column supporting a constant load, creep can cause the initial stress in the steel to double or triple with time because steel is noncreeping and thus takes over the force in the concrete due to creep. Creep can influence reinforced concrete in the following aspects.

(a) Due to creep effects, the long-term deformation of reinforced concrete structures can be significantly larger than the short-term deflection. For instance, because of the delayed effects of creep, the long-term deflection of a reinforced concrete beam can be 2–3 times larger than the initial deflection (Figure 5-50). Therefore, sufficient stiffness has to be provided during the design process to make sure that the beam deflection meets the long-term requirement. For large structures, the long-term differential creep in different parts of the structure needs to be checked to ensure no mismatching problems will be caused. For a tall building or structure, the shortage of reinforced concrete columns may cause the final height of the building and structure to be significantly shorter, and has to be taken into consideration in design and construction.

(b) The hysteresis loop shown in Figure 5-49 indicates that energy can be absorbed during cyclic loading. The energy absorption results in the damping of a structure as it is set in vibration (e.g., during an earthquake or typhoon). Note that the damping is frequency dependent, although this is often not considered in civil engineering designs, as damping is difficult to quantify in practice.

(c) In prestressed concrete design, the creep of concrete and the relaxation of steel will lead to a loss of prestress. The percentage of the prestress loss due to shrinkage and creep can be as high as 60%. It has to be taken into account in the design of a prestressed structure to

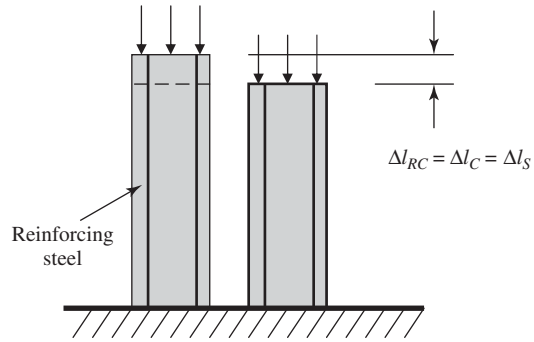

Figure 5-51 Parallel model for a reinforced concrete column

make sure that sufficient prestress can be applied. Moreover, in some cases, restressing of the prestressed tendon has to be carried out to compensate the stress caused by creep.

(d) For a reinforced concrete column, creep may lead to significant stress redistribution in concrete and in the reinforcing steel. This can be explained by a parallel model of a reinforced concrete column as illustrated in Figure 5-51. As the creep occurs only in concrete, the reinforcing steel will restrain the concrete creep through the bond between the concrete and steel. As a result, the reinforced concrete column will shorten less than a same-sized pure concrete column. This implies that the steel is compressed while the concrete is stretched. During this process, tensile stress will be generated in the concrete and compressive stress in steel. Hence, the original compressive stress level in concrete will be reduced, while in steel it will be increased. Such stress redistribution may cause the final compressive stress in steel to be 2 or 3 times higher than the original stress value. If it is not considered during the design process, overstressing in steel may cause yielding and put the structure in danger.

The misalignment or shortening of the reinforced column due to shrinkage and creep should also be considered during the design. Otherwise, the net space of a building on each floor can be compromised. For instance, in Lake Shore Towers in Chicago, combined creep and shrinkage resulted in a shortening of the vertical columns by 2.5 mm per floor (Mindess et al., 2003).

5.3.2.3 Mechanism of creep in concrete

For most materials, creep behavior is due to the time needed for atoms or molecules to rearrange themselves under load. For example, when a polymer is under stress, the polymeric chains tend to slide relative to one another. A finite time is required for the chains to go from one state (i.e., a given arrangement) to another. When loaded for a longer time, more movement will result, leading to creep. For concrete, it is believed that creep is mainly caused by the position rearrangement of water molecules that are absorbed in the layer of C–S–H gel. Creep strains originate from the deformation of a microvolume of paste, named a *creep center*, with higher energy. The creep center will deform when changing from a relatively high energy state to a relatively low energy state through an intermediate state with a higher energy due to the influence of external sources. The ability of a creep center to cross the intermediate state depends on the height of the intermediate state and the energy input from external sources. Such sources may be temperature, stress (strain energy), and variation of moisture concentration. In concrete, the nature of the creep center involves slip between adjacent particles of C–S–H under shear stress. The ease and extent of the slip depends on the process of attraction between particles. If the

particles are chemically bonded, no slip can occur. If only van der Waals interaction exists, slip can occur under some conditions. For instance, when there is a sufficient thickness of water layers between the C–S–H particles, the water can reduce the van der Waals forces and cause slippage to occur between the particles (Mindess et al., 2003).

In concrete, creep can also result from the diffusion of adsorbed water from pores in nanoscale between C–S–H layers. The thickness of the adsorbed water films that separate C–S–H particles depends on the relative humidity with which the system is in equilibrium. For saturated paste at 100% RH, the equilibrium thickness is about five water molecules thick (about 1.3 nm). If two adjacent C–S–H particles have a distance less than 2.6 nm, the equilibrium water thickness will be attained by pushing the C–S–H particles apart. If the particle positions are fixed, a disjointing pressure can be developed. The equilibrium state of water in nanoscale pores is thus determined by a combination of stress and the thickness. With application of an external stress, the disjointing pressure exerted on the water is increased. As a result, the thickness of the adsorbed water has to be decreased to maintain equilibrium, and extra water has to be diffused from the pores in the nanoscale to the stress-free capillary pores. This process leads to a bulk deformation or creep. Creep can occur in a saturated specimen at 100% RH as long as the capillary pores can take the diffused water from the pores in the nanosale. It is called basic creep. When the water movement occurs due to both diffusion and evaporation as the external RH is reduced to less than 100%, dying creep will develop. Dying creep is much larger than basic creep because that the water reduction in pores in nanoscale is much faster by dying plus diffusion than by diffusion only.

In general, the creep rate of concrete (i.e., the rate of strain increase under a given stress) increases with applied stress. Creep behavior is not necessarily linear. For many metals and ceramics, the creep rate at high temperature is proportional to the stress raised to a high power. However, at room temperature and working stress levels, the creep strain of concrete is linearly dependent on stress. In such a case, material behavior can be described by models combining springs and dashpots. The study of these models will constitute the subject matter of the next section.

5.3.2.4 Modeling of creep at low temperature (viscoelastic models)

Models with springs and dashpots can be used to describe linear creep behavior. The spring (Figure 5-52a) is a linear elastic element with direct proportionality between stress and strain. For the dashpot (Figure 5-52b), the rate of strain is directly proportional to the applied stress. This is similar to the behavior of a viscous liquid, the strain rate of which is directly proportional to the applied shear stress. Since the material can be considered as a combination of linear elastic and viscous elements, it is called a linear viscoelastic material. Using one spring and one dashpot, two different models can be created by putting the elements either in series or in parallel. The behaviour of each of these simple models is discussed below.

(a) *Maxwell model (spring and dashpot in series)*: In the Maxwell model, shown in Figure 5-53, the material is made up of two parts, a spring and dashpot, in series. The elastic

(a) Spring (b) Dashpot

Figure 5-52 Spring and dashpot for modeling viscoelastic behavior

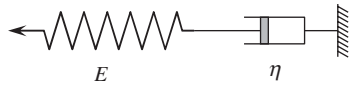

Figure 5-53 Maxwell model

(time-independent) part is represented by a spring with modulus E, and the viscous (time-dependent) part is represented by a dashpot of viscosity η. The equations regarding the equilibrium, compatibility, and constitutive relationship are as follows. For equilibrium,

$$\sigma_E(t) = \sigma_\eta(t) = \sigma(t) \tag{5-72}$$

where $\sigma_E(t)$ represents the stress in the spring, $\sigma_\eta(t)$ the stress in the dashpot, and $\sigma(t)$ the stress in the system. For compatibility,

$$\varepsilon(t) = \varepsilon_E(t) + \varepsilon_\eta(t) \tag{5-73}$$

where $\varepsilon(t)$ is the strain in the system, $\varepsilon_E(t)$ the strain in the spring, and $\varepsilon_\eta(t)$ the strain in the dashpot. The constitutive relationship is

$$\sigma_E(t) = E\varepsilon_E(t) \tag{5-74}$$

$$\sigma_\eta(t) = \eta\dot{\varepsilon}_\eta(t) \tag{5-75}$$

where E is Young's modulus of the spring and η the viscosity coefficient of the dashpot. Under an applied stress σ, the strain rate of the spring is given by

$$\frac{d\varepsilon_E}{dt} = \frac{1}{E}\frac{d\sigma}{dt} \tag{5-76}$$

The strain rate in the dashpot is given by

$$\frac{d\varepsilon_\eta}{dt} = \frac{\sigma}{\eta} \tag{5-77}$$

By differentiating Equation 5-73 and substituting Equations 5-76 and 5-77, we get

$$\dot{\varepsilon}(t) = \frac{\dot{\sigma}(t)}{E} + \frac{\sigma(t)}{\eta} \tag{5-78}$$

Now, we will examine the creep behavior and relaxation behavior of the Maxwell model.

(1) Creep behavior under constant stress applied from $0 < t < t_1$ (see Figure 5-54), under constant stress, gives

$$\frac{d\sigma}{dt} = 0, \frac{d\varepsilon}{dt} = \frac{\sigma}{\eta}, \text{ and } \varepsilon = \frac{\sigma}{\eta}t + \varepsilon(0) \tag{5-79}$$

It takes a finite time for the dashpot to respond to the loading. Therefore, at $t = 0$, $\varepsilon_\eta(0) = 0$ and the dashpot acts as if it is rigid. The initial strain results from the spring alone, and we get

$$\varepsilon(0) = \frac{\sigma}{E}, \varepsilon = \frac{\sigma}{\eta}t + \frac{\sigma}{E} \tag{5-80}$$

At $t = t_1$, the load is completely removed. The spring shortens by an amount equal to σ/E. The remaining strain is $\left(\sigma/\eta\right)t_1$. After load removal, $\sigma = d\sigma/dt = 0$, implying $d\varepsilon/dt = 0$.

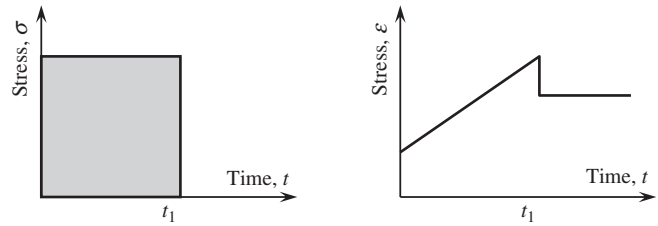

Figure 5-54 Creep behavior under constant stress for the Maxwell model

The strain will stay constant for $t > t_1$. The stress and strain are plotted against time as shown in Figure 5-54.

(2) Relaxation behavior (constant strain applied at $t = 0$) under constant strain, $d\varepsilon/dt = 0$, gives the governing equation

$$\frac{1}{E}\frac{d\sigma}{dt} = -\frac{\sigma}{\eta} \tag{5-81}$$

Integrating both sides with respect to t, and noting that $\sigma\,(0) = E\varepsilon$ (the dashpot stays undeformed) at $t = 0$, we have

$$\sigma = E\varepsilon\ \exp\left(-\frac{Et}{\eta}\right) \tag{5-82}$$

Schematically, the relaxation behavior of the Maxwell model under constant strain is shown in Figure 5-55.

(b) *Kelvin-Voigt model (spring and dashpot in parallel)*: For the Kelvin-Voigt model shown in Figure 5-56, the spring and dashpot are arranged in a parallel positions. The equations regarding the equilibrium, compatibility, and constitutive relationship are

$$\text{Equilibrium: } \sigma\,(t) = \sigma_E\,(t) + \sigma_\eta\,(t) \tag{5-83}$$

$$\text{Compatibility: } \varepsilon\,(t) = \varepsilon_E\,(t) = \varepsilon_\eta\,(t) \tag{5-84}$$

$$\text{Constitutive relationship: } \sigma_E\,(t) = E\varepsilon_E\,(t) \tag{5-85}$$

$$\sigma_\eta\,(t) = \eta\dot{\varepsilon}_\eta\,(t) \tag{5-86}$$

By substituting constitutive equations into equilibrium, we can get

$$\sigma\,(t) = \eta\dot{\varepsilon}\,(t) + E\varepsilon\,(t) \tag{5-87}$$

Equation 5-87 is the governing equation for the Kelvin-Voigt model and the creep behavior and relaxation behavior of the model will be examined as well.

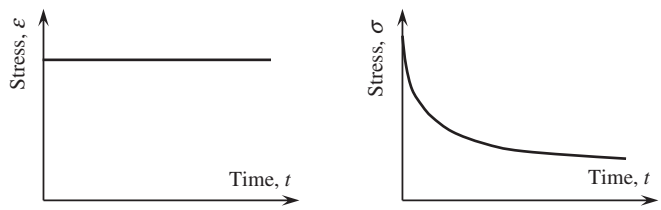

Figure 5-55 Relaxation behavior of the Maxwell model

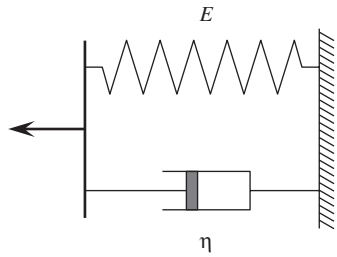

Figure 5-56 Kelvin-Voigt model

(1) Creep behavior under constant stress applied from $0 < t < t_1$. The governing equation is a first-order differential equation, which can be solved by the following procedures. Multiplying each side of the governing equation by $\exp\left(Et/\eta\right)$, we have

$$\frac{d\varepsilon}{dt}\exp\left(Et/\eta\right) + \frac{E}{\eta}\varepsilon\left(t\right)\exp\left(Et/\eta\right) = \frac{\sigma}{\eta}\exp\left(Et/\eta\right) \tag{5-88}$$

The left-hand side of the equation can be rewritten as $d\left[\varepsilon\exp\left(Et/\eta\right)\right]/dt$. Carrying out the integration, and noting that $\varepsilon\left(0\right) = 0$ (because the dashpot takes a finite time to respond), the strain is given by

$$\varepsilon\left(t\right) = \frac{\sigma_0}{E}\left(1 - e^{(-E/\eta)t}\right) \tag{5-89}$$

This equation can be used to describe the creep process diagram. When load is applied (at $t = 0$), it takes time for the dashpot to react. Thus, initially, the load is taken by the dashpot and the strain is equal to zero. Then the load is gradually transferred to the spring and the strain increases at a slower rate and has an asymptotic value of σ_0/E.

If the stress is applied at $t = 0$ and removed at $t = t_1$, as shown in Figure 5-57a, then the strain development from $t = 0$ to $t = t_1$ is a rising exponential curve, as shown in the first part of the curve in Figure 5-57b. However, for $t > t_1$, $\sigma = 0$, hence, the governing equation becomes

$$\eta\frac{d\varepsilon}{dt} = -E\varepsilon \tag{5-90}$$

Integrating, with $\varepsilon = \varepsilon\left(t_1\right)$ at $t = t_1$ as the initial condition, gives

$$\varepsilon\left(t\right) = \varepsilon\left(t_1\right)e^{-E/\eta t} \tag{5-91}$$

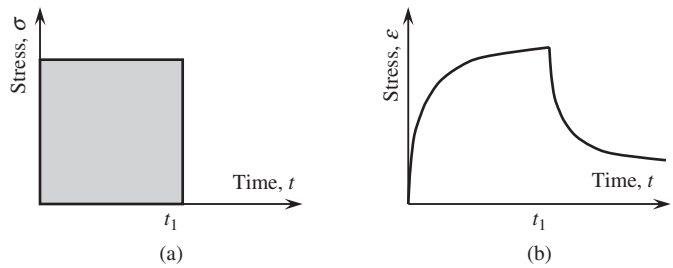

Figure 5-57 Creep behavior of the Kelvin-Voigt model

The above behavior is illustrated in the second part of the curve shown in Figure 5-57b.

(2) Relaxation behavior (constant strain applied at $t = 0$). At $t = 0$, the dashpot is theoretically rigid. In other words, the strain should be zero. To force the strain to reach a finite value, infinite stress is required. For $t > 0$, the strain is constant, implying $d\varepsilon/dt = 0$. The governing equation gives $\sigma = E\varepsilon$. The relaxation response is shown in Figure 5-58.

In describing the creep/relaxation behavior of real materials, each of the two models above has its own shortcomings. For the Maxwell model, the strain rate is constant, and after stress is removed, there is no time-dependent gradual strain recovery. For the Kelvin-Voigt model, no instantaneous material response is allowed, thus producing infinite stress when a finite strain is suddenly applied. For real materials, the applied stress is always accompanied by an instantaneous response. Subsequently, the strain will increase with time but at a decreasing rate. After the stress is removed, part of the strain is recovered immediately, while another part will be slowly recovered after a period of time. To describe the behavior of real materials, the two simple models can be combined, as shown in Figure 5-59. This combined model is called Burger's body and can be used to describe the time-dependent behavior of both concrete and wood.

5.3.2.5 Strain response under arbitrary stress history—superposition

The creep strain for a unit stress, or creep compliance $J(t)$, can be obtained experimentally from a single test (under constant stress). Once the compliance is known, the creep behavior under

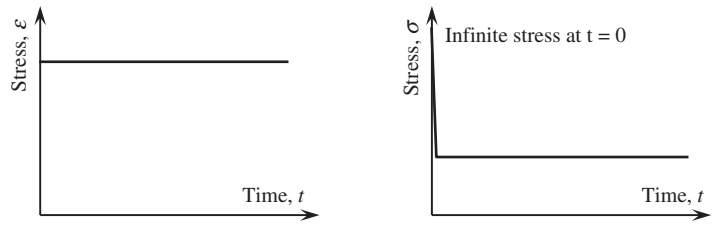

Figure 5-58 Relaxation behavior of the Kelvin-Voigt model

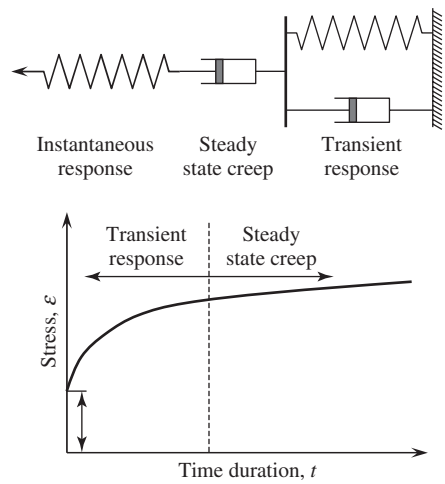

Figure 5-59 Burger's body and its response to constant stress

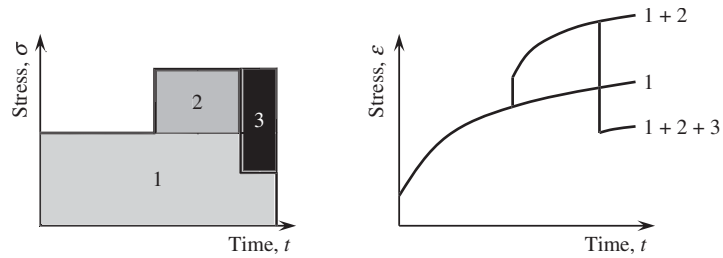

Figure 5-60 Illustration of the superposition principle

a nonconstant stress can be obtained by superposition, as illustrated in Figure 5-60. To apply superposition, any increase in stress level is replaced by a new constant stress applied at the time when the stress change takes place. The decrease in stress level is replaced by the removal of a constant stress. In the figure, the stress is shown to increase by discrete amounts. For a continuously changing stress, the stress history can be approximated with discrete stress increments occurring over very small time steps. This is the same principle behind numerical integration.

5.3.2.6 Importance of applied stress level to creep

Creep in concrete is significantly influenced by the applied stress level. For the case of concrete under a stress level less than 50% of its strength, creep in concrete is linear function of stress. For the case of a stress level higher than 50% but lower than 75% of its strength, the creep is a nonlinear function of stress. For the case of a stress level higher than 75% of a concrete's strength, creep will rapidly increase infinitely and cause structure failure, as shown in Figure 5-61. Thus, it is called unstable rupture creep. When you design a column, it is important to keep the stress level in the concrete sufficiently low, usually less than 40% of its compressive strength.

5.3.2.7 ACI equation for predicting creep

The ACI Committee 209 has suggested some equations to predict the creep values. The equations are simple mathematical formulas but provide a level of accuracy good enough for most concrete structures. The basic equation describing the creep–time relationship is

$$C_t = \frac{t^{0.6}}{D + t^{0.6}} C_{\mathrm{u}} \tag{5-92}$$

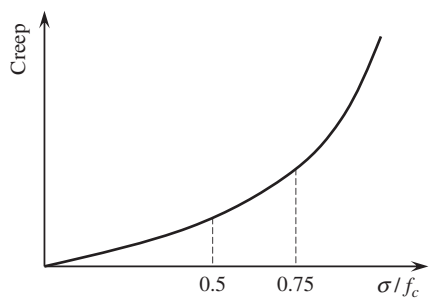

Figure 5-61 Unstable rupture creep

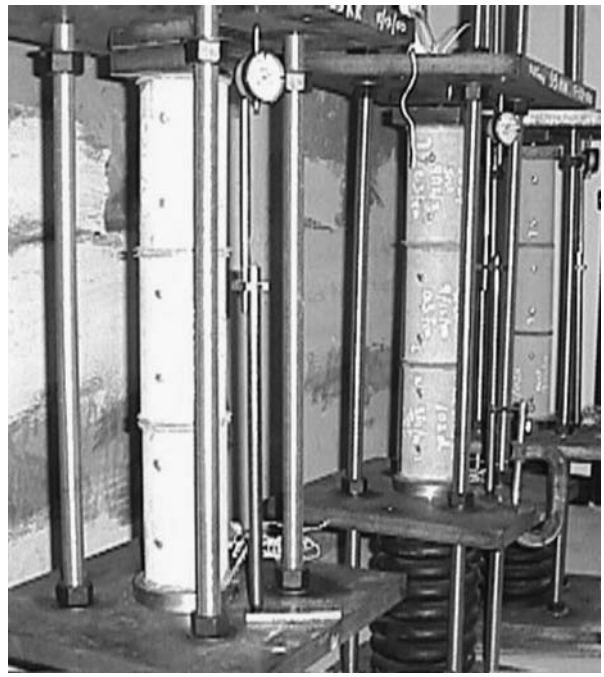

Figure 5-62 The experimental set-up for measuring creep

where C_t is the creep value at time t (in days) after being loaded, D a constant, and C_u the ultimate creep.

5.3.3 Test method for creep

The experimental setup for measuring creep is shown in Figure 5-62. It is composed of a frame with four steel bars, together with two thick steel plates. Three cylinder specimens, 100 mm in diameter and 200 mm in height, are placed between two steel plates. The bottom steel plate is supported by a strong spring. A constant load can be applied to the specimens by compressing the spring. The creep under the constant load can be monitored by a Demac gage.

5.3.4 Other important factors affecting shrinkage and creep

There are additional factors that influence the shrinkage and creep.

(a) *w/c ratio*: As both shrinkage and creep are sourced at the adsorbed water in C–S–H particles, the higher the *w/c* ratio, the more the adsorbed water and the higher the shrinkage and creep.

(b) *Aggregate stiffness (elastic modulus)*: Since the shrinkage and creep are from cement paste, nonshrinkage and noncreep aggregates play a restraining role to the paste. The stiffer aggregates will provide a higher restraining effect and hence lead to a smaller shrinkage and creep.

(c) *Aggregate fraction*: As aggregates are nonshrinking and noncreeping, as compared to cement paste, a higher aggregate fraction leads to small shrinkage and creep due to a restraining effect.

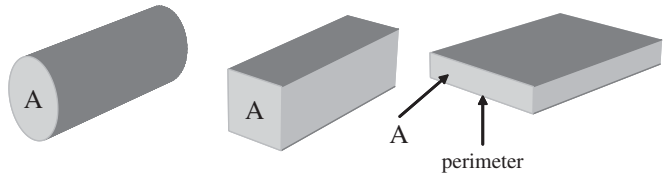

Figure 5-63 Three shapes with same section area but different perimeter

(d) *Theoretical thickness*: The theoretical thickness is defined as the ratio of the section area to the semi-perimeter in contact with the atmosphere, as shown in the following equation:

$$t_{TH} = \frac{2A}{P} \tag{5-93}$$

As can be seen from Figure 5-63, for the same section area, a higher theoretical thickness means less contact surface with the atmosphere. In other words, the distance for water migration from inside to the atmosphere is longer, making the diffusion or migration of water more difficult. Hence, a higher theoretical thickness will lead to a smaller creep and shrinkage.

(e) *Humidity*: The higher the RH, the lower the shrinkage and creep. This is because an increase in the atmospheric humidity is expected to slow down the relative rate of moisture migration.

5.4 DURABILITY

Durability of Portland cement concrete is defined as its ability to resist weathering action, chemical attack, abrasion, or any other process of deterioration to maintain its original form, quality, and serviceability when exposed to its intended service environment (Mehta and Monteiro, 2006). Durability is most likely to relate to long-term serviceability of concrete and concrete structures. Serviceability refers to the capability of the structure to perform the functions for which it has been designed and constructed after exposure to a specific environment.

Almost universally, concrete has been specified principally on the basis of its compressive strength at 28 days after casting. RC structures, on the other hand, are almost always designed with a sufficiently high safety factor. Thus, it is rare for concrete structures to fail due to lack of intrinsic strength. However, gradual deterioration, caused by the lack of durability, makes concrete structures fail earlier than their specified service lives in ever increasing numbers. The extent of the problem is such that concrete durability has been recently described as a "multimillion dollar opportunity" (Anonymous, 1988). For example, in the United States, it was reported that the decks of 2,530,000 concrete bridges had been damaged and needed repair in less than 20 years of operation. In the report of the American Society of Civil Engineers in 2005, it was estimated that 1.6 trillion U.S. dollars was needed in five years to restore the infrastructures to a normal operation condition. In the United Kingdom there are 8 high bridges in the circular express way in Southern England, and the total initial cost of construction was 28 million pounds. However, the repair cost in 2004 for the bridges reached 120 million pounds, almost 6 times as high as the initial construction cost.

To solve the durability problem, many researchers have conducted deep studies. The studies cover the carbonation, alkali aggregate reaction, reinforcing bar corrosion, sulfate attack, CH leaching, and freezing–thawing. Many researchers have extended their work from a single environmental factor to the coupling effects of multiple factors, including mechanical loading

(Ulm et al., 2000; Sun et al., 2002; Le Bellégo et al., 2003; Kuhl et al., 2004; Nguyen et al., 2007). As a result of durability studies, many countries have proposed durability-based design guidelines (DuraCrete, 2000; CCES, 2004; MDPRC, 2007).

5.4.1 Causes of deterioration and main durability problems

The classification of causes of concrete deterioration can be grouped into three categories: physical, chemical, and mechanical causes. The factors in the three groups may act alone or, in most cases, in a coupled manner.

Physical causes may include surface wear caused by abrasion, erosion, and cavitation, the effects of high temperature, or the differences in thermal expansion of the aggregate and of the hardened cement paste. An example is the alternating freezing–thawing cycle and the associated action of deicing salts, and cracking, which is common due to volume changes, normal temperature and humidity gradient, crystallization of salt in the pores, structural loading, restrained shrinkage, and exposure to fire. Chemical degradation is usually the result of an attack, either internal or external, on the cement matrix. Portland cement is alkaline, so it will react with acids in the presence of moisture and, in consequence, the matrix may become weakened and its constituents may be leached out. The most common chemical causes affecting concrete durability are (1) hydrolysis of the cement paste component; (2) carbonation; (3) cation-exchange reaction; and/or (4) reaction leading to expansion (such as sulfate expansion, alkali–aggregate expansion, and steel corrosion). Mechanical causes include impact and overloading.

As mentioned earlier, the causes responsible for concrete deterioration are either from the surrounding environment of an exposed structure or the mechanical loading a structure bears. In most cases, the degradation of a concrete structure is a result of the coupling effect of environmental factors and loading. In reality, major durability problems of concrete structures include corrosion of the reinforcing steel, freeze/thaw damage, salt scaling, alkali–aggregate reactions, and sulfate attack. The common point of these attacks is that all of them can result in cracking and spalling of the concrete.

5.4.2 Basic factors influencing durability

The durability of concrete depends, to a large extent, on its permeability and diffusivity. Permeability is defined as the property that governs the rate of flow of a fluid into a porous material under pressure. The permeability of concrete can be measured by determining the rate of water flow through a concrete specimen. The porosity in concrete can largely affect the permeability. The large amount of porosity in concrete resides at the interface between the aggregate and the cement paste. The flow of water through concrete obeys Darcy's law. In steady-state, the flow rate of water at the equilibrium flow condition described by Darcy's law can be written as

$$\frac{dq}{dt} = K\frac{\Delta HA}{L} \tag{5-94}$$

where dq/dt is the flow rate, K the coefficient of permeability, ΔH the pressure gradient, A the surface area of the specimen, and L the thickness of the specimen. As mentioned earlier, the permeability of concrete is a function of the pores inside the material. This includes two concepts: total percentage of porosity and size distribution of pores or connection of pores. Concrete is composed of aggregates, hardened cement paste, and the interface between aggregate and paste. Table 5-2 shows the permeability coefficient of hardened cement paste, aggregate, and concrete. For matured hardened cement paste, the permeability coefficient is very small even though the total porosity is not that small. The value of the coefficient of matured hardened cement

Table 5-2 Typical values of permeability coefficients of concrete materials

Type	Porosity(%)	Average Pore Size	Permeability Coefficient
HCP	20	100 nm	6×10^{-12} cm/sec
Aggregate	3–10	10 μm	$1–10 \times 10^{-12}$ cm/sec
Concrete	20–40	nm–mm	$100–300 \times 10^{-12}$ cm/sec

paste is of the same order as that observed in low-porosity aggregate made of rocks. Since a large percent of the porosity of cement paste is from pore sizes less than 0.1 μm and hidden in C–S–H particles, the low permeability coefficient implies that water does not easily move through very small gel pores and permeability is controlled by an interconnecting network of capillary pores, where 0.1 μm is usually regarded as the lower boundary of harmful pores. As hydration proceeds, the capillary network becomes increasingly tortuous as interconnected pores are blocked by the formation of C–S–H. Although concrete is made of hydrated cement paste (HCP) and aggregates that both have small permeability coefficient, its permeability coefficient is one or two magnitudes higher than that of HCP and aggregates. It can be attributed to the interface between HCP and aggregates.

Diffusivity is defined as the rate of migration of ions or moisture in concrete under the action of a higher concentration side to lower concentration side, see Figure 5-64. The difference of the two parameters is that permeability is the parameter characterizing water flow when pores inside the concrete are filled up with water, while diffusivity is the parameter describing the migration of ions or water vapor before saturation has been reached in the pores. It should be noted that there is a difference between permeability and diffusivity. One is under a pressure difference and the other a concentration difference. The two parameters are related to each other and if one of the parameters is known, the other one can be deduced indirectly. Diffusivity can be described by Fick's law. There are two types of Fick's law, the first and the second Fick's law. The first Fick's law has the linear form of

$$J = -D\frac{\partial C}{\partial x} \tag{5-95}$$

where J is the diffusion flux or mass transport rate (kg/m^2-sec), D the diffusion coefficient (m^2/sec), C the concentration of a particular ion or gas (kg/m^3), and x the distance between the higher concentration side to the lower concentration side. The second Fick's law has the form

$$\frac{\partial C}{\partial t} = D\frac{\partial^2 C}{\partial x^2} \tag{5-96}$$

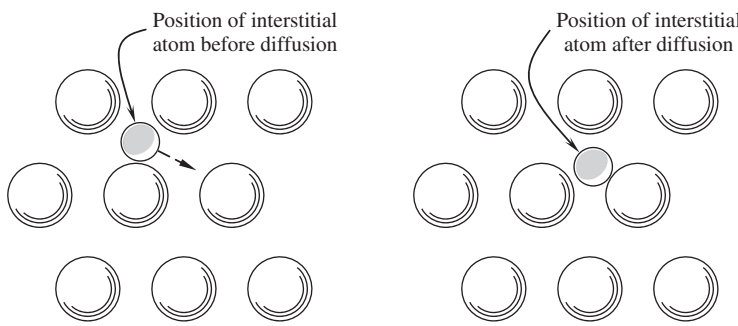

Figure 5-64 The phenomenon of diffusion

Hence, the solution of the second Fick's law for a semi-infinite plane has the form

$$C\ (x,\ t) = C_0\left[1 - \text{erf}\left(\frac{x}{2\sqrt{Dt}}\right)\right] \tag{5-97}$$

where $C(x,\ t)$ is the ion or gas concentration at distance x and time t, C_0 the ion or moisture concentration at the higher concentration surface, and erf the error function.

The two parameters, permeability coefficient and diffusivity coefficient, apply to different situations. When water is flowing through a piece of concrete or from one part to another part under a hydraulic gradient, permeability is the governing parameter. When ions, moisture, or gases (e.g., oxygen) move through concrete (either dry or wet) or ions (e.g., chloride) move through the pore solution, the process is governed by the diffusion coefficient (or diffusivity). Note that the diffusion coefficient varies for different diffusing substances. Generally speaking, since both the permeability and diffusivity are related to the pore structure of concrete, concrete with low permeability will also possess low diffusivity. Means to reduce permeability and diffusivity (e.g., use lower w/c ratio to reduce capillary porosity, specification of cement content high enough to ensure sufficient consistency and hence proper compaction, proper curing to reduce surface cracks) are generally helpful to concrete durability.

5.4.3 Measurement of the permeability coefficient

The objectives of permeability tests are to measure the flow rate of a liquid passing right through the test specimen under an applied pressure head. Concrete is a kind of porous material that allows water under pressure to pass slowly through it. There are two common practices for the evaluation of the permeability of concrete using water: the steady-flow method and the penetration-depth method. The steady-flow method is performed on a saturated specimen in which a pressure head is applied to one end of the sample, as shown in Figure 5-65. When a steady-flow condition is reached, the measurement of the outflow enables the determination of the coefficient of permeability, by using Darcy's law:

$$k_1 = \frac{(dq/dt)L}{\Delta HA} \tag{5-98}$$

where k_1 is the coefficient of permeability (m/sec), dq/dt the steady flow rate (m^3/sec), L the thickness or length of the specimen (m), ΔH the drop in the hydraulic head across the sample (m), and A the cross-sectional area of the sample (m^2).

To achieve a steady-flow state, water has to be adsorbed into all pores in the sample so that the pore surfaces do not provide friction or capillary attraction to the passage of water. However, such flow conditions take a great amount of time to be achieved in high-performance contemporary concrete, as it is dense with low porosity. Sometimes, it is impossible to reach such

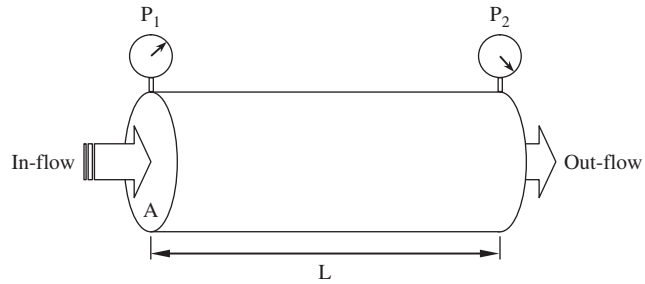

Figure 5-65 Steady-flow permeability test

Figure 5-66 Permeability cell

a condition in a year. Hence, the considerable length of time required for testing the concrete and the difficulties of attaining a steady-state outflow can be regarded as disadvantages for the steady-flow method.

In cases of good-quality concrete, the steady-flow method is not suitable for measuring the permeability of concrete. Under such conditions, the penetration-depth method has to be used. In the penetration-depth method, a permeability cell is usually used (Li and Chau, 2000), as shown in Figure 5-66. In the cell, the top and bottom parts are plastic tubes and the middle is the concrete test specimen. The circumferential surface of the concrete specimen is sealed with epoxy to make sure the 1D flow condition is achieved. The top plastic tube can be filled with water and the bottom plastic tube with air. The pressure of the air in the bottom tube can be tuned through a vacuum process. By putting the specimens in an autoclave as shown in Figure 5-67 and applying pressure, the top end of the unsaturated concrete specimen is subjected to a pressure head through the water in the tube, while the other end is under the tuned normal atmospheric conditions.

The water penetration is achieved either by measuring the volume of water entering the sample or by splitting the cylinder immediately after stopping the test and measuring the average depth of discoloration, due to wetting, which is taken as the depth of penetration. Provided the flow of water is uniaxial, the water penetration depth can be approximated to the coefficient of permeability equivalent to that used in Darcy's law, as developed by Valenta (1969):

$$k_1 = \frac{x^2 v}{2\Delta HT} \tag{5-99}$$

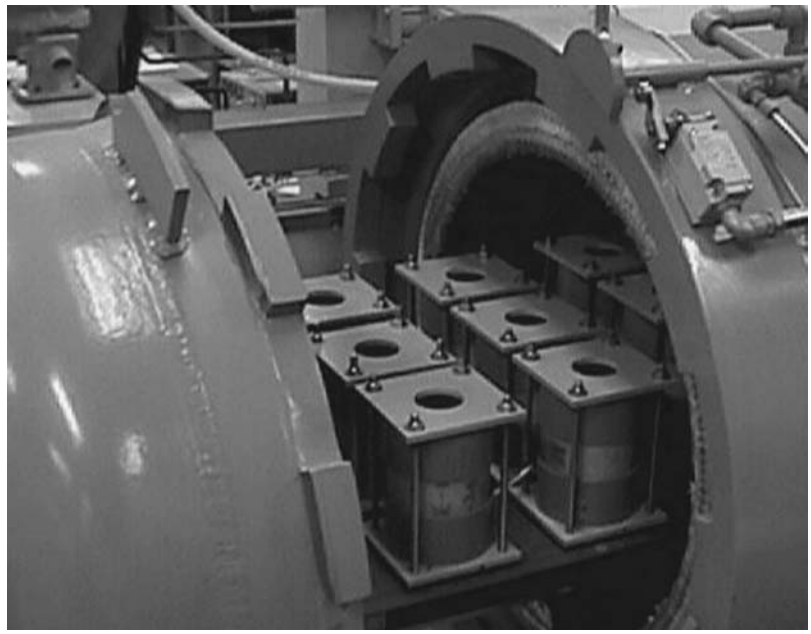

Figure 5-67 Penetration depth test with an autoclave

where x is the depth of penetration of concrete (m), v the fraction of the volume of concrete occupied by the pores, and T the time duration under pressure (sec). The value of v represents discrete pores, such as air voids, which are not filled with water except under pressure, and can be calculated from the increase in the mass of concrete during the penetration test. Bearing in mind that only the voids in the part of the specimen penetrated by water would be considered, we can write

$$v = \frac{\Delta W}{DAx} \tag{5-100}$$

in which ΔW is the gain in weight of the specimen during the penetration test, D the density of concrete, and A the cross-sectional area. Based on the penetration-depth method, it is possible to use the depth of penetration of water as a qualitative assessment of concrete permeability. In summary the steady-flow method suits concretes with relatively higher permeability, while the depth of penetration method is most appropriate for concretes with very low permeability. It is important to note that the scatter of the permeability test results on similar concrete at the same age and using the same equipment would be large.

5.4.4 Measurement of the diffusivity coefficient

In concrete technology, chloride is usually selected as the medium for diffusion testing. The main reasons for using chloride ions are as follows: first, chloride causes reinforcing steel corrosion, and, second, the size (radius) of a chloride ion is only 181×10^{-12} m, so it is small enough to fit the need for diffusion. There are basically two methods for evaluating chloride diffusion in concrete. One is called the rapid permeability test, ASTM C1202, and another is the diffusion cell test method (Li et al., 1999a). In the first method, a standard specimen has a nominal diameter of 100 mm and thickness of 50 mm, cut from the center of a cylindrical sample. Before

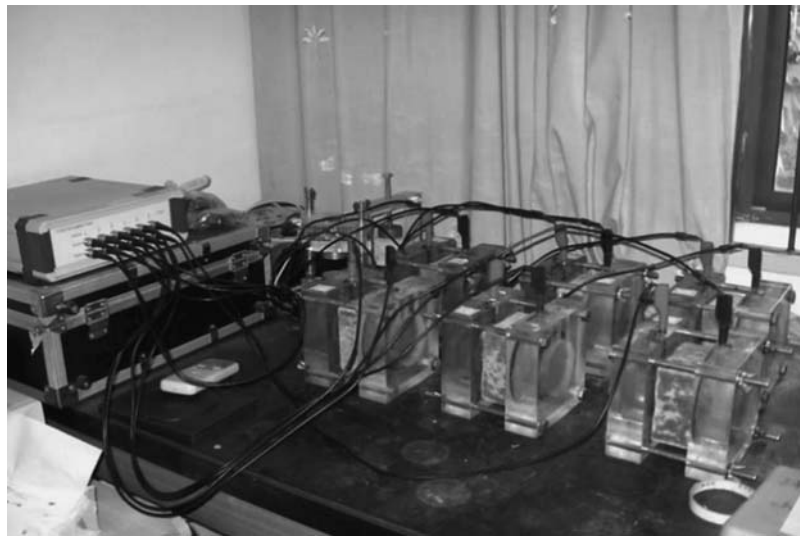

Figure 5-68 Rapid chloride permeability test setup

Table 5-3 Classification of concrete quality using chloride ion penetrability

Charge Passed (Coulombs)	Chloride Ion Penetrability
>4000	High
2000–4000	Moderate
1000–2000	Low
100–1000	Very low
<100	Negligible

mounting the specimen into the test facility, it has to be vacuumed and soaked for 22 h. The test facility includes positive and negative terminals made of plexiglass plate with an empty cell and a circular opening of the same diameter as the specimen at one surface. The specimen is mounted with two surfaces connected to the openings of the terminal using a sealing material. Next, a 3% NaCl solution is added to fill the cell on the negative terminal and 0.3 N NaOH is added to fill the cell on the positive terminal. Figure 5-68 shows the experimental setup of the rapid chloride test. A constant voltage of 60 V is then applied for 6 h. The total charge passing through the concrete specimen during testing is taken as the index of the diffusivity of concrete. Table 5-3 shows the classifications of concrete quality using such an index.

The latter method is considered a realistic test method for the chloride diffusivity of concrete due to differences of concentration. In this method, the specimens consisting of $\phi 100 \times 20$ mm ($\phi 3.94 \times 0.79$ in) slices are placed between two chambers and the edges are sealed with an epoxy resin (see Figure 5-69). After the epoxy resin is cured, saturated calcium hydroxide solution is poured into the chambers and the specimens are immersed in the solution for 5 days. This procedure is to avoid the anomalous effect due to sorption rather than diffusion of chloride ions. Then a NaCl solution with a concentration of 5 M is added into chamber A to start the chloride diffusion test. The chambers are maintained at $23 \pm 2^{\circ}$C and the concentration of the chloride diffused through the specimens in chamber B is measured periodically.

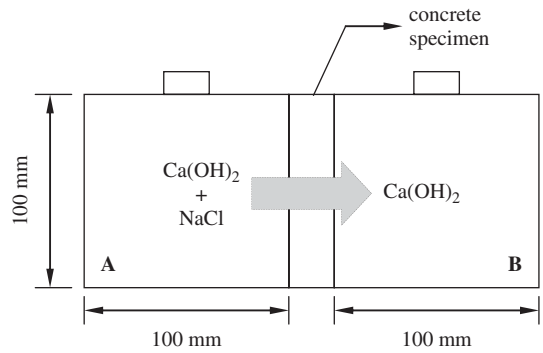

Figure 5-69 Measurement of diffusivity coefficient

A typical curve of chloride concentration in chamber B obtained from an experiment has a strong nonlinearity between the chloride concentration and time initially. However, after a test time of about 30 weeks, the curve becomes quite linear. This implies that the chloride diffusion has reached a steady state. The linear relation between concentration of chloride ions and time can be expressed as

$$C = kt - A \tag{5-101}$$

where C is the cumulative concentration of chloride ion penetration at time t in chamber B, k the slope of chloride concentration–time curve at steady state, and A a constant. In steady state, the flux of the chloride ions through the specimens can be described by Fick's first law of diffusion. For the steady-state case, this law can be written in the following form:

$$C = \frac{DC_{\mathrm{A}}}{l^2}t - A \tag{5-102}$$

where D is the diffusion coefficient in the steady state, C_{A} the concentration of chloride ions in chamber A, and l the thickness of the slice specimen. Comparing the above two equations, the diffusion coefficient can be expressed as follows:

$$D = \frac{kl^2}{C_{\mathrm{A}}} \tag{5-103}$$

It is clear that once the slope of the chloride concentration–time curve (flux) in the steady state is known, the diffusion coefficient can be calculated. In summary, the latter method is closer to the real situation of chloride penetration and can be used to obtain the diffusion coefficient. However, it is time- and labor-consuming.

5.4.5 Cracks in concrete

Cracking in concrete is another factor that influences concrete durability. The permeability and diffusivity of a concrete with a crack will be significantly higher, and hence the concrete will deteriorate fast. The cracks in concrete may be caused by many different situations and may range from very small internal microcracks that occur on the application of modest amounts of stress to quite large cracks caused by undesirable interactions with the environment, poor construction practice, or errors in structural design and detailing. In extreme cases, the structural integrity of the concrete may be seriously affected. In many other instances, however, cracks do not affect the load-carrying ability of concrete, but may affect the durability of the concrete

by providing points of easy access to the body of the concrete to aggressive agents that might otherwise not seriously affect the material.

5.4.5.1 Cause of cracking

Table 5-4 summarizes the kinds of cracking that can occur due to interactions in the concrete materials and the surroundings. In most instances, cracking originates internally, forming a network of microcracks throughout the concrete. Internal damage may be considerable before cracks are visible at the exterior surface. In other cases, such as in humidity and temperature changes, localized large cracks may occur in the structure. Cracking may be used to help determine the cause of deterioration of concrete, since in many cases characteristic cracking patterns are produced (see Table 5-5). Concrete that will resist cracking under normal environmental conditions may not remain intact under catastrophic conditions, such as fires.

5.4.5.2 Control of cracking

Cracking is best controlled during the design and construction phases. In many instances, cracking may be avoided by proper selection of materials, provided that the potential problem has been anticipated through a careful assessment of the expected environment. For example, unsoundness of cement should never be encountered when ASTM C150 or GB 175-1999 is adhered to, and

Table 5-4 Causes of cracking in concrete due to interaction with surroundings

Component	Type	Cause of Distress	Environmental Factor(s)	Variable to Control
Cement	Unsoundness	Volume expansion	Moisture	Free lime and magnesia
	Temperature cracking	Thermal stress	Temperature	Heat of hydration, rate of cooling
Aggregate	Alkali-silica reaction	Volume expansion	Supply of moisture	Alkali in cement, composition of aggregate
	D-cracking	Hydraulic pressure	Freezing and thawing	Absorption and maximum size of aggregate
Cement paste	Plastic shrinkage	Moisture loss	Wind, temperature, relative humidity	Temperature of concrete, protection of surface
	Drying shrinkage	Moisture loss	Relative humidity	Mix design, rate of drying
	Sulfate attack	Volume expansion	Sulfate ions	Mix design, cement type, admixtures
	Thermal expansion	Volume expansion	Temperature change	Temperature rise, rate of change
Concrete	Settlement	Consolidation of concrete around reinforcement		Concrete slump, cover, bar diameter
Reinforcement	Electro-chemical corrosion	Volume expansion	Oxygen, moisture	Cover, permeability of concrete

Table 5-5 Type of cracking in concrete structures

Nature of Crack	Cause of Cracking	Remarks
Large, irregular, frequently with height differential	Inadequate support, overloading	Slabs on ground, structural concrete
Large, regularly spaced	Shrinkage cracking, thermal cracking	Slabs on ground, structural concrete, mass concrete
Coarse, irregular "map cracking"	Alkali–silica reaction	Extrusion of gel
Fine, irregular "map cracking" (crazing)	Excessive bleeding, plastic shrinkage	Finishing too early, excessive troweling
Fine cracks roughly parallel to each other on surface of slab	Plastic shrinkage	Perpendicular to direction of wind
Cracks parallel to sides of slabs adjacent to joints (D-cracking)	Excessive moisture content, porous aggregate	Deterioration of concrete slab due to destruction of aggregates by frost
Cracks above and parallel to reinforcing bars	Settlement cracking	Structural slabs due to consolidation of plastic concrete around reinforcing bars near upper surface
Cracking along reinforcing bar placements, frequently with rust staining	Corrosion of reinforcement	Aggravated by the presence of chlorides

proper testing of groundwater should enable severe sulfate attacks to be avoided through the choice of an appropriate binder combination and water/cement ratio.

A chemical attack on concrete involves ingress of moisture, either as a carrier for aggressive agents or as a participant in destructive reactions. Thus, precautions in mix design and construction practice that prevents the entry of water into concrete should improve durability. Concrete of low permeability can be assured by the use of sufficient (but not excessive) quantities of cementitious materials and low water/cement ratios, proper placement, consolidation, and finishing, and adequate moist curing.

Cracking due to drying shrinkage and thermal expansion is caused by tensile stresses that are created by differential strains that occur under nonuniform drying, temperature rise, or uneven restraint. Thus, shrinkage and thermal cracking resemble flexural cracking and can be controlled by the suitable location of reinforcements, which will reduce the amount of cracking and will cause several fine cracks rather than a single large crack. The finer the crack, the less likely it is to contribute to durability problems. Crack widths less than 0.10 mm are desirable in cases where severe exposure is anticipated.

5.4.6 Corrosion of reinforcing steel

Corrosion of the reinforcing steel is regarded as the most serious durability problem. Originally, in a properly designed, constructed, and used structure, there should be little problem of steel corrosion within the concrete during the design life of that structure, because concrete provides a very high alkali environment, with pH values of 12.5–13.5, in which steel is well passivated. Unfortunately, this highly desirable condition is not always maintained during the service period of concrete structures due to the deterioration of concrete, resulting in corrosion of the reinforcement. There are two kinds of rebar corrosion: chloride-induced corrosion and carbonation-induced corrosion. The chloride-induced corrosion is caused by a localized

breakdown of the passive film on the steel, and carbonation-induced corrosion is caused by a general breakdown of passivity by neutralization of the concrete.

5.4.6.1 Carbonation-induced corrosion

Carbonation occurs due to the penetration of carbon dioxide from the atmosphere into the concrete. The chemistry of carbonation is that carbon dioxide molecules penetrate into the concrete and can react with solid calcium hydroxide. Calcium hydroxide is the hydrate in the cement paste that reacts most readily with carbon dioxide. Consequently, $Ca(OH)_2$ carbonates to $CaCO_3$:

$$CO_2 + Ca\,(OH)_2 \rightarrow CaCO_3 + H_2O \tag{5-104}$$

This is the reaction of main interest, especially for concrete made of Portland cement, even though the carbonation of C–S–H is also possible when calcium hydroxide becomes depleted. Other cement compounds can be decomposed, such as hydrated silica alumina, which produces ferric oxide. Carbonation may cause the concrete to shrink. In case of concrete with Portland cement, carbonation may even result in increased strength (Bertolini et al., 2004). Carbonation itself is not a problem; it is the consequences of carbonation on reinforced concrete that causes the major repercussions. The chemical reactions during carbonation result in a drastic decrease in the alkalinity of the concrete, from average values of 12 to 14 down to 8 or 9, with the consumption of calcium hydroxide. The reduction in alkalinity destroys the passive environment and leaves the reinforcement in a condition where it is susceptible to corrosion. Therefore, when carbonation penetrates through the rebar cover, and oxygen and moisture are present, corrosion will take place. The depth of carbonation in reinforced concrete is an important factor in the protection of the reinforcement; the deeper the carbonation, the greater the risk of the corrosion of steel. The second consequence of carbonation is that chlorides bound in the form of calcium chloroaluminate hydrates, and others bound to the hydrated phases, may be liberated due to carbonation, making the pore solution even more aggressive.

The corrosion rate is usually expressed as the penetration rate of carbonation and is measured in micrometers per year. The depth of penetration of carbonation into concrete is proportional to the square root of time. The corrosion rate can be considered negligible if it is below 2 μm/year, low between 2 and 5 μm/year, moderate between 5 and 10 μm/year, intermediate between 10 and 50 μm/year, high between 50 and 100 μm/year, and very high for values above 100 μm/year (Bertolini et al., 2004). In high-quality concrete, the rate of carbonation-induced corrosion is negligible for relative humidity (RH) below 80%. It is then assumed that corrosion propagates only while concrete is wet (i.e., RH $>$ 80%). The corrosion rate tends to decrease with time. Besides, corrosion products can reduce the corrosion rate (Alonso and Andrade, 1994). Page (1992) has illustrated the relationship between the corrosion rate in carbonated concrete and the relative humidity of the environment, where the maximum corrosion rates, of the order of 100–200 μm per year, can be reached only in very wet environments with relative humidity approaching 100%. For typical conditions of atmospheric exposure, i.e., RH $=$ 70–80%, maximum corrosion rates are between 5 and 50 μm per year.

The rate of carbonation increases with an increase in the concentration of carbon dioxide, especially in concretes with high water/cement ratio, carbon dioxide, and moisture creating the carbonic acid agent. The rate of carbonation also depends both on environmental factors (humidity, temperature, concentration of carbon dioxide) and factors related to the concrete (mainly its alkalinity and permeability). The quality of the concrete has been regarded as the most

important parameter controlling the rate of carbonation (Bentur et al., 1997). The quality of the concrete is a function of the composition of the binder (i.e., whether Portland cement or blended cement was used), the water/cement ratio, the water/binder ratio, and the curing conditions. The permeability of concrete has a remarkable influence on the diffusion of carbon dioxide and thus on the carbonation rate. The carbonation penetration slows down with decrease in the water/cement ratio, due to the decrease of the capillary porosity of the hydrated cement paste. The type of cement also influences the carbonation rate. For blended cement, hydration of pozzolanic materials or ground granulated blast furnace slag (GGBS) leads to a lower carbon hydroxyl content in the hardened cement paste, which may increase the carbonation rate. Consequently, the depth of carbonation is greater for the blended cements than for Portland cement concrete when compared on the basis of equal water/binder ratios (Bentur et al., 1997). The fly ash blended cement concretes show higher corrosion rates compared with Portland cement concrete of the same water/binder ratio.

Nevertheless, the water/cement ratio and curing are the most important factors influencing the rate of carbonation. The denser structure of concrete may slow down the diffusion of carbon dioxide. If cured properly, the lower alkalinity of cements with the addition of fly ash or blast furnace slag can be compensated by the lower permeability of their cement pastes. The rate of carbonation also varies with the humidity of concrete. In a totally dry or wet environment, there is no carbonation. The carbonation rate may be correlated to the humidity of the environment. The interval of relative humidity most critical for promoting carbonation is from 60 to 70%.

5.4.6.2 Chloride-induced corrosion

Chloride-induced corrosion in structural concrete is primarily caused by the presence of sufficient free chloride ions in the matrix. Chloride can get into the concrete at the time of mixing, either as an admixture component or in chloride-contaminated aggregates or mix water, or penetrate into the hardened concrete later on from external sources, such as seawater, salt spray, or de-icing salt placed on concrete pavements. When sufficient chlorides are present at the time of mixing, the corrosion may start at a very early service stage. For the case of chloride in the atmosphere penetrating into the concrete, the corrosion will not start until reaching a certain level of chloride accumulation. The penetrating chloride ions diffuse through the concrete cover to the rebar surface first. Then sufficient quantities of chloride ions can be accumulated. When the concentration of chloride ions in the concrete reaches a certain level (0.6 to 0.9 kilogram per cubic meter of concrete), they dissolve the protective oxidized film; thus, a localized breakdown of the passive film on the steel is formed where oxidation occurs and a galvanic cell is created. The local active areas behave as anodes, while the remaining passive areas become cathodes where reduction takes place.

The effect of the separation of the anodes and cathodes has significant consequences for the pattern of corrosion. In the concrete adjacent to the anodic areas, the concentration of positive iron ions increases, causing the pH to fall and allows soluble iron–chloride complexes to form. These complexes can diffuse away from the rebar, permitting corrosion to continue. Some distance from the electrode, where the pH and concentration of dissolved oxygen are higher, the complexes break down, iron hydroxides precipitate, and the chloride is free to migrate back to the anode and react further with the steel. The process thus becomes autocatalytic and deepens the corrosion pits rather than spreading corrosion laterally along the rebar. As the steel increases its state of oxidation, the volume of the corrosion products expands. The unit volume of Fe can be doubled if FeO is formed. The unit volume of the final corrosion product, $Fe(OH)_3 3H_2O$, is

as large as six and half times the original Fe. This expansion creates cracking and spalling inside the concrete, and finally destroys the integrity of the structural concrete and causes failures of buildings and infrastructures.

As a result, chloride-induced corrosion is localized, with penetrating attacks in a limited area surrounded by noncorroded areas. The threshold concentration of chloride ions, i.e., the critical level of the chloride ion concentration in concrete at which the surface protective layer of reinforcing steel generated in conditions of high alkalinity can be broken, is a function of the pH value, i.e., the hydroxyl ion concentration. In other words, it is the ratio of the free chloride to pH, not merely the free chloride concentration that determines the initiation of corrosion. Hausman (1967) has suggested on the basis of measurements in $Ca(OH)_2$ solutions that the threshold chloride ion concentration is about 0.6 times the hydroxyl ion concentration. Gouda (1970) has suggested another relationship in which the threshold chloride ion concentration for a pore solution of a given pH region is expressed in a logarithmic form. Both Hausman's and Gouda's data were derived from experiments in a solution rather than in concrete, and other effects in concrete may influence the threshold value. In fact, most specifications and guidelines specify the total content of chloride in concrete in terms of the percentage by weight of the original cement used. The permitted chloride content in many specifications and recommendations is smaller than about 0.2% of the cement content of the concrete (Bentur et al., 1997). In the range of 0.2 to 0.4% there is risk of inducing corrosion, but not always. Sometimes, the critical level of chloride is specified in terms of weight of chloride per unit volume of concrete, mostly in the range of 0.6 to 1.2 kg/m^3. This kind of specification is needed when assessing the chlorides in existing structures, where the total chloride content of concrete can be determined experimentally, but not the chloride content in the cement.

Under a normal atmosphere environment, the chloride-induced corrosion rate can vary from several tens of micrometers per year (of steel) to localized values of 1 mm per year (of steel), as the relative humidity rises from 70 to 95% and the chloride content increases from 1% by mass of cement to higher values. High corrosion rates always appear on heavily chloride-containing structures, such as bridge decks, retaining walls, and pillars in seawater. The corrosion rate increases when the temperature changes from lower to higher values. Once the corrosion attack begins in chloride-contaminated structures, it can lead in a relatively short time to an unacceptable reduction in the cross section of the reinforcement, even under conditions of normal atmospheric exposure. The lower limits of relative humidity near which the chloride-induced corrosion rate becomes negligible are much lower than those that make carbonation-induced corrosion negligible. The influence of temperature and humidity on the corrosion rate is through their influence on the electrochemical reactions at the steel/concrete interface and through their influence on ion transport between the anodes and cathodes. It has long been thought that the concrete resistivity is strongly related to the corrosion rate at moderate or low temperatures (Glass et al., 1991; Alonso et al., 1988). In a given set of conditions in terms of humidity and temperature, and provided corrosion has been initiated, the higher resistivity of blended cements results in a lower corrosion rate than that of Portland cement.

The signs of corrosion of reinforcing steel can be identified as rust stains and minute cracking over the concrete surface. This can be attributed to the increase in volume associated with the formation of the corrosion products and the leaching of the rust. If repairs are not taken at an early stage, corrosion damage will occur, and the corrosion of the steel will proceed further, causing severe damage through forming a longitudinal crack in parallel with the underlying reinforcement, delamination and spalling of concrete cover, as well as exposure of the steel and reduction of its cross section, which may cause a safety hazard. The cost of damage caused by

corrosion of reinforcing steel can be very large. For example, a survey by the China Academy of Engineering in 2002 reported that the annual cost due to corrosion of reinforcing steel in China reached 100 billion Chinese Yuan. So it is desirable to know clearly the mechanism of corrosion of steel and to determine the possible methods for repairing the damage caused by reinforcing steel corrosion.

5.4.6.3 Corrosion mechanisms

Corrosion of the reinforcing steel in concrete is an electrochemical process, comprising both oxidation and reduction reactions, in which the metallic iron is converted to the voluminous corrosion product ferric oxide. The process is associated with the presence of anodic and cathodic areas, and a potential difference between the two areas, arising from inhomogeneities in the surrounding liquid medium, or even in the steel itself. The differences in potential are due to the inherent variation in the structure and composition (e.g., porosity and the presence of a void under the rebar or difference in alkalinity due to carbonation) of the concrete cover, and differences in exposure conditions between adjacent parts of the steel (e.g., concrete that is partly submerged in seawater and partly exposed in a tidal zone). In general, corrosion cells are formed due to (1) contact between two dissimilar materials, such as steel rebars and aluminium conduit pipes; (2) significant variations in surface characteristics, including differences in composition, residual strain due to local cold working, applied stress, etc.; and (3) different concentrations of alkalies, chloride, oxygen, etc. Four components must be present for corrosion to occur in a macro cell: the anode, cathode, electrolyte, and metallic path. The anode is the electrode at which oxidation occurs. Oxidation involves the loss of electrons and the formation of metal ions. Corrosion occurs at the anode. The cathode is the electrode where reduction occurs. Reduction is the gain of electrons in a chemical reaction. The electrolyte is a chemical mixture, usually a liquid, containing ions that migrate in an electric field. The free electrons travel to the cathode, where they combine with the constituents of the electrolyte, such as water and oxygen, to form hydroxyl (OH^-) ions. The metallic path between the anode and cathode is essential for electron movement between the anode and cathode. For the steel corrosion in the concrete, the anode, cathode, and metallic path are on the same steel. The electrolyte is the moisture in concrete surrounding the steel. The corrosion will stop if any of these components is removed. This provides the basis for corrosion control. The process of corrosion is illustrated in Figure 5-70

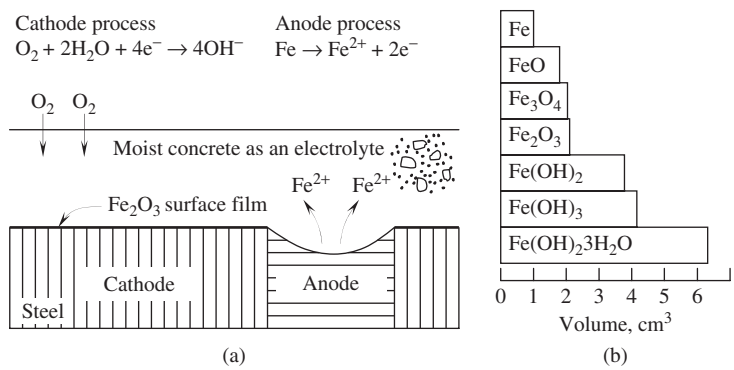

Figure 5-70 Reinforcing steel corrosion and expansion of corrosion products: (a) corrosion process, and (b) volume expansion of corrosion products

with the necessary notations of chemical reactions. At the anode site, the iron dissociates to form ferrous ions and electrons:

$$Fe \rightarrow Fe^{2+} + 2e^{-} \quad \text{(anodic reaction)} \tag{5-105}$$

The electrons move through the metal toward the cathodic site but the ferrous ions are dissolved in the pore solution. At the cathodic site, electrons combine with oxygen and water to form hydroxyl ions:

$$4e^{-} + O_2 + 2H_2O \rightarrow 4\,(OH)^{-} \quad \text{cathode reaction} \tag{5-106}$$

The hydroxyl ions move to the anode through the pore solution. At the anode, we have:

$$Fe^{2+} + 2Cl^{-} \rightarrow FeCl_2 \tag{5-107}$$

$$Fe^{2+} + 2\,(OH)^{-} \rightarrow Fe\,(OH)_2 \quad \text{ferrous hydroxide} \tag{5-108}$$

$$4Fe\,(OH)_2 + 2H_2O + O_2 \rightarrow 4Fe\,(OH)_3 \quad \text{ferric hydroxide} \tag{5-109}$$

It can be seen from the above equations that oxygen and water are needed for the initiation and propagation of the corrosion. There is no corrosion in a completely dry atmosphere, probably below a relative humidity of 40% (Mailvaganam, 1992). It has been suggested that the optimum RH for corrosion is 70 to 80%. At higher relative humidity (RH greater than 80%) or under immersion conditions, the diffusion of oxygen is considerably reduced and the environmental conditions are more uniform along the steel. Consequently, there is little corrosion. When corrosion occurs, ions need to travel through the pores in the surrounding concrete; oxygen needs to diffuse through the concrete cover. The corrosion rate is therefore affected by electrical resistance, diffusivity, and cover thickness of the concrete. The extent of steel corrosion in concrete depends on the conductivity of the electrolyte, the difference in potential between the anodic and cathodic areas, and the rate at which oxygen reaches the cathode. This controls the velocity of the anodic reaction. For steel in concrete, the strong polarization of the anodic zones under aqueous and highly alkaline conditions raises its potential close to that of the cathode, causing the surface of the steel to be passivated by the formation of an oxide layer. The passivating film prevents further reaction so that the steel remains unaltered over long periods. Another modifying effect of concrete on corrosion is that of increased electrical resistivity, which reduces the flow of electrical currents within the concrete. This is particularly true of high-density concrete (Page, 1992).

Because serious corrosion is very dangerous to a structure, engineers try to detect the corrosion to make maintenance decisions. The detection methods include visual inspection, half-cell potential measurement, and radiography, ultrasonic, magnetic perturbation/flux, and acoustic emission techniques. Here, we briefly introduce two techniques, half-cell potential measurement and acoustic emission.

Half-cell potential measurement (ASTM C876) measures the corrosion potential of the reinforcing steel using a standard reference electrode and voltmeters. One connection is made to the reinforcing steel under test and the other is made to a reference electrode, which contacts the concrete surface. The contact area should be moistened before taking the measurement. The probability of corrosion can be inferred according to the potential readings. If the potential is less negative than -200 mV, there is a better than 90% probability of noncorrosion; for a potential between -200 and -300 mV, the probability of corrosion is uncertain; for a potential more negative than -300 mV, there is a higher than 90% probability of corrosion. It should be pointed out that the above values are for copper/copper sulfate electrodes only. If a silver/silver chloride electrode or other type of electrode are used, different potential values have to be used to

judge the possibility of corrosion. A big drawback is that half-cell potential is highly dependent on the condition of the concrete at the time of measurement. For instance, moist concrete will yield different measurements from dry concrete.

The application of the acoustic emission (AE) technique to detect corrosion is relatively new (detailed information on AE can be found in Chapter 8). The principle of this application is that under the expansion of the corroded product, microcracks will develop at the interface between the corroded steel bar and the bulk matrix. The energy released by the formation of these microcracks will generate stress waves that propagate along the medium and reach the outer surface. By placing the AE transducer on the surface, the occurrence of microcracks can be detected. Since these microcracks are caused by corrosion products, the signals detected can be used to interpret the corrosion activity.

The mathematical model for calculating the stress caused by rebar corrosion at the rebar–concrete interface can be simplified as a shrink-fit model (Li et al., 1998), as shown in Figure 5-71. First, assume that the rebar can freely expand due to corrosion, with an increase of r in the radial direction. Then, we try to put the rebar back into the hole that it occupied before. Due to corrosion expansion, the rebar now is too big to fit freely in the concrete hole. To allow the rebar to fit back into the concrete, pressure has to be applied to both the surrounding concrete and the rebar. Let us consider the surrounding concrete first. This situation can be treated as an internal hole under pressure in a unbounded medium. According to the elasticity solution, the displacement caused by internal pressure p along radius direction is

$$U_r^c (r = a) = \frac{pa}{2\mu_c} \tag{5-110}$$

where p is the pressure, a the radius of hole, and μ_c the shear modulus of surrounding concrete (interface). For the rebar, it can be treated as an inclusion with pressure on the outside. The displacement along the radial direction can be written as

$$U_r^s = \frac{-p(k-1)a}{4\mu} \tag{5-111}$$

where k is the Kolosou constant, and has values of

$$k = \frac{3-v}{1+v} \qquad \text{for plane stress} \tag{5-112}$$

$$k = 3 - 4v \qquad \text{for plane strain} \tag{5-113}$$

Compatibility requires that

$$\left|U_r^c\right| + \left|U_r^s\right| = \Delta a \tag{5-114}$$

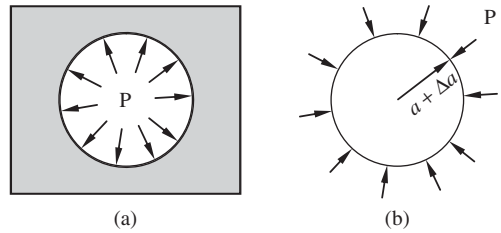

Figure 5-71 Shrink-fit model for corrosion of steel in concrete: (a) internal pressure on concrete; and (b) external pressure on steel bar

By substituting Equations 5-110 and 5-111 into 5-114, we can obtain the pressure expression as

$$p = \frac{4\mu_c\mu_s}{2\mu_s + (k_s - 1)} \frac{\Delta a}{a} \tag{5-115}$$

The stress produced at surrounding concrete interface is then derived as

$$\sigma_{\theta\theta} = \frac{4\mu_s\mu_c}{2\mu_s + (k_s - 1)\,\mu_c} \frac{\Delta a}{a} = C\frac{\Delta a}{a} \tag{5-116}$$

For steel, the shear modulus is about 81 GPa and the Kolosou constant is around 2. For concrete, the shear modulus is about 12 GPa, thus the value of C is 2.23×10^{10}. For $\Delta a/a$ equaling 0.0001, the stress produced is 2.23 MPa. Note that the stress is in fact the shear stress at the interface, and this value is large enough to create a microcrack. The stress wave generated by this microcrack can be detected by the acoustic emission transducer. Thus, it is proven that the sensitivity of the detection to rebar corrosion using the AE technique is very high (0.0001 of a radius of 10 mm is only 1 μm).

Because of the magnitude of the costs of rebar corrosion, significant efforts have been made to protect the steel in recent decades. To prevent corrosion in concrete, it is essential to lower the content of chloride to less than 0.6 kg/m^3. In this case, the protective layer on the rebar should be kept intact and thus no corrosion will be initiated. In most instances, corrosion-control methods can be described as passive. The durability performance is obtained by proper design and control of the concrete cover. Such means are usually specified in design codes: minimum concrete cover thickness, the inherent concrete properties (in terms either of design strength or maximum water/cement ratio), and the maximum allowable crack width permitted. Obviously, concrete quality is the most important parameter that controls the rate of carbonation and chloride ingress, hence the extent of reinforcing steel corrosion. Improving the quality of concrete has thus been considered the primary protection method. Next, we have to consider the four components of a corrosion cell. If one can be cut out, we can stop corrosion. It is obvious that the electrolyte in concrete is made up for the moisture condition and existing air. If we make a denser concrete, there will be less chance for moisture and air to get in, which will reduce the possibility of forming an electrolyte and prevent corrosion. We can also use cathodic protection methods to protect the reinforcing steel. For instance, using zinc as an anode can protect steel, because the corrosion occurs at the zinc anode.

The other protection strategies include increased cover, epoxy-coated rebars, stainless steel, and corrosion inhibitors. The time-to-corrosion of the embedded reinforcing steel can be significantly influenced by the amount of concrete cover over the rebar. However, as the cover increases, the rebar becomes less effective and the potential for cracking due to tensile stress, shrinkage, and thermal effects increases. Epoxy coating of the reinforcing steel can enhance the durability performance by serving as a barrier preventing the access of aggressive species to the steel surface and providing electrical insulation. Epoxy-coating can be applied in various ways, either as a liquid or as a powder which is fused on the surface. ASTM A775/A775M-04a (Standard Specification for Epoxy-Coated Steel Reinforcing Bars) has addressed the basic requirements for epoxy-coated reinforcing steels by the electrostatic spray method. In general, the performance of epoxy-coated rebars in bridge decks and parking garages in chloride environments, where chloride deicing salts are applied during winter, has been demonstrated as excellent (Clifton et al., 1975; Satake et al., 1983). However, several notable problems with the corrosion of epoxy-coated bars were reported in substructures in the Florida Keys in the United States (Clear, 1992; Clifton et al., 1975; Smith et al., 1993). The amount of damage to the epoxy coating prior to concrete casting has been considered the major contributing factor to the

poor performance. Thus, training is necessary for properly producing, handling, and applying the coating, and repairing field damage to epoxy-coated bars. Moreover, the bond properties between the concrete and the epoxy-coated rebars are not as strong as between concrete and conventional rebars, which should be improved.

There have been a few investigations on the use of stainless steel bars. It has been shown that the chloride threshold value for initiation of corrosion in a nonwelded AISI 304 (a kind of stainless steel) rebar is three to five times higher than that of a conventional rebar. However, welding the bar reduced the critical chloride level by 50%. In addition, the use of stainless rebars is an expensive solution.

Zinc coating of steel (galvanized steel) is also considered as a good means for providing corrosion resistance. It acts both as a sacrificial and barrier-type coating. But, a disadvantage is that, like other metal coatings, the zinc coating corrodes over time. The rate of corrosion under the given environmental conditions will determine the loss of coating thickness, and the time period during which it will be effective. Generally, there is a fairly linear relationship between the metal thickness and the duration of its effective service life for galvanized steel exposed to an industrial atmosphere (Chandler and Bayliss, 1985). The stability of zinc is dependent on the pH of the surrounding solution where the zinc coating is exposed. It has been found that zinc is stable at pH values below about 12.5, but it tends to dissolve at an increasing rate as the pH increases above this level. The corrosion products of zinc may be deposited at the surface of the zinc coating and seal it, thus arresting the evolution of H_2 gas and leading to passivation of the zinc coating. However, if galvanized rebars are used with ungalvanized bars, depletion of the galvanized bars will be accelerated. So if galvanized and ungalvanized bars are used in the same structure, special care should be taken to ensure complete electrical isolation of the two (Broomfield, 1997).

Corrosion inhibitors are regarded as useful not only as a preventative measure for new structures but also as a preventative and restorative surface-applied admixture for existing structures. Various corrosion inhibitors can be classified into (Trabanelli, 1986) (a) adsorption inhibitors, which act specifically on the anodic or on the cathodic partial reaction of the corrosion process, or on both reactions; (b) film-forming inhibitors, which block the surface more or less completely; and (c) passivators, which favor the passivation reaction of the steel. The mechanistic action of corrosion inhibitors is thus not against uniform corrosion but against localized or pitting corrosion of a passive metal due to the presence of chloride ions or a drop in pH value (Bertolini et al., 2004). Corrosion inhibitors admixed to the free concrete can act in two different ways: these inhibitors can extend the corrosion initiation time and/or reduce the corrosion rate after depassivation has occurred (Hartt and Rosenberg, 1989). Mixed-in inhibitors are regarded as more reliable since it is easier and more secure to add the inhibitors to the mix. Some laboratory testing has shown that certain corrosion inhibitors do not significantly affect the amount of chloride ions required to initiate corrosion, but can reduce the corrosion rate. The field performance of these products has been observed only for a relatively short period and cannot be conclusive in determining their effectiveness. Since the 1990s, fibrous composites have been introduced into concrete to replace reinforcing steel. Fibrous composites are usually made of continuous fibers (carbon, glass) as reinforcement and polymers (epoxy, polyester) as the matrix. Application of fibrous composites can completely eliminate the corrosion problem. However, the drawbacks of the material are the high price and the high temperature sensitivity.

5.4.7 Alkali–aggregate reaction

Alkali–aggregate reaction (AAR) is a reaction between alkalis in the pores of cement paste and certain forms of aggregates, which results in excessive expansion of concrete sections, and

leads to severe cracking thereafter. Two general types of attacks can occur (Tang, 1987): (1) alkali–carbonate attack with dolomitic limestone aggregate (some argillaceous dolomites) is called an alkali–carbonate reaction (ACR), and (2) alkali–silica attack with siliceous aggregates containing certain forms of amorphous or poorly crystalline silica (such as some chert, flint, opal, tridymite, cristoballite chalcedony, volcanic glasses, and some limestones) is called an alkali–silica reaction (ASR). The alkali content of cement depends on the materials from which it is manufactured and also to a certain extent on the details of the manufacturing process, but it is usually in the range of 0.4–1.6%. In concrete mixes, there may be a contribution to the alkali from other cementitious materials, such as pulverized fuel ash or ground granuated blast furnace slag, which is present. It is well known that Na_2O (sodium oxide) and K_2O (potassium oxide) are present in the cement clinker in small amounts. It is thus conventional to express the results of chemical analysis of cement in terms of these oxides. Furthermore, the alkali content in cement is generally expressed as an equivalent percentage of Na_2O by mass of cement. Since the molecular weights of Na_2O and K_2O are respectively 62 and 94, the equivalent percentage of Na_2O is calculated with the formula

$$\%Na_2O_{eq} = \%Na_2O + 0.658\%\ K_2O \tag{5-117}$$

In the cement paste, Na_2O and K_2O form hydroxides and raise the pH level from 12.5 to 13.5. The concentration of these hydroxides increases as Na_2O_{eq} increases. In such highly alkaline solutions, under certain conditions, the silica can react with alkaline. The alkali–silica reaction is the most widely spread and best understood. In this reaction, alkali hydroxides in the hardened cement paste liquor attach to the silica to form an unlimited swelling gel, which draws in any free water from osmosis and expands, disrupting the concrete matrix. Expanding gel products exerts internal stress within the concrete, causing characteristic map cracking of unrestrained surfaces (see Figure 5-72), but the cracks may be directionally oriented under the conditions of restraint imposed by the reinforcement, prestressing, or loading. Cracking resulting from alkali–silica reactions can lead to a loss of structural integrity.

Figure 5-72 Cracks caused by AAR

The degree of AAR is affected by (1) presence of water—if there is no water, there is no expansion; (2) alkali content—if the alkali content (Na_2O and K_2O) is less than 0.6%, there is no reaction, and concrete containing more than 3 kg/m^3 of alkali can be considered to have a high alkali content; and (3) concrete porosity—the internal stress may be relieved in concrete with high porosity. ASR can occur only in a moist environment: it has in fact been observed that in environments with a relative humidity below 80–90%, the alkali and reactive aggregate can coexist without causing any damage. With low effective alkali content in the concrete, i.e., when the equivalent content of Na_2O in concrete is less than 3 kg/m^3, deleterious AAR can be prevented. The expansive effect, hence the ASR effect, can be negligible. The extent of reaction depends on the amount of reactive silica present in the aggregate mix while the reactivity of the silica minerals depends on their crystal structure and composition. The porosity, permeability, and specific surface of the aggregates and the presence of Fe- and Al-rich coatings may influence the kinetics of the alkali–silica reaction. Blended cements containing pozzolana, fly ash, or blast furnace slag give a resulting alkaline solution of slightly lower pH, and addition of silica fume leads to the lowest pH. Hence, the use of pozzolana materials such as fly ash and GGBS can even prevent damage caused by ASR. These mineral additions reduce the concentration of OH^- ions in the pore solution of the cement paste. This is because hydroxyl ions are consumed by the pozzolanic reaction occurring during hydration. Furthermore, the alkali transport is slowed down because of the lower permeability of pozzolanic and blast furnace cement paste, which helps in reducing the ASR. Finally, the hydration products of the mineral additions bind alkali ions to a certain extent, preventing them from taking part in the reaction with the silica. It has also been found that by adding calcium nitrite into the concrete mix, the concrete's resistance to ASR can be significantly improved. However, the mechanism is not clear (Li et al., 1999a, 2000).

Temperature also influences the alkali–silica reaction. Normally, the ASR increases as temperature increases. AAR can be deleterious to concrete due to the expansion and possible cracking of the concrete associated with the reaction. What's more, development of the alkali–silica reaction may be very slow and its effects may show even after long periods (up to several decades). Consequently, cracking caused by an alkali–silica reaction usually takes many years and is often preceded by pop-outs on the concrete surface. Consideration must always be given to the effects of deeply penetrating cracks on the durability of the reinforcement and to the self-stress induced by the expansive reactions caused by alkali reactivity. This may be advantageous in confined sections of normally reinforced concrete members, but could prove catastrophic in the case of prestressed structures.

It is believed that AAR was first identified in 1940 in California (USA) by Stanton (Mehta and Monteiro, 2006), but only a limited number of examples were observed in practice until fairly recently. AAR causes deleterious expansion and cracking of the concrete and reduces the tensile strength, which may have consequences for the structural capacity. The significance of AAR or ASR for concrete structures has led to a surge in research activities: (1) to determine the exact nature of the reaction (which is not fully understood as yet); (2) to define the acceptable limits of alkali content, moisture content, and reactive aggregate content; and (3) to determine methods to reduce the degree of destructive expansion. Extensive research has been made in two directions. One is the development of testing methods, which are designed to reveal whether an aggregate is potentially reactive and can cause abnormal expansion and cracking of concrete. The other is the development of effective methods to prevent damage induced by AAR.

Although it is possible to determine what types of aggregates have a trend toward AAR, it is impossible to predict whether their use will result in excessive expansion or not. It has been found that a critical amount exists for each type of aggregate, which can result in serious expansion and an amount smaller or larger than this value will not cause significant swelling. Measuring

the expansion of test specimens has been considered to be the most dependable way to evaluate aggregate reactivity, and a number of test procedures have been devised. The testing methods commonly used include standard test methods, such as the mortar bar test (ASTM C227), the rock cylinder method (ASTM C586), and rapid test methods, such as ASTM C289. One of the disadvantages of standard testing methods is that most of them are very time-consuming, which is incompatible with the demands of the construction industry. Concrete prism testing (CPT) utilizes concrete prisms of $75 \times 75 \times 300-400$ mm as specimens. The prisms should be prepared with a cement content of 420 kg/m^3 and the alkali content is boosted to 1.25% Na_2O_{eq} by cement mass (total alkali content of 5 kg/m^3). The maximum aggregate size can be up to 20 mm. The test setup of CPT is shown in Figure 5-73. On the other hand, the rapid testing method, ASTM C289, only gives the potential reactivity of the aggregate, but it does not necessarily predict expansion in the real situation.

To overcome the limitation of the above-mentioned test methods, other rapid testing methods have been developed, such as the dynamic modulus test and the gel fluorescence test. The dynamic modulus can be obtained by measuring the resonant frequency and pulse velocity. It has been shown that it can provide a good indication of deterioration due to AAR. The measurement can even detect deterioration before any expansion and visible cracking occurs. It is also sensitive to the changes in environmental conditions, which activate or suppress the AAR.

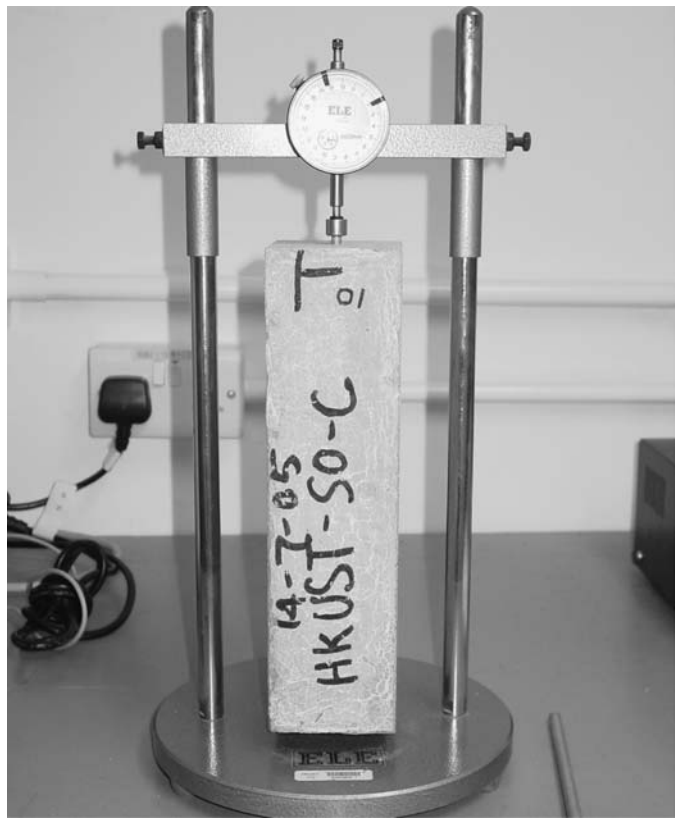

Figure 5-73 Concrete prism test setup

In the gel fluorescence test method, a 5% solution of uranyl acetate is applied on the surface of the specimen, then the specimen is viewed under an ultraviolet (UV) light. A yellowish green fluorescent glow means that AAR is present. Since AAR can cause significant deterioration and damage to concrete structures, much research has been conducted to decrease the effect of the reaction. There are numerous recommendations for minimizing the risk caused by AAR, including the following:

(a) Use nondeleterious aggregates and/or nonreactive aggregates when the alkali content of the cement is high (more than $3\,kg/m^3$).

(b) Use low-alkali Portland cement or blended cements with sufficient amounts of fly ash or slag when the active silica content of aggregate is high.

(c) Keep the concrete dry (relative humidity of the concrete less than 80%). However, the choice on the types of cements and aggregates at a construction site is usually very limited, and the environment surrounding the concrete is obviously unchangeable. In many cases, the content of silica in aggregates and/or alkalis in cement paste cannot be reduced effectively, either. The only effective way to reduce the risk of AAR is to control moisture migration in the concrete, since no AAR will occur in dry concrete even there is some silica present. Controlling of moisture diffusion in concrete can be implemented in two different levels. One is to control the local moisture diffusion around the boundary of each aggregate, that is, to control the moisture exchange between the aggregate and the surrounding cement paste. The other is to control the diffusion of moisture into and out of the surface of concrete members.

(d) Use a local diffusion-control surface coating. The control of local moisture diffusion is very important because AAR occurs right on the boundary of the aggregate. Distributions of chemicals, Na_2O, SiO_2, K_2O, and CaO, around the aggregate boundary have shown quantitatively that the reaction rim is in the range of $300\,\mu m$. Local diffusion control coating is developed based on the crystallization technique. The coating product consists of powders of finely ground rapid-setting Portland cement, treated silica sand (de-alkaline silicate), and proprietary chemical additives. They are mixed with water to form a slurry. The slurry will be applied to the reactive aggregate before the mixing of the concrete. A coating is then formed around the aggregates. Application of this technique is aimed not at completely eliminating AAR, but at reducing and slowing down the AAR rate. As a result of a slow reaction, the product of the reaction can be accommodated and deposited in the large capillary pores. Thus, the detrimental damage due to the expansion will be avoided.

(e) Use a global diffusion control coating. This method applies sunlight for curing hydrophobic weather-resistant coatings. This is a newly developed coating, which can be applied on the surface of concrete members to reduce moisture diffusion. In addition to the high resistance to moisture penetration, the coating has two other useful features. One is its ability to reduce or to eliminate VOC (volatile organic compounds), which are detrimental to the environment. The other is that it can be cured under low-power UV. UV curing is very important for long-term applications since it yields paints or coatings with excellent durability. However, conventional UV curing requires a special high-power UV lamp. This coating requires only natural light from the sun, that is, sunlight curing.

(f) The use of lithium nitrate ($LiNO_3$), calcium nitrate, or other types of nitrate, as well as other lithium compounds can control AAR-induced damage. The work of Li et al. (1999b) has demonstrated that calcium nitrate can effectively reduce AAR.

5.4.8 Deterioration caused by freeze-thawing

Concrete is a porous material. As the cement and water in fresh concrete react to form a hardened paste binding the coarse and the fine aggregates together, voids are left in the originally water-filled space among the cement grains. These voids are known as capillary pores, with a size range from approximately 5 nm to 1 μm and sometimes even larger. In addition to the capillary pores, cement paste also contains a significant volume of smaller pores called gel pores. Water content and capillary forces in these pores are important to the durability of hardened concrete, especially for those subjected to repeated cycles of freezing and thawing, which can cause disintegration of the concrete surface layers.

Concrete deterioration caused by freezing and thawing is linked to the presence of water in concrete but cannot be explained simply by the expansion of water on freezing. While pure water in the open freezes at 0°C, in concrete the water is really a solution of various salts, so its freezing point is lower. Moreover, the temperature at which water freezes is a function of the size of the pores. The freezing temperature of water in concrete pores decreases with decreasing pore size. In concrete, pore sizes cover a wide range, so there is no single freezing point. Indicatively, for saturated Portland cement paste, free water in pores larger than 0.1 mm freezes between 0 and −10°C; water in pores between 0.1 and 0.01 mm freezes between −20 and −30°C; and water in gel pores (pores less than 10 nm) freezes below −35°C (Beddoe and Setzer, 1990). Freezing begins in the outer layers and in the largest pores and extends to the inner parts and to smaller pores only if temperature drops further. Specifically, the gel pores are too small to permit the formation of ice, and the greater part of freezing takes place in the capillary pores. It is also noted that larger voids, arising from incomplete compaction, are usually air-filled and are not appreciably subjected to the initial action of frost. During freeze–thaw cycling attacks on concrete, the presence of deicing salts, like calcium and sodium chloride, in contact with concrete is a detrimental factor. The outer layers where these salts are present are more strongly affected by frost, despite their effect in lowering the freezing point, probably due to increased water saturation caused by their hygroscopic effect, with the early appearance of scaling and detachment of the cement paste that covers the aggregate, as shown in Figure 5-74.

When water freezes there is an increase in volume of approximately 9%. As the temperature of concrete drops, freezing occurs gradually inward and exerts hydraulic pressure to the unfrozen

Figure 5-74 Scaling deterioration caused by freezing–thawing

water in the capillary pores due to the volume expansion of ice. Such pressure, if not relieved, can result in internal tensile stresses that may cause local failure of the concrete. On subsequent thawing, the expansion caused by ice is maintained so that there is now new space available for additional water, which may be subsequently imbibed. During refreezing, further expansion occurs. Thus, repeated cycles of freezing and thawing have a cumulative effect. It is the repeated freezing and thawing, rather than a single occurrence of frost that causes damage. Frost action is an important factor causing concrete degradation in cold regions. When the solutions contain deicing chemicals, the deicing salts can lower the temperature of ice formation, which may be viewed as a positive effect; but they may also bring the following negative effects: (a) an increase in the degree of saturation of concrete due to the hygroscopic character of the salts; (b) an increase in the disruptive effect; (c) the development of differential stresses as a result of layer-by-layer freezing of concrete due to salt concentration gradients; (d) temperature shocks; and (e) salt crystallization in supersaturated solutions in pores (Mehta and Monteiro, 2006). Overall, the negative effects far outweigh the positive effects.

There are two other processes that can increase the hydraulic pressure of the unfrozen water in the capillaries. First, since there is a thermodynamic imbalance between the gel water and the ice, diffusion of gel water into capillaries can lead to a growth in the ice body and thus to an increase of hydraulic pressure. Second, the hydraulic pressure is increased by the pressure of osmosis caused by local increases in solute concentration due to the removal of frozen (pure) water from the original solution. The extent of damage caused by repeated cycles of freezing and thawing varies from surface scaling to complete disintegration as layers of ice are formed, starting at the exposed surface of the concrete and progressing through its depth. In general, concrete members that remain wet for long periods are more vulnerable to frost than any other concrete. It is clear that the hydraulic-pressure mechanism of frost damage has more severe consequences in a system of fully saturated pores, because in that case the pressure can be released only if the microstructure expands, which may quickly result in cracking.

In general, the loss of mass or the decrease of dynamic modulus are used as indexes of degradation. The general influence of the saturation of concrete in the deterioration mechanism is related to a value known as the critical saturation, below which the concrete is quite resistant. The critical saturation depends on body size, homogeneity, and the rate of freezing. Frost resistance is determined by the number of freeze–thaw cycles that a particular concrete can withstand before reaching a given level of degradation. To prevent a concrete from damage caused by repeated cycles of freezing and thawing, an air-entraining agent can be used. An air-entraining agent is a chemical admixture that can deliberately entrain the air into cement paste in a close space (<0.3 mm). The main types of air-entraining agents are (a) animal and vegetable fats and oils and their fatty acids; (b) natural wood resins, which react with lime in the cement to form a soluble resonate; the resin may be preneutralized with NaOH so that a water-soluble soap of a resin acid is obtained; and (c) wetting agents such as alkali salts of sulfated and sulfonated organic compounds.

The performances of an air-entraining admixture should be checked by trial mixes in terms of the requirements of ASTM C260-77 or BS 5075:Part 2:1982. The essential requirement of an air-entraining admixture is that it rapidly produces a system of finely divided and stable foam, the individual bubbles of which resist coalescence; also, the foam must have no harmful chemical effect on the cement. The beneficial effect of air entrainment on concrete subjected to freezing and thawing cycles is to create space for the movement of water under hydraulic pressure. However, there are some further effects on the properties of concrete, some beneficial, others not. One of the most important is the influence of voids on the strength of concrete at all ages.

5.4.9 Degradation caused by sulfate attack

Sulfate attack is one of main factors causing deterioration of concrete durability. It is generally regarded as an expansion due to the reaction of sulfate with some hydration products in cement paste. Portland cement itself contains sulfate as gypsum. In most cases, however, the sulfates are external to the concrete. The sulfates to which concrete can be exposed may come from contaminated aggregates, groundwater (clay soil), and seawater. Solutions of sulfates of sodium, potassium, magnesium, and calcium are common salts that may bring severe deterioration to concrete. The total sulfate content in a concrete mixture becomes a controlling factor of the degree of sulfate contact. The acceptable concentration of sulfate in concrete is about 4% by weight of cement. It is generally accepted that a sulfate attack of hydrated cement takes place by the reaction of sulfate ions with calcium hydroxide and hydrated calcium aluminates to form gypsum and ettringite. The sulfate also reacts with the tricalcium aluminate (C_3A) in the cement to form the compound ettringite. The deterioration of Portland cement concretes exposed to sulfates may be ascribed to the following reactions (Campbell-Allen and Roper, 1991):

(i) The conversion of calcium hydroxide derived from cement hydration reactions to calcium sulfate, and the crystallization of this compound with resulting expansion and disruption.

$$Ca(OH)_2 + SO_4^{2-} + 2H_2O \rightarrow CaSO_4 2H_2O + 2OH^- \tag{5-118}$$

(ii) The conversion of hydrated calcium aluminates and ferrites to calcium-sulfo-aluminates and sulfo-ferrites or the sulfate enrichment of the latter minerals. The products of these reactions occupy a greater volume than the original hydrates, and their formation tends to result in expansion and disruption.

$$C_3A + 3CaSO_4 + 32H_2O \rightarrow 3CaOAl_2O_3 3CaSO_4 32H_2O \tag{5-119}$$

(iii) The decomposition of hydrated calcium silicates.

In the presence of calcium sulfate, only reaction (ii) can occur, but with sodium sulfate, both (i) and (ii) may proceed. The sodium sulfate reacts with calcium hydroxide to form gypsum first, then with hydrated calcium aluminates or unhydrated C_3A to form ettringite, as shown in the following equations:

$$CH + N\overline{S} + 2H \longrightarrow C\overline{S}H_2 + NH \tag{5-120}$$

$$3C\overline{S}H_2 + C_3A + 26H \longrightarrow C_6A\overline{S}_3H_{32} \tag{5-121}$$

$$3C\overline{S}H_2 + C_4AH_{13} + 14H \longrightarrow C_6A\overline{S}_3H_{32} + CH \tag{5-122}$$

With magnesium sulfate, all three may occur. It means that in additional to the reaction with CH to form gypsum first and then with C_3A to form ettringite, magnesium sulfate can react with C–S–H directly as shown in the following equation:

$$C_xS_yH_z + xM\overline{S} + (3x + 0.5y - z)H \longrightarrow xC\overline{S}H_2 + xMH + 0.5yS_2H \tag{5-123}$$

From the different reaction mechanisms of different sulfates, it can be deduced that the severity of attack depends on the type of sulfate. Calcium sulfate undergoes an expansion reaction with ettringite (coming from calcium aluminate in cement), which gives rise to greater expansive effects than gypsum. Part of the formed ettringite is commonly located in the interface between the paste and aggregate, resulting in loss of bond. Sodium sulfate (Na_2SO_4) also reacts with calcium hydroxide to form gypsum, which reduces the paste strength and stiffness. Magnesium

sulfate ($MgSO_4$) reacts to form gypsum and destabilizes C–S–H, the strength-governing phase in cement paste. This is because Mg^{2+} and Ca^{2+} ions associate well, since they have equal valence and similar ionic radii, which can lead to a reaction between magnesium sulfate and the C–S–H gel. Severity of attack therefore increases from calcium sulfate to sodium sulfate to magnesium sulfate. In other words, magnesium sulfate attacks have the most damaging effect on concrete.

Generally speaking, the formation of gypsum and etringite is responsible for the expansion of concrete. The expansion caused by a sulfate attack can lead to the development of cracks in concrete. When concrete cracks, its permeability increases. The aggressive water penetrates more easily into the interior of the concrete through the cracks, thus accelerating the process of deterioration. The deterioration of concrete due to the sulfate attack is a complicated phenomenon of physical and chemical processes. Sulfate attacks can also be manifest as a progressive loss of strength of the cement paste due to loss of cohesion between the hydration products, and loss of adhesion between the hydration products and the aggregate particles in concrete.

The concrete attacked by sulfate has a whitish appearance. Usually, damage starts at the edges/corners, followed by progressive cracking/spalling. The rate of sulfate attack also increases with the concentration of sulfate and the replenishment rate (e.g., sulfate attacks on concrete and faster in flowing groundwater due to faster replenishment rate). Tests on sulfate resistance are normally conducted through storing specimens in a solution of sodium or magnesium sulfate, or a mixture of the two, see Figure 5-75. The tests may be accelerated with wetting/drying cycles that will induce salt crystallization in the pores. Effect of exposure can be estimated from (1) change in dimensions, (2) loss of strength, (3) change in the dynamic modulus of elasticity, and (4) loss of weight. The test method of ASTM C1012-04 uses immersion of well-hydrated mortar in a sulfate solution, and considers excessive expansion as a criterion of failure under sulfate attack, but this method is used only for mortar, not for concrete. Besides, the method is slow—it normally takes several months. As an alternative, ASTM C452-89 prescribes a method in which a certain amount of gypsum is included in the original mortar mix. This speeds up the reaction with C_3A, but this method is not appropriate for use with blended cements. The criterion of sulfate resistance in this method is the expansion at the age of 14 days.

Figure 5-75 Storage pond for sulfate attack test

The resistance of concrete to sulfate attack depends primarily on the permeability and diffusivity of the concrete, the type and amount of cement in the concrete, and the type and amount of mineral additives in the concrete. Low permeability and diffusivity provide the best defense against sulfate attack by reducing sulfate penetration. To achieve a low permeability and diffusivity, the water/powder ratio should be decreased to a value as small as possible and pozzolanic additives that can reduce the calcium hydroxide content and refine the pore structure of the matrix through pozzolanic reaction should be used. Reducing the water/cement ratio is more effective than reducing the calcium aluminate content in improving the sulfate resistance of concrete. The severity of sulfate attack depends on the content of C_3A and, to a lesser extent, of C_4AF in the cement. Sulfate-resisting cement has a low tricalcium aluminate content and hence less potential for expansive reaction and better resistance to sulfate attack. Reducing the amount of calcium hydroxide and hydrated calcium aluminate is also helpful in improving the sulfate resistance of concrete. Blended cements with pozzolanic materials or blast furnace slag show enhanced resistance to sulfate attack (Mehta, 1988b). For example, low-calcium fly ash is an effective blending material for combating sulfate attack of concrete. The incorporation of silica fume into a concrete mixture greatly improves the sulfate resistance, owing to the reduced amount of gypsum formation, compared with mixtures that do not contain silica fume.

The incorporation of silica fumes can also largely reduce the permeability of concrete, thus improving the sulfate resistance. The mixed utilization of silica fume and fly ash should be a much better choice for the production of high-performance concrete.

On the other hand, Mehta (1988a) has noted that it is the mineralogy rather than the chemical composition that determines the resistance to attack, and empirical guidelines based on chemical compositions of a mineral additive do not prove to be reliable. Nevertheless, Mehta (1988b) has concluded that as a first approximation, a blended cement will be sulfate resisting when made with a highly siliceous natural pozzolanic or low-alumina fly ash or slag, provided that the proportion of the blending material is such that most of the free calcium hydroxide can be used up during the course of cement hydration. Under severe conditions, hydraulic cements other than Portland cement should be used, for example, supersulfated cement and high-alumina cement. Supersulfated cement offers very high resistance to sulfates, especially if its Portland cement component is of the sulfate-resisting variety. It should be noted here that high-alumina cement should not be used in continuously warm, damp conditions, or in mass construction from which the heat of hydration cannot be easily dissipated. High-pressure steam curing improves the resistance of concrete to sulfate attack due to the change of C_3AH_6 into a less reactive phase, and also to the removal of $Ca(OH)_2$ by the reaction with silica.

5.4.10 Durability in a marine environment

Many infrastructures are built in marine environments, such as bridges, tunnels, oil platforms, and piers. The marine environment can be distinguished as being under seawater, above seawater, or in a tide zone. The deterioration of concrete structures in the marine environment in a tide zone is the most serious because it is under a combination of mechanisms, both chemical and physical in nature, as shown in Figure 5-76. Attack on concrete in the tide zone can be of various types: (a) physical erosion, (b) salt crystallization pressure, (c) leaching of sulfate attack products, (d) freezing/thawing in cold regions, and (e) chloride penetration. The tidal zone refers to the range between the mean high and mean low water levels. This zone is periodically immersed, generally on a daily basis. Corrosion of steel and spalling of concrete easily occur in this zone. Reinforcement corrosion is the most common mechanism in the deterioration of concrete structures. In marine environments, corrosion of the reinforcement is primarily due to

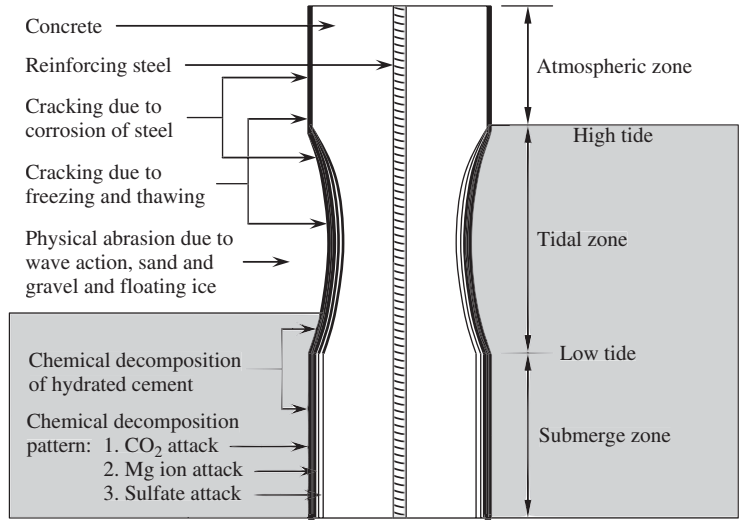

Figure 5-76 Deterioration mechanisms of concrete structure under tide zone

chloride penetration of the concrete, which results in expansion of the reinforcing steel surface, ultimately spalling the concrete surface.

Additionally, abrasion of structural elements from ice and debris occur within the tide zone. The alternating motion of waves and tides also contributes to deterioration of the concrete. A high-velocity wave and depressions and irregularities of the surface layer can cause cavitation to form in marine concrete structures. If the absolute pressure at points of surface irregularities approaches the vapor pressure of the water, minute bubbles will form and quickly collapse. The collapse of these bubble can produce minute water jets having extremely high velocities and create an intense impact wave splashing to concrete surface. This effect is very destructive to high-strength concrete. The deterioration caused by cavitation can take the form of tearing out of large pieces of concrete. Cyclic drying and capillary suction occur in the concrete just above sea level, and water carries the dissolved salts into the concrete. Subsequent evaporation causes these salts to crystallize in the pores, producing stresses that can cause microcracking. Below the low-tide line is an area where continual immersion occurs. In general, this is an area of less severe attack to the steel and concrete structures, compared with those of exposed at tidal or splash zones.

The reaction between sulfate ions and both C_3A and C–S–H takes place in concrete exposed in a marine environment, resulting in the formation of ettringite, which, as well as gypsum, fortunately, is soluble in the presence of chlorides and can be leached out of the concrete by the seawater (Lea, 1970). This happens with no expansion but gradual material loss, which is quite different from sulfate attack in other environments. To investigate the deterioration mechanism of a concrete structure in a marine environment, simulation experiments can be conducted in the laboratory with an environmental tank as shown in Figure 5-77. However, to obtain more realistic information on marine structure deterioration, exposure testing to real ocean environments should be conducted. Figure 5-78 shows the marine exposure test site in Qingdao, China.

Keys to improved durability against deterioration caused by the marine environment include (a) using concrete with low permeability, and (b) limiting the C_3A content of the cement, or using pozzolans for partial cement replacement. Mehta has indicated that the permeability of concrete is the most important factor influencing concrete performance exposed to marine environments

Figure 5-77 Seawater tank for marine environmental simulation test

(Mehta, 1980). Low permeability can reduce the penetration of salt, sulfate, and water; besides, low-permeability concrete normally has high strength and good erosion resistance to the marine environment. The rate of deterioration caused by seawater depends on the quantity of seawater absorbed by the concrete, so that all factors that contribute to obtaining a lower permeability will improve concrete structures' resistance to attack by seawater and marine environments. Mehta (1980) has noted that concretes containing even high tricalcium aluminate cements have excellent service lives in marine environments if the permeability is sufficient low.

Low-permeability concrete can be achieved by the use of a low water/cement ratio, an appropriate choice of cementitious materials, good compaction, absence of cracking, and good curing. Since salt in water can contribute to the corrosion of reinforcing steel, normally 50 to 75 mm of dense concrete cover is required for reinforced concrete structures in the marine environment. To avoid the alkali silica reaction, Mehta (1988b) has recommended using cement content that is not below 400 kg/m^3, tricalcium aluminate content below 12% and preferably between 6 and 10%, and good-quality aggregate. For ocean structures, it is preferable to use blast furnace slag cement, fly ash cement, or pozzolanic cement. Due to pozzolanic reaction of slag, fly ash, and pozzolans, a good amount of calcium hydroxide will be consumed and the large amount of secondary C–S–H generated. As a result, concrete produced by these cements has a finer pore structure, which largely reduces the transport rate of both sulfate and chloride ions.

5.4.11 Deterioration of concrete caused by multifactors

In common practice, concrete structures are exposed to different environmental conditions and deteriorate by the coupling effect of different factors. The ocean structure mentioned above under erosion, chloride diffusion, and sulfate attack simultaneously is a good example. Moreover, concrete structures have to carry the mechanical loads while being exposed to different environments. Hence, it is more realistic to study the deterioration mechanism of a concrete structure under the coupling effects of mechanical loading and a combination of environmental

Figure 5-78 The marine exposure test site in Qingdao, China

factors. Many researchers have undertaken studies along this direction. For example, Sun et al. (1999, 2002) have conducted experiments on concrete with a combination of loading, chloride diffusion, and freeze–thaw to investigate the coupling effect on performance. However, this area of research is just in its initial stage, and more effort has to be made to deeply understand the deterioration mechanism under a combination of loading and environmental factors.

DISCUSSION TOPICS

What are the strengths of concrete? Why is compressive strength an important index?
Does concrete have equal values of compressive and tensile strength? Why?
How is the indirect tension test conducted?
How is the bending test conducted?
How can shrinkage influence the quality and serviceability of a concrete structure?
How can creep influence the quality and serviceability of a concrete structure?
What are the main factors affecting the durability of concrete?
How is a permeability test conducted?
How is a chloride diffusion test conducted?
Why is durability important to a concrete structure?
How can the corrosion of reinforcing steel cause damage of concrete structure?
How can the corrosion of reinforcing steel be detected?
How can the corrosion of reinforcing steel be prevented?
Why is AAR harmful to concrete structure?
What are the methods to prevent AAR in concrete? What are their suitability and limitation?
What are the relationships between tensile, flexural, and compressive strength?
What is strain softening?
Why is Poisson's ratio of concrete not a constant in the stress range up to peak?
What is the main reason responsible for drying shrinkage?
What causes creep in concrete?
Discuss the factors affecting shrinkage and creep.
Define durability of concrete.
Discuss the main factors affecting the durability of concrete.
Do you know any incidents caused by reinforcing steel corrosion?
Can you prevent or minimize corrosion if you work as an engineer on construction site?

PROBLEMS

1. Take the transition zone into consideration and derive the Young's modulus expression using the parallel and series models. Suppose that the volume fraction ratio of the transition zone is 1% of the volume of concrete. If E_c for parallel model is 80 Gpa and for the series model is 58 Gpa, calculate volume fraction of aggregate and elastic modulus of transition zone. Assume that $E_a = 100$ GPa, and $E_m = 30$ Gpa.

2. A specimen of shrinkage-compensating concrete of $0.25 \times 0.25 \times 2.5$ m is made with 12 steel rebars (12 mm in diameter) inside of the same length. The specimen expands during the wet curing period. If $E_c = 15$ GPa, $E_s = 200$ GPa, and free expansion strain $= 0.0003$ at the time, estimate the force generated in concrete and steel. How much will be the change in the specimen length?

3. For a Kelvin model,

(a) If $E = 200$ GPa, $\eta = 6000$ GPa·s, find the initial ($t = 0$) and final ($t = \infty$) slope of the strain vs. time curve, as well as initial and final strain values for $s = 120$ MPa.

(b) For the stress input shown below, find the strain at 90 and 7200 s. Draw the curve of strain vs. time schematically.

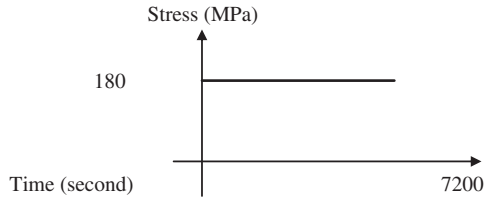

Figure P5-3

4. A specimen of concrete column (200×200 mm) is 1.5 m long with 4 steel rebars (20 mm in diameter) inside with same length. The specimen is loaded with a constant load of 600 kN under 100% relative humidity. Calculate the initial stress in steel and concrete. If the basic creep for plain concrete at 100 days is 600×10^{-6}, and the measured stress in steel at 100 days for this column is 160 MPa, estimate the percentage of creep restrained by steel. (Young's modulus of steel is 210 GPa; the modulus of elasticity of concrete is 25 GPa.) Also, calculate the length change of the specimen.

5. Suppose that the self-balanced strain due to shrinkage for a circular-shaped beam (150×500 mm) along the diameter direction follows the distribution of $\varepsilon = 0.00016(x/R)^2 - 0.0001$, where R is the radius of the circular shape. The $E_c = 20$ GPa. If the peak load, P, for this beam under pure bending is 6600 N, calculate the tensile strength for the concrete by eliminating the influence of shrinkage. The self-weight of the beam can be ignored in this problem.

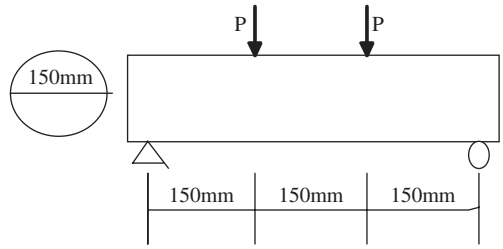

Figure P5-5

6. A reinforced concrete column with a cross section of 250×250 mm was repaired with a polymer concrete. The repaired portion is 250×100 mm at the bottom of the column. The column is 3 m long and carrying an axial load of 150 tons. The reinforcing ratio of the column is 1%. The Young's modulus of rebar and old concrete is 200 and 28 GPa. The density of reinforced concrete is 2.4. What is the minimum E requirement of the polymer concrete if the stress in old concrete has to be less than 25 MPa?

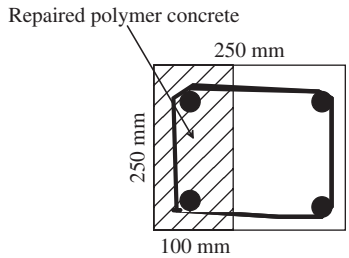

Figure P5-6

REFERENCES

Allen, R.T.L., Edwards, S. C., and Shaw, J.D.N. (1993) *The repair of concrete structures*, London: Blackie Academic & Professional.

Alonso, C. and Andrade, C. (1994) "Lifetime of rebars in carbonated concrete," In: Costa, J.M. and Mercer, A.D., eds., *Progress in understanding and prevention of corrosion*, London: Institute of Materials.

Alonso, C., Andrade, C., and González, J. A. (1988) "Relation between resistivity and corrosion rate of reinforcements in carbonated mortar made with several cement types," *Cement and Concrete Research*, **18**(5), 687–698.

Anonymous (1988) "Concrete durability—a multibillion-dollar opportunity," *Concrete International*, **10**(1), 33–35.

ASTM C1202-09 Standard test method for electrical indication of concrete's ability to resist chloride ion penetration.

Beddoe, R. and Setzer, M. J. (1990) "Phase transformations of water in hardened cement paste, a low temperature DCS investigation," *Cement and Concrete Research*, **20**, 236–242.

Bentur, A., Diamond, S., and Berke, N.S. (1997) *Steel corrosion in concrete: fundamentals and civil engineering practice*, London: E&FN Spon.

Berke, N.S., Dallaire, M.P., Hicks, M.C., and Kerkar, A. (1999) "New development in shrinkage-reducing admixtures," ACI SP 173-48, Farmington Hills, MI: American Concrete Institute, pp. 973–998.

Bertolini, L., Elsener, B., Pedeferri, P., and Polder, R. (2004) *Corrosion of steel in concrete: prevention, diagnosis and repair*, Weinheim, Germany; Wiley-VCH.

Blechman, I. (1992) "Differential equation of concrete behaviour under uniaxial short-term compression in terms of atrophy (degeneration) and its solution," *Magazine of Concrete Research*, **44**(159), 107–115.

Bloom, R. and Bentur, A. (1995) "Free and restrained shrinkage of normal and high-strength concretes," *ACI Materials Journal*, **92**(2), 211–217.

Broomfield, J. P. (1997) *Corrosion of steel in concrete: understanding, investigation and repair*, New York: E & FN Spon.

Burrows, R.W. (1998) *The visible and invisible cracking of concrete*, ACI Monograph No.11, Farmington Hills, MI: American Concrete Institute.

Campbell-Allen, D. and Roper H. (1991) *Concrete structures: materials, maintenance and repair,* New York: Longman Scientific & Technical, Wiley.

Chandler, K. A. and Bayliss, D. A. (1985) *Corrosion protection of steel structures*, Oxford: Elsevier Science.

Chen, W. F. (1981) *Plasticity in reinforced concrete*, New York: McGraw-Hill.

China Civil Engineering Society Standard (中国土木工程学会标准) (2004). *Guidelines of design and construction of durable concrete structure* (混凝土结构耐久性设计与施工指南), CCES01-2004.

Clear, K.C. (1992) "Effectiveness of epoxy-coated reinforcing steel," *Concrete International*, **14**(5), 58–64.

Clifton, J. R., Beeghley, H. F., and Mathey, R. G. (1975) "Nonmetallic coatings for concrete reinforcing bars," Building Science Series 65, U.S. Department of Commerce, National Bureau of Standards.

Damidot, D., Nonat, A., and Barret, P. (1990) "Kinetics of tricalcium silicate hydration in diluted suspension by microcalorimetric measurements," *Journal of the American Ceramic Society,* **73**(11), 3319–3322.

DuraCrete (2000) "DuraCrete—probabilistic performance based durability design of concrete structures," Final Technical Report (The European Union–Brite EuRam III), document BE95-1347/R17.

Glass, G.K., Page, C.L., and Short, N.R. (1991) "Factors affecting the corrosion rate of steel in carbonated mortars," *Corrosion Science*, **32**, 1283–1294.

Goto, T., Sato, T., Sakai, K., and Motohiko I. (1985) "Cement-shrinkage-reducing agent and cement composition," United States Patent Number 4,547,223.

Gouda, V.K. (1970) "Corrosion and corrosion inhibition of reinforcing steel, I: immersed in alkaline solutions," *British Corrosion Journal*, **5**(9), 198–203.

Hartt, W. H. and Rosenberg, A. M. (1989) "Influence of $Ca(NO_2)_2$ on seawater corrosion of reinforcing steel in concrete," American Concrete Institute, Detroit, SP 65-33, 609–622.

Hausman, D.A. (1967) "Steel corrosion in concrete," *Materials Protection,* **6**(11), 19–22.

He, Z., Zhou, X., and Li, Z. (2004) "New experimental method for studying early-age cracking of cement-based materials," *ACI Materials Journal*, **101**(1), 50–56.

Kuhl, D., Bangert, F., and Meschke, G. (2004) "Coupled chemo-mechanical deterioration of cementitious materials, part I: modeling; and part II: numerical methods and simulations," *International Journal of Solids and Structures,* **41**(1), 15–67.

L'Hermite, R.G. (1960) "Volume changes of concrete," *Proceedings of the 4th international symposium on the chemistry of cement*, Washington, DC, Vol. 2, pp. 659–694.

Le Bellégo, C., Pijaudier-Cabot, G., Gérard, B., Dubé, J. F. and Molez, L. (2003) "Coupled mechanical and chemical damage in calcium leached cementitious structures," *ASCE Journal of Engineering Mechanics,* **129**(3), 333–341.

Le Chatelier, H. (1900) "Sur les changements de volume qui accompagment le dureissement des ciments," *Bull. Societe pour 1'Encouragement de l'Industrie Nationale*, **5**(5), 54–57.

Lea, F. M. (1970) *The chemistry of cement and concrete*, London: Arnold.

Li, Z. and Chau, C.K. (2000) "A new water permeability test scheme for concrete," *ACI Materials Journal,* 97(1), 84–90.

Li, Z., Li, F., Zdunek, A., Landis, E., and Shah, S. P. (1998) "Application of acoustic emission technique to detection of reinforcing steel corrosion in concrete," *ACI Materials Journal,* **95**(1), 68–76.

Li, Z., Peng, J., and Ma, B. (1999a) "Investigation of chloride diffusion for high-performance concrete containing fly ash, microsilica and chemical admixtures," *ACI Materials Journal,* **96**(3), 391–396.

Li, Z., Mu, B., and Peng, J. (1999b) "The combined influence of chemical and mineral admixtures upon the alkali–silica reaction," *Magazine of Concrete Research,* **51**(3), 163–169.

Li, Zongjin, Mu, B., and Peng, J. (2000) "Aklali–silica reaction of concrete with admixtures—experiment and prediction," *Engineering Mechanics, ASCE*, **126**(3), 243–249.

Lyman, C. G. (1934) *Growth and movement in Portland cement concrete*, London: Oxford University Press.

Mailvaganam, N.P. (1992) *Repair and protection of concrete structures*, Boca Raton, FL: CRC Press.

Mehta, P.K. (1980) "Durability of concrete in marine environment—a review," ACI SP-65, 1–20.

Mehta, P.K. (1988a) "Durability of concrete exposed to marine environment—a fresh look." In Malhotra, V.M., ed., *Concrete in marine environment*, ACI SP-109, 1–29.

Mehta, P.K. (1988b) "Sulfate resistance of blended cements." In: Ryan, W.G., ed. *Concrete 88 workshop*, Concrete Institute of Australia, pp. 337–351.

Mehta, P.K., and Monteiro, P.J.M. (2006) *Concrete: microstructure, properties and materials*, 3rd ed., New York: McGraw-Hill.

Mindess, S., Young, J.F., and Darwin, D. (2003) *Concrete*, New York: Prentice Hall.

Ministry of Development of the People's Republic of china (中华人民共和国建设部) (2007) Chinese Design Code of Concrete Structure Durability (混凝土结构耐久性设计规范).

Mitsui, K., Li, Z., Lang, D., and Shah, S.P. (1994 "Relationship between microstructure and mechanical properties of the paste–aggregate interface," *ACI Materials Journal,* **91**(1), 30–39.

Nawa, T. and Horita, T. (2004) "Autogenous shrinkage of high-performance concrete," *Proceedings of the international workshop on microstructure and durability to predict service life of concrete structures*, Sapporo, Japan.

Nguyen, V.H., Colina, H., Torrenti, J.M., Boulay, C., and Nedjar, B. (2007) "Chemo-mechanical coupling behavior of leached concrete, part I: experimental result; and part II: modeling," *Nuclear Engineering and Design,* 237(20/21), 2083–2097.

Page, C.L. (1992) "Nature and properties of concrete in relation to reinforcement corrosion," *Corrosion of Steel in Concrete, Aachen*, Feb. 17–19.

Popovics, S. (1973) "A numerical approach to the complete stress–strain curve of concrete," *Cement and Concrete Research* **3**(5), 583–599.

Powers, T.C. (1965) "Mechanism of shrinkage and reversible creep of hardened cement paste," *Proc. Intern. Conf. Struct. Conc*., London, pp. 319–334.

Price, W.H. (1951) "Factors influencing concrete strength," *ACI Journal Proceedings,* **47**(2), 417–432.

Satake, J., Kamakura, M., Shirakawa, K., Mikami, N., and Swamy, R. N. (1983) "Long term resistance of epoxy-coated reinforcing bars." In: Crane, A. P., ed., *Corrosion of reinforcement in concrete construction*, Chichestor, U.K.: The Society of Chemical Industry/Ellis Horwood, London, pp. 357–377.

Smith, L. L., Kessler, R. J., and Powers, R. G. (1993) "Corrosion of epoxy coated rebar in a marine environment," Transportation Research Circular, 403, Transportation Research Board, National Research Council, pp. 36–45.

Sun, W., Zhang, Y.M., Yan, H.D., and Mu, R. (1999) "Damage and damage resistance of high strength concrete under the action of load and freeze–thaw cycles," *Cement and Concrete Research,* **29**(9), 1519–1523.

Sun, W., Mu, R., Luo, X., and Miao, C. (2002) "Effect of chloride salt, freeze–thaw cycling and externally applied load on the performance of concrete," *Cement and Concrete Research,* **32**(12), 1859–1864.

Tang, M. (1987) "Studies on the effect of alkali in cement and concrete in China—a review," *Durability of Building Materials,* **4**(4), 371–376.

Trabanelli, G. (1986) "Corrosion inhibitors." In: Mansfield, F., ed., *Corrosion mechanism*, New York: Marcel Dekker, Chapter 3.

Troxell, G.E., Davis, H.E., and Kelly, G.W. (1968) *Composition and properties of concrete*, 2nd ed. New York: McGraw-Hill.

Ulm, F.J., Coussy, O., Li, K.F., and Larive, C. (2000) "Thermo-chemo-mechanics of ASR expansion in concrete structure," *ASCE Journal of Engineering Mechanics,* **126**(3), 233–242.

Valenta, O. (1969) "Kinetics of water penetration into concrete as an important factor of its deterioration and of reinforced corrosion," *RILEM international symposium on the durability of concrete*, Prague, part I, pp. 177–193.

Wang, P.T., Shah, S.P., and Naaman, A.E. (1978) "Stress–strain curves of normal and lightweight concrete in compression," *ACI Journal Proceedings,* **75**(11), 603–611.

Yip, W.K. (1998) "Generic form of stress–strain equations for concrete," *Cement and Concrete Research,* **28**(1), 33–39.

CHAPTER 6

ADVANCED CEMENTITIOUS COMPOSITES

In this chapter, the advanced cement-based composites, such as fiber-reinforced concrete, polymer-modified concrete, ultra-high-strength concrete, self-compacting concrete, and engineered cement composites, are introduced. Most of them have been developed recently and have unique advantages.

6.1 FIBER-REINFORCED CEMENTITIOUS COMPOSITES

6.1.1 Introduction

Fiber-reinforced cementitious composites (FRC) are cement-based composites incorporated with fiber, mainly short and discontinuous fibers. Although fiber-reinforced concrete has a long history, a steady increase in the use of FRC began in the 1960s. The development of FRC mainly attempts to overcome the two major deficiencies of cement-based composites: a relatively low tensile strength and a rather low energy consumption capacity or toughness. The functions of the fibers in cement-based composites can be classified into two categories: shrinkage crack control and mechanical property enhancement. For shrinkage crack control, usually small amounts of low-modulus and low-strength fibers are added to restrain the early-age shrinkage and to suppress shrinkage cracking (Shah, 1991). For mechanical property enhancement, fiber reinforcement has been employed in various concrete structures to improve flexural performance (Xu and Hannant, 1992; Maalej and Li, 1994), to increase impact resistance (Mindess et al., 1987), and to change the failure mode (Li and Leung, 1992).

The amount of fiber added has a significant influence on the mechanical properties and failure mode of FRC. Based on how much fiber is added, fiber-reinforced cementitious composites can be classified into three groups. FRC employing low fiber volume fractions ($<1\%$) utilize the fibers for reducing shrinkage cracking (Balaguru and Shah, 1992). FRC with moderate fiber volume fractions (between 1 and 2%) exhibit improved mechanical properties, including modulus of rupture (MOR), fracture toughness, and impact resistance. The fibers in this class of FRC can be used as secondary reinforcement in structural members, such as in partial replacement of shear steel stirrups (Batson et al., 1972; Sharma, 1986), or for crack width control in structures (Stang and Aarre, 1992; Stang et al., 1995). In the last decade or so, a third class of FRC, generally labeled high-performance FRC, or simply HPFRC, has been introduced. HPFRC exhibits apparent strain-hardening behavior by employing high fiber content. These HPFRCs include SIFCON, slurry infiltrated 5–20% of steel fibers (Naaman and Homrich, 1989), SIMCON, slurry infiltrated 6% steel fiber mat (Krstulovic-Opara and Toutanji, 1996), and Compacte Reinforced Composite (CRC) matrix, using 5–10% finer steel fibers (Bache, 1987). The tensile strain capacity of HPFRC is typically about 1.5%.

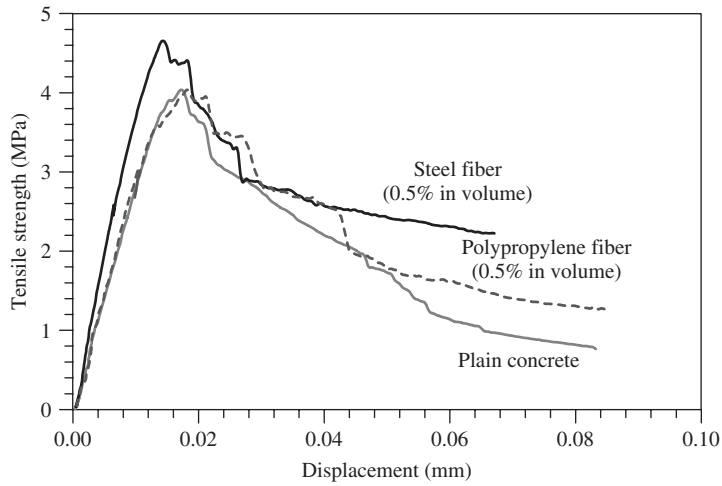

Figure 6-1 Load–displacement curves

In conventional applications of fiber cementitious composites, usually with a low volume fraction (V_f) of fibers (e.g., 0.5% steel fibers or 0.05% polypropylene fiber), the function of the fibers is apparent only after a major crack has formed in the composite. Although there is still only one major crack and the overall behavior of the composites is still characterized by strain softening after the peak load is reached, the incorporation of fibers leads to a significant increase in the total energy consumption and overall toughness of the composites, represented by the area under a stress–strain or load–displacement curve, as shown in Figure 6-1. In such cases, as long as there is no fiber fracture, the fiber debonding and pullout process can consume a great amount of energy. On the other hand, with an increase in fiber volume fraction, it is possible that microcracks formed in the matrix will be stabilized due to the interaction between the matrix and fibers through bonding, hence postponing the formation of the first major crack in the matrix. Thus, the apparent tensile strength of matrix can be increased.

Moreover, when a sufficient volume fraction of small-diameter steel, glass, or synthetic fibers is incorporated into the cement-based matrix, the fiber/matrix interaction can lead to strain hardening and multiple cracking behavior, changing the failure mode from quasi-brittle to ductile. As a result, not only the composites toughness, but also the matrix tensile strength can be significantly improved. One of the mechanisms in slowing down growth of a transverse crack in unidirectional fiber composites can be attributed to development of longitudinal cylindrical shear microcracks located at the boundary between the fiber and the bulk matrix, allowing the fibers to debond while transferring the force across the faces of the main crack. In addition to enhancing the toughness and tensile strength, the addition of fibers can also improve the bending resistance of cement-based composites. However, adding fibers has only a minor influence on the compressive strength of cement-based composites. At a small fiber volume fraction, there is almost no effect. Hence, it is not worthwhile to incorporate fibers for the purpose of enhancing compressive strength. The enhancing order of fibers on the mechanical properties of cement-based composites is toughness > flexural strength > tensile strength > compressive strength.

Although fibers can improve the mechanical properties of cement-based materials, it is important, to recognize that, in general, fiber reinforcement is not a substitute for conventional reinforcement or rebars. Fibers and rebars have different roles to play in contemporary concrete technology, and there are many applications in which both are used.

6.1.2 Factors influencing the properties

The properties of fiber-reinforced, cement-based composites can be influenced by many parameters, such as fiber type, fiber amount, matrix variation, and manufacturing methods. In this section, these parameters are discussed in detail.

(a) *Fiber type*: The fiber type can be viewed with different criteria. From the size point of view, fibers can be classified into macro- and microfibers. The diameter of macrofibers is in the range of 0. 2 to 1 mm and for microfibers is in a range of a few to tens of micrometers. Basically, microfibers are efficient in restraining microcracks and macrofibers in restraining macroscopic cracks. From the materials point of view, the fibers that are commonly used in fiber reinforced cement-based composites are carbon, glass (borosilicate and alkali resistant), polymeric (acrylic, aramid, nylon, polyester, polyethylene, polypropylene, and poly vinyl alcohol), natural (wood cellulose, sisal, coir or coconut, bamboo, jute, akwara, and elephant grass), and steel (high tensile and stainless). Different types of fibers have different values of Young's modulus, different tensile strength, different surface texture, and different elongation ability, as can be seen in Table 6-1. These characteristics influence the bond between the fibers and the matrix, crack-restraining ability, matrix property enhancement, and, hence, the global behavior of fiber-reinforced, cement-based composites as a whole.

Steel fiber is the most widely used fiber in cement-based composites, having a high modulus, high fractural strain, and high tensile strength. Steel fibers have a large distribution of diameters, and range from microfiber to macrofiber. Steel has various shapes and surface textures, as shown in Figure 6-2. Steel fibers with deformed shapes of ribs or hooks and rough surfaces are good in bond strength. One disadvantage of the steel fiber is its high specific gravity, which can increase the dead load of a composite.

Glass fiber is also commonly used in FRC, in the form of filaments. Each glass strand bundle has 204 filaments. Glass fibers are supplied in a continuous roving and can be chopped into short fibers, using a commercially available chopper. Glass fibers have high tensile strength and high fracture strain, but low modulus. Moreover, ordinary borosilicate glass fibers (E-glass) and soda-lime glass fibers (A-glass) can be easily attacked by alkali solution in cement-based composites and are thus less durable and should be used with caution. Alkali-resistant glass fibers (AR glass) contain about 16 to 20% of zirconia (ZrO_2), which protects the fibers from high alkali attack. AR glass is the most popular glass fiber used in cement-based composites. Disadvantages of glass fibers include low resistance to moisture, sustained loads, and cyclic loads.

Carbon fibers possess much higher strength and stiffness than glass fibers but are far more expensive. The strength of carbon fibers ranges from 2.2 to 5 GPa, modulus from 800 to 250 GPa, and the ultimate strain from 0.3 to 1.8%. The specific gravity ranges from 2.2 for a high-modulus

Table 6-1 Properties of different types of fibers

Fiber	Diameter (μm)	Specific Gravity	Tensile Strength (GPa)	Elastic Modulus (GPa)	Fracture Strain (%)
Steel	5–500	7.84	0.5–2.0	210	0.5–3.5
Glass	9–15	2.6	2.0–4.0	70–80	2.0–3.5
Fibrillated polypropylene	20–200	0.9	0.5–0.75	5–77	8.0
Cellulose	—	1.2	0.3–0.5	10	—
Carbon (high strength)	9	1.9	2.6	230	1.0
Cement matrix for comparison	—	2.5	3.7×10^{-3}	10–45	0.02

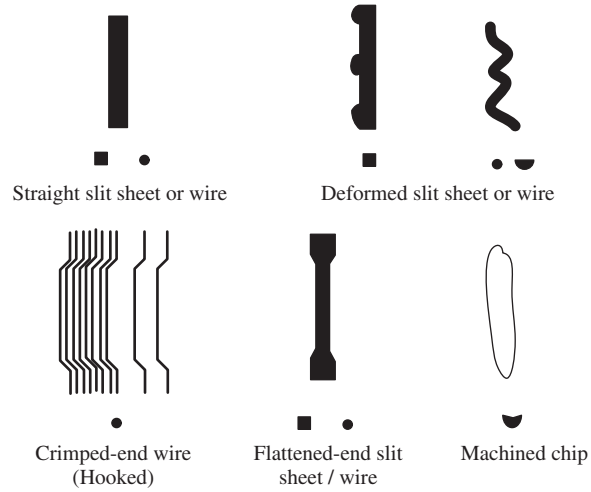

Figure 6-2 Different shapes and surface textures of steel fibers

fiber to 1.8 for a low-modulus fiber. The stronger fibers are associated with lower moduli and higher ultimate strain. Besides high strength and stiffness, carbon fibers also possess excellent resistance to moisture and chemicals, and are insensitive to fatigue. The weaknesses of carbon fiber are its low impact resistance, low ultimate strain, and high price.

Polypropylene fiber has the lowest density, the highest fracture strain, and reasonable tensile strength, but its modulus is quite low. Polypropylene fiber has both microfiber and macrofiber sizes.

To get multiple-cracking and strain-hardening responses, two fundamental requirements have to be satisfied when a fiber is selected. First, the fibers should be strong enough to carry the total load at the position of the first matrix transverse crack. Second, the bond at the fiber–cement interface should be strong enough to transfer the forces from the fiber to the matrix and thus build up the tensile stress in the matrix. According to previous studies, polyvinyl acetate (PVA) fiber shows a very promising potential in improving the interfacial bond and achieving multiple cracking.

(b) *Fiber volume ratio*: Another important factor that greatly influences FRC properties is the fiber volume fraction ratio, which is defined as the ratio of the fiber volume to the total volume of FRC. As mentioned earlier, at a low fiber volume ratio, the addition of fibers mainly contributes to the energy-consuming property. At a higher fiber volume fraction ratio, the tensile strength of the matrix can be enhanced and the failure mode can be changed.

For a low fiber volume fraction case, the ultimate stress of FRC is usually reached when the matrix reaches its ultimate stress. According to the rule of mixtures, the ultimate strength of the composites can be written as

$$\begin{aligned}\sigma_{cu} &= V_m\sigma_{mu} + V_f\sigma_f \\ &= V_m E_m \varepsilon_{mu} + V_f E_f \varepsilon_{mu} \\ &= V_m E_m \varepsilon_{mu} + V_f \frac{E_f}{E_m}\sigma_{mu}\end{aligned} \tag{6-1}$$

where σ_{cu} = ultimate stress in fiber-reinforced concrete
σ_{mu} = ultimate stress in the matrixo
σ_f = stress in the fiber
E_m = Young's modulus of matrix
ε_{mu} = ultimate strain
V_m = matrix volume ratio
V_f = fiber volume ratio

For a high fiber volume fraction, the ultimate strength is essentially determined by the ultimate strength of the fibers, σ_{fu}, as the matrix's contribution can be ignored due to cracking. Hence,

$$\sigma_{cu} = V_f \sigma_{fu} \tag{6-2}$$

where σ_{cu} = ultimate stress in fiber-reinforced concrete
σ_{fu} = ultimate stress of fiber
V_f = fiber volume ratio

If we plot Equations 6-1 and 6-2 as a function of V_f, Figure 6-3 can be obtained. The intersection of the two lines separates the failure modes of the single crack and multiple cracks. Thus, by equating the above two equations, the minimum fiber volume fraction for obtaining multiple cracks failure mode can be obtained as

$$V_f^{\text{minimum}} = \frac{\sigma_{mu}}{\sigma_{fu} + \left(1 - \dfrac{E_f}{E_m}\right)\sigma_{mu}} \tag{6-3}$$

It can be seen from Equation 6-3 that the critical fiber volume fraction depends only on the fiber and matrix ultimate strength, according to the theory applied here. However, in a real situation, many other factors, such as the bond between the fiber and the matrix and the ultimate strain of the fiber, can influence the minimum fiber volume ratio that is required to obtain a multicrack failure mode.

(c) *Matrix variation*: The properties of the matrix influence the bond with the fibers and the mechanical properties of FRC, such as ultimate tensile strength. The FRC matrix can be modified using mineral admixtures, such as fly ash, slag, silica fume, and metakaolin. It can also be modified by adding some water-soluble polymers. Changing the matrix composition can

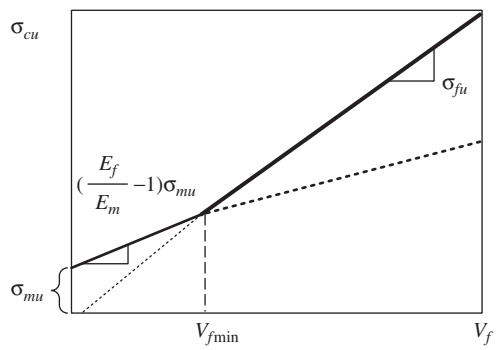

Figure 6-3 Relationship between stress and fiber volume fraction

increase the bond properties with the fibers, improve the matrix toughness, and enhance the matrix tensile strength and, hence, the mechanical properties of FRC.

(d) *Processing methods*: Recent studies have shown that the response of fiber-reinforced composites also depends on the methods of processing. The commonly used industrial processing methods for producing FRC products include the Hatschek process, normal casting, the pultrusion process, the Reticem process, and the extrusion process. Different processing methods produce FRC products with different densities, and bonds and, hence, different mechanical properties. The Hatschek process was originally developed for producing FRC products with asbestos fibers using a dewater process, as shown in Figure 6-4. However, as more and more countries have restricted the use of asbestos fiber due to health considerations, the process is now mainly used to produce thin-wall products, such as sidings, using cellulose fibers. The normal casting method is the same as for normal concrete casting. The Hatschek process and casting are suitable only for short and discrete fibers. Both the pultrusion process and Reticem process are used for FRC products with continuous fibers. The pultrusion setup is shown in Figure 6-5. It can be seen that after passing through a slurry bath, the fibers are enforced by passing through a die or by forming a designed shape by the filament method. Here pultrusion was employed to incorporate continuous fibers into the cement matrix. Composites with a fiber volume ratio of more than 10% can be produced. The strain-hardening type of response was the direct result, with a tremendous enhancement in tensile strength.

Extrusion technology is an economical mass-production method. A typical extrusion process is shown in Figure 6-6. During the extrusion process, the dough-like material is pushed out through a die by an augur. The advantages of extrusion in producing FRC products are that the

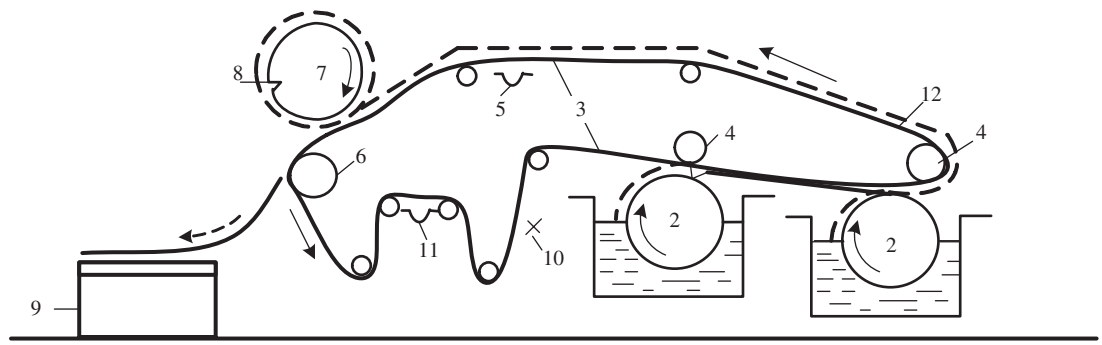

Figure 6-4 The Hatschek process

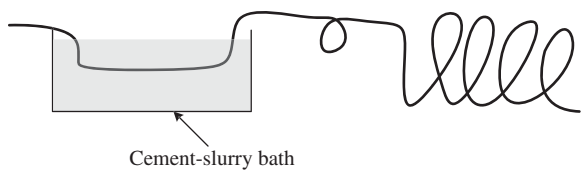

Figure 6-5 The pultrusion process

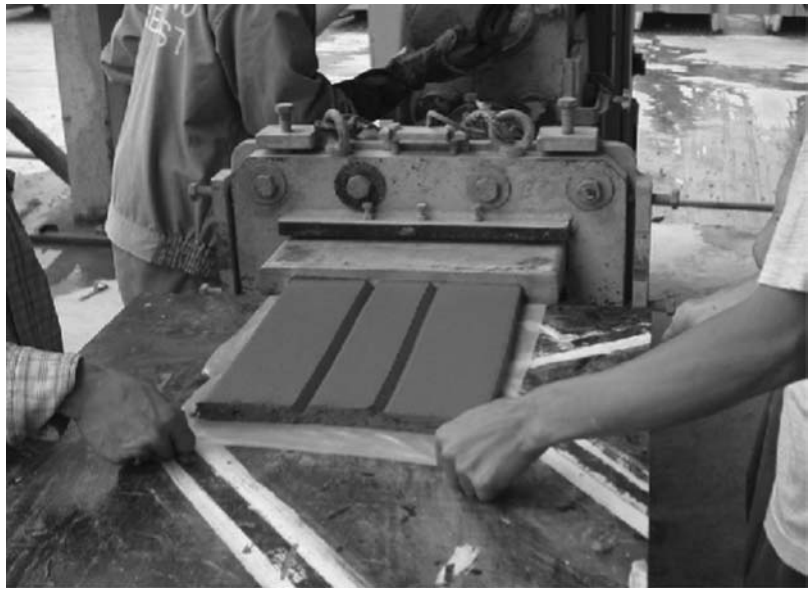

Figure 6-6 The extrusion process

products formed under high shear and high compressive forces are denser and stronger, fiber alignment is controllable, and the product shape is flexible and good for mass production. With properly designed dies and properly controlled material mixes and viscosities, the fibers can be aligned in a load-bearing direction. Thus, extrusion can lead to a strain-hardening type of response. It is obvious that special processing compacted matrices with fibers of a low porosity controls fiber direction and distribution and improves the interfacial bond between the fibers and the matrix, which, in turn, leads to a class of high-performance fiber-reinforced composites with strain hardening. Extruded specimens can achieve a better performance than cast specimens, provided other conditions are similar.

Nowadays, except for the traditional products, such as bricks, tiles, and pipes, finely structured ceramic honeycomb units and completely shaped plastic doors and windows can also be produced using the extrusion technique. The advantages of the extrusion technique lie in its mass production capability, product manufacture flexibility, its ability to manufacture products with complicated shapes, and its capability of improving the material properties under high shear and high compressive force. Great research attention has been devoted to the feasibility of applying the extrusion technique in the manufacture of cement-based materials. Shao et al. (1995) at Northwestern University experimented with a screw-type extruder and successfully extruded various types of products, including sheets and tubes. They proved that extrusion is a promising alternative for fabricating cement composites with short fiber reinforcement. Stang and Pedersen (1996) applied the extrusion technique to pipe manufacture. They developed a novel type of extrusion that combines the ease of material mixing and only a few requirements for material preprocessing, with a high degree of accuracy and stability of the newly extruded material. Li and Mu (1998) extruded fiber-reinforced cement-based thin plates with a width to thickness ratio of 50:1. Li et al. (1996) studied the influence of mineral admixtures such as silica fume and metakaoline on cement-based extrudates, and showed beneficial effects and formulation hits. Li et al. (2005) have successfully extruded short-fiber-reinforced geopolymer thin plates (6 mm

thick) and made a significant improvement in extrudate formulas. Generally speaking, the matrix formed through the extrusion process is dense and good in flexural strength. It can provide a seal effect for the phase-changing materials.

6.1.3 Fiber–cement bond properties

Since the bond between the fiber and cement matrix plays a very important role in FRC, significant research activity has been conducted to characterize the interfacial bond properties and fiber debonding and pullout behavior. Theoretically, two analytical approaches have been developed to interpret the material properties for fiber debonding and pullout problems (Stang et al., 1990): stress-based and energy release rate-based approaches. According to the stress-based criterion, debonding of the fiber from the matrix will take place when the maximum shear stress at the interface reaches a critical value. According to the energy release rate criterion, debonding will propagate only when the energy flowing into the interface exceeds the value of the specific resistance energy.

The fiber cement bond properties can be measured by a pullout test. Fabrication of the specimens for pullout testing is complicated and can be achieved using different methods. Li et al. (1991) have utilized a specially made brass mold to prepare specimens. A brass-guided plate with 16 holes was used to provide alignment of fibers during construction. Small springs attached to the frame of the mold were used to keep the fibers straight. During testing, this guide plate was used to separate the pullout section of the specimen from the anchored end and to provide for the transfer of the load. Since measurement of debonding on only one side (bottom portion) was desired, epoxy droplets were placed on the other side (top portion) of the specimens, thus providing anchorage of the fibers in the matrix. Hence, it could be reasonably assumed that the slip of the fiber during the tests would occur only on the pullout side. Furthermore, one specimen was prepared with epoxy-resin anchorage provided on both sides. This specimen was used to measure the deformation of the fiber inside the guide plate, which was subsequently subtracted from the slip displacement of pullout test specimens, as described in the following sections.

The specimen being held in the mechanical fixture is shown in Figure 6-7. The specimen is connected to the U-shaped loading fixture by means of a stainless steel rod (loading rod) 6.3 mm

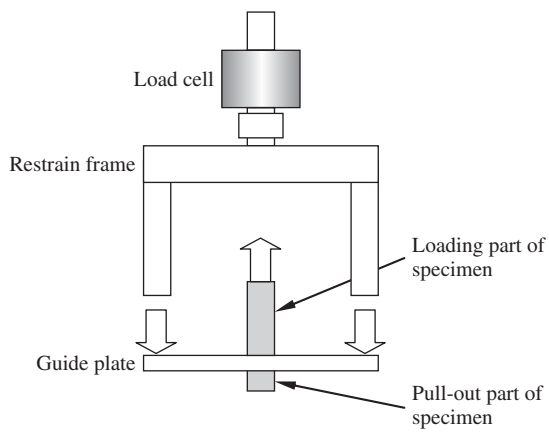

Figure 6-7 Specimen being held in the mechanical fixture

(0.25 in.) in diameter. The loading fixture is connected to the servo hydraulic actuator and the entire specimen fixture moves with the actuator. A restraining frame that can make contact with the specimen's brass guide plates is connected to a load cell and is used to resist the upward movement of the guide plate. Subsequently, load is transferred from the brass guide plate to the matrix. This load is being reacted against by the fibers, which are the only means of connecting the top and bottom portion of the specimen. The load is transferred to the top of the specimen and thereafter to the loading fixture through bending of the loading rod.

Two extensometers (1.905 mm or 0.075 in. range) mounted across the guide plate with a 12.5-mm (0.5-in.) gage length were used to measure the slip displacement of the fiber debonding and pullout. The average output of the extensometers was used as the feedback signal in the control of the servo hydraulic system. The pullout tests were performed at a rate of 0.0254-mm opening of extensometer transducers per minute. Once the magnitude of slip exceeded the transducers range, the mode of the control was switched to stroke control and the entire fiber length was pulled out of the matrix.

A typical pullout load–slip displacement plot is shown in Figure 6-8. It can be seen from the figure that, originally, the load and displacement had a linear relationship. Then, nonlinear behavior appears until the leak load is reached. After that, a sudden drop of the load is experienced and is followed by a gradual decrease of the load with displacement, representing a fiber pullout from the matrix. By utilizing the characteristic points on the curve, the interface properties, such as the interface stiffness parameter, shear bond strength, frictional bond strength, and surface energy, release rate can be interpreted, as demonstrated by Li et al. (1991).

Typical pullout fibers from a three-point bending test are demonstrated in Figure 6-9. It can be seen that the steel fibers are kept intact after being pulled out, and the two sides have similar amounts of fiber left. This proves that the pullout test can reflect the true situation in fiber-reinforced, cement-based composites under mechanical loading.

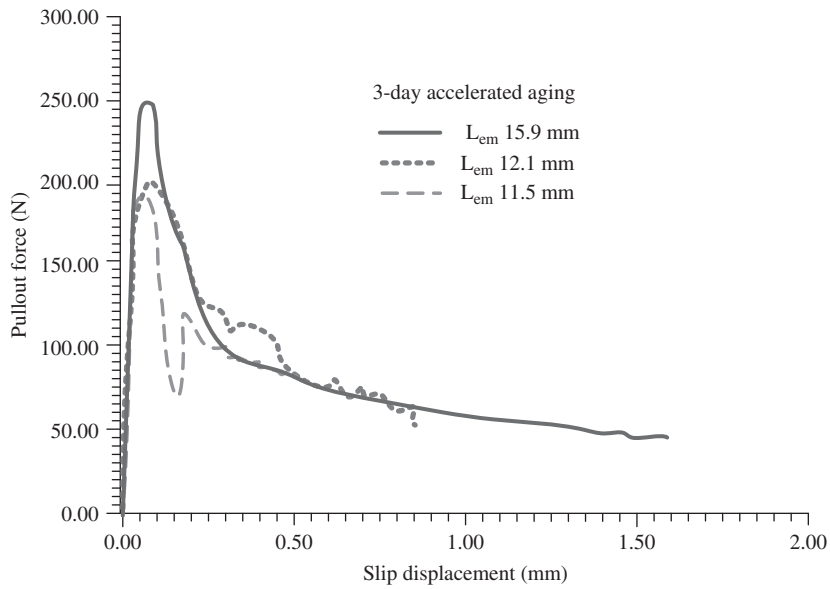

Figure 6-8 Experimental results of fiber pullout test

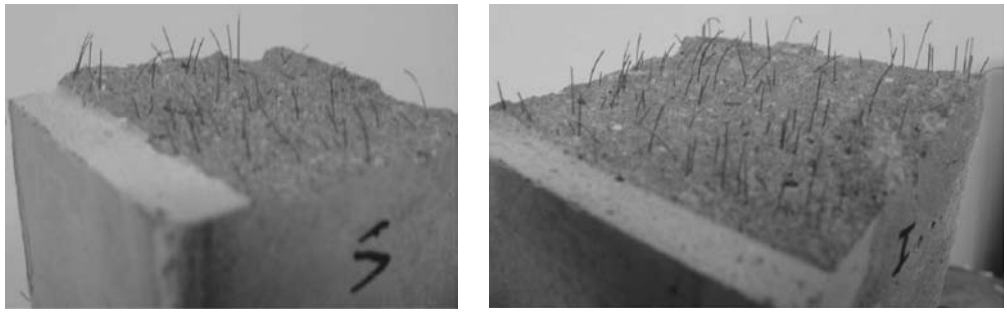

Figure 6-9 Typical pullout fibers from a three-point bending test

6.1.4 Mechanical properties

As mentioned earlier, the incorporation of fibers into cement-based composites mainly improves their toughness, bending, and tensile properties. In this section, we discuss the effect of fibers on these properties.

(a) *Tension*: Incorporation of fibers into cement-based composites can largely improve the tensile behavior of the composites, including toughness, tensile strength, and failure mode. Usually, fiber-reinforced cement-based composites can be classified into two categories, according to their global tensile responses: strain softening or strain hardening. The strain-softening type of fiber-reinforced cement-based composites is usually reinforced with a low volume of short fibers. This kind of composite, containing about 1% fiber, is typically used for bulk field applications involving massive volumes of concrete. Figure 6-1 illustrates the tensile responses of such composites, with the incorporation of low-volume fiber fraction. For comparison, it also shows the stress–deformation curves for a plain concrete specimen. For steel fiber-reinforced concrete specimens, the length, diameter, and volume fraction of the steel fiber are 48 mm, 0.5 mm, and 0.5%. For polypropylene fiber-reinforced concrete specimens, the length and volume fraction of the fibrillated polypropylene fiber are 50 mm and 0.5%. It can be seen from the figure that although all the specimens display a softening behavior after the peak load is reached, the areas under the load–deformation curve are different and are larger for fiber-reinforced specimens than for plain concrete specimens. This implies that the fiber-reinforced specimens require more energy for fracture than do the plain concrete specimens. For a strain-softening type of failure, usually only one major crack is formed in the specimen. The fracture process of the material can be divided into four stages: the linear elastic stage (0–35% of peak load), the randomly distributed damage stage (35 to about 80% of the prepeak load), the microcrack localization stage (during the loading period between 80% of pre-peak load and 80% of post-peak load), and the major crack propagation stage (the period after 80% of post-peak load).

A failure mode with multiple matrix cracking can be obtained when the cement-based composite is reinforced with either a high-volume fraction of short fibers or with aligned continuous fibers. Such high-volume fiber composites have been used in thin sheets (e.g., curtain walls), slurry-filled cementitious composites, and concrete. A typical strain-hardening curve for steel fiber-reinforced cementitious composites is shown in Figure 6-10. There is a special point (marked B on the curve) called the *bend over point* (BOP) at which the matrix contribution to the tension capacity reaches a maximum. The stress–strain curve shown in the figure can be roughly divided into four stages. Stage 1 is from O to A in the figure, which is characterized by the elastic behavior of the composite until a few microcracks are initiated and are randomly

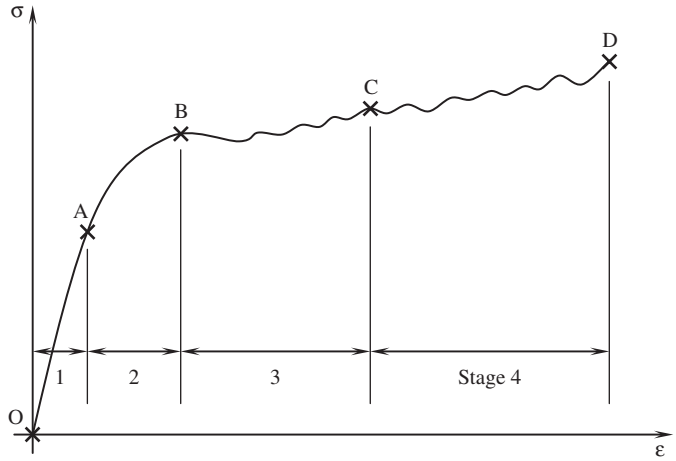

Figure 6-10 Strain-hardening behavior of steel fiber-reinforced cementitious composite

dispersed at end of this stage. Stage 2 is from A to B. In this stage, randomly distributed microcracks start to localize and form the first major crack across the specimen's cross section at point B. The BOP corresponds to the end of stage 2. The third stage is from B to C. In this stage, the incremental loading carried purely by the fibers at the position of the first crack is transferred back to the matrix through the bond and this process builds up the tensile stresses in the matrix again. When the tensile stress exceeds the tensile strength of the matrix, the next matrix crack will form. The multiple cracking process continues until the minimum crack spacing is reached, at which the tensile stress is transferred from the fibers back to the matrix cannot reach the tensile strength of the matrix. The process leads to an almost uniform distribution of fine matrix cracks. The fourth stage is from C to D. In this stage, no further matrix crack is expected and the additional load is sustained only by the fibers until failure of the fibers is reached. The phenomenon of strain hardening with multiple cracks is observed not only for continuous fiber-reinforced, cement-based composites, but also for short fiber-reinforced concrete. Figure 6-11 shows the test results of short steel fiber-reinforced concrete under uniaxial tension test (Li and Li, 1998).

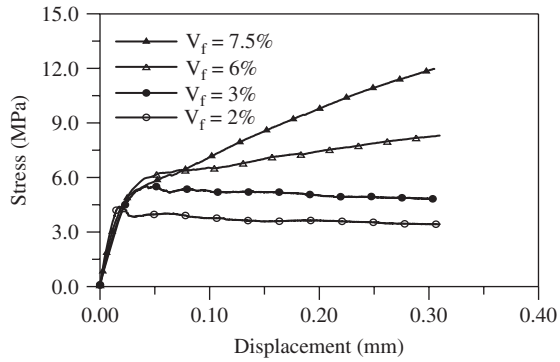

Figure 6-11 Tensile response of short steel fiber-reinforced concrete

The steel fiber used has a length of 32 mm, and an equivalent diameter of 0.8 mm with a tensile strength of 810 MPa and Young's modulus of 200 GPa.

It can be seen from the figure that with the increase of the fiber volume fraction ratio, not only is the area under stress–strain curves increased, but the tensile strength is also increased. Moreover, the failure mode changes from strain softening to strain hardening. To study the multiple cracking and associated interfacial bond behavior, experiments have been conducted on the cementitious composites reinforced with continuous glass, polypropylene, and steel fibers. Three recently developed techniques—laser holographic interferometry, quantitative optical microscopy, and MOR interferometry—were employed in the investigation.

So far, the applications of FRC in structural components are limited for inhibiting cracking, improving resistance to impact or dynamic loading, and resisting material disintegration, such as for airport runways and pavements. The limitation of the applications of FRC is partly due to the high cost of the fibers. For example, for steel fiber-reinforced concrete (SFRC), 1% by volume will increase the cost by US$52 per cubic meter of concrete.

(b) *Bending*: Fiber-reinforced, cement-based composites can achieve very good flexural strength and ductility. Figure 6-12 shows that an extruded fiber-reinforced, cement-based plate exhibits a larger deflection under four-point bending. Figure 6-13 shows the load–deflection curves for an extruded thin FRC plate. It can be seen from the figure that there is larger deformation with a reasonably high stress, hence the area under the stress–strain curve is larger. The area under the load–deflection curve for bending can be used as an index to estimate the energy-absorbing capacity or toughness of the material. Increased toughness also means improved performance in resisting fatigue, impact, and impulse loading. Moreover, the improved toughness also leads to a better ductility.

To characterize the toughness of FRC beam specimens under bending, the concept of toughness index has been proposed. The toughness index utilizes a ratio of the area under the

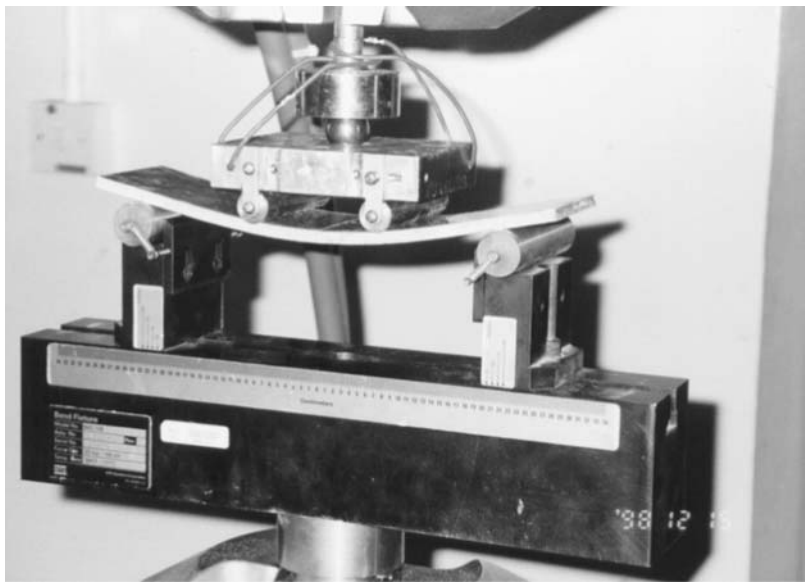

Figure 6-12 Large deflection of an extruded thin plate

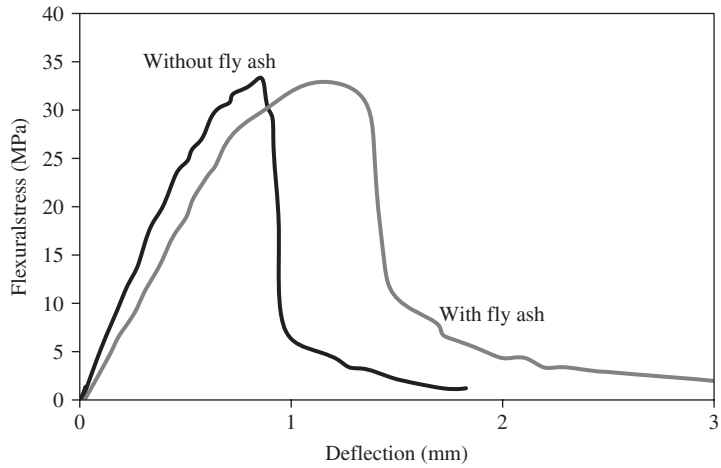

Figure 6-13 Stress–deflection curves of an extruded FRC thin plate

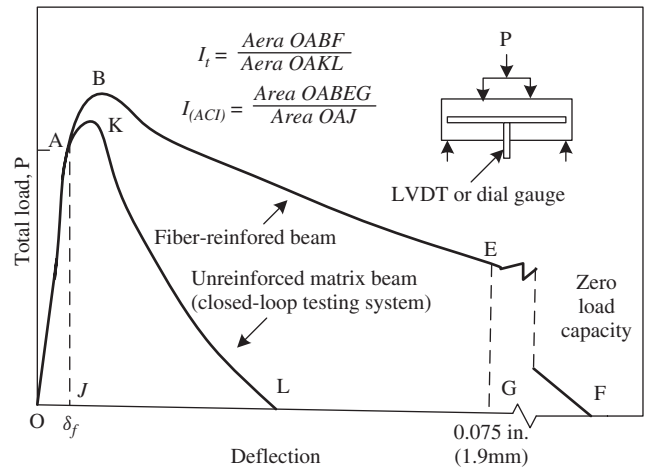

Figure 6-14 Definition of toughness index by ACI

load–deflection curve of an FRC beam up to a specified deflection value to the area upto the first crack, or simply an area up to a specified deflection value. For instance, the ACI Committee 544 defines the toughness index as the ratio of the area of the load–midspan deflection curve to 1.9 mm to the area of the curve up to the first cracking, as shown in Figure 6-14. ASTM C1080 defines three toughness indexes, I_5, I_{10} and I_{30}, as follows:

$$I_5 = \text{area of the load–midspan deflection curve to } 3\delta/\text{area of the curve up to } \delta$$

$$I_{10} = \text{area of the load–midspan deflection curve to } 5.5\delta/\text{area of the curve up to } \delta$$

$$I_{30} = \text{area of the load–midspan deflection curve to } 15.5\delta/\text{area of the curve up to } \delta$$

where δ is the deflection of the beam corresponding to the first crack of the beam under bending. As shown in Figure 6-15, I_5, I_{10}, and I_{30} roughly represent the areas of 5, 10, and 30 times the

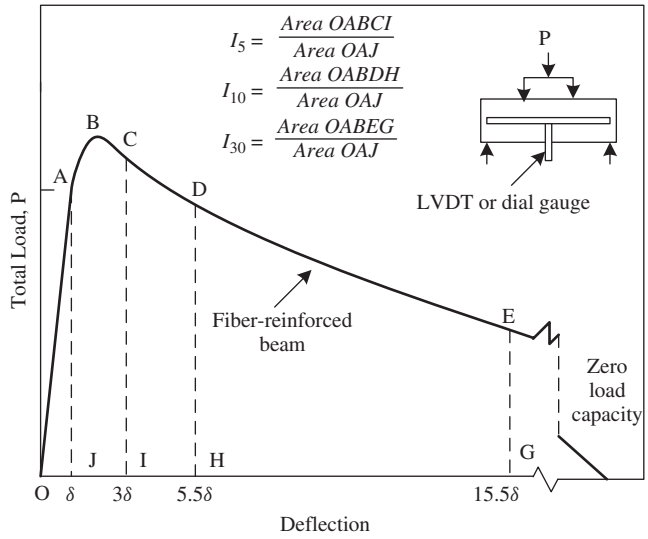

Figure 6-15 Definition of toughness index by ASTM

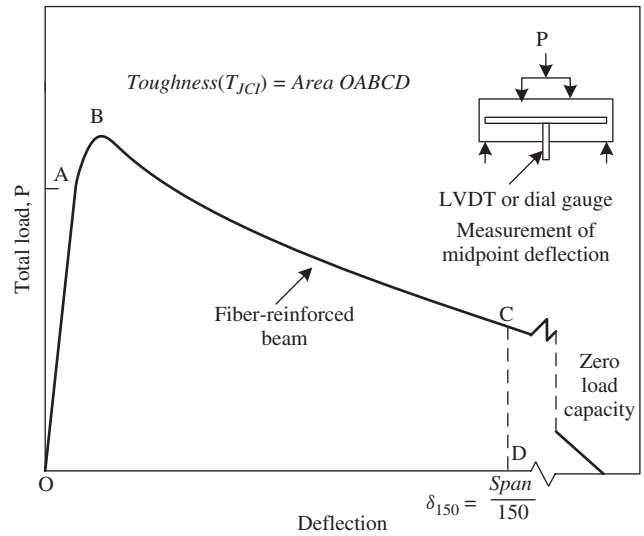

Figure 6-16 Definition of toughness index by JCI

area up to the first crack. The Japan Concrete Institute defines the toughness index as the area of the load–midspan deflection curve up to the value of 1/150 span, as shown in Figure 6-16.

6.1.5 Hybrid FRC

As mentioned earlier, fibers can be distinguished as microfibers and macrofibers, according to their normal diameter and length. Fibers are also made from different materials that bring different properties into different fibers. A hybrid FRC uses more than two different fibers simultaneously

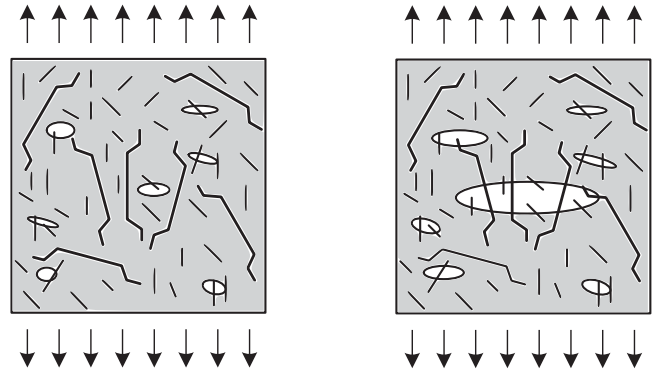

Figure 6-17 Hybrid macrofiber- and microfiber-reinforced cementitious composite

to optimize their advantages. For example, by incorporating micro- and macrofibers into a cement-based composite at same time, the microfibers can restrain the development of the microcrack, while the macrofibers can control the propagation of macrocracks, as shown in Figure 6-17. Hence, the benefits of different size scales in restraining different size of crack can be fully utilized.

Recently, Chen and Qiao (2010) demonstrated that a proper hybrid combination of steel fibers and polyvinyl alcohol (PVA) microfibers enhances the resistance to both crack nucleation and crack growth. On the other hand, combining different types and lengths of fibers can optimize the performance of FRC for specific benefits, such as improved processing, improved mechanical performance, improved durability, and reduced cost. Yao et al. (2003) have constructed three types of hybrid composites using fiber combinations of polypropylene (PP) and carbon, carbon and steel, and steel and PP fibers. Their test results showed that the fibers, when used in a hybrid form, could result in superior composite performance compared to their individual fiber-reinforced concretes. Among the three types of hybrids, the carbon–steel combination gave concrete of the highest strength and flexural toughness, because of the similar modulus and the synergistic interaction between the two reinforcing fibers. Peled et al. (2000) studied the performance of extruded thin sheet with hybrid fibers and found that the bending properties can be significantly improved, as shown in Figure 6-18. A preliminary study on the hybrid FRC has demonstrated the good potential of such a composite, but how to get uniform dispersion of the different fibers remains a big issue in this type of composite.

6.1.6 FRC products

Based on the matrix composition, fiber volume fraction, type of fibers, and manufacturing process, many fiber-reinforced, cement-based products can be manufactured. The following products are introduced due to their common applications in practice or potential utilization in the future.

Fiber-reinforced concrete: Concretes contain coarse aggregates, and the existence of coarse aggregates in the matrix, brings some difficulties for fiber distribution or dispersion. Thus, the volume fraction of fibers is highly limited. For fiber-reinforced concrete used in practice, the applicable fiber volume fraction ranges from 0.4 to 2% for steel fibers and 0.06 to 0.5% for polypropylene fibers. The matrix is usually proportioned following the procedures used for plain concrete.

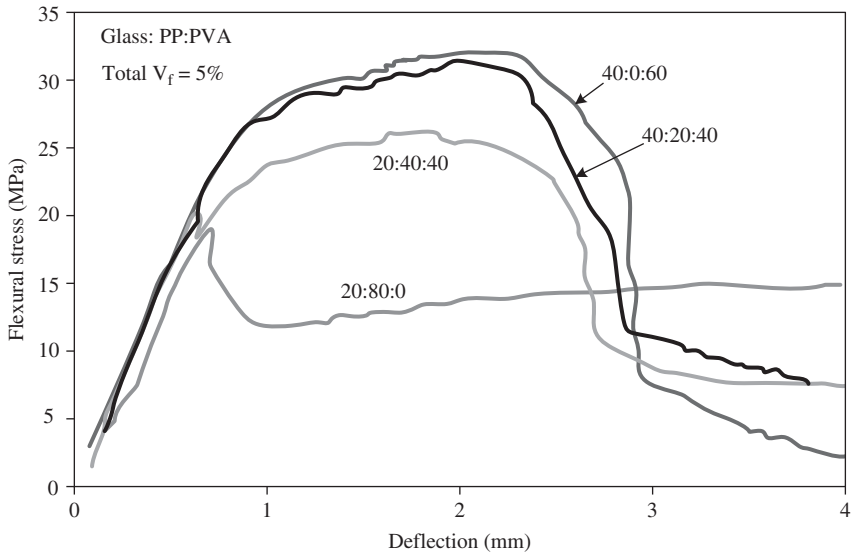

Figure 6-18 Flexural response of hybrid composites combing glass/PP/PVA fibers (Peled, et. al., 2000)

Fiber-reinforced mortar: Since mortar contains only fine aggregates, it is relatively easier to incorporate a larger amount of fibers into the matrix. The fiber volume fraction ranges from 1 to 5%. It applies to a wide range of manufactured products, such as glass fiber-reinforced sheets, polymeric fiber-reinforced panels, and tiles.

Fiber-reinforced cement paste: There are no aggregates in cement paste, so the incorporation of fiber is much easier. Larger amounts of fibers can be incorporated, with volume fractions ranging from 4 to 10% or up.

Slurry-infiltrated fiber concrete (SIFCON): SIFCON is a special type of fiber-reinforced cement paste or mortar, which is produced by infiltrating a bed of fibers with cement or mortar slurry (Naaman, 1992). Since the fibers are placed into the mold (bed) by hand, large amounts of fiber can be added, with volume fractions from 4 to 22%. This type of high-volume steel-reinforced cement composite has demonstrated a unique high performance and hence attracted great attention. Table 6-2 compares the mechanical properties of SIFCON with normal FRC. It can be seen that SIFCON can largely increase the compressive strength of the composites due to a large amount of steel fibers added. At such a high percentage, the

Table 6-2 Comparison of properties of SIFCON with normal FRC

Property	SIFCON	FRC
Compressive strength (psi)	12,000–22,000	5000–8000
Flexural strength (psi)	4000–8000	1000–2000
Compressive/Flexural	About 3:1	4–5:1
Strain at failure	0.02–0.08	0.005–0.01
Modulus	3–6	3–6

fibers contribute not only directly to the compressive resistance of the composite through parallel support, but also indirectly to the resistance through the confining effect on the matrix. The flexural strength of SIFCON can reach 60 MPa, which is about 4–10 times that of normal FRC. Moreover, SIFCON demonstrates much better ductility than normal FRC. The ratio of compressive strength to flexural strength is 3 and the fracture strain can reach 8%. Hence, SIFCON can be treated as an ultra-high-performance, cement-based composite. However, it requires a hand layup to make a fiber bed and thus is time-consuming.

Compacted reinforced composite: The compacted reinforced composite is made of cement, silica fume, steel microfibers, fine aggregate, and rebars. The fiber volume ratio can reach 15% and up. Fibers in such large quantities fundamentally alter the nature of cementitious matrices. The responses clearly indicate the large increase in both strength and ductility. Microcracking is stabilized, and homogeneous distribution of microcracks can be found even at very high strain levels of 1%, which is 100 times the strain of plain concrete. Thus the bending capacity of a beam made up of this kind of material approximates to that of structural steel.

Extruded fiber-reinforced products: As discussed earlier, extrusion is a good method for producing high-quality fiber-reinforced, cement-based composites. In the last few decades, the extrusion technique has been utilized in laboratories for new product development, and in industry for mass production. Along this line, researchers at Northwestern University and the Hong Kong University of Science and Technology have studied the feasibility of applying the extrusion technique in the manufacture of short-fiber-reinforced, cement-based materials. Shao et al. (1995) have successfully extruded various types of products, including sheets (6 mm thick and 75 mm wide) and tubes. Stang and Pedersen (1996) applied the extrusion technique specifically in pipe manufacture. They developed a novel type of extrusion combining ease of material mixing and few requirements for material preprocessing, with a high degree of the accuracy and stability of the newly extruded material. Mori and Baba (1994) produced molded cementitious products by screw extruders. Their work mainly focused on material aspects of the extrusion process control. A series of experiments were performed by them to show the relationship between particle size (silica sand), extrusion velocity and pressure, water cement ratio, and flexural strength for plates 12 mm in depth and 60 mm in width. Li and Mu (1998) have extruded a wide and thin sheet, with cross section of 6 mm × 300 mm, using a single screw and a two-section vacuum extruder. The barrel of the above extruder is 100 mm in diameter. In the extrusion process, elastic and viscous properties were studied by a coaxial cylinder rheometer (Rheocord 9000, HAAKE) to obtain smooth and homogeneous products under continuous operation. HKUST also manufactured products with the incorporation of foam plastic and phase-changing material for heat insulation purposes, as shown in Figure 6-19. Such products are very light with a unit weight less than 800 kg/m^3, and can float on water. Li et al. (2004) studied the heat resistance of the extruded product with the incorporation of perlite. In addition, imitation wood-products using wood particles or dust have also been developed, as shown in Figure 6-20. These products can be sawed and nailed, just like wood.

The extrusion technique has been transferred into industry-scale production. Figure 6-21 shows a wall panel with a hollow cross section being extruded out of the die and on the conveyor belt. The panel has a cross section of 60 × 600 mm, with a hollow area ratio of 50%. Several other types of products have also been manufactured. One is a panel of solid cross section, with the incorporation of expanded perlite or foam plastic. Such a product is very light and has very good heat and acoustic insulation properties. Moreover, the panel is very easily machined, as

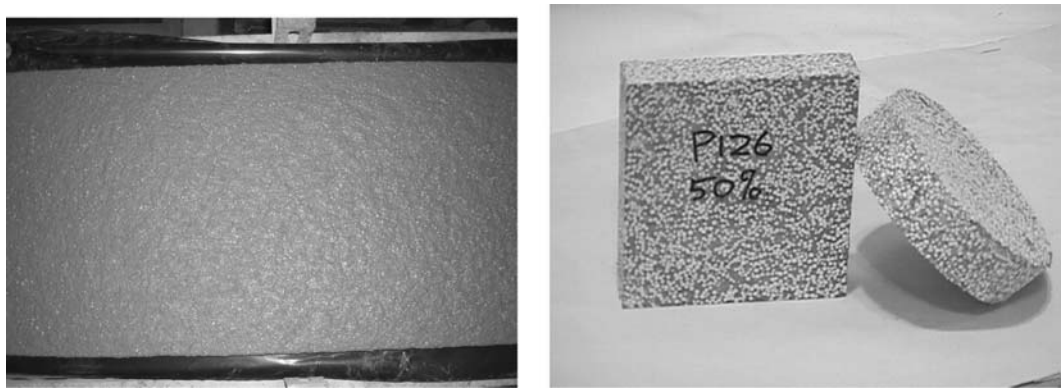

Figure 6-19 Extruded heat insulation products

Figure 6-20 Extruded imitation wood-products

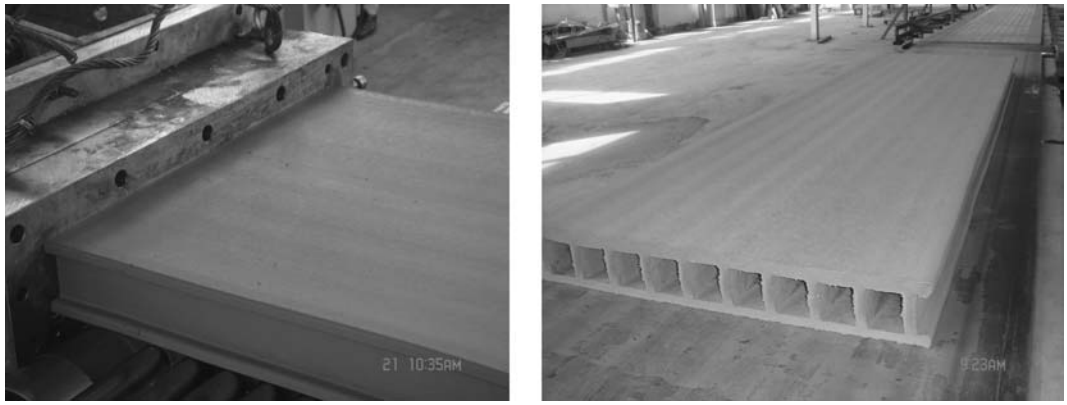

Figure 6-21 Extrusion process in a plant

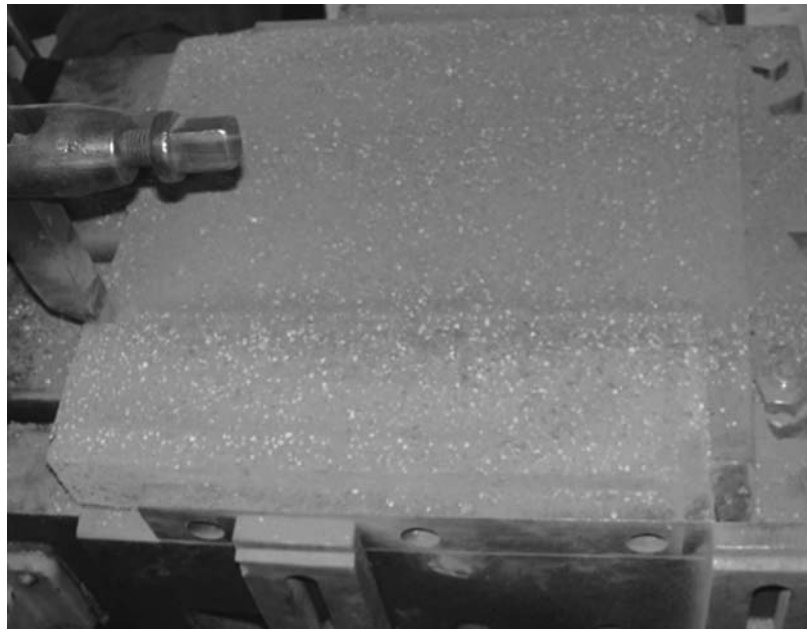

Figure 6-22 Extruded products can be easily machined (milling)

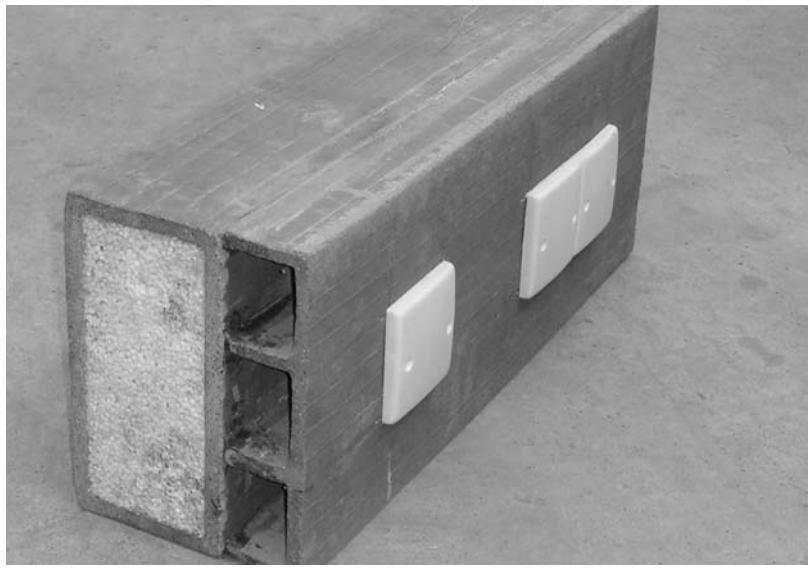

Figure 6-23 Industry-extruded products with several different functions

shown in Figure 6-22. Other industrial extruded products include functional blocks with cable channels and a heat insulation core, as shown in Figure 6-23, and a structural wall panel with a heat insulation core, as shown in Figure 6-24. Such a wall panel has a compressive strength of around 15 MPa and thus can carry the loads transferred from other components. Meanwhile, the heat insulation core provides excellent performance in reducing the heat transfer from the outside to the inside of a room.

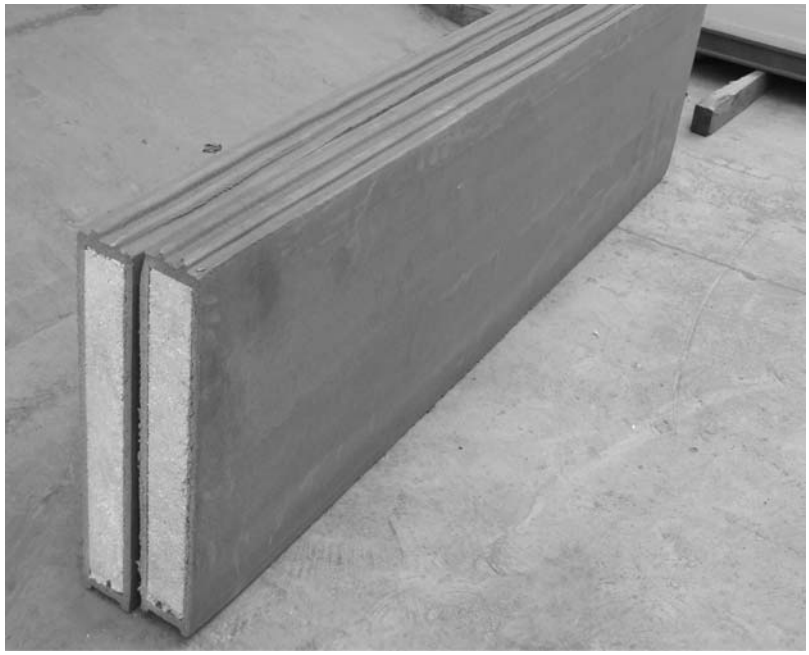

Figure 6-24 Industry-extruded wall panel with heat insulation core

Another popular product of fiber-reinforced cement-based composites, the engineering cement composite (ECC), is introduced in detail in a later section.

6.2 HIGH-STRENGTH CEMENTITIOUS COMPOSITES

6.2.1 High-strength concrete

High-strength concrete is defined as concrete made with normal-weight aggregates with a compressive cylindrical strength higher than 50 MPa. Here high strength means high compressive strength only. Although there are no differences in the raw materials used to make normal-strength concrete and those used to make high-strength concrete, more stringent quality control and more care in the section of materials are needed.

Usually, for the aggregate to be used in making high-strength concrete, it is better to choose one with a high crushing strength, if possible. The maximum size of aggregate is usually limited to 20 mm. The limitation on maximum aggregate size is to reduce the influence of the transition zone and to get a more homogeneous material. The moisture content in aggregates has to be carefully calculated to make sure the right w/c or w/b ratio is secured. The materials proportion of high-strength concrete is different from normal-strength concrete. The cement content is usually high, in the a range of 400–600 kg/m^3. The higher cement content is the result of limiting the maximum aggregate size and the need for workability under the smaller w/c ratio condition, as is discussed later. Moreover, the higher cement content also leads to a more homogenous concrete structure. Frequently, water-reducing admixtures and mineral admixtures such as fly ash, slag, and silica fume are incorporated in the mix for high-strength concrete.

The w/c or w/b ratio is a key parameter in making high-strength concrete. From Abrams' law and the gel space ratio introduced earlier, it is easily seen that a low w/c or w/b ratio can lead to high compressive strength. Thus, the basic measure usually taken in making high-strength concrete is to reduce the w/c or w/b ratio from the values for normal-strength concrete or about 0.5 or higher to about 0.3 or lower. However, lowering the w/c or w/b ratio will lead to the loss of workability, especially fluidity. This disadvantage is overcome in concrete proportions by adding superplasticizers and increasing the cement content. As discussed ealier, a superplasticizer can separate cement particles from flocculation and thus release the entrapped water by cement particle clusters, either by electrostatic repulsion or steric effect. Hence, the workability of concrete can be improved. Increasing the cement content can increase the total amount of water used in the concrete mix and provide more paste for the lubrication effect, which leads to an enhanced workability.

Incorporating mineral admixtures, especially silica fume, is another key factor in producing high-strength concrete. As discussed in Chapter 3, silica fume is a by-product of the ferro-silicon manufacturing process, with very small particle size and high reactive silica. Due to the small size of around nanometers, silica fume can easily pack into the gaps among cement particles of size 20 mm on average, to form a much denser microstructure. Due to its highly reactive amorphous nature, silica fume can react with calcium hydroxide (CH) and water to produce secondary C–S–H, which is very efficient in filling up large capillary spaces, thus further improving the density of the microstructure and reducing the porosity of concrete. Subsequently, the strength and permeability of the concrete are enhanced. Moreover, due the reduction of CH and permeability, the penetration rate and amount of carbon dioxide, oxygen, chloride, and moisture in the concrete are reduced. The possibility for leaching, alkali aggregate reaction (AAR), carbonation, corrosion, and sulfate attack is reduced and hence the overall durability of high-strength concrete is enhanced. Table 6-3 provides typical mix proportions for a normal-strength and a high-strength concrete. It can be seen that the high-strength concrete has incorporated both silica fume and a superplasticizer. Figure 6-25 shows the responses of the two concretes under compressive load. It can be clearly seen that the stress development of high-strength concrete is much faster than normal-strength concrete. It implies that high-strength concrete also has high early strength.

In addition to compressive strength, the microstructure and failure modes under compression of high-strength concrete are quite different from those of normal-strength concrete. From a microstructure point of view, high-strength concrete looks more homogeneous than normal-strength concrete due to the limitation of the maximum aggregate size and the increase of cement content. The extent of porosity in the transition zone is greatly reduced. Sometimes, the existence of the transition zone is almost eliminated. Also, the number of microcracks in high-strength concrete associated with shrinkage, short-term loading, and sustained loading is significantly less than that in normal-strength concrete. As for the failure mode, high-strength concrete usually has a vertical crack going through the aggregate and shows a more brittle mode of fracture and less

Table 6-3 Mix proportions of normal concrete and high-strength concrete

	Binder				
	Cement	**Silica Fume**	**Water**	**Sand**	**Gravel**
NSC	1		0.5	1.5	2.4
HSC	0.9	0.1	0.3	1	1.8

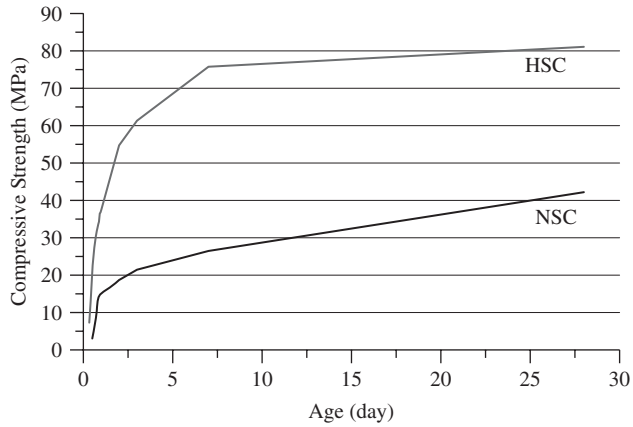

Figure 6-25 Compressive stress development of normal-strength concrete (NSC) and high-strength concrete (HSC)

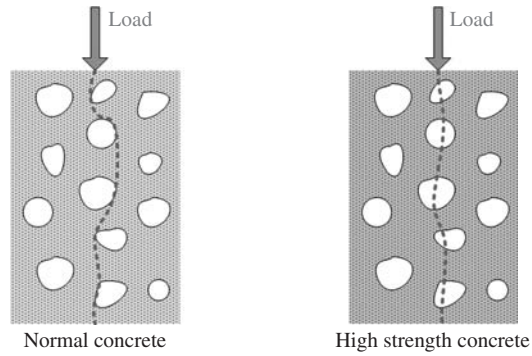

Figure 6-26 Failure mode of normal concrete and high-strength concrete under compression

volumetric dilation, while for normal-strength concrete the major crack usually passes around coarse aggregate, as shown in Figure 6-26.

6.2.2 MS concrete

MS stands for *microsilica*, and an MS concrete contains a large amount of microsilica, usually up to 15% by weight of cement. There are some commercially available MS concretes in the United States and Europe. The microstructure and properties of MS concrete have the following characteristics.

In MS concretes, the amount of CH is greatly reduced due to the pozzolanic reaction of silica fume. The C–S–H formed in MS concrete in the presence of reactive pozzolans is slightly different from that formed during normal hydration. In particular, the C/S ratio is reduced from 1.7 to 1.4, but the silicate structure is not significantly different. It is likely that both types, "normal" (C/S = 1.7) and "pozzolanic" (C/S $\sim$ 1.4), co-exist, giving rise to a mean value of around 1.5. The addition of microsilica can reduce or eliminate the macroporosity (>100 nm diameter) that dominates permeability. Hence, MS concrete can be very impermeable.

Table 6-4 Effectiveness of microsilica in reducing permeability of concrete

Cement Content (Lb/Yd^3)	WDRA[a] (wt.%)	Microsilica (wt.%)	Water-to-Powder Ratio	Permeability Coefficient, K (m/s)
170	0	0	2.38	120×10^{-10}
170	1	0	2.09	1160×10^{-10}
170	0	10	2.32	10×10^{-10}
170	1	10	2.10	4×10^{-10}
170	2	20	2.02	0.6×10^{-10}
420	0	0	0.89	0.5×10^{-10}
420	1	0	0.81	620×10^{-15}
420	0	10	0.97	95×10^{-15}
420	1	10	0.82	18×10^{-15}
420	2	20	0.79	21×10^{-15}
675	0	0	0.52	7×10^{-15}
675	0	10	0.56	136×10^{-15}
675	1	10	0.47	40×10^{-15}
675	1[b]	10	0.44	8×10^{-15}
845	0	0	0.43	14×10^{-15}
845	1	0	0.49	41×10^{-15}

[a]Lignosulfonate-based water reducing agent.
[b]Naphthalene-based super plasticizer.

With the incorporation of large amounts of microsilica, the interfacial zone of MS concrete has a denser and more uniform structure that is similar to that of the bulk paste. The small particle size of the microstructure inhibits the development of segregated water films, which probably are the cause of the porous zone and which inhibit the growth of oriented CH crystals. Similarly, the bond between the paste and other embedded materials, such as fibers, will also be improved.

The effectiveness of microsilica in reducing the permeability of concrete was demonstrated a long time ago. Typical figures are given in Table 6-4. These data show that even with low cement content and high w/c ratios, low-permeability coefficients can be attained due to incorporation of silica fume. The efficiency factor is about 10 for a 10% incorporation of silica, i.e., replacement of 1 part cement for 1 part microsilica is equivalent to adding 10 parts cement. In other words the reduction in permeability with 10% of microsilica is approximately equivalent to doubling the cement content. This assessment is based on well-cured concretes. Inadequate curing will have a greater detrimental effect on MS concrete than on conventional concrete, because the pozzolanic reaction will be inhibited.

The refined pore structure increases the chemical resistance of MS concrete and reduces the access of oxygen. Alkalinity reduction caused by the pozzolanic reaction is not significant. Diamond (1985) has measured a pH > 12 after 145 days hydration in a concrete with the presence of 30% microsilica. MS concrete has been exposed to salt spray in Kristiansand, Norway for over 10 years without any outward sign of corrosion.

When chlorides are added to MS concrete, the chloride ions do not appear to be bound by the hydration products to the same extent as in conventional concretes. Thus, depassivation can occur at lower dosages of added chlorides. However, ingress of external chloride ions is significantly reduced, by at least a factor of 10 (about 1×10 cm/sec). The rate of corrosion in

the presence of equal amounts of chloride ions is the same regardless of the microsilica content of the concrete; i.e., there is no negative influence of microsilica to nullify or outweigh the beneficial effects of a refined pore structure.

The effectiveness of microsilica in controlling AAR has been well established in several independent studies. In Iceland, 7.5% microsilica is routinely added to all cement for this purpose. Recently, Diamond et al. (2004) have shown that the addition of microsilica does reduce the concentration of alkali (K^+ and OH^-) in the pore solution. The low permeability and reduction in CH content should also improve the resistance to sulfate attacks and acids. It has been demonstrated that microsilica performs better than other pozzolans at equivalent additions. Field trials under severe conditions in Oslo, Norway have shown good performance over a 20-year period (Herfurth and Nilsen, 1993).

6.2.3 DSP materials

DSP stands for *densified with small particles*. DSP concrete is very similar in composition to MS concrete. It is reasonable to expect that the behavior of DSP materials can be estimated from MS concrete properties. Although there is no clear gap between MS concrete and DSP materials, DSP materials have the following unique characteristics: (1) DSP concretes usually have much lower w/b ratio ($\sim$0.20); (2) DSP concretes incorporate much higher microsilica content ($>$20 wt.%); and (3) DSP concrete's requirement on particle packing is more stringent.

It is critical to achieve an optimum particle packing for DSP concrete and hence the grading of aggregates and size distribution of binder particles have to be carefully selected. The aggregates used for DSP concrete are usually very special. For instance, a convoluted stainless steel aggregate is frequently used.

With such compacted particle packing, large quantities of a dispersing agent (usually a superplasticizer) have to be used, due to the very low w/p ratios. Under such low w/p ratios, only about 50% of the cement is able to hydrate. Thus, roughly, DSP concrete has 50% unhydrated cement particles. These particles act like a hard core to help the hydrate carry the compressive load. Due to the pozzolanic reaction of a large amount of silica fume, the CH formed as a reaction product is reduced to very low levels. Large massive crystals of CH are not observed, and the microstructure is very uniform in contrast to that of regular cement paste. The porosity of DSP concrete is very low and the pore structure is quite different than normal Portland cement concrete, as demonstrated in Figure 6-27. There is a good reason to believe that no capillary pores are present in DSP.

The strength development of DSP concrete is very rapid, after a delayed setting time of 15–20 h. In about 2 days, the compressive strength of DSP can reach 100 MPa. The strengths can continue to increase with extended moist curing. A compressive strength of 345 MPa is the highest reported value for DSP. This may be the result of eliminating macroporosity. It is important that complete dispersion of the microsilica be achieved. The use of a chemically dispersed agent is not sufficient if low shear mixing is used. High shear mixes will allow compressive strengths to be significantly increased. It is possible to achieve paste strength over 200 MPa (see Figure 6-28) by optimizing processing.

Like high-strength concrete, DSP materials are extremely brittle. The ratio of compressive to flexural strength is in the range of 10–12:1 for paste, and 7–12:1 for mortar. Thus, reinforcement will be needed to improve ductility. Regarding other physical properties, the abrasion resistance of DSP is excellent. A screw feeder for fly ash made from DSP has a reported lifetime of 1250 h compared with the 250 h of one made of steel with a wear-resistant carbide coating. The permeability of DSP would be expected to be extremely low because of the optimized particle

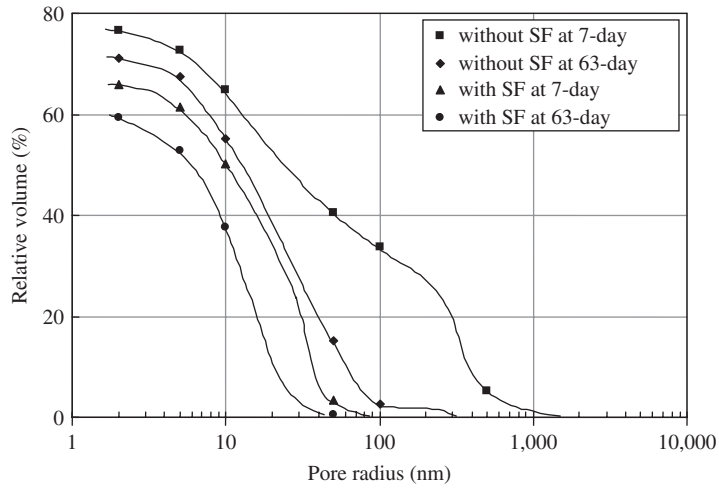

Figure 6-27 Effects of the addition of silica fume on pore size distribution

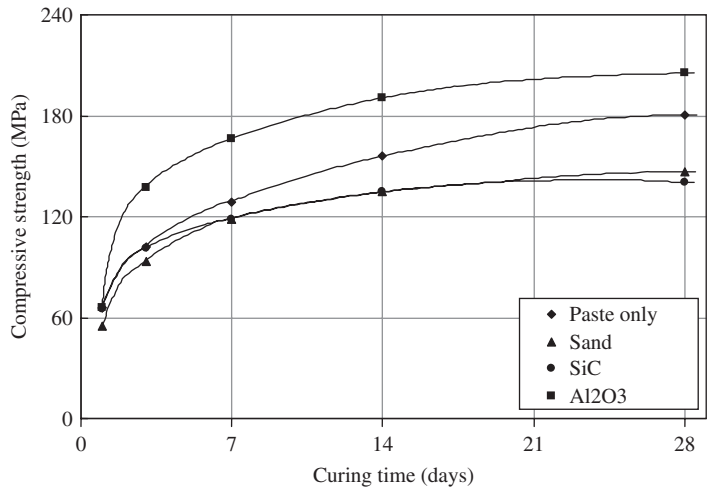

Figure 6-28 Strength development of DSP

packing, low w/p ratio, and the pozzolanic reaction products of the high microsilica content. The DSP commercial product DASH 47 has an air permeability even lower than that of cast aluminum. Another DSP commercial product, Density formulation, has good corrosion resistance.

DSP is usually utilized to make molds and tools. DSP has excellent ability to withstand temperature cycling without losing its properties up to 200–250°C. When the temperature is higher than this limit, large degradation in mechanical properties occurs. To overcome this limit, impregnation with high-temperature polymers (Novolac epoxy resin) has been used. It is verified by experiments, as shown in Table 6-5, that vacuum impregnation can significantly improve flexural strength.

Table 6-5 Temperature resistance of DSP

Temp. (°C)	Wt. Loss (%)	Flexural Strength (psi) before PI	Flexural Strength (psi) after PI	Vac. Leak Rate (torr/min) before PI	Vac. Leak Rate (torr/min) after PI
200	4.5	4,650	4,850	0.1	n/a
300	5.0	4,200	4,900	6.0	0
400	6.2	3,850	6,550	11.0	0
550	6.6	3,500	6,250	18.0	0.3
700	7.0	2,450	12,850	100.0	n/a

6.2.4 MDF materials

MDF stands for *macrodefect-free*. MDF cement was invented by the British chemical company ICI in 1982 (Birchall et al., 1982). The term macrodefect-free alludes to the relatively large internal voids that are present in conventionally mixed pastes, due to entrapped air and inadequate dispersion. These internal flaws act as crack initiators and reduce the original strength. MDF is a composite of cement and polymer. The raw materials used to produce MDF are cement, either Portland cement or calcium aluminate cement, water-soluble polymers, such as polyvinyl alcohol or polyvinyl acetal, and water. Water-soluble polymer is added to cement as a rheological aid to make a dough-like material.

The processing method for MDF is twin roll mixing, as shown in Figure 6-29. The dough-like MDF material is processed under high shear and then stretched into a thin sheet. The polymer is indispensable for this kind of mixing, providing necessary cohesion and allowing a close packing of cement grains to be achieved. More recent studies show that the polymer is more than a rheological aid. It reacts with the cement to create a viscoelastic material that is capable of forming a cohesive dough, which can be easily shaped. The extracted thin sheet is then put into a press under a modest pressure (7–10 MPa). The pressing process removes the entrapped air and makes the paste free of large defects, giving it a high flexural strength.

The typical formulation of MDF cement is given in Table 6-6, using calcium aluminate cement and polyvinyl alcohol. This cement–polymer combination gives the highest flexural strength (250–300 MPa). When Portland cement is used, strengths exceed 100 MPa. The microstructure of MDF is very dense and the cement grains are close-packed and bound together by the polymer matrix. Surrounding each cement grain is a rim of hydrated material, about 0.25 μm wide, which also contains polymer. This interface region also contributes to bonding since it forms a percolating network. There is no capillary porosity present.

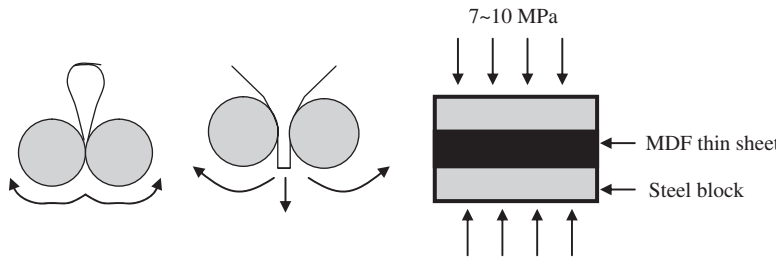

Figure 6-29 Processing method of MDF

Table 6-6 Compositions of representative MDF materials

Constituent	Parts of Weight	Weight %	Volume %
Calcium aluminate cement	100	84.3	65.2
Polyvinyl alcohol/acetate	7	5.9	12.3
Glycerin	0.7	0.6	1.4
Water	11	9.3	21.1

When the polymer is removed by heating at high temperature, a capillary pore network is formed, with mean pore diameters around 0.1 to 0.0075 μm. The residual flexural strength is about 20 MPa. The pore system can be filled by further hydration or by impregnation with another polymer. A polymer-free MDF cement has a flexural strength of about 75 MPa. A major drawback to the commercialization of MDF cement is its sensitivity to water. Nearly two-thirds of the dry strength can be lost after 3 weeks of immersion in water. The exact mechanism of strength loss is not yet known with certainty, but the following explanation is proposed. MDF develops its high strength only after drying at 80–100°C. Removal of water creates a strong but brittle PVA matrix. Water can be reabsorbed to form a soft, weak, rubbery polymer. The water eventually reaches the cement grains, which continue to hydrate and destroy the interface region. Eventually a hydrated matrix will become the sole binder and the limiting wet strength will approach 20 MPa. The addition of a commercial organo-titanate can effectively prevent this loss of strength. It appears that the titanate reacts chemically with PVA, thereby reducing the rate at which it can absorb water. It may also modify the interphase region. The properties of MDF lie between conventional cement paste and a sintered ceramic, as listed in Table 6-7. Its fairly high fracture toughness makes it a good candidate for a ballistic protection. Frost resistance is not a problem even when the strength is reduced by exposure to moisture, because there should be no freezable water.

6.2.5 Ultra-high-strength concrete

Ultra-high-strength concrete (UHSC) is defined as concrete that has a compressive strength greater than 150 MPa. When this type of composite was developed in France, it was called reactive powder concrete (RPC) because it contained a larger amount of active silica fume, as discussed in Chapter 1. It is different from high-strength concrete not only because it does not have coarse aggregates, but also in the amount of powders and fibers. A comparison of normal-strength, high-strength, and ultra-high-strength concrete is given Table 6-8.

Table 6-7 Comparisons of the properties of sintered alumina, MDF cement, and conventional cement paste

Properties	Sintered Alumina	MDF Cement	Portland Cement
Compressive strength (MPa)	2, 100	300	70
Flexural strength (MPa)	350	150	20
Modulus of elasticity (GPa)	40	45	35
Fracture toughness ($MPa \cdot m^{1/2}$)	5	3	0.3
Density (kg/m^3)	3700	2400	2700
Thermal expansion ($10^{-6}/°C$)	7	10	15

Table 6-8 Characteristics of conventional concrete, high-strength concrete, and ultra-high-strength concrete

	Conventional Concrete	High-Strength Concrete	Ultra-High-Strength Concrete
Compressive strength (MPa)	<50	~100	>200
Water–binder ratio	>0.5	~0.3	<0.2
Chemical admixture	Not necessary	WRA/HRWRA necessary	HRWRA essential
Mineral admixture	Not necessary	Fly ash (and/or) silica fume commonly used	Silica fume, (and/or) fine powder essential
Fibers	Beneficial	Beneficial	Essential
Air entrainment	Necessary	Necessary	Not necessary
Processing	Conventional	Conventional	Heat treatment and pressure
Steady-state chloride diffusion ($\times 10^{-12}$ m^2/s)	1.00	0.60	0.02

Table 6-9 Examples of compositions of ultra-high-strength concrete

	Cement	Water	Superplasticizers	Silica Fume	Fine Sand	Quartz Flour
No.1	1	0.28	0.060	0.33	1.43	0.3
No.2	1	0.15	0.044	0.25	1.10	—

6.2.5.1 Composition of ultra-high-strength concrete

To illustrate the composition of ultra-high-strength concrete, two examples are given Table 6-9. The key characteristics of the ultra-high-strength concrete can be summarized as follows. (1) UHSC has very low water–binder ratio. The water-to-binder ratio of UHSC is less than 0.15, very close to that of MDF. However, since there is no polymer, UHSC can have very good fluidity just like normal concrete. (2) UHSC has a large quantity of silica fume (and/or other fine mineral powder). The incorporation of silica fume in UHSC can reach 25% by weight of cement, similar to that of DSP. (3) UHSC aggregates contain only fine sand. Since there are no coarse aggregates, UHSC looks more like a homogenous material. Also, it is easy to incorporate large amounts of fibers into UHSC due to lack of coarse aggregates. (4) UHSC contain a high dosage of superplasticizers. It is due to the high percentage of silica fume and very low w/b ratio. With such high dosage of superplasticizer, UHSC can achieve a very good flowability.

Depending on the level of compressive strength, postset heat treatment and application of pressure before or during setting may be necessary.

6.2.5.2 Microstructure of ultra-high-strength concrete

Based on the observations made by optical microscopy, SEM, and TEM, the microstructure of ultra-high-strength concrete can be described as follows. (1) On a millimeter scale, the material is more homogeneous as there is no coarse aggregate, and a large amount of binders is used. (2) There is an absence of a pronounced transition zone between the sand and the paste. This is the result of a low w/b ratio and the dispersion effect of the superplasticizer. (3) There is a low

or negligible presence of Portlandite because of the pozzolanic reaction of a large amount of silica fume. By using mercury intrusion porosimetry, it was also found that UHSC has (4) a low porosity (1 to 3%) as a result of the low w/b ratio and pozzolanic reaction, (5) a proportionally lower volume of capillary porosity (10% of total porosity), and (6) a strong component of pores with a diameter 2.5 nm. The above-mentioned microstructural features lead to low water absorption, low gas permeability, and low chloride diffusivity.

6.2.5.3 Brittleness

Ultra-high-strength concrete is considerably more brittle than conventional concrete. This can be seen by comparing the uniaxial compressive stress–strain curve of conventional concrete with that of an ultra-high-strength concrete, as shown in Figure 6-30. These curves were obtained with a digitally controlled, closed-loop test system. The post-peak response of ultra-high-strength concrete is considerably steeper than that of conventional concrete. In practice, fibers are essential for UHSC to overcome the brittleness. With the incorporation of fibers, the flexural strength can reach 50 MPa, as shown in Figure 6-31.

6.2.5.4 Applications

Ultra-high-strength concrete can be used for prestressed concrete structures and nuclear waste storage. The first application of UHSC was a pedestrian bridge constructed in Sherbrook, Canada with ultra-high-strength concrete of 200 MPa. The footbridge was built with post-tensioned, precast elements made with UHSC, having a fiber amount of 200 kg per cubic meter. The thickness of the bridge deck was only 35 mm. UHSC has also been used to build the Shawnessy light rail Train Station in Calgary, Canada. The thin-shelled canopies, 5.1 by 6 m, and just 20 mm thick, supported on single columns, protect commuters from the elements, as shown in Figure 6-32. In China, UHSC has been applied as pavement cover plate for high-speed railways as shown in Figure 6-33. The UHSC has compressive strength $\geq$ 130 MPa, flexural strength = 18 MPa, a modulus of elasticity = 48 GPa, penetration quantity of chloride ions $<$ 40 C, and a frost-resistance grade $>$ 500. Investigation has also been conducted on the resistance to impact

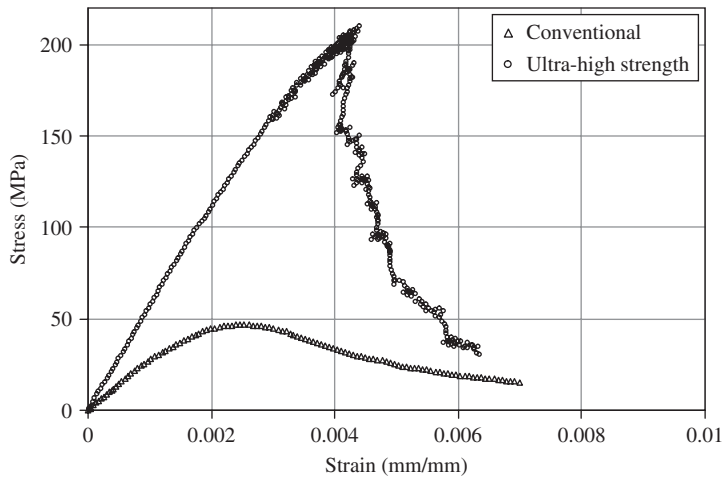

Figure 6-30 Comparison of stress–strain curves of representative conventional and ultra-high-strength concretes

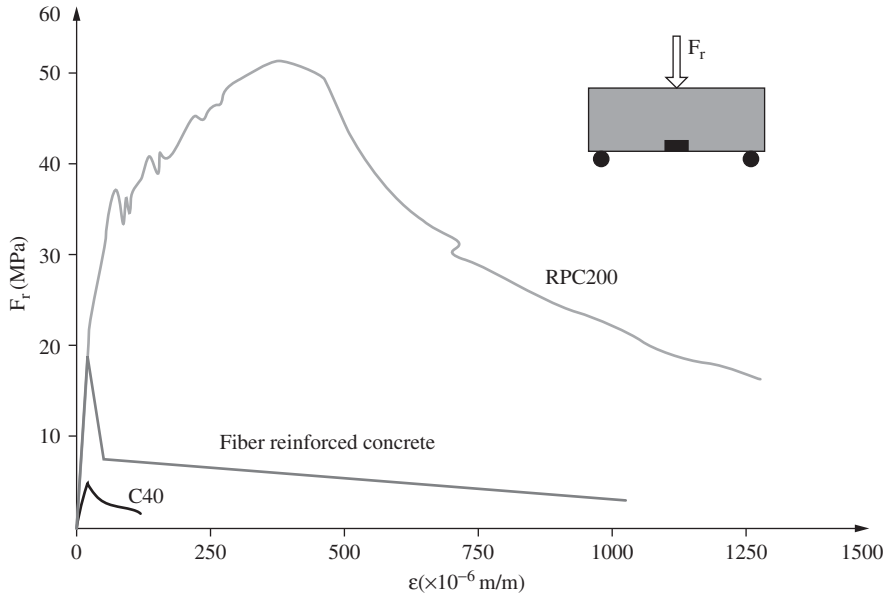

Figure 6-31 Flexural strength comparison

Figure 6-32 The thin-shelled canopies of the Shawnessy Light Rail Train Station in Calgary, Canada

of UHSC. As shown in Figure 6-34, UHSC is extremely brittle without the addition of fibers. However, when 3 or 4% of fiber is added, its resistance to impact is significantly improved. UHSC has been utilized to cast reinforced beams. The cross section of a beam made of UHSC is very close to that of steel and so is the self-weight. Recently, UHSC has been commercialized by Lafarge under the brand name Ductal.

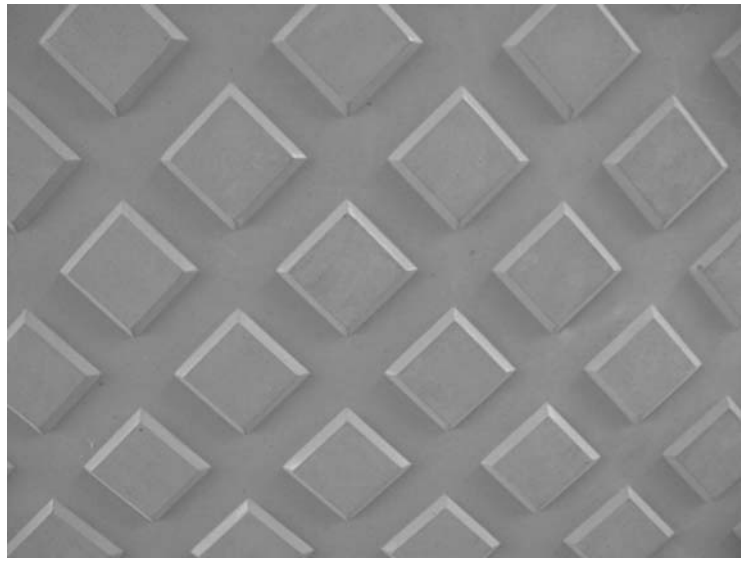

Figure 6-33 Application of UHSC in Pavement Cover Plate in high speed railway in China

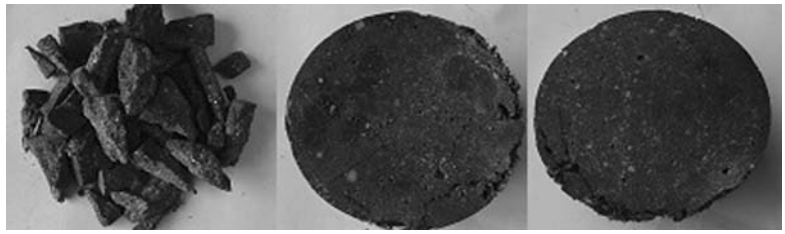

Figure 6-34 Fiber influence on UHSC impact resistance

The fibers used in UHSC are usually special steel fibers 12 mm long and 0.2 mm in diameter, originally used in rubber tire production. The cost of UHSC with fibers is about US$1242 per cubic meter, whereas without fibers, the cost is US$332 per cubic meter. The advantages for ultra-high-strength concrete for use in nuclear waste storage are low porosity and reduced transport potential.

6.3 POLYMERS IN CONCRETE

6.3.1 Introduction

Polymers are used in concrete production in three major forms. In the first, polymer is used directly as the binder to replace Portland cement in gluing aggregates together, and is called polymer concrete. In the second, polymer is applied as an impregnating agent to penetrate a Portland cement concrete member to enhance its properties, and is called polymer-impregnated concrete. And last, polymer is used as an admixture added into concrete, known as polymer-modified concrete or latex-modified concrete, as the polymer used in this category is mainly latex.

6.3.2 Polymer concrete

Polymer concrete (PC) is produced by premixing a two-part polymer system, composed of monomers or prepolymers together with hardeners (cross-linking agent), which is then added to aggregates to produce a hardened plastic material with aggregate as filler. Other components used include catalyst, plasiticizer, fire retardant, and fibers. The function of the plasticizer is to improve the workability of polymer concrete. The reason for adding the fire retardant is to improve the poor resistance of polymer concrete to high temperature or fires. The polymer is a homopolymer if it is made by the polymerization of one monomer, and a copolymer when two or more monomers are polymerized. Polymer concrete has been made with a variety of resins and monomers. The common used monomers or prepolymers for PC are (1) methyl methacrylate (MMA), (2) polyester prepolymer-styrene, and (3) epoxide prepolymer. Polyester resins are attractive because of moderate cost, the availability of a great variety of formulations, and moderately good properties. Epoxy resins are generally higher in cost, but may offer advantages such as adhesion to wet surfaces (ACI, 1998). The properties of polymer concrete are largely dependent on the properties and the amount of the polymer used, modified somewhat by the effects of the aggregate and the filler materials. The composites do not contain a hydrated cement phase, although Portland cement can be used as a filler.

The term polymer concrete refers to a family of products, including mixtures of concrete and mortar. The improvement of properties of hardened concrete by the addition of polymers is well documented (ACI, 1997). The advantages of PC include high tensile and flexural strengths, excellent adhesion, good resistance to attack by chemicals; very low water sorption, high water resistance, good resistance to abrasion; good freeze–thaw stability, and greater strength. The main disadvantages of PC include a low Young's modulus, high creep values, shrinkage varying with the polymer used, sensitivity to high temperature, and high price. The main application areas for PC is in making facade plates, sanitary products, panels, floor tiles, pipes, and industrial flooring. It is used in various precast and cast-in applications in construction work, skid-resistant overlays in highways, plaster for exterior walls, and resurfacing of deteriorated structures. In addition, PC is also widely used as repair material, in particular for concrete carriageways, around the world nowadays. In Japan, PC mortars are used as grouts for repairing cracks and delaminations of concrete structures, patching materials for damaged concrete structures, and rustproof coatings for corroded reinforcing bars. In the United States, polymer mortar and concrete are employed as the main patching materials for repair work and overlays for bridge decks in cast-in-place applications, and in precast applications (Chandra and Ohama, 1994).

Only limited numbers of polymer systems are appropriate for the repair of wet concrete surfaces. In general, the aggregates used in polymer concrete should be dry in order to obtain the highest strengths. High temperatures can adversely affect the physical properties of certain polymer concrete, causing softening. Service temperatures should be evaluated prior to selecting polymer concrete systems for such use. Epoxy systems may burn out in fires where the temperature exceeds 230°C and can significantly soften at lower temperatures. Users of polymer concrete must consider its poor fire resistance. Conventional concrete generally cannot bond to cured polymer concrete, and compatibility of the systems should be considered.

Many polymer concrete patching materials are primarily designed for the repair of highway structures where traffic conditions allow closing of a repair area for only a few hours. However, polymer concrete is not limited to that usage and can be formulated for a wide variety of applications. Polymer concrete is used in several types of applications: (1) fast-curing, high-strength patching of structures, and (2) thin (5 to 9 mm thick) overlays for floors and bridge decks. Polymer mortars have been used in a variety of repairs where only thin sections (patches and overlays) are required. Polymers with high elongation and low modulus of elasticity are

particularly suited for bridge overlays. Polymer concrete is especially suitable for areas subject to chemical attack.

Polymer concrete is mixed, placed, and consolidated in a manner similar to conventional concrete. With some harsh mixtures, external vibration is required. A wide variety of prepackaged polymer mortars is available, which can be used as mortars or added to selected blends of aggregates. Depending on the specific use, mortars may contain variable aggregate gradations intended to impart unique surface properties or aesthetic effects to the structure being repaired. Polymer mortars are trowelable and are specifically intended for overhead or vertical applications. Epoxy mortars generally shrink less than polyester or acrylic mortars. Shrinkage of polyester and acrylic mortars can be reduced by using an optimum aggregate grading.

Rapid curing generally means less time for placing and finishing operations. Working times for these materials are variable and depending on ambient temperatures, may range from less than 15 minutes to more than one hour. Also, high or low ambient and concrete temperatures may significantly affect polymer cure time or performance. The coefficients of thermal expansion of polymer materials are variable from one product to another, and are significantly higher than conventional concrete. Shrinkage characteristics of polymer concrete must be evaluated so that unnecessary shrinkage cracking is avoided. The modulus of elasticity of polymer concrete may be significantly lower than that of conventional concrete, especially at higher temperatures. Its application in load-carrying members must be carefully considered.

Organic solvents may be needed to clean equipment when using polyesters and epoxies. Volatile systems such as methyl methacrylate evaporates quickly and presents no cleaning problems. However, such systems are potentially explosive and require nonsparking and explosion-proof equipment.

6.3.3 Polymer-impregnated concrete

Polymer impregnated concrete (PIC) is produced by impregnating a monomer and catalyst into a hardened concrete and polymerizing it using steam or infrared heater in situ. The procedures for making PIC are as follows: (1) precasting hardened Portland cement concrete; (2) drying the precast conventional concrete; (3) displacing the air from the open pores; (4) saturating the open pore structure by diffusion of low-viscosity monomers or a prepolymer–monomer mixture; and (5) in situ polymerization with heating.

The compressive strength of PIC can reach 140 MPa, and the tensile strength 15 MPa. PIC usually has very low permeability and diffusivity. Subsequently, PIC has excellent chemical resistance and superior durability. Thus, PIC is commonly used to produce structural industry floors, sewer pipes, storage tanks for seawater, structural members for desalination plants and distilled water plants, and tunnel liners. PIC is also very expensive due to the complicated processing procedures and the cost of the polymer; thus, usage is limited.

6.3.4 Polymer (latex)-modified concrete

Polymer (usually latex)-modified concrete is produced by adding polymer (latex) into a Portland cement concrete mixture during the mixing process. The processing procedures are the same as normal Portland cement concrete. Since the early 1950s, it has been known that certain polymers can be added to cementitious mortars, to overcome some of the problems of pure cement-based repair materials. The polymers used as admixtures for cementitious systems are normally supplied in the form of latex and are used to gauge the cementitious mortar as a whole or as partial replacement of the mixing water. Such mortars afford similar alkaline passivation protection to the steel as conventional cementitious materials do, and can be readily placed in

Table 6-10 Characteristics of different latexes

Latex Type	Acronym	Solids (%)	Viscosity (cps)	MFFT[a] (°C)	pH
Styrene–butadiene	SB	47	20–50	12	10
Acrylic copolymers	PAE	47	20–100	10–12	9–10
Styrene acrylic copolymers	SA	48	75–5000	10–18	6–9
Polyvinyl acetate	PVA	55	1000–2500	15	4–5

[a]MFFT: Minimum film forming temperature

a single application with a 12- to 15-mm thickness that gives adequate protective cover. It was shown (Isenberg and Vanderhoff, 1974) that when a latex was incorporated in a cementitious mortar, a network of polymer strands formed, interpenetrating the cement matrix.

Latex can be either natural or man-made. Natural latex comes from rubber trees and man-made latex is created by synthetic processes. The most widely used latexes with Portland cement are copolymers of styrene–butadiene (SB); 100% acrylic copolymers (PAE), styrene acrylic (SA), vinyl acetate ethylene (VAE), and polyvinyl acetate (PVA). As the names indicate, these latexes are composed of organic polymers that are combinations of various monomers, such as styrene, acrylic, butadiene, and vinyl acetate. The general properties of the above mentioned copolymers are given in Table 6-10. The form of latex is usually a dispersion of very small particles of an organic polymer in water. These particles are typically in the range of 1500–2500 angstroms (10^{-10} m), i.e., 0.15 to 0.25 μm, in diameter. The solid content in a latex emulsion is about 50%. The application of latex in Portland cement concrete requires about 15% of solid content by weight of cement. In this case, about 30% of emulsion by weight of cement has to be added. Thus, 15% of water by weight of cement is brought into concrete. The water has to be reduced from the free water for concrete mixing.

The reaction of latex-modified Portland cement involves two processes: the hydration of the cement and the coalescence of the latex. The chemistry and reaction processes of cement hydration occurs in the same way as in conventional mortar and concrete. Meanwhile, with water being removed from the latex emulsion, the latex particles get closer. With continual water removal, the latex particles can eventually coalesce into a film, coating the hydrate and aggregate surface with a semi-continuous plastic film.

As the latex particles coalesce and form a semi-continuous film, moisture can be maintained around the cement particles, permitting the cement hydration process to continue and reduce the need for an external wet cure. This process occurs after the material reaches initial set and is common in both mortar and concrete applications. For many mortar applications, the materials are formulated with some latex so that no external curing is needed, even right after placement, whereas for most concrete applications, the normal curing procedure is 1 day of moist cure followed by air drying for the remainder of the cure time. For the moist cure of concrete, damp burlap and polyethylene films are typically used.

Usually, surfactants are added to the latex formulation to prevent latex particles from coagulating due to the influence of severe mechanical or chemical conditions, such as high shear or calcium ions in Portland cement. However, these surfactants can bring a large number of air voids into latex-modified mortar or concrete due to the nature of the surfactant to foam. Thus, an antifoam agent has to be added to the latex to control the air content in the Portland cement mix.

Latexes can influence the properties of mortar or concrete in both the plastic stage and the hardened stage. In the plastic stage, the combined characteristics of latex and antifoam will cause some air to be entrained in the mix. Values are typically in the range of 5–9% for

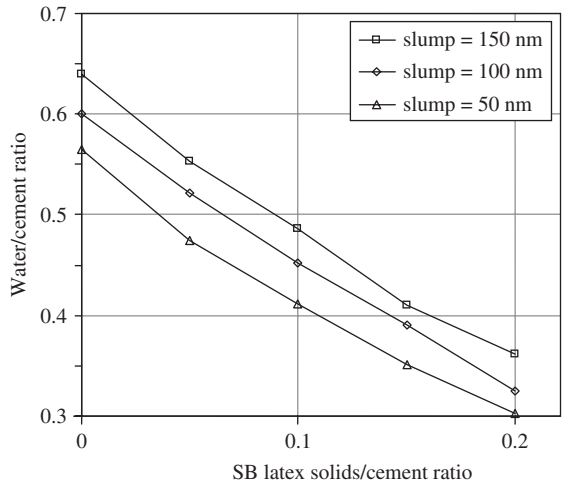

Figure 6-35 Workability of styrene/butadiene latex improved concrete

mortar and 4–6% for concrete. The entrained air voids act as a lubricant and hence improve the workability of the modified concrete. One more factor contributing to the improved workability is the dispersing effect of surfactants on the latex combined with the water. The improvement on the slump value is evident from the experimental results, as shown in Figure 6-35.

The setting time of latex-modified mixes is usually controlled by the hydration of the Portland cement. The available working time for finishing, however, can be considerably shorter than an unmodified composite due to the latex drying and film formation initiated by evaporation of water from the surface of the mix. This causes the formation of a crust on the surface, which can tear if overfinished and is the major difference in finishing latex-modified Portland cement mixes and mixes without latex. In the hardened stage, latexes can improve adhesion properties, tension and flexural properties, permeability, and chemical resistance of latex-modified mixes.

The bond between the latex-modified mixes and existing concrete is an important property when latex-modified concrete (LMC) is used as a repair material. The bond as a repair material is desired so that the new material remains in place, preferably for the life of the parent concrete. The ideal bond would be one that exceeds the tensile and shear strength of the parent concrete so that if failure occurs, it does so in the parent concrete. The latter yields good reproducibility as well as mode of failure, thus indicating when bond strength exceeds the strength of the materials bonded. The different bond strengths can be measured by different methods. The tension-bond strength can be measured by a pull-off test. It is done on a parent concrete slab with the disk-like specimens of LMC material adhering to it (Figure 6-36). Then dollies are attached on the top surface of the disk specimen and followed by a pull-off process to measure the bond strength (Figure 6-37). The shear bond strength can be measured with a prismatic specimen of size $100 \times 100 \times 300\,\text{mm}^3$. The specimen is cast using normal concrete into a slanted shape. After the concrete is hardened, another half of the beam specimen is cast with LMC material on top of the parent concrete to form a test prism, as shown Figure 6-38. The specimen is then tested under bending to determine the shear bond strength.

The bond of SB latex-modified mortar to concrete is chemical in nature, thus creating a homogeneous combination of the two materials. Bond tests have demonstrated that ultimate failure is in the parent concrete. It is reported that mortars modified with SB, PAE, and PVA

Figure 6-36 Casting of disk-like specimens for pull-off strength measurement

Figure 6-37 Measurement of pull-off strength using a pull-off tester

latexes exceed the bond strength of the unmodified control by factors of 2–3. The pore-sealing effects of latex in a concrete mix results in a major reduction of its permeability to both gases and liquids, as listed in Table 6-11. Carbonation studies have shown that the addition of latex to concrete significantly reduces the depth of carbonation of the concrete. Chloride permeability is also reduced.

The compressive strength of LMC can be measured by a cube specimen. If the LMC is very sticky, the casting of cubic specimens for determination of compressive strength should use

Figure 6-38 Casting of prisms for slant shear measurement

Table 6-11 Permeability of different types of concrete

Permeability Rating	Charge Passed (C)	Type of Concrete
High	>4000	High water/cement, conventional (>0.6) PCC
Moderate	2000–4000	Moderate water/cement, conventional (0.4–0.5) PCC
Low	1000–2000	Low water/cement, conventional (<0.4) PCC
Very low	100–1000	Latex-modified concrete, internally sealed concrete
Negligible	<100	Polymer-impregnated concrete, polymer concrete

plastic molds with a size of $50 \times 50 \times 50\,\text{mm}^3$, as shown in Figure 6-39. In addition, since shrinkage is an important parameter for LMC, drying shrinkage measurement should be made. The specimen size for the determination of drying shrinkage is $25 \times 25 \times 285\,\text{mm}^3$. Moreover, the modulus of elasticity of LMC can be measured with a cylinder specimen of size $\phi 100 \times 200\,\text{mm}^3$. The typical mechanical properties of concretes containing polymers are given in Table 6-12. It can be seen that both PC and PIC have much better properties than LMC.

In the early 1980s, polymer-modified repair mortars were blended on site using sand, cement, latex, and water. This resulted in some problems of unsatisfactory mortars due to the lack of adequate quality control (poor proportion, inadequate labor, unsatisfactory mixes, etc.). To overcome this problem, complete "bag and bottle" mixes of latex and preblended sand cement were developed. These packs were ready to be used on site without any further addition. A further development was packing redispersible spray-dried polymer powders blended with graded sand, cement, and other additives into a bag. The site application was carried out only by adding appropriate amount of water (Mirza et al., 2002). Polymer-modified cementitious mortars are mainly used for the repair of reinforced concrete where the cover to be replaced is less than 30 mm in thickness. In some instances they are used in conjunction with a protective coating in thin cover situations when the cover is less than 12 mm (Shaw, 1984).

Figure 6-39 Casting of cubic specimens for determination of compressive strength

Table 6-12 Typical mechanical properties of concretes containing polymers

	PC		LMC			PIC	
	Polyester	Polymerized (MMA)[a]	Control		LMC Containing Styrene Butadiene, Air Cured	Control Unimpregnated	MMA Impregnated Thermal-Catalytical Polymerization
	Polymer/Agg. Ratio of 1:10	1:15	Moist Cured	Air Cured			
Compressive strength (MPa)	125	140	40	10	33	37	125
Tensile strength (MPa)	14	10	3.7	2.1	4.3	2.9	10
Flexural strength (MPa)	35	21	7.4	4.2	10	5.1	16
Elastic modulus GPa	35	38	20	—	11	25	43

[a]Methyl methacrylate

LMC can be used for emergency concreting jobs in mines, tunnels, ceramic tile adhesives and grouting, swimming pool finishes, and industrial floor toppings, as well as the production of high-strength precast products. As a coating, it has been used for basement and exterior walls, skid-resistant surfaces on concrete pavement and ship decks, and maintenance coatings on steel. LMC is the most commonly used repair material, especially for overlays on bridge decks or concrete highways.

Concrete roadways are normally reinforced with steel mesh, and, in general, most highway deterioration is associated with corrosion of the reinforcement (Batis et al., 2003). Under heavy traffic loading and exposure to harsh environments, deterioration of concrete roadways frequently occurs. Such problems are faced by most modern cities, for example, Hong Kong, one of the busiest cities in Asia. The roads in Hong Kong (HK) are heavily used with over 580,000 vehicles running daily on 1900 km of roads, including over 900 highway bridges within a small territory of size about 1100 km^2. To maintain these roads in good condition is indeed a challenging job as well as a multimillion-dollar burden. In the financial year 1998/1999, the Government of the HK Special Administrative Region (HKSAR) spent a total of around HK$1.22 billion on road maintenance and minor improvement, in which about 51%, or HK$624 million, was used on the maintenance of concrete roadways (HKSAR Highways Department, 2006).

Roadway maintenance works inevitably occupy road space and disrupt normal traffic. Hence, one basic requirement is that the repaired portion should set and harden fast to minimize the disturbance to traffic. Concrete roadway maintenance works can be broadly classified into corrective repairs and programmed works. With a background of high traffic demand, acute land constraints, and growing community expectation, all roadway repair works are carried out under an extremely tight working program and within limited hours.

If the thickness of an overlay is less than 30 mm, repair mortar for a concrete roadway is demanded (Hassan et al., 2001) because latex-modified mortar has no minimum thickness requirement, and has with the following properties: (1) consistent physical properties with concrete; (2) fast hardening, within hours; (3) superior bonding strength to the substrates; (4) good volume stability and matching color; and (5) appropriate workability, surface finishing, and durability. If the thickness of an overlay is greater than 30 mm, latex-modified concrete is preferred. The majority of concrete applications incorporating a latex modifier have been used in bridge and carpark deck overlays for over twenty years. Thousands of bridges in the United States have been protected with latex-modified concrete. The overlay can last over 20 years.

For most applications, type I/II Portland cements are suitable for latex-modified mixes. Most sands that are suitable for quality mortar and concrete are suitable for latex-modified mixes. The *w/c* ratio is usually less than 0.4, and the latex solids–cement ratio for many applications is 15%. The two typical mixture compositions of mortar and concrete modified with latex are given in Table 6-13. It should be pointed out that LMC is very sensitive to high temperature. At high temperature (i.e., 29.4°C or above) and under conditions of rapid drying, latex systems will cause a skin or crust to form. For underwater applications LMC should be used with caution since it needs air to dry.

The property modifications of LMC depend on the composition of the polymer. For instance, concrete modified with styrene–butadiene and acrylate latexes is superior in water resistance than concrete modified with vinyl acetate latex. In addition, the monomer ratio can affect concrete properties. An SB latex with a styrene–butadiene ratio of 35/65 can produce concrete with a lower compressive strength than latex with a styrene–butadiene ratio of 50/50.

Table 6-13 Typical mixture proportioning of mortar and concrete modified with latex

	Mortar Parts by Weight	Concrete Parts by Weight
Portland cement	1.00	1.00
Sand	3.50	2.50
Stone	—	2.00
Latex, 48% solids	0.31	0.31
Water	0.24	0.24
Flow, ASTM C230, cm	12	0
Slump, ASTM C143, in.	—	6–8

6.3.5 Selection of LMC as repair materials

The selection of LMC as a repair material is based on the following factors: (1) job nature, including the total repair area (volume), thickness, and allowed working time before reopening to traffic; (2) compatibility between the repair materials and the original concrete; (3) the total budget for the repair work; and (4) service quality of suppliers. Patch repairs are discrete repairs carried out in small areas on a structure or concrete roadway. They are generally less than half a square meter in area and are applied by hand (Kay, 1992). The repair material may be cementitious, polymer-modified, or a straight polymer mortar with an aggregate of fine sand or other filler. The repair system may include bonding aid, reinforcement primer, repair mortar, pore filler leveling mortar, and protective coatings. In repairs of large volume it may not be appropriate or economical to use hand-applied mortars.

Although there is a wide variety of materials available for repair of concrete highways, in most repair work, polymer-modified and resin-based repair materials are bonded directly to concrete or other cementitious materials. It is, therefore, important to understand the similarities and differences in the mechanical and physical properties of repair materials and the original concrete. Typical properties of the different repairing systems are given in Table 6-14. Bond and compressive strengths are obviously important properties in any repair case, and they have to be satisfied first. ASTM C881 (ASTM, 2002) covers two-component, epoxy resin bonding systems for application to Portland cement concrete, which are able to be cured under humid conditions and bond to damp surfaces. ASTM C881 provides the compressive strength requirement of an epoxy resin bonding system for use in load-bearing applications for bonding concrete to hardened concrete and other materials, and as a binder for epoxy mortars and concretes, showing that the strength at 24 and 48 h were 14 and 40 MPa, respectively. Generally, a minimum early compressive strength development of the repair material for a concrete roadway of 20 MPa would be considered strong enough for rubber-tired traffic (Crovetti, 2005). At such a strength level, the corresponding flexural strength of the repair material is normally within 10%, that is, around 2 MPa, which is another important criterion for allowing early opening to traffic (FHWA, 2006).

In additional compressive strength, there are some other material properties that can be of equal to or of greater importance than the bond and compressive strengths (Warner, 1984), and these should be considered.

(a) *Coefficient of thermal expansion*: It is important to use a repair material with a coefficient of expansion similar to that of the existing concrete. Thermal compatibility is particularly important when patches have a large volume. If there is a large difference in the thermal

Table 6-14 Physical properties of typical products used in concrete roadway repairs

	Epoxy Resin Grouts, Mortars, and Concretes	Polyester Resin Grouts, Mortars, and Concretes	Cementitious Grouts, Mortars, and Concretes	Polymer-Modified Cementitious Systems
Compressive strength (MPa)	55–110	55–110	20–70	10–80
Modulus of elasticity (GPa)	0.5–20	2–10	20–30	1–30
Flexural strength (MPa)	25–50	25–30	2–5	6–15
Tensile strength (MPa)	9–20	8–17	1.5–3.5	2–8
Elongation at break (%)	0–15	0–2	0	0–5
Linear coefficient of thermal expansion per °C	$25–30 \times 10^{-6}$	$25–35 \times 10^{-6}$	$7–12 \times 10^{-6}$	$8–20 \times 10^{-6}$
Water absorption, 7 days at 25°C (%)	0–1	0.2–0.5	5–15	0.1–0.5
Maximum service temperature under load (°C)	40–80	50–80	>300°C (dependent on mix design)	100–300
Rate of development of strength at 20°C	6–48 h	2–6 h	1–4 weeks	1–7 days

properties of the two materials, significant changes in temperature could lead to failure either at the interface or within the material of lower strength. This should be considered in all situations.

(b) *Shrinkage*: Since most repairs are made on older Portland cement concrete in which major shrinkage has been completed, the repair material should be essentially low shrinkage in nature to avoid shear at the interface. Shrinkage of cementitious repair materials can be reduced in a number of ways.

(c) *Modulus of elasticity*: The modulus of elasticity of repair materials should be as close as possible to the old concrete being repaired. If the moduli of the two materials differ too much, large differences in stress can be generated under parallel loading or in deformations under a series loading in the two materials. Either case can result in failure of the repaired structures.

(d) *Color properties*: For repair of architectural concrete surfaces and concrete highways, the color of the repair material should not differ appreciably from the adjacent surface. Trials should be made on the jobsite mockup prior to beginning the actual production work.

(e) *Cost*: The total cost of the materials is another important consideration in material selection for repair of concrete highways.

(f) *Compatibility*: Compatibility is the most important property for a repair material. Compatibility means the properties of a repair material match well the properties of the materials to be repaired, and hence two materials can work together to carry out the external loading and to withstand the impact of the environment.

The widely used methods for evaluating the performance of rapid repair mortars are listed in Table 6-15.

Table 6-15 Testing methods for evaluating the performance of repair mortars

Test	Method of Testing
Determination of compressive strength	BS 6319-2:1983
Measurement of pull-off strength	BS 1881-207:1992
Determination of shear strength	BS En 12615:1999
Measurement of shrinkage	ASTM C531-00
Determination of modulus of elasticity	BS 1881-121:1983
Compressive strength of parent concrete	BS EN 12390-3:2002

6.3.6 General application guideline

Different types of repair mortars require different kinds of treatment and are suitable for different application conditions. Therefore, the application procedures for repair materials recommended by the corresponding manufacturers should be followed. The general steps in the repair of concrete highways using the different repair mortars are as follows:

Step 1: Cut (saw cut is recommended) the boundary of the repair location to avoid feather-edging and to provide a square edge.

Step 2: Clean the surface and remove all faulty materials, including dust, unsound or contaminated material, oil, paint, grease, and corrosion deposits.

Step 3: The repair surface should be water saturated or primed with a primer in accordance with the manufacturer's instructions.

Step 4: A fresh mixture of the repair materials should be mixed in the recommended proportions, and then placed in a position with proper compaction, according to the manufacturer's instructions;

Step 5: The repair portion should be protected from damage and for a suitable curing period before opening to traffic.

6.4 SHRINKAGE-COMPENSATING CONCRETE

Shrinkage-compensating concrete is an expansive concrete. Its expansion occurs at an early stage before the drying shrinkage and is compensated for by the drying shrinkage occurring later on. In Figure 6-40, the early-age volume change of a normal Portland cement concrete specimen and an expansive concrete are schematically drawn to compare the behavior of two types of concretes and to illustrate the mechanism of an expansive concrete.

6.4.1 Expansive materials and mechanisms

Shrinkage-compensating concrete can be made in two ways. One is by using expansive cement, such as types K, M, S, and O. Another way is by adding suitable expansive admixture to normal Portland cement concrete.

Expansive cements are usually special Portland cements with some expansive chemical compounds added. For instance, type K cement is Portland cement plus anhydrous tetracalcium trialuminosulfate, $C_4A_3\bar{S}$, additional calcium sulfate, and uncombined calcium oxide (lime). Type M cement is a blend of Portland cement and high alumina cement plus additional gypsum.

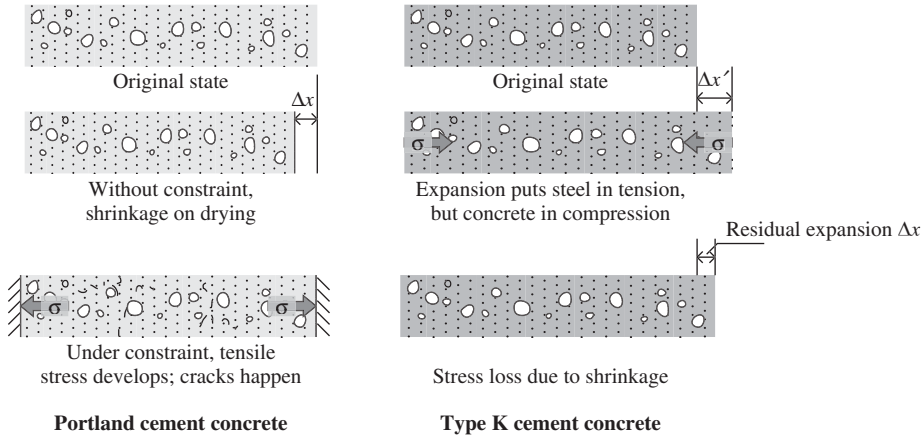

Figure 6-40 Performance of shrinkage-compensating concretes

Type S cement is Portland cement with a large amount of C_3A and gypsum. In China, in special Portland expansion cements, aluminum sulfate expansive cement (or sulfoaluminate expansive cement) is normally used for shrinkage compensation, which is produced with ($C_4A_3\bar{S} + C_2S$) clinker and gypsum. The expansive admixtures used include various expansive agents made of $C_4A_3\bar{S}$ clinker, alumite (alumstone), and anhydrous gypsum, of sulfoaluminate clinker, alumite (alumstone), and anhydrous gypsum, or MgO.

The main mechanism of expansive concrete is the growth of the expansive hydration products right after setting under moist conditions, such as etringite (AFt), monosulfoaluminate (AFm), and MH. These hydration products have a good crystal structure and large volume expansion with a high crystal growth pressure. They can increase the volume of concrete through the growth of the crystals (Chatterji and Jeffery, 1966; Okushima et al., 1968). It should be pointed out that, even though these hydration products have a large volume expansion compared to the original raw compounds, the volume is still less than the total volume of the compounds and water. Hence, the expansion is only realized under moist conditions. Moreover, the growth of such crystals should occur before the concrete matures. Otherwise, as discussed in Chapter 2, unsoundness can occur and the hardened concrete can be damaged by the cracks formed by the aggressive movement of the later-formed crystal. An air entraining agent can also act as a expansion admixture because it causes an increase of the concrete volume due to the entrained air voids.

In practice, it is more convenient to produce an expansive concrete using an expansive agent plus normal Portland cement than to produce it with expansive cement. In China, the production of expansion agents has been rapidly increased. A common dosage for expansive agents is from 5 to 15% by weight of cement, for replacement. The main characteristic of shrinkage-compensating concrete is in its expansion, usually expressed as the restrained expansion rate. The expansion rate can be measured using a restrained frame (Wang, 2006), as shown in Figure 6-41. To measure the restrained expansion, a expansion concrete or mortar is cast around the frame and the restrained strain is measured after demolding. The experiment is designed in this way so as to reflect the true situation of the concrete expansion by considering the minimum reinforcement required. It has been found from experiments that the restrained expansion rate can reach $(11-18) \times 10^{-4}$ if the expansive agent replacement percentage is in the range of 12 to 15% (Wang, 2006).

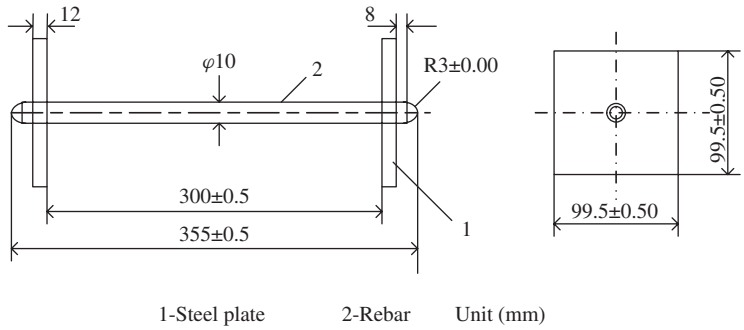

Figure 6-41 A restrained frame for expansion rate measurement on concrete

Table 6-16 A typical mix proportion of shrinkage-compensating concrete (kg/m^3)

Series	Binder	Coarse Aggregate	Fine Aggregate	Water	Water Reducer	*w/c*
1[a]	347	1056	754	184.1	0.00	0.53
2[b]	338+22	1030	810	187.2	2.16	0.55
3[b]	470+30	1038	692	172.5	5.00	0.37

[a]M. W. Hoffman and E. G. Opbroek (1997) ACI, *Concrete International*, **1**(3), 19–25. Binder is type K cement.
[b]D. M. Wang (2006), *High performance expansive concrete*, Publisher of Hydraulic and Hydropower of China, Beijing. Binder is cement plus expansive agent (2: $f_c = 30$ MPa and 3: $f_c = 60$ MPa).

The mix proportion of expansive concrete is slightly different than that of normal Portland cement concrete. When type K cement is used in concrete, a minimum cement content of 305 kg/m^3 is required to ensure adequate expansion. Moreover, a minimum of 0.15% reinforcement has to be added. The incorporation of reinforcement is aimed at providing a suitable restraint before compensating the dry shrinkage to avoid even earlier cracking due to expansion. When an expansive agent is used to produce shrinkage-compensating concrete, the mix proportion procedures are similar to those for normal Portland cement concrete. As discussed above, the amount of expansive agent used is expressed as the percentage of binder to be replaced. Usually, other mineral admixtures, such as slag or fly ash and water-reducing admixtures are used together with the expansive agent. In this case, it should be noted that pozzolans and water-reducing admixtures have a trend in reducing expansion. A typical mix proportioning of shrinkage-compensating concretes using either type K cement or expansion agents is given in Table 6-16.

6.4.2 Properties

The properties of shrinkage-compensating concrete, both in fresh and hardened stages, have their own characteristics different from those of normal Portland cement, which need to be paid attention to in order to fully utilize the advantages and avoid the limitations.

(a) *Workability*: In the fresh stage, shrinkage-compensating concrete tends to be stiff but highly cohesive. The slump loss of the expansive concrete at a temperature of 32°C or higher and in dry conditions is more serious than that of normal concrete. This will cause a reduction of both strength and expansion. The reason for this is the large amount of AFt formed in the early stage. To solve this problem, cool water with ice added should be used to lower

the temperature of the concrete mixture to below 29°C. Because of the quicker stiffening and setting of expansive concrete under hot and windy conditions, plastic shrinkage cracks easily occur and create more serious problems than normal Portland cement. Hence, a careful early-age curing is a must for expansive concrete.

(b) *Strength*: Shrinkage-compensating concrete made of type K cement is usually prepared with a *w*/*c* ratio from 0.4 to 0.65. Under such conditions, the paste matrix in shrinkage-compensating concrete is denser, and the interface between the aggregates and paste is stronger. Subsequently, the compressive strength of shrinkage-compensating concrete is much higher than that of normal Portland cement concrete. For shrinkage-compensating concrete with a expansive agent, an enhanced compressive strength is also normally observed. However, for different grades of concrete, the improvement levels are different. For normal-strength concrete with a projected 28-day compressive strength of 30 MPa, the strength improvement due to the incorporation of an expansive agent is not obvious. However, for high-strength concrete with a projected 28-day compressive strength of 60 MPa, the improvement of compressive strength can reach 15 to 20% (Wang, 2006).

(c) *Microstructure*: The hydration rate of shrinkage-compensating concrete is usually higher than that of normal Portland cement concrete. The microstructure of shrinkage-compensating concrete at an early age contains a large number of AFt crystals. With the process of hydration, C–S–H can fill in the spaces occupied by water and surround the AFt crystals. Hence, a much denser microstructure can be produced.

(d) *Durability*: As shrinkage-compensating concrete has a denser microstructure and a higher gel-to-space ratio, its resistance to water penetration and ion diffusion is greatly improved. As a result, the migration rate of water, and the diffusion rate of chloride ions, oxygen, and carbon dioxide into the concrete are reduced. Generally speaking, shrinkage-compensating concrete has better durability than normal concrete in respect of carbonation, corrosion of steel bar, freezing–thawing, chemical resistance, and leaching.

6.4.3 Applications

Although studies on expansion cement and expansive concrete started in the 1950s, the application of expansive concrete only became somewhat popular in the 1980s. It has been reported that shrinkage-compensating concrete has been mostly utilized in structural elements, such as slabs, pavement, runways, prestressed beams, and water- and sewage-handling structures (Mehta and Monteiro, 2006). In China, many buildings and infrastructures have been built up with shrinkage-compensating concrete. The following are good examples (You and Li, 2005).

(a) *Bank of China in Qingdao*: The underground structure of the building with an area of 6500 m^2 has been built up partially with shrinkage-compensating concrete. The total amount used was 1200 m^3 with 12 to 13.5% of expansion agent added.

(b) *Car park at Beijing Airport*: This structure has four stories underground and two above ground. To solve the leakage problem due to shrinkage cracking, shrinkage-compensating concrete was utilized. The binder composition for the concrete was 340 kg/m^3 Portland cement, 110 kg/m^3 slag, and 55 kg/m^3 of expansion agent. The slump flow was greater than 550 mm and the 28-day compressive strength was 80 MPa.

(c) *Beijing National Stadium (Birdnest)*: The ground-floor slab of the stadium has a thickness of 650 mm and a large area. It adopted a shrinkage compensating concrete for construction.

Other examples include Terminal 3 Building of Beijing National Airport, the Beijing Tongchan building, Gongbei Port Square in Zhuhai, and the East Square building in Beijing.

6.5 SELF-COMPACTING CONCRETE

Self-compacting concrete (SCC) or self-consolidation concrete is a high-fluidity concrete (HFC). Self-compacting means it can be easily placed and consolidated by its own gravity in a formwork, even with highly congested reinforcements, without external consolidation by vibration. It is characterized by its high filling capacity caused by high visco-plastic deformability, resistance to segregation, and an ability to maintain a stable composition throughout transportation and placing. SCC has the advantages of fast construction, noise reduction, good formability, and energy effectiveness. SCC enables concrete to be placed in structures that would otherwise have been impossible to construct with concrete, and has undergone dramatic improvements in construction efficiency of extralarge-scale structures, such as bridge tower pile cap (Figure 6-42).

Self-compacting concrete was first systematized by Okamura in 1988 in Japan. At the beginning, he named it "high-performance concrete" (HPC). SCC/HPC was initially developed to meet the need of construction in Japan. The postwar reconstruction of Japan in the 1960s led to a boom in building and infrastructure construction. As Japan is a major earthquake region, most structures have to be heavily reinforced to be earthquake-proof, especially at beam–column joints. Because of these situations and the need for speedy project delivery, many structures could not be built with sufficient compacted concrete. Within a decade or two, many reinforced concrete structures deteriorated. To solve the durability issue of new concrete construction, a project was started by H. Okamura of the University of Tokyo. His investigation found that insufficient compaction was the most common cause of deterioration of concrete structures and suggested an increase in the flowability of the fresh mixture to eliminate compaction, i.e., "self-compacting" concrete mixtures (Kuroiwa et al., 1993).

In Europe, a large, industry-led (NCC Sweden, GTM-Vinci France, and six other partners) research project was funded by the European Commission in 1997 (Grauers, 1997). The European

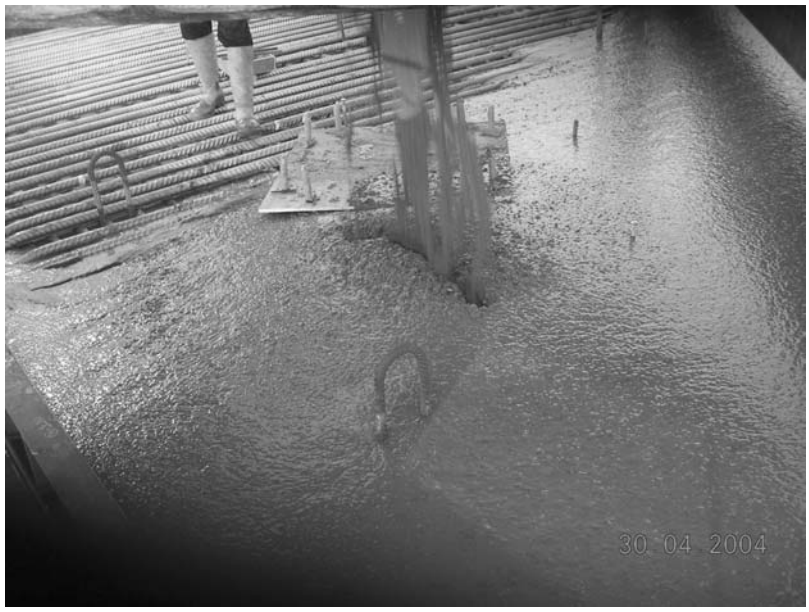

Figure 6-42 Application of self-compacting concrete for in situ piles

SCC project proved that SCC was practical for application using a variety of local materials, and that the expected benefits were obtainable in real construction practice. The working group on SCC set up under RILEM TCI45-WSM was converted to a new RILEM workgroup (TCI74-SCC), and its guidelines on SCC were published in 2000 (Petersson and Skarendahl, 2000).

The fluidity of self-compacting concrete was realized with the invention of high range of water-reducing admixtures or superplasticizers. The alternative approach to raising consistency was to increase the cement paste content.

6.5.1 Advantages of self-compacting concrete

SCC is considered an environmentally friendly material. First, the application of SCC on a construction site can eliminate the need for vibration to compact the concrete. The compaction of fresh concrete by vibration is generally recognized as a heavy physical job and an unpleasant activity in the concrete construction process. The vibration can cause high noise levels, up to 90 dB, that are not good for public health, especially the health of the operators. Second, the acceleration generated by vibrators can reach 0.70 to 4 m/s^2 and has potential to injure the vibrator operator. Hence, eliminating the vibration significantly improves health and the environment on a concrete construction site (Bartos and Cechura, 2001). Third, some skill and experience are needed for vibrator operators in compacting fresh concrete into a satisfactory concrete. Lack of experienced workers in many regions may lead to low quality of concrete. The application of SCC can solve this problem and ensure consistent high quality for concrete structures. The application of SCC also makes automation of construction possible, leading to higher productivity. This is envisaged not only in precast concrete production; but also for in situ concreting operations.

The introduction of SCC benefits architects and structural engineers, and ultimately the users of buildings. New types of structural elements, which were not possible with traditional concrete, can be produced using SCC. Such elements include different types of steel–concrete structural elements with more complex shapes, that are thinner with a much heavier reinforced cross section.

6.5.2 Property evaluation of fresh self-compacting concrete

The major difference between traditional concrete and SCC is the flowability in the fresh stage. Due to its water-like fluidity, the methods utilized to evaluate the workability of traditional concrete in the fresh stage are not suitable for SCC. Thus, starting from the invention of SCC, much research has focused on property evaluation of SCC in the fresh stage. Up to now, standardized yet, many test methods, though not have been widely recognized worldwide, and are presented in this section.

6.5.2.1 Slump flow test

The slump flow test is the most common test method for measuring the flowability of SCC. The apparatus employed and the procedures followed are very similar to the slump test for conventional concrete stipulated in BS 1881: Part 102 (BSI, 1983) or ASTM C143 (ASTM, 2005a). The only differences between slump and slump flow tests are the following. (1) No tamping is allowed when filling the concrete into the slump cone for the slump flow test. (2) The slump flow test measures the time that is needed for SCC to spread into a circular-shaped configuration with a nominal diameter of 500 mm, named T500, as the index of flow velocity. Usually, it requires SCC to have a T500 less than 8 seconds (Shindoh and Matsuoka, 2003; Khayat et al., 2004; Felekoglu et al., 2007; Gesoglu and Ozbay, 2007; Sonebi et al., 2007). (3) The slump flow test

also measures the maximum nominal diameter that the SCC can reach after lifting the slump cone without limiting the time. Usually, the SCC should be able to reach a nominal diameter of 600 mm. And (4) the flow test can also provide some information on the cohesiveness of SCC through visual inspection. If the SCC has insufficient cohesiveness, the coarse aggregate in SCC cannot flow with the mortar, and the sand particles cannot flow with the water. Thus, the coarse aggregates will be left in the central region of the slump patty, and a layer of thin mortar will appear on the outside ring of the slump patty, as shown in Figure 6-43. To evaluate this type of phenomenon, Daczko and Kurtz (2001) proposed a visual stability index (VSI), and the assessment criteria adopted by ASTM (ASTM, 2005b) are summarized in Table 6-17.

6.5.2.2 V-funnel test

The V-funnel test was first proposed by Ozawa et al. (1995), and can be used to evaluate the ability of SCC to pass through a small space. As shown in Figure 6-44, the apparatus for a V-funnel test consists two parts: a V-shaped top connected to a rectangular bottom. There is a

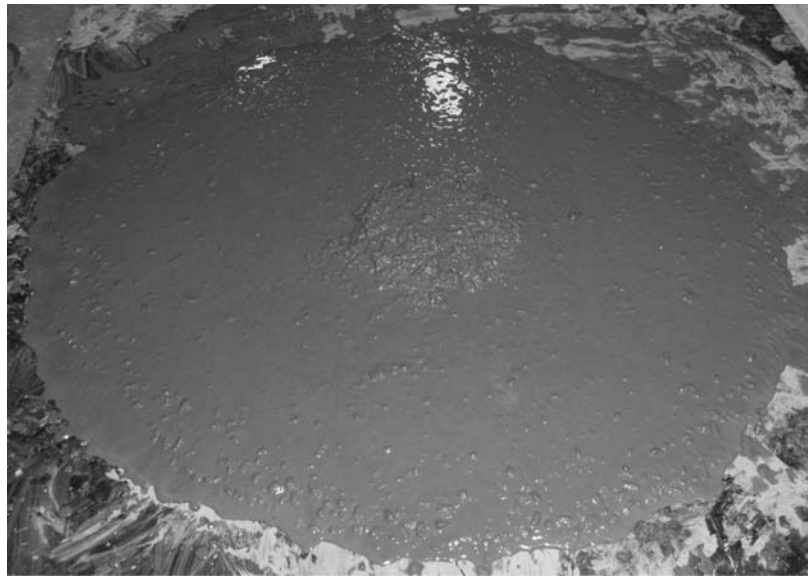

Figure 6-43 Phenomenon of SCC lack of cohesiveness

Table 6-17 Visual stability index (VSI) values

VSI Value	State	Description and Criteria
0	Highly stable	No evidence of segregation or bleeding
1	Stable	No evidence of segregation; slight bleeding observed as a sheen on the concrete mass
2	Unstable	A slight mortar halo $\leq$ 10 mm and/or aggregate pile in the center of the concrete mass
3	Highly unstable	Clear segregation evidenced by a large mortar halo $\geq$ 10 mm and/or a large aggregate pile in the center of the concrete mass

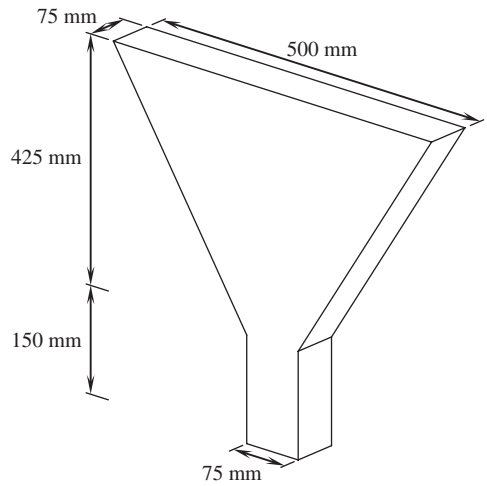

Figure 6-44 Schematic diagram of a V-funnel

Table 6-18 Recommended values of V-funnel time

Source	Range (sec)
European Federation of National Trade Associations (2002)	6–12
Precast/Prestressed Concrete Institute (2003)	6–10
Self-compacting Concrete European Project Group (2005)	≤25
Hwang et al. (2006)	<8

gate at the bottom of the apparatus. To perform the V-funnel test, the bottom gate is first closed to shut off the orifice and then SCC is filled gently into the V-funnel until it reaches the top edge. After leveling the top surface of the SCC, the bottom gate is opened to discharge the SCC. The period from the time the bottom gate is opened to the time when the concrete has been discharged to such extent that light can be seen through the orifice is recorded as the V-funnel time. The V-funnel time is a measure of the flowability of SCC. A shorter V-funnel time means a higher flowability, while a longer V-funnel time means a lower flowability. The recommended ranges of V-funnel time, according to various researchers and guidelines, are summarized in Table 6-18 for comparison. It can be observed that the recommended values vary in a rather wide range.

6.5.2.3 J-ring test

The J-ring test was developed in Japan (J-ring means Japanese ring). The J-ring test measures the ability of SCC to pass through reinforcing steel. A typical J-ring is shown in Figure 6-45. A number of 12-mm-diameter, plain, round steel bars are fixed uniformly along the circumference of a circular steel ring with external diameter of 360 mm, internal diameter of 300 mm, and thickness of 30 mm. They are used to simulate the obstructive effects of the steel reinforcing bars in the mold. The J-rings used by different researchers are basically similar except for the spacing between the steel bars, which varies from 30 to 120 mm (Grunewald and Walraven, 2001;

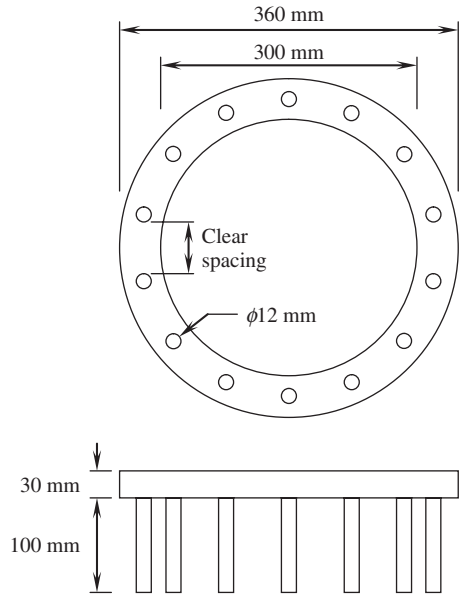

Figure 6-45 Schematic diagram of a J-ring

Daczko, 2003; Khayat et al., 2004). Ideally, the clear spacing between the steel bars of the J-ring should be the same as the minimum clearance of the steel reinforcing bars in the mold to truly reflect the actual situation.

The J-ring is usually used together with a flow test setup by putting the ring outside the slump cone to obstruct the flow of SCC. The flowability of SCC is measured in terms of the reduction in flow of SCC after passing the J-ring as compared to the free slump flow without a J-ring (Brameshuber and Uebachs, 2001; Daczko, 2003; Khayat et al., 2003; ASTM, 2006). The passability of SCC can also be indexed in terms of the difference in the height of concrete between the inside and outside of the J-ring (RILEM, 2002; European Federation of National Trade Associations, 2002; Precast/Prestressed Concrete Institute, 2003). Similar to the slump flow test, visual inspection after the J-ring test should be carried out to detect any signs of segregation. In general, segregation tends to be more serious with the J-ring in place due to the blockage effect of the reinforcing bars.

Table 6-19 shows the acceptance requirements of a J-ring test recommended by different researchers, and the guidelines either in the flow reduction or in the height difference as measures

Table 6-19 Recommended acceptance requirement for J-ring test

Source	Measurement	Range (mm)
Brameshuber and Uebachs (2001)	Flow reduction	$\leq$50
European Federation of National Trade Associations (2002)	Height difference	$<$10
RILEM (2002)	Height difference	$<$10
Precast/Prestressed Concrete Institute (2003)	Height difference	$<$15
ASTM (2006)	Flow reduction	$\leq$50

of the passability of SCC. Regarding the flow reduction, 50 mm is an index accepted by all researchers and guidelines.

6.5.2.4 U-box test

The U-box test was originally developed in Japan (Hayakawa et al., 1993). In this test, a specially designed U-shaped tube, comprising a storing compartment, a filling compartment, and an opening between the two compartments, is employed (Okamura et al., 2000).

The procedures for the U-box test are as follows. Firstly, the sliding gate separating the two compartments is closed and the concrete is filled gently into the storing compartment until the compartment is full; the top surface of the concrete is then troweled flat. Secondly, the sliding gate is opened quickly. Due to the hydrostatic pressure, the concrete in the storage compartment is pushed to fill the filling compartment until it completely stops. Ideally, the height in the storage and filling compartment should become the same. However, a level difference between the two compartments may exist due to the friction of the wall of the compartments and the viscosity of the concrete. After the concrete has stopped flowing, the height of the concrete in the filling compartment is measured. The filling height is an integrated measure of the filling ability and passing ability of the concrete.

6.5.2.5 L-box test

The L-box test was developed to assess the flowability and passing ability of SCC (Yonezawa et al., 1992). A typical apparatus for an L-box test is illustrated in Figure 6-46. It comprises a vertical compartment to store the concrete and a horizontal one to be filled by the concrete flowing from the vertical compartment. The dimensions of the vertical compartment can range from 60 to 100 mm in breadth, 150 to 300 mm in width, and 400 to 600 mm in height. The length of the horizontal trough varies among different L-box versions, ranging from 600 to 710 mm

Figure 6-46 An L-box apparatus

(RILEM, 2002; Sonebi, 2004; Self-Compacting Concrete European Project Group, 2005; Testing-SCC Project Group, 2005a), but the most commonly used version has a length of 700 mm. A sliding gate is inserted at the bottom of the vertical compartment. A number of plain, round steel bars are also inserted as obstacles to simulate the reinforcement in the mold. The number of reinforcing bars to be inserted should be decided according to the net spacing of reinforcing bars in the mold. If no information on the real situation is available, an obstacle arrangement of three 12-mm, plain, round steel bars with center-to-center spacing of 53 mm can be used.

The procedures for the L-box test are as follows. Firstly, the sliding gate separating the vertical compartment and the horizontal trough is closed and the concrete is filled gently into the vertical compartment. Then, after the top surface of the concrete is troweled flat, the sliding gate is opened quickly. Next, the concrete in the vertical compartment will be pushed by the hydrostatic pressure to flow along the horizontal trough, passing the obstacle. If the concrete has sufficient fluidity and passability, it will reach the end wall of the horizontal trough with a certain height.

After the flow of the concrete has ceased, the height of the concrete at the end wall, h_1, and the height of the concrete at the vertical compartment, h_2, are measured. The blocking ratio defined by h_1/h_2 can be estimated as a measure of the passability of the concrete. In addition, the time difference between two given points in the horizontal channel can be used as a measure of the viscosity of the concrete (RILEM, 2002; Gesoglu and Ozbay, 2007). The recommended values of blocking ratio are summarized in Table 6-20. A blocking ratio higher than 0.80 is usually suggested.

6.5.2.6 Sieve segregation test

The sieve segregation test was developed in the 1990s by Fujiwara (1992) to measure the segregation stability of SCC. In this method, a 2-liter (about 4.8-kg) concrete sample is taken from a concrete batch and placed gently over a 5-mm aperture sieve. Because the sieve is porous, the fine portion of the concrete that is incapable of adhering to the aggregate particles on the sieve will drip through the apertures of the sieve to the base receiver placed underneath. After 5 min, the sieve is removed without agitation and the weight of the material collected in the base receiver is measured. Since this method pours SCC directly from the batch to the sieve, it is called a direct pouring sieve method.

A modified sieve segregation test was developed in France (Association Francaise de Genie Civil, 2000) and later adopted in many countries in Europe (RILEM, 2002; Self-Compacting Concrete European Project Group, 2005; Testing-SCC Project Group, 2005b). In this method, 10 liters of a concrete sample taken from a batch is placed gently in a 300-mm-diameter container. The sample is then covered by a lid, put in a level position, and left undisturbed to allow any sedimentation of the coarse aggregate particles and bleeding of water to take place. After

Table 6-20 Recommended values of blocking ratio

Source	Range
European Federation of National Trade Associations (2002)	>0.8
Swedish Concrete Association (2002)	>0.8
RILEM (2002)	0.80–0.85
Precast/Prestressed Concrete Institute (2003)	>0.75
Self-compacting Concrete European Project Group (2005)	≥0.8

15 minutes, 2 liters (about 4.8 kg) of the top portion of the concrete sample is poured gently onto the sieve at a height of 500 mm. The fine portion of the concrete without sufficient adhesion to the aggregate particles will drip through the openings of the sieve to the base receiver underneath. After 2 min, the sieve is removed without agitation and the weight of the material collected in the base receiver is measured. Since this method pours SCC on the sieve after placing it in a container for a while, it is called an indirect pouring method. The segregation index, SI, for both methods, is calculated using the formula

$$\mathrm{SI} = \frac{M_\mathrm{p}}{M_\mathrm{c}} \times 100\% \tag{6-4}$$

where SI is the segregation index of SCC; M_p is the mass of the material collected from the base receiver; and M_c is the mass of the concrete poured onto the sieve. The segregation index measures the adhesive ability of the SCC matrix to coarse aggregates. A low segregation index represents a high adhesion, whereas a high segregation index represents a low adhesion of SCC.

As revealed in Table 6-21, all the recommendations impose an upper limit on the acceptable segregation index for SCC, no matter which method is used. In general, the recommended upper limit of the segregation index for the direct pouring method is 10%, while the recommended upper limit of the segregation index for the indirect pouring method is 20%.

6.5.2.7 Noncontact resistivity measurement

Li et al. (2009) have characterized fresh SCC properties with electrical resistivity measurements. The study adopts a noncontact resistivity measurement method that can provide accurate and reliable information for fresh SCC. The influence of various minerals, chemical admixtures, and rheological modifying agents on fresh SCC's properties can be identified by resistivity measurement. Figure 6-47 shows the electrical resistivity development with time for samples SCC-0 and NC. The proportions of the two concretes are shown in Table 6-22. It can be seen from the figure that the curve shapes of samples SCC-0 and NC are different. Firstly, the resistivity of NC develops faster than that of SCC-0. Secondly, there is an extreme point (P), as shown in Figure 6-47, followed by a temporary decreasing range, on the curve of sample SCC-0, which is not experimentally observed in normal concrete. From Table 6-22, it can be seen that a superplasticizer was added in SCC-0 while no superplasticizer was used in NC, which caused the delay of the C–S–H formation. The transformation of hydration products AFt to AFm occurred when sulfate ions were not sufficient for the hydration system, releasing ions (Ca^{2+} and SO_4^{2-}) and increasing the solid volume (AFt has lower density than AFm). The consequence is an electrical resistivity decrease until enough C–S–H formation offsets such a trend and the electrical resistivity increases again. In sample NC, the C–S–H formation is not delayed and

Table 6-21 Recommended values of segregation index

Source	Pouring Method	Range
Fujiwara (1992)	Direct	<5%
Khayat et al. (1998)	Direct	<10%
European Federation of National Trade Associations (2002)	Indirect	≤15%
Lachemi et al. (2003)	Direct	<10%
Testing-SCC Project Group (2005b)	Indirect	5–15%
Self-Compacting Concrete European Project Group (2005)	Indirect	≤20%

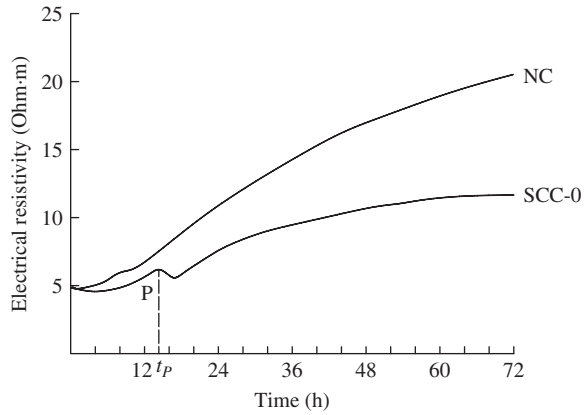

Figure 6-47 The electrical resistivity of SCC and normal concrete

Table 6-22 Mix proportions of concrete per cubic meter (kg/m^3)

							Viscosity Modifying Agent	
Name	**Water**	**Cement**	**Fly Ash**	**Sand**	**Coarse Aggregate**	**SP**	**Weight**	**Type**
NC	176	352	235	744	819	—	—	—
SCC-0	176	352	235	744	819	1.76	—	—
SCC-1	176	352	235	744	819	1.76	0.29	MC
SCC-2	176	352	235	744	819	1.76	0.29	PAM
SCC-3	176	352	235	744	819	1.76	0.29	CMC

its content increases with the hydration process covering the possible decreasing trend of the electrical resistivity caused by the phase transformation.

A superplasticizer is necessarily used in SCC to improve fluidity, which often has a retarding effect on the hydration process. Therefore, the extremum point becomes an obvious characteristic of SCC on the electrical resistivity curve. Figure 6-48 shows the electrical resistivity development with time for four SCC samples: SCC-0 without a viscosity-modifying agent (VMA) and SCC-1 through SCC-3 containing one of the VMAs, as shown in Table 6-22. All the curves follow a similar pattern to that presented earlier. There is an extremum point (P), followed by a temporary decreasing range on each curve. It can be seen that the addition of each of the VMAs leads to an electrical resistivity increase during the measurement period and the extremum point shifts to the left or the right.

The electrical resistivity increase in the SCC mixes with a VMA is attributed to the air entrapped by VMA addition. The air bubbles act as insulators for ion conduction and cause the electrical resistivity to become higher than that of mix SCC-0 without VMA, when other factors are the same.

6.5.3 Characteristics of mix proportion of SCC

The SCC mix proportion has some unique characteristics compared to that of conventional concrete. For example, the cement-based paste content in SCC is much more elevated due to the need to keep a good workability under low water–powder ratios. The increased paste content is used to supplement the decreased volume of the coarse aggregate, and to assure the required viscosity

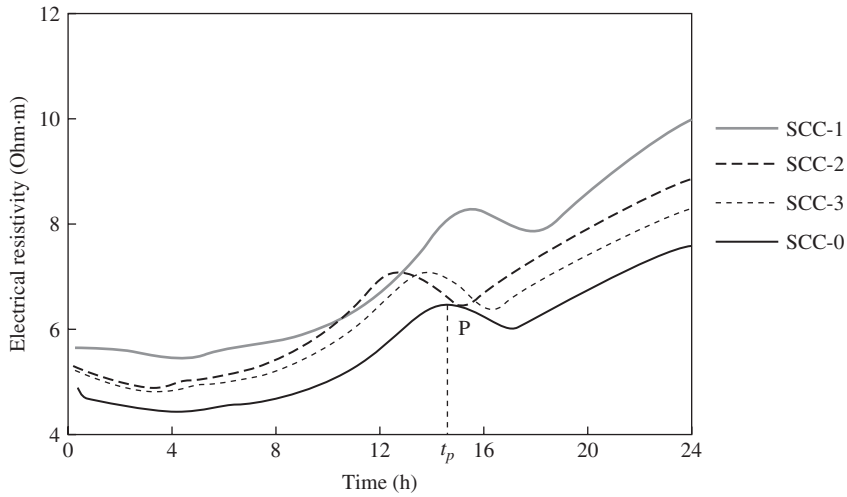

Figure 6-48 The electrical resistivity curves of SCC with various VMAs up to 24 hours

of the paste at lower water–powder ratios. Usually, the powder content is increased up to 600 kg/m^3 or more, and the water content is restrained to an adequately low level. Various mineral admixtures are utilized to increase the powder content. High fluidity is produced with the help of high-performance superplasticizers, and suitable cohesiveness is reached with the addition of a viscosity-modifying agent or powder.

The characteristics of the mix proportions of SCC are somewhat near to those of high-strength concrete. Hence, high-strength concrete can be easily transformed to SCC, and vice versa. However, to make SCC, the rheology of the matrix must be measured first to ensure that the matrix can maintain a uniform distribution of coarse aggregates. From the rheological point of view, a fresh SCC mixture should have low yield stress and moderate viscosity (Khayat et al., 1999; Bonen and Shah, 2005). The low yield stress is necessary to achieve high flow ability and high filling ability, while a moderate viscosity is essential to maintain good cohesiveness. Based on the mix design methodology and the methods to achieve the rheological requirements, currently, two major categories of SCC can be identified: the powder-type SCC and the VMA-type SCC (Bonen and Shah, 2005). The characteristics of the mix proportions of the two categories of SCCs are discussed separately in the following sections.

6.5.3.1 Power type of SCC mixtures

In general, powder-based SCC mixtures are developed from traditional concretes through the use of improved mix proportions. However, the relative proportions of SCC mixtures are quite different from those of conventional concrete. As shown in Figure 6-49, for a given total volume, the coarse aggregate volume of SCC mixes is much smaller than that of conventional concrete; the sand volume of SCC mixes is larger than that of conventional concrete; the cementitious material content of SCC mixes is much higher than that of conventional concrete; while the water volume of SCC mixes is similar to that of conventional concrete. Compared with relative mix proportions of a conventional concrete mixture with that of a SCC mixture, it can be observed that a SCC mixture generally consists of a lower coarse aggregate content, higher paste volume and lower water/cement (w/c) ratio. Actually, it is these characteristics in SCC mixtures that are responsible for the excellent workability of SCC.

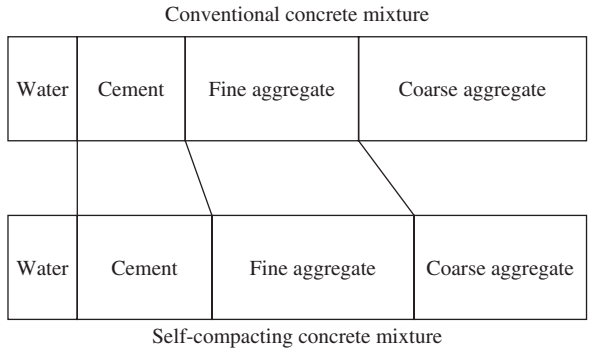

Figure 6-49 Mix proportions of conventional and self-compacting concrete mixtures

A low aggregate content in the concrete mixture is essential for the high performance of SCC mixtures because it can reduce the frequency of collision and contact between aggregate particles and thus reduce the solid-to-solid friction resulting from the particle interactions and shearing actions of the aggregate particles when they are moving relative to each other. Hence, the deformability and the flow speed of fresh SCC can be enhanced.

With a reduced coarse aggregate content but slightly increased fine aggregate content in SCC mixtures, the fine aggregate to total aggregate (F/T) ratio is increased. Typical values are increased from 0.40 for conventional concrete mixtures to higher than 0.50 for SCC mixtures (Yurugi et al., 1993; Saak et al., 2001; Bonen and Shah, 2005). Such an increase in the F/T ratio helps maintain a moderate viscosity of the concrete to avoid localized increase in the shear stress and improve the deformability (Okamura and Ozawa, 1994).

Apart from the F/T ratio, the volume of paste (i.e., water + powder) of an SCC mixture is increased as compared to that of a conventional concrete mixture. In conventional concrete mixtures, the function of the paste when the concrete is still plastic is mainly to fill the voids among the aggregate particles. However, in SCC mixes, the paste functions as a medium for lubricating the aggregate particles suspended therein, to provide the required workability and deformability (Petrou et al., 2000; Roussel, 2006; Toutou and Roussel, 2006). It should be pointed out that the increase of the paste volume of SCC mixtures is achieved by an increase in the powder content with a lower water/binder (w/b) ratio. The total water content remains almost unchanged as compared with typical conventional concrete mixes. The w/b ratio of SCC mixtures should be set in a range in which both deformability and cohesiveness of the SCC are high. It has been found, from practice, that a w/b ratio ranging from 0.30 to 0.45 gives the SCC mixtures satisfactory performance.

The powders utilized in powder-type SCCs include silica fume, fly ash, and ground limestone fines with different size distribution. In Europe and Japan, ground limestone, slag, fly ash, and silica fume are utilized. In the United States, the powders used are mostly fly ash and silica fume.

According to Khayat (2000), SCC mixtures having a powder content (powder content here means particles finer than 80 μm) of 500 to 600 kg/m^3 can effectively improve the cohesiveness and reduce the superplasticizer demand. Likewise, the ACI Committee 237 (2007) recommends that for initial trial mixing, a relatively high powder content (powder content here means particles finer than 125 μm) of 386 to 475 kg/m^3 should be adopted.

6.5.3.2 Viscosity-modifying agent type SCC

In a VMA type of SCC, to satisfy the rheological requirements of SCC, superplasticizer and—VMAs are incorporated into SCC mixtures. The incorporation of superplasticizers can largely decrease the SCC yield stress with a limited influence on the viscosity (Khayat, 1999; Wallevik, 2003). The incorporation of VMA can significantly improve the cohesiveness of the SCC. VMAs are usually water-soluble polymers, and can dissolve in the mixing water and adsorb cement particles. The polymer can hold water tightly and provide sufficient adhesion to the aggregate. As reported by Khayat and Guizani (1997), incorporation of 0.07% by mass of cementitious materials of a welan gum VMA in a highly fluid concrete significantly reduces the bleeding by more than 85% and the segregation by 45%. Rols et al. (1999) also reported that incorporation of 0.005% of starch-based VMA significantly reduced the aggregate sedimentation of concrete. Sometimes, VMA can be used to overcome the negative impacts resulting from the poor aggregate grading used in SCC mixtures (Lachemi et al., 2003). In summary, the VMA-type SCC utilizes polymers to improve the viscosity of SCC and is proportioned based on the use of both superplasticizer and VMA. In these kinds of concrete mixtures, the required workability or flowability is controlled by the superplasticizer dosage, while the required segregation stability (viscosity) of the SCC mixture is adjusted by the VMA usage.

The differences in mix proportions of traditional concrete, powder-type SCC, and VMA-type SCC are schematically shown in Figure 6-50. It can be seen from the figure that among the three types, traditional concrete contains the highest amount of coarse aggregates, the smallest amount of sand, the lowest cementitious materials, and the least water. The VMA type of SCC contains a moderate to high content of cementitious material, moderate water content, almost no or very small amounts of mineral admixture, moderate sand content, moderate coarse aggregate content, high superplasticizer content, and a certain amount of VMA. The powder type of SCC contains the highest content of cementitious materials, the highest sand content, the lowest coarse aggregate content, high mineral powder content, relatively high water content, and relatively high superplasticizer content.

6.5.4 SCC pressure on formwork

The applications of SCC in a precast plant are more extensive than those in concrete cast in place on a construction site. One technical issue limiting SCC's application on a construction

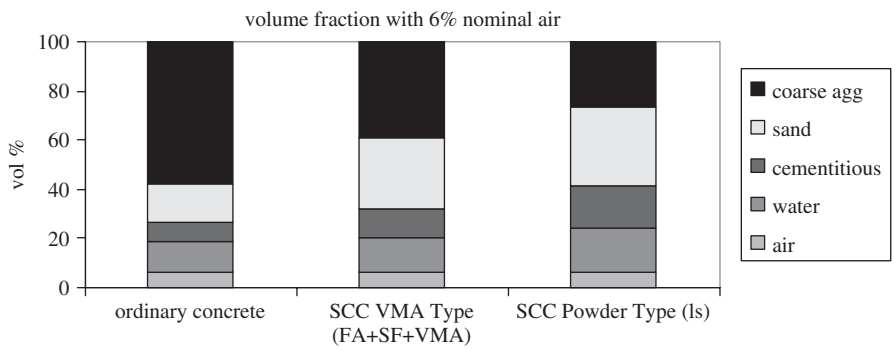

Figure 6-50 Mix proportions of traditional concrete, powder-type SCC, and VMA-type SCC

site is a lack of knowledge about the lateral pressure generated by SCC on the formwork (Shah et al., 2009).

Formwork pressure depends on the fluidity and cohesion of the SCC, rate of vertical rise, and the method of placing (from the top or from the bottom). Some design guidelines, such as "The European Guidelines for Self-Compacting Concrete (SCC) Specification, Production and Use," suggests that in formwork design, including supports and fixing systems, it should normally be assumed that the full hydrostatic concrete pressure is applied to the formwork. Such type of design, of course, is safe and conservative. However, it may overestimate the pressure that leads to unnecessary increased cost. It has been reported and confirmed that the formwork pressure of SCC can be smaller than the hydrostatic pressure (Fedroff and Frosch, 2004). This is due to the buildup of a 3D structure when the concrete is left to rest. A similar phenomenon has been observed by Khayat and Omran (2009) and Lange et al. (2009). In Khayat and Omran's work (2009), a portable device was developed to monitor lateral pressure exerted by SCC. Their study shows that the formwork pressure exerted by SCC on site can be predicted by the simulation of the device through the analytical model that they built up. In the works Lange et al. (2009), a formwork pressure model was built based on a threefold SCC performance. The model considers that SCC exhibits a pressure decay. The model is relatively simple and easy, and has been successfully used in tall wall construction.

Formwork pressure and 3D structure rebuilding of SCC is highly influenced by the mixture proportion and raw materials composition, in which the powder materials play an important role. It has been found that cement with lower alkali/C_3A content produces lower formwork pressure than cement with a higher content (Shah et al., 2009). Moreover, shows the same study that replacement of cement with metakaolin clay is very effective in reducing the formwork pressure of SCC.

If the SCC is pumped from the bottom, then, locally, pressure can be increased close to the pump entry point, especially on restart, if there is an interruption in pumping. This pressure increase has to be taken into account in formwork design. If not, the pressure is underestimated, and may cause large deformation or even failure of the structural formwork.

6.5.5 Applications of SCC

Due to its attractive advantages, SCC has been widely used throughout the world. Full-scale trials and demonstrations were carried out in the early 1990s, and self-compacting concrete was first used in significant practical applications in Japan (Hayakawa et al. 1993). The gradual increase in volume consumption in Japan reached its peak in the construction of the two anchorages of the Akashi–Kaikyo bridge in 1997. A total of 600,000 m^3 of different varieties of SCC were placed, which remains the most prominent landmark application of SCC and the largest single application to date. In India, large application of SCC was commenced during the Delhi Metro Project in 2003 (Vachhani et al., 2004). However, the annual consumption of SCC in India ranges only from 50,000 to 100,000 m^3, about 0.1% of the total concrete production (Asmus and Christensen, 2009). In China, due to the booming infrastructure construction in the last few decades, the applications of SCC have been speeded up. A steel fiber-reinforced SCC with compressive strength of 60 MPa has been used in the construction of the new China Central TV station. The project comprises two towers of height 234 m, inclined at 6 degrees toward each other. Columns of size 1900 × 1500 mm are used to support the tower. C60 steel fiber-reinforced SCC is used to build up the columns to meet the requirements of crack control and to fit the complex shape (Yan and Yu, 2009). In Beijing, a C60 self-consolidating concrete was also used in Tower A of the International Trade Center, Phase 3, which is 330 m in height. The columns

Table 6-23 The mix proportion of a C60 self-compacting concrete (kg/m^3)

Cement	Fly Ash	Sand	Crushed Limestone	Water	Superplasticizer
360	240	800	840	175	7.1

Table 6-24 Properties of the fresh and hardened C60 concrete

Fresh Concrete After 1 Hour of Casting				Compressive Strength (MPa)		
Air Content (%)	Slump (mm)	Slump Flow (mm)	Flowing Time[a] (sec)	3-day	7-day	28-day
2.4	250	665	21	43	60	84

[a]Flowing time through V-funnel

in the core wall are huge, with a cross-sectional area of 3.6 m^2, and C60 SCC is used for these columns. The mix proportion of the concrete for this project is given in Table 6-23 and its properties are given in Table 6-24. Moreover, C50 SCC has been applied in a famous project in Beijing—the Birdsnest which is the National Olympics stadium. The outer shell of the stadium is composed of irregular steel elements. Many concrete columns have been built up between the outer steel structure and the inner concrete stand to support the stand system. There are a total of 124 steel tubular columns, 228 inclined beams, 600 inclined poles, and 112 Y-shaped poles. They had to be interwoven with 3D contorted annular beams. It is very difficult, if not impossible, using traditional concrete due to the limited space for compacting. Hence, SCC was selected for construction of these columns and poles (Yan and Yu, 2009). In Hong Kong, a multipurpose commercial building has been designed and constructed, that has 118 stories and is 495 m in height. High-strength SCC of grade 90 was used to construct the concrete core of the building to reduce the dead load and column size (Zhang et al., 2009). The main mix parameters for the SCC were cementitious material content of 600 kg/m^3, water to binder ratio of 0.26, and a liquid PC-based superplasticizer at a dosage of 3 L per 100 kg of cementitious material. The main requirements for the SCC are (1) mean compressive strength of 90 MPa and a target strength at 28 days of 104 MPa; (2) mean modulus of elasticity of 39 GPa at 28 days; (3) T500 $<$ 15 sec and slump flow of 700 mm in 120 sec; (4) pumpable to a height of 320 m; and (5) casting temperature of concrete lower than 25°C on site. In the United States, the 15-km Los Angeles Sewer Tunnel renovation project has used 37,000 m^3, which made it the largest SCC project in North America.

The application of SCC has also been extended into hydraulic engineering, such as dam construction (An et al., 2009). Rock-filled concrete (RFC) is a new type of mass concrete structure developed in China. It utilizes large rock blocks, up to 300 mm, as the filler and SCC as the "binder" or "grout" to build up the dam and other massive concrete structures. The first application of RFC in China was a gravity dam in a reservoir project in Beijing. The dam, 13.5 m in height and 2000 m^3 in volume, was constructed in 2005. Following the success of this project, RFC has also been applied in the construction of an auxiliary dam in the Baoquan water-storage project. The dam is 42 m in height, in which the top 3 m are constructed with RFC. In addition, RFC has also been applied in caisson backfill construction of the Xiangjiaba hydropower project, the third largest hydropower station in China. The greatest depth of the caisson is 54.7 m and the total volume is 80,000 m^3. The consumption of RFC for this project was about 70,000 m^3.

6.6 ENGINEERED CEMENTITIOUS COMPOSITE

Engineered cementitious composites (ECC) are special types of random short-fiber-reinforced, cement-based composites. The representative characteristic of ECC is its excellent ductility and toughness. The early work at the National Science Foundation Center of Advanced–Cement-Based-Materials at Northwestern University in the United States has demonstrated that cement-based composite manufactured by the extrusion technique with a few percent of polyvinyl alcohol fibers does show great improvement in ductility (Shao et al., 1995). The work continued at HKUST and showed that extruded plates can reach a large deflection under four-point bending (Li and Mu, 1998). The concept of ECC was developed by Li (1998) and Li et al. (2001a).

The theoretical mechanism in the development of ECC was an extension from the pioneering research by the IPC group (Aveston et al., 1971), which applied fracture mechanics concepts to analyzing fiber-reinforced cementitious composite systems. In ECC, micromechanics was employed to optimize the microstructure of the composite, in which the mechanical interactions between the fiber, matrix and interface were taken into account. Marshall and Cox (1988) showed that steady-state crack propagation can prevail over the typical Griffith-type crack when the following equation is satisfied:

$$J_{\text{tip}} = \sigma_{\text{ss}}\delta_{\text{ss}} - \int_0^{\delta_{\text{ss}}} \sigma(\delta)d\delta \tag{6-5}$$

where J_{tip} is the energy density at the crack tip; σ_{ss}, the constant ambient tensile stress; δ_{ss}, the constant crack opening; and $\sigma(\delta)$, the closing pressure as a function of the crack opening, δ. J_{tip} approaches the matrix toughness $K_{\text{m}}^2/E_{\text{m}}$ at small fiber content. The matrix fracture toughness K_{m} and Young's modulus E_{m} are sensitive to the mix design, such as w/c ratio and sand content. The right-hand side of Equation 6-5 can be interpreted as the energy supplied by external work minus the energy dissipated by the deformation of the inelastic springs at the fracture process zone. The inelastic spring concept is a convenient means of capturing the inelastic processes of fiber deformation/breakage and interface debonding/slippage of those fibers bridging across the crack faces in the process zone. Hence, Equation 6-5 expresses the energy balance during steady-state crack propagation.

Figure 6-51 schematically illustrates this energy balance concept on a fiber bridging the stress–crack opening relationship. The right-hand side of Equation 6-5 is shown as the area A

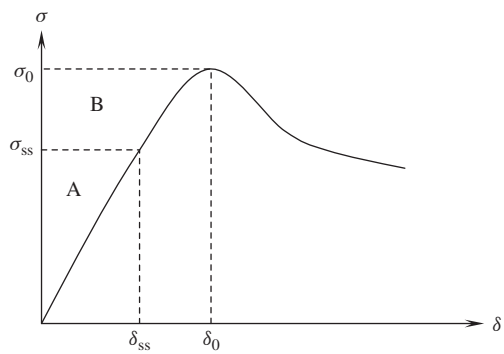

Figure 6-51 Schematic illustration of energy balance concept on a fiber bridging stress-crack opening stress-strain curve

and is referred to as the complementary energy. Since the maximum value (area B) of this complementary energy J_b' occurs when σ increases to the peak stress σ_0, and δ to the crack opening δ_0, it implies an upper limit on the matrix toughness as a condition for strain hardening:

$$\frac{K_m^2}{E_m} \leq \sigma_0\delta_0 - \int_0^{\delta_{ss}} \sigma(\delta)d\delta \equiv J_b' \tag{6-6}$$

It is clear from Equation 6-6 that successful design of an ECC requires the tailoring of fiber, matrix, and interface properties. Specifically, the fiber and interface properties control the shape of the $\sigma - \delta$ curve and are therefore the dominant factors governing J_b'. Composite design for strain hardening requires the tailoring of the fiber/matrix interface to maximize the value of J_b'. Similarly, the matrix composition must be designed so that the value of $J_m = K_m^2/E_m$ is not excessive.

The shape of the curve and especially the rising branch associated with J_b', shown in Figure 6-51, is related to a number of fiber/matrix interaction mechanisms, including debonding and frictional pullout. It also involves many parameters such as fiber content V_f, diameter d_f, length L_f, and stiffness E_f, chemical bond G_d, and the interface frictional bond τ_0. The peak value of the $\sigma - \delta$ curve is mainly governed by V_f, d_f, L_f, τ_0 in the case of simple friction pull-out. An analytic expression of $\sigma - \delta$ and σ_0 obtained by Li (1992) can be utilized as a base for theoretical analysis of ECC. In the case when both the interface chemical bond and slip hardening are present, an analytic expression of $\sigma - \delta$ found by Lin et al. (1999) can be employed.

ECC can be made with the same ingredients as regular concrete but without the use of a coarse aggregate. ECC can be produced by mixing, in a similar way to produce traditional mortar. Due to the simple production method, mixing is needed. ECC is suitable for mass production. It can be easily molded and shaped into different products reinforced with short random fibers, usually polymer fibers. Since the introduction of the concept in the 1990s, ECC has undergone major evolution in materials development. Li and co-workers (1998, 2000, 2001b) developed self-compacting ECC via a constitutive rheological approach. The high flowability was achieved with the utilization of a polyelectrolyte-type superplasticizer. In addition, extrusion of ECC has also been demonstrated (Stang and Li, 1999). Spray ECC, equivalent to shotcreting but replacing the concrete with ECC, is also being developed at the University of Michigan.

In mechanical behavior, ECC exhibits tensile strain-hardening behavior with strain capacity in the range of 3–7%, yet the fiber content is typically 2% by volume or less, which allows ECC to have very good bending ductility, like a piece of metal sheet. The fact that ECC can be bent to such a large deflection is due to the distinctively coated fibers embedded in the cementitious materials that are allowed to slide within the cementitious matrix.

Because ECC has excellent pseudo-ductility, investigations have been conducted on applications in practice. These include the repair and retrofitting of pavements or bridge decks (Lim and Li, 1997; Kamada and Li, 2000; Zhang and Li, 2002), the retrofiting of building walls to withstand strong seismic loading (Kanda et al., 1998; Kesner and Billington, 2002), and the design of new frame systems. These studies reveal the unique characteristics of ECC or R/ECC (steel-reinforced ECC) in a structural context, such as high damage tolerance in beam–column joints (Parra-Montesinos and Wight, 2000), super resistance to shear load, (Kanda et al., 1998; Fukuyama et al., 1999), higher energy absorption (Fischer and Li, 2003), excellent delamination and spall resistance (Lim and Li, 1997; Kamada and Li, 2000; Zhang and Li, 2002), high deformability, and tight crack width control for durability (Maalej and Li, 1995). ECC technology has been used on projects in Japan, Korea, Switzerland, Australia, and the United States. Many unsolved problems of traditional concrete—lack of durability, failure under severe strain, and the resulting expenses of repair—have been a driving force in the application of ECC.

6.7 TUBE-REINFORCED CONCRETE

Steel has the advantages of high strength and excellent ductility. When steel is used as a structural member, especially a compressive member, the cross section is usually small and hence stiffness is limited. Concrete has advantages in compressive strength and stiffness as a compressive member, due to a large cross section. Hence, by utilizing a steel tube and concrete to form a steel tube-reinforced concrete column, the compressive strength, ductility, and stiffness of the column can be easily satisfied simultaneously. Moreover, as discussed in Chapter 5, due to the confinement of the steel tube, the performance of a concrete-filled steel tube (CFST) column is greater than that of just a steel tube plus concrete core. The enhancement in construction speed, load-carrying capability, and ductility are superior to that of reinforced concrete columns.

The tubes used for CFSTs can be circular, square, or even rectangular in shape, as shown in Figure 6-52. The behavior of a circular CFST is much better than that of a square or rectangular CFST. Moreover, the processing method for circular tubes is usually relatively easier and cheaper. Spiral welding is always used for circular steel tube when the thickness of the plate is less than 20 mm. Under such a welding method, the quality of the weld can be guaranteed. When the thickness of the plate is greater than 20 mm, longitudinal butt welds are adopted, with only one weld necessary for a circular tube. However, for a square tube, at least two or even four welds are necessary to form a box cross section. It is obvious that the cost of circular tube processing is cheaper than that for square tubes. More importantly, the butt weld in a circular tube carries the tensile force only during the loading period, while the butt welds in square tubes are under complex stress conditions.

Concrete-filled tube structures have been used for many construction and structural purposes, such as saving the formwork and speeding up the construction work, compressive strength enhancement for short axially loaded columns, stiffness enhancement of steel structures, and ductility enhancement for seismic-resistant structures. In a CFST structural member, the concrete fill provides compressive strength and stiffness to the steel and reduces the potential for local buckling. The steel tube provides formwork to minimize the cost of the concrete placement, constrains the concrete under uniaxial compression, and reinforces the concrete for axial tension, bending, and shear, as well as providing sufficient ductility for the structure. Both circular and square CFSTs can be designed according to the "unified theory" suggested by Zhong (1995). CFST columns are particularly well suited for short axially loaded columns due to the significant increase in compressive strength of concrete because of the confinement effect of the steel tube. A good example that demonstrates the application of the short CFST in Tianjin Station, Tianjin, China is shown in Figure 6-53.

CFST columns are particularly well suited for braced frames, since great axial strength and stiffness are needed, so braced frames are adopted for the majority of the buildings constructed with CFT columns. Braced-frame–CFT column connections are fundamentally different than

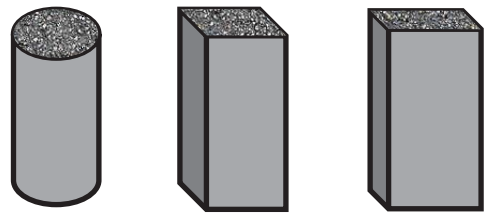

Figure 6-52 Tubes used for CFST

Figure 6-53 Application of CFST as a short axially loaded column in Tianjin Station, China (Photo provided by Linhai Han)

moment frame connections, since they transfer relatively large axial forces to the column, which must be distributed between the steel and concrete. The ductility demands are different in braced frames because dissipation is achieved through brace buckling rather than flexural yielding of the beams. In 2009, the Guangzhou TV and sightseeing tower was topped up with a braced frame–CFST system, see Figure 6-54. The Tower is 610 m in height, and the 610-m-tall twisted, tapering tube is formed by the rotation between two ellipses, which form a "waist" in the center of the building. The tower will be completed and open to the public in 2010.

The CFST structure is also suitable for arch structures due mainly to compressive forces that are generated in the structure. Recently, CFST arch bridges have been widely applied in China. More than 30 arch bridges, with spans longer than 200 m, have been built. The CFST arch bridge with the longest span of 460 m, shown in Figure 6-55, was built in Chongqing, China, and is named the Wushan Bridge.

Recently, hollow concrete-filled tubular structures or composite concrete-filled tubular structures have attracted great attention in both research and application. The advantages of hollow CFST over solid CFST are (1) saving materials and reducing self-weight; (2) providing room for utilities such as cables, pipe installations; (3) increasing the effectiveness of the cross section (such as a higher moment of inertia); and (4) easier and more economic assembly. A typical cross section of a hollow CFST or composite concrete-filled tubular member is shown in Figure 6-56. The studies have shown that the structural behavior of hollow CFST members is highly influenced by the coefficient of the confining effect of the steel tube on the concrete circular core, and the ratio of the empty area to the solid area (Huang et al., 2010). Typical failures of hollow CFST are shown in Figure 6-57.

Due to the advantages of hollow CFST, it has been rapidly utilized in practice, especially for tall bridge piers. In China, more than 10 bridge piers higher than 100 m have utilized the composite type of the pier shown in Figure 6-58. The concrete-filled steel tube structure includes

(a) (b)

Figure 6-54 (a) Guangzhou TV Tower under construction and (b) site view of finished tower in China (Photo provided by Linhai Han)

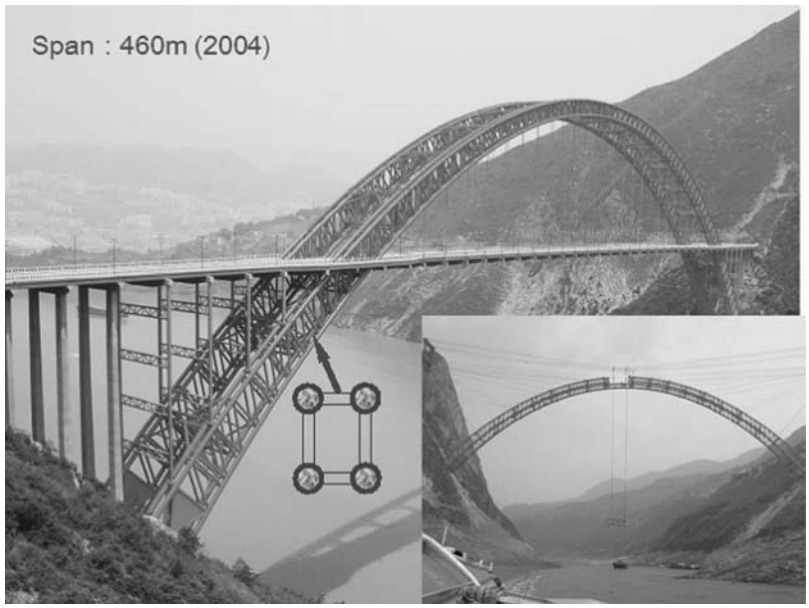

Figure 6-55 Wushan CFST arch bridge, Chongqing China

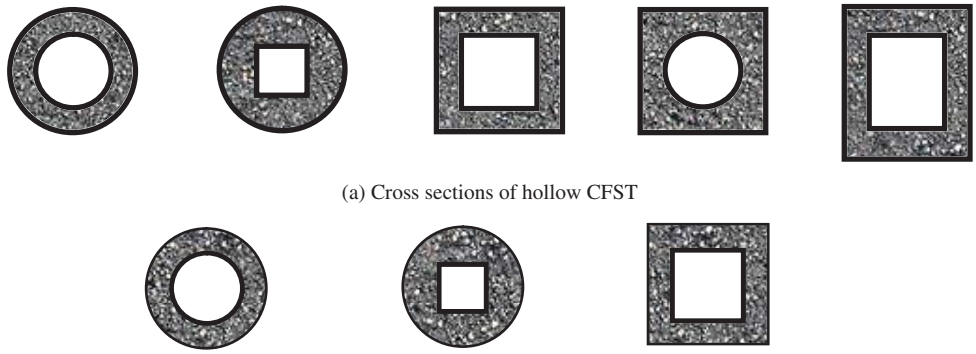

(a) Cross sections of hollow CFST

(b) Cross sections of fibrous-composite-tube (Outside) reinforced concrete with steel inside

Figure 6-56 Typical cross sections of hollow CFST or composite concrete-filled tubular member

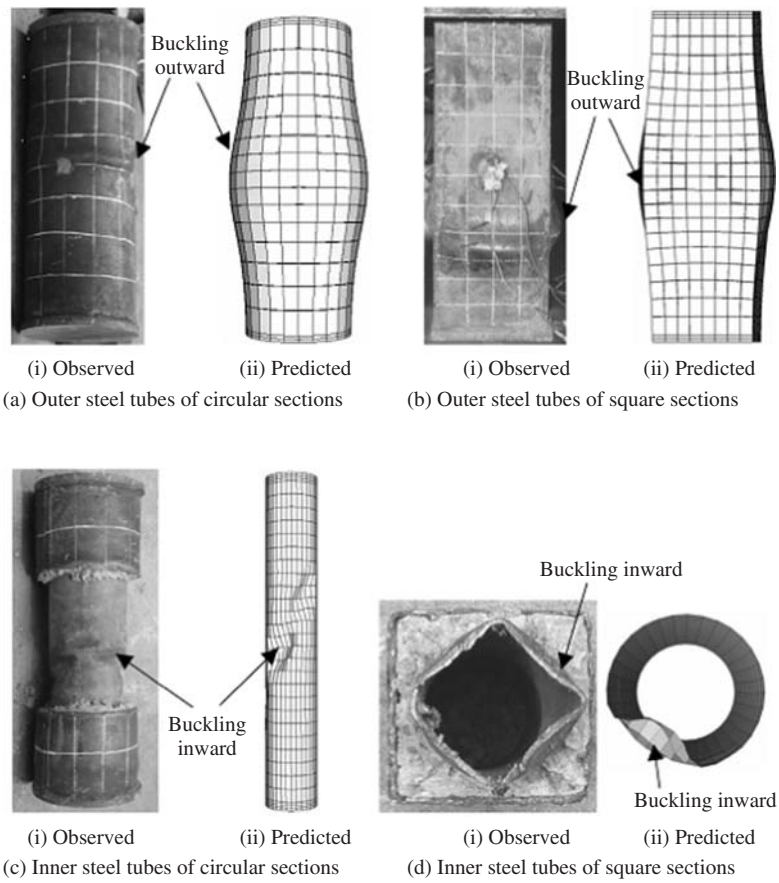

(i) Observed (ii) Predicted
(a) Outer steel tubes of circular sections

(i) Observed (ii) Predicted
(b) Outer steel tubes of square sections

(i) Observed (ii) Predicted
(c) Inner steel tubes of circular sections

(i) Observed (ii) Predicted
(d) Inner steel tubes of square sections

Figure 6-57 Typical failure of hollow CFST

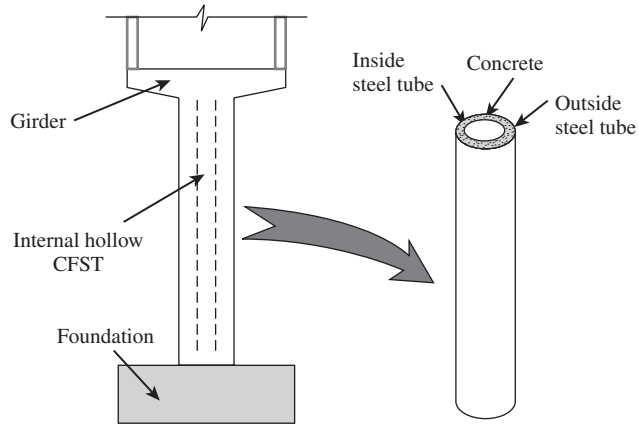

Figure 6-58 Composite type of tall bridge pier

a steel tube having an inner surface and a concrete core cast within the steel tube. Under normal conditions, the concrete core is bonded with the inner surface of steel tube to form a unique structure. However, a separating layer interposed between the inner surface of the steel tube and the surface of the concrete core may form so that the steel tube may not be bonded to the concrete core. Such a layer may be caused by shrinkage or bleeding. To eliminate the separating layer, expansive concrete is preferred in such a tube-reinforced concrete structure.

6.8 HIGH-VOLUME FLY ASH CONCRETE

Fly ash (pulverized fuel ash) is a by-product of an electricity generating plant using coal as fuel. It used to be disposed of as industrial waste. Because a large amount of fly ash can be produced by power plants every year, fly ash disposal became a major environmental issue in many countries. To solve the disposal problem, since the early 1960s, many countries have started to incorporate fly ash into concrete. It was found that the incorporation of fly ash has certain advantages and some disadvantages as a result of research carried out for the past 40 years or so. The major advantages of fly ash concrete are low cost, low energy demand, and low hydration heat. The disadvantages of fly ash concrete are low early-age strength and longer initial setting time. Depending on the amount of fly ash incorporated in the concrete, there are two categories of fly ash concrete: regular fly ash concrete and high-volume fly ash concrete. The regular fly ash concrete utilizes about 25–30% of fly ash by weight of Portland cement and is widely used for massive structures, such as gravity dams. In recent years, attempts have been made in many countries to utilize a large amount of fly ash in concrete without losing its early-age compressive strength. The high-volume fly ash (HVFA) concrete that has been developed recently uses fly ash of 60% or more by weight of cement. Desirable mechanical and durability properties of HVFA concrete have been achieved by careful selection of mix proportions and the use of chemical superplasticizers (Langley et al., 1989). The useful features of HVFA concrete are low Portland cement content (about 150 kg or less per cubic meter), which means fly ash concrete can be produced at less cost and less energy demand than conventional concrete; high early and high ultimate strength, so that some HVFA concrete's compressive strength is greater than 45 MPa at 28 days, with early-age strength in the range of 30 to 35 MPa at 7 days; and high durability in chemically aggressive environments.

6.9 STRUCTURAL LIGHTWEIGHT CONCRETE

Structual lightweight concrete is defined as a concrete having compressive strength in excess 17 MPa with a bulk density less than 1950 kg/m^3. To make lightweight concrete, light weight aggregate has to be used. Nowadays, structural lightweight concrete can made 25% lighter than normal-weight concrete but with a compressive strength up to 60 MPa (Guo et al., 2000). Structural lightweight concrete has shown enhanced durability in chemical resistance, frost resistance, fire resistance, and permeability reduction. The coefficient of thermal expansion of structural lightweight concrete is only around one-third that of normal-weight concrete, with a value of $7 \times 10^{-6}/^{\circ}$C. Hence, the insulating thermal conductivity of lightweight concrete can be reduced by over 25%. The improved fire resistance of structural lightweight concrete can be attributed to a lower expansion coefficient and a lower reduction of strength at elevated temperatures. Moreover, structural lightweight concrete has been applied in building and infrastructure construction since the 1920s. In the United States, Europe, and China, many bridges and tall buildings have utilized high-performance lightweight concrete.

6.10 HEAVYWEIGHT CONCRETE

Heavyweight concrete is defined as a concrete having bulk density in the range of 3360–3840 kg/m^3, and is utilized for special purposes. Heavyweight concrete has been used for the prevention of seepage from radioactive structures due to the harmful effect of radioactive rays (x-rays and gamma rays as well as nuclear radiation) on living organisms. It is mainly used in laboratories, hospitals, and nuclear power plants. The most important point about heavyweight concrete is the determination of the w/c ratio. The favored w/c ratio for heavyweight concrete is 0.40. Another important point for heavyweight concrete is that the cement dosage should be both high enough to allow for radioactive impermeability and low enough to prevent splits originating from shrinkage. The recommended cement dosage should be greater than 350 kg/m^3.

Recently, a new type of heavyweight concrete has been developed to provide soundproofing (Li et al., 2003). In this type of concrete, the aggregates were made of heavyweight metal balls coated with a layer of soft rubber as shown in Figure 6-59. In fact, such aggregates can play the role of a locally resonance unit, and with this effect, sound at certain frequencies can be effectively blocked. Figure 6-60 shows experimental results of sound shielding with different construction materials, including gypsum board, concrete plate, and plastics. It can be seen that at around 180 Hz, the sound transmission loss for heavyweight concrete reaches 45 dB while for all other materials is 25 dB. This implies that ability of heavyweight concrete in sound shielding at a frequency of 180 Hz is 100 times higher than for other building materials.

6.11 DISCUSSION TOPICS

What factors influence the properties of fiber-reinforced concrete?
What is the most beneficial effect by incorporating fibers into concrete?
What are two types of responses in tension of fiber-reinforced concrete?
Define the toughness index in bending for fiber-reinforced concrete.
Define ultra-high-strength and high-strength concrete.
What are the major differences between normal-strength and high-strength concrete?
What is MS concrete?

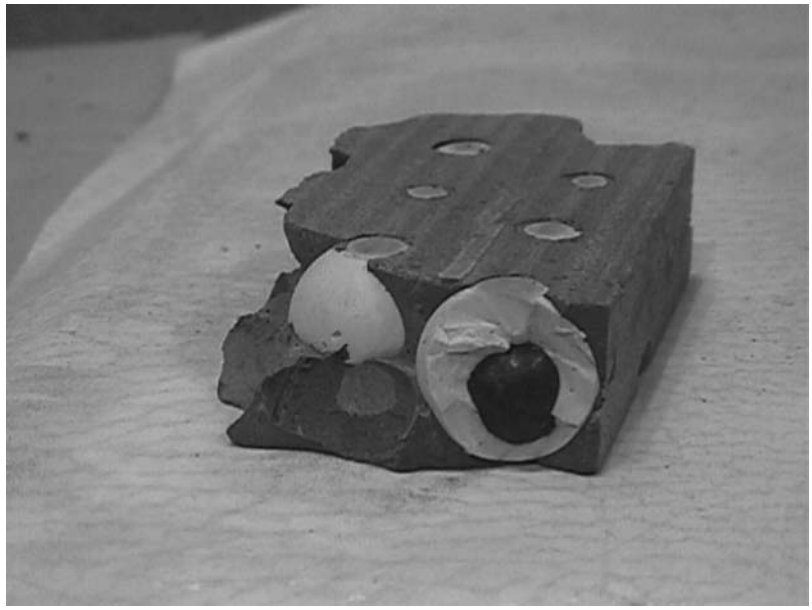

Figure 6-59 Heavyweight concrete for soundproofing

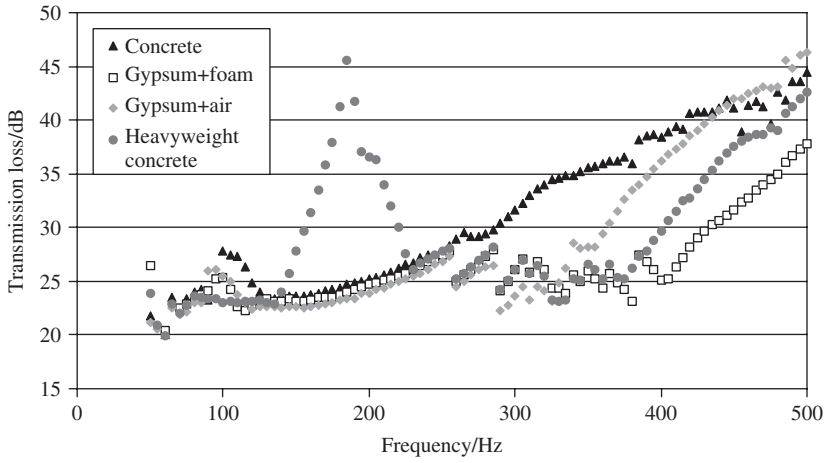

Figure 6-60 Experimental results of sound shielding with different construction materials

What does DSP stand for?
What are the similarities and differences between MS and DSP?
What does MDF stand for?
Why has MDF not become popular yet?
How many common ways are there to incorporate the polymer into concrete?
What are the main applications for polymer-modified concrete?
How can shrinkage be compensated for?

Can you think of a case suitable for the application of fiber-reinforced concrete?

Can you design a fiber-reinforced concrete with strain-hardening behavior?

How can you improve concrete strength using micro engineering?

Suppose that you are a civil engineer. Which materials would you recommend for the emergency repair of a concrete road?

What aspects should you pay attention when you apply shrinkage-compensating concrete?

What is the mechanical background in the design of ECC?

Why can ECC sustain a large deformation without collapse?

Define SCC.

Define UHSC.

How can high flowability be achieved for SCC?

How can the viscosity or cohesiveness of SCC be improved?

List two common types of SCC and discuss the differences between them.

List a few examples in which ECC has obvious advantages over common concrete.

Discuss the advantages of UHSC. What will be the potential of the applications of UHSC?

What is CFT?

Discuss the advantages of CFT.

What are the main functions of a tube and concrete in a CFT?

Discuss the differences between a short, axially loaded CFT and a slender CFT column with bending.

What are the advantages and disadvantages of high-volume fly ash concrete?

List some applications of lightweight concrete.

List some applications of heavyweight concrete.

PROBLEMS

1. Derive the differential equation for a fiber pullout issue by referring to the following figure, where P is the axial force acting on the fiber, and q is shear force per unit length, with $q = \mathrm{KU}$ for perfect bond. The Young's modulus of the fiber is E_f and the area is A.

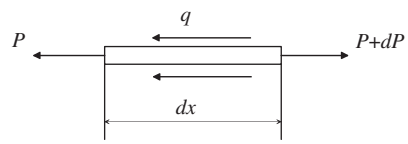

Figure P6-1

2. Solve the differential equation with the boundary conditions of $X = 0$, $U'(0) = 0$; and $x = L$, $E_\mathrm{f}AU'(L) = P^*$

3. A continuous fiber-reinforced cement specimen is loaded in uniaxial tension. The Young's modulus of the cement paste is 20 GPa and tension strength is 5 MPa. The Young's modulus of fiber is 210 GPa.

(a) If V_f is 1% and a total of 50 fibers with a diameter of 0.2 mm are used, when the stress in FRC reaches 5 MPa, what is the stress in cement paste and fiber?

(b) At which stress of FRC will a crack appear in the cement paste? Draw stress distribution in fiber and in matrix along the fiber length starting from the matrix crack position right after the cement paste cracks (suppose that the force incremental is negligible during the crack develop).

REFERENCES

ACI (1997) 503.4-92 Standard specification for repairing concrete with epoxy mortars, American Concrete Institute.

ACI (1998) 503R-93 (Reapproved 1998) Use of epoxy compounds with concrete, American Concrete Institute.

ACI Committee 237 (2007) Self-consolidating concrete, ACI 237R-07, ACI publications.

An, X.H., Huang M. S., Zhou, H., and Jin, F. (2009) "Rock-filled concrete in China—self compacting concrete for massive concrete." In: Shi, Yu, Khayat, and Yan, eds. *RILEM procedings, PRO 65, Design, performance and use of self-consolidating concrete, SCC'2009,* Beijing, pp. 615–627.

Asmus, S.M.F. and Christensen, B. J. (2009) "Status of self consolidating concrete (SCC) in Asia Pacific," In: Shi, Yu, Khayat, and Yan, eds. *RILEM procedings, PRO 65, Design, performance and use of self-consolidating concrete, SCC'2009*, pp. 35–42.

Association Francaise de Genie Civil (2000) "Betons auto-placants—recommendations provisorires," Documents Scientifiques et Techniques.

ASTM (2002) C881 Specification for epoxy-resin-base bonding systems for concrete, American Society for Testing and Materials.

ASTM (2005a) Standard test method for slump of hydraulic-cement concrete, ASTM C143/C143M, American Society for Testing and Materials.

ASTM (2005b) Standard test method for slump flow of self-consolidating concrete, ASTM C1611/C1611M, American Society for Testing and Materials.

ASTM (2006) Standard test method for passing ability of self-consolidating concrete by J-ring, ASTM C1621/C1621M, American Society for Testing and Materials.

Aveston, J., Cooper, G.A. and Kelly, A. (1971) "Single and multiple fracture." In: *The properties of fiber composites*. Guildford, UK: IPC Science and Technology Press, pp. 15–26.

Bache, H.H. (1987) "Introduction to compact reinforced composites," *Nordic Concrete Research*, **6**, 19–33.

Balaguru, P. and Shah, S. (1992) *Fiber reinforced cement composites*. New york: McGraw Hill.

Bartos P.J.M. and Cechura J. (2001) "Improvement of working environment in concrete construction by the use of self-compacting concrete," *Structural Concrete*, **2**(3), 127–131.

Batis, G., Routoulas, A., and Rakanta, E. (2003) "Effects of migrating inhibitors on corrosion of reinforcing steel covered with repair mortar," *Cement & Concrete Composites*, **25**, 109–115.

Batson, G., Jenkins, E., and Spatney, R. (1972) "Steel fibers as shear reinforcement in beams," *ACI Journal*, **69**(10), 640–644.

Birchall, J.D., Kendall, K., and Howard, A.J. (1982) Hydraulic cement composition, US patent 4,353,74.

Bonen, D. and Shah, S.P. (2005) "Fresh and hardened properties of self-consolidating concrete," *Progress in Structural Engineering and Materials*, **7**(1) 14–26.

Brameshuber, W. and Uebachs, S. (2001) "Practical experience with the application of self-compacting concrete in Germany," *Proceedings of the 2nd international symposium on self-compacting concrete*, Tokyo, Japan, pp. 687–696.

British Standards Institution (1983) Testing concrete—method for determination of slump, BS 1881: Part 102.

Chandra, S. and Ohama, Y. (1994) Polymers in concrete, Boca Raton, FL: CRC Press.

Chatterji, S. and Jeffery, J.W. (1966) "The volume expansion of hardened cement paste due to the presence of 'dead burned' CaO," *Magazine of Concrete Research*, **19**(55), 65–68.

Chen, Y. and Qiao, P.Z. (2010) "Crack growth resistance of hybrid fiber reinforced cement matrix composites," *Journal of Aerospace Engineering*, accepted.

Crovetti, J. (2005) "Early opening of Portland cement concrete pavements to traffic," report submitted to Wisconsin Department of Transportation.

Daczko, J.A. (2003) "A comparison of passing ability test methods for self-consolidating concrete," *Proceedings of the 3rd international RILEM symposium on self-compacting concrete*, RILEM Publication SARL, pp. 335–344.

Daczko, J. and Kurtz, M. (2001) "Development of high volume coarse aggregate self-consolidating concrete," *Proceedings of the 2nd international symposium on self–compacting concrete*, pp. 403–412.

Diamond, S. (1985) "Very high strength cement-based materials," *Materials Research Society Symposia Proceedings* **42**, 233–243.

Diamond, S., Sahu, S., and Thaulow, N. (2004) "Reaction products of densified silica fume agglomerates in concrete," *Cement and Concrete Research*, **34**(9), 1625–1632.

European Federation of National Trade Associations (2002) Specification and guidelines for self-compacting concrete.

Federal Highway Administration (2006) Highway concrete technology development and testing, IV, FHWA-RD-02-085, U.S. Department of Transportation.

Fedroff, D. and Frosch, R. (2004) "Formwork for self-consolidating concrete," *Concrete International*, **26**(10), 32–37.

Felekoglu, B, Turkel, S., and Baradan, B. (2007) "Effect of water/cement ratio on the fresh and hardened properties of self-compacting concrete," *Building and Environment*, 42(4), 1795–1802.

Fischer, G. and Li, V.C. (2003) "Deformation behavior of fiber-reinforced polymer reinforced engineered cementitious composite (ECC) flexural members under reversed cyclic loading conditions," *ACI Structures* Journal, **100**(1), 25–35.

Fujiwara, H. (1992) "Fundamental study on the self-compacting property of high-fluidity concrete," *Proceedings of Japan Concrete Institute*, **14**(1), 27–32.

Fukuyama, H., Matsuzaki, Y., Nakano, K., and Sato, Y. (1999) "Structural performance of beam elements with PVA-ECC." In: Reinhardt, H., and Naaman, A., eds., *Proceedings of High performance fiber Reinforced cement composites 3 (HPFRCC 3)*, Reinhardt and A. Naaman, Mainz, Germany Chapman & Hall, pp. 531–542.

Gesoglu, M. and Ozbay, E. (2007) "Effects of mineral admixtures on fresh and hardened properties of self-compacting concretes: binary, ternary and quaternary systems," *Materials and Structures*, **40**(9), 923–937.

Grauers, M. (1997) "Rational production and improved working environment through using self-compacting concrete," EC Brite-EuRam Contract No. BRPR-CT96-0366.

Grunewald, S. and Walraven, J.C. (2001) "Parameter-study on the influence of steel fibers and coarse aggregate content on the fresh properties of self-compacting concrete," *Cement and Concrete Research*, **31**(12), 1793–1798.

Guo, Y.S., Kimura, K., Li, M.W., Ding, J.T., and Huang, M.J. (2000) "Properties of high performance lightweight aggregate concrete." In: Helland, S., Holand, I., and Smeplass, S., eds. *Proceedings second international symposium on structural lightweight aggregate concrete*, Norway, pp. 548–561.

Hassan, K.E., Brooks, J.J., and Al-Alawi, L. (2001) "Compatibility of repair mortars with concrete in a hot-dry environment," *Cement & Concrete Composites*, 23, 93–101.

Hayakawa, Y., Matsuoka, Y., and Shindoh, T. (1993) "Development and application of super-workable concrete." In: Bartos, P.J.M., eds., *Special concrete: workability and mixing*, London: E&FN Spon, pp. 183–190.

Herfurth, E.A. and Nilsen, T. (1993) "Advances in dry shotcrete technology by means of microsilica," *Proceedings of the 5th engineering foundation conference*, Uppsala, Sweden, Code 18378.

HKSAR Highways Department (2006) Publications and Press Releases, on the website www.hyd.gov.hk/eng/home/index.htm.

Huang, H., Han, L.H, Tao, Z., and Zhao, X.L. (2010) "Analytical behaviour of concrete-filled double skin steel tubular (CFDST) stub columns," *Journal of Constructional Steel Research*, **66**(4), 542–555.

Hwang, S.D., Khayat, K.H., and Bonneau, O. (2006) "Performance-based specifications of self-consolidating concrete used in structural applications," *ACI Materials Journal*, **103**(2), 121–129.

Isenberg, J.E. and Vanderhoff, J.W. (1974) "Hypothesis for reinforcement of Portland cement by polymer latexes," *Journal of American Ceramic Society*, **57**(6), 242–245.

Kamada, T. and Li, V.C. (2000) "Effects of surface preparation on the fracture behavior of ECC/concrete repair system," *Cement and Concrete Composites*, **22**(6), 423–431.

Kanda, T., Watanabe, S., and Li, V. C. (1998) "Application of pseudo strain hardening cementitious composites to shear resistant structural elements." In: Fracture mechanics of concrete structures, proceedings FRAMCOS-3, AEDIFICATIO Publishers, D-79104 Freiburg, Germany, pp. 1477–1490.

Kay, T. (1992) Assessment and renovation of concrete structures, Longman Scientific & Technical; England.

Kesner, K. and Billington, S.L. (2002) "Experimental response of precast infill panels made with DFRCC," *Proceedings, DFRCC int'l workshop*, Takayama, Japan, pp. 289–298.

Khayat, K.H. (1999) "Workability, testing, and performance of self-consolidating concrete," *ACI Materials Journal*, **96**(3), 346–353.

Khayat, K.H. (2000) "Optimization and performance of air-entrained, self-consolidating concrete," *ACI Structural Journal*, **97**(5), 526–535.

Khayat, K.H. and Guizani, Z. (1997) "Use of viscosity-modifying admixture to enhance stability of fluid concrete," *ACI Materials Journal*, **94**(4), 332–340.

Khayat, K.H. and Omran, A.F. (2009) "Evaluation of SCC formwork pressure." In: Shi, Yu, Khayat, and Yan, eds *RILEM Procedings, PRO 65, Design, performance and use of self-consolidating concrete, SCC'2009*, pp. 43–55.

Khayat, K.H., Ghezal, A., and Hadriche, M.S. (1998) "Development of factorial design method models for proportioning self-consolidating concrete." In: Malhotra, V.M., ed., Nagataki symposium on vision of concrete: 21st century, pp., 173–197.

Khayat, K.H., Ghezal, A., and Hadriche, M.S. (1999) "Factorial design models for proportioning self-consolidating concrete," *Materials and Structures*, **32**(223), 679–686.

Khayat, K.H., Hu, C. and Laye, J.M. (2003) "Importance of aggregate packing density on workability of self-consolidating concrete," *Proceedings of the 1st North American conference on the design and use of self-consolidating concrete*, Hanley-Wood Publication, Addison, USA, pp. 55–62.

Khayat, K.H., Assaad, J. and Daczko, J., (2004) "Comparison of field-oriented test methods to assess dynamic stability of self-consolidating concrete," *ACI Materials Journal*, **101**(2), 168–176.

Krstulovic-Opara, N. and Toutanji, H. (1996) "Infrastructural repair and retrofit with HPFRCCs." In: Naaman, A.E. and Reinhardt, H.W., eds., *High performance fiber reinforced cement composites* 2, London: E&FN Spon, pp. 423–439.

Kuroiwa, S., Matsuoka, Y., Hayakawa, M., And Shindoh, T. (1993) "Application of super workable concrete to construction of a 20-story building." In: Zia, P., ed., *Proceedings of symposium on high performance concrete in severe environment*, American Concrete Institute, pp. 147–161.

Lachemi, M., Hossain, K.M.A., Lambros, V., and Bouzoubaa, N. (2003) "Development of cost-effective self-consolidating concrete incorporating fly ash, slag cement, or viscosity-modifying admixtures," *ACI Materials Journal*, **100**(5), 419–425.

Lange, D.A., Lin, Y.S., and Henschen, J. (2009) "Modeling formwork pressure of SCC." In: Shi, Yu, Khayat, and Yan, eds., *RILEM Procedings, PRO 65, Design, performance and use of self-consolidating concrete, SCC'2009*, Beijing, pp. 56–63.

Langley, W., Carette, G., and Malhotra, V. (1989) "Structural concrete incorporating high volume of class-F fly ash," *ACI Materials Journal*, **86**(5), 507–514.

Li, F. and Li, Z. (1998) "Tensile strain hardening behavior of cementitious composites reinforced with short steel fibers," *Key Engineering Materials*, 145–149, 965–970.

Li, V.C. (1992) "Post-crack scaling relations for fiber reinforced cementitious composites," *ASCE Journal of Materials in Civil Engineering*, **4**(1), 41–57.

Li, V.C., (1998) "Engineered cementitious composites–tailored composites through micromechanical modeling," Fiber reinforced concrete: present and the future, Eds. N. Banthia et al, CSCE, Montreal, pp. 64–97.

Li, V. C. and Leung, C.K.Y. (1992) "Steady state and multiple cracking of short random fiber composites," *ASCE Journal of Engineering Mechanics*, **118**(11), 2246–2264.

Li, V.C., Kong, H.J., and Chan, Y.W. (1998) "Development of self-compacting engineered cementitious composites," *Proceedings, international workshop on self-compacting concrete*, Kochi, Japan, pp. 46–59.

Li, V.C., Kong, J. and Bike, S. (2000) "High performance fiber reinforced concrete materials." In: Leung, C.K.Y., et al., eds., *Proceedings of high performance concrete—workability, strength, and durability*, China, pp. 71–86.

Li, V.C., Kong, J., and Bike, S. (2001b) "Constitutive rheological design for development of self-compacting engineered cementitious composites," *Proceedings of the 2nd international workshop on self-compacting concrete*, Tokyo, Japan.

Li, V.C., Wang, S. and Wu, C. (2001a) "Tensile strain-hardening behavior of PVA-ECC," *ACI Materials Journal,* **98**(6), 483–492.

Li, Z. and Mu, B. (1998) "Application of extrusion for manufacture of short fiber reinforced cementitious composite," *Journal of materials in Civil Engineering, ASCE*, **10**, 2–4.

Li, Z. and Xiao, L.Z. (2009) "Characterization of fresh self consolidating concrete properties with electrical resistivity," *Second international symposium on design, performance and use of self-consolidating concrete*, Beijing, China.

Li, Z. Mobasher B., and Shah, S.P. (1991) "Characterization of interfacial properties in fiber-reinforced cementitious composites," *Journal of the American Ceramic Society*, **74**(9), 2156–2164.

Li, Z., Mu, B., and Chui, S. (1996) "The systematic study of the properties of extrudates with incorporated metakaolin or silica fume," *ACI Materials Journal*, **96**(5), 574–579.

Li, Z., Shen, P., and Siu, A. (2003) "Sound proof concrete," *Magazine of Concrete Research*, **55**(2), 177–181.

Li, Z. Zhou, X., and Shen, B. (2004) "Systematic study of fiber-reinforced cement extrudates with perlite subjected to high temperatures," *Journal of Materials in Civil Engineering*, ASCE, **16**(3) 221–229.

Li, Z., Zhang, Y., and Zhou, X. (2005) "Short fiber reinforced geopolymer composites manufactured by extrusion," *Journal of Materials in Civil Engineering*, **17**(6), 624–631.

Lim, Y.M. and Li, V.C. (1997) "Durable repair of aged infrastructures using trapping mechanism of engineered cementitious composites," *Journal of Cement and Concrete Composites*, **19**(4), 373–385.

Lin, Z., Kanda, T. and Li, V.C. (1999) "On interface property characterization and performance of fiber reinforced cementitious composites," *Journal of Concrete Science and Engineering*, **1**, 173–184.

Maalej, M. and Li, V.C. (1994) "Flexural/tensile strength ratio in engineered cementitious composites," *Journal of Materials in Civil Engineering*, ASCE, **6**(4), 513–528.

Maalej, M. and Li, V.C. (1995) "Introduction of strain hardening engineered cementitious composites in the design of reinforced concrete flexural members for improved durability," *ACI Structural Journal* **92**(2), 167–176.

Marshall, D. and Cox, B.N. (1988) "A J-integral method for calculating steady-state matrix cracking stress in composites," *Mechanics of Materials*, **7**, 127–133.

Mehta, P. K. and Monteiro, P.J.M. (2006) *Concrete: microstructure, properties, and materials*, 3rd ed. New york: McGraw-Hill.

Mindess, S., Banthia, N., and Yan, C. (1987) "The fracture toughness of concrete under impact loading," *Cement and Concrete Research*, **17**(2), 231–241.

Mirza, J., Mirza, M.S., and Lapointe, R. (2002) "Laboratory and field performance of polymer-modified cement-based repair mortars in cold climates," *Construction and Building Materials*, **16**, 365–374.

Mori, A. and Baba, A. (1994) "A method for predicting the operating characteristics curing extrusion molding process for cementitious materials." In: Brandt, A.M., Li, V.C., and Marshall, I.H., eds., *Proceedings of the international symposium on brittle matrix composites* 4, Warsaw, pp. 492–501.

Naaman, A.E., and Homrich, J.R. (1989) "Tensile stress-strain properties of SIFCON," *ACI Materials Journal* **86**(3), 244–251.

Naaman A.E. (1992) "SIFCON: Tailored properties for structural purpose," *High performance fiber reinforced cement composites, RILEM proceedings,* 15. London: E&FN SPON, pp. 18–38.

Okamura, H. and Ozawa, K. (1994) "Self-compactable high-performance concrete in Japan." In: Zia, P., ed. *Proceedings of the international workshop on high performance concrete*, Detroit, MI: American Concrete Institute, pp. 31–44.

Okamura, H., Ozawa, K., and Ouchi, M. (2000) "Self-compacting concrete," *Structural Concrete*, **1**(1), 3–17.

Okushima, M., Kondo, R., Muguruma, H. and Ono, Y. (1968) "Development of expansive cement with sulphoaluminous cement clinker," *5th international symposium on the chemistry of cement*, Tokyo, 4, pp. 419–430.

Ozawa, K., Sakata, N., and Okamura, H. (1995) "Evaluation of self-compactability of fresh concrete using the funnel test," *Concrete Library of JSCE*, **25**, 59–75.

Parra-Montesinos, G. and Wight, J.K. (2000) "Seismic response of exterior RC column-to-steel beam connections," *ASCE Journal of Structural Engineering*, **126**(10), 1113–1121.

Peled, A., Cyr, M., and Shah, S.P. (2000) "Hybrid fibers in high performance extruded cement composites," *Proceedings of fifth RILEM symposium on fiber reinforced concretes*, Lyon, France, pp. 139–147.

Petersson O. and Skarendahl A. (2000) "Self-compacting concrete," *Proceedings of the 1st international symposium*, Stockholm 1999. Cachan, France: RILEM Publications.

Petrou, M.F., Harries, K.A., Gadala-Maria, F., and Kolli, V.G. (2000) "A unique experimental method for monitoring aggregate settlement in concrete," *Cement and Concrete Research*, **30**(5), 809–816.

Precast/Prestressed Concrete Institute (2003) PCI interim SCC guidelines TR-6-03: interim guidelines for the use of self-consolidating concrete in precast/prestressed concrete institute member plants.

RILEM Technical Committee 145 (2002) *Workability and rheology of fresh concrete: compendium of tests*, RILEM Publications SARL.

Rols, S., Ambroise, J., and Pera, J. (1999) "Effects of different viscosity agents on the properties of self-leveling concrete," *Cement and Concrete Research*, **29**(2), 261–266.

Roussel, N. (2006) "A thixotropy model for fresh fluid concretes: theory, validation and applications," *Cement and Concrete Research*, **36**(10), 1797–1806.

Saak, A.W., Jennings, H.M., and Shah, S.P. (2001) "New methodology for designing self-compacting concrete," *ACI Materials Journal*, **98**(6), 429–439.

Self-Compacting Concrete European Project Group (2005) The European guidelines for self-compacting concrete, BIBM, CEMBUREAU, EFCA, EFNARC and ERMCO.

Shah, S.P. (1991) "Toughening of cement-based materials with fiber reinforcement," *Mater. Res. Soc. Symp. Proc.*, **211**, 3–13.

Shah, S.P., Ferron, R.F., Tregger, N.A., Ferrra, L., and Beacraft, M.W. (2009) "Self-consolidating concrete: now and future." In: Shi, Yu, Khayat, and Yan, eds., *RILEM Procedings, PRO 65, Design, Performance and use of self-consolidating concrete, SCC'2009*, Beijing, pp. 3–15.

Shao, Y., Marikunte, S., and Shah, S.P. (1995) "Extruded fiber-reinforced composites," *Concrete International*, **17**(4), 48–52.

Sharma, A.K. (1986) "Shear strength of steel fiber reinforced concrete beams," *ACI Proceedings*, **83**(4), 624–628.

Shaw, J.D.N. (1984) Concrete repair—materials selection, *Civil Engineering*, August, pp. 53–58.

Shindoh, T. and Matsuoka, Y. (2003) "Development of combination-type self-compacting concrete and evaluation test methods," *Journal of Advanced Concrete Technology*, **1**(1), 26–36.

Sonebi, M. (2004) "Applications of statistical models in proportioning medium-strength self-consolidating concrete," *ACI Materials Journal*, **101**(5), 339–346.

Sonebi, M. Grunewald, S. and Walraven, J. (2007) "Filling ability and passing ability of self-consolidating concrete," ACI Materials Journal, **104**(2), 162–170.

Stang, H. and Li, V.C. (1999) "Extrusion of ECC-Material." In: Reinhardt, M., and Naaman, A., eds., *Proceedings of high performance fiber reinforced cement composites* 3 (HPFRCC 3), Chapman & Hall, pp. 203–212.

Stang, H. and Pedersen, C. (1996) "HPFRCC-extruded pipes," In: Chong, K.P., ed., Materials for the new millennium, New York: American society of Civil Engineers 2, pp. 261–270.

Stang, H., Li, Z., and Shah, S.P. (1990) "Pull-out problem: stress versus fracture mechanical approach," *Engineering Mechanics, ASCE*, **116**(10), 2136–2150.

Stang, H., Aarre, T. (1992) "Evaluation of crack width in FRC with conventional reinforcement," *Cement & Concrete Composite*, **14**(2), 143–154.

Stang, H., Li, V.C., and Krenchel, H. (1995) "Design and structural applications of stress-crack width relations in FRC," *Materials and Structures*, **28**(4), 210–219.

Swedis Concrete Association (2002), "Self-compacting concrete, recommendations for use," concrete Report No. 10(E) 84 pp.

Testing-SCC Project Group (2005a) Guidelines for testing fresh self-compacting concrete.

Testing-SCC Project Group (2005b) Measurement of properties of fresh self-compacting concrete.

Toutou, Z. and Roussel, N. (2006) "Multiscale experimental study of concrete rheology: from water scale to gravel scale," *Materials and Structures*, **39**(286), 189–199.

Vachhani, S.R., Chaudary, R., and Jha, S.M. (2004) "Innovative use of SCC in Metro Construction," *ICI Journal*, **4**, 27–32.

Wallevik, O.H. (2003) "Role in rheology in developing new breeds of concrete and construction techniques," *Proceedings of the international symposium—celebrating concrete: people and practice*, pp. 441–450.

Wang, D.M. (2006) *High performance expansive concrete*. Publisher of hydraulic and hydropower of China, Beijing, in Chinese.

Warner, J. (1984) "Selecting repair materials," *Concrete Construction*, **29**(10), 865–873.

Xu, G. and Hannant D.J. (1992) "Flexural behavior of combined polypropylene network and glass fiber reinforced cement," *Cement and Concrete Composites*, **14**, 51–61.

Yan, P.Y. and Yu, C.H. (2009) "Application of self consolidating concrete in Beijing,." In: Shi, Yu, Khayat, and Yan, eds., *RILEM Proceedings, PRO 65, Design, performance and use of self-consolidating concrete, SCC'2009*, Beijing, pp. 817–822.

Yao, W., Li, J., and Wu, K.R. (2003) "Mechanical properties of hybrid fiber-reinforced concrete at low fiber volume fraction," *Cement and Concrete Research*, **33**(1), 27–30.

Yonezawa, T., Izumi, I., Okuno, T., Sugimoto, M., Shimuno, T., and Azakuna, T. (1992) "Reducing viscosity of high strength concrete using silica fume," *Proceedings of the 4th CANMET/ACI international conference on fly ash, silica fume, slag and natural pozzolans in concrete*, pp. 665–680.

You, B.K. and Li, N.Z. (2005) "Expansive agent and shrinkage compensating concrete," Publisher of China Building Materials Industry, Beijing, in Chinese.

Yurugi, M., Sakata, N., Iwai, M., and Sakai, G. (1993) "Mix proportion for highly workable concrete," *Proceedings of the international conference of concrete 2000*, Dundee, UK.

Zhang, J. and Li, V.C. (2002) "Monotonic and fatigue performance in bending of fiber-reinforced engineered cementitious composite in overlay system," *Cement and Concrete Research*, **32**(3), 415–423.

Zhang, S.Q., Hughes, D., Jeknavorlan, A.A., Nishimura, T., and Yang, K. (2009) "Self compacting concrete, worldwide experience," In: Shi, Yu, Khayat, and Yan, eds., *RILEM Procedings, PRO 65, Design, performance and use of self-consolidating concrete, SCC'2009*, Beijing, pp. 831–840.

Zhong, S.T. (1995) *Concrete filled steel tubular structures*, Heilongjiang Science-Technology Publisher, Harbin.

CHAPTER 7

CONCRETE FRACTURE MECHANICS

7.1 INTRODUCTION

According to the tensile stress–strain curve, materials can be divided into brittle materials, quasi-brittle materials and ductile materials (see Figure 1-10). As shown in Figure 1-10a, brittle materials break suddenly when the stress reaches maximum. As shown in Figure 1-10b, quasi-brittle materials can show a strain-softening behavior, i.e., stress decreases with strain increase, if a proper loading control is provided. As shown in Figure 1-10c, ductile materials show a long, plastic plateau before failure. Glass is a typical brittle material, concrete is a typical quasi-brittle material, and low-carbon steel at normal temperatures is a typical ductile material. Fracture occurs as a brittle failure mode. Fracture mechanics is the study of stress and displacement fields in a material in the region surrounding a crack tip.

It has long been known that there are a lot of sources of microcracks inside a cement-based material such as concrete. It has been shown that both stress–strain behavior and the failure mode of cement paste and concrete are governed by a process of microcrack propagation. Thus, the failure of concrete under loading is closely related to crack formation and propagation. Hence, fracture mechanics fits concrete naturally. To understand the nature of concrete behavior, it is essential to understand its fracture mechanism. Before discussing the concrete fracture mechanism, it is necessary to briefly review the basic concepts of fracture mechanics.

7.1.1 History of fracture mechanics

The industrial revolution in Europe in the 19th century broadened the application of materials, especially metals. The vastly increasing use of metals, moreover, caused a number of accidents, including broken axles or wheels of trains, explosion of boilers, and chains giving way on suspension bridges. Most of the accidents were a result of the fracture of metal components. It was found that the failures often occurred under conditions of low stress, which made them unexpected. These accidents attracted great attention and initiated extensive investigations. The investigations revealed that the preexisting flaws in materials caused stress concentrations, which were mainly responsible for such accidents. To explain this, let us look at theoretical cohesive stress.

In a metal, the structure is formed by metallic lattices. The strength of a metal is sourced at the metallic bonds. With metallic bonding, the valence electrons become detached from individual parent atoms and move freely within the solid as an electron gas. When the atoms give up their electrons, they become positive ions. It is easy to see that there is an equilibrium condition for two ions at which the forces between them are balanced.

Ideally, the strength of a solid depends on the strength of its atomic bonds. Thus, to obtain an approximation to at least the order of magnitude of the fracture strength, we can consider the interaction between ions. Let us consider the cubic lattice with a balanced spacing, b_0, as

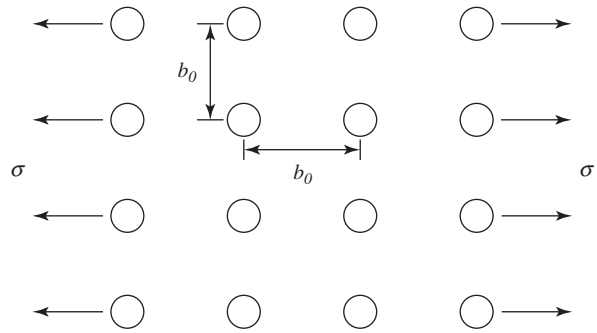

Figure 7-1 Lattice structure under stressing

shown in Figure 7-1. Furthermore, if we assume that only adjacent neighbors interact, we have the situation shown in Figure 7-2. Two ions will attract each other when $b > b_0$ and repel each other when $b < b_0$. Let F be the force acting on the ions and Δl the length change between two ions ($\Delta l = b - b_0$). We can write the stress and strain expressions as

$$\sigma = \frac{F}{b_0^2} \tag{7-1}$$

and

$$\varepsilon = \frac{\Delta l}{b_0} \tag{7-2}$$

Subsequently, the F–b form can be transferred into a σ-ε curve that can be further simplified as a sine curve:

$$\sigma = \sigma_{\max} \sin(2\pi\varepsilon) \tag{7-3}$$

The differential of the above equation gives

$$\left.\frac{d\sigma}{d\varepsilon}\right|_{\varepsilon=0} = \sigma_{\max} 2\pi = E \tag{7-4}$$

Thus, we can estimate the strength for ideal materials as

$$\sigma_{\max} = \frac{E}{2\pi} \approx \frac{E}{6} \tag{7-5}$$

However, in the real world, the material strength is usually much lower than the above theoretical prediction. For instance, E for steel is 210 GPa; thus, according to the above equation, we have

$$\sigma_{\max} \approx \frac{E}{6} = 35\,\text{GPa} \tag{7-6}$$

The tensile strength measured for reinforcing steel is about 0.3–0.6 GPa. There is a big difference between the real value and the theoretical predicted value. Why? This is because of the preexisting flaws inside a material, which can cause stress concentrations and uneven distributions. The stress concentration may lead to very high stress that causes a local failure, which results in a low apparent strength, indexed with normalized stress. These phenomena initiated the study of fractures.

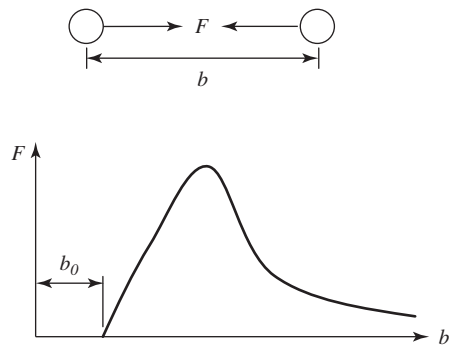

Figure 7-2 Force acting on two neighboring ions

Linear elastic fracture mechanics (LEFM) theory was developed in 1920 with Griffith (1921) as the founder. His original interest was on the effect of surface treatment on the strength of solids. It had been observed, experimentally, that small imperfections had a much less damaging effect on the material properties than large imperfections. This was theoretically puzzling because at that time people believed that the stress concentrations caused by imperfections should be same for imperfections of different sizes. Griffith tackled this dilemma by developing a new criterion for fracture prediction by taking the crack size into consideration. LEFM had essentially two criteria: stress-based and energy-based. What Griffith developed was an energy-based criterion. He utilized a compliance concept and dealt with both fixed-load and fixed-displacement cases. Griffith showed that an instability criterion could be derived for cracks in brittle materials based on the variation of potential energy of the structure, as the crack grew. The Griffith approach was global but could not easily be extended to accommodate structures with finite geometries subjected to various types of loads. The theory was considered to apply only to a limited class of extremely brittle materials, such as glasses or ceramics.

The stress-based LEFM criterion was first developed by Inglis (1913), who provided the solution of maximum stress for a solid weakened by an elliptical cavity subjected to a uniform stress normal to the semi-axis of the ellipse. Later on, Irwin defined the fundamental concept of a *stress intensity factor* and the critical stress intensity factor (K_{IC}), which is a material property. The fundamental postulate of LEFM is that crack behavior is determined solely by the value of the stress intensity factor (SIF) at the crack tip, which is a function of the applied load and the geometry of the cracked structure. The SIF, thus plays an important role in LEFM applications, for example, in fatigue crack growth analyses. The stress values in the vicinity of a crack tip are usually expressed as a function of SIF. According to the stress expressions, it can reach infinity, termed a singularity. However, in a real material, this is impossible. Hence, researchers inferred that an inelastic zone must exist in front of a crack tip. This assumption triggered the study of nonlinear fracture mechanics. Nonlinear fracture mechanics mainly focused on the determination of the size of the plastic zone in front of a crack tip. The representative work in determining the size of the plastic zone included Irwin's plastic zone correction (Irwin, 1958, 1960), Dugdale's cohesive zone model (1960), and Rice's J-integral (1968). These works confirmed that there is a small plastic zone in front of a crack tip and provided equations to calculate the size of the plastic zone. It was also proved that for a material with a small size of plastic zone, LEFM could still be applied.

A broad range of disciplines, from nanoscaled materials science to meter-scaled engineering applications, was involved in the development of fracture mechanics. Small-scale materials

science concerned itself with the fracture processes on the scale of atoms and dislocations to that of impurities and grains and provided an understanding on the origin and driving force of microcracks. Large-scale engineering mechanics provided analysis methods for stress and deformation determination around the crack tip as well as design criteria based on crack analysis for structures. The prediction on fracture strength could be checked experimentally. In the study of fracture mechanics, one should be able to answer the following questions:

(a) How is a crack formed? What is the driving force of a crack?
(b) What is the maximum tolerated crack size corresponding to the service load?
(c) What is the maximum stress a structure can carry with an existing crack size?
(d) What is the fatigue life of a structure with a certain initial crack size?
(e) What are the essential conditions for a crack to grow?
(f) How often should a structure be inspected for cracks?

7.1.2 Development of concrete fracture

Concrete is a multiple-scale composite material, mainly composed of hardened cement paste and aggregates. Due to the nature of cement hydration, shrinkage and creep occur. Microcracks and sometimes even macrocracks evidently exist, in concrete from the very beginning. Hence, failure of concrete structures is usually accompanied by propagation of cracks in the concrete matrix. Understanding and modeling how and when concrete fails are not only critical for designing concrete structures, but also important for developing new cement-based materials. Except for the physical formation of a crack, the failure of concrete is softening without a plateau. The plasticity is not applicable to concrete. On the other hand, it is natural to apply fracture mechanics to concrete due to the preexistence of cracks inside.

Fracture mechanics was first applied to concrete in 1961 by Kaplan (1961). Based on the observations that microcracks occurred in concrete, he made an effort to ascertain whether the Griffith crack theory was a necessary condition for rapid crack propagation and consequent fracture of concrete or not, by conducting three-point bending tests. Since then, a large number of tests have been conducted to examine the applicability of fracture mechanics to concrete. For instance, Shah and McGarry (1971) concluded that the critical crack length was likely to depend on the volume, type, and the size of aggregate particles from the experimental observations. One characteristic of concrete fracture was that it had a large fracture process zone. Castro-Montero et al. (1990) conducted a laser holographic interferometry test on a concrete plate loaded vertically at a central circular hole with two notches along the horizontal diameter from the edge of the hole. The fracture process zone was identified by plotting the difference between a strain field experimentally measured by holography and a strain field from a linear elastic solution. The results showed that a large fracture process zone existed both behind and in front of the crack tip. Ouyang et al. (1991) applied the acoustic emission technique to determine internal microcrack positions for three-point bending testing of a concrete beam. They found that most of the acoustic emission events were located at both sides of the plane containing the notch, which indicated that the fracture process zone had a substantial width. From the observation of the large fracture process zone in concrete, it was concluded that the criterion of LEFM could not be directly applied to predict concrete fracture behavior. Thus, researchers had to look for a modified method of fracture mechanics to solve concrete fracture problem.

Since the 1980s, models with more than one fracture parameter to have been proposed to explain the fracture processes in concrete. Hillerborg et al. (1976) proposed a fictitious crack model, which is somewhat similar to Dugdale's model used in metals. Bazant and Oh (1983) have

proposed a crack band model based on the concept of strain softening to explain the fracture process of concrete. Wecharatana and Shah (1982, 1983) used a compliance based model to calculate the length of the fracture process zone, which was represented by traction forces resulting from aggregate or fiber interlock. They observed that *R*-curves could be considered a material property, provided the length of the process zone and the inelastic energy absorbed in the process zone were included in the analysis. Jenq and Shah (1985) introduced a two-parameter fracture model. It was demonstrated that these two parameters—the critical stress intensity factor at the tip of the effective crack and the elastic critical crack opening displacement—were size independent. In 1984, Bazant developed a size effect law to model concrete fracture.

In the later 1980s and 1990s, intensive research was undertaken and applications of fracture mechanics in design of beams, anchorage, and large dams became more common. However, concrete fracture mechanics is not yet mature. Some people have predicted that the concrete fracture mode will govern the concrete design code in the future.

7.2 LINEAR ELASTIC FRACTURE MECHANICS

Linear elastic fracture mechanics studies the stress and deformation distribution in the region in front of a crack tip of brittle materials. It utilizes a single parameter as an index of the fracture criterion. Two criteria are used in LEFM: one is stress-based and other energy-based. The fracture index in the stress-based criterion is the stress intensity factor and in the energy-based case is the surface energy release rate.

Originally, fracture mechanics was developed from elasticity problems in dealing with inside defects, such as circular or elliptical holes.

7.2.1 Stress concentration factor and intensity factor at a crack tip

(a) *Stress concentration factor*: The presence of defects in materials influences the stress distribution in the materials and subsequently the mechanical properties of the materials. This can be illustrated by a plate with an elliptical hole, as shown in Figure 7-3, where the elliptical hole represents the defect. The existence of the hole in the plate alters the stress distribution in the surrounding area and leads to a maximum stress, $\sigma_{\max}$, being formed at

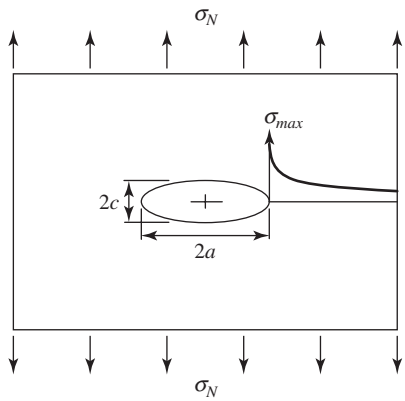

Figure 7-3 A specimen with an elliptical hole under tensile loading

the edge of the hole. The σ_{max} is much larger than the normal stress, σ_N. This phenomenon is called a stress concentration. The stress concentration factor, K_t, for the given loading condition in Figure 7-3, can be expressed as

$$K_t = \frac{\sigma_{max}}{\sigma_N} = 1 + \frac{2a}{c} \tag{7-7}$$

where a and c are the long and short radii of the ellipse, respectively. It can be seen from the equation that when $a = c$, i.e., for a circular hole, then $K_t = 3$. It should be noted that K_t depends not only on the shape of the hole, but also on the loading pattern on the specimen. For instance, for a plate with a circular hole under pure shear, as shown in Figure 7-4, the value of K_t is 4.

It can also be seen from Equation 7-7 that the value of K_t largely depends on the ratio of a/c. With an increase of the a/c ratio, the value of K_t increases. The value of K_t tends to approach infinity for a very narrow ellipse or sharp crack. Hence, K_t cannot be a material parameter under such a condition. This indicates that the conventional analysis

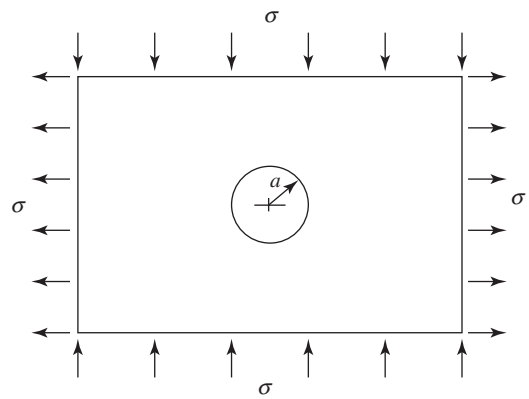

Figure 7-4 A thin plate with a circular hole subjected to pure shear

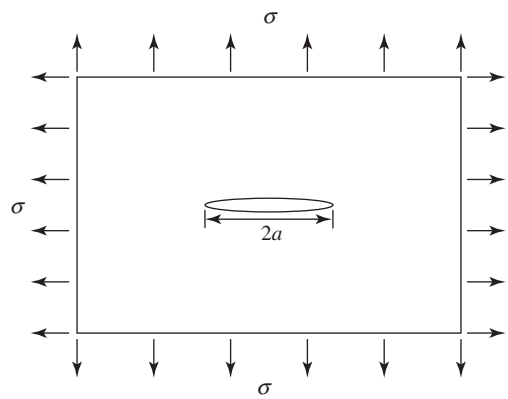

Figure 7-5 A specimen with a mode I crack

based on the concentration factor is not valid for a structure with a sharp crack; therefore, fracture mechanics should be introduced.

(b) *Stress intensity factor*: In fracture mechanics, cracks are classified into mode I (opening mode), mode II (shearing mode), mode III (tearing mode), and mixed mode (I+II or I+III). The stress expressions in the vicinity of a crack tip for the three basic modes can be derived from the elasticity (Irwin, 1958). Similar to the case of stress concentrations, the stress expressions depend not only on the specimen geometry, but also on the loading pattern acting on the specimen. Figure 7-5 shows a thin plate with a central crack subjected to two-dimensional axial tension. The crack length is usually expressed as a. It corresponds to a crack tip. If a crack has two crack tips, such as central crack, it has two crack lengths, $2a$. If a crack has only one crack tip, such as edge crack, it has only one crack length, a.

Clearly, Figure 7-5 is a mode I case and the elastic stress field in the vicinity of a crack tip has the form

$$\begin{aligned}
\sigma_{xx} &= \frac{K_{\mathrm{I}}}{\sqrt{2\pi r}} \cos\frac{\theta}{2}\left(1 - \sin\frac{\theta}{2}\sin\frac{3\theta}{2}\right) \\
\sigma_{yy} &= \frac{K_{\mathrm{I}}}{\sqrt{2\pi r}} \cos\frac{\theta}{2}\left(1 + \sin\frac{\theta}{2}\sin\frac{3\theta}{2}\right) \\
\sigma_{xy} &= \frac{K_{\mathrm{I}}}{\sqrt{2\pi r}} \cos\frac{\theta}{2}\sin\frac{\theta}{2}\cos\frac{3\theta}{2}
\end{aligned} \tag{7-8}$$

where r is the distance from crack tip to the point, θ the angle between r and the x-axis, and K_{I} is the stress intensity factor, defined as

$$K_{\mathrm{I}} = \sigma\sqrt{\pi a} f\,(a/b) \tag{7-9}$$

where σ is the applied stress (or normal stress) on the structure, a the crack length, b the size of the structure, and $f(a/b)$ the geometry factor.

For a uniaxial tensile plate with a central crack, we have

$$f\left(\frac{a}{b}\right) = \sqrt{\sec\left(\frac{\pi a}{2b}\right)} \tag{7-10}$$

For a uniaxial tensile plate with a single-edge crack, we have

$$f\left(\frac{a}{b}\right) = 1.12 - 0.231\frac{a}{b} + 10.55\left(\frac{a}{b}\right)^2 - 21.72\left(\frac{a}{b}\right)^3 + 30.39\left(\frac{a}{b}\right)^4 \tag{7-11}$$

For a three-point bending beam with span equal 4 times of beam height,

$$f\left(\frac{a}{b}\right) = \frac{1.99 - \frac{a}{b}\left(1 - \frac{a}{b}\right)\left[2.15 - 3.93\left(\frac{a}{b}\right) = 2.70\left(\frac{a}{b}\right)^2\right]}{\sqrt{\pi}\left(1 + 2\frac{a}{b}\right)\left(1 - \frac{a}{b}\right)^{3/2}} \tag{7-12}$$

The expressions of $f(a/b)$ for other geometries can be obtained from the tables in the fracture analysis handbook (Tada et al., 2000). The value of $f(a/b)$ approaches unity when the ratio a/b approaches zero, for most loading cases and geometries.

Both the stress intensity factor K_{I} and the stress concentration factor K_{t} are used to account for the increase of stresses due to a defect. When the defect is a sharp crack, K_{I} has a limiting

value but K_t approaches infinity. The value of K_I accounts for the singularity of the stress field in the crack tip, and is a function of load, specimen geometry and size, boundary condition, and crack length.

The fundamental postulate of linear elastic fracture mechanics is that crack behavior is determined solely by the value of the stress intensity factor at the crack tip, which is a function of the applied load and the geometry of the cracked structure. The SIF, thus plays a very important role in LEFM applications, for example, in fatigue crack growth analyses. SIF can be obtained using the Airy stress function with complex variables:

$$\Phi(Z) = \mathrm{Re}\, Z + iIMZ \tag{7-13}$$

where $Z = x + iy$.

However, numerical methods are usually used for the evaluation of the SIFs in engineering structures, because of their complex configurations and loading status. A 1 to 5% accuracy of SIFs can be obtained by the most used numerical methods. It is good enough for general engineering problems except for numerical simulation of fatigue crack growth. The finite element method (FEM) has a long and well-documented history in fracture mechanics applications. The boundary element method (BEM) is also a well-established numerical technique in fracture mechanics. The procedures of general displacement-based SIF computation method in fracture mechanics problems can be expressed as follows.

The displacement fields of the crack problems are first obtained through the application of numerical methods such as FEM or BEM. To achieve better results for the displacement fields, specially designed crack tip elements, such as quarter-point elements, have been often used. Then, SIFs are extracted from the obtained displacement fields by the techniques deduced from LEFM. A lot of techniques have been developed to extract SIFs from the displacement fields. These techniques may be divided into two classes of procedures: local displacement field procedures and global displacement field procedures. Local displacement field procedures are based on the asymptotic analysis of the displacements on the crack line near a crack tip:

$$v = \frac{8}{E}\sqrt{\frac{r}{2\pi}}K_I + O(r^{3/2}) \tag{7-14}$$

$$u = \frac{8}{E'}\sqrt{\frac{r}{2\pi}}K_{II} + O(r^{3/2}) \tag{7-15}$$

where v and u are the crack opening displacements (COD) normal and tangential to the crack line, respectively; r the distance from the crack tip along the crack line; and K_I and K_{II} the mode I and mode II SIFs at the crack tip, respectively. $E' = E$ is for plane stress, and $E' = E/(1 - \upsilon^2)$ for plain strain, where E and ν are the Young's modulus and Poisson's ratio, respectively.

Apparently, by using Equations 7-14 and 7-15, only the displacement data near a crack tip are used to extract the SIFs. An advantage of local displacement extraction techniques is that they can be readily programmed with a simple post-processing algorithm. Note that Equations 7-14 and 7-15 are exactly valid only for $r \to 0$, so in numerical calculations the nodal positions, which will be used to extract SIFs, must be chosen to be very small. On the other hand, since the gradient of the displacement field is singular as $r \to 0$, the errors of the displacements near the crack tip, even with the use of specially designed crack tip elements, are much bigger than those far away from the crack tip. Unfortunately, when using Equations 7-14 and 7-15 to extract SIFs, it is not clear what value of r should be chosen for obtaining the best results. Lim et al. (1992) and Pang (1993) systematically studied these techniques, and they indicate that

the displacement extrapolation techniques exhibited some erratic characteristics and are highly sensitive to the nodal displacement distribution. In other words, fortuitously, more accurate displacements do not always give more accurate SIFs because of the interaction between the error in the approximate displacements and the error in Equations 7-14 and 7-15.

It is natural to imagine that if the SIFs are extracted from the total COD data on the crack line, the accuracy will be greatly improved. The global displacement extraction procedure is based on the use of a path-independent J-integral, which is defined as

$$J = \int_S (Wn_1 - t_j u_{j,1})\, dS \tag{7-16}$$

where S is an arbitrary contour surrounding the crack tip; W the strain energy density that can be expressed by $1/2\sigma_{ij}\varepsilon_{ij}$, where σ_{ij} and ε_{ij} are the stress and strain tensors, respectively; and $t_j = \sigma_{ij} n_i$, the traction components, where n_i are the components of the unit outwardly normal to the contour path. The relationship between the J-integral and SIFs is given by

$$J = \frac{K_{\mathrm{I}}^2 + K_{\mathrm{II}}^2}{E} \tag{7-17}$$

The advantages of using Equations 7-16 and 7-17 to extract SIFs are that the total COD data are used, although indirectly, and the numerical calculations of the J-integral are not significantly sensitive to the displacement near fields where the big errors of the displacement fields are encountered. This makes the accuracy of SIFs extracted from Equations 7-16 and 7-17 much better than that of SIFs that extracted from Equations 7-14 and 7-15. The disadvantages of this procedure are that (1) more post processing work is needed; (2) the integral in the right-hand side of equation 7-16 involves the calculation of stress or strain tensors along a new contour, which will introduce more errors than if the integral only involves displacement fields along the crack line itself; and (3) it is not easy to extend this method to 3D crack problems.

Within the scope of LEFM, the physical meaning of the J-integral is the energy release rate G when the crack tip has a virtual crack extension Δa:

$$J = G = \Delta U / \Delta a \tag{7-18}$$

where ΔU is the change in strain energy. By using the energy release rate method to extract SIFs, a second analysis of the crack problem should be carried out, and the size of Δa is based more on experience; however, the results are as good as those use the J-integral method. Another advantage of the energy release rate method is that it can be used in 3D crack programs.

Cooper et al. (1995) compared the two procedures mentioned above on a set of about forty basic test problems by using finite element analysis. They concluded that the continued use of local fitting procedures for SIFs is not recommended, other than possibly for rough hand estimates, and for applications in which reliable estimates of SIFs are sought, path-independent integrals represent a superior choice.

Recently, a self-similar crack expansion method (SSCE) was proposed by Xu (1998) and Xu et al. (1997) to evaluate SIFs for the cracks in an infinite medium or semi-infinite medium. By taking advantage of the crack self-similarity, a relation between the SIFs and the crack opening volume defined by the integral of COD over the crack face is established. Since only COD data are needed and all the COD data are used, highly accurate SIF results have been obtained by using the SSCE method. Also the post-processing is small, and this method is valid for the analysis of 3D crack problems. However, if a crack is not self-similar, such as a crack in a finite body, an additional integral including the traction derivatives around the boundary of the finite body is needed to evaluate the SIFs.

A reliable, highly accurate and easily implemented procedure to extract the SIFs should have the following features: (1) The procedure should make full use of the COD data to increase the accuracy of the results, and the information of COD fields should not be wasted. (2) The numerical calculation should only involve displacement fields to avoid additional errors from the numerical calculation of other field quantities, such as stress or strain components. (3) The postprocessing should be as small as possible, i.e., no new contouring and remeshing are needed. (4) The procedure can be easily applied to mixed-mode crack problems with arbitrary crack shapes. And (5) the errors of obtaining SIFs can be directly estimated from the error information of the COD data.

For mode II, the stress expressions are

$$\sigma_{xx} = \frac{-K_{\mathrm{II}}}{\sqrt{2\pi r}} \sin\frac{\theta}{2}\left(2 + \cos\frac{\theta}{2}\cos\frac{3\theta}{2}\right) \tag{7-19}$$

$$\sigma_{yy} = \frac{K_{\mathrm{II}}}{\sqrt{2\pi r}} \cos\frac{\theta}{2}\left(\sin\frac{\theta}{2}\sin\frac{3\theta}{2}\right)$$

$$\sigma_{xy} = \frac{\mathrm{K_{II}}}{\sqrt{2\pi r}} \cos\frac{\theta}{2}\left(1 - \sin\frac{\theta}{2}\sin\frac{3\theta}{2}\right)$$

$$K_{\mathrm{II}} = \sigma_{xy}\sqrt{\pi a} \tag{7-20}$$

For mode III, the stress expressions are

$$\sigma_{xz} = \frac{-K_{\mathrm{III}}}{\sqrt{2\pi r}} \sin\frac{\theta}{2}$$

$$\sigma_{yz} = \frac{K_{\mathrm{III}}}{\sqrt{2\pi r}} \cos\frac{\theta}{2} \tag{7-21}$$

The stress intensity factor is one of the most important concepts of fracture mechanics. It is also called fracture toughness. A crack extension will occur when the critical fracture toughness of the material is reached. Therefore, fracture toughness is expected to be a material property.

According to the stress expression, the stress approaches infinity at a crack tip where r tends to zero. This phenomenon is termed the stress singularity at the tip of an elastic crack. Since an infinite stress cannot develop in real materials, a certain range of the inelastic zone must exist at the crack tip.

The stress intensity factor can serve as a fracture criterion. A crack propagates whenever K_{I} is equal to a threshold value, i.e.,

$$K_{\mathrm{I}} = K_{\mathrm{Ic}} \tag{7-22}$$

where K_{Ic} is the critical stress intensity factor for a mode I crack. The value of K_{Ic} is regarded as the material fracture parameter in linear elastic fracture mechanics.

7.2.2 Griffith strain energy release rate

An energy-based fracture criterion was first developed by Griffith (1921). Crack propagation can also be described by an energy-based criterion. The energy-based fracture criterion was built up on an equilibrium state of a structure with a crack. To demonstrate such an equilibrium state, one might consider a unit thickness plate with a crack subjected to tension, as shown in Figure 7-6.

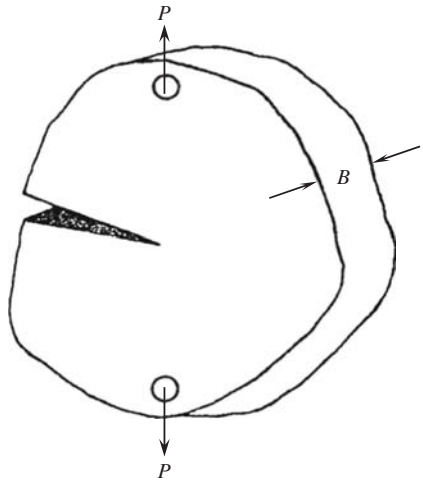

Figure 7-6 A specimen with an edge crack under loading

For simplicity, body forces are neglected. The total potential energy in the structure can be expressed as

$$\Pi = U - F + W \tag{7-23}$$

where $U = U(a, \varepsilon)$ is the strain energy of the structure and a function of crack length and strain, F the work done by the external (applied) load, and W the energy for crack formation. The condition for the structure to have an equilibrium state is that the first-order derivative of total potential energy equals zero during an infinitesimal crack extension, da, and this results in

$$\frac{\partial}{\partial a}(F - U) = \frac{\partial W}{\partial a} \tag{7-24}$$

It should be noted that since a change of the equilibrium state results from a change of the crack length, the equation is taken as a derivative with respect to the crack length, a. By introducing G as the strain energy release rate for the propagation of a unit length of crack in a structure with unit thickness, we have

$$G = \frac{1}{B}\frac{\partial}{\partial a}(F - U) \tag{7-25}$$

Consider a cracked plate of thickness B under a load P, as shown in the previous figure. Under an action of the load, the load-application points undergo a relative displacement v. For a fixed-load case, when the crack increases in size by an amount da, and the displacement will increase by an amount of dv. Hence, the work done by the external force is Pdv. Thus we have

$$G = \frac{1}{B}\left(\frac{\partial F}{\partial a} - \frac{\partial U}{\partial a}\right) = \frac{1}{B}\left(P\frac{\partial v}{\partial a} - \frac{\partial U}{\partial a}\right) \tag{7-26}$$

Since $U = 0.5\ Pv = 0.5\mathrm{CP}^2$, we can write

$$G = \frac{1}{B}\left(P^2\frac{\partial C}{\partial a} + CP\frac{\partial P}{\partial a} - \frac{1}{2}P^2\frac{\partial C}{\partial a} - CP\frac{\partial P}{\partial a}\right) = \frac{P^2}{2B}\frac{\partial C}{\partial a} \tag{7-27}$$

For the condition of fixed displacement, we have

$$G = -\frac{P^2}{2B}\frac{\partial C}{\partial a} \tag{7-28}$$

Define $G_c = 1/B(dW/da)$ as the critical strain energy release rate of the materials; then $G = G_c$ represents the condition for the equilibrium state of the structure during crack propagation. Since any propagation of an initial crack means catastrophic failure of a structure made of linearly elastic materials, it can be used as a failure criterion for such materials. Generally, the strain energy release rate, G, is a function of the applied load, structural geometry, and boundary conditions, whereas the critical strain energy release rate, G_c, is a material fracture constant for linearly elastic materials. Since G provides the energy for a crack extension, it is also termed the crack driving force.

The value of G can be evaluated based on a load–deflection curve. It has been shown that for a linearly elastic material under a plane stress condition a relationship between G and K exists as

$$G_I = \frac{K_I^2}{E} \tag{7-29}$$

where E is Young's modulus. For the plane strain case, we have

$$G_I = \frac{K_I^2}{(1-\nu^2)E} \tag{7-30}$$

7.3 THE CRACK TIP PLASTIC ZONE

According to the elastic stress field solutions, a stress singularity exists at the tip of an elastic crack. However, in practice, materials tend to exhibit a yield stress, above which they deform plastically. There is always a small plastic zone around the crack tip in a metal, and a stress singularity cannot exist. The plastic region is known as the crack tip plastic zone. A rough estimate of the size of the plastic zone is simple to make. For a plane stress case, Figure 7-7 shows the magnitude of stress σ_v in the plane $\theta = 0$.

At a distance r_p^* from the crack tip, the stress is higher than the yield stress σ_{ys}. To a first approximation, this r_p^* is the size of plastic zone. The r_p^* can be calculated by substituting σ_{ys}

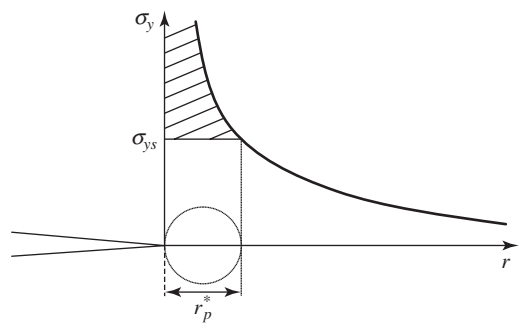

Figure 7-7 Estimation of the plastic zone in front of a crack tip

with σ_y:

$$\sigma_y = \frac{K_I}{\sqrt{2\pi r_p^*}} = \sigma_{ys} \tag{7-31}$$

and we have

$$r_p^* = \frac{K_I^2}{2\pi\sigma_{ys}^2} = \frac{\sigma^2 a}{2\sigma_{ys}^2} \tag{7-32}$$

However, the size of the actual plastic zone must be larger than r_p^* because it will not satisfy equilibrium by just simply cutting off the stress area above the yield stress. To estimate the actual size of the plastic zone, Irwin suggested an effective crack size method that shifted the stress curve to front of the crack tip a distance of δ, as shown in Figure 7-8. Note that δ must be large enough to balance the load that is carried by the area of the singularity hat.

$$\delta\sigma_{ys} = \int_0^{\lambda} \sigma_{yy}\, dr - \lambda\sigma_{ys} \tag{7-33}$$

After substituting the expression for σ_{yy} into Equation 7-33, and integrating, we get

$$(\delta + \lambda)\sigma_{ys} = \sigma\sqrt{2a\lambda} \tag{7-34}$$

This can be further rewritten as

$$(\delta + \lambda)^2 = \frac{\sigma^2 2a\lambda}{\sigma_{ys}^2} = \frac{2K_I^2\lambda}{\pi\sigma_{ys}^2} = 4\lambda^2 \tag{7-35}$$

Since $\lambda << a$, we have

$$\lambda = \frac{\sigma^2\pi(a + \lambda)}{2\pi\sigma_{ys}^2} \approx r_p^* \tag{7-36}$$

Therefore, it can be verified that the actual size of the plastic zone is twice that of the value of r_p^*, i.e.,

$$r_p = 2r_p^* = 2\frac{K_I^2}{2\pi\sigma_{ys}^2} = \frac{K_I^2}{\pi\sigma_{ys}^2} \tag{7-37}$$

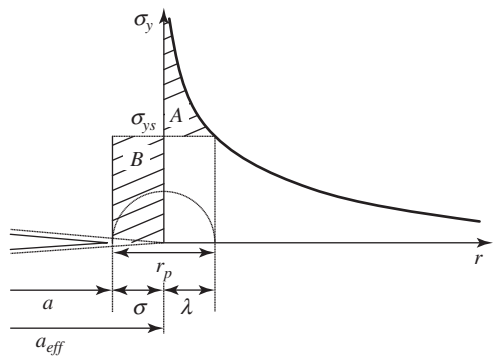

Figure 7-8 Effective crack size method for the plastic zone

A different approach to find the size of plastic zone was followed by Dugdale (1960). Dugdale assumed the length of plastic zone to be much greater than the thickness of the sheet and modeled the plastic zone as a yield strip ahead of the crack tip. Dugdale applied the superposition method to calculate the size of the plastic zone. The detailed procedures are stated as follows.

It was assumed that the crack had a crack length of $a + \rho$ by considering the plastic zone. However, the crack edges, a distance of ρ in front of the physical crack tip, was under the action of the yield stress, σ_{ys}, tending to close the crack in this region. Part of ρ was not really cracked; the material could still bear the yield stress. The size of ρ was chosen such that the stress singularity disappears: K should be zero. This means that the stress intensity factor K_σ, due to uniform stress σ, had to be compensated by the stress intensity factor K_ρ, due to the edge closing stress, σ_{ys}:

$$K_\sigma = -K_\rho \tag{7-38}$$

This equation permitted determination of ρ in the following manner. The stress intensity factor at crack tip is due to wedge forces p shown in Figure 7-9, and given as

$$K_A = \frac{p}{\sqrt{\pi a}}\sqrt{\frac{a+x}{a-x}} \tag{7-39}$$

And for the case shown in Figure 7-10, the stress intensity factor was given by

$$K_B = \frac{p}{\sqrt{\pi a}}\sqrt{\frac{a-x}{a+x}} \tag{7-40}$$

If the wedge forces were distributed from s to the crack tip (as in the Dugdale case) the stress intensity becomes

$$K_\rho = \frac{p}{\sqrt{\pi a}}\int_s^a \left(\sqrt{\frac{a+x}{a-x}} + \sqrt{\frac{a-x}{a+x}}\right)dx \tag{7-41}$$

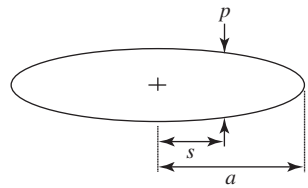

Figure 7-9 A crack under a pair of wedge forces on the right side

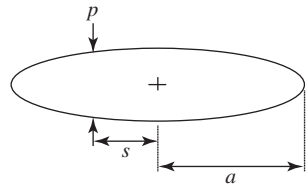

Figure 7-10 A crack under a pair of wedge forces on the left side

The integral result is

$$K_\rho = 2p\sqrt{\frac{a}{\pi}}\arccos\frac{s}{a} \tag{7-42}$$

Applying this result to the Dugdale crack, the integral had to be taken from $s = a$ to $a + \rho$. Hence, a had to be substituted for s and $a + \rho$ for a, while $p = \sigma_{ys}$.

$$K_\rho = 2\sigma_{ys}\sqrt{\frac{a+\rho}{\pi}}\arccos\frac{a}{a+\rho} \tag{7-43}$$

According to Dugdale, this stress intensity should be equal to K_σ,

$$K_\sigma = \sigma\sqrt{(a+\rho)\,\pi} \tag{7-44}$$

It followed that ρ could be determined from

$$\frac{a}{a+\rho} = \cos\frac{\pi\sigma}{2\sigma_{ys}} \tag{7-45}$$

By expanding the two sides in a Taylor series and neglecting the higher-order terms in the series development of the cosine, ρ was found as

$$\rho = \frac{\pi^2\sigma^2 a}{8\sigma_{ys}^2} = \frac{\pi K^2}{8\sigma_{ys}^2} \tag{7-46}$$

This result can be compared with

$$r_p = \frac{K_I^2}{\pi\sigma_{ys}^2} \tag{7-47}$$

because the value of π is close to $8/\pi$. When the plastic zone is small compared to the crack size, LEFM can still be used to find the stress and displacement distributions in front of the crack tip. However, if the plastic zone is larger with respect to the crack, the application of LEFM is doubtful, because of the validity of the expressions for K, which are based on elastic solutions only.

7.4 CRACK TIP OPENING DISPLACEMENT

A certain size of the inelastic zone always exists at a crack tip in a real material. The presence of the inelastic zone allows the crack to open a small amount. The crack opening displacement (COD) is a general term and can be any point along a crack. The crack tip opening displacement (CTOD) is the displacement at the point of the crack tip. Therefore, COD is a function but CTOD a number. In LEFM, the critical value of CTOD is related to the critical value of SIF or energy release rate. Hence, one may use crack tip opening displacement as a fracture criterion.

To better understand the CTOD fracture criterion, let us consider an infinite plate with a crack of size $2a$, subjected to tension, as shown in Figure 7-11. The crack opening displacement for the structure can be expressed as

$$\text{COD} = \frac{4\sigma}{E}\sqrt{a^2 - x^2} \tag{7-48}$$

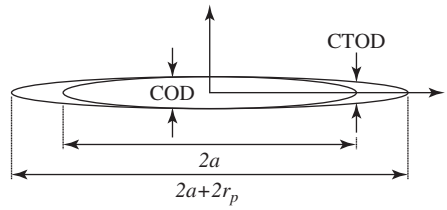

Figure 7-11 Sketch of crack opening displacement

It can be seen that if there is no crack propagation, when $x = a$, then CTOD = 0. When $x = 0$, COD reaches maximum,

$$\mathrm{COD}_{x=0} = \frac{4\sigma}{E}a \tag{7-49}$$

Since the stress is usually two or three orders of magnitude smaller than Young's modulus, COD is much smaller than the crack length. By introducing the crack length extension, r_p; we can write,

$$\mathrm{COD} = \frac{4\sigma}{E}\sqrt{\left(a + r_\mathrm{p}\right)^2 - x^2} \tag{7-50}$$

where $a + r_\mathrm{p}$ is the effective crack size. Since CTOD is the value of COD at the position of $x = a$, it follows that

$$\mathrm{CTOD} = \frac{4\sigma}{E}\sqrt{2ar_\mathrm{p}} \tag{7-51}$$

It can be shown that

$$r_\mathrm{p} = \frac{K_\mathrm{I}^2}{\pi\sigma_\mathrm{ys}^2} \tag{7-52}$$

where σ_ys is the yield stress of the material. Substituting r_p into Equation 7-51, we have

$$\mathrm{CTOD} = \frac{4\sqrt{2}K_\mathrm{I}^2}{\pi\sigma_\mathrm{ys}E} = \frac{4\sqrt{2}}{\pi\sigma_\mathrm{ys}}G_\mathrm{I} \tag{7-53}$$

It can be further written as

$$\mathrm{CTOD} = \frac{K_\mathrm{I}^2}{m\sigma_\mathrm{ys}E} = \frac{G_\mathrm{I}}{m\sigma_\mathrm{ys}} \tag{7-54}$$

where $m = \pi/4\sqrt{2}$ and is a constant. When CTOD reaches its critical value, the crack will propagate. Thus, we have one more criterion for the unstable crack as

$$\mathrm{CTOD} = \mathrm{CTOD}_\mathrm{c} \tag{7-55}$$

The parameters K_Ic and G_Ic can be related to CTOD_c as

$$K_\mathrm{Ic} = \sqrt{mE\sigma_\mathrm{ys}\mathrm{CTOD}_\mathrm{c}} \tag{7-56}$$

and

$$G_\mathrm{Ic} = m\sigma_\mathrm{ys}\mathrm{CTOD}_\mathrm{c} \tag{7-57}$$

Thus, once CTOD_c is known, K_Ic and G_Ic can be obtained from the equations.

7.5 FRACTURE PROCESS IN CONCRETE

To study fracture progress in concrete, uniaxial tension tests have been carried out with monitoring of the microcrack occurrence using the acoustic emission technique. The test setup is shown in Figure 7-12. As can be seen from the figure, four LVDTs (linear variable differential transformers) are used to cover the whole test portion of the concrete specimen. An adoptive control method is used that allows the control mode to be switched among the LVDTs and hence the major crack formation can be captured by one of them, and the opening displacement of the major crack can be used as a feedback signal to control the movement of the actuator of the test machine. Six acoustic emission transducers are placed on the surfaces of the specimens. They are used to detect the wave signal generated by the occurrence and the propagation of cracks during the loading process. The acoustic emission (AE) information can be used to locate the positions of the microcracks or propagation path of major cracks and to interpret the fracture properties of concrete.

Figure 7-13 shows the tensile stress, accumulated AE event number, and AE event rate as functions of time for a plain concrete tension specimen. The AE data analysis can be divided into five regimes according to the stress level (loading stage) for the convenience of analysis. In the first regime, which is the initial portion of the stress–displacement curve from the start of testing to when the stress reaches about 40% of peak load, no AE event occurred, implying that

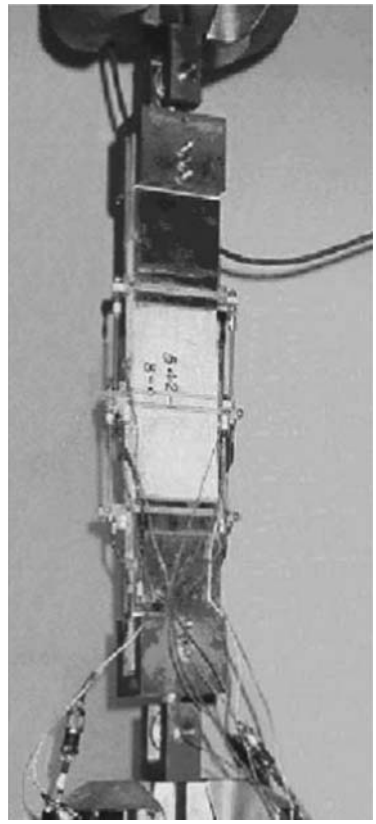

Figure 7-12 Uniaxial tension test setup for unnotched specimens

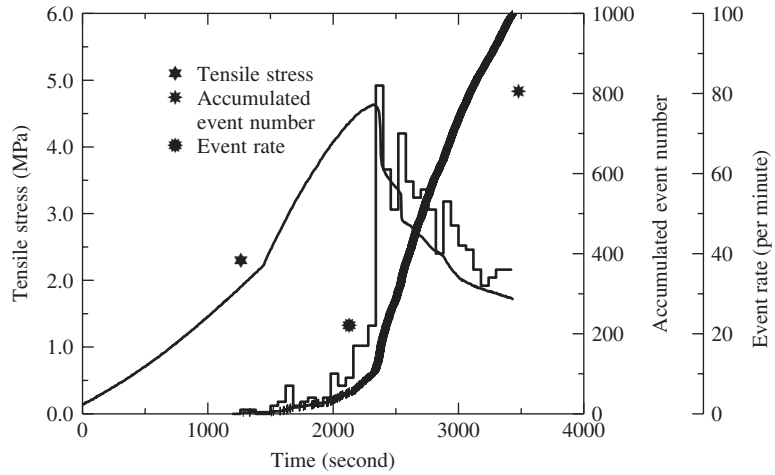

Figure 7-13 Tensile stress and accumulated acoustic events as function of time

there was no microcrack. In the second regime, where the stress level is within $0.4 - 0.8f_t$, AE activity starts to be detectable at around 40% of the peak stress f_t, and the AE events gradually increase with the stress increase but with a small slope. At this stress level range, the defects, voids, and other preexisting flaws in the mortar–aggregate interfaces within the concrete begin to form microcracks and propagate. Later on, with the increment of the external load, AE events gradually increase as more and more damage forms. When the stress level closes to $0.8f_t$, the AE event rate becomes much higher. This implies that AE activity is closely related to the stress level before the peak stress. The interface defects continue to propagate and branch inside the mortar matrix. Matrix cracks (and also voids) begin to link. The consequent propagation and linking of these cracks will lead to the formation of a macrocrack in the ensuing regime.

A significant increase of the AE event rate occurs when the stress approaches the peak value, f_t. This implies that a major crack may have formed and begun to propagate. The fracture process zone around the crack tip becomes the major emission source. After this loading stage, with the stress level decreased, the AE event rate becomes relatively lower. A map of the microcrack can be obtained by the analysis of AE event source locations. Figure 7-14 shows the distribution of the microcracks that occurred during the loading stage between 0.4 and $0.8f_t$, between pre-peak $0.8f_t$ and peak stress, and between peak and post-peak stress $0.8f_t$. It can be seen from Figure 7-14a that the AE events registered on the source location maps, or the microcracking activities, are randomly and relatively sparsely distributed in the test portion of the specimen. When the stress level proceeds into the regime between pre-peak $0.8f_t$ and peak stress, significant AE events take place in a narrow region of the specimen, clearly showing a strain localization. In the stage from peak stress f_t to post-peak $0.8f_t$, the localization phenomena become more obvious (see Figure 7-14c). During this loading stage, emissions from those defects within the specimen tend to be dominated by a localized area, namely, around a macrocrack (Li and Li, 2000). A similar phenomenon has also been reported by Li and Shah (1994).

One more phenomenon that can be observed from the microcrack map is that the area spread by microcracks seems quite large, which is quite different from the case in a metal. This phenomenon could be evidenced by other investigations that focused on the fracture process zone, especially its size and its distribution. Castro-Montero et al. (1990) used laser holographic interferometry, with an accuracy of a quarter of a micron, to study displacement fields at the crack

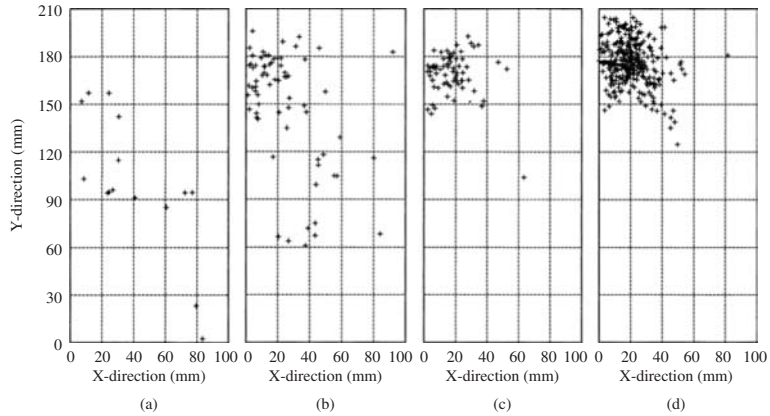

Figure 7-14 The distribution of microcracks that occurred during the loading stage between (a) 0.4 and $0.8f_t$, (b) pre-peak $0.8f_t$ and peak stress, (c) peak and post-peak $0.8f_t$, and (d) after post-peak $0.8f_t$.

tip. The region where the experimentally determined strain field differed significantly from the LEFM solutions was taken to be the fracture process zone. As shown in Figure 7-15, they reported a large wake zone (labeled B) behind the observed crack tip. This zone increased with crack extension, whereas the zone in front of the tip (labeled A) remained practically consistent in size. They concluded that most of the toughening in concrete occurs in the wake zone. This fact may suggest that the increasing size of the wake process zone rather than the constant size of the crack tip process zone should be primarily responsible for the growing *R*-curve behavior in concrete. Similar observations have been reported for other quasi-brittle materials (Sakai et al., 1988; Homeny and Vaughn, 1990). By using the dye-penetration method, Swartz and Refai (1989) found that the fracture process zone varies along the specimen thickness.

The large area spread by microcracks in concrete is termed microcrack shielding. The reasons for the shielding are that during fracture, the high stress state near the crack tip causes the preexisting flaws, which resulted from the water-filled pores, air voids acquired during casting, and shrinkage and thermal shock due to the nature of hydration process, to grow into microcracks. Microcrack shielding is a major characteristic for the fracture processing zone in concrete. Other characteristics for the fracture process zone in concrete are further indicated in Figure 7-16. Crack deflection occurs when the path of least resistance is around a relatively strong particle or along a weak interface (see Figure 7-16b). This mechanism has been studied in detail by Faber and Evans (1983). An other important toughening process in concrete is grain bridging (Van Mier, 1991) as shown in Figure 7-16c. Bridging occurs when the crack has advanced beyond an aggregate that continues to transmit stresses across the crack until it ruptures or is pulled out. Also, during grain pullout, or the opening of a tortuous crack, there may be some contact (or interlock) between the faces (see Figure 7-16d). This causes energy dissipation through friction, and some bridging across the crack.

It is obvious that a crack process zone in concrete is not small. In this case, the applicability of LEFM solutions is questionable, although LEFM can still be applied when there is a small yield zone, as we indicated earlier.

Shah and McGarry (1971) conducted a three-point beam test on cement paste, mortar, and concrete specimens. They found that hardened cement paste was a notch-sensitive material. The presence of a notch significantly reduced the tensile or flexural strength of the paste. On

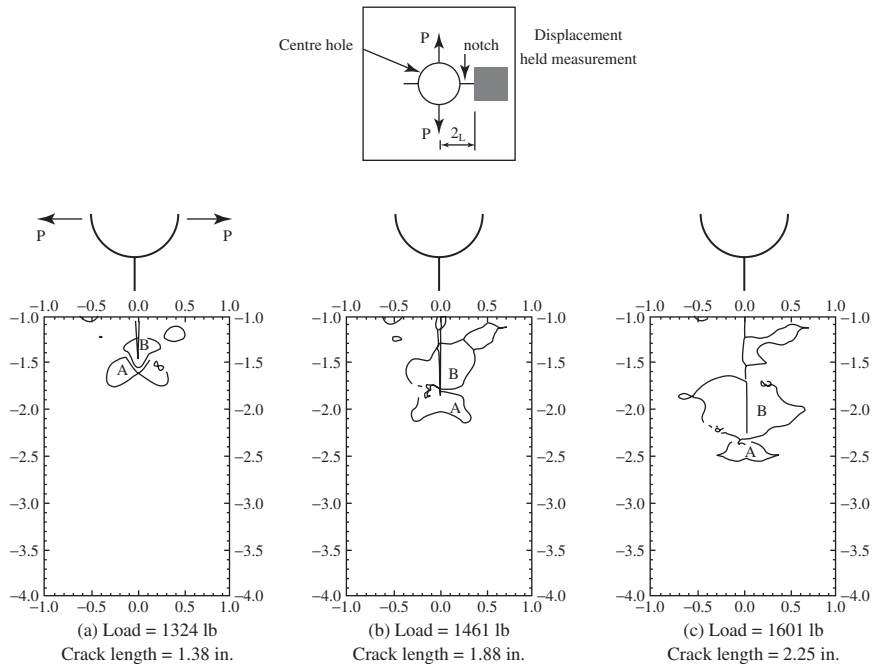

Figure 7-15 Fracture test with laser holographic interferometry observations

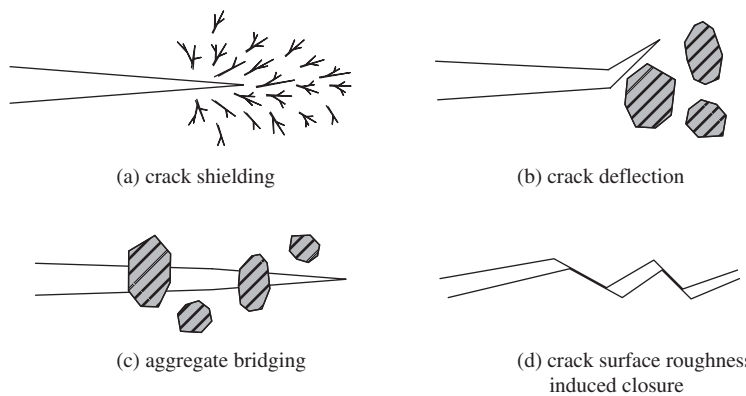

Figure 7-16 Possible mechanisms for the fracture process zone in concrete

the other hand, mortar and concrete, with the normally used amounts and volume of stone particles, were notch-insensitive materials. Even for cement paste that showed notch sensitivity there was no brittle behavior, and the direct application of LEFM had to be verified. Higgins and Baily (1976) tested three-point bend beams with different depths but the same cement paste, and calculated the critical stress intensity factor using linear elastic fracture mechanics. However, they found values of the critical stress intensity factor to be size-dependent, as shown in Figure 7-17. This was due to the fact that linear elastic fracture mechanics did not take the stable crack growth associated with the fracture process zone into account. In other words, in

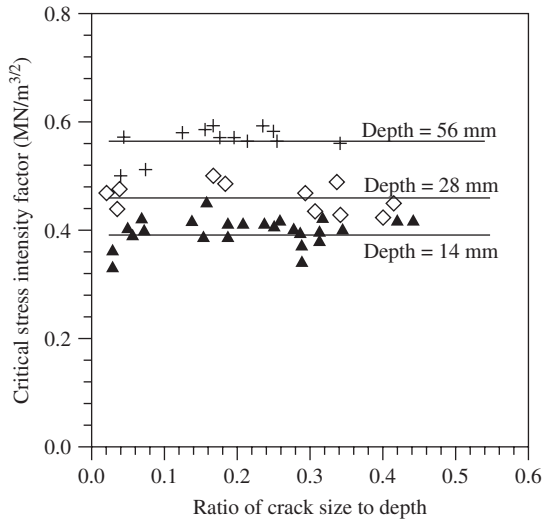

Figure 7-17 Dependency of the stress intensity factor on the crack size in concrete

linear elastic fracture mechanics, the initial crack length, rather than sum of the initial crack length and the crack extension, was used to determine the critical stress intensity factor.

The experimental results have demonstrated that LEFM cannot be directly applied to cement-based composites, especially concrete. For LEFM materials, one parameter is sufficient to describe its failure toughness. For concrete, if only one parameter is considered then one observes that the fracture toughness increases with increasing compressive strength or increasing strain rate. Such single-parameter representation is misleading since concrete, in fact, becomes more brittle as its compressive strength increases. The presence of a sizable fracture process zone and its contribution to the fracture toughness of concrete have to be taken into consideration for concrete fracture mechanics. In other words, nonlinear fracture mechanics should be used for modeling concrete fracture.

7.6 NONLINEAR FRACTURE MECHANICS FOR CONCRETE

Fracture behavior of concrete is greatly influenced by its fracture process zone. Since the work of Kaplan (1961), many attempts have been made to apply fracture mechanics to concrete. As summarized in Section 7.5, linear elastic fracture mechanics cannot be directly applied to concrete due to the sizeable fracture process zone, aggregate bridging, and tortuous, zigzag crack path. It is difficult to determine the exact position of the crack tip in concrete due to particle bridging and variation of the fracture process zone along the thickness direction. An accurate description of concrete fracture needs to specify the torturous three-dimensional crack path, as well as the inelastic material response within the fracture process zone. To simplify the application of fracture mechanics to the failure of concrete, most recently available models attempt to simulate mode I concrete fracture with an effective straight-line crack. The variation of the fracture process zone along the structure thickness or width is usually neglected. The inelastic fracture process zone may be taken into account by a cohesive pressure acting on the crack faces.

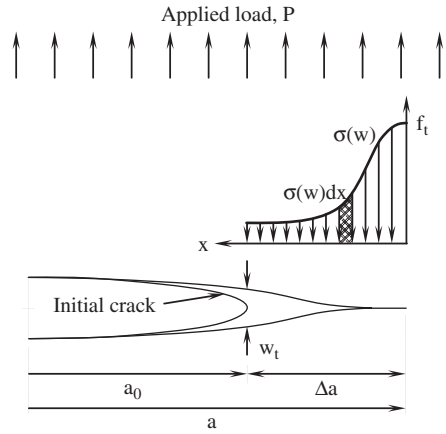

Figure 7-18 Modeling of cohesive stress for a quasi-brittle crack

By analoging Dugdale's model, an effective inelastic crack or effective quasi-brittle crack in a concrete can be drawn. Figure 7-18 shows such a crack, where the initial crack length is noted as a_0 and the length of the associated fracture process zone is presented by a crack extension of Δa. Since the crack extension does have the ability to consume energy, a continuously distributed cohesive stress is modeled over Δa.

Differing from the yield stress in Dugdale's model for metals, the cohesive pressure, $\sigma(w)$, in concrete has to be modeled as a monotonic decreasing function of crack separation displacement, w, because of its strain-softening behavior. The shape of $\sigma(w)$ can be determined by referring to the postpeak portion of the stress–displacement curve of a concrete under uniaxial tension as a function of the crack opening displacement, w. The value of $\sigma(w)$ is set equal to the concrete tensile strength f_t at the end of the fracture process zone, where $w = 0$, and gradually is reduced toward the original crack tip. The value of $\sigma(w)$ at the original crack tip is usually set to 0 to simplify the computation process. This cohesive pressure tends to close the crack, just like the yield stress in Dugdale's model. It should be noted that the effective crack extension is usually not the same as the length of the real fracture process zone because of the difficulty in determining the variation of the actual fracture process zone along the thickness or the width direction.

When a concrete structure with an effective quasi-brittle crack is subjected to loading, the applied load will result, at a certain level, in an energy release rate G at the tip of the effective quasi-brittle crack. The energy release rate G is composed by two portions: (1) the energy release rate in creating two surfaces generated by remote stress during specimen loading (the material surface energy), and (2) the energy release rate in overcoming the local cohesive pressure, $\sigma(w)$, during the separation of the new surfaces. As a result, the total energy release rate, G_{It}, for a mode I quasi-brittle crack can be expressed as

$$G_{It} = G_{I\sigma} + G_{\sigma(w)} = G_{I\sigma} + \int_0^{CTOD} \sigma(w)\, dw \tag{7-58}$$

where G_{Ic} is the strain energy rate to create two new crack surfaces due to remote stress for a mode I crack; $\sigma(w)$the normal traction pressure, which is a function of the crack opening displacement w, as explained earlier; and CTOD the crack tip opening displacement. The crack shape is assumed to be a line. Two terms representing two types of energy dissipation mechanisms for the fracture process have been introduced in the equation. The Griffith-Irwin energy

dissipation mechanism is represented by a nonzero stress intensity factor and the Dugdale-Barenblatt energy dissipation mechanism is represented by the traction term. It seems that it is proper to use these two energy dissipation mechanisms to describe the propagation of a quasi-brittle crack. However, one may approximately use models based only on a single fracture energy dissipation mechanism, either the Griffith-Irwin energy dissipation mechanism by assuming $\sigma(w) = 0$, or the Dugdale-Barenblatt energy dissipation mechanism by assuming $K_I = 0$, to simplify the mathematical derivation. Based on the different energy dissipation mechanism used, nonlinear fracture mechanics models for quasi-brittle materials may be classified as a fictitious crack approach and an equivalent-elastic crack approach (or an effective-elastic crack approach). Fracture models using only the Dugdale-Barentblatt energy dissipation mechanism are usually referred to as the fictitious crack approach, whereas fracture models using only the Griffith-Irwin energy dissipation mechanism are usually referred to as the effective-elastic crack approach.

In the category of the fictitious crack approach, Hillerborg et al. (1976) have proposed a cohesive model with $K_I = 0$. Bazant and Oh (1983) have developed a crack band model using a similar concept. It is noted that by assuming $K_I = 0$, some computational efficiency may be accomplished. However, a single Dugdale-Barenblatt energy dissipation mechanism may only achieve a global energy balance by selecting model parameters. Some actual features associated with crack propagation, such as crack profile, computed based on the pure cohesive model, may not match with those experimentally measured.

In the effective-elastic crack approach category, two representative models are the two-parameter model and the size effect model. In the effective-elastic crack models, instead of the original crack length, an effective-elastic crack length is used. The equivalence between the actual and the corresponding effective crack can be prescribed explicitly. Since a stable crack extension before the peak load is present in concrete, the critical effective-elastic crack length at failure of the materials is different from the initial crack length. To predict the failure condition of the materials, two conditions are needed to determine the critical load and the corresponding crack length. Most of these effective crack models use two or more fracture parameters to define the inelastic fracture process.

7.7 TWO-PARAMETER FRACTURE MODEL

7.7.1 The model

Using the concept of the effective elastic crack, Jenq and Shah (1985) proposed a two-parameter fracture model. In their model, two parameters, crack tip opening displacement and the stress intensity factor (K_I), corresponding to the effective-elastic crack, are used to describe the fracture properties of concrete. Jenq and Shah used a beam under three-point bending for the investigation. Figure 7-19 shows the geographical feature and loading pattern for such a specimen. It can be seen from the figure that it is easier to measure the crack mouth opening displacement (CMOD) than CTOD, because the crack tip is unclear.

Figure 7-20 shows a typical stress–CMOD curve of loading and unloading. It can be seen that after unloading from peak stress to zero stress, CMOD cannot return to zero. This means that CMOD contains some plastic deformation, and so does CTOD. Figure 7-21 illustrates the relationship between CMOD and CTOD.

If accounting for the quasi-brittle features of concrete, the $\mathrm{CMOD_c}$, the CMOD value at peak load, can be divided into two parts, the elastic and plastic parts:

$$\mathrm{CMOD_c} = \mathrm{CMOD_c^e} + \mathrm{CMOD_c^p} \tag{7-59}$$

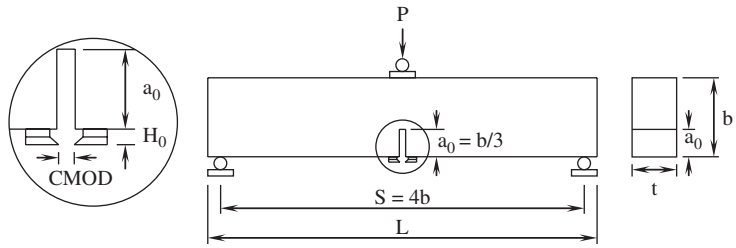

Figure 7-19 Three-point bending test setup for the two-parameter model

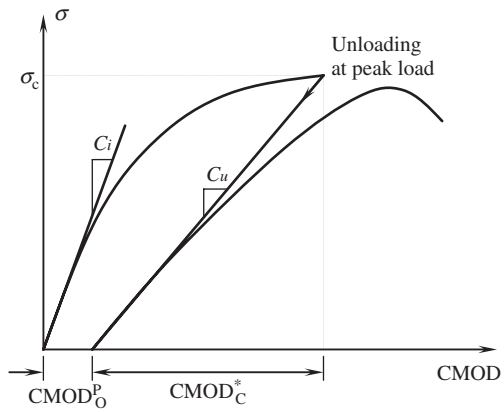

Figure 7-20 Loading and unloading procedure

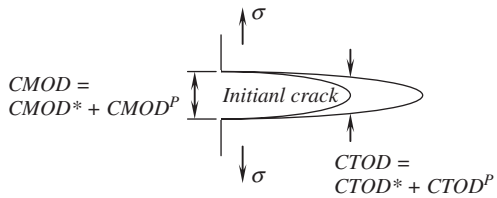

Figure 7-21 The schematic of CMOD and CTOD

The procedures to separate these two components involve a loading and unloading process. The measured value of CMOD_c^e and the maximum stress σ_c, can be further substituted into the following LEFM equations to calculate the critical effective-elastic crack length, a_c, and then the critical stress intensity factor, K_{Ic}^S, based on maximum stress σ_c and critical effective-elastic crack length, a_c:

$$\mathrm{CMOD}_c^e = \frac{4\sigma_c a_c}{E_t} g_2\left(\frac{a_c}{b}\right) \tag{7-60}$$

and

$$K_{Ic}^S = \sigma_c \sqrt{\pi a_c} g_1\,(a_c/b) \tag{7-61}$$

The value of the critical crack tip opening displacement $\mathrm{CTOD_c}$ can then be determined based on the obtained values of $\mathrm{CMOD_c^e}$:

$$\mathrm{CTOD_c^e} = \mathrm{CMOD_c^e} g_3\left(\frac{a_c}{b}\right) \tag{7-62}$$

In the above three equations, g_1, g_2 and g_3 are geometrical functions for calculating $\mathrm{K_{Ic}^S}$, $\mathrm{CMOD_c^e}$, and $\mathrm{CTOD_c^e}$, respectively. As an example, for a three-point bending beam with a span-to-height ratio of 4, the expressions are (Murakami et al., 1987)

$$g_1\left(\frac{a_c}{b}\right) = \frac{1.99 - \frac{a_c}{b}\left(1 - \frac{a_c}{b}\right)\left[2.15 - 3.93\frac{a_c}{b} + 2.70\left(\frac{a_c}{b}\right)^2\right]}{\sqrt{\pi}\left(1 + 2\frac{a_c}{b}\right)\left(1 - \frac{a_c}{b}\right)^{3/2}} \tag{7-63}$$

$$g_2\left(\frac{a_c}{b}\right) = \frac{1.73 - 0.85\frac{a_c}{b} + 31.2\left(\frac{a_c}{b}\right)^2 - 46.3\left(\frac{a_c}{b}\right)^3 + 2.70\left(\frac{a_c}{b}\right)^4}{\left(1 - \frac{a_c}{b}\right)^{3/2}} \tag{7-64}$$

$$g_3\left(\frac{a_c}{b}, \frac{a_0}{a_c}\right) = \left\{\left(1 - \frac{a_0}{a_c}\right)^2 + \left(1.081 - 1.149\frac{a_c}{b}\right)\left[\frac{a_0}{a_c} - \left(\frac{a_0}{a_c}\right)^2\right]\right\}^{1/2} \tag{7-65}$$

From the experimental results obtained by using beams with three-point bending, Jenq and Shah (1985) found that for the beams with different sizes but made of the same material, the values of K_{Ic}^S and $\mathrm{CTOD_c^e}$ were basically constant. As a result, they proposed that the critical fracture property of a quasi-brittle material might be characterized by the values of K_{Ic}^S and $\mathrm{CTOD_c^e}$. For a given material, structures with different geometry and sizes when subjected to the critical fracture load (the peak load) would satisfy the following two conditions:

$$\begin{aligned} K_I &= K_{Ic}^S \\ \mathrm{CTOD} &= \mathrm{CTOD_c} \end{aligned} \tag{7-66}$$

where K_I and CTOD are the stress intensity factor and the crack tip opening displacement, which can be calculated based on LEFM. Also, it is noted that $\mathrm{CTOD_c^e}$ is simply denoted as $\mathrm{CTOD_c}$. This is why it is called the two-parameter model. It should be emphasized that K_I and CTOD are functions of the applied load, structural geometry and size, as well as the crack length, whereas K_{Ic}^S and $\mathrm{CTOD_c^e}$, which are defined in terms of the critical effective-elastic crack, are fracture material parameters depending only on the material. Only when the fracture load and crack tip opening displacement meet the two necessary conditions will a concrete structure start fracture failure. It is seen from the above-mentioned procedure of determining the values of K_{Ic}^S and $\mathrm{CTOD_c^e}$ in the two-parameter fracture model that the effective-elastic crack exhibits a compliance equal to the unloading compliance of the actual structure. Therefore, the two parameter model determines the critical fracture state based on its elastic response.

The existence of $\mathrm{CTOD_c}$ can be justified from the fact that all materials have some sort of initial flaws. This is especially true for concrete. When material is subjected to an external load, these flaws will open, propagate, and sometimes coalescence with other cracks. The opening displacement can be directly linked to the value of CTOD. At the critical fracture load, the crack opening displacement at the initial crack tip can be defined as $\mathrm{CTOD_c}$. For quasi-brittle materials

such as concrete, the stable crack extension occurs before the critical fracture. Since $CTOD_c$ is defined at the tip of the initial crack, it may primarily account for the growth in size of the weak process zone.

7.7.2 Determination of fracture parameters for the two-parameter model

The RILEM Technical Committee 89-FMT on Fracture Mechanics of Concrete Test Methods has proposed a method for the determination of fracture parameters based on the two-parameter model. It recommended using the three-point bending beam with $s/b = 4$ to obtain K_{Ic} and $CTOD_c$. The size of the beam depends on the maximum size of the aggregate and is listed in the Table 7-1.

A typical beam is shown in Figure 7-22. As can be seen from the figure, the initial notch-to-depth ratio should be 1/3 and the notch width should be less than 5 mm. After casting, the specimens should be cured at 100% relative humidity (RH) and at $23 \pm 2^{\circ}C$ until 4 hr before testing. A minimum of 4 specimens are required for each batch of concrete.

The test should be conducted with a closed-loop controlled materials testing machine, using CMOD as a feedback signal. The CMOD and the applied load should be recorded continuously during a test. It is preferred to use a clip gage to measure the CMOD. The loading rate should be controlled so that the peak load is reached in 5 minutes. After reaching the peak load in a monotonic increasing mode, an unloading process should be carried out before it passes 95% of the peak load. When the applied load reaches 0, reloading may be applied according to the test need.

As shown in Figure 7-20, a typical load–CMOD curve can provide the information concerning initial stiffness (compliance), unloading stiffness (compliance), and leak load. To obtain the critical stress intensity factor K_{Ic}^{S}, and the critical crack tip opening displacement $CTOD_c$, the critical effective-elastic crack length has to be determined. This can be done by the following procedures.

By substituting the stress expression into the expression for CMOD and noting that $C_i = CMOD/P$, E can be calculated as

$$E = \frac{6Sa_0 g_2(\alpha_0)}{C_i b^2 t} \tag{7-67}$$

Table 7-1 Relationship between maximum size of aggregate and size of the beam

D_{max} (MM)	Depth, D (MM)	Width, B (MM)	Length, L (MM)	Span, S (MM)
1 to 25	150 ± 5	80 ± 5	700 ± 10	600 ± 5
25.1 to 50	250 ± 5	150 ± 5	1100 ± 10	1000 ± 5

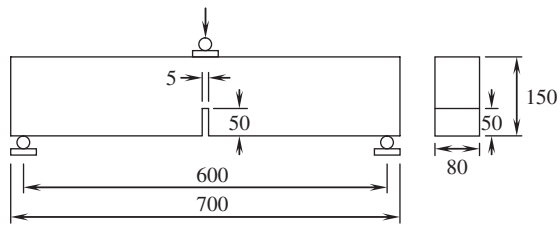

Figure 7-22 A typical beam geometry for determination of fracture parameters (mm)

where C_i is the initial compliance calculated from the load–CMOD curve and $g_2(\alpha_0)$ is

$$g_2(\alpha_0) = 0.76 - 2.28\alpha_0 + 3.78\alpha_0^2 - 2.04\alpha_0^3 + \frac{0.66}{(1-\alpha_0)^2} \tag{7-68}$$

where $\alpha_0 = (a_0 + \mathrm{HO})/(b + \mathrm{HO})$, in which HO is the height of the holding plates for the clip gage or LVDT and a_0 is the initial notch length.
Similarly, E can also be expressed using unloading compliance, C_u, as

$$E = \frac{6Sa_c g_2(\alpha_c)}{C_u b^2 t} \tag{7-69}$$

where C_u is the unloading compliance within 95% of the peak load calculated from the load–CMOD curve, and the geometrical function $g_2(\alpha_c)$ is the same as the expression of $g_2(\alpha_0)$, except that α_c should be used instead of α_0 as shown:

$$\alpha_c = \frac{a_c + \mathrm{HO}}{b + \mathrm{HO}} \tag{7-70}$$

Since the modulus of elasticity of concrete should be the same, i.e., $E = E$, the two expressions for E above should be equal, so we have:

$$\frac{6Sa_0 g_2(\alpha_0)}{C_i b^2 t} = \frac{6Sa_c g_2(\alpha_c)}{C_u b^2 t} \tag{7-71}$$

Therefore, the critical crack length can be obtained as

$$a_c = \frac{C_u a_0 g_2(\alpha_0)}{C_i g_2(\alpha_c)} \tag{7-72}$$

It should be noted that $g_2(\alpha_c)$ is also a function of a_c and hence numerical procedures are usually needed to solve for a_c. After knowing a_c and substituting the stress expression into the critical stress intensity factor expression, we have

$$K_{Ic}^S = 3(P_c + 0.5W_h)\frac{S\sqrt{\pi a_c}\, g_1(\alpha_c)}{2b^2 t} \tag{7-73}$$

where P_c is the peak load, $W_h = W_0 S/L$, and W_0 is the self-weight of the beam, and $g_1(a_c)$ is,

$$g_1(\alpha_c) = \frac{1.99 - \alpha_c(1-\alpha_c)\left[2.15 - 3.93(\alpha_c) + 2.70(\alpha_c)^2\right]}{\sqrt{\pi}(1+2\alpha_c)(1-\alpha_c)^{3/2}} \tag{7-74}$$

in which $\alpha_c = a_c/b$.

The $\mathrm{CTOD_c}$ can be calculated using the equation

$$\begin{aligned} \mathrm{CTOD_c} &= \mathrm{CMOD_c}\sqrt{\left[(1-\beta_0)^2 + (1.081 - 1.149\alpha_c)\left(\beta_0 - \beta_0^2\right)\right]} \\ &= \frac{6(P_c + 0.5W_h)Sa_c g_2(\alpha_c)}{Eb^2 t}\sqrt{\left[(1-\beta_0)^2 + (1.081 - 1.149\alpha_c)\left(\beta_0 - \beta_0^2\right)\right]} \end{aligned} \tag{7-75}$$

where $\beta_0 = a_0/a_c$.

It has been shown that the values of K_{Ic}^S evaluated at the effective elastic crack are independent of the dimensions of the notched beams by large round-robin tests. However, $\mathrm{CTOD_c}$ has not been verified, since it is a small quantity and difficult to measure.

7.7.3 Some applications of the two-parameter model

(a) *Material length, Q*: When the values of K_{Ic}^{S} and $CTOD_c^e$ are known for a concrete, some material characteristic properties can be identified. For example, a material length, Q, can be defined as

$$Q = \left(\frac{E \times \text{CTOD}_c}{K_{Ic}^{s}} \right)^2 \tag{7-76}$$

The material length is proportional to the size of the fracture process zone for the same material. It is found that the values of Q range from 12.5–50 mm for hardened cement paste, 50–150 mm for mortar, and 150–350 mm for concrete. Hence, the material length, Q, can be used as a brittleness index for a material: the larger value of Q, the less brittle the material.

(b) *Size effect*: Experimental results have indicated that the strength of concrete usually decreases with increasing size of the structure and then remains constant, as shown in Figure 7-23, where the nominal strength of a three-point bend beam is equal to its failure load (peak load) divided by its cross-sectional area. This size effect on concrete strength may be primarily explained by the fracture process zone. When a concrete structure is loaded, the strain energy produced by the applied load is converted to the energy consumed to create a new fracture surface and the energy absorbed in the fracture process zone. For larger sizes of structures, the latter is negligible compared to the former, whereas for small-sized structures, the latter can be comparable to the former. Therefore, the larger the structure's size, the lower the nominal strength. However, the concrete strength approaches a constant when the sizes of concrete structures become very large.

This size effect on concrete tensile strength can be predicted by using the fracture mechanics approach. The nominal stress of a concrete structure can be obtained directly as

$$\sigma_N = \frac{K_{Ic}}{\sqrt{\pi a_c} f\left(\frac{a_c}{b}\right)} \tag{7-77}$$

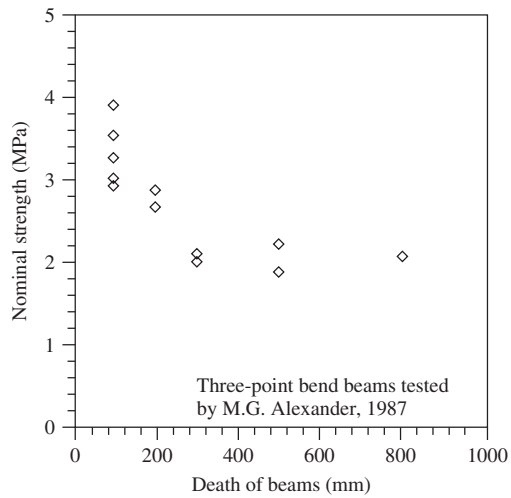

Figure 7-23 Strength of concrete beams of different sizes

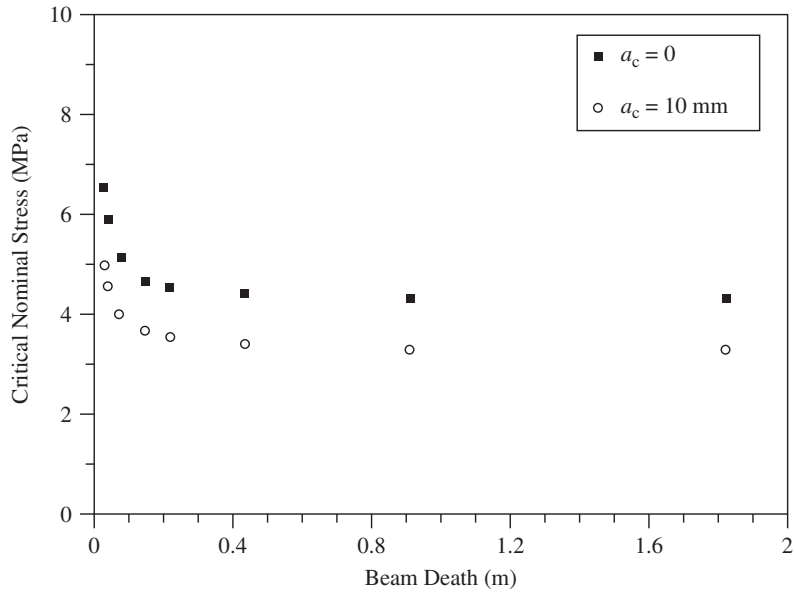

Figure 7-24 Critical nominal stress predicted by the two-parameter model

If the values of K_{Ic} and a_c are determined from the two-parameter model, the size effect on the tensile nominal strength of concrete can be predicted by the above equation. The results obtained for three-point bending are shown in Figure 7-24, which shows a similar trend with the experimental values.

The two-parameter model can also be applied to an unnotched structure, as illustrated in Figure 7-25. By assuming that the material length Q is equal to 20 mm, which is the average material length of concrete and mortar, the influence of the structural size on the modulus of rupture (MOR) of unnotched beams predicted by the two-parameter model is plotted in the figure. It is seen that the CEB-FIP size effect MOR compares favorably with the prediction by the two-parameter model.

(c) *High-strength concrete*: Typical high-strength concrete has a matrix that is very strong and stiff, is compact, and possesses well-bonded aggregate–mortar interfaces. Due to its composition, several of the toughening mechanisms found in normal concrete are absent during the fracture process. Microcracking at interfaces, flaws, and voids are infrequent, and cracks propagate through the coarse aggregate instead of being deflected by them. Carrasquillo et al. (1981) observed these differences, and concluded that as its compressive strength f_c increases, concrete behaves more like a homogeneous material. This decrease in toughness leads to an increase in brittleness. Designers have been forced to confine high-strength concrete with steel to prevent catastrophic failure, especially under seismic loading. Obviously, a less brittle material would make the design safer. Also, as seen earlier, an increase in brittleness implies a decrease in nominal strength. Figure 7-26 shows a plot of critical crack extension against compressive strength. It is seen that the critical crack extension decreases with increasing compressive strength. Thus, the two-parameter model correctly simulates the observed brittle response of high strength concrete.

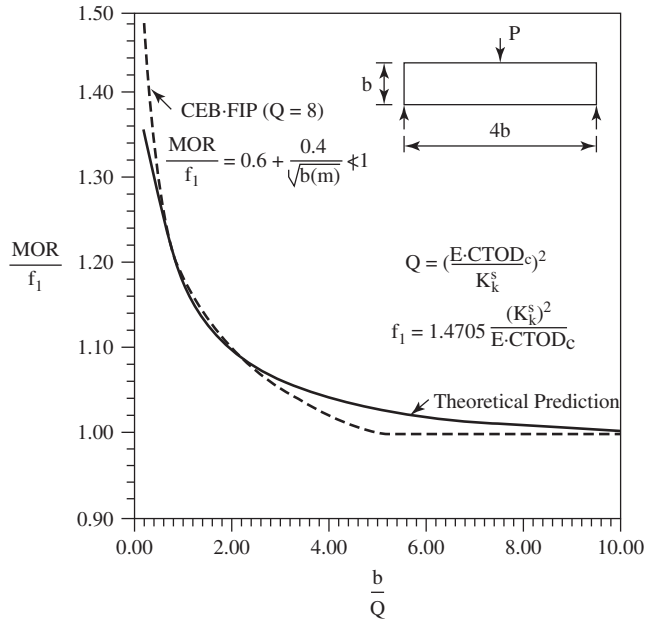

Figure 7-25 Effect of beam depth on MOR by the two-parameter fracture model and CEB-FIP model code

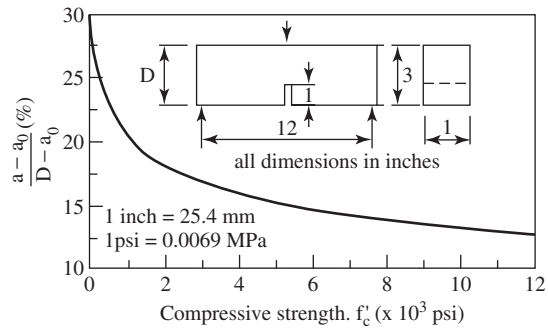

Figure 7-26 Critical crack extension against compressive strength

7.8 SIZE EFFECT MODEL

7.8.1 Bazant's model

Size effect is a characteristic behavior for nonlinear fracture in concrete, in which the nominal strength (stress at maximum load) of a structure is a function of structural size. In 1972, Walsh reported experimental evidence of the size effect from the nominal strength of notched concrete beams under three-point bending (Walsh, 1972). One year later, Leicester (1973) described the size effect on the strength of structures made of metals, timber and concrete in a nominal stress form:

$$\sigma_N = A_1 D^{-s}, \quad s \geq 0 \tag{7-78}$$

where A_1 is a constant, D the characteristic dimension of the structure, and s the size coefficient, which is a measure of the size effect for a structure with different geometries and loading patterns. The so-called size effect law was developed by Bazant (1984). Bazant and Kazemi (1990) have simulated the fracture of quasi-brittle materials by an effective-elastic crack. For two-dimensional similarity, the ratio of initial crack length, a_0, to the characteristic dimension, D, is kept constant for different sized structures. D represents the depth of a beam, or the width of a plate. It is, however, an important requirement that the third dimension (thickness) be kept constant. For these geometrically similar structures, the nominal stress at failure is described as

$$\sigma_{\mathrm{N}} = \frac{c_{\mathrm{n}} P_{\mathrm{c}}}{tD} \tag{7-79}$$

where P_{c} is the critical fracture load (or the peak load), t the thickness of a structure, and c_{n} a coefficient representing different types of structures; $c_{\mathrm{n}} = 1$ for a tensile plate and $c_{\mathrm{n}} = 1.5\,S/b$ for a beam (S is span; b is depth). It is noted that the value of c_{n} is a constant for a series of geometrically similar structures. D is the characteristic dimension of the structure or specimen. For a simply supported beam, D can be defined as the height (depth) of the beam. When the beam is subjected to three- point bending under elastic conditions, we have

$$\sigma_{\mathrm{N}} = \frac{M_{\mathrm{c}} \dfrac{D}{2}}{\dfrac{tD^3}{12}} = \frac{\dfrac{P_{\mathrm{c}} S}{4} \dfrac{D}{2}}{\dfrac{tD^3}{12}} = \frac{3S}{2D} \frac{P_{\mathrm{c}}}{tD} = \frac{c_{\mathrm{n}} P_{\mathrm{c}}}{tD} \tag{7-80}$$

where $c_{\mathrm{n}} = 3S/2D$ is a constant for a series of geometric similar structures with S representing the span of the beam. The variable t is the width (thickness of the beam) and is taken as a constant for a series of geometric similar structures to simplify the analysis. Likewise, under a plastic bending condition, we have

$$\sigma_{\mathrm{N}} = \frac{P_{\mathrm{c}} S}{tD^2} = \frac{S}{D} \frac{P_{\mathrm{c}}}{tD} = \frac{c_{\mathrm{n}} P_{\mathrm{c}}}{tD} \tag{7-81}$$

where $c_n = S/D$ is a constant for a series of geometric similar structures, with S representing the span of the beam.

Elastic analysis with an allowable stress criterion or any method of analysis with a failure criterion based on stress or strain, as well as plastic limit analysis, exhibits no size effect. In other words, geometrically similar structures or specimens of different sizes will fail at the same σ_{N}. LEFM, however, does show a size effect. From the expression of energy release rate and stress intensity factor, we can write

$$G_{\mathrm{I}} = \frac{K_{\mathrm{I}}^2}{E'} = \frac{\sigma_{\mathrm{N}}^2 \pi a D}{E' D} \tag{7-82}$$

Then the nominal stress can be obtained as

$$\sigma_{\mathrm{N}} = \sqrt{\frac{G_{\mathrm{I}} E' D}{\pi a D}} = \frac{\text{constant}}{\sqrt{D}} \tag{7-83}$$

after considering that $(D_1/a_1) = (D_2/a_2) = \cdots = (D/a) =$ constant. From Equation 7-83, we can see that LEFM has a very simple size effect: $\sigma_{\mathrm{N}} \propto 1/\sqrt{D}$.

For nonlinear concrete fracture mechanics, the size effect is more complicated. Let us consider two geometrically similar specimens as shown in Figure 7-27. Assume that (a) total

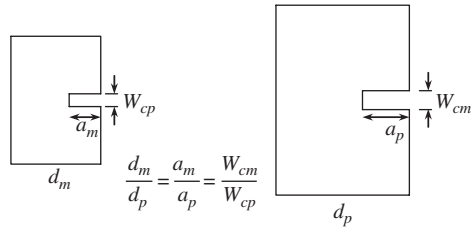

Figure 7-27 Two geometrically similar specimens with a crack

energy released at failure, W_{total}, depends on fracture length, fracture bandwidth, or area of the fracture zone; (b) cracks at failure are similar (i.e., following geometric similarity); and (c) failure does not occur at the crack initiation stage.

According to assumption (a), the total energy can be written as function of nominal stress, specimen geometry, and crack geometry:

$$W_{\text{total}} = W(\sigma_{\text{N}}, t, d, a, w_{\text{c}}) \tag{7-84}$$

Let $\alpha_1 = a/d$ and $\alpha_2 = w_{\text{c}}/d$, then Equation 7-84 can be rewritten as

$$W_{\text{total}} = W(\sigma_{\text{N}}, t, d, \alpha_1, \alpha_2) = F(\sigma_{\text{N}}, t, d) f(\alpha_1, \alpha_2) \tag{7-85}$$

where $F(\sigma_{\text{N}}, t, d)$ represents the energy consideration in the specimen without a crack and $f(\alpha_1, \alpha_2)$ the crack influence on energy consumption.

For $F(\sigma_{\text{N}}, t, d)$, we have

$$F(\sigma_{\text{N}}, t, d) = \iint \frac{1}{2}\sigma \, d\varepsilon \, dv = \iint \frac{1}{2}\sigma \frac{d\sigma}{E} \, dv = \frac{\sigma_{\text{N}}^2}{2E} t d^2 \tag{7-86}$$

Hence, we have

$$W_{\text{total}} = \frac{\sigma_{\text{N}}^2}{2E} t d^2 f(\alpha_1, \alpha_2) \tag{7-87}$$

Differentiate W_{total} with respect to the crack length, a, and we have

$$\begin{aligned} \frac{\partial W_{\text{total}}}{\partial a} &= \frac{\sigma_{\text{N}}^2}{2E} t d^2 \frac{\partial f(\alpha_1, \alpha_2)}{\partial a} = \frac{\sigma_{\text{N}}^2}{2E} t d^2 \left[\frac{\partial f(\alpha_1, \alpha_2)}{\partial \alpha_1} \frac{\partial \alpha_1}{\partial a} + \frac{\partial f(\alpha_1, \alpha_2)}{\partial \alpha_2} \frac{\partial \alpha_2}{\partial a} \right] \\ &= \frac{\sigma_{\text{N}}^2}{2E} t d^2 \left[\frac{\partial f(\alpha_1, \alpha_2)}{\partial \alpha_1} \frac{\partial \alpha_1}{\partial a} + \frac{\partial f(\alpha_1, \alpha_2)}{\partial \alpha_2} \frac{\partial \alpha_2}{\partial a} \right] = \frac{\sigma_{\text{N}}^2}{2E} t d^2 \left[\frac{\partial f(\alpha_1, \alpha_2)}{\partial \alpha_1} \frac{1}{d} \right] \\ &= \frac{\sigma_{\text{N}}^2}{2E} t d \bullet g(\alpha_1, \alpha_2) \end{aligned} \tag{7-88}$$

Substituting $\partial W_{\text{total}}/\partial a = tG_{\text{I}}$, gives

$$\frac{\sigma_{\text{N}}^2 t d}{2E} g(\alpha_1, \alpha_2) = tG_{\text{I}} \tag{7-89}$$

then

$$\sigma_{\text{N}} = \sqrt{\frac{2EG_{\text{I}}}{d g(\alpha_1, \alpha_2)}} \tag{7-90}$$

It may be assumed that the geometrical function $g(\alpha_1, \alpha_2)$ is positive, i.e., $g\prime(\alpha_1, \alpha_2) > 0$. Then we can expand $g(\alpha_1, \alpha_2)$ with respect to α_2, at $\alpha_2 = 0$:

$$g'(\alpha_1, \alpha_2) = g(\alpha_1, 0) + g'(\alpha_1, 0)\alpha_2 + \cdots \tag{7-91}$$

By substituting equation 7-91 into 7-90, we get

$$\sigma_N = \sqrt{\frac{2EG_I}{d[g(\alpha_1, 0) + g'(\alpha_1, 0)\alpha_2]}} = \sqrt{\frac{B'EG_I}{1 + d/d_0}} \tag{7-92}$$

where $B' = 2/g'(\alpha_1, 0)w_c$, and $d_0 = g'(\alpha_1, 0)w_c/g(\alpha_1, 0)$.

Furthermore, by considering the area under a simplified stress–strain curve with a post-peak response, as shown in Figure 7-28, G_I can be computed as:

$$G_I = \frac{1}{tda}\iint \sigma \, d\varepsilon \, dv = \frac{w_c f_t^2}{2}\left(\frac{1}{E} - \frac{1}{E'}\right) \tag{7-93}$$

By substituting this expression into Equation 7-92, we get

$$\sigma_N = \frac{Bf_t}{\sqrt{1 + \frac{d}{d_0}}} = \frac{Bf_t}{\sqrt{1 + \beta}} \tag{7-94}$$

where $B = \sqrt{B'w_c E\frac{1}{2}\left(\frac{1}{E} - \frac{1}{E'}\right)}$ and $\beta = \dfrac{d}{d_0}$

Figure 7-29 shows the size effect law together with the strength criterion and the LEFM criterion. It can be seen that the nominal strength of a series of geometrically similar structures is conventionally described by a strength criterion, which is a constant regardless of structural size and may be used only for relatively small structures. On the other hand, the single parameter failure criterion based on LEFM predicts a linear curve for the nominal strength, and this criterion may be used only for relatively large structures. The above equation is based on nonlinear fracture and thus provides a smooth curve for the nominal strength of various sizes of structures. It can be seen from the figure that for a small structure, the size effect law approaches the strength criterion, and for a large size, it approaches the LEFM solution.

The brittleness parameter, β, may be obtained by calculating the parameter, D_0, as the value of D at the intersection of the horizontal strength criterion, $\sigma_N = Bf_t$, with the inclined asymptote, $\sigma_N = c_n\sqrt{G_f E'/g(\alpha_0)D}$ from LEFM, as shown in Figure 7-29. Equating these two expressions yields D_0, and then $\beta = D/D_0$ or

$$\beta = \frac{B^2 f_t^2 g(\alpha_0)}{c_n E' G_f} D \tag{7-95}$$

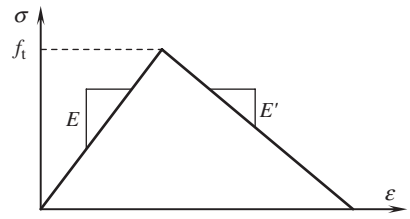

Figure 7-28 A simplified stress–strain curve with post-peak response

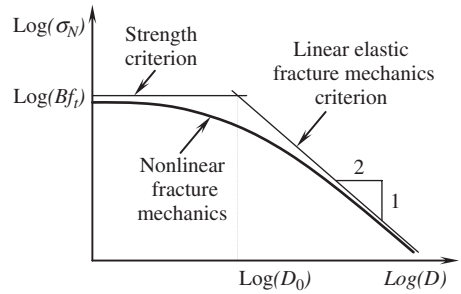

Figure 7-29 The size effect law, together with the strength criterion and the LEFM criterion

The brittleness number, β, depends not only on the material fracture parameter G_f but also on the structural geometry function $g(a_0/D)$. Since the value of $B = \sigma_N/f_t$ relates to the nominal strength of a very small structure on the basis of the strength criterion, the above equation may be suitable for small structures. For relatively large structures, the brittleness parameter, β, may also expressed as (Bazant and Pfeiffer, 1987)

$$\beta = \frac{D}{c_f}\left[\frac{g(\alpha_0)}{g'(\alpha_0)}\right] \tag{7-96}$$

Based on these definitions, the brittleness of structures relates not only to the material but also to the geometry and size of the structure. The greater the value of β, the more brittle the structure. For $\beta < 0.1$, the strength criterion may be used; for $0.1 < \beta < 10$, the size effect model should be used; for $\beta > 10$, the LEFM criterion may be used.

Since an effective-elastic crack is used in the size effect law, the critical energy release rate for a certain size of structure, G_{Ic}, can be written as

$$G_{Ic} = \frac{K_{Ic}^2}{E} = \frac{\sigma_N^2 \pi a_c}{E} g_1^2\left(\frac{a_c}{D}\right) = \frac{\sigma_N^2 D}{E c_n^2} g\left(\frac{a_c}{D}\right) \tag{7-97}$$

where $a_c = a_0 + \Delta a_c$ is the critical crack length, which is expressed as the sum of the initial crack length a_0 and the effective crack extension Δa_c. The geometrical function is defined as

$$g\left(\frac{a_c}{D}\right) = \frac{c_n^2 \pi a_c}{D} g_1^2\left(\frac{a_c}{D}\right) \tag{7-98}$$

Bazant proposed to use the critical energy release rate and the critical crack extension for an infinitely large structure, with G_f and c_f as fracture parameters of a quasi-brittle material. The parameters G_f and c_f are defined as

$$G_f = \lim_{D\to\infty} G_{Ic} \tag{7-99}$$

and

$$c_f = \lim_{D\to\infty} \Delta a_c \tag{7-100}$$

Substituting G_{Ic} expression into Equation 7-99, we have

$$G_f = \lim_{D\to\infty} \frac{\sigma_N^2 D}{E c_n^2} g\left(\frac{a_c}{D}\right) = \lim_{D\to\infty} \frac{B^2 f_t^2 D_0}{E c_n^2} \frac{D}{D + D_0} g\left(\frac{a_c}{D}\right) \tag{7-101}$$

Note that

$$\lim_{D\to\infty}\frac{D}{D+D_0}=1 \tag{7-102}$$

and

$$\lim_{D\to\infty} g\left(\frac{a_c}{D}\right)=g\left(\frac{a_0}{D}\right) \tag{7-103}$$

These two results from Δa_c are negligible compared to the initial crack length when the structure size approaches infinity. Thus, we have

$$G_f=\frac{B^2 f_t^2 D_0}{E c_n^2} g\left(\frac{a_0}{D}\right) \tag{7-104}$$

This equation relates the material fracture parameter G_f to a infinite size structure with a characteristic size of D_0.
The value of c_f can be determined from Equation 7-96 as

$$c_f=\frac{g\left(\frac{a_0}{D}\right)}{g'\left(\frac{a_0}{D}\right)}D_0 \tag{7-105}$$

or

$$D_0=\frac{g'\left(\frac{a_0}{D}\right)}{g\left(\frac{a_0}{D}\right)}c_f \tag{7-106}$$

This equation represents a relationship between c_f and D_0. Substituting the expression for D_0 as a function of c_f into $G_f=\left(B^2 f_t^2 D_0/E c_n^2\right) g\left(a_0/D\right)$, we get

$$Bf_t=c_n\sqrt{\frac{EG_f}{c_f g'\left(a_0/D\right)}} \tag{7-107}$$

Through these equations, the values of D_0 and Bf_t are related to the fracture parameters G_f and c_f. Further substituting Equations 7-104 and 7-106 into Equation 7-94, we can get

$$\sigma_N=c_n\sqrt{\frac{EG_f}{c_f g'\left(\frac{a_0}{D}\right)+g\left(\frac{a_0}{D}\right)D}} \tag{7-108}$$

This equation describes the nominal strengths for a series of geometrically similar structures made of the same quasi-brittle material. Once the fracture parameters, G_f and c_f, are known for a given material, the nominal strength can be determined. The influence of geometry is taken into account by the functions $g\left(a_0/D\right)$ and $g'\left(a_0/D\right)$. Since the functions $g\left(a_0/D\right)$ and $g'\left(a_0/D\right)$ are constants for geometrically similar structures, the nominal strength, σ_N, decreases with increase of D.

This equation also provides a handy method to determine G_f and c_f through experiments. To explain this, let us rewrite the equation as

$$c_n^{-2}\sigma_N^2=\frac{EG_f}{c_f g'\left(\frac{a_0}{D}\right)+g\left(\frac{a_0}{D}\right)D} \tag{7-109}$$

Inversing the equation gives

$$\frac{1}{c_n^{-2}\sigma_N^2} = \frac{c_f g'\left(\frac{a_0}{D}\right) + g\left(\frac{a_0}{D}\right)D}{EG_f} = \frac{c_f g'\left(\frac{a_0}{D}\right)}{EG_f} + \frac{g\left(\frac{a_0}{D}\right)D}{EG_f} \tag{7-110}$$

If we take $1/c_n^2\sigma_N^2$ as y, D as x, and $c_f g'(a_0/D)/EG_f$ and $g(a_0/D)/EG_f$ as constants, we have a linear equation.

7.8.2 Method of Bazant et al. to determine G_f and c_f

(a) *Specimens and test procedures*: The three-point bending beams to be used, as shown in Figure 7-30, should have a span-to-depth ratio not less than 2.5. The initial notch-to-depth ratio is between 0.15 and 0.5. The notch width should be as small as possible and should not exceed 0.5 times the maximum aggregate size. The width and the depth of the beam, b, must not be less than $3d_a$, where d_a is the maximum size of the aggregate.

Specimens of at least three different sizes, characterized by beam depth $b = b_1, b_2, \ldots, b_n$, and spans $S = S_1, S_2, \ldots, S_n$, must be tested. The smallest depth b_1 must not be larger than $5d_a$, and the largest depth b_n must not be smaller than $10d_a$. The ratio of b_n and b_1 must be at least 4. The ratios of the adjacent sizes should be approximately constant. The choice of $b_i/d_a = 3, 6, 12$, and 24 is preferable. At least three identical specimens should be tested for each beam size. The geometrical ratios should be same for all specimens. It is important that the thickness t be kept constant.

Specimens should be loaded at constant displacement rates. The loading rates should be such that the maximum load is reached in about 5 minutes. Although an ordinary uniaxial testing machine may be used, a machine with high strength or closed-loop control is better. All tests should be performed on the same machine and in an identical manner.

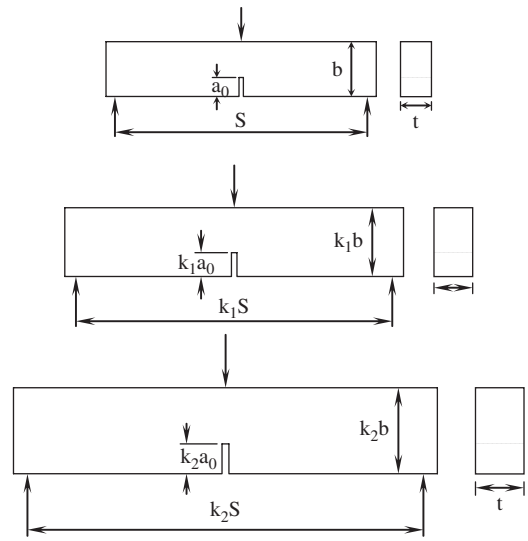

Figure 7-30 Series of geometrically similar structures

(b) *Test results and calculations*: First, the corrected maximum loads, P_j^0 should be obtained by taking the weight of the specimen into account:

$$P_j^0 = P_j + \frac{S_j}{2L_J} W_j \tag{7-111}$$

where P_j is the maximum load, S_j the span, L_j the total length, and W_j the weight of the specimen j.
By introducing

$$Y_j = \left(\frac{b_j t}{P_j^0}\right)^2 \tag{7-112}$$

and

$$X_j = b_j \tag{7-113}$$

for $j = 1, 2, 3, \ldots, n$, a linear regression $Y = Ax + C$ can be plotted. The values of the slope A and the intercept C can be obtained as

$$A = \frac{\sum_{j=1}^{n} \left(X_j - \overline{X}\right)\left(Y_j - \overline{Y}\right)}{\sum_{j=1}^{n} \left(X_j - \overline{X}\right)^2} \tag{7-114}$$

and

$$C = \overline{Y} - A\overline{X} \tag{7-115}$$

where

$$\overline{X} = \frac{1}{n} \sum_{j=1}^{n} \left(X_j\right) \tag{7-116}$$

and

$$\overline{Y} = \frac{1}{n} \sum_{j=1}^{n} \left(Y_j\right) \tag{7-117}$$

are the centroids of all the data points.
The geometrical factor $g(a_0/b)$ or $g(\alpha_0)$ is calculated as

$$g\left(\alpha_0\right) = \left(\frac{S}{b}\right)^2 \pi \alpha_0 \left[1.5 g_1\left(\alpha_0\right)\right]^2 \tag{7-118}$$

The value of $g_1(\alpha_0)$ is determined according to ratios of S/b. For $S/b = 2.5$,

$$g_1\left(\frac{a_0}{b}\right) = \frac{1.0 - 2.5\frac{a_0}{b} + 4.49\left(\frac{a_0}{b}\right)^2 - 3.98\left(\frac{a_0}{b}\right)^3 + 1.33\left(\frac{a_0}{b}\right)^4}{\left(1 - \frac{a_0}{b}\right)^{3/2}} \tag{7-119}$$

For $S/b = 4$,

$$g_1\left(\frac{a_0}{b}\right) = \frac{1.99 - \frac{a_0}{b}\left(1 - \frac{a_0}{b}\right)\left[2.15 - 3.93\left(\frac{a_0}{b}\right) + 2.70\left(\frac{a_0}{b}\right)^2\right]}{\sqrt{\pi}\left(1 + 2\frac{a_0}{b}\right)\left(1 - \frac{a_0}{b}\right)^{3/2}} \tag{7-120}$$

For $S/b = 8$,

$$g_1\left(\frac{a_0}{b}\right) = 1.11 - 1.552\frac{a_0}{b} + 7.71\left(\frac{a_0}{b}\right)^2 - 13.55\left(\frac{a_0}{b}\right)^3 + 14.25\left(\frac{a_0}{b}\right)^4 \tag{7-121}$$

Linear interpolation may be used to obtain $g_1(\alpha_0)$ for the other values of S/b. The values of the material fracture energy G_f can be determined from

$$G_f = \frac{g\ (\alpha_0)}{EA} \tag{7-122}$$

The critical value of the fracture process zone length, c_f, can be further obtained from

$$c_f = \frac{g\ (\alpha_0)}{g'\ (\alpha_0)}\frac{C}{A} \tag{7-123}$$

where $g'(\alpha_0)$ is

$$g'\ (\alpha_0) = \frac{dg\ (\alpha_0)}{d\alpha}\Big|_{\alpha=\alpha_0} \tag{7-124}$$

To verify the linear regression, one needs to calculate the following statistical parameters:

$$s_x^2 = \frac{1}{n-1}\sum_{j=1}^{n}\left(X_j - \overline{X}\right)^2 \tag{7-125}$$

$$s_y^2 = \frac{1}{n-1}\sum_{j=1}^{n}\left(Y_j - \overline{Y}\right)^2 \tag{7-126}$$

$$s_{x|y}^2 = s_{y|x}^2 = \frac{n-1}{n-2}\left(s_y^2 - A^2 s_x^2\right) \tag{7-127}$$

$$\omega_{y|x} = \frac{s_{y|x}}{\overline{Y}} \tag{7-128}$$

$$\omega_x = \frac{s_x}{\overline{X}} \tag{7-129}$$

$$\omega_A = \frac{s_{y|x}}{A s_x\sqrt{n-1}} \tag{7-130}$$

$$\omega_C = \frac{s_{y|x}}{C\sqrt{n-1}}\sqrt{1+\frac{1}{\omega_x^2}} \tag{7-131}$$

$$\text{and} \quad m = \frac{\omega_{y|x}}{\omega_x} \tag{7-132}$$

where X_j are the specimen sizes, Y_j the measured data points, s the square deviation, ω the coefficient of variation, and m the relative width of the scatter band. The value of ω_A should not exceed 0.10 and the values of ω_C or m should not exceed 0.20; otherwise, the result is highly uncertain. To avoid a large scatter, very broad size ranges should be used.

It should be noted that a slight error in the calculation of A can significantly alter the value of G_f. Therefore, extreme care should be exercised in determining the slope A of the regression line. The value of c_f has been reported as $c_f = 13.55$ mm for a concrete with a maximum aggregate size of 13 mm, and $c_f = 1.90$ mm for a mortar with a maximum aggregate size of 5 mm.

7.9 THE FICTITIOUS MODEL BY HILLERBORG

7.9.1 The model

The basic premise of the present analysis is that the best available fracture model for concrete is the cohesive crack of the fictitious crack model, pioneered and generalized by Hillerborg et al. (1976). Hillerborg proposed a fictitious crack model based on the assumption of strain localization and consideration of the softening curve of the cohesive stress versus the separation of a crack. The assumption has been verified by experiments conducted in uniaxial tension tests by Li and Shah (1994) and Li and Li (2000). Figure 7-31 shows the deformations measured at different portions of a specimen under tension as a function of time. Initially, the deformations are almost identical at different parts of the specimen. Then some deviation occurs, indicating nonuniform strain development. Finally, only one LVDT keeps increasing in tension strain, while the other LVDTs show compression. This means that the tensile strain is concentrated in the region covered by that particular LVDT, showing significant strain localization.

In Hillerborg's model, the elastic part of the stress–deformation curve is neglected and the post-peak response can be characterized by a stress–elongation curve. The area under the entire curve is denoted as G_F, and is given by

$$G_F = \int_0^{w_c} \sigma(w)\, dw \tag{7-133}$$

where w_c is the critical crack separation displacement when the softening stress is zero. The crack width w is usually defined as zero at the peak load. The material fracture toughness, G_F, represents the energy absorbed per unit area of crack. The computation of G_F is per definition for the complete separation of the crack surfaces, where the crack area A is the projected area and not the real area. The beauty of the model is that the softening stress–separation displacement curve, $\sigma = \sigma(f_t, w)$, represents a type of constitutive relationship and can be easily incorporated into a

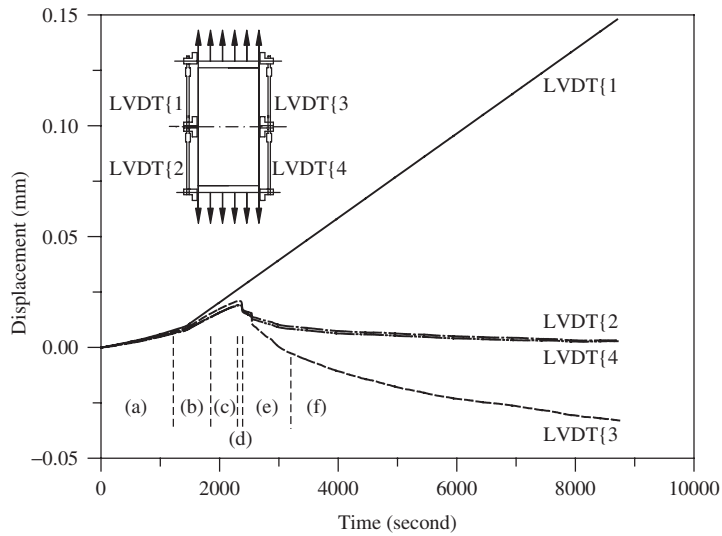

Figure 7-31 Deformations measured at different portions in a specimen as a function of time

numerical analysis. The expression of $\sigma = \sigma(f_t, w)$ can be linear, for example, $\sigma = f_t(1 - w/w_c)$ or exponential, for example, $\sigma = f_t e^{-A(w/w_c)}$.

The fictitious crack model requires three parameters: f_t, G_F, and the shape of $\sigma(w)$. When the shape of $\sigma(w)$ is given, the material fracture property is determined by the values of f_t and G_F. Along this line, a new parameter, the characteristic length, is proposed by combining f_t and G_F into

$$l_{ch} = \frac{EG_F}{f_t^2} \tag{7-134}$$

where l_{ch} is proportional to the length of the fracture process zone. The value of l_{ch} for concrete roughly ranges from 100 to 400 mm. The length of the fracture process zone in concrete from the initial crack tip is of the order of $0.3 - 0.5l_{ch}$.

7.9.2 Determination and influence of the $\sigma(w)$ relationship

The cohesive model requires a unique $\sigma(w)$ curve to qualify the energy dissipation. The choice of the $\sigma(w)$ function influences the prediction of the structural response significantly. The local fracture behavior, for example, the crack opening displacement, is particularly sensitive to the shape of $\sigma(w)$. Many different shapes of $\sigma(w)$ curves, including linear, bilinear, trilinear, exponential, and power functions, have been previously used.

The critical value of the crack opening displacement plays an important role in the energy calculation. Hillerborg et al. (1976) simply used $w_c = 0.01 - 0.02$ mm. On the other hand, Cedolin et al. (1987) obtained values of f_t and w_c based on their test results and numerical modeling. They tested two mixes of concrete with a water to cement ratio of 0.5. The first mix had a maximum aggregate size of 12 mm, $E = 34.2$ GPa and $f_c = 41.6$ MPa, where f_c is the compressive strength of the concrete cylinder specimen. For the first concrete mix, Cedolin et al. estimated $f_t = 4$ MPa and $w_c = 0.035$ mm using a least-squares data fitting procedure based on the solution of an inverse problem, and assumed the shape of the stress–strain curve. The second mix of concrete had a maximum aggregate size of 8 mm, $E = 39.0$ GPa and $f_c' = 41.6$ MPa. For this second concrete mix, the values of $f_t = 3.6$ MPa and $w_c = 0.037$ mm were estimated.

Roelfstra and Whittmann (1986) proposed a bilinear curve for $\sigma(w)$ with σ_1 and w_1 defined as the intersection point coordinates, see Figure 7-32. They tested three-point bend concrete beams to determine the values of f_t, w_c, σ_1 and w_1. The concrete used had a water to cement ratio of 0.58, and maximum aggregate sizes of 3, 8, and 16 mm, respectively. For the concrete mix with a maximum aggregate size of 3 mm, the values of $f_t = 4.7$ MPa, $w_c = 0.077$ mm, $\sigma_1 = 0.57$ MPa, and $w_1 = 0.017$ mm were obtained. For the concrete mix with a maximum aggregate size of 8 mm, the values of $f_t = 4.0$ MPa, $w_c = 0.100$ mm, $\sigma_1 = 0.64$ MPa, and $w_1 = 0.022$ mm were obtained. For the concrete mix with a maximum aggregate size of 16 mm, the values of $f_t = 4.4$ MPa, $w_c = 0.123$ mm, $\sigma_1 = 0.82$ MPa, and $w_1 = 0.020$ mm were obtained.

Cho et al. (1984) and Liaw et al. (1990) used a trilinear curve for $\sigma(w)$ as shown in Figure 7-33. In this model, the values of w_1 and w_2 were determined according to the compressive strength, f_c'. It was reported that for 23.9 MPa $< f_c' <$ 34.5 MPa, $w_1 = 0.37f_c' - 2.54, w_2 = 5w_1$, and $w_c = w_2 + 228.6$, whereas for 34.5 MPa $< f_c' <$ 62.5 MPa, $w_1 = 19 - 0.26f_c', w_2 = (18.2f_c' - 1.25)w_1$, and $w_c = w_2 + 228.6$. Here all the crack opening displacements are given in micrometers.

Gopalaratnam and Shah (1985) proposed an exponential curve for $\sigma(w)$, as shown in Figure 7-35, in which A and B are constants depending on the concrete mix. Based on the experimental data obtained, they reported $A = -0.06163$ and $B = 1.01$ for concrete with $f_c' = 33 - 47$ MPa, with the crack opening displacement also in micrometers. Note that no value of

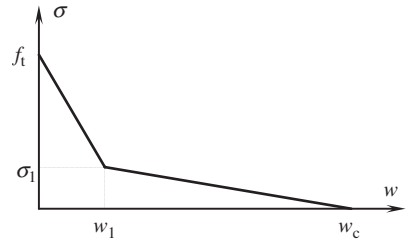

Figure 7-32 Bilinear curve modeling of the closing pressure

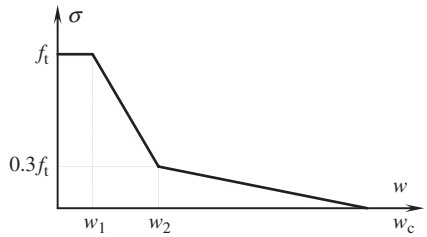

Figure 7-33 Trilinear curve modeling of the closing pressure

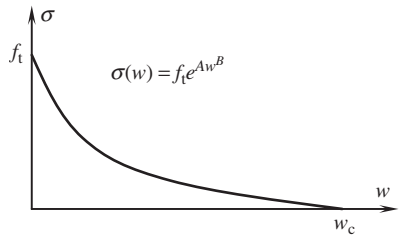

Figure 7-34 Exponential curve modeling of the closing pressure

w_c is found using this approach. The value of w corresponding to $\sigma(w) = 0$ depends on the constants A and B selected in Figure 7-34. A similar exponential relationship for $\sigma(w)$ was also suggested by Cedolin et al. (1987).

A power function for $\sigma(w)$ was suggested by Du et al. (1992), as shown in Figure 7-35. It is noted that the $\sigma(w)$ function suggested by Du et al. has a sudden drop after the initial opening of the crack.

It should be emphasized that the assessment of the fracture behavior of a concrete structure is largely influenced by using different functions; therefore, reasonable and accurate determinations of the curve and the corresponding parameters become crucial for the cohesive crack approach. Experimental determination directly from tension tests has been suggested, but it is difficult and the results may vary with specimen size and shape. Thus, the concept that the shape of the softening curve is a material property is currently not accepted by many researchers in the field.

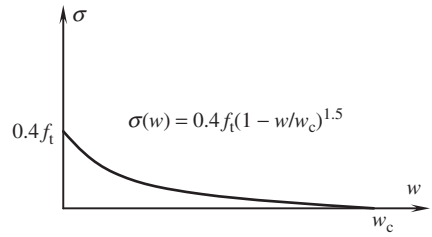

Figure 7-35 Power curve modeling of the closing pressure

7.9.3 Test method to determine G_F

A three-point bend beam is recommended to be used. The size of the beam depends on the maximum size of aggregate. The notch depth is equal to half the beam depth ±5 mm, and the notch width at the tip should be less than 10 mm. The notch should be sawed under wet conditions at least one day before testing. The curing ambient temperature should be $20 \pm 2^{\circ}$C. The beam should be stored in lime-saturated water until 30 min before testing. The peak load should be reached within 30–60 sec with a deformation accuracy of at least 0.01 mm, and a load accuracy 2%. The post–peak measurement is an essential requirement. Closed-loop control or a very stiff test machine is required.

For the most used test setup, as shown in Figure 7-36, the weight of the beam needs to be considered using the usual equation,

$$\sigma_w = \frac{btS^2\rho g}{8}\frac{6}{t(b-a_0)^2} \tag{7-135}$$

where b is the height of the beam, t the thickness of the beam, S the span, and a_0 the length of the notch. For a normal concrete beam, with $a_0/b = 0.5$, we get,

$$\sigma_w \approx \frac{7000S^2}{b} \tag{7-136}$$

where S and b are in meters and σ_w in Pa. As a result, $\sigma_w \approx 0.4$ MPa is obtained for $S^2/b = 6.4$.

The total load P is $P = P_w + P_a$, where P_a is the applied load and P_w is self weight of the beam. Since $W = W_0 + W_1 + W_2$, where W_0 is the area below the measured $P_a - \delta$ curve, and $W_1 = P_w\delta_0$, the δ value when $P_a = 0$, W_2 approximately equals to W_1; thus,

$$W = W_0 + 2P_w\delta_0 \tag{7-137}$$

By assuming that energy absorption takes place only in the fracture zone, the fracture energy per unit projected area can be calculated by

$$G_F = \frac{W_0 + 2P_w\delta_0}{(b-a_0)\,t} \tag{7-138}$$

A rather deep notch has been used to keep a low maximum bending moment for the test. Thus, the assumption that energy absorption takes place only in the fracture zone can be considered valid.

In addition to the downward loading pattern, the lateral loading and upward loading are other possible patterns to determine G_F, as shown in Figures 7-37 and 7-38, respectively.

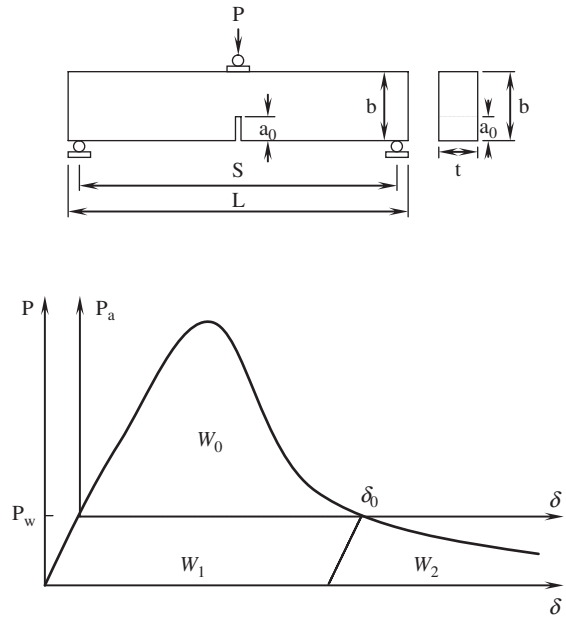

Figure 7-36 Experimental setup and load-displacement curve

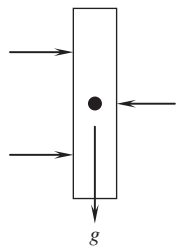

Figure 7-37 Lateral loading setup

By noting the influence of gravity in these two loading patterns, which are different from the downward loading pattern, we can readily write the G_F expressions. For a lateral loading pattern, G_F can be calculated as

$$G_F = \frac{W_0}{(b - a_0)\, t} \tag{7-139}$$

and for an upward loading pattern, G_F can be calculated as

$$G_F = \frac{W_0 - P_w \delta_0}{(b - a_0)\, t} \tag{7-140}$$

A round-robin test among different laboratories was performed to measure the value of G_F using different sizes of beams. The results of the tests showed that the values of G_F are size-dependent. On average, the values of G_F increased by 20% when the beam depth increased by factor of 2, and by 30% when the depth increased by a factor of 3. This size dependency on

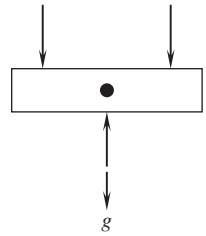

Figure 7-38 Upward loading setup

the G_F values may partially be due to the unwanted energy absorption outside the fracture zone. The value of G_F was found to be 90 N/m from some experiment results.

7.10 *R*-CURVE METHOD FOR QUASI-BRITTLE MATERIALS

7.10.1 General description of the *R*-curve

According to energy principles, the necessary condition for a structure in an equilibrium state during crack propagation is that the first order of derivative of the potential energy with respect to the crack length be equal to zero:

$$\begin{aligned} \frac{\partial (F - U + W)}{\partial a} &= 0 \\ \frac{\partial (U - F)}{\partial a} &= \frac{\partial (W)}{\partial a} \end{aligned} \tag{7-141}$$

where U is the strain energy of the structure, F the work done by the applied force, and W the energy required for crack formation. The second part of the above equation can be rewritten as

$$G_q = R \tag{7-142}$$

where $G_q = (1/t)[\partial (U - F) / \partial a]$ is the energy release rate for the propagation of a unit length of crack in a structure with a unit thickness (t is the thickness of the structure), and

$$R = \frac{\partial W}{t \partial a} \tag{7-143}$$

is the fracture resistance of the material. Taking R as a constant that is independent of crack length is approximately true only for cracks under plane strain. In the case of plane stress, R varies with the amount of crack growth. The R-curve method was developed based on such observation of the incremental of the resistance with increase of the stable crack extension for a plane stress case. For a crack in a sheet thin enough for plane stress to occur, when it is subjected to a certain stress level, the crack starts propagating. However, the crack growth is stable and fracture does not yet occur. If the stress level is kept constant, the crack propagates only over a small distance, and then stops.

A further increase of the stress is required to maintain the crack growth: although the crack is longer, it can withstand a higher stress. In other words, for a linear elastic material, R is a material constant and any extension of the initial crack means catastrophic failure of the structure. However, for a quasi-brittle material, R is a function of crack extension increment, i.e., R is a

rising function of crack extension. When the value of G_q increases, due to the increase of applied load, the value of R also increases due to the incremental of crack length. Therefore, $G_q = R$ can only serve as a necessary condition for failure. A crack may be stable or unstable depending on the change trend of the function of G_q. Thus, another condition is needed to describe the onset of unstable crack propagation in quasi-brittle materials. This condition is defined as

$$\frac{\partial G_q}{\partial a} = \frac{\partial R}{\partial a} \tag{7-144}$$

This equation can be regarded as a sufficient condition for catastrophic propagation, while $G_q = R$ serves as a necessary condition. To use the two equations to describe the failure of a structure, both G_q and R should be known. Generally, G_q is a function of the applied load, structural geometry, and boundary conditions and can be obtained from analytical or numerical stress analysis. However, the fracture resistance R is an unknown function depending on the material fracture properties and structural geometry.

For a simple case, the function of the fracture resistance R can be obtained through a graphical approach. To illustrate this approach, let us take a look at Figure 7-39. In the figure, the horizontal axis represents crack length and the vertical axis represents G or the R function. The curve represents the G function. It can be seen that the lower two straight lines satisfy the condition of $G_q = R$. However, after the point $G_q = R$, the lines are in the safety region under the G function. Hence, catastrophic fracture will not occur. Instead, a stable crack increase stops. For the top straight line, its point intersects with the G function with satisfies both $G_q = R$ and $\partial G_q/\partial a = \partial R/\partial a$, and hence signals an unstable crack propagation.

The equation of the top line can be written as

$$G = G_i + \left(\frac{dG}{da}\right)_i (a - \Delta a_c) \tag{7-145}$$

where G_i is the G value at the intersect point, $(dG/da)_i$ the slope of the G function at the intersection point, and Δa_c the a value at the intersection point, which also represents the critical crack extension.

At $a = -a_0$, $G = 0$. We have

$$G_i = \left(\frac{dG}{da}\right)_i a_0 + \left(\frac{dG}{da}\right)_i \Delta a_c \tag{7-146}$$

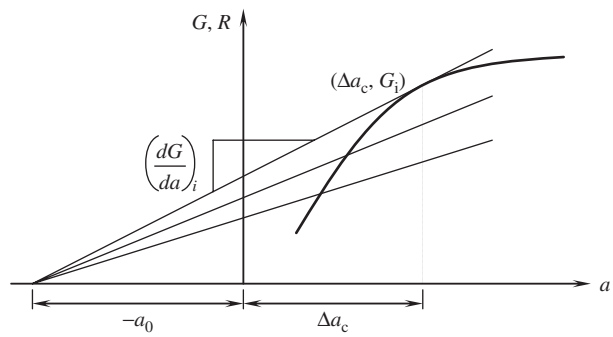

Figure 7-39 A graphical approach for the determination of fracture resistance

Let

$$a_0 + \Delta a_c = \alpha a_0 \tag{7-147}$$

Then we have

$$a_0 = \frac{\Delta a_c}{\alpha - 1} \tag{7-148}$$

and Equation 7-146 becomes

$$(\alpha - 1)G_i = \alpha(\Delta a_c)\left(\frac{dG}{da}\right)_i \tag{7-149}$$

or

$$\frac{\alpha}{\alpha - 1}(\Delta a_c)\frac{dG}{d(\Delta a_c)} - G = 0 \tag{7-150}$$

This is a typical form of the Euler equation and its solution can be obtained by the variable exchange technique as

$$G = \beta(\Delta a_c)^{(\alpha-1)/\alpha} \tag{7-151}$$

where β is a constant.

For a complex case, two methods may be used to measure or construct *R*-curves. The experimental method monitors positions of the crack length during the loading process and constructing the *R*-curve using $R = \mathrm{G}$. It can be done either in a single test from successive values of G during slow crack growth or in a series of tests from the instability point of each test. For a single test, usually a film record is made during the test to derive the slow growth curve. The film recording method has shown a fair accuracy. However, the crack tip observed on specimen surface may not coincide with the tip of the effective crack. This will greatly influence the determination of R, especially for concrete.

Another method is to construct the *R*-curve using semi-analytical and semi-experimental methods. The *R*-curve can be constructed from a purely mathematical derivation first. Then the unknown constants in the mathematical functions of *R*-curve are determined, using the relatively easily measured fracture parameters.

7.10.2 *R*-curve based on an equivalent-elastic crack (Ouyang et al.)

Based on the two conditions for unstable crack propagation, a governing differential equation for the *R*-curve can be derived. The *R*-curve obtained by solving this differential equation is interpreted as the envelope of the energy release rate for a series of structures with the same specimen geometry and initial crack length, but different sizes.

The energy release rate G_q, as shown in Figure 7-40, can be expressed in a Taylor's series at a critical point, c,

$$G_q = (G_q)_c + \sum_{n=1}^{\infty} \frac{1}{n!}\left(\frac{d^n G_q}{da^n}\right)(a - a_c)^n \tag{7-152}$$

where a_c is the critical crack length, $(G_q)_c$ is the value of G_q at the critical point, and the subscript c indicates the critical point.

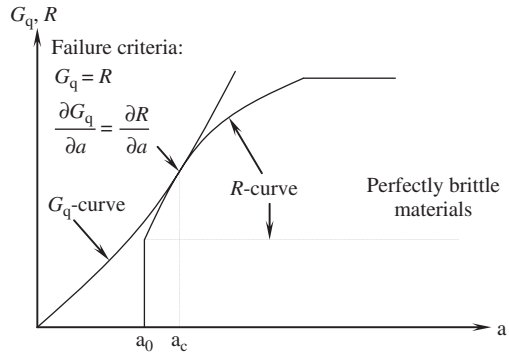

Figure 7-40 Schematic of the *R*-curve

Using $G_q = 0$ at $a = 0$ results in the following equation:

$$\left(G_q\right)_c = -\sum_{n=1}^{\infty} \frac{1}{n!} \left(\frac{d^n G_q}{da^n}\right) (a - a_c)^n \tag{7-153}$$

For materials with a precritical stable crack length, a_c is proportional to the initial crack length, a_0, i.e.,

$$a_c = a_0 + \Delta a_c = \alpha a_0 \tag{7-154}$$

where α describes the prescribed precritical stable crack growth ($\alpha \geq 1$), and may be regarded as a brittleness index.

Substituting a_c into $(G_q)_c$, one gets,

$$\left(G_q\right)_c = -\sum_{n=1}^{\infty} \frac{1}{n!} \left(\frac{d^n G_q}{d\Delta a_c^n}\right) \left(\frac{\alpha}{\alpha - 1}\right)^n (-c)^n = 0 \tag{7-155}$$

Replacing $(G_q)_c$ with R and rearranging the terms, one gets

$$R + \sum_{n=1}^{\infty} \frac{1}{n!} \left(\frac{d^n R}{dc^n}\right) \left(\frac{\alpha}{\alpha - 1}\right)^n (-c)^n = 0 \tag{7-156}$$

where $c = \Delta a_c$. If the *R*-curve is an envelope of the *G*-curves for a certain category of structure, every point on the *R*-curve corresponds to a critical point for particular structures. Therefore, c is a variable. From the mathematical point of view, the above equation can be classified as an Euler equation. The solution of the equation can be written as

$$R = \sum_{n=1}^{\infty} \beta^n (a - a_0)^{d_n} \tag{7-157}$$

For $n = 1$, Broek (1987) obtained the solution as

$$R = \beta_0 (a - a_0)^{d_0} \tag{7-158}$$

with

$$d_0 = \frac{\alpha - 1}{\alpha} \tag{7-159}$$

This *R*-curve can be used for materials with a small crack extension, such as metals. For quasi-brittle materials, more terms have to be considered. Ouyang et al. (1991) developed an expression for $n = 2$ as follows:

$$\frac{1}{2}\left(\frac{\alpha}{\alpha - 1}\right)^2 c^2 \frac{d^2R}{dc^2} - \frac{\alpha}{\alpha - 1} c \frac{dR}{dc} + R = 0 \tag{7-160}$$

Letting $t = \ln c$, we have

$$\frac{dR}{dc} = \frac{dR}{dt}\frac{dt}{dc} = \frac{1}{c}\frac{d_y R}{dt} \tag{7-161}$$

and

$$\frac{d^2R}{dc_2} = \frac{1}{c^2}\left(\frac{d^2R}{dt^2} - \frac{dR}{dt}\right) \tag{7-162}$$

Then, Equation 7-160 can be rewritten as

$$\frac{1}{2}\left(\frac{\alpha}{\alpha - 1}\right)^2 \frac{d^2R}{dt^2} - \frac{\alpha}{\alpha - 1}\frac{dR}{dt} + R = 0 \tag{7-163}$$

The solution of Equation 7-163 can be easily obtained through the characteristic equation. After substituting the original parameters back into the solution, we have

$$R = \beta_1 (a - a_0)^{d_1} + \beta_2 (a - a_0)^{d_2} \tag{7-164}$$

where

$$d_1 = \frac{1}{2} + \frac{\alpha - 1}{\alpha} + \left[\frac{1}{4} + \frac{\alpha - 1}{\alpha} - \left(\frac{\alpha - 1}{\alpha}\right)^2\right]^{1/2} \tag{7-165}$$

and

$$d_2 = \frac{1}{2} + \frac{\alpha - 1}{\alpha} - \left[\frac{1}{4} + \frac{\alpha - 1}{\alpha} - \left(\frac{\alpha - 1}{\alpha}\right)^2\right]^{1/2} \tag{7-166}$$

where α, β_1, and β_2 are constants. Once these constants are determined, the *R*-curve can be plotted as a known function. The values of α, β_1, and β_2 have to be determined based on experimental results. They are dependent on the geometrical function and material fracture property of any given size of structure. As an example, a method using an infinitely sized specimen and fracture parameters from the size effect law are introduced for simplicity.

According to LEFM, for an infinite size specimen, we have

$$G_q = \frac{\sigma^2 \pi a f_1^2}{E} \tag{7-167}$$

where f_1 is a geometrical factor of infinitely sized structure for the stress intensity factor. For the tension mode specimen its value is 1.0 for center crack specimen, and 1.12 for single edge crack tensile specimen.

Substituting Equations 7-164 and 7-167 into the two basic definitions of the R-curve, Equations 7-142 and 7-144, a relationship between β_1 and β_2 can be obtained, and the R-curve becomes

$$R = \beta_2 \psi \, (a - a_0)^{d_2} \tag{7-168}$$

where

$$\psi = 1 - \left(\frac{d_2 \alpha - \alpha + 1}{d_1 \alpha - \alpha + 1} \right) \left(\frac{\alpha a_0 - a_0}{a - a_0} \right)^{d_2 - d_1} \tag{7-169}$$

Only two parameters, α and β_2, need to be further determined. By utilizing the critical crack extension, c_f, and the fracture toughness, G_f, for an infinite-size structure, obtained by the size effect law, the condition of $R = G_\mathrm{f}$ when $a = \alpha a_0 = a_0 + c_\mathrm{f}$ yields the following equations:

$$\alpha = 1 + \frac{c_\mathrm{f}}{a_0} \tag{7-170}$$

and

$$\beta_2 = \frac{G_\mathrm{f} \, (d_1 \alpha - \alpha + 1)}{\alpha \, (d_1 - d_2) \, (\alpha a_0 - a_0)^{d_2}} \tag{7-171}$$

After obtaining α, β_2, and ψ, the R-curve can be finally determined. The R-curve obtained in such a way is regarded as an envelope of the G_q-curves of a series of structures with the same geometry and initial crack length, but different sizes.

DISCUSSION TOPICS

Why did people develop linear fracture mechanics?

Describe the stress criterion and energy criterion for LEFM.

What is a singularity?

Why do we have to consider the plastic zone in front of a crack tip?

What is the superposition method?

What is the Dugdale model?

Why can LEFM not be applied to concrete directly?

Describe the special characteristics of a concrete fracture process?

What is the two-parameters model?

Describe the size effect law.

What is the main difference between the fictitious model and the size effect law?

Show how to construct R-curve for concrete.

Show how to determine the necessary parameters for a two-parameters model, the size effect law, and the R-curve approach.

What are the differences in fracture behaviour for a cement paste and a normal-strength concrete?

Do you think fracture-based design will soon become dominant for civil engineers? Why?

For shear and flexural design of reinforced concrete structures, which one is more suitable to use in fracture mechanics as a design guideline?

PROBLEMS

1. A type of steel has a K_{II} value of 66 MPa$\sqrt{m}$ and an ultimate strength, σ_u, of 840 MPa. If the allowed stress in the material is half of its ultimate strength, what will be the corresponding allowed crack length? For a crack length of 1.25 mm, what will be the allowed stress value?

2. Consider a cylindrical pressure vessel as shown in Figure P7-2, with $R = 1.5$ m, $h = 0.025$ m, $\sigma_y = 1500$ MPa, and $K_{IC} = 60$ MPa$\sqrt{m}$. Assuming that the vessel is designed on the basis of the yield stress, σ_y, reduced by a safety factor of 4, solve the following problems:

(a) Get the expression for the normal stress, σ, in the wall of the vessel as a function of the internal pressure p.

(b) Assuming that $K_I = 1.12\sigma\sqrt{\pi a}$, calculate the failure pressure for a minimum detectable flaw size of $a = 1.5$ mm.

(c) Calculate the critical crack depth at the design pressure.

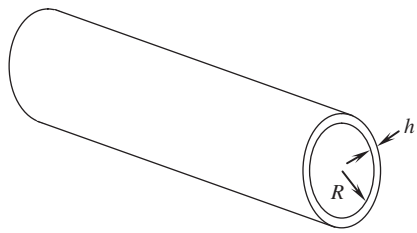

Figure P7-2 A cylindrical pressure vessel

3. Consider a crack located parallel to the edge of a thin, semi-infinite plate, as shown in Figure P7-3. The edge of the plate is loaded by a concentrated force, P, as shown in the figure, and the thickness of the plate is b. Determine an approximation for the stress intensity factor of the configuration.

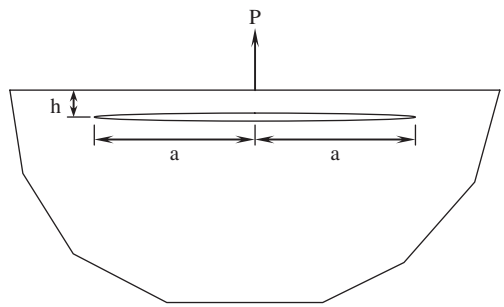

Figure P7-3 A thin plate with a crack near the edge

4. Derive the following expression for E:

$$E = \frac{6Sa_0g_2(\alpha_0)}{C_i b^2 t} \tag{7-172}$$

from the equation of $\text{CMOD}_c = (4\sigma_c a_0/E)g_2(\alpha_0)$, where t is the beam thickness and b the beam height, referring to Figure P7-4 (self-weight of the beam can be ignored).

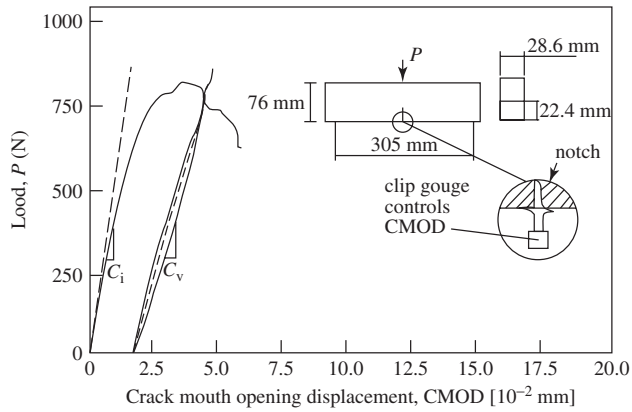

Figure P7-4 A typical measured load–CMOD curve

5. Determine the value of K_I for a round crack, as shown in Figure P7-5a, loaded by normal tensile stress σ over $e < r < b$ by considering the case shown in Figure P7-5b.

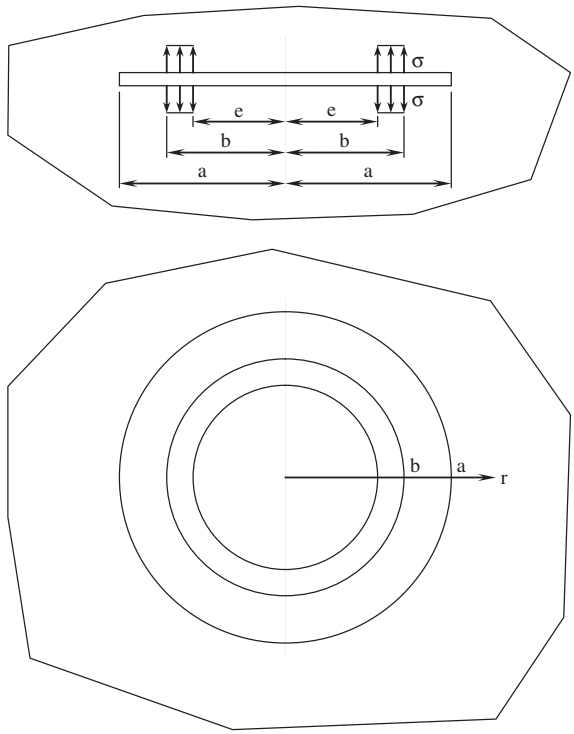

Figure P7-5a A round crack under symmetrical loading

$$K_{\mathrm{I}} = \frac{2p}{\sqrt{\pi a}}(a - \sqrt{a^2 - b^2})$$

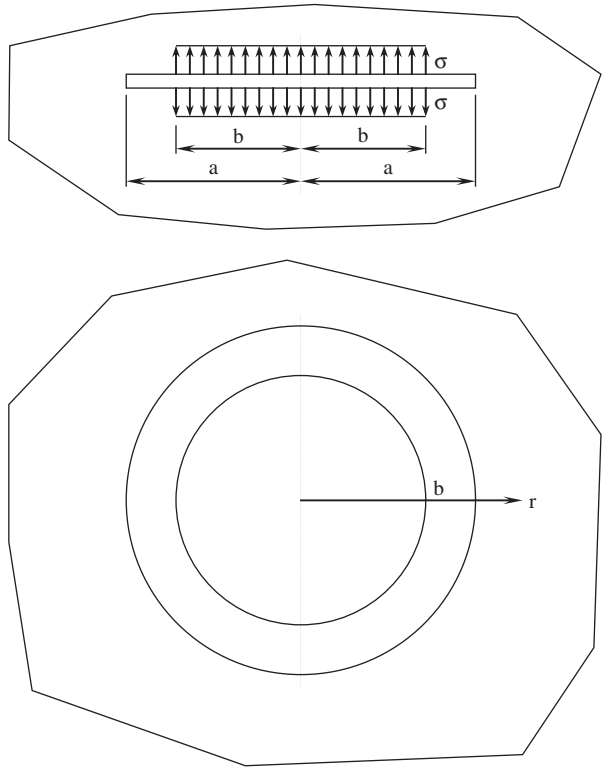

Figure P7-5b A round crack under distributed loading

6. For $n = 2$, derive the solution of the R-curve (with detailed procedures) given by

$$R + \sum_{n=1}^{\infty} \frac{1}{n!}\left(\frac{d^n R}{dc^n}\right)\left(\frac{\alpha}{\alpha - 1}\right)^n (-c)^n = 0 \tag{7-173}$$

7. Consider a semi-infinite crack in a thin plate as shown in Figure P7-7. The faces of the crack are subjected to normal line loads. The stress intensity factor is

$$K_{\mathrm{I}} = \frac{2p}{\sqrt{2\pi l}} \tag{7-174}$$

Suppose the yield stress is σ_{ys}. Compute the plastic zone on the basis of the Dugdale model.

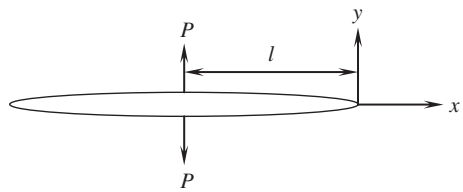

Figure P7-7 A semi-infinite crack in a thin plate

8. Using the configuration shown in Figure P7-8, show that for plane stress, we have the following (*Hint*: The relationship between K and G for mode I can be applied to mode II):

$$K_{II} = \frac{P}{t\sqrt{2h}} \tag{7-175}$$

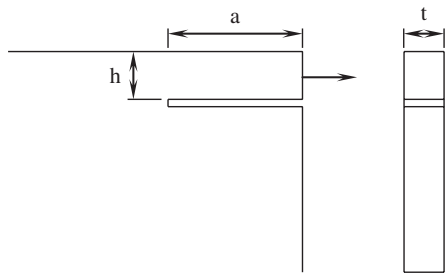

Figure P7-8 A thin plate with an edge crack under plane stress

9. Consider two series of three-point bending tests, one series on concrete specimens and the other on cement paste specimens. The setup of the test is shown in Figure P7-9 and the test results are provided in Table 7-2. Solve the following problems:

(a) By using beam theory, calculate the modulus of rupture for all six specimens. (Actually, it is not strictly valid to use beam theory. However, for simplification, some people still use it to get an approximate result.) What can you say about the notch sensitivity of the two materials?

(b) Use the compliance method to find G_{Ic} for all specimens. Can LEFM be applied to either paste or concrete?

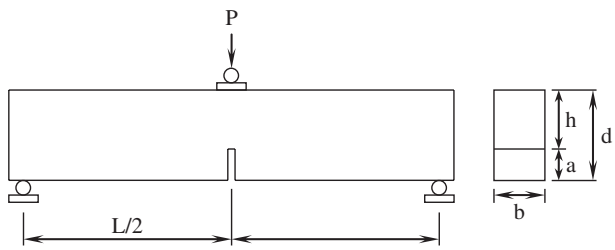

Figure P7-9 Specimen configuration used in the bending tests

Table 7-2 Results of two series of 3-point bending tests

b (mm)	*L* (mm)	*a* (mm)	*d* (mm)	*h* (mm)	*P* (paste) (N)	*P* (concrete) (N)
50	450	25	150	125	3,685	5,148
75	675	37.5	225	187.5	6,772	11,588
100	900	50	300	250	10,422	20,560

REFERENCES

Bazant, Z.P. (1984) "Size effect in blunt fracture: concrete, rock, metal," *Journal of Engineering Mechanics, ASEC*, **110**(4), 518–535.

Bazant, Z. P. and Kazemi, M. T. (1990) "Determination of fracture energy, process zone length and brittleness number from size effect, with application to rock and concrete," *International Journal of Fracture*, **44**, 111–131.

Bazant, Z. P. and Oh, B. H. (1983) "Crack band theory for fracture of concrete," *Materials and Structures, RILEM*, **16**, 155–177.

Bazant, Z.P. and Pfeiffer, P.A. (1987) "Determination of fracture energy from size effect and brittleness number," *ACI Materials Journal*, **84**(6), 463–480.

Broek, D. (1987) *Elementary engineering fracture machanics*, 4th ed. Hingham: Martinus Nijhoff.

Carrasquillo, R. L., Slate, F. O., and Nilson, A. H. (1981) "Microcracking and behavior of high strength concrete subject to short-term loading," *Journal of the American Concrete Institute*, **78**(3), 179–186.

Castro-Montero, A., Shah, S.P., and Miller, R.A. (1990) "Strain field measurement in fracture process zone," *Journal of Engineering Mechanics, ASCE*, **116**(11), 2463–2484.

Cedolin, L., DeiPoli, S., and Iori, I. (1987) "Tensile behavior of concrete," *Journal of Engineering Mechanics, ASCE*, **113**(3), 431–449.

Cho, K.Z., Kobayashi, A.S., Hawkins, N.M., Barker, D.B., and Jeang, F.L. (1984) " Fracture process zone of concrete cracks," *Journal of Engineering Mechanics, ASCE*, **110**(8), 1174–1184.

Cooper, D.B., Meda, G., and Sinclair, G.B. (1995) "A comparison of crack-flank displacement fitting for estimating K with a path independent integral," *International Journal of Fracture*, **70**(3), 237–251.

Du, J., Yon, J.H., Hawkins, N.M., Arakawa, K., and Kobayashi, A.S. (1992) "Fracture process zone for concrete for dynamic loading," *ACI Materials Journal*, **89**(3), 252–258.

Dugdale, D.S. (1960) "Yielding of steel sheets containing slits," *Journal of the Mechanics and Physics of Solids*, **8**(2), 100–104.

Faber, K.T. and Evans, A.G. (1983) "Crack deflection processes, I: theory," *Acta Metallurgica*, **31**(4), 565–576.

Gopalaratnam, V.S. and Shah, S.P. (1985) "Softening response of plain concrete in direct tension," *ACI Journal*, **82**(3), 310–323.

Higgins, D.D., and Bailey, J.E. (1976) "Fracture measurements on cement paste," *Journal of Materials Science*, **11**(11), 1995–2003.

Hillerborg, A., Modeer, M., and Petersson, P.E. (1976) "Analysis of crack formation and crack growth in concrete by means of fracture mechanics and finite elements," *Cement and Concrete Research*, **6**(6), 773–782.

Homeny, J. and Vaughn, W.L. (1990) "R-curve behavior in a silicon carbide whisker/alumina matrix composite," *Journal of the American Ceramic Society*, **73**(7), 2060–2062.

Inglis, C. E. (1913) Stresses in a plate due to the presence of cracks and sharp corners. *Transactions of the Institution of Naval Architects*, **55**, 219–241.

Irwin, G.R. (1958) *Fracture, Handbook der Physik*, VI. Flugge, ed., Berlin Springer, pp. 551–590.

Irwin G.R. (1960) Plastic zone near a crack and fracture toughness. *Proceedings of the 7th Sagamore Conference*, p. IV–63.

Jenq, Y. S. and Shah, S. P. (1985) "A two parameter fracture model for concrete," *Journal of Engineering Mechanics*, **111**(4), 1227–1241.

Kaplan, M. E. (1961) Crack propagation and fracture of concrete, *Journal of ACI*, **58**(5), 591–610.

Leicester, R.H. (1973) Effect of size on the strength of structures, Report paper No. 71, CSIRO Forest Products Laboratory, Division of Building Research Technology, Commonwealth Scientific and Industrial Research Organization, Australia.

Li F. and Li, Z. (2000) "AE monitoring of fracture of fiber reinforced concrete in tension," *ACI Materials Journal*, **97**(6), 629–636.

Li Z. and Shah, S.P. (1994) "Microcracking localization in concrete under uniaxial tension: AE technique application," *ACI Materials Journal*, **91**(4), 372–389.

Liaw, B.M., Jeang, F.L., Du, J.J., Hawkins, N.M., and Kobayashi, A.S. (1990) "Improved non-linear model for concrete fracture," *Journal of Engineering Mechanics, ASCE*, **116**(2), 429–445.

Lim, I.L., Johnston, I.W., Choi, S.K., and Murti, V. (1992) "An improved numerical inverse isoparametric mapping technique for 2D mesh rezoning," *Engineering Fracture Mechanics*, **41**(3), 417–435.

Murakami, Y., et al. (1987) *Stress intensity factors handbook.* New York: Pergamon.

Ouyang, C., Landis, E., and Shah, S.P. (1991) "Damage assessment in concrete using quantitative acoustic emission," *Journal of Engineering Mechanics, ASCE*, **117**(11), 2681–2698.

Pang, H.L.J. (1993) "Linear elastic fracture mechanics benchmarks: 2D finite element test cases," *Engineering Fracture Mechanics* **44**(5), 741–751.

Rice, J.R. (1968) "A path independent integral and the approximate analysis of strain concentration by notches and cracks," *Journal of Applied Mechanics, ASME*, **35**(6), 379–386.

Roelfstra, R.E. and Wittmann, F.H. (1986) A numerical method of link strain softening with fracture in concrete. In: Wittmann, F.H., ed., *Fracture toughness and fracture energy in concrete.* Amsterdam: Elsevier Science, pp. 163–175.

Sakai, M., Yoshimura, J., Goto, Y., and Inagaki, M. (1988) "R-curve behavior of a polycrystalline graphite: microcracking and grain bridging in the wake region," *Journal of the American Ceramic Society* **71**(8), pp. 609–616.

Shah, S. P. and McGarry, F. J. (1971) "Griffith fracture criterion and concrete," *Journal of the Engineering Mechanics Division, ASCE*, **97**(6), 1663–1676.

Swartz, S.E. and Refai, T. (1989) Cracked surface revealed by dye and its utility in determining fracture parameters. In: Mihashi, H., et al., eds., *Fracture toughness and fracture energy: test method for concrete and rock.* Brookfield VT: Balkema, pp. 509–520.

Tada, H., Paris, P.C., and Irwin, G.R. (2000) *The stress analysis of cracks handbook*, New York : ASME Press.

Van Mier, J.G.M. (1991) "Mode I fracture of concrete: discontinuous crack growth and crack interface grain bridging," *Cement and Concrete Research*, **21**(1), 1–15.

Walsh, P.F. (1972) "Fracture of plain concrete," *Indian Concrete Journal*, **46**(11), 469–470.

Wecharatana, M. and Shah, S.P. (1982) "Slow crack growth in cement composites," *Journal of Structural Engineering*, **108**(6), 1400–1413.

Wecharatana, M. and Shah, S.P. (1983) "Predictions of nonlinear fracture process zone in concrete," *Journal of Engineering Mechanics*, **109**(5), 1231–1246.

Xu, Y. (1998) "Self-similar crack expansion method for two-dimensional cracks under mixed mode loading conditions," *Engineering Fracture Mechanics*, **59**(2), 165–182.

Xu, Y., Moran, B., and Belytschko, T. (1997) "Self-similar crack expansion method for three-dimensional crack analysis," *Journal of Applied Mechanics, Transactions ASME* **64**(4), 729–736.

CHAPTER 8

NONDESTRUCTIVE TESTING IN CONCRETE ENGINEERING

8.1 INTRODUCTION

8.1.1 General description

There are two kinds of tests, destructive and nondestructive, that can be utilized to assess the properties of concrete material or structures. Destructive testing obtains the materials or structural properties or information through the actions that destroy the integrity of the materials or structures, while nondestructive testing obtains the information without destroying the integrity of the materials or structures. Hence, nondestructive testing can be defined as the measurement, inspection, or analysis of materials, existing structures, and processes of manufacturing without destroying the integrity of the materials and structures. The common terms used in this field are as follows:

NDT: nondestructive test
NDI: nondestructive inspection
NDE: nondestructive evaluation
QNDE: quantitative nondestructive evaluation

The first three terms are basically the same. The last term, QNDE, emphases the quantitative nature and is more difficult to apply. The application fields of NDT include the following:

(a) *Quality control of concrete materials and structures,* including hydration processing monitoring, strength development evaluation, curing process monitoring of concrete, welding quality evaluation of reinforcing steel, and/or porosity assessment in matured concrete members

(b) *In-service inspections of concrete materials and structures,* including inspection on the corrosion degree and rate, residual strength, fatigue damage, existing crack length, debonding of an interface, and impact damage

Nondestructive testing in concrete engineering (NDT-CE) is an important tool for assessing the quality and maturity of a concrete structure during construction, which helps decision making in construction procedures and speed. For new constructions, NDT-CE can act as a quality-control tool to evaluate reliability, to assess integrity, and to monitor the conditions of a construction as a whole or in part. NDT-CE is very useful for condition assessments of serviceability and stability of concrete structures and for maintenance and renovation decision making of aged buildings

and infrastructures by estimating the properties and performance of materials and structures. NDT-CE can localize and measure the defects or damage inside a structure for repair or removal purposes. It also can be used to find the position of the prestressed elements to avoid their being destroyed by accidental drilling. In general, NDT-CE can make a significant contribution to evaluating and guaranteeing a building safety and protecting invaluable monuments at low cost, and in a rapid and simple manner. The following are some general requirements for a practical NDT-CE technique:

It must be effective for determining the quantities of interest.
It must be accurate, with the ability to determine shape, size, and depth of the defective areas.
It must be insensitive to the surface condition and the shape of the object to be tested.
It must be efficient in terms of labor and equipment, and rapid and simple to use.
It must be economical, with low cost for equipment and maintenance.
It must be unobtrusive to the surrounding environment.
It must be safe for operators and equipment.
It must be convenient to the users.
It is better to be noncontacting.
It should be able to inspect large areas as well as localized areas.

For a specific NDT-CE technique, it is difficult to satisfy all of the above requirements, but it should at least meet some of these requirements, and the more the better. The performance of concrete in a building is often different from that in the laboratory. Hence, in situ testing directly on a concrete structure becomes important.

It is said that many NDT methods have been tried on concrete structures but none of them has proved satisfactory. This is partially true, because concrete, the most widely used building material, is an inhomogeneous, porous, and highly variable material. The average values of the concrete properties depend on the raw material types and proportions, and they vary with water content, curing conditions, the microstructure of hardened binders, the cement mix, the type, shape, orientation, size, and distribution of the aggregate, as well as the state of the concrete reinforcement. Another problem on the NDT application to concrete structures is that a building or bridge structure is usually very large. All of these factors have created problems in producing an accurate result. In regard to the NDT-CE techniques themselves, even if they can perform well in some aspects, they also have their own limitations.

Generally speaking, to better apply NDT-CE techniques, one needs to thoroughly understand the problem of the concrete structures or materials to be tested, and to select NDT-CE techniques correctly, with a sound knowledge of the basis of the testing techniques and devices to be used. Usually, this requires interdisciplinary cooperation, prior knowledge of the specimen, calibration of the instruments, and experienced operators. Since the 1980s, NDT-CE techniques have been developed into a more advanced stage. Many excellent results have been achieved with these techniques, benefitting from the advanced development of digital electronics and computer technology. Measurements are mostly automatically performed by computer-controlled instruments and the test results are automatically analyzed and displayed on a computer screen in an easily understood way. The analyzing and displaying process is usually called digital signal processing. Significant improvements were achieved in the 1990s in ultrasonic pulse echo testing, in the application of radar and the impact echo technique, in data analysis, and in the interpretation and simulation of test results.

In NDT-CE, an allowable tolerance philosophy is frequently applied. First, there is always a detection limit in an NDT method and this limit has to be tolerated. Second, even when a flaw

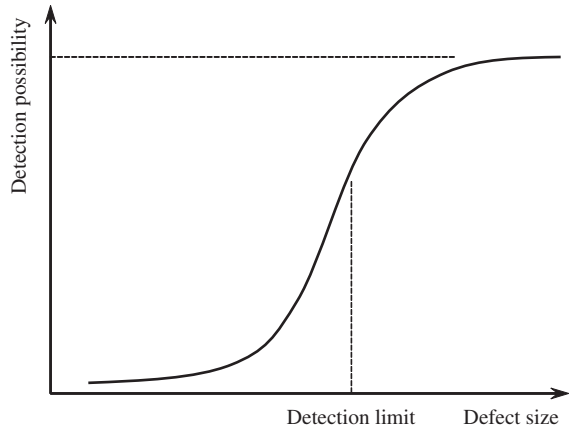

Figure 8-1 No clear cutoff in detection resolution

or crack is detected, it can be allowed to remain if its size is less than a critical value. Moreover, tolerance can be applied to the inspection interval on different concrete structures, according to their importance and from economic considerations. When conducting NDT, there may not be a clear cutoff in the detection resolution, as shown in Figure 8-1; hence, probability theory is very useful in NDT-CE.

8.1.2 Principles and classifications

Generally speaking, NDT is a technique to know the properties or to "see" the structures inside the component to be inspected, especially for optically opaque components, without damaging it. There are many NDT techniques available, such as mechanical techniques, elastic wave techniques, electromagnetic techniques (EMT), and optical techniques (OT). There are four main aspects related to a specific NDT technique. The first is the physical principle on which the technique is based, called *principle* for simplicity. The second aspect is the NDT techniques employed, termed *method*. The third is the equipment used to perform the function specified, and the fourth is the signal processing scheme adopted. Any advances in these four aspects would improve the performance of the relevant NDT technique.

Among the four aspects, the principle is the most important, because it is the foundation of an NDT technique. The principle controls the way to link the received signals to the materials properties and to interpret material or structural conditions and qualities. Different NDT techniques depend on different physical rules. For example, the principle of elastic wave technique involves the physical rules on elastic wave behavior. The capability and the limitation of an NDE technique essentially depends on the basic physical rules followed.

The NDT method means the manner or way to realize the measurement, and is the key aspect of an NDT technique. Following a principle, there are lots of possible methods. For example, there is the transmission method and the reflection method for wave-related NDT techniques. The equipment is a physical medium to undertake the NDT measurements and is designed based on the principle and method. The equipment determines whether an NDT technique can be applied or not.

The signal processing scheme is the way to extract useful information from the gathered signals. The bases of interpreting the measured data are the principles of the method followed,

but the signal processing scheme sometimes plays a significant role in the data interpretation procedure. Nowadays, signal processing (SP) has become an essential and necessary procedure in NDT measurements. Signal processing can be analog or digital. Digital signal processing (DSP) has become more and more popular due to the rapid development of advanced computer techniques and mathematical analysis tools.

The difference between in terminology words "signal" and "information" should be pointed out. The signal is something that a sensor directly measures. Information is something interpreted from a signal. The signal is the information carrier. Sometimes, there are many signals received, but little information can be interpreted. In this situation, the signal may be noisy or may lack ways to be interpreted. Having less signals but carrying more information is more desirable.

The NDT techniques can be classified into different categories according to the above-mentioned four aspects. That is to say, they can be classified as to what kind of physical principle they follow, what methods they adapt, what kind of equipment they use, and what kind of signal processing scheme they use. They can also be classified according to the final goals the technique is intended to reach, or the objectives defined in the technique.

Plenty of NDT-CE techniques can be found in practice. Some are mechanical techniques like building dynamics, impact echo, ultrasound, and acoustic emission techniques. Some are electromagnetic techniques like eddy current, electrochemical methods, microwaves, nuclear magnetic resonance method, magnetic method, and radiography. Some are optical methods, like interferometry, infrared thermography, and fiber optic sensors. Computer tomography and other imaging techniques are also used as NDT-CE techniques.

According to the physical working principle, NDT-CE techniques can be roughly classified into three categories: (1) direct measurement, (2) load-induced reaction measurement, and (3) measurements through inquiring agency.

8.1.2.1 Direct-measurement NDT-CE techniques

Sometimes the information or properties of a material can be directly measured or interpreted through NDT measurement. This kind of testing is referred to as the direct NDT-CE technique. Direct-measurement NDT-CE techniques should be solidly based on a fundamental physical principle. For example, the density can be obtained by weighing the object, providing its volume is known. The weighing technique also can be used to determine the moisture content of a concrete sample. The procedure involves weighing the sample, drying the sample, and reweighing the dried sample. The weight difference is directly related to the moisture content. Another example is the half-cell potential measurement technique, which is the most commonly used electrochemical NDT-CE technique for reinforced concrete structures. It measures the macrocurrent of the corroding steel bars of reinforced concrete, and then the corrosion condition can be easily deduced. The magnetic leakage technique measures the premagnetized magnetic field of the steel-reinforced concrete, and the deformation of the magnetic field can indicate fracture of the steel rebar.

The direct NDT-CE testing technique is usually simple, but, like the weighing–drying–weighing technique, for example it is not suitable for in situ applications. It is still useful in practice for testing structures by means of a slightly destructive manner—samples could be taken from the structure, e.g., by coring from a column, beam, slab, or wall.

8.1.2.2 Load-induced reaction measurement NDT-CE techniques

This kind of technique is used to detect the response of an object to be tested by loading it to a certain level. However, the load should be controlled in a reasonable range without damaging

the test specimen. The signals gathered reflect the nature of the test object. Building dynamics is an example. In building dynamics, the natural frequency or eigenfrequency of a structure (a building, a bridge, etc.) is excited by a random load and measured. The mode shapes can also be determined when needed. These data can be compared with the theoretical prediction of the model of this structure to extract information about the integrity, stiffness, stability, and some macrodefects. Another example is the impact echo method, which measures the dynamic response of a structure to an applied impact load.

8.1.2.3 Measurement through inquiring agent NDT-CE techniques

These methods use an inquiring agent as a probe, and the agent usually is a wave packet. They can be divided into active and passive techniques. In the active technique, a wave packet is generated by the test instrument and then transmitted into the materials to be inspected. Examples are ultrasonic testing and microwave testing. The probe agent, the wave packet, interacts with the matrix material and embedded objects, if existing. Then, it gives out a signal, which carries the information on the specimen. In passive techniques, the wave packet stems from the tested specimen itself and carries information about the process the specimen is undergoing. An example is the acoustic emission NDT-CE technique.

The most widely used inquiring agents in NDT-CE are mechanical waves (acoustic waves and ultrasonic waves), electromagnetic waves (ultrahigh frequencies (UHF), L-band, and S-band microwaves), infrared lights, lights, and X-ray and gamma-ray radiation. From a physical point of view, infrared light, light, and X-ray and gamma-ray radiation are essentially electromagnetic waves.

8.1.3 Components of NDT-CE

As aforementioned, NDT-CE stands for nondestructive testing in concrete engineering. It is a relatively young area in NDT applications, and large-scale experiments only started in the 1980s. NDT-CE activities can be viewed in different categories: (1) the test objects or problem, and (2) the testing method. However, these categories interweave. A problem may require several different NDT techniques, or a technique may be used for attacking several test objects or problems.

8.1.3.1 Testing objects

The testing objects of NDT-CE may include masonry buildings, usually low, multistory residential or office buildings made of concrete blocks, concrete bridges, tall buildings, dams, highways, and airport runways. Differing from NDT applied in other fields, the test structures in NDT-CE are usually much larger, more complicated in shape, and more complex in properties. Hence, NDT-CE usually requires more carefully designed inspection plans and several different techniques.

8.1.3.2 Testing problems

The test problems of NDT-CE can be viewed from the load-carrying abilities and environment resistance abilities.

(a) *Strength*: The strength of a concrete cast on site can be very different from the strength measured in a laboratory. Moreover, the strength of concrete can vary with its service life. Hence, determination of concrete strength on site is a big issue for NDT-CE. In addition, if

a concrete structure has gone through a fire, the residual strength of the damaged concrete has to be determined in order to make decisions for renovation work. The true steel yield stress of a concrete structure during service and after a natural disaster has to be determined using NDT-CE, for maintenance purposes.

(b) *Cracks and fractures*: Concrete is a quasi-brittle and tension-weak material. In addition, due to the boundary constraints in shrinkage and creep, large tensile stresses can be generated in concrete. When such a stress exceeds its tensile strength, concrete will crack. The existence of cracks can induce many durability problems, as they can channel many harmful agents into the concrete. Thus, detecting the properties of cracks in concrete is a big challenge. The detection of a crack includes the length and width of the crack, the position of the crack, and the propagation rate of the crack. From these parameters, it can be judged whether the crack is active or not, or dangerous or not.

(c) *Thickness*: The thickness measurement of a pavement, a restraining wall, the cover of a reinforcing steel, and slab is an important quality assurance issue in concrete structure construction and maintenance.

(d) *Moisture*: Moisture or water in a concrete structure can play an important role in deterioration. It can cause a lot of durability problems, such as corrosion, CH leaching, alkali aggregate reaction (AAR) expansion, and leakage. Hence, detection of the moisture location and content is a common NDT-CE problem.

(e) *Corrosion*: Corrosion is the most serious and dangerous durability problem, and also is the most commonly encountered durability problem. Corrosion can crack the concrete cover and make it spall. Corrosion can also significantly reduce the effective area of the reinforcing steel and put a concrete structure in danger, especially a prestressed concrete structure. It is obvious that the detection of corrosion occurring, corrosion rate, and corrosion degree is one of the most important issues of NDT-CE.

(f) *Debonding*: Debonding is the separation of two adjacent materials originally bonded together. Debonding is usually an indication of serious damage or deterioration of a concrete structure. Frequently encountered debonding problems include those caused by corrosion in losing the adhesive effect and interfaces damaged by shear stress.

8.1.3.3 Testing methods

The classification principle of NDT-CE methods was briefly discussed in Section 8.1.2 and more details of commonly used NDT-CE methods are described in the following sections. Here, only a brief introduction is provided for most NDT-CE methods.

(a) *Mechanical wave techniques (MWT)*: These techniques take the mechanical waves as the working agency. The principle of these techniques is the generation and propagation of laws concerning mechanical waves. Ultrasonic waves, acoustic waves, and subacoustic waves are mechanical waves. A special feature of these waves is that they are directly related to the mechanical properties of the media they propagate through, hence, this is a remarkable advantage for determining the mechanical performance of the materials. Mechanical wave NDT techniques are widely used in NDT-CE, and are also some of the most popularly used conventional NDT techniques. They can be used in a wide range of objectives, as a tool for measurement, detection, and monitoring. They can meet most of the requirements for NDE in civil engineering. They are accurate in determining shape, size, and depth of the defective areas, with high sensitivity, deep penetration, low cost, and they are easy and fast to operate and convenient for in situ use.

Mechanical waves are not harmful to the human body, which is an important advantage over radiation.

The basic theory involved in MWT methods is elastic wave generation, propagation, and reception. Wave propagation involves reflection, transmission, and scattering, as well as diffraction and interference. The wave packet transmitted into the materials to be tested interacts with the material and changes its own parameters as a result, which carries the information about the properties of the test object. The most frequently measured wave parameters are amplitude, phase, and frequency, as well as the transmission time when the wave passes through the object, which is usually called time of flight (TOF). It is important to establish some relations between these wave parameters and the properties of the object to be tested.

Mechanical wave techniques can be active or passive. In the active ones, the testing apparatus produces the mechanical waves. In the passive techniques, the mechanical waves stem from the test object itself. The main mechanical wave NDT-CE techniques are ultrasound testing, impact echo, and acoustic emission.

(i) *Ultrasonic techniques (UT)*: The ultrasonic technique works in the ultrasonic band. Most ultrasonic inspection is done at frequencies between 0.1 and 25 MHz (human hearing range is 20 Hz to 20 kHz.). Ultrasonic waves are mechanical waves that consist of oscillations or vibrations of the atomic or molecular particles about the equilibrium position of these particles. This method introduces high-frequency sound waves into materials for the detection of surface and subsurface flaws in the material and hence is an active NDT method. The sound waves travel through the material and are reflected at the interfaces. The reflected sound wave or the first arrival time can be displayed and analyzed to define the presence and location of flaws or dislocations. UT has the following advantages: accurate, convenient to use, cheap to buy and maintain, as well as low labor requirements. In addition, UT can detect almost every kind of defect.
Usually pipzoelectric transducers (PZT) or transducer arrays are used to generate ultrasound in UT. The waves used can be continuous (CW) or impulse (PW). PW ultrasound is now the dominant technique. The ultrasonic waves propagate in the material and are reflected or scattered by the materials inside the specimen or at the interface of the structure of the specimen. The reflected or scattered wave pulse, especially the backscattered wave pulse, is usually referred as an echo. To receive ultrasound, the same emitting transducer/array could be used, or another one. The receiver can be placed at the same side of the emitter (reflection mode) or opposite the emitter (transmission mode). Both the emitter and the receiver can be individual or in an array. These form a great variation in NDT-CE-UT testing methods. The last, but not insignificant, procedure is signal processing and display. Signal processing, especially digital signal processing, is so important that it has become the essential part of an UT technique.

(ii) *Acoustic emission (AE)*: The acoustic emission method is a passive NDT method. It relies on detection of the energy released due to microcracks, dislocations, and inclusions in concrete. The beauty of the AE technique is that it can provide information about an active crack that could be dangerous to a structure.

(iii) *Impact echo (IE)*: The impact-echo method usually generates an impact on a concrete specimen and then measures the response of the specimen under the action of the impact. Through time domain and frequency domain analysis of the received response, the properties of concrete, such as the dynamic modulus and Poisson's ratio, can be interpreted. Moreover, the damage degree of the material or structure can be interpreted from the changes of the stiffness.

(b) *Electromagnetic wave technique (EMT)*: Among NDT methods in concrete engineering, the electromagnetic wave technique is one of the most powerful, as most nonmetal materials are amenable to electromagnetic waves. This kind of technique uses a special band of electromagnetic waves as the inquiring agent and is an active method. It can be applied in either a noncontact or a contact mode, and measurements can be taken in a remote as well as in a real-time manner. It possesses a lot of advantages over other techniques.

Electromagnetic waves cover a very wide range of frequency in the scientific sense. According to the different frequency ranges, from lower to higher, they have different nomenclature, such as radio waves, high-frequency waves (RF), very high-frequency waves (VHF), ultra-high-frequency waves, microwaves (L-band, S-band, etc.), infrared light (IR), and light, X-rays. In NDT engineering, they are usually referred to according to what kind of electromagnetic wave is used as the working agent. The electromagnetic wave techniques are usually related to relatively lower frequency, namely, the frequency from RF to the S-band, usually called microwaves. Microwave testing in the reflection mode is often called the radar technique, whereas the infrared light, light, and X-ray techniques, etc. are usually regarded as other independent NDT techniques. For most cases, the frequency range for EMT is from 90 MHz to 1 GHz, and the electrical techniques are well developed in this band.

EMT is suitable mostly for testing nonmetallic materials. It can penetrate much more deeply than ultrasound and is very sensitive in detecting the metal objects inside the nonmetal matrix, like steel bars in concrete. It can detect a flat defect, which is difficult to detect by X-ray techniques. It is not sensitive to aggregate size and type. By means of a microwave technique, radar, a 6-mm-diameter steel bar and 20 by 20-mm voids can be detected when the cover thickness is around 200 mm. It does not require knowledge of the specific state of the testing surface, such as the shape, oil pollution, or roughness. It can make one-sided access to an object under testing, and it can precisely locate the internal faults. It has a wide range of measurement, from microns in paint coatings to meters in concrete.

The operation of the measurement system is fast and simple. Electromagnetic shielding, by the microwave technique, can detect only the surface of a metal object but not the insides. Not can it give information on the structures beyond a metallic sheet. In addition, the equipment is relatively expensive. EMT is based on the physical laws of microwave generation and propagation; thus, problems similar to those in UT would be encountered. These include electromagnetic wave (EMW) generation, propagation and reception, reflection, transmission, and scattering, as well as diffraction and interference.

The most frequently measured parameters of the wave are amplitude, phase, and frequency, as well as the time of flight. It is important to establish some relations between these wave parameters and the properties of the object to be tested. The most reliable and reproducible results are obtained by determining the wave velocity, reflection coefficient, and the attenuation and the velocity of the microwave packet to be tested. The wave velocity and the reflection and absorption of the wave depend on the electromagnetic parameters of the material, such as their permittivity, permeability, and conductivity, and the geometrical parameters of the object, such as their thickness, shape, orientation, direction, etc. Usually, in different frequencies, a wave exhibits different characteristics. Hence, by measuring the time of fight of microwaves, the attenuation during passing through the testing object, or the reflection/transmission coefficients, one can deduce the parameters of the test object, and hence deduce information about the structure and the mechanical properties.

The microwave NDT technique can be used to perform building inspections and quality control and to detect steel objects, as well as moisture, water content, and cracks. It is well suited for locating the lateral positions of rebars, the location of metallic ducts, and metallic

T-girders and metallic anchors in prefabricated three-layer concrete elements, the location of plastic and metallic leads, measurement of cover thickness of concrete, and moisture measurement of concrete. The artificial birefringence properties can be found for ceramics and cement with microwaves, of which the wavelength is between 7.5 and 12.5 mm, similar to that of photoelasticity with visible light (Dannheim et al., 1995). Hence, visualizing the inside of specimen is possible with microwaves.

A very powerful EMT instrument is ground-penetrating radar (GPR). A GPR image can profile a bridge pile in a bridge scour investigation. A maximum frequency should be recommended in a GPR survey design for clutter reduction. It is suggested that the wavelength should be ten times larger than the characteristic dimension for geological materials (Davidson et al., 1995). For most cases, the frequency range is from 90 MHz to 1 GHz and the pulse repetition frequency is 25 Hz. The following typical results could be reached: a scour depth of 1.2 m relative to the general riverbed; a filling consisting of a sandy layer 0.5 m deep overlying gravel 0.8 m thick at the center of the hole; and a water depth of about 1 m. The GPR measurement is fast enough to detect a large area like a 10,000-m^2 airport pavement (Weil, 1995).

The EMT technique can make reliable assessment of the integrity of a structure and locate tendons and metal ducts (diameter 85 mm) to offer information on geometrical dimensions. It can detect defects in concrete members, voids in tendon ducts, compression faults, or honeycombing (voids from 80 to 160 mm) in concrete. The EMT technique is not sensitive to aggregate size. For example, for aggregate size 8 to 32 mm and cover thickness 340 ± 10 mm, the lateral position of a reinforcement could be found with an accuracy of ± 10 mm (Attoh-Okine, 1995). A microwave moisture content meter offers on-line water content monitoring in clay (Kalinski, 1995).

(c) *Optical techniques*: These techniques use light waves as the inquiring agent, and are also the active methods. The main techniques are based on interferometry and energy transportation. The representative technique of the former is electronic speckle pattern interferometry (Jones and Wykes, 1989; Hung, 1982), and of the latter is the infrared detection (Reynolds, 1988; Favro et al., 1991).

Interferometric methods utilize the principle of interferometry of two lights to measure the surface change of a concrete specimen. The examples include holographic, moire, and electronic speckle pattern interferometry methods.

Infrared thermography utilizes the principles of radiation theory. By measuring the surface temperature difference due to the difference in radiation of the materials underneath, infrared thermography can detect debonding and moisture content in concrete materials or structures.

(d) *Electrical and electrochemical methods*: These methods usually measure the electrical parameters, such as potential, current, or resistivity that can be influenced by property changes of the concrete material or structure, and hence these electrical parameters are used to interpret the concrete properties. Examples include noncontact resistivity measurement, half-cell potential measurement, and corrosion current measurement.

Other electrical methods for detecting reinforcement corrosion are available. One such technique is based on electrical resistance measurements on a thin section of in situ reinforcement (Vassie, 1978). The electrical resistance of the reinforcement bar is inversely proportional to its thickness; therefore, as the thin slice is gradually consumed by corrosion, it becomes thinner, with a corresponding increase in resistance. In this technique, to facilitate measurements, the probe is normally incorporated into a Wheatstone bridge network (Figure 8-2). One of the probes is protected from corrosion, while the other arm is the in-place portion of the reinforcement. The measured resistance ratio can be used to monitor the corrosion rate. The significant disadvantages are the need for positioning the exposed arm of the probes during construction and the concerns

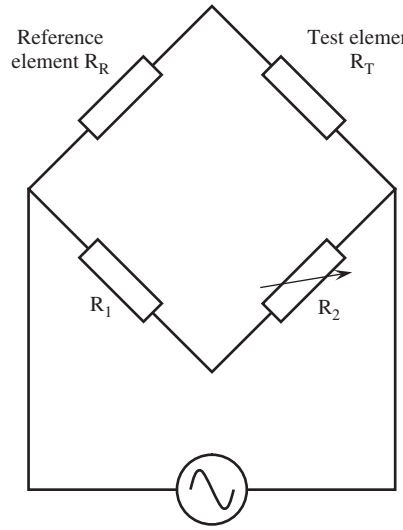

Figure 8-2 Basic circuit for the electrical resistance probe technique

of associated sampling techniques required for locating the probes in a large structure subject to localized corrosion.

(e) *Magnetic methods*: Magnetic techniques utilize magnetic fields as an essential tool to detect or interpret material properties. As far as applications in concrete structures go, currently there are three different aspects of magnetic field phenomena: (1) alternating current excitation of conducting materials and their magnetic inductance; (2) direct current excitation resulting in magnetic flux leakage fields around defects in ferromagnetic materials; and (3) nuclear magnetic resonance (Malhotra and Carino, 2004). The magnetic induction method is applicable only to ferromagnetic materials, in which the test equipment circuitry resembles a simple transformer and the test object acts as a core (Figure 8-3). With a piece of metal close to the coil of the transformer, the inductance increases and the change in induced current depends on the

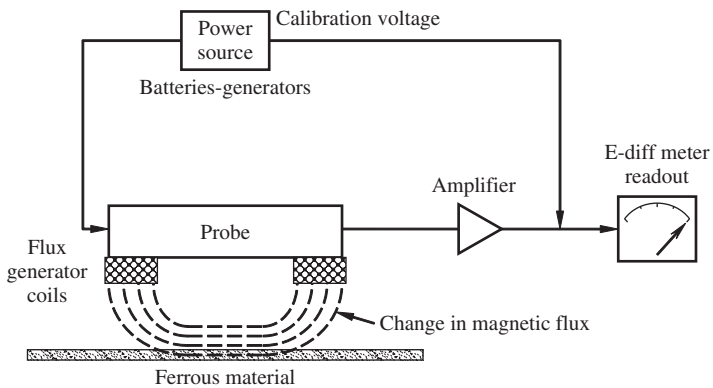

Figure 8-3 Principle of an induction meter used to locate reinforcement

magnetization characteristics, location, and geometry of the metal. The inductance of the coil can be used to measure coil-to-place distance if the relationship between mutual inductance and the coil-to-place distance is known. The magnetic induction theory has resulted in the development of equipment for determining the location, sizes, and depth of reinforcement or depth of concrete cover, such as a cover meter to detect the location of embedded steel.

Magnetic flux leakage (MFL) nondestructive testing consists of magnetizing a test part, generally a ferromagnetic material, and scanning its surface with some form of flux-sensitive sensor for the leakage field (Bray and Stanley, 1997). The fundamental theory of MFL has been explained elsewhere (Bray and McBride, 1992; Bray and Stanley, 1997). When ferromagnetic materials are magnetized, magnetic lines of force (or flux) pass through the material and complete a magnetic path between the poles, which increases from zero at the center of the specimens to increased density and strength toward the outer surface. When cracks or defects exist in materials, they can lead to perturbations of the magnetic flux. Its magnetic permeability is drastically changed and the leakage flux provides a basis for nondestructive identification of such discontinuities. The amount of leakage flux produced also depends on the defect geometry. Broad, shallow defects will not produce a large outward component of leakage flux. What's more, a defect whose long axis is parallel to the lines of flux will not produce leakage flux either. By sensing the magnetic flux along a test member, damage location can be deduced. MFL techniques are suitable for the detection of surface or near-surface anomalies in ferromagnetic materials, such as detection area reduction in reinforcements and breakage of tendons in prestressed cables. Internal defects in thick parts may not be detected because the magnetic lines of flux nearly bypass the defect with little leakage. These techniques generally do not require mechanical contact with the testing object and are very amenable to automatic signal recognition schemes, both of which are of great benefit for automated, high-speed inspection.

Nuclear magnetic resonance (NMR) is based on the interaction between nuclear magnetic dipole moments and a magnetic field. Magnetic resonance occurs in electrons, atoms, molecules, and nuclei in response to excitation by certain discrete radiation frequencies as a result of a space quantization in a magnetic field. The NMR technique can be used as a basis for determining the amount of moisture content in concrete by the detection of a signal from the hydrogen nuclei in the water molecules. Careful surface preparation is required and the object for testing must be clean and originally demagnetized. The test requires a source of high-current electric power to magnetize the object. The operation is relatively messy and good operator skill is needed to interpret the results.

Magnetic particle testing is another nondestructive magnetic method, mainly for steel structures. In this method, the object is magnetized and covered with magnetic powder. Surface and/or near-surface discontinuities in the magnetized materials may create leakage in the magnetic field, which, consequently, may affect the orientation of the particles above those areas. A variation of this test involves using wet fluorescent particles visible in back light through a borescope. The magnetic particle technique can be used for locating surface cracks, laps, voids, seams, and other irregularities. Some subsurface defects can also be detected to a depth of about 0.635 mm (0.25 in.) (Newman, 2001). This method is relatively fast, simple to administer, and inexpensive, but there is a limited depth penetration for these methods. Magnetic particle testing has a long history and has been implemented into many standards and specifications. This method is a most effective way to nondestructively detect surface and near-surface discontinuities in ferromagnetic material.

(f) *Building dynamics*: Building dynamics measures the vibration of a concrete building under random dynamic loading with a very small amplitude. The measured wave form is analyzed in both the time and frequency domains to induce the fundamental frequencies and modal modes.

The analysis is extended into the change of the stiffness of the structure to access the damage degree of the building under inspection.

Building dynamics techniques are widely used in structural engineering. Simple methods are useful for assessing localized integrity, such as delamination, while more complex methods are used in pile integrity testing, determination of member thickness, and examination of the change of stiffness of members affected by cracking or other deterioration. In general, there are three categories of dynamic response methods for NDT purposes: modal analysis, resonant, and damping techniques. The test equipment for building dynamics techniques is roughly composed of two parts, one generating mechanical vibrations and the other sensing these vibrations. The pulse-echo method is simple and easy to apply to building dynamics technique. It involves measuring the reflected shock waves caused by a surface hammer and analyzing them in the time and/or frequency domains. Dynamic response testing of large structures may similarly involve hammer impacts or the application of vibrating loads. The vibration response is recorded by carefully located accelerometers. Through measuring the natural frequencies and/or the rate of attenuation (or damping) of the vibrations of the building structure, information about the dynamic properties, defects, and damage of the building structure, even individual member stiffness, can be obtained.

The resonant frequency technique is also widely used in deriving the dynamic properties of a building structure. Since every elastic object has many resonant frequencies, which are related to its stiffness and mass distribution, many physical characteristics of the object may be determined from the characteristics of the induced vibration. Typical vibration mode shapes include flexural, longitudinal, and torsional, as well as fundamental and higher orders. Usually, the fundamental flexural and extensional modes are most easily excited and are important for NDT inspection of building structures. When the test object is caused to vibrate in one of its natural or resonant modes by an applied external force, its mode shape can reveal the configuration and composition of the test object. This method is mainly used to determine the dynamic modulus of elasticity, stiffness and Poisson's ratio. Several factors may influence the results of the resonant frequency method in the inspection of concrete structures, including mix proportions and properties of aggregates (Jones, 1962); specimen-size (Obert and Duvall, 1941; Kesler and Higuchi, 1954); and curing conditions (Obert and Duvall, 1941; Kesler and Higuchi, 1953).

The damping test is another method for testing building dynamics. Damping is closely related to the dynamic motion of an object. When a solid object is subjected to dynamic forces, the amplitude of its free vibration will decrease with time after the exciting forces are removed. This is because some of the internal energy of the vibrating object is converted into heat. This phenomenon is called damping. What's more, solid objects exhibit a hysteresis loop, i.e., the downward stress–strain curve due to unloading does not exactly retrace its upward path. In addition, engineering materials always exhibit mechanical relaxation by an asymptotic increase in strain resulting from the sudden application of a fixed stress, and, conversely, by an asymptotic relaxation in stress whenever they are suddenly strained (Bray and McBride, 1992). This mechanical relaxation has an associated relaxation time, the direct result of which is the significant attenuation of vibrations whenever the imposed frequency has a period that approximates to the relaxation time. Normally, the damping effect is characterized by the specific damping capacity, Y, which is given by

$$Y = \frac{\Delta W}{W} \tag{8-1}$$

where ΔW is the energy dissipated in one cycle; and W the total energy of the cycle. Damping is a relaxation process, which is governed by a characteristic time that corresponds to the peak

frequency and is referred to as the relaxation time. The specific damping capacity and associated dynamic response of the material are characterized by the damping coefficient, which can be expressed by

$$\alpha = \frac{1}{N} \ln \left(\frac{A_0}{A_n} \right) \tag{8-2}$$

where α is the damping ratio; A_0 the vibration amplitude of the reference cycle; and A_n the vibration amplitude after N cycles. The specific damping capacity ($\Delta W/W$) for the material is calculated as

$$\frac{\Delta W}{W} = 1 - e^{-2\alpha} \tag{8-3}$$

The damping test methods require an input vibration pulse and an associated output signal. The test body is first caused to vibrate in one of its natural vibration modes, the input signal is then interrupted, and the vibration decay of the test object is measured.

(g) *Radiography or radiometry*: These types of NDT methods utilize X-rays or γ-rays as the agency for detecting the internal defects or microstructure of a concrete material or structure. The techniques of radiometry and radiography are based on radioactive sources, such as X-rays, γ-rays, or neutrons. Both X-rays and γ-rays have very small wavelength. X-rays have a wavelength range from 3 to 0.03 nm, while γ-rays wavelength is much smaller. As the wavelengths of light decrease, they increase in energy. Thus, X-rays and γ-rays are both at the high-energy end of the electromagnetic spectrum and can penetrate matter with some attenuation. The attenuation of radiation passing through matter is exponential and may be expressed as

$$I = I_0 \exp(-\mu X) \tag{8-4}$$

where I is the energy intensity of the beam at a particular location; I_0 the incident energy intensity; μ the linear absorption coefficient; and X the distance from member surface.

The absorption coefficient depends on the composition of the material. Thus, the measured intensity (with a detector or a radiation-sensitive film) can provide information on the material. In radiographic methods, a radiation source and photographic film are placed on opposite sides of a test object. The result, after exposing the film, is a photographic image of the member's interior. Defects inside the member can thus be identified. These techniques are generally fast and reliable, and can provide information unavailable by other means. However, they involve complex technology, high initial costs, and specific training and licensing requirements. X-rays can go through about 1 m of concrete. Applications include determining the distribution of aggregate particles, three-dimensional configuration of air voids inside concrete, segregation, and the presence of cracks. However, X-ray equipment is very expensive and operated with high voltage. As the use of γ-rays does not require electricity, γ-ray equipment has gained a considerable market. However, γ-ray equipment has to be properly shielded and additional safety blocks are required to prevent exposure to radioactive materials. The γ-ray technique is especially valuable for determining the position and condition of reinforcements, voids in the concrete, or the grouting quality of post-tensioned structures.

In radiometric methods, a radiation source and a detector are placed on the same or opposite sites of a concrete member. The number of electric pulses produced at the detector is a measure of the dimensions or physical characteristics (e.g., density or composition of the concrete member). γ-Rays are most commonly used in radiometry systems for concrete, although neutron radiometry has been used for asphalt concrete and soil. For the detection of γ-rays, the Gieger-Müller tube is most commonly used. When high-energy radiation passes through

concrete, some energy is absorbed, some energy passes through, and a significant amount is scattered by collisions with electrons in the concrete. So when employing γ-rays in examining concrete, there are basically two modes of transmission: the direct transmission mode and the backscatter mode. For the former, depending on source, a γ-ray can go through 50–300 mm of concrete. The latter essentially measures concrete within 100 mm of the surface. Some examples of applications include (1) measurement in the transmission mode with internally embedded probes in fresh concrete to monitor the density and hence the degree of consolidation; and (2) noncontact backscatter measurement allows the monitoring of the density of a relatively thin pavement.

(h) *Computer tomography*: This technique is a powerful postprocessing for X-ray or γ-ray measurement. It can slice the object under inspection into three dimensions with very thin segments and recompose them into a whole image of the internal microstructure.

Since the most widely used inquiring agent in NDT-CE are mechanical waves (acoustic waves and ultrasonic waves) and electromagnetic waves, understanding the basic wave theory is essential to managing NDT-CE. Thus, the following sections concentrate on a review of wave theories, including wave reflection and transmission.

8.2 REVIEW OF WAVE THEORY FOR A 1D CASE

A wave is a physical phenomenon, a disturbance or variation that transfers energy progressively from point to point in a medium. It may take the form of an elastic deformation or of a variation of pressure, electric or magnetic intensity, electric potential, or temperature. The most important part of this definition is that a wave is a disturbance or variation that travels through a medium. The medium through which the wave travels may experience some local oscillations as the wave passes by, but the particles in the medium do not travel with the wave. The disturbance may take any of a number of shapes, from a finite width pulse to an infinitely long sine wave. Waves can be divided into mechanical waves and electromagnetic waves. The main difference between mechanical and electromagnetic waves is that a mechanical wave needs a medium to travel through while an electromagnetic wave can travel in a vacuum. Mechanical waves can be divided into body waves that travel through the interior of a solid body, and surface waves that travel along a surface of a solid body. The body wave can be further divided into P-waves and S-waves. P-waves are also known as primary, compressional, or longitudinal waves. In a longitudinal wave, the particle vibration direction is the same as the wave propagation direction. P-waves can travel through both solids and liquids. S-waves are also known as secondary, shear, or transverse waves. In shear waves, the particle vibration direction is perpendicular to the wave propagation direction. The most important surface waves for engineering purposes include Rayleigh waves and Love waves. In a homogeneous elastic half-space, only P-waves, S-waves, and Rayleigh waves can exist. Love waves can be developed only when a half-space is overlain by a layer of material with a lower body wave velocity.

A wave is a disturbance that propagates through a transmission medium, usually with the transference of energy. While a mechanical wave exists in a medium (on which deformation is capable of producing elastic restoring forces), waves of electromagnetic radiation (and probably gravitational radiation) can travel through a vacuum, that is, without a medium. Waves travel and transfer energy from one point to another, often with little or no permanent displacement of the particles of the medium (that is, with little or no associated mass transport); instead, there are oscillations around almost fixed locations.

8.2.1 Derivation of the 1D wave equation

For an elastic solid, that is homogeneous, isotropic, and linear elastic, we have the following equations:

By Hooke's law

$$\begin{aligned}\varepsilon_{xx} &= \frac{1}{E}\left[\sigma_{xx} - \upsilon\left(\sigma_{yy} + \sigma_{zz}\right)\right]\\ \varepsilon_{yy} &= \frac{1}{E}\left[\sigma_{yy} - \upsilon\left(\sigma_{xx} + \sigma_{zz}\right)\right]\\ \varepsilon_{zz} &= \frac{1}{E}\left[\sigma_{zz} - \upsilon\left(\sigma_{yy} + \sigma_{xx}\right)\right]\end{aligned} \tag{8-5a}$$

$$\begin{aligned}\varepsilon_{xy} &= \frac{\sigma_{xy}}{2\mu}\\ \varepsilon_{yz} &= \frac{\sigma_{yz}}{2\mu}\\ \varepsilon_{zx} &= \frac{\sigma_{zx}}{2\mu}\end{aligned} \tag{8-5b}$$

and for the displacement–strain relationship

$$\begin{aligned}\varepsilon_{xx} &= \frac{\partial U_x}{\partial x}\\ \varepsilon_{yy} &= \frac{\partial U_y}{\partial y}\\ \varepsilon_{zz} &= \frac{\partial U_z}{\partial z}\end{aligned} \tag{8-6}$$

$$\text{and}\quad \begin{aligned}\varepsilon_{xy} &= \frac{1}{2}\left(\frac{\partial U_x}{\partial y} + \frac{\partial U_y}{\partial x}\right)\\ \varepsilon_{yz} &= \frac{1}{2}\left(\frac{\partial U_z}{\partial y} + \frac{\partial U_y}{\partial z}\right)\\ \varepsilon_{zx} &= \frac{1}{2}\left(\frac{\partial U_x}{\partial z} + \frac{\partial U_z}{\partial x}\right)\end{aligned} \tag{8-7}$$

For a one-dimensional strain case, we have the displacement expression

$$\begin{aligned}U_x &= U\left(x, t\right)\\ U_y &= U_z = 0\end{aligned} \tag{8-8}$$

and strain expressions

$$\begin{aligned}\varepsilon_{xx} &= \frac{\partial U_x}{\partial x}\\ \varepsilon_{yy} &= \varepsilon_{zz} = \varepsilon_{xy} = \varepsilon_{yz} = \varepsilon_{zx} = 0\end{aligned} \tag{8-9}$$

For the stress expressions, we have

$$\begin{aligned}\sigma_{xx} &\neq 0\\ \sigma_{yy} &= \frac{\nu}{1-\nu}\sigma_{xx}\\ \sigma_{zz} &= \frac{\nu}{1-\nu}\sigma_{xx}\end{aligned} \tag{8-10}$$

Substituting into Equation 8-5, we have

$$\begin{aligned}\varepsilon_{xx} &= \frac{1}{E}\left[\sigma_{xx} - \nu\left(\sigma_{yy} + \sigma_{zz}\right)\right]\\ &= \frac{1}{E}\frac{(1+\nu)(1-2\nu)}{1-\nu}\sigma_{xx}\end{aligned} \tag{8-11}$$

Or in term of stress, we have

$$\begin{aligned}\sigma_{xx} &= E\frac{1-\nu}{(1+\nu)(1-2\nu)}\varepsilon_{xx}\\ &= (\lambda + 2\mu)\,\varepsilon_{xx}\end{aligned} \tag{8-12}$$

Considering an element, as shown in Figure 8-4, we can write the equilibrium equation as

$$\frac{\partial \sigma_{xx}}{\partial x}\Delta x\,\Delta y\,\Delta z = \rho\,\Delta x\,\Delta y\,\Delta z\frac{\partial^2 U}{\partial t^2} \tag{8-13}$$

$$\text{or} \quad E\frac{1-\nu}{(1+\nu)(1-2\nu)}\frac{\partial^2 U}{\partial x^2} = \rho\frac{\partial^2 U}{\partial t^2} \tag{8-14}$$

Furthermore, we can derive the one-dimensional wave equation as follows:

$$\frac{\partial^2 U}{\partial x^2} = \frac{1}{C_L^2}\frac{\partial^2 U}{\partial t^2} \tag{8-15}$$

where C_L is called the longitudinal wave velocity. For the current case, i.e., a one-dimensional strain case, C_L equals

$$C_L^2 = \frac{E}{\rho}\frac{1-\nu}{(1+\nu)(1-2\nu)} = \frac{\lambda + 2\mu}{\rho} \tag{8-16}$$

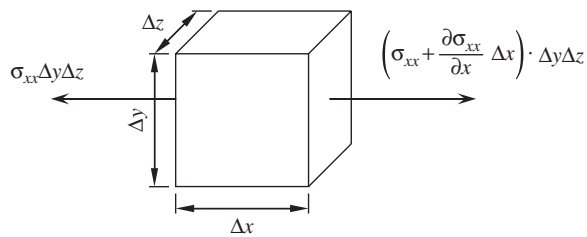

Figure 8-4 A unit element for stress consideration

For the one-dimensional stress case, we have

$$C_L^2 = \frac{E}{\rho} \tag{8-17}$$

8.2.2 Solution for a 1D wave equation

8.2.2.1 Longitudinal wave case

The wave equation for the longitudinal case is

$$\frac{\partial^2 U}{\partial x^2} = \frac{1}{C_L^2}\frac{\partial^2 U}{\partial t^2} \tag{8-15}$$

where C_L represents the longitudinal wave velocity, and

$$C_L^2 = \frac{E}{\rho} \qquad \text{for plane stress} \tag{8-18}$$

$$C_L^2 = \frac{\lambda + 2\mu}{\rho} \qquad \text{for plane strain} \tag{8-19}$$

It is clear that the wave equation is a partial differential equation and a function of both space coordinates and time. To get the solution for the wave equation, let us introduce two new parameters, α and β, and assume that

$$\begin{aligned} \alpha &= t - \frac{x}{C_L} \\ \beta &= t + \frac{x}{C_L} \end{aligned} \tag{8-20}$$

Furthermore, we can get:

$$\frac{\partial}{\partial t} = \frac{\partial}{\partial \alpha} + \frac{\partial}{\partial \beta} \tag{8-21}$$

$$\text{and} \quad \frac{\partial^2}{\partial t^2} = \frac{\partial^2}{\partial \alpha^2} + 2\frac{\partial^2}{\partial \alpha \partial \beta} + \frac{\partial^2}{\partial \beta^2} \tag{8-22}$$

$$\text{and} \quad \frac{\partial}{\partial x} = \frac{1}{C_L}\left(-\frac{\partial}{\partial \alpha} + \frac{\partial}{\partial \beta}\right) \tag{8-23}$$

$$\text{and} \quad \frac{\partial^2}{\partial x^2} = \frac{1}{C_L^2}\left(\frac{\partial^2}{\partial \alpha^2} - 2\frac{\partial^2}{\partial \alpha \partial \beta} + \frac{\partial^2}{\partial \beta^2}\right) \tag{8-24}$$

Substituting Equations 8-20 through 8-24 into wave Equation 8-15, one gets

$$\frac{\partial^2 U}{\partial \alpha \partial \beta} = 0 \tag{8-25}$$

Now we can solve this equation easily through an integral process. The first integral is made with respect to β, and we have

$$\frac{\partial U}{\partial \alpha} = \bar{f}(\alpha) \tag{8-26}$$

The second integral is made with respect to α, giving

$$U = f(\alpha) + g(\beta) \tag{8-27}$$

$$\text{or} \quad U = f\left(t - \frac{x}{C_L}\right) + g\left(t + \frac{x}{C_L}\right) \tag{8-28}$$

This is the so called D'Alembert solution. The term $f(t - x/C_L)$ represents a pulse propagated with the velocity of C_L in the positive x-direction while $g(t + x/C_L)$ represents a pulse propagated with the velocity of C_L in the negative x-direction.

8.2.2.2 Transverse wave case

For a transverse wave, the particle vibrates in the y-direction while the wave moves in the x-direction, as shown in Figure 8-5. Thus, we have

$$\begin{aligned} U(x,t) &= \omega(x,t) = 0 \\ v(x,t) &\neq 0 \end{aligned} \tag{8-29}$$

Consequently, we have

$$\begin{aligned} \frac{\partial v}{\partial x} &\neq 0 \\ \gamma_{xy} &= \frac{\partial v}{\partial x} \end{aligned} \tag{8-30}$$

Furthermore, we can write

$$\sigma_{xy} = \mu \frac{\partial v}{\partial x} \tag{8-31}$$

where μ is the shear modulus of materials. The equilibrium equation can be written as

$$\frac{\partial \sigma_{xy}}{\partial x} \Delta x \Delta y \Delta z = \rho \Delta x \Delta y \Delta z \frac{\partial^2 v}{\partial t^2} \tag{8-32}$$

$$\text{or} \quad \frac{\partial^2 v}{\partial x^2} = \frac{1}{C_T^2} \frac{\partial^2 v}{\partial t^2} \tag{8-33}$$

$$\text{where} \quad C_T^2 = \frac{\mu}{\rho} \tag{8-34}$$

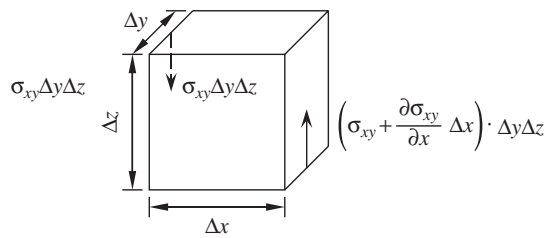

Figure 8-5 A unit element for the transverse wave case

Note that

$$C_L^2 = \frac{E}{\rho} \qquad \text{for plane stress} \tag{8-18}$$

$$C_L^2 = \frac{\lambda + 2\mu}{\rho} \qquad \text{for plane strain} \tag{8-19}$$

Thus, for the plane strain case, we have

$$\frac{C_L^2}{C_T^2} = \frac{2(1-v)}{1-2v} \tag{8-35}$$

For the plane stress case, we have

$$\frac{C_L^2}{C_T^2} = 2(1+v) \tag{8-36}$$

The solution of the S-wave equations can be obtained by using the same methods and procedures as the longitudinal wave case. The solution of the S-wave equation is

$$U(x,t) = f\left(t - \frac{x}{C_T}\right) + g\left(t + \frac{x}{C_T}\right) \tag{8-37}$$

This is exactly the same as the longitudinal case, Equation 8-28, with a substitution of C_T to C_L.

8.2.2.3 Observations on the D'Alembert solution

Since the D'Alembert solution for the longitudinal case and the transverse case has the same form, here we utilize the longitudinal case as an example. For the expression of

$$U(x,t) = f\left(t - \frac{x}{C_L}\right) + g\left(t + \frac{x}{C_L}\right) \tag{8-28}$$

the first differential with respect to x yields

$$\frac{\partial U}{\partial x} = -\frac{1}{C_L} f'\left(t - \frac{x}{C_L}\right) + \frac{1}{C_L} g'\left(t - \frac{x}{C_L}\right) \tag{8-38}$$

and the first differential with respect to t leads to

$$\frac{\partial U}{\partial t} = f'\left(t - \frac{x}{C_L}\right) + g'\left(t - \frac{x}{C_L}\right) \tag{8-39}$$

Thus, we have

$$\begin{aligned} \frac{\partial U}{\partial x} &= -\frac{1}{C_L}\left[\frac{\partial U}{\partial t} - 2g'\left(t + \frac{x}{C_L}\right)\right] \\ &= \frac{1}{C_L}\left[\frac{\partial U}{\partial t} - 2f'\left(t + \frac{x}{C_L}\right)\right] \end{aligned} \tag{8-40}$$

Hence, for $g' = 0$, we have

$$\begin{aligned} \sigma_{xx} &= (\lambda + 2\mu)\frac{\partial U}{\partial x} \\ &= -\rho C_L \frac{\partial U}{\partial t} \end{aligned} \tag{8-41}$$

and for $f' = 0$, we have

$$\sigma_{xx} = \rho C_L \frac{\partial U}{\partial t} \tag{8-42}$$

This means that the stress can be expressed as a function of the rate of wave propagation and different directions give different signs. The term ρC_L is also called acoustic impedance.

8.2.2.4 Specific solution of a wave equation

It should be noted that although the D'Alembert solution has a very clear physical meaning for a moving wave along either the positive x-direction or the negative x-direction, and sometimes its specific wave form can be obtained by utilizing the initial condition, it does not get a specific solution for most wave cases. Here, we introduce a generally applicable method to get the explicit solution of the wave equation, the variable separation method. It is a commonly used simple method. In this section, we use this method to show how to obtain an explicit solution for the wave equation. For the wave equation with a form of

$$\frac{\partial^2 U}{\partial x^2} = \frac{1}{C_L^2} \frac{\partial^2 U}{\partial t^2} \tag{8-15}$$

the solution of U must be a function of both x and t. The variable separation method assumes that x and t can be completely separated in the expression for U, i.e.

$$U = T \cdot X \tag{8-43}$$

where T is a function of t only when X is a function of x only. Then, substitution of the expression into the wave equation leads to two normal differential equations of T and X

$$X'' + \lambda X = 0 \tag{8-44}$$

$$T'' + \lambda C_L^2 T = 0 \tag{8-45}$$

It is much easier to solve the two normal differential equations using characteristic equations. The constants accompanying the solution can be determined by the boundary conditions and the initial conditions. To further examine the features of the wave equation solution, let us take a look at the solution in the form of

$$U\ (x, t) = A \cos\left[k\ (x - C_L t)\right] = A \cos\left(kx - \omega t\right) \tag{8-46}$$

where A is the amplitude of a wave, a measure of the maximum disturbance in the medium during one wave cycle or the maximum distance from the highest point of the crest to the mean value. The units of the amplitude depend on the type of wave: waves on a string have an amplitude expressed as a distance (meter), sound waves as pressure (pascal), and electromagnetic waves as the amplitude of the electric field (volt/meter). The amplitude may be constant (in which case the wave is a continuous wave), or may vary with time and/or position. The form of the variation of amplitude is called the envelope of the wave.

The variable k is called the wave number, which represents how many complete waves occur in a given period. The wave number is related to the wavelength by the equation

$$k = \frac{2\pi}{\lambda} \tag{8-47}$$

The physical meaning of the wavelength (denoted as λ) is the distance between two sequential crests (or troughs). This generally is measured in meters; it is also commonly measured in nanometers for the optical part of the electromagnetic spectrum.

The variable ω is called angular frequency, representing the frequency in terms of radians per second. It is related to the frequency by

$$\omega = 2\pi f = \frac{2\pi}{T} \tag{8-48}$$

where T is the period of the wave motion and is the time required for one complete cycle in the oscillation of a wave. The frequency f defines the number of periods per unit of time (for example, one second) and is measured in hertz. The frequency and period are related by

$$f = \frac{1}{T} \tag{8-49}$$

In other words, the frequency and period of a wave are reciprocals of each other. There are two velocities that are associated with waves. The first is the phase velocity, which gives the rate at which the wave propagates, and is given by

$$\upsilon_{\mathrm{p}} = \frac{\omega}{k} = \lambda f \tag{8-50}$$

The second is the group velocity, which gives the velocity at which variations in the shape of the wave's amplitude propagate through space. This is the rate at which information can be transmitted by the wave. It is given by

$$\upsilon_{\mathrm{g}} = \frac{\partial \omega}{\partial k} \tag{8-51}$$

For a fixed $t(t = t_{\mathrm{i}})$, $U\ (x,\ t)$ becomes a periodic function in x as shown in Figure 8-6. The length between two positive peaks or two negative peaks is called the wavelength:

$$\lambda = \frac{2\pi}{k} \tag{8-52}$$

where k is the wave number. For a fixed x, we have a traveling harmonic wave

$$\begin{aligned} U\ (x_i, t) &= A\cos\left[k\ (x_i - C_{\mathrm{L}}t)\right] \\ &= A\cos\left[kx_i - kC_{\mathrm{L}}t\right] \\ &= A\cos\left[kx_i - \omega t\right] \end{aligned} \tag{8-53}$$

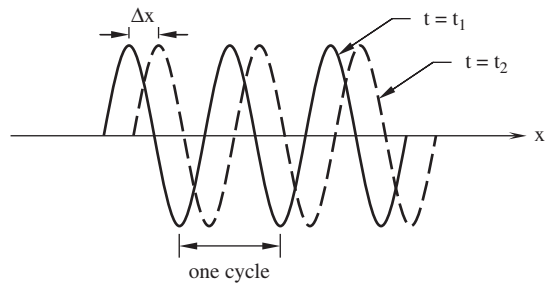

Figure 8-6 A representative periodic function

We can derive the following relationships:

$$\begin{aligned} T &= \frac{2\pi}{\omega} \\ f &= \frac{1}{T} = \frac{\omega}{2\pi} \\ \omega &= 2\pi f \\ k &= \frac{2\pi f}{C_{\mathrm{L}}} \end{aligned} \tag{8-54}$$

Example of the variable separation method

Solve the following 1D wave equation using the variable separation method.

$$\begin{aligned} U_{xx} &= \frac{1}{C_{\mathrm{L}}^2} U_{tt} \\ U\,|_{x=0} &= 0 \\ U\,|_{x=l} &= 0 \end{aligned}$$

Solution:

$$\begin{aligned} \text{Let} \quad U &= XT \\ \frac{\partial^2 U}{\partial x^2} &= X''T \\ \frac{\partial^2 U}{\partial t^2} &= T''X \\ X''T &= \frac{1}{C_{\mathrm{L}}^2} T''X \\ \Rightarrow \frac{X''}{X} &= C_{\mathrm{L}} \frac{T''}{T} = -\lambda \end{aligned}$$

Then, we have

$$\begin{aligned} &X'' + \lambda X = 0 \\ &T'' + \lambda C_{\mathrm{L}}^2 T = 0 \\ &\text{For} \quad X'' + \lambda X = 0, \\ &r^2 + \lambda = 0 \\ &r = \pm\sqrt{-\lambda} \end{aligned}$$

The first case is $\lambda < 0$:

$$X(x) = C_1 e^{\sqrt{-\lambda}x} + C_1 e^{-\sqrt{-\lambda}x}$$

From boundary conditions $X(0) = 0$ and $X(\mathrm{l}) = 0$,

$$\begin{cases} C_1 + C_2 = 0 \\ C_1 e^{\sqrt{-\lambda}l} + C_2 e^{-\sqrt{-\lambda}l} = 0 \end{cases}$$

and $C_1 = C_2 = 0$ (no meaning).

The second case is $\lambda = 0$:

$$X(x) = C_1 x + C_2$$

From boundary conditions $X(0) = 0$ and $X(\mathrm{l}) = 0$,

$$\begin{cases} C_2 = 0 \\ C_1 l + C_2 = 0 \end{cases}$$

Again, $X(x) \equiv 0$ (No meaning)
The third case is $\lambda > 0$:

$$X(x) = C_1 \cos\sqrt{\lambda}x + C_2 \sin\sqrt{\lambda}x$$

From boundary conditions $X(0) = 0$ and $X(\mathrm{l}) = 0$,

$$\begin{cases} C_1 = 0 \\ C_2 \sin\sqrt{\lambda}l = 0 \end{cases}$$

Since $C_2 \neq 0$, $\sin\sqrt{\lambda}l = 0$

$$\sqrt{\lambda}l = n\pi, \sqrt{\lambda} = \frac{n\pi}{l}, \lambda = \frac{n^2\pi^2}{l^2}$$

$$\Rightarrow X(x) = C_2 \sin\frac{n\pi}{l}x$$

From $T'' + \lambda C_{\mathrm{L}}^2 T = 0$

Let $T(t) = A\cos\frac{n\pi C_L}{l}t + B\sin\frac{n\pi C_L}{l}t$

Thus,

$$U(x,t) = \left(A'\cos\frac{n\pi C_{\mathrm{L}}}{l}t + B'\sin\frac{n\pi C_{\mathrm{L}}}{l}t\right)\sin\frac{n\pi x}{l}$$

8.3 REFLECTED AND TRANSMITTED WAVES

As mentioned above, the major types of body waves are longitudinal (P-) waves and transverse (S-) waves. For longitudinal waves, the propagation and particle motion directions are the same. Longitudinal waves can propagate in solids, liquids, and gases and are the most widely utilized wave modes for nondestructive testing of materials and structures. On the other hand, shear waves have particle motion transverse to the direction of the propagation of the wave. Shear waves cannot pass through liquids and are thus limited to solid inspection only. The reflection and transmission behavior of the wave front at an interface plays an important role in ultrasonic investigations. The wave front defines the leading edge of a stress wave as it propagates through a medium. The reflection and transmission describe the behavior of the wave front at an interface of two different materials. The acoustic impedance ratio of two materials plays an important role in determining the reflection and transmission parameters. The acoustic impedance is defined as a product of density and wave velocity of a material.

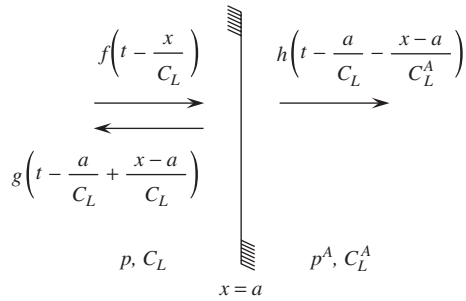

Figure 8-7 One-dimensional wave propagation at an interface between two mediums

The reflection and transmission behavior of the wave front at an interface plays an important role in ultrasonic investigations and provides the basis of determining the presence of a flaw and other anomalies. Here, let us consider a one-dimensional wave propagation case, as in Figure 8-7. The figure shows that two media have different material properties with a boundary, in which ρ and C_{L} are the density and longitudinal wave velocity for medium I, while ρ^{A} and $C_{\mathrm{L}}^{\mathrm{A}}$ are for medium II. A plane wave traveling in medium I approaches the boundary from the left. This wave front is parallel to the boundary and is designed as the incident wave. Upon striking the boundary, part of the energy is reflected back to medium I and part of it is transmitted into medium II through the boundary. Their portions of energy transmitted and reflected are a function of the properties of media I and II. The displacements for incident (i), reflected (r), and transmitted (t) waves are as follows:

$$\begin{aligned} U^i &= f\left(t-\frac{x}{C_{\mathrm{L}}}\right) \\ U^r &= g\left(t-\frac{a}{C_{\mathrm{L}}}+\frac{x-a}{C_{\mathrm{L}}}\right) \\ U^t &= h\left(t-\frac{a}{C_{\mathrm{L}}}-\frac{x-a}{C_{\mathrm{L}}^{\mathrm{A}}}\right) \end{aligned} \tag{8-55}$$

where U^{i} is the displacement of incident wave; U^{r} the displacement of reflected wave; U^{t} the displacement of transmitted wave; C_{L} the longitudinal wave velocity for medium I; and $C_{\mathrm{L}}^{\mathrm{A}}$ for medium II.

At the interface ($x = a$), stress continuity and displacement compatibility have to be satisfied. From these conditions, we can obtain the relationships

$$\begin{aligned} A_{\mathrm{R}} &= \frac{1-\dfrac{\rho^{\mathrm{A}}C_{\mathrm{L}}^{\mathrm{A}}}{\rho C_{\mathrm{L}}}}{\dfrac{\rho^{\mathrm{A}}C_{\mathrm{L}}^{\mathrm{A}}}{\rho C_{\mathrm{L}}}+1}A_{\mathrm{I}} = \frac{1-z}{z+1}A_{\mathrm{I}} \\ A_{\mathrm{T}} &= \frac{2\rho C_{\mathrm{L}}}{\rho^{\mathrm{A}}C_{\mathrm{L}}^{\mathrm{A}}+\rho C_{\mathrm{L}}}A_{\mathrm{I}} = \frac{2}{z+1}A_{\mathrm{I}} \end{aligned} \tag{8-56}$$

where A_R is the displacement amplitude of reflected wave; A_I the displacement amplitude of incident wave; and A_T the displacement amplitude of transmitted wave; and

$$\sigma_R = \frac{\frac{\rho^A C_L^A}{\rho C_L} - 1}{\frac{\rho^A C_L^A}{\rho C_L} + 1}\sigma_I = \frac{z-1}{z+1}\sigma_I = R\sigma_I$$
$$\sigma_T = \frac{2\rho^A C_L^A}{\rho^A C_L^A + \rho C_L}\sigma_I = \frac{2z}{z+1}\sigma_I = T\sigma_I \tag{8-57}$$

where R and T are the reflection and transmission parameters. These expressions show that the ratio of the acoustic impedances completely determines the nature of the reflection and transmission at the interface. They can be plotted as a function of the ratio of acoustic impedance of the two materials, as shown in Figure 8-8. Let's look at a few extreme cases.

For $\rho^A C_L^A / \rho C_L = 0$, $T = 0$ and $R = -1$, which means that the incident wave is reaching a free surface. No stress can be transmitted. To satisfy the zero stress boundary condition, the displacement must be twice the displacement of the incident wave. The reflected wave has the same amplitude as the incident wave but opposite polarity. It implies that a free end will reflect a compression wave to a tension wave with identical amplitude and shape and vice versa.

For $\rho^A C_L^A / \rho C_L = 1$, it means the same materials, $T = 1$ and $R = 0$. The wave is completed transmitted.

For $\rho^A C_L^A / \rho C_L = \infty$, it goes to infinity, which means that an incident wave is approaching a fixed end. No displacement can occur, $U^t = 0$. The stress at the boundary is twice that of the incident wave and the reflected wave has the same amplitude and polarity as the incident wave.

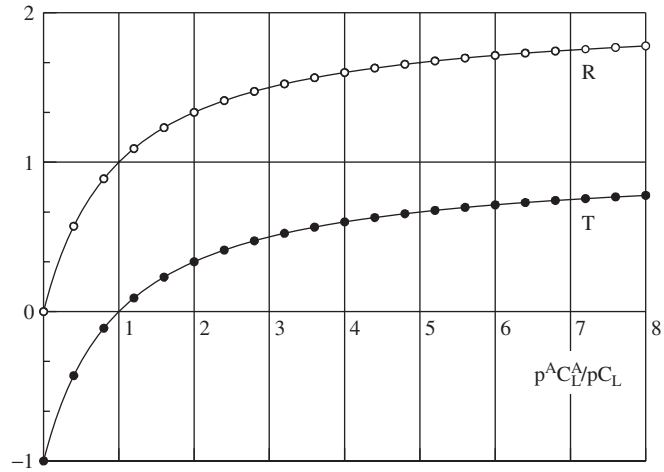

Figure 8-8 The reflection and transmission coefficients vs. acoustic impedance

When the wave fronts propagate on the boundary between two materials with different properties, with an angle not normal to the interface, the reflection and transmission will depend on the angle. Let θ be the wave incidence angle. The reflection angle of the wave is also θ. However, the angle of transmission, β, is a function of the angle of incidence, θ, and the ratio of wave velocities in the two media as given by Snell's law:

$$\sin\beta = \frac{C_{\mathrm{L}}^{\mathrm{A}}}{C_{\mathrm{L}}}\sin\theta \tag{8-58}$$

Stress waves can change their mode of propagation when striking a boundary at an oblique angle. Depending on the angle of incidence, a P-wave can be partially reflected as both P- and S-waves and can be transmitted as both P- and S-waves. An S-wave reflects and transmits at angles, determined using Snell's law, which are less than the angles of reflection and transmission for a P-wave.

8.4 ATTENUATION AND SCATTERING

An acoustic wave traveling through engineering materials will lose energy for a variety of reasons. This behavior can lead to a loss in amplitude and is sometimes called attenuation. Attenuation is generally expressed in the form of

$$P = P_0 e^{aL} \tag{8-59}$$

where P_0 is original pressure level at a source or a reference point; P the pressure level at measured place; a the attenuation coefficient (nepers per meter); and L the distance between the two points P_0 and P.

Ultrasonic pulse attenuation is typically expressed in units of decibels (dB). Decibels are based on a logarithmic scale and are convenient to use over a large range. The relative sound pressure level (SPL) is defined as

$$\mathrm{SPL} = 20\log\frac{P}{P_0} \tag{8-60}$$

Considering two points,

$$\mathrm{SPL}_1 - \mathrm{SPL}_2 = 20\log\frac{P_1}{P_2} \tag{8-61}$$

$$\text{or} \quad \alpha\mathrm{L} = 20\log\frac{P_1}{P_2} \tag{8-62}$$

As an example, let us look at an attenuation test conducted on an aluminum specimen. The test results showed that a pulse traveling 200 mm had an amplitude of 70% as great as that of a pulse, which had traveled 100 mm. For this case, the α is

$$\alpha = \frac{20}{L}\log\frac{P_1}{P_2} = \frac{20}{0.1}\log\frac{1}{0.7} = 31\ \mathrm{dB/m} \tag{8-63}$$

It should be pointed out that a and α have a relationship of $\alpha = 8.686\,a$.

8.5 MAIN COMMONLY USED NDT-CE TECHNIQUES

8.5.1 Ultrasonic technique

8.5.1.1 Principle of ultrasound

As mentioned earlier, the ultrasonic technique (UT) is based on time-varying deformations or vibrations in materials, which are generally referred to as acoustics. All material substances are composed of atoms, which may be forced into vibrational motion about their equilibrium positions. Many different patterns of vibrational motion exist at the atomic level, but most are irrelevant to acoustics and ultrasonic testing. Acoustics is focused on particles that contain many atoms that move in unison to produce a mechanical wave. When a material is not stressed in tension or compression beyond its elastic limit, its individual particles perform elastic oscillations. When the particles of a medium are displaced from their equilibrium positions, internal (electrostatic) restoration forces arise. It is these elastic restoring forces between particles, combined with the inertia of the particles, which lead to the oscillatory motions of the medium. There are many different UT methods, such as pulse velocity, pulse echo, frequency shift, ultrasonic resonance spectroscopy, 3D images, time of flight diffraction (TOFD), and synthetic aperture focusing technique (SAFT). Among all the existing NDT methods, the pulse velocity and pulse echo methods (PE) are the dominant ones. All the UT methods obey the laws of elastic waves, but different methods follow different physical principles.

The following are the basic characteristics of elastic waves. Two kinds of elastic waves propagate in a homogenous isotropic solid medium: the longitudinal wave and the transverse wave. The velocity of the longitudinal wave and the transverse wave has been given in Equations 8-28 and 8-37. It can be seen from the expressions that the wave velocities are functions of the Young's modulus, Poisson's ratio, and the density of the material only. Hence, when the ultrasonic velocities and density of the material are known, then the elastic modulus can be easily deduced. This forms the basis of the pulse velocity method.

There are another two important wave types in solids. One is the surface wave and the other is the plate wave. Surface waves, also called Rayleigh waves, travel from the surface of a relatively thick, solid material penetrating to a depth of one wavelength. Surface waves combine both a longitudinal and transverse motion to create an elliptical orbit motion. The major axis of the ellipse is perpendicular to the surface of the solid. As the depth of an individual atom from the surface increases, the width of its elliptical motion decreases. Surface waves are generated when a longitudinal wave intersects a surface near the second critical angle and they travel at a velocity between 0.87 and 0.95 of a shear wave. Rayleigh waves are useful because they are very sensitive to surface defects (and other surface features) and they follow the curvature of a surface. Because of this, Rayleigh waves can be used to inspect areas that other waves might have difficulty in reaching. Plate waves are similar to surface waves except they can be generated only in a thin, plate-like specimen, a few wavelengths thick. Lamb waves are the most commonly used plate waves in NDT. Lamb waves are complex vibrational waves that propagate parallel to the test surface throughout the thickness of the material. Propagation of Lamb waves depends on the density and the elastic properties of the material. They are also influenced a great deal by the test frequency and material thickness. Lamb waves are generated at an incident angle in which the parallel component of the velocity of the wave in the source is equal to the velocity of the wave in the test material. Lamb waves can travel several meters in steel and so are useful to scan plates, wire, and tubes.

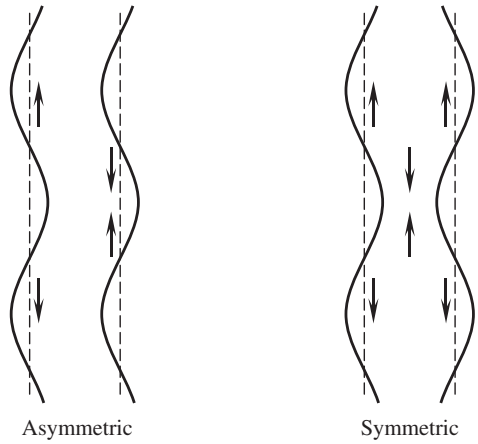

Figure 8-9 Asymmetric and symmetric Lamb waves

With Lamb waves, a number of modes of particle vibration are possible, but the two most common are symmetrical and asymmetrical, as shown in Figure 8-9. The complex motion of the particles is similar to the elliptical orbits for surface waves. Symmetrical Lamb waves move in a symmetrical fashion about the median plane of the plate. This is sometimes called the extensional mode because the wave is "stretching and compressing" the plate in the wave motion direction. Wave motion in the symmetrical mode is most efficiently produced when the exciting force is parallel to the plate. The asymmetrical Lamb wave mode is often called the *flexural mode* because a large portion of the motion is in a normal direction to the plate, and little motion occurs in the direction parallel to the plate. In this mode, the body of the plate bends as the two surfaces move in the same direction.

The ultrasonic waves will be attenuated during propagation. There are three main mechanisms: beam spreading, absorption by the medium, and scattering by inhomogeneities, as discussed in the previous section. The ultrasonic wave is also subjected to reflection, refraction, diffraction, and scattering when it encounters an interface between two media with different acoustic impedances. The elastic wave behavior at the interface obeys Snell's law and is complex. The longitudinal wave and transverse wave can transform each other, which is called mode conversion. The reflection factor depends on the difference of the acoustic impedance Z_i of the two materials and the incidence angle, as mentioned earlier. In the simplest case, the wave is of normal incidence, there is no mode conversion, and the reflection factor can be obtained by using Equation 8-57. The reflected wave and the scattered wave are usually called echoes. The time of flight of an echo is determined by the distance it is propagated and the wave velocity

$$t = \frac{2h}{c} \tag{8-64}$$

where h is the thickness of the specimen. Combining the data of the reflection ratio and the TOF, one can deduce the thickness and material type of the layers. This forms the theoretical basis of the pulse echo method. All the velocity, TOF, and reflection ratio data can be used to form a 2D or 3D image of the specimen by means of computer tomography (CT), synthetic aperture focusing technique, C-scan, or B-scan methods.

8.5.1.2 Technical features and advances

When applying UT to concrete or other cement-based materials and structures, some difficulties can be encountered due to the material features. First, concrete is an inhomogeneous, porous, multiscale, and heterogeneous building material. Reinforced concrete is also anisotropic. The elastic wave behavior becomes more complicated when it propagates in these kinds of materials. Second, the surface condition of a cement-based material such as concrete is usually very rough as compared to metals, which makes the coupling between the UT transducer and the concrete surface difficult to realize. Finally, concrete constructions, such as buildings and bridges, are usually very large and have very complicated shapes that bring complexity to the carrying out of inspection and analysis of the complicated data collected. All of these require attention to the special technique features on conventional NDT-UT techniques.

(a) *Working frequency*: To overcome the difficulties mentioned above, first of all, relative lower frequencies, say hundreds of kHz, are usually used for UT inspection in concrete rather than the higher frequencies used for UT applications in the metallurgical field. Ultrasonic wave scattering is significantly dependent on the frequency, and the higher the frequency, the stronger the scattering. Under UT frequency ranges, the scattering is proportional to the fourth order of the frequency. Hence, using lower frequencies in concrete can greatly reduce the clutter and noise generated by the scattered waves at the boundaries of aggregates. Specifically, a low-frequency wave, with a wavelength as large as 4–5 times of the nominal size of the maximum aggregate, is preferred for UT inspection in concrete. Low-frequency waves can also penetrate deep into the specimen, as the attenuation of elastic waves is reduced as the working frequency goes down. However, since the resolution of UT inspection is limited to half the wavelength, the working frequency cannot go too low, otherwise there is insufficient resolution.

(b) *Acoustic coupling*: Mechanical waves may lose significant strength at an interface between air and a solid material because the difference of the acoustic impedance between air and solid materials is very large. As more than 95% of ultrasound energy will be reflected from a smooth air–solid interface, UT-NDT is very effective for detecting cracks or voids inside solids. Hence, a coupling between a UT transducer and solid material to be inspected is a necessary measure to ensure a meaningful measurement. In the case of a concrete structure, the surfaces of the specimens are usually in a rough condition from the UT point of view, and it is difficult to couple the transducers well. To make a good contact for a UT transducer with concrete, the concrete surface is usually smoothed with sandpaper before coupling materials are applied. The commonly used coupling materials include fast-set glue, grease, and oil. Some kinds of fast-solidifying cement have also been developed as a couplet for UT inspection in concrete (Krause et al., 1995).

To test large structures like bridge piles, the cross-hole sonic logging technique (CSL) is very useful (Sack and Olson, 1995). The coupling problem can be partly solved by the CSL method. A set of parallel tubes is built in the structure. The tubes are filled with water, and the ultrasonic transducers (probes) are hung inside the tubes. The probes are worked in the transmission mode without coupling problems. It is easy to take the measurements of the ultrasonic pulse velocity of the B-scan, etc. CSL also can work in the tomogram configuration. By means of the new digital technique, the states of the object tested at different periods can be compared. That is to say, it can be used as a both instant and long-term monitor. The CSL technique can undertake quality assurance of drilled shafts, slurry walls, steel footings, piers and dams, etc.

(c) High-power transducer: Another way to overcome the coupling problem, is to develop a stronger emitter and a more sensitive receiver. In the 1990s, an airborne ultrasonic flaw detector

was developed. A pair of powerful 40-kHz transducers produce an ultrasound beam to punch through and test brick or concrete samples without contact (APCNDT, 1998). The powerful transducers matched the high-performance electrical circuits, which greatly enhanced the ability of the NDT-UT instruments.

(d) Signal processing and displaying techniques: Recently, a fast sampling frequency and low-cost analogue to digital transform device (ADT) has been developed and is readily available. It allows the digital signal processing of high-frequency signals to become possible. Relying on the DSP, such as by applying spectrum analysis, digital filtering, self/co-relations, and artificial neural networks, the application of traditional UT has become broader. Now signal processing is so important that it is an essential part of an UT technique.

(e) *Wave propagation and modeling*: In concrete, the ultrasonic wave propagation is complicated. To understand the phenomenon computer modeling and simulation can be performed by modern powerful computers. The production parameters, such as the maximum aggregate size, cement mix, moisture content, and pore size are selected to meet practical conditions.

8.5.1.3 Applications

The applications are wide for UT. For example, it can be used for quality assurance, condition assessment, and reliability evaluation, can locate and identify defects, cracks, fractures, voids, and inhomogeneities, can measure the thickness and size of defects, and can estimate the strength of concrete for bridges, drilled shafts, slurry walls, and dams.

(a) *Scanning technique for flaw detection*: The pulse-echo method is the simplest and most common ultrasonic application method. In this method, a single piezoelectric transducer is used to excite an acoustic wave in the object being examined and it moves around to detect the inside flaws by receiving the reflected signal and by using an imaging technique. There are three kinds of scan methods for flaw detection—A-scan, B-scan, and C-scan—in the presentation of pulse-echo data.

The A-scan is known as an amplitude scan. It can be done by placing a transducer directly against the solid material to be examined and making contact between the transducer and the sample with grease. It displays the signal received in an amplitude to time base. An adjustable threshold of the amplitude level is used to suppress the noise. Suppose that the transducer emits an acoustic pulse, the generated acoustic pulse passes into the specimen and is reflected by the acoustic impedance discontinuities caused by the presence of flaws. The returned echo signal is received at the transducer and is amplified and displayed as a function of time on an oscilloscope. Since the amplitude of the returned echo depends on the size and shape of the flaw, a rough estimate of the size of the flaw can be obtained by measuring the amplitude of returned echo. Figure 8-10 shows the flowchart of the A-scan technique.

As there are usually many signals stemming from the multireflection and multiscattering from the inside structure boundaries or the inhomogeneities, the A-scan is difficult to understand and it is easy to lose a lot of information at times, especially for applications in civil engineering. An alternative display format is the B-scan, which is widely used in medical diagnostics. In the B-scan, the echoes are displayed as bright points, of which the brightness is proportional to the echo amplitude, the point is located in a line, and the distance from the starting point of the line represents the time of flight of the echo. The line direction is along the ultrasonic wave direction of propagation. By scanning the ultrasonic wave source along a line, a two-dimensional plot is formed. Hence, a B-scan display forms a longitudinal cross-sectional plot of the specimen tested. In other words, one can use a set of A-scan data to form a B-scan data set.

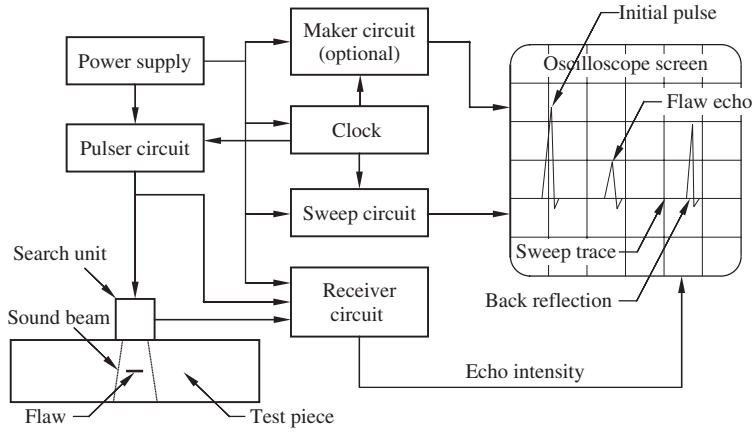

Figure 8-10 Sketch of the A-scan technique

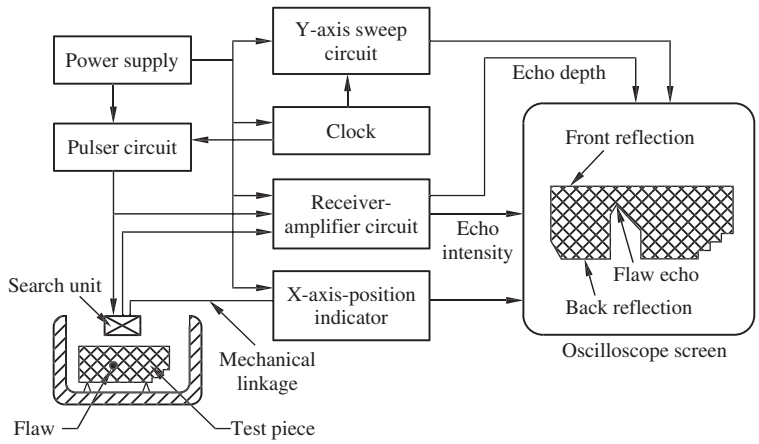

Figure 8-11 Schematics of B-scan technique

The B-scan is also called a brightness scan, in which the returned echo signal is used to modulate the intensity of the spot on an oscilloscope. This format provides a quantitative display of time-of-flight data obtained along a line on the test piece. The B-scan display shows the relative depth of reflectors and is used mainly to determine size (length in one direction), location (both position and depth), and, to a certain degree, the shape and orientation of large flaws. By this means, a crude picture of the structure within a material can be presented, as shown in Figure 8-11. B-scan is very popular in the medical field. The A-scan and B-scan systems are almost identical, but there are some differences between the two methods. B-scan allows the imaginary cross section to be viewed; in B-scan, echoes are indicated by bright spots on the screen rather than by deflections of the time trace. The position of a bright spot along the axis orthogonal to the search unit position axis indicates the depth of the echo within the test piece.

Another widely used display format is called a C-scan. The ultrasound source is moved on a two-dimensional surface. Every source point opens a time window at a fixed distance. Only

the echoes inside the window are displayed in a bright point format, of which the brightness is proportion to the amplitude of the echo. The co-ordinates of the point displayed are just those of the source. Thus, a lateral cross-sectional plot is formed. The depth in the specimen corresponds to the time window distance selected. B-scan and C-scan methods give more information than A-scan. For both B-scan and C-scan, digital image processing (DIP) techniques can be applied to extract more information. C-scan provides a semi-quantitative or quantitative display of signal amplitudes obtained over an area of the test piece surface. This information can be used to map out the position of flaws on a plan view of the test piece, as shown in Figure 8-12. A C-scan format also records time-of-flight data, which can be converted and displayed by image-processing equipment to provide an indication of the flaw depth. C-scan has an electronic depth gate that can allow echo signals to be received within a limited range to exclude the display of the front and back reflections.

(b) *S-wave reflection method for fresh concrete monitoring*: This ultrasonic technique has been proven to be very effective for nondestructive measurement of fresh and hardened cementitious composites. In the 1990s, a shear wave reflection method was developed at Northwestern University for hydration process monitoring of fresh concrete.

The method utilizes high-frequency (2.25-MHz) ultrasonic waves continuously monitoring the setting and hardening of concrete. The test setup is schematically shown in Figure 8-13. The

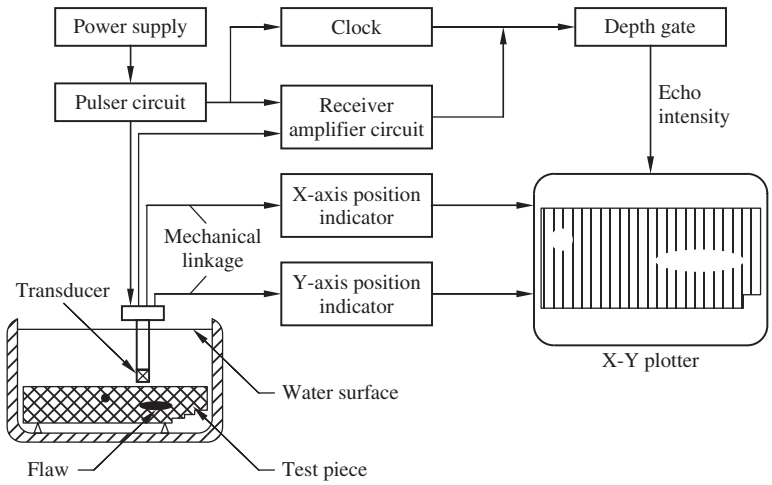

Figure 8-12 General description of C-scan technique

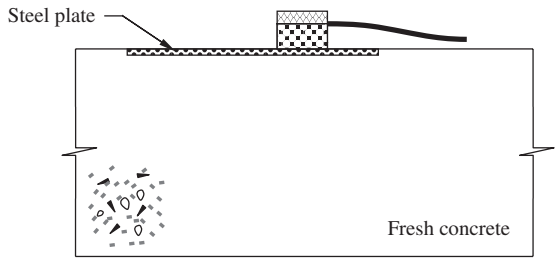

Figure 8-13 S-wave reflection method for monitoring concrete setting and hardening

transducer is placed on the top surface of a steel plate in contact with fresh concrete. The principle of the shear wave reflection measurement consists of monitoring the reflection coefficient of the ultrasonic waves at an interface formed between the steel plate and the concrete to be tested. Since a shear wave cannot pass though a liquid, the reflection factor at beginning of the hydration is very high. However, with the hydration process, the concrete changes into a more solid condition, and the reflection of the shear wave becomes weak due to the partial wave transmission into the concrete. Hence, the change of the reflection factor at the interface between steel plate and the concrete is related to the hydration process. The reflections of the shear waves from the steel–concrete interface are received from the transducer in the time domain. To calculate the reflection coefficient, the received signals in the time domain are transformed into the frequency domain by using the fast Fourier transform algorithm. The reflection loss, L, is then defined as

$$L = 1 - \frac{F_2(f)}{F_1(f)} \tag{8-65}$$

where the $F_2(f)$ is the amplitude of the reflection from steel–concrete interface in the frequency domain and $F_1(f)$ the amplitude of the emitted signal in the frequency domain. Typical reflection loss versus time is plotted in Figure 8-14. It can be seen that the curve can be divided into three stages. Up to point A, the reflection loss is almost 0, i.e., the shear wave is almost complete reflected. This implies that the concrete is in a liquid state. From point A to point B, the reflection loss is gradually increased, which implies that concrete is under a fast hardening process. After point B, the reflection loss curve becomes very flat, which signals that the concrete has reached the maturity stage.

The relationship between the reflection loss and the setting time, as well as the compressive strength of the concrete, can be established through a careful calibration process. Figure 8-15 shows the relationship between the setting time and the time at which point A in the reflection loss curve occurs. It can be seen that there is a linear relationship between the two parameters. Hence, there is a potential to utilize point A as an index to predict the setting time for concrete. Figure 8-16 shows the relationship between compressive strength and reflection loss factors. It can be seen that a bilinear relationship exists between the two parameters. The transition point is between 6 and 15 hours after casting. It can be seen from the figure that the compressive strength of a cement-based composite can be estimated from the reflection loss factor of a shear wave.

(c) *Longitudinal transmission method for fresh concrete*: This method utilizes ultrasonic waves to investigate the setting and hardening of cement-based materials, and was developed by

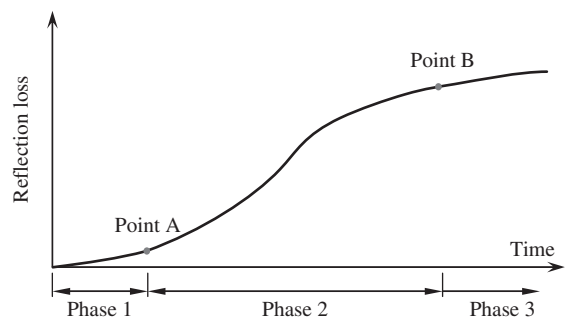

Figure 8-14 A typical reflection loss verus time plot

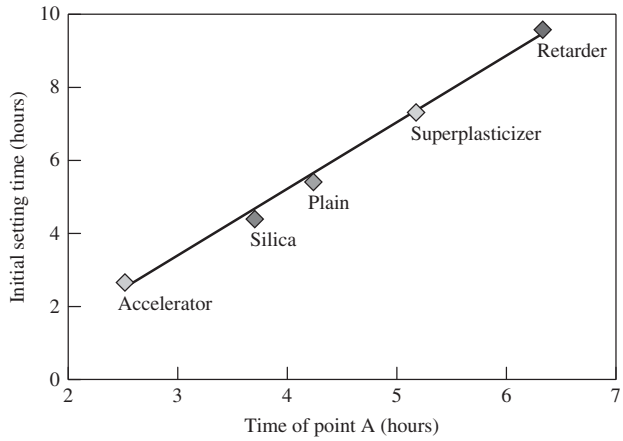

Figure 8-15 Relationship between setting time and reflection loss

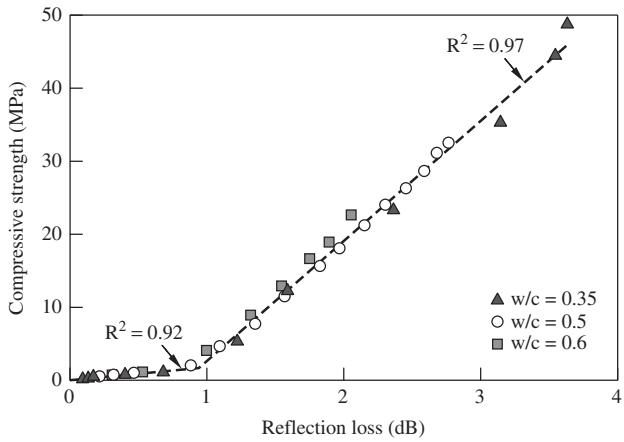

Figure 8-16 Relationship between compressive strength and reflection loss

Grosse and Reinhardt (1994). It measures the flight time of an ultrasonic pulse traveling through a known distance and then calculates the wave velocity. During the setting and hardening process, fresh concrete changes from a liquid state to a plastic state and then to a solid state. The wave velocity keeps increasing with the process. By interpreting the characteristic points on the wave velocity versus time curve, the behavior of fresh concrete can be identified. Furthermore, since the wave velocity is directly related to the modulus of elasticity of the concrete, the development of the modulus of elasticity can be interpreted by this method.

A typical apparatus for this technology is shown in Figure 8-17. The walls of the container are made of Plexiglas. At the center of the apparatus, a transmitter and a receiver are fixed on opposite sides of the container, and fresh concrete is placed between the two transducers. Once the container is fully filled with fresh concrete, the transmitter starts to emit a P-wave and the receiver receives the signal. The measurement can be continuously conducted and recorded. Since the distance between the two transducers is known, it is easy to calculate the velocity.

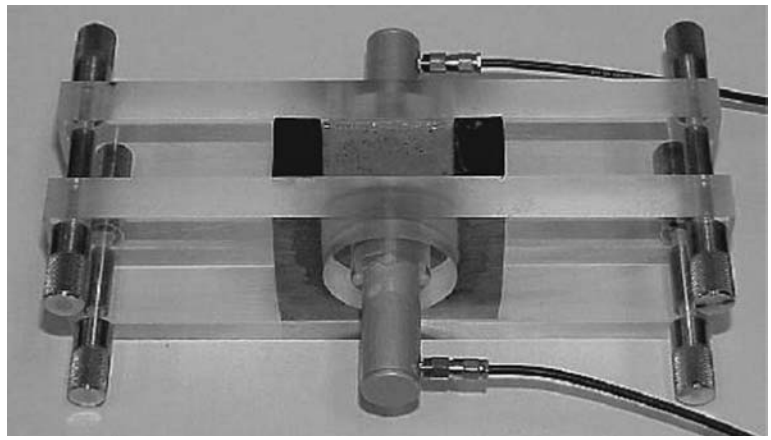

Figure 8-17 A typical apparatus for using the longitudinal transmission method

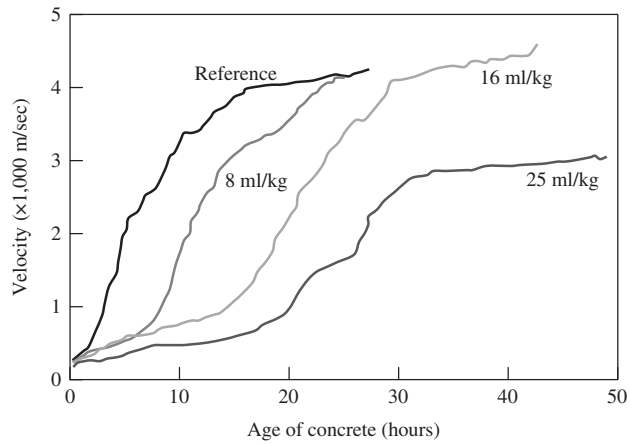

Figure 8-18 A representative plot of wave velocity versus time

A typical plot of the wave velocity versus time is shown in Figure 8-18. One limitation of this method is that it is difficult to perform on site.

(d) *Embedded transmission method for fresh concrete*: To make the transmission method feasible for on-site hydration monitoring of fresh concrete, an embedded ultrasonic system has been developed at the Hong Kong University of Science and Technology (Qin and Li, 2008). The measurement system includes a functional generator, power amplifier, pre-amplifier, and oscilloscope. An electrical pulse is first generated by an Agilent 33120A functional generator. Before being applied to the transmitter, the pulse is amplified by a power amplifier. The transmitter is excited by the input electrical pulse and then vibrated in its resonance mode, emitting ultrasonic waves. An electrical field is applied along the polarization direction, and, therefore, the ultrasonic waves are of the longitudinal type. The ultrasonic waves can be received by the receiver through changing the mechanical energy into electrical energy. The voltage of the receiver can be measured and recorded by the oscilloscope though a pre-amplifier. The oscilloscope is a 12-bit Agilent 5462A digital oscilloscope with a sampling frequency of 1 MHz.

This embedded ultrasonic system has many advantages. First, it has good coupling between the transducer and the matrix. Second, the method is very effective for hydration measurement of large-scale or underground concrete structures. Last, but not least, it can also be used to continuously monitor the structure during its entire service life. For a concrete structure, early-age performance can be monitored by the new system to provide guidance for construction quality control. After the concrete is cured and the strength is fully developed, the system can be used to detect damage accumulation or even impending disasters. Compared with traditional ultrasonic nondestructive methods, this method is inexpensive and effective for any-scale concrete structures. It meets all the health monitoring requirements of concrete structures from the fresh stage to the hardened stage.

The key element in the system is the homemade PZT. The transducer fabrication process includes the following steps: cutting PZT rods, welding coaxial wires to the positive and negative electrodes, coating the epoxy layer for insulation, coating the conductive layer as a shielding layer, and grounding. First, small PZT rods about 2 cm long were cut from a big PZT plate (from Hong Kong Piezo). The length direction was set along the poling direction. After welding a coaxial cable to the two electrodes of the piezo-rod, the patch and the coaxial cable were insulated using a thin layer of epoxy. Due to the embedment requirement, the insulation layer was laid very carefully. The insulation between the power line and the instrument circuit has little effect on the capacitive coupling. Capacitive coupled interference was mainly reduced by shielding the instrument circuit, using an envelope of high conductive material such as aluminum or copper that physically surrounds the instrument. Here, silver paint was used as the shielding layer. The shield was connected at one point to ground, thereby, encasing the circuit in a zero-voltage surface. Figure 8-19 shows the fabrication of the transducers.

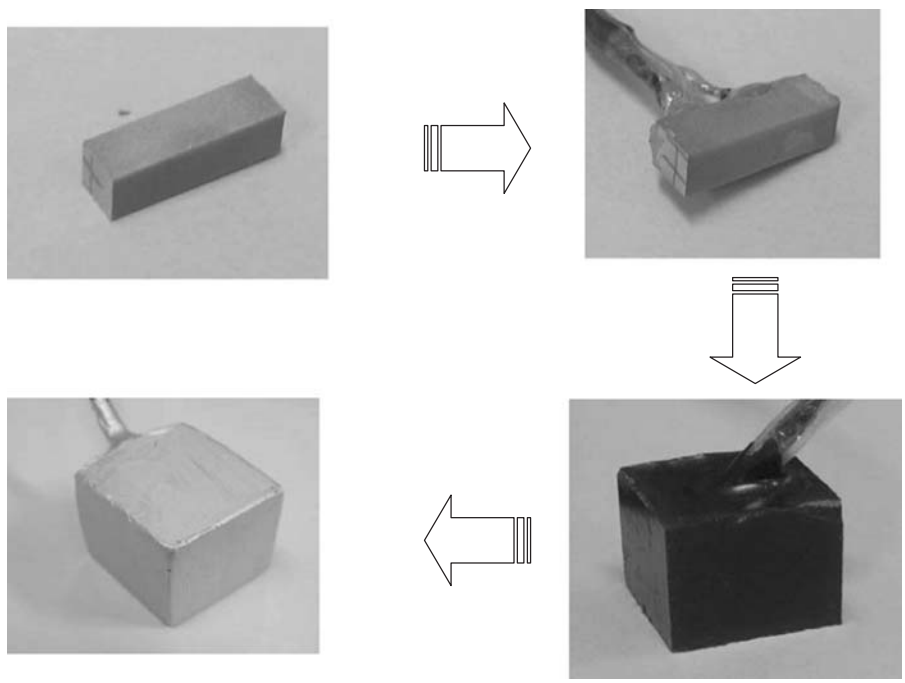

Figure 8-19 Fabrication process of the transducer

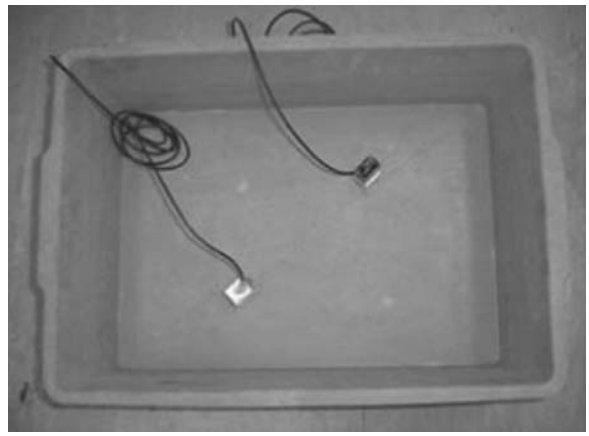

Figure 8-20 Placement of the transducers before casting

To measure the hydration process of fresh cement-based materials, the transducers should be fixed in a predetermined position in a formwork before the casting of fresh concrete or other cement-based materials. As an example, Figure 8-20 shows a placement of the transducers on the bottom of a plastic mold before casting. For this experiment, cement paste with a w/c ratio of 0.4, was mixed thoroughly for 5 minutes, and then was poured into the mold followed by a proper compaction to remove the entrapped air bubbles. After casting the fresh sample in the plastic box, the measurements were immediately started. During the experiment, one transducer, which was excited by an electrical pulse, acted as the signal source, while the other transducer acted as the receiver for ultrasonic signals. Figure 8-21 shows the input and output signals recorded by the two sensors. The input electrical signal is a step function of several hundred volts. The recorded signal from the receiver has very low amplitude, from several millivolts to several volts. The travel time is the interval between the onset time of the input pulse and the onset time

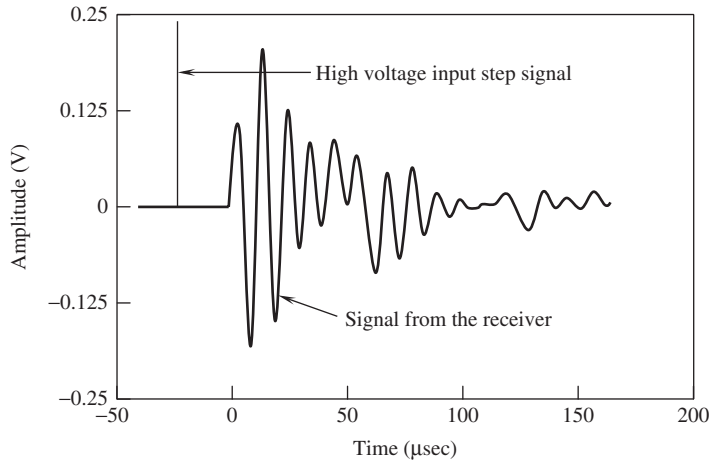

Figure 8-21 Input and output signals recorded by two sensors

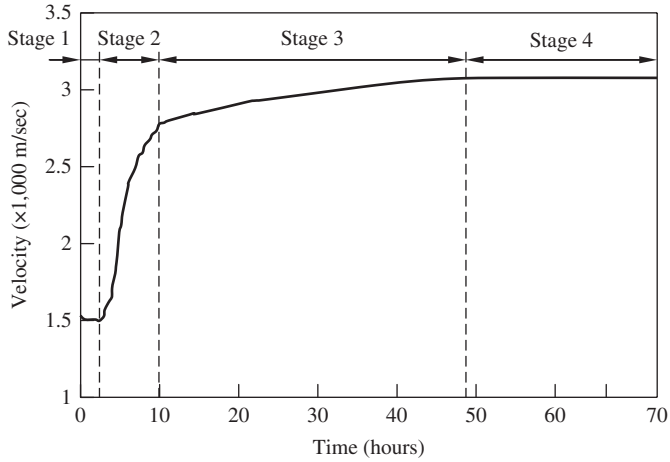

Figure 8-22 Development of the acoustic velocity in fresh concrete

of the received signal. A threshold is preset based on the noise level. The time when the signal exceeds the threshold is the onset time. In this study, because of the good coupling between the sensor and the specimen, the signal-to-noise level is quite high. It is easy to determine the onset time accurately according to the threshold. Knowing the travel distance, the velocity can be calculated.

Figure 8-22 shows the development of the velocity in fresh concrete paste. Based on the characteristic points on the experimental curves, evolution of ultrasonic pulse velocity (UPV) can be divided into four stages. In the first stage, the UPV remains nearly constant at around 1500 m/s. This period is related to the dissolution and dynamic balance stages of cement hydration. The wave velocity is very close to that of water. A period of rapid increase in the UPV appears after the dissolution and dynamic balance period, which corresponds to the rapid development of hydration products. When a critical quantity of hydration products is reached, percolation of solid phase seems to occur, and the UPV starts to increase. In stage 2, more and more hydration products are produced and intersected, and the stiffness or the modulus of the material increases rapidly. As a result, the UPV increases notably. In stage 3, the cement hydration process proceeds into diffusion control, and the growth rate of the hydration products slows down. The UPV thereafter increases slightly. In stage 4, a high hydration degree is reached and further hydration becomes minimal. Thus, the velocity development reaches a plateau. After the wave velocities are obtained, the wavelength, λ, and the dynamic modulus of elasticity, E, of the cement paste specimen at different ages can be calculated using the following equations:

$$\lambda = \frac{C_L}{f} \tag{8-66}$$

$$E = \rho C_L^2 \tag{8-67}$$

where C_L is the longitudinal wave velocity, f the resonant frequency, and ρ the density of the cement paste.

The calculated results are shown in Figure 8-23 for wavelength and in Figure 8-24 for dynamic modulus. It can be seen that at an early age, the wavelength decreases sharply due to the fast increase of the resonant frequency, although the velocity increases considerably in

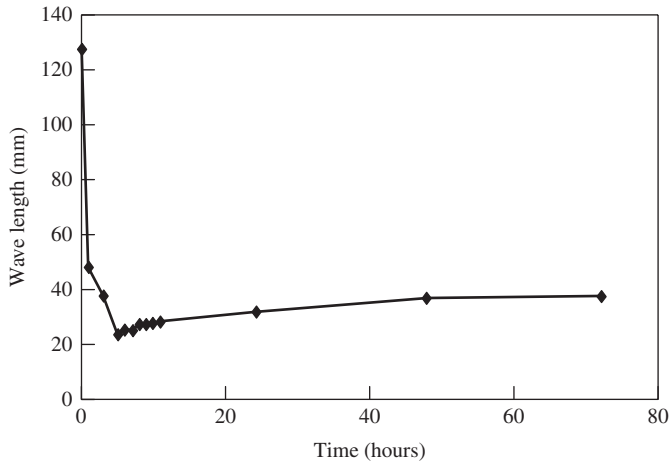

Figure 8-23 The calculated values of wavelength

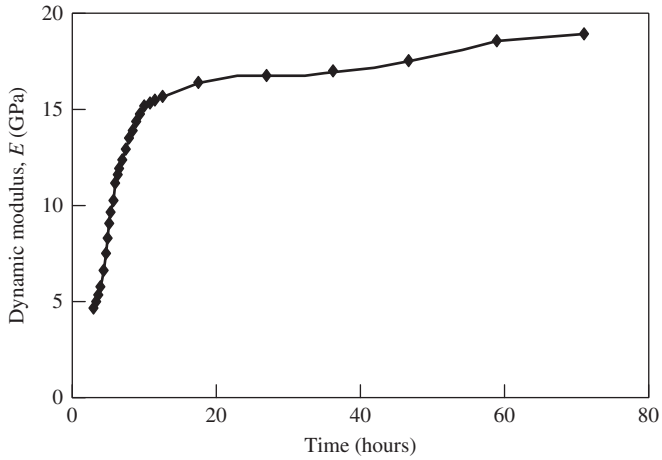

Figure 8-24 The calculated values of a dynamic Young's modulus

the same period. The dynamic modulus of elasticity increases with the hydration process. The mechanical properties and the microstructure development of the material can be assessed by using the calculated modulus.

8.5.2 Acoustic emission technique

The acoustic emission (AE) technique is one of the most important passive NDT techniques—it simply listens to "sounds" generated within materials. Acoustic emission is the physical process of an object quickly releasing its inner elastic energy in the form of stress waves when the object is subjected to external loads and/or environmental action. These stress waves, referred to as AE signals, are generated from localized sources, such as dislocations, microcracking, debonding, and other inside micro- as well as macrochanges in a stressed material. In concrete,

AE sources may also include the local stress distributions associated with chemical action, such as alkali–aggregate reaction and corrosion of steel inside concrete. The AE signals carry the source information and follow the elastic wave propagation rules in concrete materials. AE activities, thus, can reflect the damage process in a stressed specimen. The locations where AE events occur and the material properties inside the object can be deduced from the received AE signals.

These form the basis of the NDT-AE as an acoustic passive NDT technique. In other words, the NDT-AE is a technique to characterize the material properties and to identify the structure of the test specimen, or even occurring inside the specimen, by means of receiving these AE signals and analyzing their characteristics. The AE technique can be used to monitor the change of material conditions in real time and to determine the location of these emission events as well. It cannot detect a crack that already exists but is not propagated. Since AE is a result of local stress redistribution, any micromechanisms that will cause stress release can be the sources of AE. Some typical AE sources in concrete are summarized as follows:

- Microcrack and macrocrack initiation and propagation due to loading
- Separation of reinforcing members
- Mechanical rubbing of separated surfaces
- Corrosion of reinforced steel inside concrete
- Debonding of different interfaces, such as the interfaces between steel bar and concrete and between ceramic tile and concrete substrate
- Matrix cracking due to formation of aggressive chemical product, such as ASR gel
- Fiber debonding, fracture, and pull-out in fiber-reinforced concrete
- Damage generated by environmental attack

The AE signal could be affected by several factors simultaneously, such as the structure and shape of the specimen, the quality and state of the specimen material, the strength of the loading, the position and direction of the loading, and the rate and process of the loading. For concrete, the w/c, cement type and property, the size and type of aggregates, the technology of processing, the age of the concrete, and so on all affect the AE process. Hence, generally, AE signals are very complex as well as random and blurred. The positive result of this is that an AE signal carries abundant information. The negative result is that the AE signal can be too complex to extract useful information.

Due to the nature of AE, the most important aspect of NDT-AE is the physical basis. Compared with the UT technique, where the source property of the ultrasonic wave is a known factor, the NDT-AE just wants to find the properties of the ultrasound source, that is to say, how to establish the roles on the relation between the quantities to be tested and the behavior of AE signals. Because of the complexity of the AE phenomena, most of these roles are empirical. A great deal of research to reveal these relations has been performed, on the mechanism of acoustic emission, the properties of ultrasonic transducers, the acoustic wave propogation theory, etc. This has led the AE technique onto a more solid and wider physical basis, and the application of NDT-AE has rapidly expanded.

The application of the AE principle relies strongly on the techniques of data acquisition and signal processing. It is difficult to make a prediction when and where AE events will emerge. Hence, it is difficult to record AE events precisely. To characterize the AE source, unlike the NDT-CE-UT, multichannel receiving techniques are necessary for NDT-CE-AE. From an analysis point of view, the more channels, the better. However, from the technical point of view,

to adding channels requires, great effort due to the increasing interaction among channels and the fast expanding data and cost of equipment.

The early AE testing instruments used analogue electrical devices. The ability to capture instantaneous AE events and to process AE signals is low with these instruments. Early successful applications of NDT-AE as a practical industrial applied technique started around the middle of 1960s in the United States, where it was used to monitor and to test a rocket shell. The development of NDT-AE techniques was slow until the numerical data acquisition AE instrument was developed by the middle of 1980s. Thanks to the rapid development of the numerical electrical techniques and computer technology, with the assistance of solid electrical circles, high-speed analog-to-digital converters, DSP technologies, and modern computer data acquisition, the capture and storage an instant AE signal that is precise and synchronized became possible and easy. More and more fast and reliable new numerical data processing methods have become available. These led the NDT-AE technique to have a reliable basis in both of hardware and software.

After about three decades of research and practice, the AE technique has made great progress and has become a very powerful nondestructive technique. Successful applications are to be extended over more and more areas.

When an AE event occurs at a source within the material, the stress wave travels directly from the source to the receiver in the form of body waves. Surface waves may then arise from mode conversion. When the stress waves arrive at the receiver, the transducer responds to the surface motions that occur. AE signals cover a wide range of energy levels and frequencies. Modern instrumentation can record AE signals in concrete in the range of 50 kHz to about 1 MHz. At lower frequencies, background noise from the test equipment becomes a problem. At very high frequencies, the attenuation of the signals is severe. AE signals are usually divided into two basic types, the burst type and the continuous type. The former corresponds to individual emission events, while the latter refers to an apparently sustained signal level from rapidly occurring emission events (Bray and Stanley, 1997). The most important role for a data analysis method in the AE technique is to acquire an integrated and meaningful AE wave form.

There are several ways to characterize the material behavior based on acoustic emissions, including event counting, rise time, spectrum analysis, AE source location (defect location), energy analysis, signal processing, and signal duration. For example, AE activities (event rate, accumulated event numbers, count rate, and count summation etc.) have been used to predict the onset and extent of damage in concrete and relate to the imposed stress level. Frequency components, rise time, and amplitude of AE signals have been used to distinguish different sources at different stress levels. The source location of an AE event can be determined based on the time differences among the recorded signals by an array of transducers, and has been used to monitor microcrack localization in concrete and fiber-reinforced concrete under uniaxial tension, and the fracture process zone in concrete under uniaxial tension.

The first representative investigation of AE from metals was carried out by Kaiser, who established the so-called Kaiser effect: “the absence of detectable acoustic emissions at fixed sensitivity level, until previously applied stress levels are exceeded.” Concrete and fiber-reinforced concrete are multiphase and flaw-rich composite materials. When subjected to a load, microcracks tend to form along flaws as the load increases, which makes it very suitable for AE monitoring. Unlike other NDE techniques, this technique indicates only active flaws and cannot determine the presence of other kinds of flaws. It responds to changes in flaw size instead of the total size. Therefore, continuous monitoring is required to detect a flaw extension whenever it occurs.

The application of AE in concrete has been studied for the past 30 years. Almost all the applications of the AE technique for concrete are focused on the fracture process zone. An

extensive series of investigations has been carried out by Maji and Shah (1988), Li and Shah (1994), Maji et al. (1990), Ouyang et al. (1991), and Landis et al. (1993). In these tests, concrete, mortar, and low-volume-fraction FRC specimens were loaded, in either direct tension or bending, to study the damage initiation and propagation within the materials. Both notched (Maji and Shah, 1989) and unnotched (Li and Shah, 1994) specimens were investigated. Deconvolution techniques were used by Maji et al. (1990), Ouyang et al. (1991), Li (1996), and Suaris and van Mier (1995) to study the orientation and the mode of microcracking. The relative amplitudes of AE signals at different transducer positions were used to distinguish tension and shear microcracks in mortar and aggregate–matrix interfaces.

For fiber-reinforced concrete, Li and Shah (1994) attempted to use the AE technique to study the tensile fracture of short steel fiber-reinforced concrete. Li et al. (1998) improved this AE measuring system for unnotched fiber-reinforced concrete specimens with relatively high volume fractions of fibers. An adaptive AE trigger signal identifier was developed for an adaptive trigger AE measurement system. An automated P-wave arrival time determination method was developed for pinpointing the location of thousands of AE events by using an adaptive low-pass filter (Li et al., 2000).

The AE technique has also been explored for detecting reinforcing steel corrosion in concrete. Li et al. (1998) examined the correlation between the characteristics of an AE event and the behavior of rebar corrosion in HCl solution, and the possibility of the corrosion detection of rebars inside concrete through an accelerated corrosion experimental method. The theoretical prediction and experimental results have shown that the AE technique is able to detect rebar corrosion at an early corrosion stage.

8.5.2.1 AE measurement system

The main elements of a modern AE instrumentation system are schematically shown in Figure 8-25. A complete AE measurement system includes AE transducers, preamplifiers, trigger, digitizer, and computer. The AE transducers are mainly made of piezoelectric composites, preferably wideband, with a linear phase response and small size. These transducers are used to convert the surface displacements into electric signals. The voltage output from the transducer is directly proportional to the strain in the PZT, which depends, in turn, on the amplitude of

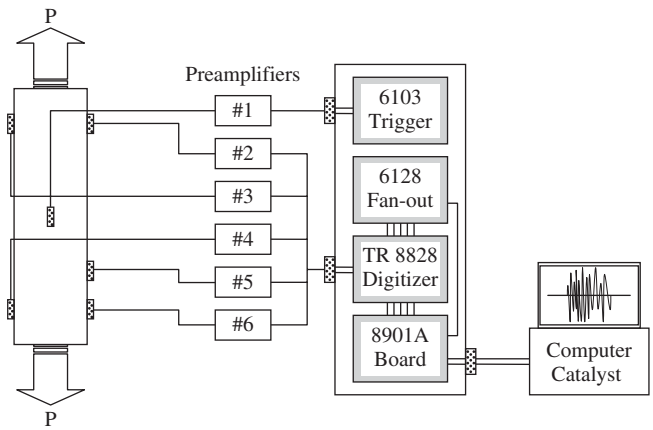

Figure 8-25 Acoustic emission measurement system

the surface displacement. Preamplifiers are normally necessary because the outputs from the transducers are usually low. The pre-amplifiers have two functions. One is to amplify the signal received by the AE transducers, usually using two magnification scales, 40 and 60 dB. The other function is to act as a filter.

Usually, a bandpass filter is installed in the pre-amplifier with a bandwidth of 30 kHz to 1 MHz. Only signals within this range can get through. A trigger is useful and the triggering is initiated when the output voltage of the transducer exceeds a preset reference voltage (threshold), such that the lower level background noises can be rejected. An analog–digital converter is used to digitize a signal in real time and store the digitized data in a memory. A computer is usually utilized to control the AE system and record the AE signals. The radiation patterns of acoustic emission sources are formed according to the same principle described earlier for ultrasonic transducers. In industrial applications, the AE sensors usually are located relatively farther from the source.

8.5.2.2 AE source location method

The AE source location can be deduced by using the time differences among the first-wave arrival times of the AE transducers. Figure 8-26 shows a typical set of AE signals. There are four individual signals in the figure, representing four channels. Each signal is obtained by a

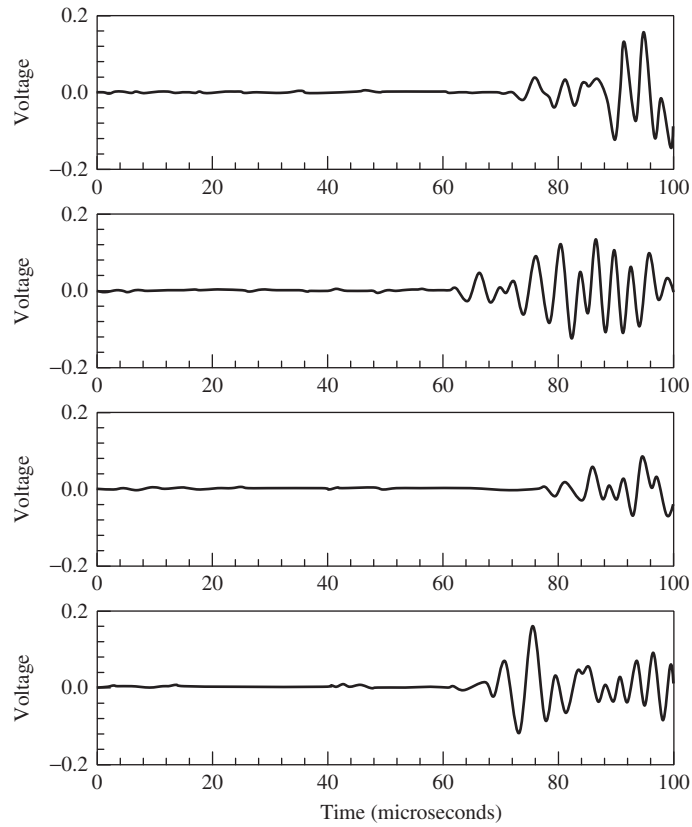

Figure 8-26 Typical set of AE signals

specific transducer located at a specific position. It can be seen from the figure that the first arrival time of the wave is different for different signals because the distances from the transducer to the source of AE are different. The differences in these first arrival times provide a base for locating the AE sources, as discussed in next section.

For the difference in these arrival times, for a two-dimension case, we can write the error between the distance from transducer 1 to the AE source and the distance from transducer i to the AE source as

$$e_{1i} = \sqrt{(x - x_1)^2 + (y - y_1)^2} - \sqrt{(x - x_i)^2 + (y - y_i)^2} - \Delta t_{1i} C \tag{8-68}$$

where x and y are coordinates of the AE source to be determined and $x_1(x_i)$ and $y_1(y_i)$ are the coordinates of the transducers. The term Δt_{1i} represents the difference in arrival time between transducer 1 and i ($i = 2, 3, \ldots, n$) and C is the wave velocity. For an ideal situation, the error expression should be zero and the AE source location should be easily determined by an intersection of two sets of equations. However, for a real experiment, error always exists. To minimize the test error, the following method is developed. First, the square of individual error is summed:

$$\begin{aligned} e &= \sum_{i=2}^{n} (e_{1i})^2 \\ &= \sum_{i=2}^{n} (d_1 - d_i - \Delta t_{1i} C)^2 \end{aligned} \tag{8-69}$$

where

$$\begin{aligned} d_1 &= \sqrt{(x - x_1)^2 + (y - y_1)^2} \\ d_i &= \sqrt{(x - x_i)^2 + (y - y_i)^2} \end{aligned} \tag{8-70}$$

Then, the total error is differentiated with respect to x and y, giving

$$\begin{aligned} f_1(x, y, C) &= \frac{\partial e}{\partial x} \\ &= 2 \sum_{i=2}^{n} \left(\frac{x - x_1}{d_1} - \frac{x - x_i}{d_i} \right) (d_1 - d_i - \Delta t_{1i} C) \end{aligned} \tag{8-71}$$

$$\begin{aligned} f_2(x, y, C) &= \frac{\partial e}{\partial y} \\ &= 2 \sum_{i=2}^{n} \left(\frac{y - y_1}{d_1} - \frac{y - y_i}{d_i} \right) (d_1 - d_i - \Delta t_{1i} C) \end{aligned} \tag{8-72}$$

By setting $f_1(x, y, C)$ and $f_2(x, y, C)$ to zero, the values of x and y can be solved by employing a numerical method, provided that the value of the wave velocity is known. Moreover, if the error equation is differentiated with respect to wave velocity, C, one gets,

$$\begin{aligned} f_3(x, y, C) &= \frac{\partial \mathrm{e}}{\partial C} \\ &= 2 \sum_{i=2}^{n} \Delta t_{1i} (\Delta t_{1i} C + d_i - d_1) \end{aligned} \tag{8-73}$$

It should be pointed out that solving Equations 8-71 through 8-73 together will provide not only the source location but also the wave velocity.

The method is easy to expand to a 3D case. In this case, Equation 8-68 becomes

$$e_{1i} = \sqrt{(x-x_1)^2 + (y-y_1)^2 + (z-z_1)^2} - \sqrt{(x-x_i)^2 + (y-y_i)^2 + (z-z_i)^2} - \Delta t_{1i} C \tag{8-74}$$

The sum of the square of the errors for a 3D case will take the same expression as shown in Equation 8-70. However, the expressions for d_1 and d_i will take the form

$$\begin{aligned} d_1 &= \sqrt{(x-x_1)^2 + (y-y_1)^2 + (z-z_1)^2} \\ d_i &= \sqrt{(x-x_i)^2 + (y-y_i)^2 + (z-z_i)^2} \end{aligned} \tag{8-75}$$

Consequently, the differential with respect to x, y, z and C are in the forms of

$$\begin{aligned} f_x(x,y,z,C) &= \frac{\partial e}{\partial x} \\ &= 2\sum_{i=2}^{n} \left(\frac{x-x_1}{d_1} - \frac{x-x_i}{d_i} \right) (d_1 - d_i - \Delta t_{1i} C) \end{aligned} \tag{8-76}$$

$$\begin{aligned} f_y(x,y,z,C) &= \frac{\partial e}{\partial y} \\ &= 2\sum_{i=2}^{n} \left(\frac{y-y_1}{d_1} - \frac{y-y_i}{d_i} \right) (d_1 - d_i - \Delta t_{1i} C) \end{aligned} \tag{8-77}$$

$$\begin{aligned} f_z(x,y,z,C) &= \frac{\partial e}{\partial z} \\ &= 2\sum_{i=2}^{n} \left(\frac{z-z_1}{d_1} - \frac{z-z_i}{d_i} \right) (d_1 - d_i - \Delta t_{1i} C) \end{aligned} \tag{8-78}$$

$$\begin{aligned} f_C(x,y,z,C) &= \frac{\partial e}{\partial C} \\ &= 2\sum_{i=2}^{n} \Delta t_{1i} (\Delta t_{1i} C + d_i - d_1) \end{aligned} \tag{8-79}$$

Setting the four equations equal to zero and solving them will provide the coordinates of the AE source location, x, y, and z, and the wave velocity, C, for a 3D problem.

8.5.2.3 Characterization of AE signals

As mentioned earlier, traditionally the AE signals have been characterized by the so-called wave-shape parameters such as the number of ring echoes, the total energy, the number of AE events, the rate of AE events, the rise time of the wave pulse, the wave pulse length, and the spectrum. An AE test records the AE signal wave-shape parameters first, then by means of some preestablished relationships estimates the material properties under inspection.

As an update, the Physical Acoustics Company (PAC) has developed software, PAC-PARS, using an artificial neural network (ANN) analysis system to characterize AE signals in a more advanced way. It uses twelve basic parameters in an AE signal to form a tensor space. The components of the tensor are load, number of channels, rise time of the pulse, the number of ring echoes, total energy, amplitude, average signal level, the ratio of pulse length over rise time, the product and pulse length, the ratio of the number of ring echoes over pulse length, the product of the number of ring echoes, and the pulse length. Over the tensor space, detailed analysis, such the analysis of eigenvalues and eigenvectors, mode recognition and ANN, can be performed to extract useful information fast and accurately.

Besides the wave-shape analysis, wave-form analysis has been developed as a new scheme to extract information from AE signals. It is based on the AE signal wave form in the time domain and the well-developed analysis techniques, such as frequency spectrum, autorelation function, and corelation function, to extract information from a wave packet. To realize the wave form analysis, the equipment must have the ability to capture the transient wave impulse and the ability of real-time processing. The high-speed numerical AE system (NAES) instrument makes this possible, in an easy and reliable manner.

No NDT technique, other than the AE technique, is so strongly reliant on the instrument used, and only good digital AE instruments can give satisfactory results. The specification of the transient wave record greatly affects the performance of the AE system, of which the most important are the sampling rate, precision, and memory length for one record (a hit). In practice, the sampling rate should be at least 4 or 5 times as fast as the highest frequency of the AE signal to receive the details of the AE signals and hence more information. The maximum dynamic range of the amplitude is determined by the precision of the analog–digital converter (ADC)

$$\text{Dynamic range} = 6 \times \text{bits of ADC(dB)} \tag{8-80}$$

That is to say, the dynamic range is limited to below 48 dB for an 8-bit ADC theoretically. The AE pulse duration is determined by the product of the memory length for one sampling and the sampling period, which is the inverse of the sampling rate. For a certain expected length of AE signal, enough memory length should be kept. High sampling rate and long hitting of the AE signal and multichannel receiver requires the very fast postprocessing of data.

8.5.2.4 Laboratory applications

NDT-AE is widely applied in fracture mechanics for metals and composite materials. In civil engineering, it has also been widely used to detect crack formation and propagation in a concrete specimen under load action, to detect corrosion of reinforcing steel under severe environment conditions, or to monitor a debonding process of external decoration attached to concrete structures.

(a) *Detection crack occurrence in concrete under uniaxial tension*: In this example of AE application, a method developed to study crack occurrence and propagation in concrete is introduced. The set-up for the test is shown in Figure 8-27. Except for four LVDT transducers, five piezoelectric transducers are mounted on the side surfaces of the specimen to pick up the acoustic emission signals originating from the materials, mainly the working portion of the specimen. The mix proportion for the plain concrete specimen is 1:0.45:2:0.65 (binder:water:sand:coarse aggregate, by weight). The specimens were tested about 30 days after casting. The test portion in the center, after gluing the loading plates onto each end, had a length of 210 mm, a width of 100 mm, and a depth of 20 mm.

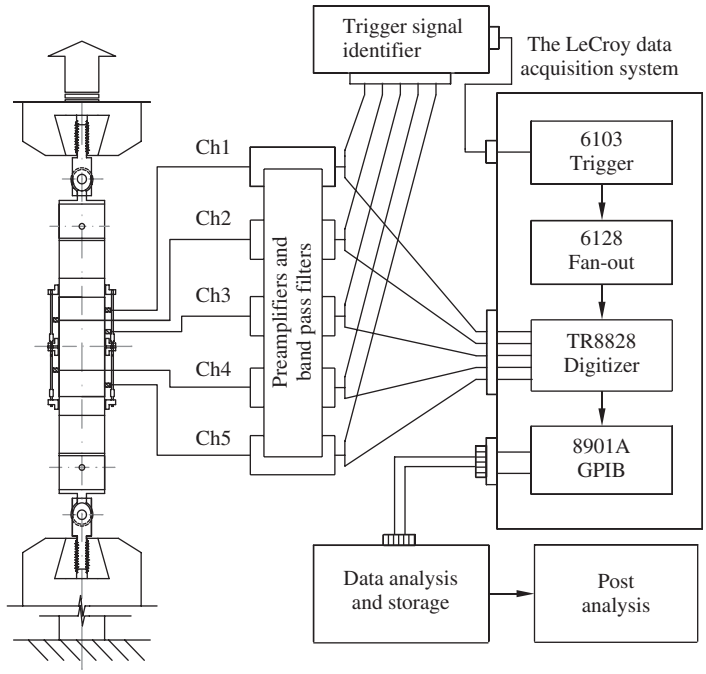

Figure 8-27 Experimental setup for studying crack occurrence

The acoustic emission measurement system shown in Figure 8-27 was used to acquire AE data during the test. The system was much the same as the one that was described by Li and Shah (1994). There is a major difference, however, in that an eight-channel adaptive AE-trigger-signal identifier was employed in the system. The adaptive triggering was actualized by comparing the signal level to a reference voltage (adjustable) with the help of voltage comparators, and then the identifier can "identify" the first signal, whose amplitude exceeds the threshold, among the all signals. By using this trigger identifier, all channels can be used as a trigger. Hence, the requirement of presetting a trigger channel is eliminated. In addition, possible omission of AE events due to the geographical arrangement of a preset trigger can be eliminated.

During the test, the preamplifier gain was set at 60 dB and the sampling frequency was set at 6.25 MHz. Considering the maximum frequency of AE signals from concrete to be normally within 1 MHz, this frequency was much higher than the one required by the Nyquist theorem (Oppenheim and Schafer, 1975). Each digitized signal from a channel is set at 4 K (4096) sample points and the threshold was selected as 49 dB. When the external load was increased to near the concrete capacity, diversified fracture events could occur, such as preload microcracks, voids, or other defects, which will propagate due to stress concentrations in the vicinities. During this process, energy is released and an acoustic wave is generated. The level of energy released or the amplitude of the waves depends on the types of fracture events. Thus, in principle, it is possible to detect these fracture events by monitoring the acoustic emission activity. The occurrences of AE events were somewhat related to the imposed stress level. The activity can be characterized by an AE event count and event rate. The source locations can be determined if enough transducers are used for monitoring. Bearing this view in mind, five identical PZT transducers are mounted on the unnotched specimen to monitor the damage and the fracture during the uniaxial tensile testing.

A plain concrete specimen was tested in direct tension and monitored by AE measurement in mean time. Figure 7-31 (see Chapter 7) shows its deformation–time curves. It can be seen from the figure that the deformations in the specimen vary a lot at different loading stages. The tensile stress, accumulated event number, and event rate as a function of time for the plain concrete is depicted in Figure 8-28. In this figure, it can be seen that the AE data is closely related to the stress level (loading stage). In the figure, stress is the nominal stress calculated from the imposed tensile load divided by the original cross-sectional area. Displacement is the deformation measured by the control LVDT that catches the formation of major crack.

The source locations of the AE events or microcracks have been calculated using the method introduced in the previous section and the source location map has been plotted in Figure 8-29. It should be pointed out that identification of damage localization can be clearly

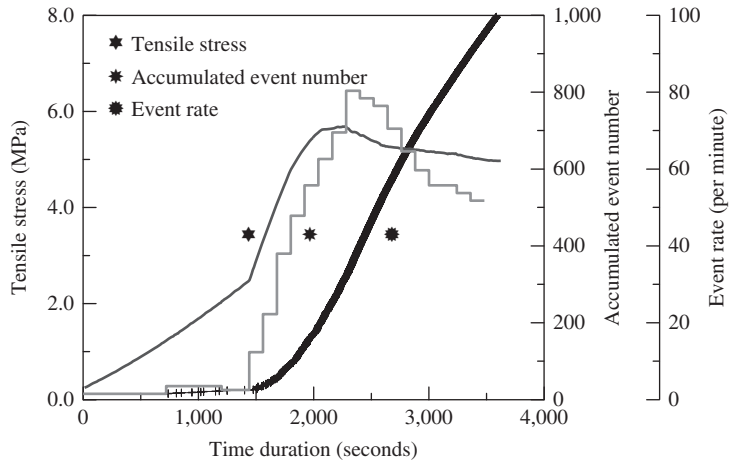

Figure 8-28 The tensile stress, accumulated even number, and event rate for plain concrete

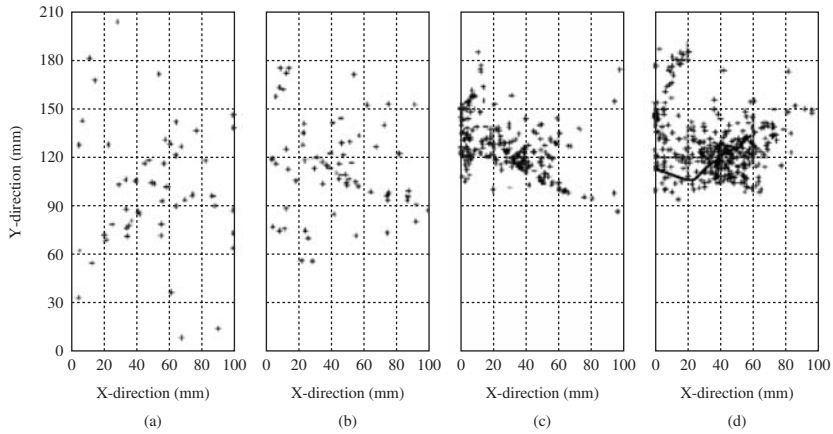

Figure 8-29 The source location map of the measured AE events

observed in the figure for regime (c), which corresponds to a stress level from $0.8f_t$ to f_t. A major crack has developed from the localization zone and is propagated across the width of the specimen. The phenomenon agrees with the findings of Li and Shah (1994) very well.

(b) *Corrosion detection*: The feasibility of the application of the AE technique to detect corrosion of reinforcing bars in concrete has been studied by Li et al. (1998). The physical background of this application is that under the expansion of the corroded parts, microcracks will be developed in the interface and bulk matrix, and energy will be released. Subsequently, a stress wave will be generated, which propagates along the medium and will reach the outer surface. By placing the AE transducer on the surface, the occurrence of microcracks can be detected. Since these microcracks are caused by corrosion products, the signals detected can be used to interpret the corrosion activity.

The mathematical model for calculating the stress caused by rebar corrosion at the rebar–concrete interface can be simplified as a shrink-fit model. First, let us assume that the rebar can freely expand due to corrosion with an increase of r in radius direction. Then, we try to put the rebar back into the hole that it occupied before. Due to corrosion expansion, the rebar now is too big to fit freely in the concrete hole. To allow the rebar to fit back into concrete, pressure has to be applied to both the surrounding concrete and the rebar. Let us consider the surrounding concrete first. This situation can be treated as a hole under internal pressure in an unbounded medium. According to the elasticity solution, the displacement caused by internal pressure p along radius direction is

$$U_r^c (r = a) = \frac{pa}{2\mu_c} \tag{8-81}$$

where p is the pressure, a is the radius of hole, and μ_c is the shear modulus of the surrounding concrete (interface). For the rebar, it can be treated as an inclusion with pressure on the outside. The displacement along the radial direction can be written as

$$U_r^s = \frac{-p\,(k-1)\,a}{4\mu} \tag{8-82}$$

where k is the Kolosou constant, with values

$$k = \frac{3-v}{1+v} \qquad \text{for plane stress} \tag{8-83a}$$

$$k = 3 - 4v \qquad \text{for plain strain} \tag{8-83b}$$

Compatibility requires that

$$\left|U_r^c\right| + \left|U_r^s\right| = \Delta a \tag{8-84}$$

Thus, we can obtain the pressure expression as

$$p = \frac{4\mu_c\mu_s}{2\mu_s + (k_s - 1)} \frac{\Delta a}{a} \tag{8-85}$$

The stress produced in the surrounding concrete interface is then derived as

$$\begin{aligned} \sigma_{\theta\theta} &= \frac{4\mu_s\mu_c}{2\mu_s + (k_s - 1)\,\mu_c} \frac{\Delta a}{a} \\ &= C\frac{\Delta a}{a} \end{aligned} \tag{8-86}$$

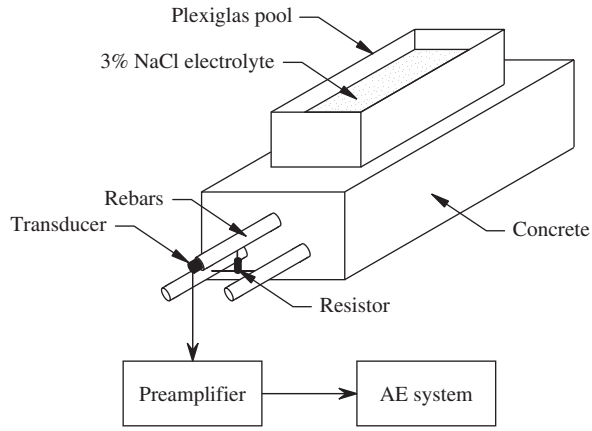

Figure 8-30 Experimental setup for a corrosion test of reinforcement

For steel, the shear modulus is about 81 GPa and the Kolosou constant is around 2. The shear modulus for concrete is about 12 GPa. Thus, the value of C is 2.23×10^{10}. For $\Delta a/a$ equaling 0.0001, the stress produced is 2.23 MPa. Note that the stress is, in fact, the shear stress in the interface and this value is large enough to create a microcrack. The stress wave generated by this microcrack can be detected by an acoustic emission transducer. This proves that the detection sensitivity of the AE technique to rebar corrosion is very high (0.0001 for a radius of 10 mm is only 1 μm!).

An experimental setup for corrosion testing is shown in Figure 8-30. The specimen used in the experiment was a concrete block with dimensions of $300 \times 300 \times 175$ mm. The mix proportion of the concrete was 1:0.6:2.5:2.5 (B:W:S:A) by weight. Three deformed rebars, 25 mm in diameter, were placed in the concrete block. One was positioned about 25 mm from the top surface of the concrete and the other two 250 mm below the top surface. All the reinforcing bars were coated with epoxy resin, 25 mm in length, at the edge surface where they entered the concrete, to prevent edge effect. The two rebars placed at the bottom of the concrete specimen were electrically connected to the top rebar by a shunt resistor, which made galvanic current measurement possible. An acrylic tank was attached on the top surface of the concrete specimen. The reinforced concrete specimen underwent a cyclic exposure of salt solution with 15% of solid NaCl electrolyte. The exposure cycle consisted of 3 days wet and 4 days dry to simulate the condition of wet/dry cycling of seawater on concrete bridge decks and substructures. The AE transducers were mounted on the two ends of the top rebar that was to be corroded. The output of the AE transducers was amplified and filtered by a preamplifier and transferred into digital signals by an A/D module. The digital signals were fed into a computer via shielded coaxial cables.

Half-cell and galvanic current were also measured to monitor the corrosion activities of the reinforcing steel. Figure 8-31 shows the comparison of the accumulated number of AE signals with the measured values of galvanic current. It can be seen that there is a significant increase in AE signals at about 20 days into exposure that is most likely due to microcracking caused by the building up of corrosion products on the rebar. However, the measurement of galvanic current shows no obvious change at this time. A sudden increase in galvanic current is found at approximately 32 days exposure time. Also, the half-cell potential became more negative, to about -420 mV, at the same time. It is thus verified that AE monitoring can detect corrosion earlier than the other two corrosion-detecting techniques.

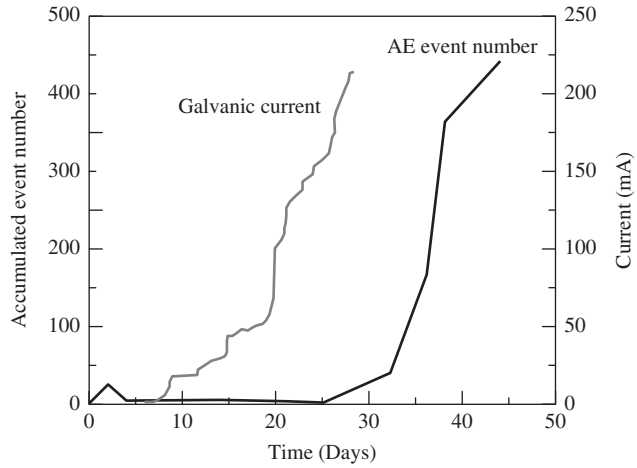

Figure 8-31 Comparison of the accumulated number of AE signals with galvanic current

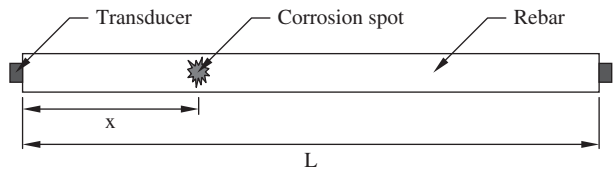

Figure 8-32 Measurement of the location of corrosion

For the arrangement of the AE transducers in this way, the AE source location becomes a one-dimensional problem. Referring Figure 8-32, suppose that * is the position of the corrosion, and the length of reinforcing bar is L. Then the distance from corrosion source to the AE transducer on the left is x and that on the right is $L - x$. If the time difference between the first arrival times at the two transducers is Δt and the wave velocity of steel is C, we can write the following equation:

$$(L - x) - x = \Delta t \cdot C \tag{8-87}$$

and solving the equation for x and gives

$$x = \frac{L - \Delta tC}{2} \tag{8-88}$$

Based on this equation, the source locations of corrosion have been calculated for the test specimen. The results are shown in Figure 8-33. To verify the calculated results, the specimen was broken and the reinforcing steel was taken out, as shown in Figure 8-34. Direct comparison shows a good agreement between the predicted corrosion locations and real ones on the rebar.

(c) *Debonding detection of ceramic tiles on concrete*: The decoration of concrete buildings using ceramic tile finishes is common practice throughout the world. The external finishes not only improve the stark appearance of concrete, but also offer some degree of protection

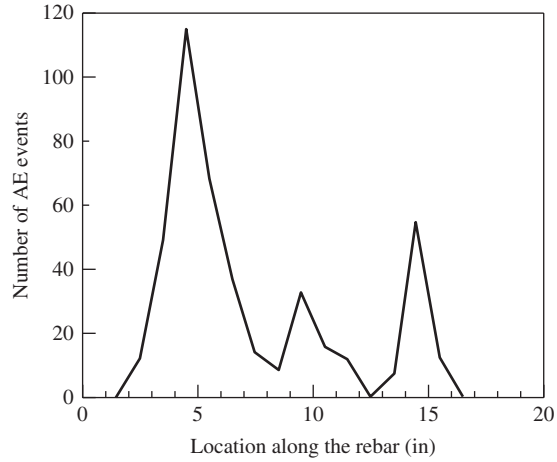

Figure 8-33 Calculated source locations of corrosion

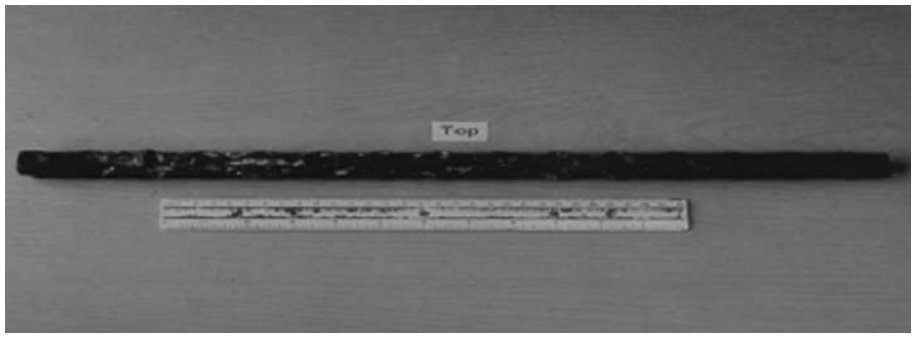

Figure 8-34 The actual corrosion conditions of the reinforcement

from carbonation attack to the concrete surface beneath. Unfortunately, almost every building experiences some degree of failure on the ceramic tile finishes. Most of this failure manifests itself as hollowing, cracks, discoloration, or disintegration of the finishing materials, or by the finishing material separating from the substrate. Thus, debonding is a common and an inevitable occurrence of tile finishes. To prevent or avoid the danger of tiles falling off, damage monitoring during the service period is very important. Its ability to detect weak signals makes the AE technique a strong candidate for this task.

To investigate the feasibility of the AE technique in monitoring the debonding process between the ceramic tiles and concrete, a push-off test was conducted. To prepare the push-off specimens, concrete cubes of size 150 × 150 × 150 mm were cast. The specimens were made by fixing ceramic tiles of 150 × 150 mm to one surface of the cubes with adhesive material. Two loading conditions were applied in this test, monotonic and cyclic loading. The specimens were cured in water at 20°C at room temperature for 26 days after tile fixing. One day before testing, the specimens were taken out of the curing chamber. An L-shaped steel plate was attached to the tile with epoxy resin. The steel plate was used to transfer the load to the tile–adhesive interface.

The test setup is shown in Figure 8-35. As can be seen from the figure, the specimen was tied on a flat rectangular plate that was connected to a servo hydraulic actuator of the testing

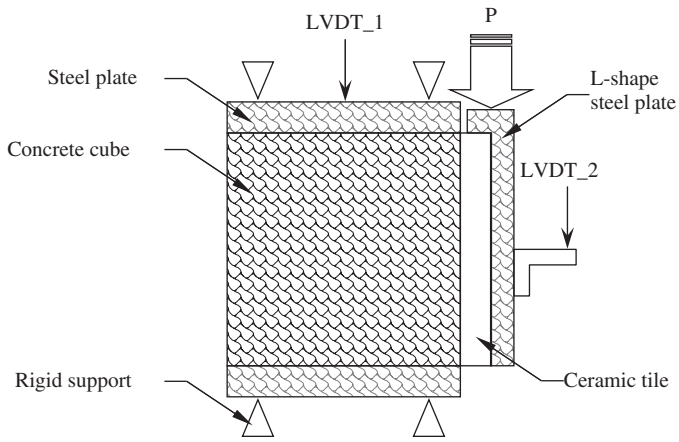

Figure 8-35 Test setup for debonding detection of ceramic tiles on concrete

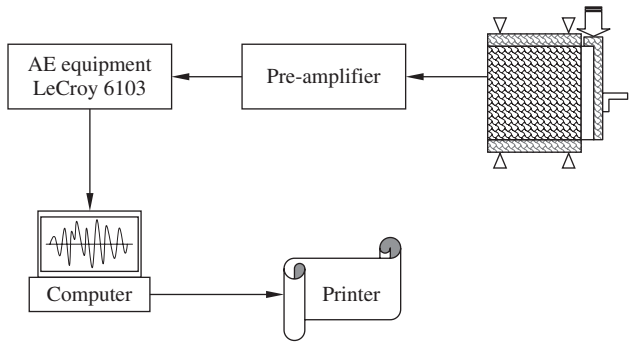

Figure 8-36 The AE measurement system for debonding detection

machine, through two C-clamps. The entire specimen/fixture could move up with the actuator. A steel rod, connected to the load cell, made contact with the top surface of the L-shaped steel plate with the help of a ball socket joint. A restraining force was provided by resisting the upward movement of the loading fixture, pushed by the L-shaped steel plate, which in turn pushed the ceramic tile downward. Two LVDTs, which were fixed between the top surface of the specimen and the rigid wing of the steel rod, were used to measure the displacement of the top of the L-shaped steel plate relative to the surface of the concrete cube. To study the damage accumulation process of the interface during push-off testing, an AE measurement system was utilized, as shown in Figure 8-36. The system consisted of transducers, preamplifiers, and A/D modules. Six piezoelectric transducers were glued on the two opposite surfaces of the specimen to monitor the acoustic emission activities. These transducers had an essentially flat amplitude response, approximately in the frequency range from 0.1 to 1.2 MHz. The preamplifiers had a bandwidth of 0.02 to 1.2 MHz and a gain of 40 to 60 dB. In the system, channel 1 was used as a trigger channel and was connected to a LeCroy 6103 amplifier trigger module. The other five channels were used as working channels and were connected to five TR8828D digitizer modules. A LeCroy 6128 fan-out module was used to receive the signal from the LeCroy 6103 amplifier and to trigger all working channels simultaneously. A LeCroy 8901A interface board

was used to communicate with a personal computer via a GPIB board. The operation of the LeCroy system was controlled by a Physical Acoustics Catalyst program, which also stored the digitized data on the computer's hard disk. Three thousand data points were stored for each channel at a digitizing rate of 16 MHz.

The electrical signal from each sensor was pre-amplified with a gain of 60 dB. A bandpass filter with a range from 30 to 500 kHz was used to eliminate undesirable low and high frequencies. A threshold of 46 dB was selected to ensure a high signal/noise ratio. A complete set of the acoustic signals obtained from the push-off test is plotted in Figure 8-37. It can be seen that the first arrival times are different for different channels. This provides, as mentioned earlier, the basis for the interpretation of the damaged or debonded areas. The 3D-source locations of AE events are deduced using the algorithm mentioned earlier.

Figure 8-38 shows the AE event occurrence under cyclic (a) and monotonic (b) loading. It can be clearly seen that prior to 30% of the peak load, there was no AE activity. From 30 to 70% of the peak load, AE activities increased slowly. After 70% of the peak load, the rate of the occurrence of the AE events shows an obvious increase. For the specimens tested under cyclic loading with 20 repeated cycles prior to 50% of the peak load, the Kaiser effect can be observed, as shown in Figure 8-39. The figure shows the loading history with superposition of the AE events from the test. In the first cycle (*OABC*), the AE events started at point *A*, and ended at point *B*, at the maximum load for the cycle. No events occurred on the unloading part.

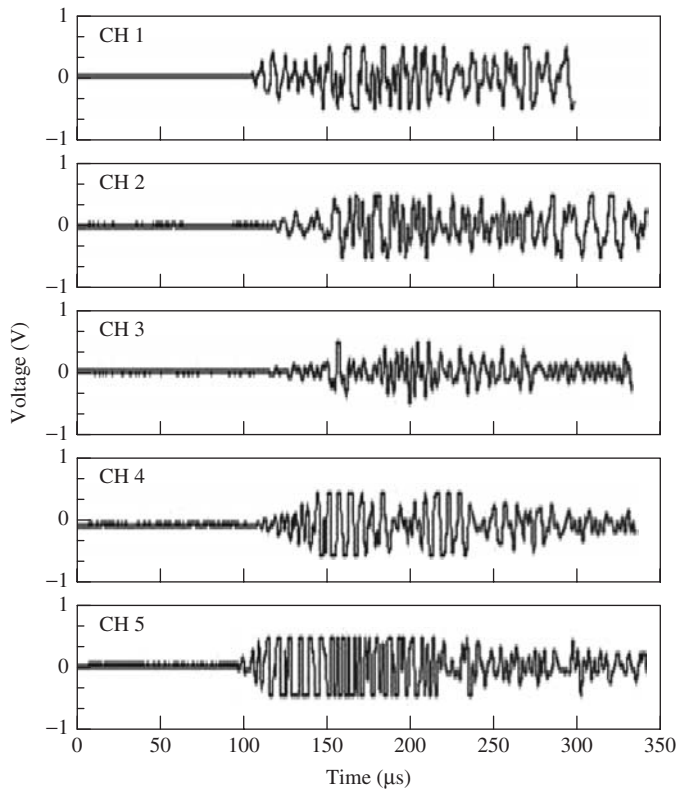

Figure 8-37 A typical set of acoustic emission signals on ceramic tiles

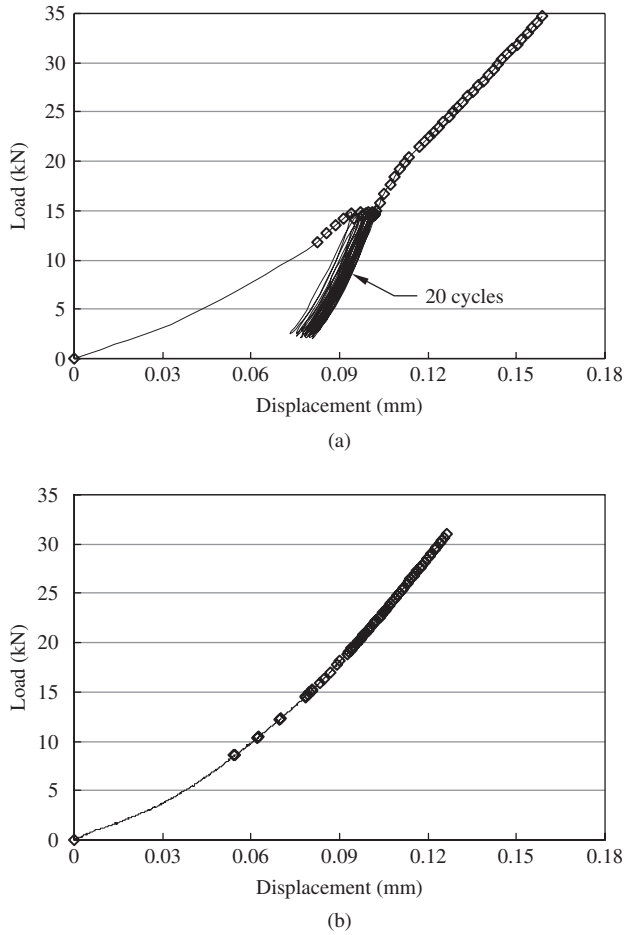

Figure 8-38 Acoustic emission under (a) cyclic and (b) monotonic loading of push-off test

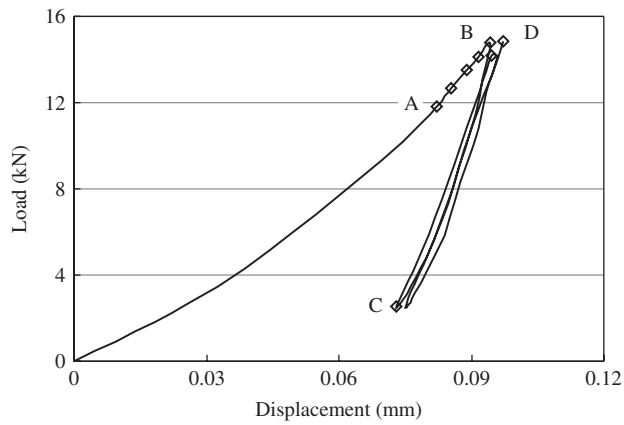

Figure 8-39 Kaiser effect observed under cyclic loading of push-off test

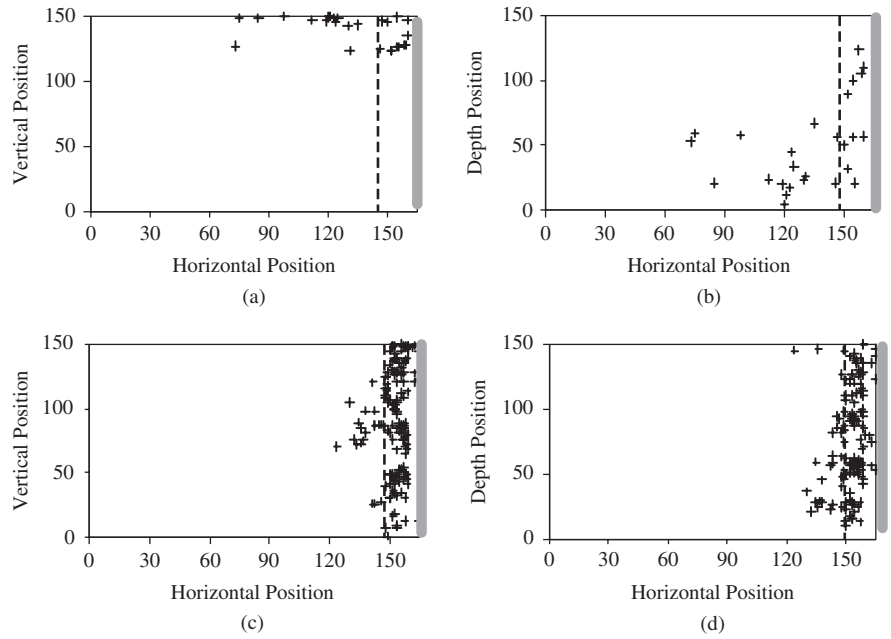

Figure 8-40 Acoustic emission of relative locations before (a, b) and after (c, d) 70% of peak load under push-off test

In the second loading cycle, AE events did not occur until point D, close to the maximum load of the previous cycle. Similar phenomena were observed for the other 18 loading cycles.

The interpreted AE sources are plotted in Figure 8-40, where (a) and (b) show the source locations for AE events that occurred prior to 70% of peak load for the case of monotonic loading. We can see that the events were randomly distributed in the horizontal and depth directions of the specimen, while in vertical direction AE events were concentrated in the top of specimen, which means that the shear stress in this region was bigger and the main macrocrack may have started from the top of the specimen. The majority of AE events registered after 70% of the peak load showed a trend to localize on a narrow band in the specimen, as can be seen from Figure 8-40 (c) and (d). A clustering of event locations is concentrated around the final failure plane.

(d) *Further research*: Due to the limitations of current AE technology, further research is needed to improve its performance. From the theoretical prediction point of view, the inverse of AE source properties is one of the most challenging problems. Only with a well-established reverse theory, can the nature of microcracks in the process zone be clearly understood, the relations between AE characteristics and the microcrack formation, localization, and propagation be resolved, and the relationship between the unknown quantities and the measured AE signal wave-type parameters and wave forms be established. From the hardware point of view, a more advanced acquisition system with sufficient channels needs to be developed. The hardware development should absorb the advances in computer technology so the information can be obtained much faster and with real-time processing. From the software point of view, DSP techniques should be adopted for in situ displaying of the crack sources and propagation pattern, damage degree, and safety evaluation.

AE is well suited for laboratory experiments but can be very time-consuming and difficult to monitor on site. However, the AE technique can serve as a dynamic method of flaw detection

and its use is actively growing (Brandes et al., 1998). A potentially important application of quantitative AE is to monitor bridges and buildings to assess the degree of damage and service life. To know the history and the present situation, AE might be a suitable tool, but powerful analysis software must be provided. This must also rely on the wave-form analysis and combined multidisciplinary NDT techniques, and new data fusion techniques are needed. Data fusion is the systematic integration of multisensor information (Gros, 1997) and can be defined as the overall understanding of a phenomenon.

8.5.3 Impact echo

Hammers are used in the evaluation of piles (Steinbach and Vey, 1975; Brendenberg, 1980; Olson and Wright, 1990), and produce energetic impacts with long contact times, which are acceptable for testing long, slender structures, but are not suitable for detecting flaws within thin structures such as slabs and walls. Impact sources with shorter-duration impacts, such as small steel spheres and spring-loaded, spherically tipped impactors, have been used for detecting flaws within slab and wall structures (Carino et al., 1986; Sansalone and Carino, 1988). The use of small ball bearings as impact sources was regarded as one of several key breakthroughs in impact-echo (IE) research in the mid-1980s (Sansalone, 1997). Such a source produces a well-defined and mathematically simple input, which in turn generates waves with characteristics that facilitate signal interpretation. Ball bearing impactors are easy to use and the frequency content of the resulting stress waves can be tuned to fit the size of the structure and the sizes of flaws to be detected. The data acquisition system should have a sampling frequency of at least 500 kHz. The optimal sampling frequency depends on the thickness of the test object, but for testing relatively thin members, a high sampling rate is more effective. Nowadays, the impact-echo test equipment can be portable and has a wide range of applications in the inspection of concrete, both in laboratory and field conditions. The impact-echo technique is more precise than the rebound hammer method.

In these studies, the partial or complete discontinuities of piles, such as voids, abrupt changes in cross section, weak concrete, and soil intrusions, and the location of these irregularities can be detected by the impact-echo technique. Carino and Sansalone initiated experimental and theoretical studies to develop an impact-echo method for testing structures other than piles (Carino et al., 1986; Sansalone and Carino, 1988). They used the impact-echo technique to detect interfaces and defects in concrete slab and wall structures, including cracks and voids in concrete, depths of surface-opening cracks, voids in prestressing tendon ducts, thicknesses of slabs and overlays, and delaminations in slabs. The impact-echo technique has also been used in layered-plate structures, including concrete pavements with asphalt overlays (Sansalone and Carino, 1988; Sansalone and Carino, 1990). Lin and Sansalone (1997; 1997) developed a new method for determining the P-wave velocity in concrete on the basis of the impact-echo technique.

8.5.3.1 Principle

The impact echo technique is an important and widely used mechanical wave NDT technique in civil engineering. Impact echo is actually a very old nondestructive testing method. In ancient times, people used this method to evaluate the quality of stone by striking the stone and listening to the ringing sound by ear. This is an active NDT technique. A hammer, a dropped ball, or a layer beam can be used to generate a mechanical acoustic vibration of the specimen and emit acoustic waves into the air. Defects and anomalies change the sounds. The sounds could be

received by means of a microphone in air or a transducer on the specimen surface. IE works in the acoustic and low ultrasonic frequency band. The received signals are analyzed mainly by the fast fourier transform (FFT). The multireflection between the flaw surface and the top surface of the specimen forms a periodic vibration source to produce a peak in the frequency spectrum of the echo. The multireflection process can also occur inside the flaw, say in the void, which gives out the specific peaks in the frequency spectrum. The geometry of the flaw, such as the depth h, can be deduced from the measured frequency peak f, provided the velocity C of the ultrasonic waves in the specimen is known:

$$h = \frac{C_i}{2f_i} \tag{8-89}$$

where the subscript represents the wave type of the corresponding frequency peak. In most cases, the wave type is a longitudinal one. It is useful to detect cracks, delaminations, and voids beneath the surface of concrete.

The IE signal actually is the response of the specimen under the impulse loading. This is the main difference of IE from UT and also causes the difference in the wave-emitting technique. In IE, the sound is produced by mechanical impulse by the use of a hammer or in another similar manner; in UT the sound is usually produced by a PZT, an ultrasonic probe. Another difference between UT and IE is the frequency ranges they cover. The IE usually works in the acoustic frequency band, and the UT in the ultrasonic band. As the IE signals are the response of an object, they might carry the fingerprints of this object. By choosing proper advanced DSP methods, one might find out more information from IE testing. Compared to the NDT-CE-UT, the coupling problem of IE is trivial if the receiver uses a microphone, because it uses the air as a couplet. Thus, it is easy to assess surfaces that are rough and complicated in shape, which are found more frequently in NDT-CE. On the other hand, when the PZT is used, all types of waves, including longitudinal waves, transverse waves, and surfaces waves, can be received. As the first arrival wave must be the longitudinal one, the longitudinal wave is dominant.

An impact-echo test system normally consists of three components: an impact source, a receiving transducer, and a digital processing oscilloscope or wave-form analyzer, which is used to capture the transient output of the transducer, store the digitized wave forms, and perform signal analysis. The force–time history of an impact may be approximately a half-sine curve, and the duration of the impact is the contact time, which determines the frequency content of the stress pulse generated by the impact—the shorter the contact time, the broader the range of frequencies contained in the pulse. As the contact time decreases, the higher-frequency components can be generated and smaller defects can be detected. In using the impact-echo method to determine the locations of flaws within an object, tests are performed at regularly spaced points along "scan" lines marked on the surface. Examination of the amplitude spectra from these scans reveals the depth and approximate size of defects that may be present. However, interpretation of test data requires in-depth understanding of the technique (Mailvaganam, 1992). The selection of the impact source is a critical aspect of a successful impact-echo test system.

8.5.3.2 Application

IE can be used to detect and locate flaws, fractures, voids, and laminations in ground decks, concrete pavements, and walls. The depth of the flaws can also be measured. The general nonhomogeneous forms might be identified by the method suggested above. IE can also be utilized to interpret the dynamic modulus of a material.

The development of a standard test method for flaw detection using the impact-echo technique is difficult because of the many variables and conditions that may be encountered in field

testing, in which the type of defects and shapes of structures are frequently met. ASTM C1383 (2004) has proposed a standard test method based on the use of the impact-echo method to measure the thickness of plate-like concrete members. This method includes two procedures. Procedure A is used to measure the P-wave velocity in concrete based on the travel time of the P-wave between two transducers at a known distance. In procedure B, the plate thickness is determined using the P-wave velocity measured in procedure A. The data analysis procedure in ASTM C1383 considers the systematic errors associated with the digital nature of the data on procedures A and B.

8.5.3.3 Dynamic modulus measurement

The dynamic modulus of concrete can be measured by an impact-echo technique. Jin and Li have developed a new device to conduct such an experiment (Jin and Li, 2001). The device is schematically shown in Figure 8-41. The system includes a box made of sponge, an 8-mm steel sphere, an accelerometer, and a digitized oscilloscope with a fast Fourier transform function. To measure the dynamic modulus, a cylindrical specimen is put into the hole in the sponge box with the accelerometer fixed at the bottom of the specimen. Then the steel ball is dropped onto the top surface of the specimen. The vibration generated by such an impact will be detected by the accelerometer and recorded by the oscilloscope. The recorded wave form will be transferred into a frequency spectrum later, for dynamic modulus determination.

For concretes, the dynamic modulus measurement can be carried out on the same specimen at different ages to investigate the influence of age on the development of dynamic modulus. To interpret the dynamic modulus of concrete, the wave forms recorded by the oscilloscope have to be transformed into a frequency spectrum. Figure 8-42 shows a typical spectrum for a concrete specimen at different ages. It can be seen from the figure that the first two resonance frequencies do shift from lower values to high values regularly with age all the time. Thus, the resonance frequencies do reflect the process and degree of hydration, setting and hardening.

After determining f_1 and f_2, the dynamic Poisson's ratio can be calculated using the method developed by Subramaniam et al. (1999). The formula used to calculate Poisson's ratio is

$$\nu = A_1 \left(\frac{f_2}{f_1}\right)^2 + B_1 \left(\frac{f_2}{f_1}\right) + C_1 \tag{8-90}$$

where f_1 and f_2 are the measured first and second longitudinal resonance frequency, respectively; and

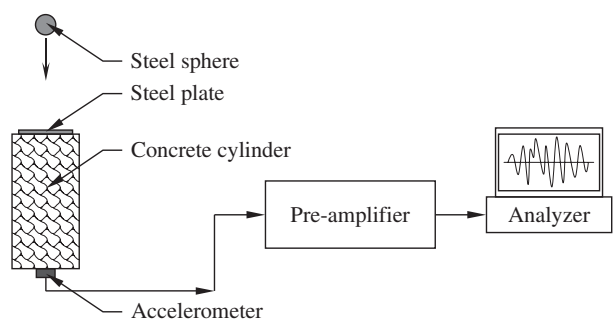

Figure 8-41 Experimental setup for resonance measurements

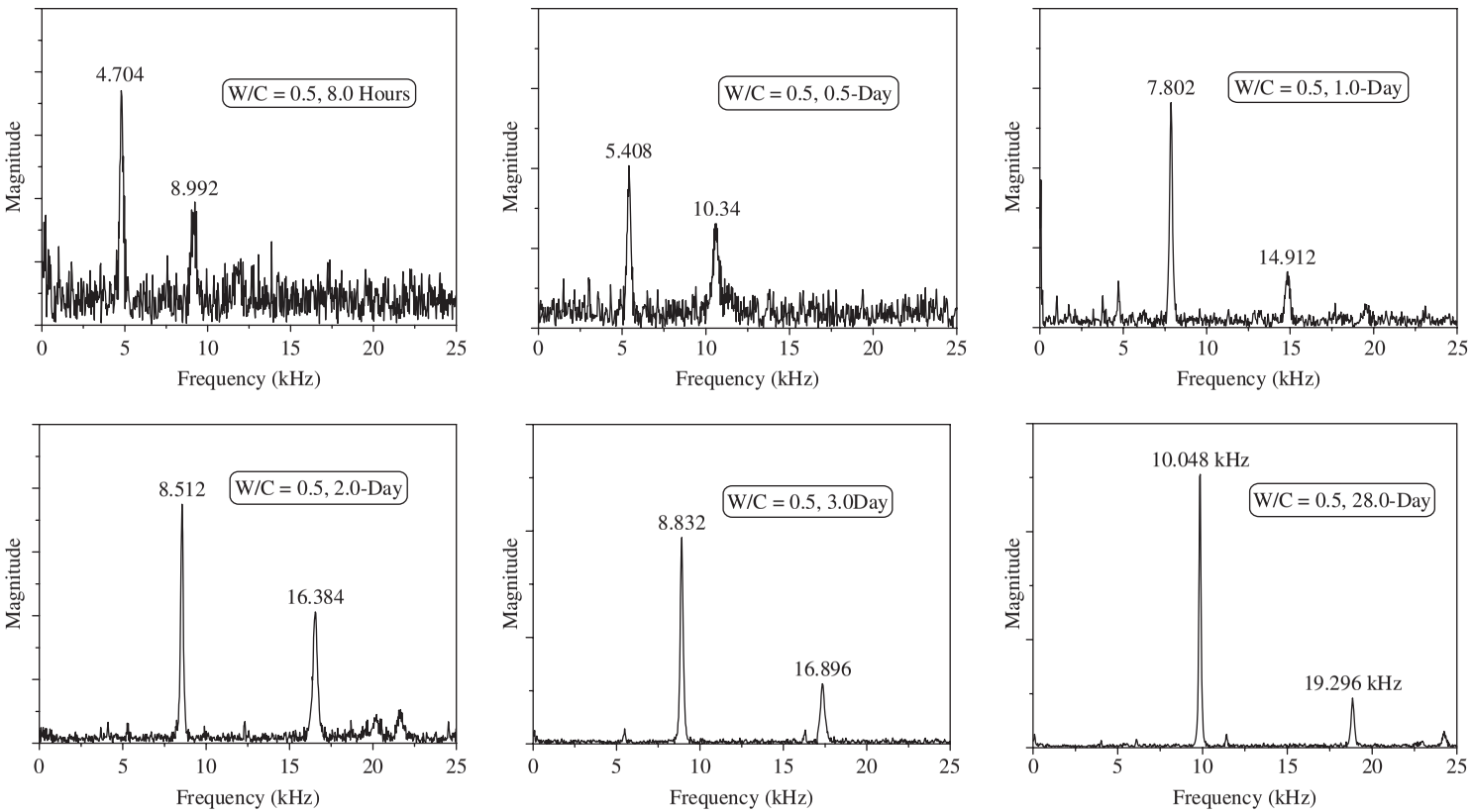

Figure 8-42 Typical spectrum for a plain concrete ($w/c = 0.5$)

$$A_1 = -8.6457\left(\frac{L}{D}\right)^2 + 24.443\left(\frac{L}{D}\right) - 12.478 \tag{8-91}$$

$$B_1 = 34.599\left(\frac{L}{D}\right)^2 - 101.72\left(\frac{L}{D}\right) + 56.172 \tag{8-92}$$

$$C_1 = -34.681\left(\frac{L}{D}\right)^2 + 105.98\left(\frac{L}{D}\right) - 62.731 \tag{8-93}$$

where L/D is length to diameter ratio.

The calculated Poisson's ratio from the experiments is plotted as a function of age in Figure 8-43. Generally speaking, Poisson's ratio values show a very small variation within the range 0.18 to 0.21 and can be regarded as constant. This is consistent with the findings of Boumiz et al. (1996), who observed that the Poisson's ratio of cement paste and mortar were more or less constant after curing for 12 hours.

After Poisson's ratio is obtained, the dynamic modulus can be calculated using its value and the longitudinal resonance frequencies (Subramaniam et al., 1999). The formula used to calculate the dynamic modulus is

$$E_d = 2(1+\nu)\rho\left(\frac{2\pi f_1 R_0}{f_n^1}\right)^2 \tag{8-94}$$

$$\text{where } f_n^1 = A_2(\nu)^2 + B_2(\nu) + C_2 \tag{8-95}$$

$$A_2 = -0.2792\left(\frac{L}{D}\right)^2 + 1.4585\left(\frac{L}{D}\right) - 2.1093 \tag{8-96}$$

$$B_2 = 0.0846\left(\frac{L}{D}\right)^2 - 0.5868\left(\frac{L}{D}\right) + 1.3791 \tag{8-97}$$

$$C_2 = 0.285\left(\frac{L}{D}\right)^2 - 1.7026\left(\frac{L}{D}\right) + 3.3769 \tag{8-98}$$

and R_0 is the radius of the solid cylinder and ρ the mass density.

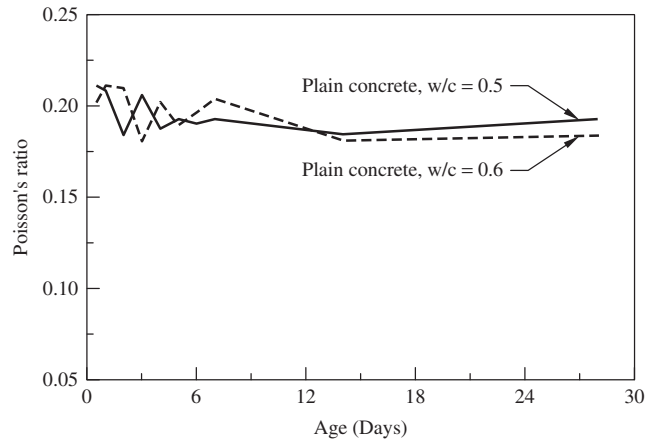

Figure 8-43 Poisson's ratio versus age

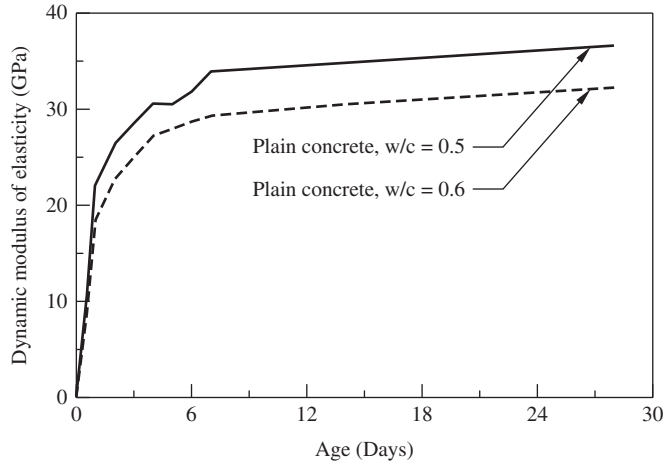

Figure 8-44 Dynamic modulus versus ages

The calculated results for the dynamic modulus are plotted as a function of age in Figure 8-44. It can be seen from the figure that the dynamic modulus increases rapidly, up to the age of 4 days, then the rate decreases and the curve becomes flat. The influence of the w/c ratio can also be clearly seen from the figure, and a higher w/c ratio leads to a lower dynamic modulus at all ages.

8.5.3.4 Surface cracking measurement by impact echo

To detect the finer crack on a concrete surface that cannot be easily observed by the naked eye, the impact echo technique can be used. The impact echo setup for surface crack measurement is shown in Figure 8-45. As can be seen from the figure, it consists of one impact source and two receivers. When the surface wave is generated by an impact source, usually a steel ball, the wave propagates along the surface of the material or specimen. The stress wave can be picked up by two transducers. If there is no crack between the two transducers, the responses of the two transducers are almost identical. However, if there is a crack between the two transducers, the response of the second transducer will show a significant difference from the first one; hence, the existence of a crack can be determined. The detection of a surface crack using the impact echo method usually utilizes *self-calibration*, developed by Achenbach et al. (1992). The self-calibration method can cancel uncertain parameters of the source characteristics term and the receiver response term, by utilizing the FFT form of the captured time domain signal, V_{AB}, V_{AC}, V_{DB}, and V_{DC}. In this, V_{AB} and V_{AC} represent a stress wave signal, generated by an impact (wave source) at location A and received by the near accelerometer at locations B and C, in the frequency domain, respectively. V_{DC} and V_{DB} represent stress wave signals, generated by an impact (wave source) at location D and received by the accelerometer at locations C and B, in the frequency domain, respectively.

The signal transmission function between locations B and C, d_{BC}, can be obtained using the following equation:

$$d_{BC} = \sqrt{\frac{V_{AC}V_{DB}}{V_{AB}V_{DC}}} \tag{8-99}$$

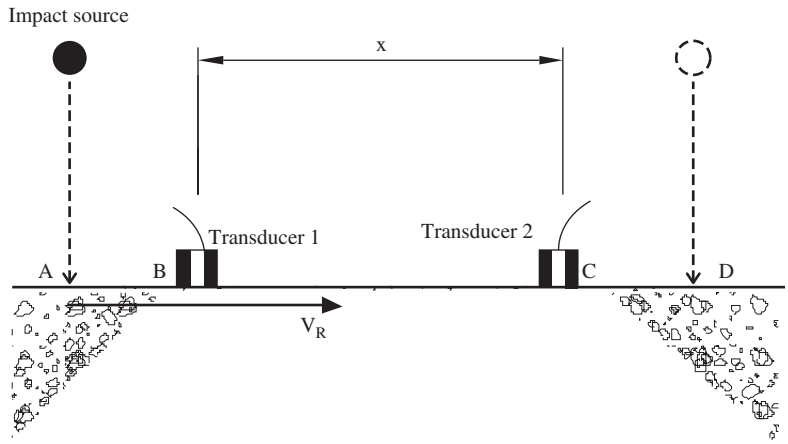

Figure 8-45 Surface wave velocity measurement for concrete strength assessment

where d_{BC} is a function of frequency and can be visualized as the ratio of the amplitude of the signal from the far accelerometer to that of the near accelerometer. Thus, a transmission value of unity indicates no amplitude loss (completely transmission) as the wave propagates from B to C, whereas a value of zero indicates complete signal amplitude loss (no transmission). In the case of a point source, d_{BC} values should be less than 1, even for perfect transmission materials due to some loss from attenuation.

Usually, an impact event will generate waves propagated in all directions. Some wave components propagate along the surface while others reflect at free boundaries. By setting an appropriate window, the surface wave or the first P-wave reflection from the opposing side of the specimen can be distinguished. The d_{BC} measurement can be used to detect a surface crack in concrete. Clearly, if there is a crack between two transducers, the d_{BC} values will suffer a severe reduction in almost all the frequency ranges.

8.5.4 Penetrative radar technique

The penetrative radar technique was developed based on the theory of electromagnetic waves. When electromagnetic waves propagate in a medium, the wave velocity v is

$$v = \frac{c}{n} \tag{8-100}$$

where c is the velocity of light, and n the index of refraction. For a homogeneous medium,

$$n = \sqrt{\varepsilon\mu} \tag{8-101}$$

where ε and μ are the relative permittivity and relative magnetic permeability of the material, respectively. The relative magnetic permeability almost equals unity for most materials. For a mixture consisting of j constituents with volume V_j, the relative permittivity can be regarded as the linear combination of its constituents,

$$\varepsilon = \sum_{i=1}^{j} V_i \varepsilon_i / V \tag{8-102}$$

where V is the total volume of the mixture. Hence, one could deduce the volume component from the measured velocity provide the materials of the constituents are known.

From the point of view of concrete quality control, water content is one of the most important parameters. Fortunately, the relative permittivity of water is about 81, whereas that of cement paste and normal aggregates is about 5. Hence, the measurement is very sensitive to the water content. The accuracy is about 3 to 5% for a normal concrete mixture. Moreover, since the relative permittivity of air is 1, it is feasible to use EM wave propagation to detect the porosity for a dry concrete. The time of flight can be used to measure the thickness by the formula

$$\text{Thickness} = \frac{150t}{\sqrt{\varepsilon}} \tag{8-103}$$

The scattered wave is usually called an echo, and its amplitude is related to several material parameters. By means of some inverse procedures, one can deduce the characteristic of a layered structure (Attoh-Okine, 1995). By scanning, the echo information, amplitudes, phases, TOF echo data can be used to form an image, or can be used as raw data for tomography.

As concrete is a composite mixture, the scattered wave from the aggregate will form a cluster. The scattering at an interface is strongly dependent on the difference of the complex permittivity of the two materials. As the permittivity of a normal aggregate and a cement matrix is similar, the scattered EM waves from the interface are usually much weaker than ultrasonic waves. This is another advantage of the EM wave to detect water or air defects in concrete that have very different permittivities. For the same reason, the test results are also not sensitive to the aggregate size.

One should be aware of the limitation by the nature of the physical laws. For example, the power reflection coefficient R from air to a board made of lossless material with a perpendicular incidence is

$$R = 4r^2 \sin^2(\beta d) \Big/ \left[(1 - r^2)^2 + 4r^2 \sin^2(\beta d)\right] \tag{8-104}$$

where $\beta = 2\pi/\lambda$, λ is the wavelength in the medium, d the thickness of the board, and r the amplitude reflection coefficient, which can be expressed as

$$r = (1 - n)/(1 + n) \tag{8-105}$$

in which n is the relative refractive index. Hence, the penetrating ability of a microwave strongly depends on the frequency when the thickness of a plate is fixed. When the thickness is equal to the integer times of the wavelength, then $R = 0$, which means that the technique cannot realize the existence of the board by reflection.

In the case of testing involving waves, the wavelength is the most critical parameter. The resolution and sensitivity of the measurements are all related to the wavelength used. The lateral resolution is mainly limited by the wavelength. The depth resolution depends mostly on the width of the wave pocket. Electromagnetic waves totally reflect from a metal sheet even if the thickness of the sheet is only a few tenths of a millimeter. Hence, it is hardly possible to detect the parts inside or behind the metal components.

Ground penetrative radar (GPR) is a very powerful EMT instrument. A basic radar system consists of a control unit, antennas (one is used for transmitting and one receiving pulses), an oscillographic recorder, and a power converter for DC operation. In the inspection of concrete, it is desirable to use a radar antenna with relatively high resolution so that the small layer of a concrete member can be detected. Radar can be employed in the rapid investigation of concrete structures, such as for measuring the thickness of structural members, for determining the spacing and depth of reinforcement, and for detecting the position and extent of voids and other types

of defects in bare or overlaid reinforced concrete decks. In the testing of concrete, normally short-pulse radar is used, which is the electromagnetic analog of sonic and ultrasonic pulse-echo methods. In this method, the equipment generates electromagnetic pulses, which are transmitted to the member under investigation by an antenna close to its surface. The pulse travels through the member and its propagation velocity is determined by the electrical permittivity. The relative permittivity of the concrete is determined predominantly by the moisture content of the concrete. Typical relative permittivity values for concrete range between 5 (oven-dry concrete) and 12 (wet concrete) (Bungey and Millard, 1996).

The radar technique utilizes the EM wave as an enquiring agent to get information on concrete materials or structures, such as the thickness and defects inside. A GPR can image the bridge pile profile in a bridge scour investigation. A maximum frequency should be recommended in a GPR survey design for clutter reduction. It is suggested that the wavelength λ be ten times larger than the characteristic dimension for geological materials (Davidson et al., 1995). For most cases, the frequency range is from 90 MHz to 1 GHz and the pulse repetition frequency is 25 Hz. The following typical results can be achieved: a scour depth of 1.2 m relative to the general riverbed; a filling consisting of a sandy layer 0.5 m deep with overlying gravel 0.8 m thick at the center of the hole; and a water depth of about 1 m (Davidson et al., 1995). The GPR measurement is fast enough to be suitable to detect a large area like a 10,000 m^2 pavement at an airport (Weil, 1995).

8.5.4.1 Application

Microwave NDT techniques can be used to perform building inspection and quality control and to detect steel objects as well as moisture, water content, locating and cracks. It is well suited for locating the lateral position of rebars, metallic ducts, metallic T-girders, and metallic anchors in prefabricated three-layer concrete elements; locating plastic and metallic leads, and measuring the cover thickness and moisture content of concrete. Artificial birefringence properties can be found for ceramics and cement with microwaves, of which the wavelength is between 7.5 and 12.5 mm. This is similar to that of photoelasticity with visible light (Dannheim et al., 1995). Hence, to visualize inside the specimen is possible with microwaves.

EMT techniques can make reliable assessment of integrity. It can locate tendons and metal ducts (diameter 85 mm) and offer information on geometrical dimensions. It can detect concrete member defects, voids in tendon ducts, compression faults or honeycombing (voids from 80 to 160 mm) in concrete. However, using the EMT technique to measure concrete is not sensitive with aggregate size. For example, for aggregate size of 8 to 32 mm, and cover thickness 340 $\pm$10 mm, the lateral position for reinforcement could be within an accuracy of $\pm$10 mm (Attoh-Okine, 1995). A microwave moisture content meter offers on-line water content monitoring in clay (Kalinski, 1995).

8.5.4.2 Digital image processing (DIP) and modeling

As the microwave frequency is usually very high, the AD device for the microwave signal itself is either very expensive or unavailable with the present technique. The DSP in NDE-CE-EMT is different from other NDT-CE techniques. In NDE-CE-EMT, the AD converter acts on the radar image, which corresponds to the B-scan plot in NDT-CE-UT. Then the general digital image processing technique can be used normally. In this case, the DSP routines, e.g., artificial neural networks, frequency analysis, and digital filtering, can be used to effectively draw the information from the image.

Interpreting the radar image is not so easy sometimes. If the simulation technique is used together with the analysis of the radar response image, the void as well as the shape of the void can be discovered, while it is very difficult to discover the shape of a void only from direct test results.

8.5.5 Optical techniques

These kinds of techniques use light waves as the inquiring agent. They are also active methods. The main techniques are based on interferometry and energy transportation. A representative technique of the former is electronic speckle pattern interferometry (Jones et al., 1989; Hung, 1982), and of the latter is infrared thermography (Favro et al., 1991; Milne and Carter, 1988).

8.5.5.1 Electronic speckle pattern interferometry

Electronic speckle pattern interferometry (ESPI) is a powerful laser based measurement technique (Butter et al., 1971; Hung and Liang, 1979). The essential principle is the same as holographic interferometry (HI). ESPI realizes HI by means of a video technique instead of by photography. The reflected light is superposed to a reference laser beam. The resultant interference pattern is recorded by a CCD camera. The interference patterns before and after loading are recorded and the resultant fringe pattern reflects the displacement fields of the illuminated surface. A phase-shift technique resolution of the order of 20 nm can be reached. ESPI is a noncontacting, full-field technique to measure and monitor the 3D-displacement field of an optical diffusely scattering object (Jones and Wykes, 1989). The surface area to be monitored can be more than $70 \times 80\ \text{cm}^2$, depending on the geometrical arrangement. Because ESPI needs a reference beam, isolation of the vibration ion from the environment is important, but difficult to realize.

Speckle pattern shearing interferometry (SPSI), also called shearography (Hung 1982) is an advanced technique stemming from ESPI. In contrast to HI or ESPI, SPSI measures the derivatives of the surface displacement directory. It does not respond to the rigid body motions. By a special set of optical elements, the light beam scattered from the object surface splits in to two beams separated by a small distance in the lateral direction, which is what the shearing really means, which interfere with each other. As the two beams come from the same source, this method is very stable against environmental vibrations. The advantage of this method is that it measures the surface strain directly instead of displacements. Hence, SPSI can work in larger displacement cases than ESPI.

Both ESPI and SPSI can be used as a real-time micro crack monitors. By means of the phase-shifting technique, quantitative evaluation of fringes is possible.

8.5.5.2 Infrared thermography

Sunlight is an electromagnetic wave. It travels at 3×10^8 m/sec in a vacuum. Sunlight can be visible or invisible according the wavelength. Table 8-1 shows the range of the wavelength of visible light. If wavelength $\lambda < 0.4\,\mu\text{m}$, it is called ultraviolet; if the wavelength falls between 700 and 1500 nm ($0.7\,\mu\text{m} < \lambda < 1.5\,\mu\text{m}$), it is called near-infrared. If the wave length falls between 1,500 nm to 20,000 nm ($1.5\,\mu\text{m} < \lambda < 20\,\mu\text{m}$), it is called mid-infrared; and if the wavelength falls between 20,000 and 100,000 nm ($20\,\mu\text{m} < \lambda < 100\,\mu\text{m}$), it is called far infrared.

As mentioned above, infrared is a waveband in the electromagnetic spectrum that lies just beyond red and is invisible to the naked eye. According to the physical law, all matter with a temperature above absolute zero, i.e., -273°C, radiates heat. Heat radiation is synonymous with infrared radiation, or we can say that all objects emit infrared radiation. The intensity of the emitted radiation depends on two factors: the temperature of the object and the ability of the

Table 8-1 Wavelength ranges of visible light

Wavelength (nm)	Color
400–450	Violet
450–480	Blue
480–510	Blue-green
510–550	Green
550–570	Yellow-green
570–590	Yellow
590–630	Orange
630–700	Red

object to radiate or its emissivity. The amount of infrared radiation of an object increases with the rise of temperature. When a material body is conducting heat flow, the effects of the material thermal properties and internal structure means that the heat distribution within the body can be the presented in the surface temperature field, and the infrared radiance emitted from the body can be related to its surface temperature. Based on this principle, infrared thermography can be used to inspect the surface temperature field of materials, and further to interpret its internal structural states.

According to Planck's law, the thermal radiation power of a blackbody per unit of area, unit of solid angle, and unit of frequency, f, can be written as

$$u(f,T) = \frac{2hf^3}{c^2} \cdot \frac{1}{e^{hf/kT} - 1} \tag{8-106}$$

where f is the frequency, T the temperature on the Kelvin scale, h Planck's constant (h = 6.626 $\times$ 10^{-34} J/sec), c the speed of the light (c = 299,792,458 m/sec), and k Boltzmann's constant (k = 1.380 $\times$ 10^{-23} J/K). This formula mathematically follows from calculation of the spectral energy distribution in a quantized electromagnetic field that is in complete thermal equilibrium with the radiating object.

By integrating the above equation over the power output, Stefan's law is obtained:

$$W = \sigma \cdot A \cdot T^4 \tag{8-107}$$

where σ is the Stefan-Boltzmann constant with a value of 5.670 $\times$ 10^{-8} $Wm^{-2}K^{-2}$. The wavelength λ, for which the emission intensity is highest, can be obtained by Wien's law:

$$\lambda_{max} = \frac{b}{T} \tag{8-108}$$

where b is Wien's displacement constant, of value 2.897 $\times$ 10^{-3} mK.

For surfaces that are not blackbodies, one has to consider the (generally frequency-dependent) emissivity correction factor $\varepsilon(f)$. This correction factor has to be multiplied with the radiation spectrum formula before integration. The resulting formula for the power output can be written in a way that contains a temperature-dependent correction factor, which is (somewhat confusingly) often called ε as well:

$$W = \varepsilon \cdot \sigma \cdot A \cdot T^4 \tag{8-109}$$

When an analysis of the surface temperature field is required, the surface temperature profile of an object will have to be recorded and an infrared camera is required for scanning and recording. An infrared camera is a radiometer that measures the radiated electromagnetic energy. Once the parameters are defined, the radiometric values registered by the camera can be converted into temperature values. The fundamental equation of thermography is introduced as follows. The radiance N_{CAM} received by the camera is expressed by

$$N_{\text{CAM}} = \varepsilon N_{\text{obj}} + (1 - \varepsilon) N_{\text{env}} \tag{8-110}$$

where ε is the object emissivity, N_{obj} the radiance from the surface of the object, and N_{env} the radiance of the surrounding environment. If an object has a very high emissivity coefficient, e.g., $\varepsilon > 0.9$, we can roughly write

$$N_{\text{obj}} \approx N_{\text{CAM}} \tag{8-111}$$

In this case, a direct relationship can be derived between the radiometric signal and the temperature of the object using Equation 8-111. However, in many cases, ε is not big enough and a correction is needed to accurately interpret the properties of the object under inspection. One such correction method is introduced in a later section.

A system used for thermographic inspection and based on principles presented above must be composed of many subsystems, such as a scanner, an infrared camera, an image acquisition and analysis system, a portable display monitor, and a thermal stimulation system. The mechanism of a thermographic inspection system is described as follows: the scanner contains a gas-cooled multielement detector. The gas cooling is used as a reference and to eliminate electronic noise. The camera converts electromagnetic energy into electronic video signals. These signals are then amplified and transmitted to a high-resolution portable display monitor. Parts of the scanning system are very sensitive and can identify temperature differences as small as 0.1°C or less. A range of lenses can be used so that surfaces can be inspected from as close as one meter or up to several hundred meters from the structure. The portable display monitor portrays the image in monochrome or color, and, generally, the hotter the area, the lighter the image, and the cooler the area, the darker the image. This portrayed image can be video-recorded, in real time, and the system provides an instant thermal picture. The displayed image can be stored in a computer, where further analysis of the captured data can be carried out. The complete thermographic inspection system is illustrated in Figure 8-46.

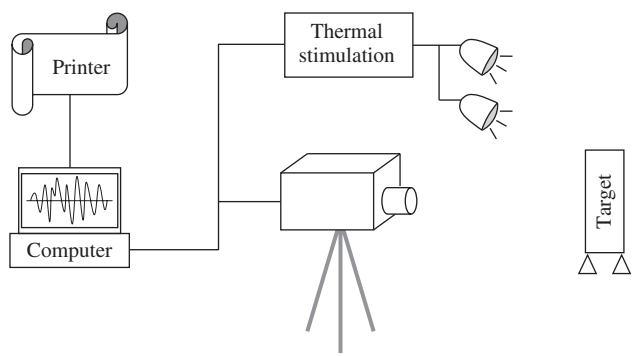

Figure 8-46 Typical active infrared NDT experimental setup

There are two different ways in which infrared equipment can be deployed for thermography nondestructive evaluation, depending on the specific application envisaged. In general, a thermograph can be deployed either in a passive or an active fashion. In the passive configuration, the infrared camera is pointed at the scene, focusing on the object to be inspected, while no external thermal perturbation is applied. Applications such as building inspection make use of this mode of operation, where the surface temperature distribution, as is, contains relevant information concerning the possible presence or absence of any defects. In the active configuration, an externally applied thermal stimulation is needed to generate meaningful contrasts that will yield the detection of subsurface abnormalities. In general, the heat will be conducted away by the mass of the structure. If there are defect areas, the heat will not dissipate there at the same rate as in the sound areas. With this phenomenon, information can be drawn from the inspection, since the surface temperature distribution of a certain object is related to the subsurface structure.

The first attempt to detect anomalies and air leaks in buildings using IR techniques was reported by an AGA salesman in 1965. From 1975 to 1985 there was rapid progress and the potential of nondestructive evaluation of materials by infrared thermograph was increasingly exploited, especially in the 1980s with the availability of commercial infrared cameras whose video signals were compatible with black-and-white television standards. Results have been reported at different international conferences in the united states (SPIE: thermo-sensing) and in Canada (symposium on remote sensing). Most research work on infrared thermography for civil engineering applications has been carried out during the last 10 years. This method has now gained widespread popularity because it is a nondestructive technique that is quick, safe, and easy to implement.

Under certain ambient conditions, a building with surface defects in the form of debonding mosaic tiles or delaminating render emits differing amounts of infrared radiation. Using a suitably modified infrared camera, the surface of a building can be scanned rapidly and areas that are defective will show up as a result of the differential transmittance of infrared radiation. A surface with an even texture, free of cracks and delaminations, will appear quite uniform when viewed by the infrared camera. If there is a defect, the ambient temperature conditions and solar gain will make the surface heat up and cool down at different rates. Different buildings can be situated in different locations that may be surrounded by different complex environmental conditions, which can lead to abnormal distributions of surface temperature fields. Some subsurface defects may be filled with air; some may be partially filled with moisture. In the sunshine or on a cloudy day, these defects present different behaviors, which could impose some potential difficulties for interpreting the results obtained from an infrared thermograph.

Consider a thin tile, in which one surface is in contact with air and is exposed to the sun. The other surface is in contact with the wall. The equation for the temperature of an element of the tile is

$$B\frac{dT}{dt} = H - K(T - T_0) \tag{8-112}$$

where B is the heat capacitance per unit area of the tile, H the heat flow onto the tile/air surface due to the sunlight, and K the thermal conductivity between the tile and the wall. In the most simplified model, T_0 is the wall temperature, which remains constant because of its large thermal capacitance. In a more sophisticated model, the temperature of the thick wall varies across the thickness section of the wall, which is in contact with tile on one surface and with the room air on the other. The temperature variation of the wall is such that its surface on the tile side will follow the change of the tile temperature, while the temperature of its indoor surface remains constant. Since the heat flow is determined by the temperature gradient, an equivalent temperature T_0 can be found such that $K(T - T_0)$ is equal to the actual heat flow from the tiles to the wall.

The values of B and K may vary across the plane of the tile due to the variation of the tile/wall bound conditions, thus causing a temperature variation, which can be detected by a thermal camera. Here, the lateral thermal conduction, the thermal conduction of the surface/air, is ignored. These factors can be ignored only within a short period of time when the tile temperature is varying. Over a period (several hours), the thermal conduction to air and the lateral conduction will result in an uniform temperature distribution all over the tiles, and the defects behind the tile will not be easily detected. Therefore, it is important that the thermograph measurements should be carried out within the transient period.

(a) *Heating process*: Supposed a tile is at T_0 at $t = 0$. This would be the condition in the morning before sunrise, where $H = 0$. A heat flow is quickly imposed on the tile, and could be due to the sunrise, building shadow movement, or the clearing up of clouds. The time-dependent temperature is then followed, by solving the equation below with the proper initial conditions:

$$T = T_0 + \frac{H}{K}(1 - e^{-K_t/B}) \tag{8-113}$$

It is seen that the time constant in the exponential expression depends on K/B, and the steady state is $T_0 + H/K$. In practice, within $t = 5B/K$, $T(t)$ will reach 99% of its steady value. This steady value, which is actually only quasi-steady because the lateral thermal conduction and air conduction are not considered, will gradually be taken over by these much slower processes. A quasi-steady-state thermograph should therefore be taken at times after $5B/K$ but before the lateral conduction takes over.

A debonding defect is a hollow space between the tile and wall. The hollow space could be filled with water, caused by rain or moisture condensation due to the high humidity in Hong Kong, or caused simply by air. However, the two filling media, air and water, have different effects on the thermal properties, B and K, of the tiles. An air pocket (void) with its poor thermal conductivity will have a reduced K but little influence on B. The surface temperature next to an air hole will then be higher than in intact areas during both the transient and quasi-steady-state stages. A water-filled cavity will probably have a larger K because of the improved thermal contact, even though water probably has about the same heat conductivity as cement, and will increase the thermal capacitance of the tile if the water is considered as part of the tile. Its surface temperature will therefore be lower than an intact tile. Laboratory tests (see next section) are in complete agreement with the above predictions.

(b) *Cooling process*: For a cooling process, the initial temperature is then $T_0 + H/K$ where the tiles are still in a quasi-steady state. The solution to the equation is then

$$T = T_0 - \frac{H}{K}e^{-K_t/B} \tag{8-114}$$

Due to lower thermal conductivity, an air-filled defect will cause a faster decrease, or a lower local temperature, while a water-filled hole will have a higher temperature.

(c) *Laboratory calibration*: To establish a link between the abnormal isotherms recorded on the inspected target surface and the presence of a subsurface defect, it is necessary to establish a baseline for comparison by calibrating the known defects in the laboratory. The basic principle of (transient) infrared thermograph consists of flashing heat to a specimen and subsequently recording the IR images (also called thermograms). Subsurface defects having different thermal properties with respect to the bulk of material will have an effect on the diffusion of the thermal front inside the material.

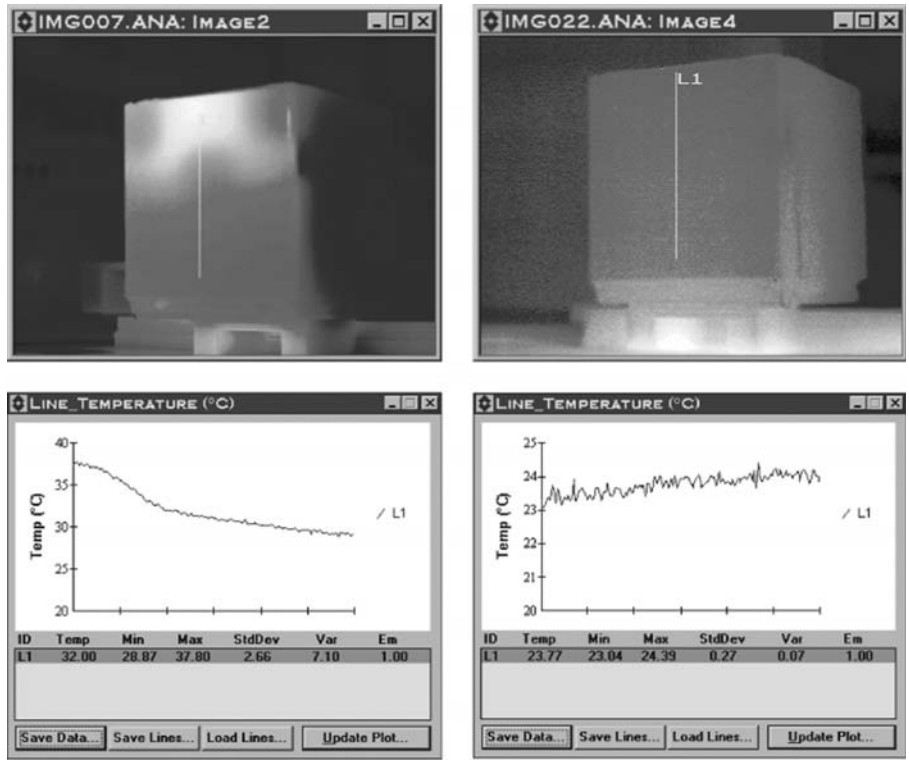

(a) (b)

Figure 8-47 Surface temperature distribution of a debonded tile sample with the upper half dry and the lower half filled with water: (a) uniform heating of the inspected face, and (b) after cooling for half an hour

Two procedures for calibration are used: (i) reflection, where both the thermal source and the IR camera are located on the same side of the tile wall; and (ii) transmission, where the thermal source and the IR camera are located on opposite sides of the tile wall.

Case 1. Debonded area filled with water: Filling the debonded area with water would lead to a lower surface temperature during heat inflow and a higher temperature during heat outflowing. An example of such an analysis was calibrated in the laboratory, as shown in Figure 8-47.

Before testing, the upper half of the tile sample was kept dry and the lower half was soaked with water, and an external thermal source was applied to one side of the tile sample, with the isotherm pattern on the same side being recorded. It was noticed that the surface temperature of the bottom half (wet) was lower than that of top portion of the tile, see Figure 8-47a. Once the thermal source was withdrawn, the tile sample would start to cool off. After half an hour, it was noted that the surface temperature of the bottom half (wet) in the IR image was higher, see Figure 8-47b. This was due to the fact that the moist areas retained more heat energy than the sound dry areas because of the higher thermal capacity of water.

Case 2. Debonded area filled with air: Another common phenomenon is the filling of the debonded area with air, which will lead to a higher surface temperature during heat flowing

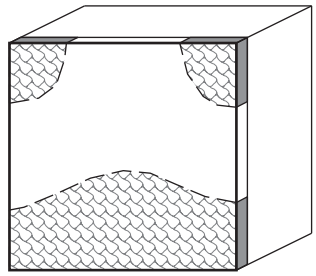

(a)

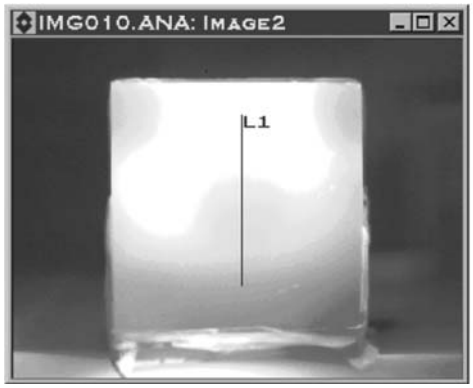

(b)

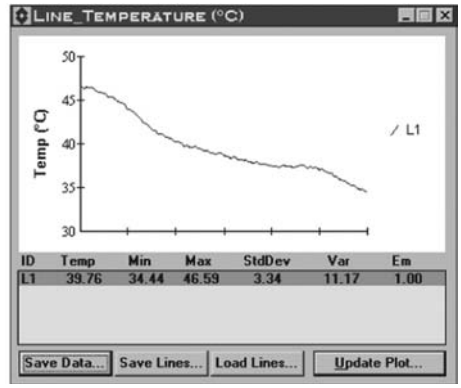

(c)

Figure 8-48 Tile with debonded area filled with air

in and a lower surface temperature during heat outflow. Figure 8-48 shows thermograms obtained on a tile sample with air defects under an external thermal stimulation. Figure 8-48a shows the areas of the bonded and debonded tile samples. Under an external heat stimulation, the thermal image presented different temperature distributions, as shown in Figure 8-48b. The high-temperature region was in the debonded area and the line profile also shows that the higher temperature was on the front surface of the debonded area, see Figure 8-48c.

8.5.5.3 Buildings inspection

As described in the previous section, a favorable condition for field inspection is a steep thermal gradient between the environment and the target object. This usually occurs in the morning after sunrise and in the afternoon before sunset, or due to the slow movement of shadows or clouds. The steep gradient stimulates the transient behavior of the tiles. When the finishing material has a perfect bond with the substrate, the incidence of heat on the surface is conducted away by the mass of the substrate (concrete wall). However, when there are debonding areas filled with moisture in the finishing materials, their thermal properties will be different. Figure 8-49 shows a corresponding thermogram of such a case. The survey was performed in the morning during the sunrise. Before the survey was conducted, it had been rainy for several days and it was very likely that condensed moisture or water was trapped in the defect areas (indexed by

Figure 8-49 The lower-temperature areas (indexed by upward arrows) indicating the defected areas filled with water or moisture

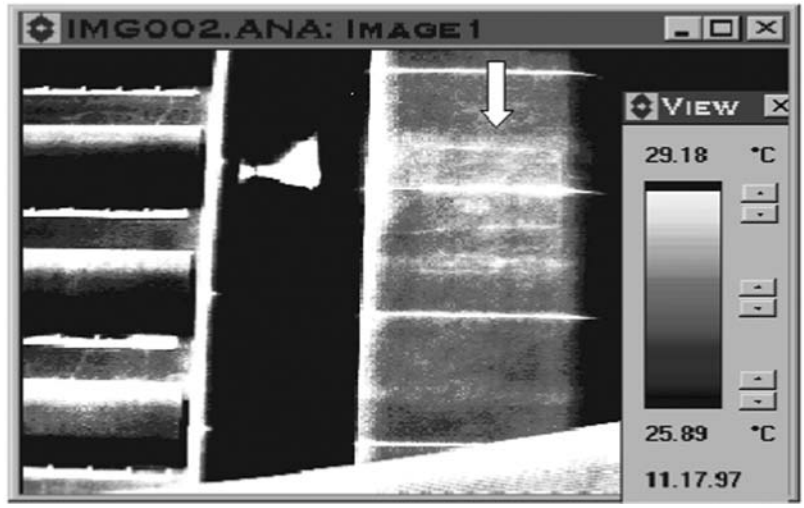

Figure 8-50 Thermogram indicating air-filled defect area of the external wall

arrows). Due to water having infiltrated the porous material, thereby increasing its specific heat, the surface temperature of the defect area was lower than the sound areas.

For the cases of air-filled debonding, the thermograms behave differently. When the sun shines on the surface, it begins to heat the tile-clad wall, and the surface over a debonding or potential void filled with air will heat up faster, because the fracture plane of the defect acts as a small insulator, trapping the heat in the tile. These "hot spots" on the surface are generally 2–3°C higher than the surrounding areas and can be easily detected by an IR camera. Figure 8-50 identifies this type of pattern. The higher-temperature regions in the figure are suspected to be severely debonded areas on the walls, which is later confirmed by the tapping technique.

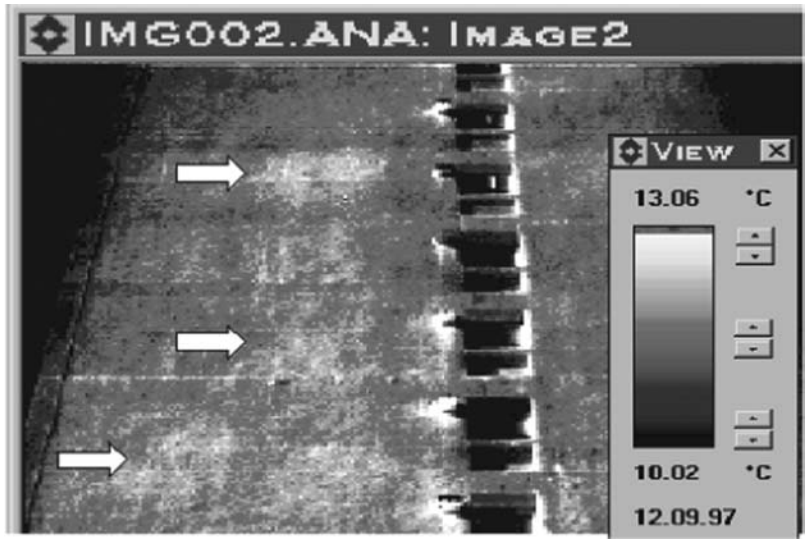

Figure 8-51 Thermogram indicating several small air-filled defect areas on the external wall of building

Moreover, even fairly small defects can be detected by the thermography technique. In Figure 8-51, the smallest "hot spot" was only about 50 × 50 mm in size. Debonded areas like this are generally held in place by the interlocking of the surrounding materials. However, any small defect has a potential to propagate into a large detachment. Hence, it should be marked for future surveys to monitor its size stability.

(a) *Reflection correction*: As mentioned in the earlier sections, an IR camera in front of an object detects not only the emitted radiance but also a part of the radiance due to reflection of the ambient fluxes by the object surface, whose reflectivity is nonzero. It is necessary to take into account this phenomenon for objects with reflective surfaces, such as ceramic tiles, when interpreting the survey results. As we know, in the fundamental thermograph equation, the radiance N_{CAM} received by the IR camera is expressed by

$$N_{CAM} = \tau_{atm}\varepsilon N_{obj} + \tau_{atm}\rho N_{env} + (1 - \tau_{atm})N_{atm} \tag{8-115}$$

where τ_{atm} is the transmission coefficient of the atmosphere in the spectral window of interest, ε the object emissivity (the object is considered opaque), ρ the object reflectivity, N_{obj} the radiance from the surface of the object, N_{env} the radiance of the surrounding environment considered as a blackbody, and N_{atm} the radiance of the atmosphere (supposed constant). If the transmission coefficient of the atmosphere is considered to be close to unity, Equation 8-115 can be simplified as follows:

$$N_{CAM} = \varepsilon N_{obj} + \rho N_{env} \tag{8-116}$$

If the emissivity is very high (more than 0.9), according to the Kirchhoff laws, $\varepsilon = 1 - \rho$, Equation 8-116 can be further reduced to $N_{obj} \approx N_{CAM}$. According to some relationships, camera signals can be converted to radiance N_{obj} and temperature T_{obj} values. If the emissivity ε is not high enough, but with perfectly diffuse reflection, the temperature of an object can also be qualitatively obtained from the radiance N_{CAM} received by the IR camera.

For ceramic tiles, the emissivity is about 0.6–0.8, not high enough to ignore the effect of the surface reflection. Moreover, due to the smooth surface, more specular than diffuse, the intensity of the reflected radiation is not constant in all directions. In an actual survey, the specular reflection toward the camera will yield apparent hot spots or strips in the IR images. Hot spots or strips would be falsely interpreted as damage zones following the active thermography principle discussed previously. Consequently, extreme care is required and an adequate approach should be undertaken when IR thermography is to be employed for materials having specular reflective surfaces. We here take the reflectivity to be the sum of a specular component and a diffuse component:

$$\rho = \rho_s + \rho_D \tag{8-117}$$

We define the diffuse radiance N_D as the total diffuse energy leaving the surface per unit area and per unit time, so that

$$N_D = \varepsilon N_{obj} + \rho_D N_{env} \tag{8-118}$$

In Equations 8-116 and 8-118, it is known that N_{obj} is related to the surface temperature of unit area, N_{CAM} and N_D are related to the detected temperatures by the IR camera for the unit area with and without specular reflection toward the camera, respectively. The temperature detected by the IR camera can be overestimated due to reflectivity. Moreover, the specular reflection will create parasitic hot spots that further complicate the thermogram interpretation.

The most effective way to solve the problem is to remove the influence of specular reflection. This can be done by grabbing the images continually at the same zone (for example, mounting the camera on a tripod, when the images are recorded and neither the object nor camera is moved), and recording the thermography images during a dual transient period, i.e., right after a thermal source is applied and then withdrawn abruptly. During the daytime, a favorable weather condition for this purpose is when the sky is partially cloudy. The movement of a cloud leads to a change from sunshine to shadow and back to sunshine again, providing an opportunity to record the transient behavior with or without specular reflection for the wall tiles under inspection. In sunshine, the object is thermally stimulated but with a reflective disturbance; under cloud cover, the effect of surface reflection is minimized and the detected temperature by the IR camera corresponds to the actual surface temperature of the object. Due to the rapid change of temperature in the transient period, a grab rate of 30 sec/frame is suggested.

When the images are taken in this way, the points of interest will always be in exactly (or very near) the same place in all the images. Figure 8-52 shows some results of the images taken using this approach, and each image was grabbed at a different time (but for the same position). In image 1, we marked down the X/Y coordinates of three points, P1, P2, and P3. By using the "Trending Analysis" program, the three points (that we placed in image 1) were automatically placed at exactly the same pixel locations in all of the images (see Figure 8-52a), and the graph showing the temperature variation of the spots over the series of images is shown in Figure 8-52b.

In Figure 8-52, it is found that in about 15 minutes, the detected temperatures by the IR camera for the three fixed points are different due to the motion of the clouds. The temperature of P3 is higher than that of other two points both with clouds and without clouds, indicating the zone near this point is a damaged area with a subsurface filled with air. The temperature of P1 is lower at all times, indicating the region near P1 is a sound area. It should be noted that the temperature change of P2 is somewhat different as compared to these two points. Without clouds, its temperature is higher than that of P1, and only slightly lower than that of P3. But with clouds (stage AB, C, DE, and FG in Figure 8-52b), the detected temperature of P2 is nearly equal to that of P1, indicating the influence of specular reflection on P2. Hence, we can conclude that the

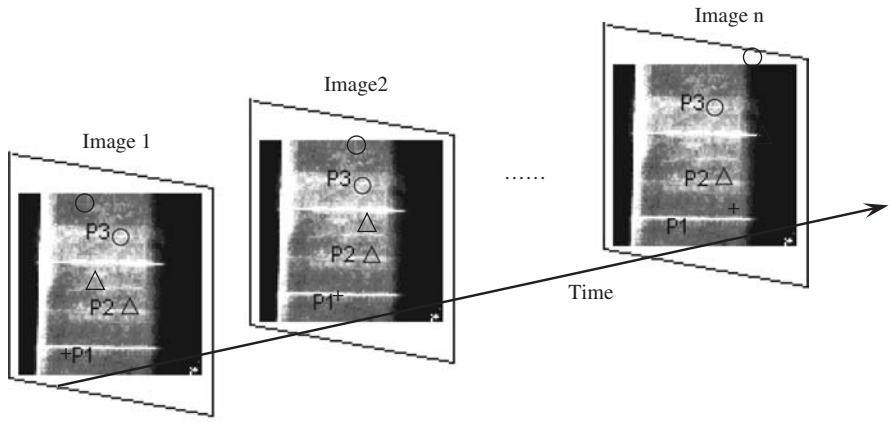

(a)

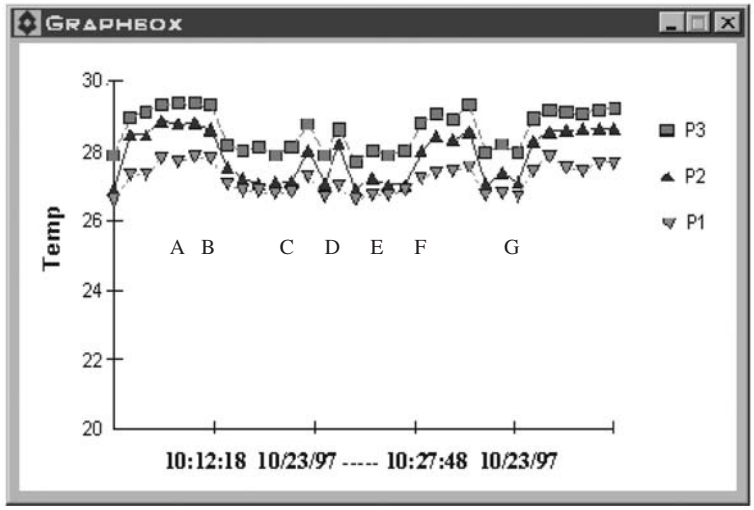

(b)

Figure 8-52 (a) Thermal trend analysis approach and (b) the development of the spots over the series of images at different times

actual surface temperatures of points P1 and P2 are almost same, and the region near point P2 is also a sound area. The higher temperature of P2 in the case without clouds, caused by the effect of specular reflection, might be falsely interpreted as a damaged zone if the object was stimulated by sunshine all the time. After all, the proposed approach is very useful to eliminate the effect of reflection and make possible interpretation and analysis, with a high degree of accuracy.

(b) *Space resolution*: Before discussing the space resolution of an infrared thermograph camera, let us first talk about the field of view. The field of view (FOV) is defined as the area of an object to be inspected that can be viewed by an infrared thermograph camera. It depends on the lens of the system and the distance between the camera and the object. Another term frequently encountered is the instantaneous field of view (IFOV). A camera usually consists of

Table 8-2 The field of view and instantaneous field of view for a typical camera

Distance to Object	Field of View	IFOV
1 m	0.35 × 0.26 m	1.1 × 1.1 mm
5 m	1.76 × 1.32 m	5.5 × 5.5 mm
10 m	3.52 × 2.63 m	11 × 11 mm
50 m	17.6 × 13.2 m	55 × 55 mm

many detectors, arranged in an array. The smallest cell in the array is called a picture element or pixel. The area covered by each pixel is the IFOV. For instance, if a camera has 320 × 240 detectors, it has 76,800 cells. The field of view will be distributed on these cells. As an illustration, Table 8-2 shows the field of view and instantaneous field of view for a typical camera (with a 20 by 15-degree lens) at different distances.

It is fair to say that the IFOV is a measure for the spatial resolution from cameras with focus parallel array detectors. The spatial resolution, also called geometrical resolution, is one of the most important parameters for viewing, as well as for temperature measurement of an object. It determines how well an object under inspection can be measured. For the case where the object to be measured covers IFOV completely, the pixels will receive radiation from the object only and the temperature can be correctly measured. However, if the object to be measured cannot cover IFOV completely, i.e., IFOV is larger than the object, the detector will pick up radiation from other objects surrounding or behind the object to be inspected and hence an inaccurate result will be obtained. Moreover, the optics distorts the image, e.g., chromatic aberration, spherical aberration, and a number of other deficiencies, which implies that radiation coming from objects outside the IFOV will fall onto the detector. Hence the real size of the measurement spot is substantially bigger than the IFOV. The IFOV is therefore a measure of the absolute lower limit for measurement.

(c) *Angle correction*: The IFOV is usually defined perpendicular to the object. In other words, it is the area seen from a camera when the camera looks at the object at a right angle. However, in many cases, the projection of the detector on the object does not always hit the object at a right angle. When the detector is projected onto the object with an angle α, the surface that the detector hits is bigger than that it hits at a right angle, as shown in Figure 8-53. Considering that the radiation from an object varies with the angle of view as

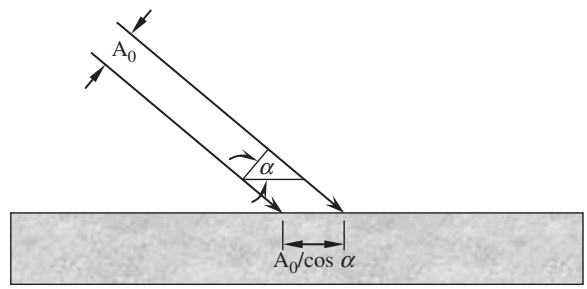

Figure 8-53 The projection area of an angled detection beam

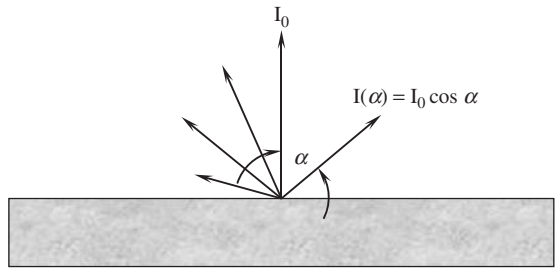

Figure 8-54 The radiation from an object with the angle of view

shown in Figure 8-54, if we combine the two effects sketched above, i.e., the radiator being looked at by a thermal camera at an angle of α, the expression for the received radiation can be obtained:

$$\frac{A_0}{\cos \alpha} I_0 \cos \alpha = A_0 I_0 \tag{8-119}$$

It can be seen that the camera sees the same radiation from a diffuse radiator, no matter what the angle of incidence. However, in reality no perfectly diffuse bodies exist. A good rule of thumb is that most bodies are Lambertian radiators up about 50 degrees from the normal. After that the emissivity usually goes down.

8.6 NONCONTACTING RESISTIVITY MEASUREMENT METHOD

Many nondestructive methods are based on measuring the changes in electrical properties, including electrical resistance, dielectric constant, and polarization resistance, of concrete. These methods can be classified into electrical and electrochemical nondestructive methods. The electrical resistance of an electrolyte is directly proportional to the length and inversely proportional to the cross-sectional area and is expressed by

$$R = \rho \frac{L}{A} \tag{8-120}$$

where R is the resistance in ohms, ρ the resistivity in $\Omega \cdot$ m, L the length in m, and A the cross-sectional area in m^2. The changes in electrical properties of concrete are closely related to the evaporable water content in concrete, which varies with water/cement ratio, degree of hydration, and degree of saturation. The ion concentration in water varies with time, too. The conduction of electricity by moist concrete is essentially electrolytic and can be used to interpret the properties of concrete, despite the complex relationship between the concrete's moisture content and its dielectric constant. The electrical resistance depends on the size of concrete specimen, while the resistivity is essentially a material property, so that electrical resistivity is more widely used for characterizing concrete property in electrical methods. Resistivity measurement can provide a rapid nondestructive assessment of concrete surface areas, crack size, reinforcing steel corrosion, and cement hydration.

To detect steel corrosion, the ability of the corrosion current to flow through the concrete is assessed in terms of the electrolytic resistivity of the material. An in situ resistivity measurement setup, in conjunction with half-cell measurement, is shown in Figure 8-55. In this test technique, normally low-frequency alternating current is applied and the current flowing between the outer

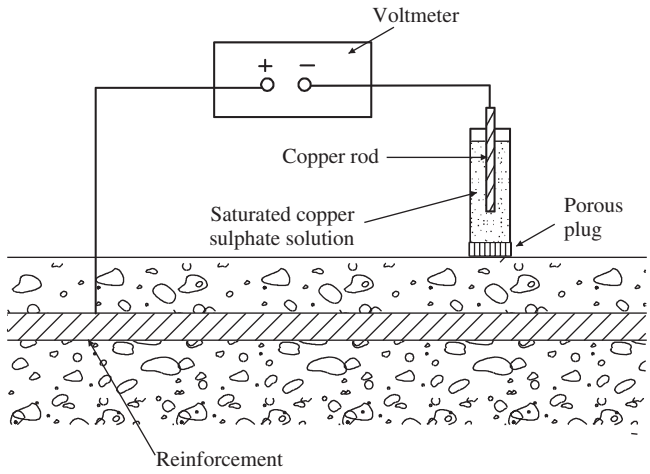

Figure 8-55 Reinforcement potential measurement by the half-cell method

Table 8-3 Classification of the likelihood of corrosion by half-cell potential

Potentials over an area	> −0.20 V CSE[a]	−0.20 V ~ −0.35 V CSE	< −0.35 V CSE
Probability of steel corrosion	> 90% no corrosion	Uncertain	> 90% corrosion

[a]Copper sulfate electrode.

probes and the voltage between the inner probes are measured. Since the ability of the corrosion current to flow through concrete increases with decreasing resistivity, the measured resistivity ρ can be used together with potential measurements to assess the likelihood of corrosion. Classification of the likelihood of corrosion can be obtained following the values in Table 8-3 when half-cell potential measurements show that corrosion is possible. As far as the test results are interpreted, highly negative corrosion potential or a high gradient in a potential map imply that corrosion is thermodynamically favorable. If the resistivity is also low, there is a high chance to have significant corrosion actually occurring in the reinforcing steel.

The resistivity can also be used as a measure of the degree of hydration of cement-based materials. In the past, such measurement always employed contacting electrical resistivity apparatus, which has many drawbacks. Recently, Li and Li (2002) and Li et al. (2003) have invented a noncontacting electrical resistivity apparatus to measure the resistivity of cement-based materials. The measuring system of this nondestructive testing method is shown in Figure 8-56, which adopts the transformer principle. The electrical circuit contains a primary coil with wound wires and a ring-type cementitious specimen acting as the secondary coil of the transformer. The primary coil is the input coil of the transformer and the secondary coil is the output coil. When AC is applied to the primary coil, mutual induction causes current to be induced in the secondary coil. With the measurement of the induction current in a cement-based specimen, the curve of resistivity versus time can be obtained. By interpreting the behavior of the resistivity curve, the hydration characteristics of cement-based materials can be obtained. The characteristics include the hydration stages, setting times, and strength development. It has been found that the noncontact electrical resistivity measurement provides a good nondestructive way to determine and assess the setting time and mechanical properties of the cement-based materials during the entire

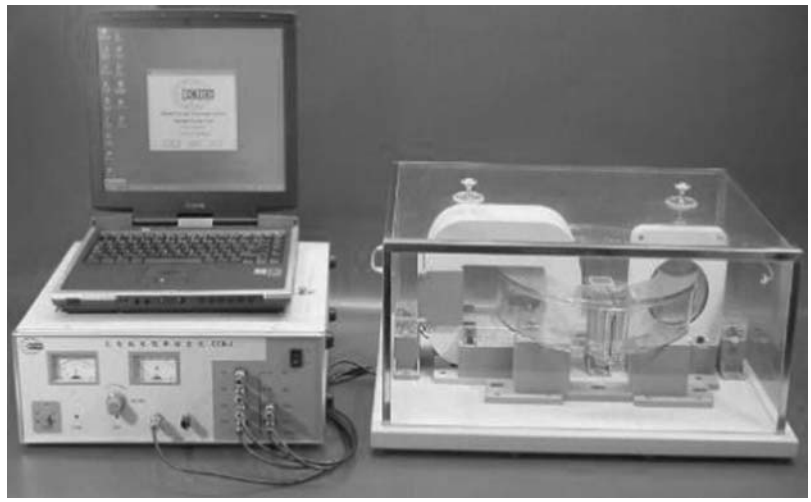

Figure 8-56 A noncontact resistivity test apparatus for cement-based materials

setting process. In general, fresh concrete behaves essentially as an electrolyte with a resistivity of the order of 1 Ω·m, a value in the range of semiconductors, while hardened concrete has a resistivity of the order of 10 Ω·m, a reasonably good insulator.

The Wenner four-probe technique has been used for soil testing for many years and it has recently been adopted in applications for testing in situ concrete. In this method, four electrodes are placed in a straight line, on, or just below, the concrete surface at equal spacing, as shown in Figure 8-57. A low-frequency alternating electrical current is passed between the two outer electrodes while the voltage drop between the inner electrodes is measured. The apparent resistivity, ρ, is calculated as

$$\rho = \frac{2\pi sV}{I} \tag{8-121}$$

where s is the electrode spacing, V the voltage drop, and I the current. This method can also be used in applications for detecting pavement thickness. Since concrete and subgrade pavement materials have different electrical characteristics, the change in slope of the resistivity vs. pavement depth curve will indicate pavement thickness (Vassie, 1978). When testing a concrete pavement, the electrode system may be adjusted at 25- or 50-mm spacings for the initial readings, and then expanded to 25-mm increments for successive readings, thereby extending to a spacing equal to the pavement depth plus 75–150 mm (Malhotra and Carino, 2004).

The corrosion of steel in concrete is an electrochemical process that requires a flow of electrical current for the chemical corrosion reactions to proceed. The electrochemical method can be used to detect signs of rebar corrosion, based on an electrochemical process, through measuring the electric potential of the reinforcing bars (Newman, 2001). Some tests use the half-cell method of measurement described in Chapter 2, in which a copper/copper sulfate half-cell is used. In this technique, an electrical connection is made to the reinforcement at a convenient position. The electric potential difference between the anode and the cathode is measured by a voltmeter; and if the values are more negative than 350 mV, the probability of corrosion is in excess of 90 percent. In practice, a series of measurements can be taken at grid points to map the probable corrosion activity. This technique has been standardized by ASTM C876. According to

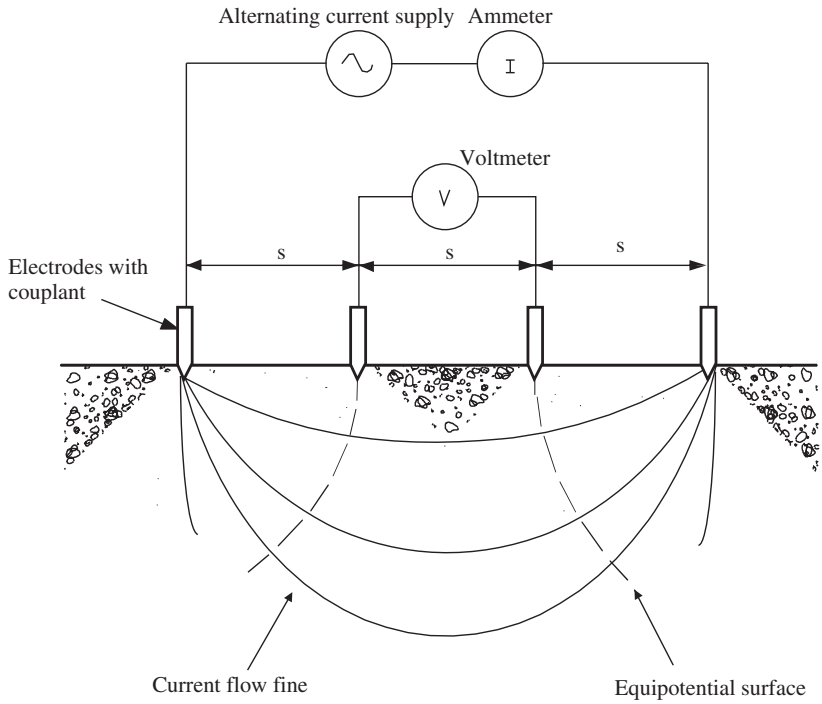

Figure 8-57 Four-probe resistivity test of concrete

this standard, the difference between two half-cell readings taken at the same location with the same cell should not exceed 10 mV when the cell is disconnected and reconnected. In addition, the difference between two half-cell readings taken at the same location with two different cells should not exceed 20 mV. This method is readily utilized in the field, but trained operators are required. What's more, the actual rate of corrosion (such as the percent loss of section) is not provided by this method. The interpretations of these potentials vary with investigator and agency.

The variations of electrical resistivity are closely related to the physical and chemical properties of cement-based materials at early ages. Resistivity is used to study and analyze the hydration process of young cement-based materials (Khalaf and Wilson, 1999; EL-Enein et al., 1995; Levita et al., 2000). Early studies of concrete resistivity applied a DC voltage on the concrete specimen, then obtained electrical resistance according to Ohm's law. There are several disadvantages to DC voltage probing, such as the polarization effect, the release gas effect, and the change of ion distribution (Lakshminarayanan et al., 1992; Banthia et al., 1992). These factors will cause the measured results to be inaccurate, hence, using AC voltage as the probing signal is more reasonable. In recent years, there have been many papers concerning this subject (Hughes et al., 1985). These conventional methods for resistance measurements (consequently, resistivity) of cement-based materials are usually conducted by measuring the AC current and the AC voltage between two plate electrodes placed at opposite sides of a prism specimen (McCarter et al., 1981). Obviously, the contact between the electrodes and specimen plays an important role in determining the accuracy of the measurement. Loose contacts will lead to inaccurate and sometimes ridiculous results. To improve the contact, some researchers inserted fresh cement paste or colloidal graphite between the electrodes and concrete (McCarter et al.,

1981; Whittington et al., 1981), and others used external force to fasten the electrodes and concrete specimen from two ends.

These measures are effective only at the beginning of experiments. As the hydration of cement proceeds, shrinkage will occur, which can lead to some fissures appearing in the electrode–concrete boundary. If this phenomenon occurs, the experiment cannot be continued. In addition, the cement paste is highly alkaline (pH 12.5–13.5), so the electrodes are gradually corroded within several days. Due to the poor connection problem, the data obtained by this kind of method are suspect. Besides, fresh cement paste and colloidal graphite can diffuse inside the specimen being measured, which affects the measured results.

8.6.1 Principle of the novel method

The schematic of the resistance measurement for the novel method is shown in Figure 2-15 (Chapter 2), in which there are no electrodes, and the cement-based specimen is a ring with a rectangular section. The specimen ring acts as a secondary transformer coil.

When an AC voltage is applied on the primary coil of the transformer, a toroidal voltage (V) will be inducted in the secondary, i.e., in the specimen ring. Subsequently, a toroidal current (I) will be incurred inside the specimen ring. Supposing the impedance of specimen ring is Z:

$$Z = V / I \tag{8-122}$$

This principle can be represented by an equivalent circuit as shown in Figure 8-58. In the figure, R is resistance, and C capacitance; then

$$\begin{aligned} V &= R \cdot I_R \\ \mathbf{I} &= \mathbf{I}_C + \mathbf{I}_R \end{aligned} \tag{8-123}$$

The impedance of the specimen is the parallel connection of R and C:

$$Z = R\left[1 + (\omega CR)^2\right]^{-1/2} = R\left[1 + (2\pi fCR)^2\right]^{-1/2} \tag{8-124}$$

where Z is the impedance of specimen ring, R the resistance of specimen ring, C the capacitance of specimen ring, and f the probing frequency. According to the phase difference between the toroidal voltage V and the toroidal current I, R can be obtained:

$$R = V / (I \cos\varphi) \tag{8-125}$$

where V is the toroidal voltage, I the current passed through specimen ring, and φ the phase difference between V and I.

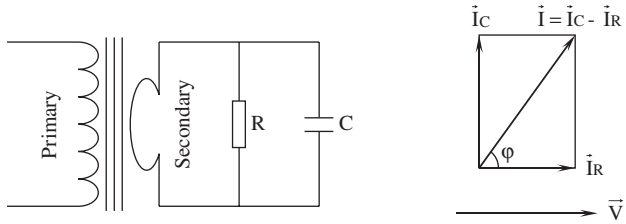

Figure 8-58 An equivalent circuit for the resistivity measurement

8.6.2 Formulation of resistivity calculation

The resistance can be found from Equation 8-125. Since the resistance of a specimen depends on the geometric parameters, resistance is therefore not significant for material research. The resistivity is a necessary parameter for comparison between different specimens. Due to the geometric form of the ring, the resistivity cannot be directly calculated from R. In these circumstances, a formula for resistivity calculation was derived from integral equations. As shown in Figure 8-59, the cross section of the specimen is rectangular. In fact, the cross section of a specimen ring can be either rectangular or circular. However, a rectangular section is recommended due to the ease of mold making. On the other hand, this shape can meet drill sampling for hardened cement-based materials. The procedures of formula derivation for the resistivity calculation are as follows. For a conductor, such as a metal wire, the resistance R can be represented by

$$R = \rho L/S \tag{8-126}$$

where ρ is the electrical resistivity of conductor, L the length of conductor, and S the cross section of conductor. For a conducting ring with rectangle section, as shown in Figure 8-59, the rectangle section can be divided into many area elements:

$\Delta R_1, \Delta R_2, \Delta R_3, \ldots$ are the resistance elements

r_{in} the internal radius

r_{ex} the external radius

ΔS the area element

$\Delta S = h\Delta r$

The circumferences for different radii are

$$\begin{aligned}
L_i &= 2\pi r_i, \qquad i = 1 \text{ to } n, \qquad n = (r_{\text{ex}} - r_{\text{in}})/\Delta r \\
\Delta R_1 &= \rho L_1/\Delta S_1 = \rho 2\pi r_1/\Delta S_1 = \rho 2\pi r_1/h\Delta r, \qquad r_1 = r_{\text{in}} + \Delta r \\
\Delta R_2 &= \rho L_2/\Delta S_2 = \rho 2\pi r_2/\Delta S_2 = \rho 2\pi r_2/h\Delta r, \qquad r_2 = r_1 + \Delta r \\
\Delta R_3 &= \rho L_3/\Delta S_3 = \rho 2\pi r_3/\Delta S_3 = \rho 2\pi r_3/h\Delta r, \qquad r_3 = r_2 + \Delta r \\
&\vdots \\
\Delta R_n &= \rho L_n/\Delta S_n = \rho 2\pi r_n/\Delta S_n = \rho 2\pi r_n/h\Delta r, \qquad r_n = r_{n-1} + \Delta r
\end{aligned} \tag{8-127}$$

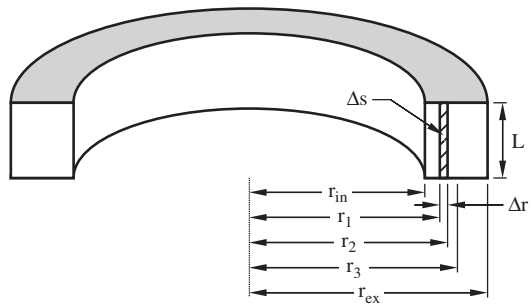

Figure 8-59 Cross sections of the resistivity measurement ring

Supposing the whole resistance is R, which equals all resistance elements connected in parallel. Then

$$\begin{aligned} 1/R &= 1/\Delta R_1 + 1/\Delta R_2 + 1/\Delta R_3 + \cdots \\ &= \sum_{i=1}^{\infty} 1/\Delta R_i \\ &= \left(h/2\pi\rho\right) \int_{r_{\text{in}}}^{r_{\text{ex}}} (1/r)\, dr \\ &= \left(h/2\pi\rho\right) \ln\left(r_{\text{ex}}/r_{\text{in}}\right) \end{aligned} \tag{8-128}$$

$$\text{hence, } R = \frac{2\pi\rho}{h \ln\left(r_{\text{ex}}/r_{\text{in}}\right)} \tag{8-129}$$

The resistivity ρ can be obtain as

$$\rho = \frac{Rh \ln\left(r_{\text{ex}}/r_{\text{in}}\right)}{2\pi} \tag{8-130}$$

The rectangular section ring can be made of cement-based materials, because the resistivities of cement-based material are larger than those of metals (metal conductor ρ 10^{-6}–10^{-4} Ω·cm). In addition, the electrical current is produced by ion movement and the frequency used in the experiments is lower (1–20 kHz). Thus, there is no skin effect inside the concrete. The current density in the specimen section is proportional to $1/r$. These initial conditions can satisfy the requirements of the equations used in the derivation process.

When the resistance R is obtained from Equation 8-125, concurrently, the relative resistivity can be found by Equation 8-130, which can be used to accurately calculate the resistivities of cement-based products.

8.6.3 Measuring system

The measuring system of the novel method is shown in Figure 8-60, which consists of a generator, amplifier, oscilloscope, transformer core, current sensor, data acquisition interface, and computer. The generator produces a sine wave at a given frequency. The amplifier magnifies the sine wave to match the transformer primary, and the data acquisition interface samples the data needed and transfers them to computer. The sampling period is 5 minutes. An oscilloscope is used to observe the phase between the toroidal voltage and current. This system can operate continuously. To understand this system clearly, it is necessary to give the relevant parameters of this system. The signal applied on the primary of transformer is a sine wave of 1 kHz frequency, the turn number of the transformer primary is 36, and the secondary toroidal voltage is 1.2 V. The measuring range of the leakage current clamp is 0–100 mA, and the resolution is 0.1 mA.

Before measuring the resistances of cement-based specimens, a circuit of parallel connection by a resistor and a capacitor is used to assess the accuracy of the measuring system. The values measured by this method, such as resistance, and capacitance, are perfectly coincident with the nominal values. The phase relations between V and I are correct, when using a pure resistance to simulate the cement specimen. The phase measured is zero. These results proved that the system is credible.

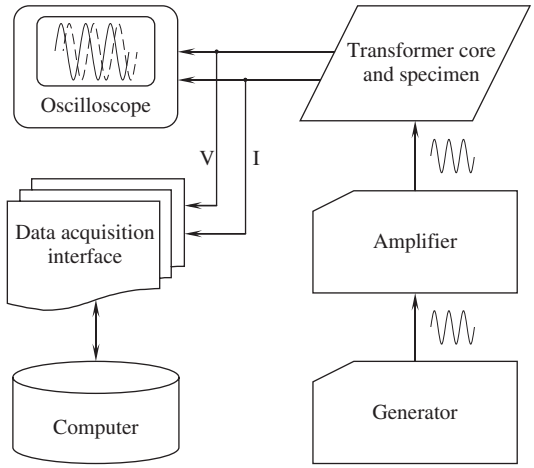

Figure 8-60 Measurement system for the resistivity test

8.6.3.1 Resistivity measurements of cement specimens

When using this system to monitor the resistivity of a cement-based paste for studying the hydration process, the paste has to be cast in a mold. The geometric shape of the mold is shown in Figure 2-15 (see Chapter 2), and the mold is cast in the position shown in Figure 2-15. If using the system to measure the resistivity of hardened cement-based materials, it is necessary to make a specimen of this material, because the specimen has to be a ring with rectangular section (as demold shape). This shape can be taken using drill sampling. After such a specimen is finished, it is placed in the window of transformer core, and the current leakage clamp and transformer core are opened.

Some results of resistivity measurements for OPC pastes and OPC mortars in different w/c ratios have been measured. The relevant curves are given in Figures 8-61 and 8-62. Since the purpose of this discussion is to present the novel method of electrical resistivity measurement for cement-based materials, analyses concerning the measured curves have not be given.

8.6.3.2 Repeatability

To observe the repeatability of this system, three specimens of cement paste with the same water–cement ratio ($w/c = 0.5$) have been measured. The repeatability is excellent. The measured results are shown in Figure 8-63.

8.6.3.3 Calibration

The simplest calibration is to measure the electrical resistivity and phase of a closed circuit with a resistor or with a resistor plus capacitor, and to compare the theoretical values from an equivalent circuit. For this purpose, a sinusoidal wave form with frequency 1 kHz is again used. The primary turns of the transformer are 36 and the secondary toroidal voltage generated is 2.5 V. In the first calibration case, only one resistor of 600 Ω is used. The measured current by the sensor in this case is 4.1 mA. The theoretically calculated result is

$$2.5\text{V}/600 = 4.17\,\text{mA} \tag{8-131}$$

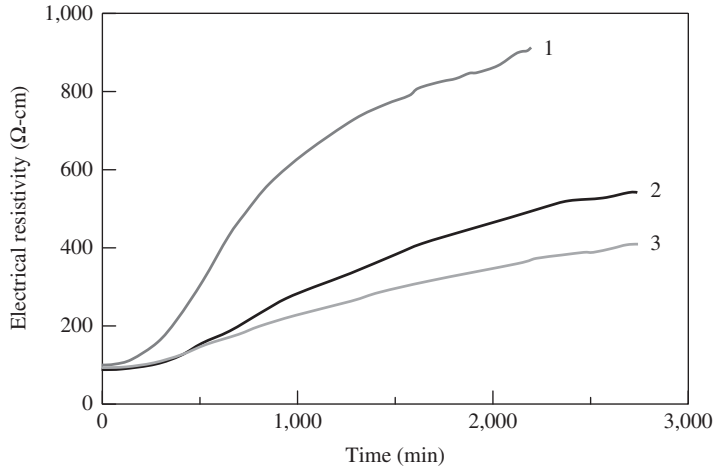

Figure 8-61 Resistivity of cement pastes (w/c = 1. 0.30, 2. 040, 3. 0.50)

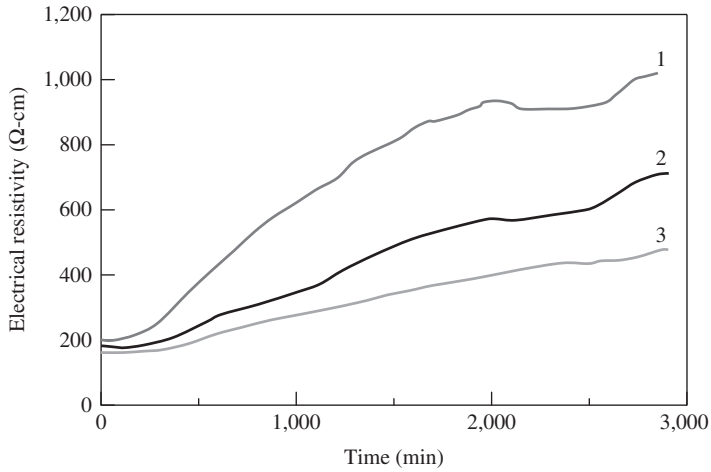

Figure 8-62 Resistivity of mortars (cement/sand = 1, w/c = 1. 0.35, 2. 0.50, 3. 070)

In the second calibration case, one 600-Ω resistor and one 2.2-μF capacitor are used. The measured output of the current sensor is 35 mA and measured phase shift from the oscilloscope is 83 degrees. The theoretical calculated results are 34.5 mA and 83.1 degrees, respectively.

To further prove the reliability of this method, a standard aqueous solution of potassium chloride has been used in the experiments to verify the measurement accuracy. The parameters of the standard KCl solution are as follows: 7.455 g (0.1 mol) KCl per kg of distilled water. The KCl is extra pure (max. 0.0001% Al), and the temperature of the solution is 25°C. The conductivity of such a solution is given in David (1994), and the resistivity is $\rho = 0.77993$. The result measured by this method is almost coincident with the value given in the reference, the difference between both values is less than 0.4%. So it can undoubtedly be said that the principle and the accuracy of the novel method are accurate and credible.

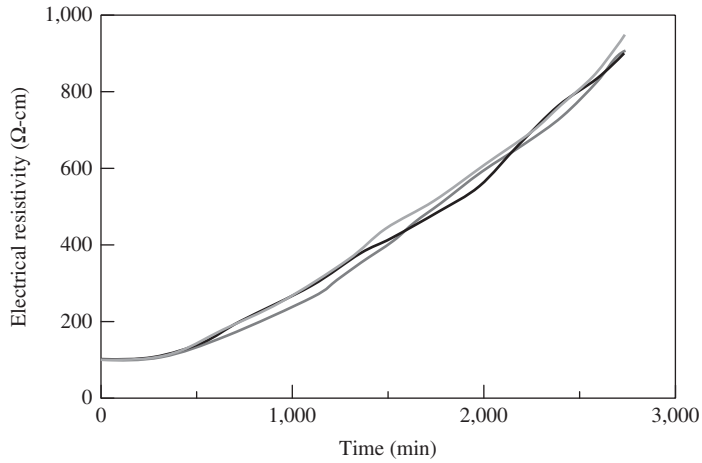

Figure 8-63 Repeatability of the measuring system

8.6.4 Applications

8.6.4.1 Hydration dynamics

Noncontact electrical resistivity measurement can be used to study the dynamics of the cement hydration process, which includes the stages of dissolution, dynamic balance, setting, hardening, and hardening deceleration. The corresponding application details of this method have already been included and discussed in the Section 2.2.4 (Chapter 2); therefore, they are not reiterated here.

8.6.4.2 Setting time

As mentioned in Section 3.1.6.1 (Chapter 3), the measurement of the concrete setting time can be conducted according to ASTM 403, using the experimental setup shown in Figure 3-8. Resistivity measurement can also be used to determine concrete setting time. Introduction of this innovative method in determining concrete setting time is presented in detail in Section 3.1.6.2.

8.6.4.3 Porosity

A new method using resistivity measurement to determine the porosity in cement-based materials has been developed by Zhang and Li (2009). They developed a general effective media (GEM) model to predict the porosity using the measured resistivity values. The equation is as follows:

$$\phi = \left[(1-\phi_c)\,F^{-1/t} + \phi_c\right] \cdot \left(\frac{M^{1/t} - F^{1/t}}{M^{1/t} - 1}\right) \tag{8-132}$$

where ϕ is the capillary porosity in cement-based materials; F the resistivity formation factor determined by ρ and ρ_0; ρ the overall resistivity of a cement-based system, which can be provided by noncontact resistivity measurement; ρ_0 the resistivity of the capillary pore phase, which can be determined experimentally by measuring the pore solution extracted from the specimen; M the magnification coefficient between ρ_1 and ρ_0; ρ_1 the resistivity of the phase consisting of C–S–H gel, CH, and unhydrated cement particles; ϕ_c the value of the percolation

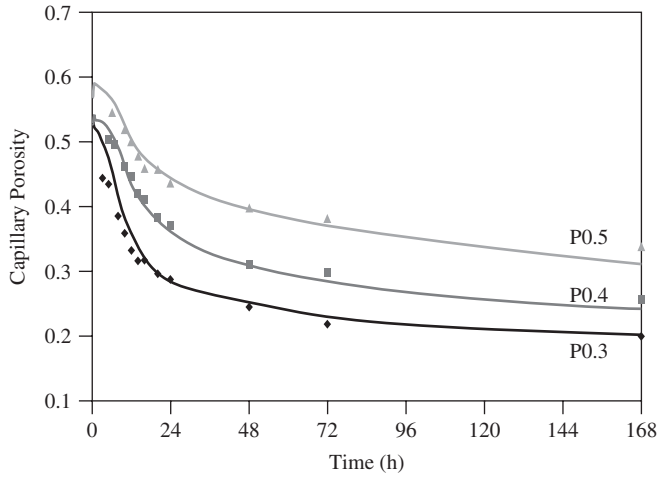

Figure 8-64 Comparison of theoretically predicted and measured porosity (solid lines are the theoretical porosity developments from GEM-based equation; dots are the experimental results from the MIP test)

threshold, below which the low-resistivity capillary pore phase is isolated by the other phase; t a free parameter that is the critical exponent for electrical conductivity.

When we consider the capillary porosity ϕ as a function of the formation factor F, then ρ_1 (or M), ϕ_c, and t are the three parameters in the equation. By applying the parameter values in traditional research, the equation can be rewritten as

$$\phi = \left[(1 - 0.18)\, F^{-1/2} + 0.18\right] \left(\frac{400^{1/2} - F^{1/2}}{400^{1/2} - 1} \right) \tag{8-133}$$

Once the F values are determined by resistivity measurement, the porosity can be predicted by this equation. Figure 8-64 shows a comparison between the porosity predicted by the equation and that measured by the MIP technique. The results show a good agreement.

8.6.4.4 Other applications

The noncontact resistivity measurement method has also been applied to study the influences of mineral and chemical admixtures on the hydration process of cement-based materials and the relationship between compressive strength and resistivity values. Very promising results have been obtained (Xiao et al., 2007; He et al., 2006; Li et al., 2003; Wei and Li, 2005; Wei et al., 2008; Xiao and Li, 2006).

DISCUSSION TOPICS

Why is NDT needed?
Which wave will travel faster, a P wave or an S-wave?
Why is acoustic impedance an important index?
Where are sources for attenuation?

What are the differences among A-scan, B-scan, and C-scan?
In what way is the acoustic emission method unique?
How does infrared thermography detect defects below the surface of a materials?
Can you give some examples of NDT in concrete engineering?
How are the durability problem and NDT related?
Do you trust the results of a single NDT method? How can you improve the accuracy?

PROBLEMS

1. Consider an elastic rod with Young's modulus E, mass density of ρ, and a length of L, which is rigidly clamped at $x = L$, as shown in the figure. The rod is initially at rest. At time $t = 0$, the end $x = 0$ is subjected to a pressure $p(t)$.

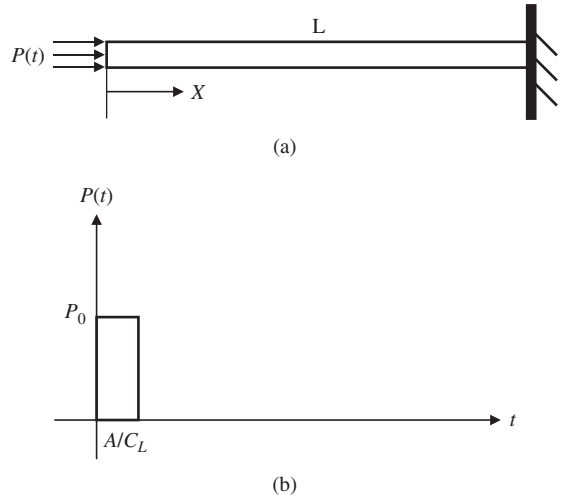

Figure P8-1

(a) If the material is brittle, and much weaker in tension than in compression, and if p_0 exceeds the tensile strength of the rod, at what time would you expect the rod to fail (A is not negligible)?

(b) Is it possible that the material in case (a) will not fail if the length of a square wave can be adjusted? What is the minimum requirement for the length, A.

2. Solve the following 1D wave equation using the variable separation method:

$$U_{xx} = \frac{1}{C_{\mathrm{L}}^2} U_{tt}$$

$$U\,|_{x=0} = 0$$

$$U_x\,|_{x=l} = 0$$

3. To monitor the hydration process of fresh concrete, an experimental setup has been developed as shown in the following figure. An ultrasonic transducer is attached on the surface of a steel mold. It sends a shear wave signal to the specimen and receives the reflected signal from the steel–concrete interface. The material properties of steel are Young's modulus, $E = 200$ GPa; Poisson's ratio, $\nu = 0.3$; and relative density, $\rho = 7.8$. The properties of fresh concrete at one day are Poisson's ratio, $\nu = 0.2$; and

relative density, $\rho = 2.3$. If the reflection factor measured from the first interface at 1 day is -0.77, calculate the modulus of the concrete at that time. What will be the reflection factor at the age of 1 day at the second interface?

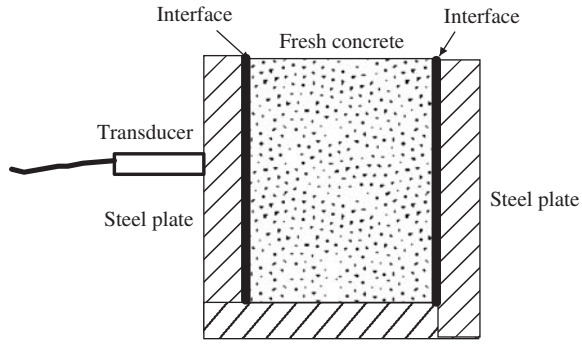

Figure P8-3

4. Consider an elastic rod with Young's modulus E, mass density of ρ, and length of L, which is rigidly clamped at $x = L$ ($L = 2.4$ m), as shown in the figure. The rod is initially at rest. At time $t = 0$, the end $x = 0$ is subjected to a pressure $p(t).p_0 = 5\,\text{MPa}$. The tensile strength of the material is 6 MPa (compressive strength is much higher).

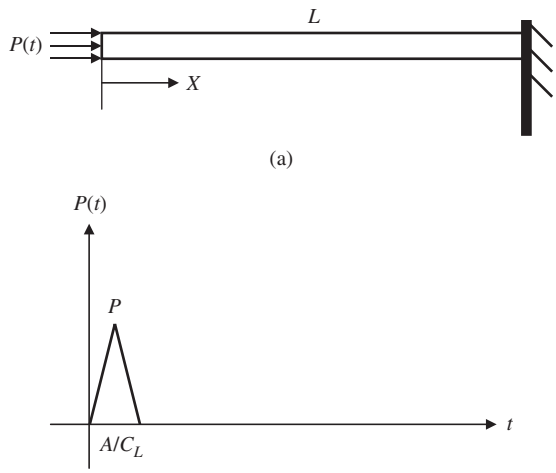

Figure P8-4

(a) Will the rod be fail? If so, where and when? ($A = 0.2$ m)

(b) Find the value of attenuation coefficient at which the material will not fail.

5. For the infrared thermograph technique, find the solution of the heat transfer differential equation of

$$B\frac{dT}{dt} = H - K(T - T_0)$$

$$\text{Initial condition}: t = 0,\ T = T_0.$$

(Detailed procedures are required.)

6. The resistivity of a fresh concrete can be measured using the transformer principle. The cement-based ring specimen acts as a secondary in the transformer. For a concrete ring with the shape and dimension shown in the following figure, show that the resistivity can be calculated by using the following equation:

$$\rho = R_{\text{total}} \frac{h}{2\pi} \left(\left[\ln \frac{r_3}{r_2} + \frac{r_4}{r_4 - r_3} \ln \frac{r_4}{r_3} - \frac{r_1}{r_2 - r_1} \ln \frac{r_2}{r_1} \right] \right)$$

where R_{total} is the total resistance of concrete ring:

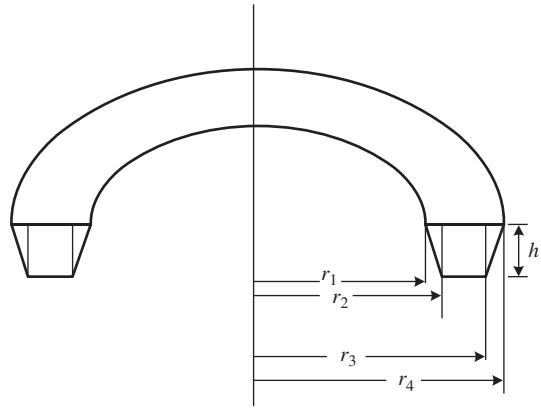

Figure P8-6

7. To detect the corrosion in a reinforcing steel bar, three acoustic emission transducers were used. The arrangement of the transducers is shown in the following figure. The first arrive-time differences between transducer 1 and 2 is 105 μsec and between transducer 1 and 3 is 156 μsec. Find out the position of the corrosion.

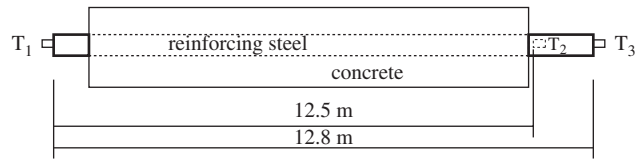

Figure P8-7

8. A concrete beam was repaired for the cracks using the injection method. To ensure the repairing quality, the ultrasonic pulse method with a shear wave was used to evaluate the resin injection. The recorded pulse amplitude from the front interface of repair material and repaired concrete is −0.48 (see the drawings). The properties of concrete are $E = 30$ GPa, $\nu = 0.2$, and $r = 2.4$. If the repair material has a Poisson's ratio (ν) of 0.33 and density (r) of 1.6,

(a) What will be the modulus of elasticity of repair material?

(b) What will be the amplitude of the reflected pulse from the back interface of the repair material and repaired concrete if there is an air gap at the back interface?

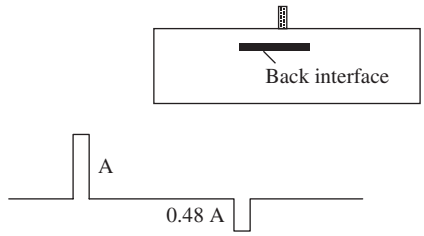

Figure P8-8

9. A material has the following properties: for plane strain case, C_L (P-wave velocity) = 5612 m/s, C_T (shear wave velocity) = 3000 m/s, and density $\rho = 7800\,kg/m^3$. Find Poison's ratio, the shear modulus, and Young's modulus for the material. Calculate C_L for the plane stress case.

REFERENCES

Achenbach, J. D., Komsky, I. N., Lee, Y. C., and Angel, Y. C. (1992) "Self-calibrating ultrasonic technique for crack depth measurement," *Journal of Nondestructive Evaluation*, **11**(2), 103–108.

American Standards for Testing and Materials (2004) Standard test method for measuring the P-wave speed and the thickness of concrete plates using the impact-echo method, ASTM C1383-04.

Attoh-Okine, N. (1995) "Use of artificial neural networks in ground penetrating radar applications in pavement evaluation and assessment." In Schickert, G. and Wiggerhanser, H., eds., *International Symposium Non-Destructive Testing in Civil Engineering(NDT-C, E)*, Sept. 26–28, Berlin, pp. 93–100.

Banthia, N., Djeridane, S., and Pigeon, M. (1992) "Electrical resistivity of carbon and steel micro-fiber reinforced cements," *Cement and Concrete Research*, **22**(5), 804–814.

Boumiz, A., Vernet, C., and Cohen Tenoudji, F. (1996) "Mechanical properties of cement pastes and mortars at early ages," *Advanced Cement Based Materials*, **3**(4), 94–106.

Brandes K., Herter J., Helmerich R., (1998) Assessment of remaining fatigue life of steel bridges assisted by adaptive NDT, ISNDT-CE [P77], 1233–1240

Butters, J. N. and Leendertz, J. A. (1971). "Holographic and Video Techniques Applied to Engineering Measurement," *Journal of Measurement and Control*, **4**, 349–354.

Bray, D. E. and McBride, D. (1992) *Nondestructive testing techniques*, New York: Wiley.

Bray, D. E. and Stanley, R. K. (1997) *Nondestructive evaluation: A tool in design, manufacturing and service*, Boca Raton, FL: CRC Press.

Brendenberg, H., ed. (1980) *Proceedings of International Seminar on the Application of Stress-Wave Theory on Piles*, Stockholm, June.

Bungey, J. H. and Millard, S. G. (1996) *Testing of concrete in structures*, 3rd ed., Glasgow, U.K.: Blackie Academic & Professional.

Carino, N. J., Sansalone, M., and Hsu, N. N. (1986) "A point source-point receiver technique for flaw detection in concrete," *Journal American Concrete Institute*, **83**(2), 199.

Dannheim, H., Haedrich, H., and Ruckdaeschel, R. (1995) "Measurements of stresses in ceramics and cement with microwaves." In Schickert, G. and Wiggerhanser, H., eds., *International Symposium Non-Destructive Testing in Civil Engineering(NDT-C, E)*, Sept. 26–28, Berlin, p. 1041.

Davidson, N., Padaratz, I., and Forde, M. (1995) "Quantification of bridge scour using impulse radar." In Schickert, G. and Wiggerhanser, H., eds., *International Symposium Non-Destructive Testing in Civil Engineering(NDT-C, E)*, Sept. 26–28, Berlin, pp. 61–68.

El-Enein, S. A. A., Kotkata, M. F., Hanna, G. B., Saad, M., El Razek, M. M. A. (1995) "Electrical conductivity of concrete containing silica fume," *Cement and Concrete Research*, **25**(8), 1615–1620.

Favro, L. D., Ahmed, T., Crowther, D., Jin, H. J., Kuo, P. K., and Thomas, R. I. (1991) "Infrared thermal-wave studies of coatings and composites," *Proceedings SPIE*, **1467**, Thermosense VIII, Orlando, FL, pp. 290–294.

Gros, X. E. (1997) *NDT data fusion*, London: Arnold.

He, Z., Li, Z. J., Chen, M. Z., and Liang, W. Q. (2006) "Properties of shrinkage-reducing admixture-modified pastes and mortar," *Materials and Structures RILEM*, **39**(4), 445–453.

Hewlett, P. C. (1998) *Lea's chemistry of cement and concrete*, 4th ed., London: Arnold.

Hung, Y. Y. (1982) "Shearography: A new optical method for strain measurement and non-destructive testing," *Optical Engineering*, **21**(3), 391–395.

Hung, Y. Y. and Liang, C. Y. (1979) "Image-shearing camera for direct measurement of surface strains," *Applied Optics*, **18**(7), 1046–1051.

Hughes, B. P., Soleit, A. K. O. and Brierley, R. W. (1985) "New technique for determining the electrical resistivity of concrete," *Magazine of Concrete Research*, **37**(133), 243–248.

Jennings, H. M. and Pratt, P. L. (1980) "On the reactions leading to calcium silicate hydrate, calcium hydroxide and ettingite during the hydration of cement," *Proceedings of the 7th International Congress on the Chemistry of Cement*, Vol. II, Paris: Editions Septima, Paris, pp. II-141–146.

Jin, X. Y. and Li, Z. J. (2001) "Dynamic property determination for early-age concrete," *ACI Materials Journal*, **98**(5), 365–370.

Jones, R. (1962) *Non-destructive testing of concrete*, London: Cambridge University Press.

Jones, R. and Wykes, C., (1989) *Holographic and speckle interferometry*, 2nd ed., London: Cambridge University Press.

Kalinski, J. (1995) "On-line water content monitoring in clay by means of microwave method and instrumentation." In Schickert, G. and Wiggerhanser, H., eds., *International Symposium Non-Destructive Testing in Civil Engineering(NDT-C, E)*, Sept. 26–28, Berlin, p. 1005.

Kesler, C. E. and Higuchi, Y. (1953) "Determination of compressive strength of concrete by using its sonic properties," *Proceedings of the ASTM*, **53**, 1044.

Kesler, C. E. and Higuchi, Y. (1954) Problems in the sonic testing of plain concrete, *Proceedings of the International Symposium on Nondestructive Testing of Materials and Structures*, Vol. 1, Paris: RILEM, Paris, p. 45.

Khalaf, F. M. and Wilson, J. G. (1999) "Electrical properties of freshly mixed concrete," *Journal of Materials in Civil Engineering*, **11**(3), 242–248.

Krause, M. et al. (1995) "Comparison of pulse-echo-methods for testing concrete." In Schickert, G. and Wiggerhanser, H., eds., *International Symposium Non-Destructive Testing in Civil Engineering(NDT-C, E)*, Sept. 26–28, Berlin, pp. 281–296.

Lakshminarayanan, V., Ramesh, P. S., and Rajagopalan, S. R. (1992) "A new technique for the measurement of the electrical resistivity of concrete," *Magazine of Concrete Research*, **44**(158), pp. 47–52.

Landis, Eric N., and Shah, Surendra P. (1993) "Recovery of microcrack parameters in mortar using quantitative acoustic emission," *Journal of Nondestructive Evaluation*, **12**(4), 219–232.

Levita, G., Marchetti, A., Gallone, G., Princigallo, A., and Guerrini, G.L. (2000) "Electrical properties of fluidified Portland cement mixes in the early stage of hydration," *Cement and Concrete Research*, **30**(6), 923–930.

Li, Z. (1996) "Microcrack Characterization in Concrete under Uniaxial Tension," *Magazine of Concrete Research*, **48**(176), 219–228.

Li, Z. and Li, W. (2002) "Contactless, Transformer-Based Measurement of the Resistivity of Materials," United States Patent 6639401.

Li, Zongjin and Wei Xiaosheng (2003) "The electrical resistivity of cement paste incorporated with retarder," *Journal of Wuhan University of Technology-Materials Science Edition*, **18**(3), 76–78.

Li, Z., Li, F.M., Li, X.S., and Yang W.L. (2000) "P-Wave Arrival Determination and AE Characterization of Concrete," *Journal of Engineering Mechanics*, **126**(2), 194–200.

Li, Z., Wei, X., and Li, W. (2003) "Preliminary interpretation of Portland cement hydration process using resistivity measurements," *ACI Materials Journal*, **100**(3), 253–257.

Li, Zongjin and Shah, Surendra P. (1994) "Microcracking localization in concrete under uniaxial tension: AE technique application," *ACI Materials Journal*, **91**(4): 372–389.

Li, Zongjin, Li, Faming, Zdunek, A., Landis, E., and Shah, S. P. (1998) "Application of acoustic emission to detection of rebar corrosion in concrete," *ACI Materials Journal*, **95**(1): 68–76.

Lide, David R. (Editor-in-chief) (1994) *Handbook of Chemistry and Physics*, 75th ed., Boca Raton, FL: CRC Press, pp. 5–86.

Lin, J. M. and Sansalone, M. (1997) "A procedure for determining P-wave speed in concrete for use in impact-echo testing using a Rayleigh wave speed measurement technique," *Innovations in Nondestructive Testing*, SP-168, Detroit, MI: American Concrete Institute.

Lin, J. M., Sansalone, M., and Streett, W. B. (1997) "A procedure for determining P-wave speed in concrete for use in impact-echo testing using a P-wave speed measurement technique," *ACI Material Journal*, **94**(6), 531–539.

Mailvaganam, N. P. (1992) Repair and protection of concrete structures, Boca Raton, FL: CRC Press.

Maji, A. K., and Shah, S. P. (1988) "Process zone and acoustic emission measurement in concrete," *Experimental Mechanics*, **28**, 27–33.

Maji, A. K., and Shah, S. P. (1989) "Application of acoustic emission and laser holography to Study Micro-Fracture in Concrete," *Nondestructive Testing of Concrete*, SP-112, Detroit, MI: American Concrete Institute, pp. 83–109.

Maji, A. K., Ouyang, C., and Shah, S. P. (1990) "Fracture mechanism of quasi-brittle material based on acoustic emission," *Journal of Material Research*, **5**(1), 206–217.

Malhotra, V. M. and Carino, N. J. (2004) *Handbook of nondestructive testing of concrete*, 2nd ed., Boca Raton, FL: CRC Press.

McCarter, W. J., Forde, M. C., and Whittington, H. W. (1981) "Resistivity characteristics of concrete," *Proceedings of the Institution of Civil Engineers (London), Part 1: Design & Construction*, **71** (2), pp. 107–117.

Ménétrier, D., Jawed I., Sun, T. S., and Skalny, J. (1979) "ESCA and SEM studies on early C3S hydration," *Cement and Concrete Research*, **l9**(4), 473–482.

Milne, J. M. and Carter, P. (1988) "A transient thermal method of measuring the depths of sub-surface flaws in metals," *British Journal of Nondestructive Testing*, **30**(5), 333–336.

Newman, A. (2001) *Structural renovation of buildings: Methods, details, and design examples*, New York: McGraw-Hill.

Obert, L. and Duvall, W. I. (1941) "Discussions of dynamic methods of testing concrete with suggestions for standardization," *Proceedings of the ASTM*, **41**, 1053.

Oppenheim, Alan V. and Schafer, Ronald W. (1975) *Digital signal processing*, Englewood Cliffs, N.J.: Prentice Hall.

Olson, L. D. and Wright, C. C. (1990) "Seismic, sonic, and vibration methods for quality assurance and forensic investigation of geotechnical, pavement, and structural systems." In dos Reis, H. L. M., ed., *Proceedings of Conference on Nondestructive Testing and Evaluation for Manufacturing and Construction*, Hemisphere, p. 263.

Ouyang, C. S., Landis, E., and Shah, S. P. (1991) "Damage assessment in concrete using quantitative acoustic emission," *ASCE Journal of Engineering Mechanics*, **117**(11), 2681–2698.

Qin L., and Li, Z.J. (2008) "Monitoring of cement hydration using embedded piezoelectric transducers," *Smart Materials and Structures*, **17**(5), Article Number 055005.

Reynolds, W. N., (1988) "Inspection of laminates and adhesive bonds by pulse-video thermograph," *NDT International*, **21**(4), 229–232.

Sack, D. and Olson L. (1995) "High speed testing technologies for NDT of structures." In Schickert, G. and Wiggerhanser, H., eds., *International Symposium Non-Destructive Testing in Civil Engineering(NDT-C, E)*, Sept. 26–28, Berlin, pp. 43–50

Sansalone, M. (1997) "Impact-echo: The complete story," *ACI Structural Journal*, **94**(6), 777–786.

Sansalone, M. and Carino, N. J. (1988) "Impact-echo method: Detecting honeycombing, the depth of surface-opening cracks, and ungrouted ducts," *Concrete International*, **10**(4), 38–46.

Sansalone, M. and Carino, N.J. (1990) "Finite element studies of the impact-echo response of layered plates containing flaws." In McGonnagle, W., ed., *International advances in nondestructive testing*, 15th ed., New York: Gordon & Breach, pp. 313–336.

Steinbach, J. and Vey, E. (1975) "Caisson evaluation by stress wave propagation method," *ASCE Journal of Geotechnical Engineering*, ASCE, **101**(4), 361–378.

Suaris, W. and van Mier, J. G. M. (1995) "Acoustic emission source characterization in concrete under biaxial loading," *Materials and Structures*, **28**(182), 444–449.

Subramaniam, K. V., Popovics, J. S., and Shah, S. R. (1999) "Fatigue response of concrete subjected to biaxial stresses in the compression-tension region," *ACI Materials Journal*, **96**(6), 663–669.

Vassie, P.R. (1978) "Evaluation of techniques for investigating the corrosion of steel in concrete," Department of the Environment, Department of Transport, TRRL Report SR397, Crowthorne, U.K.

Wei, X. S. and Li, Z. J. (2005) "Study on hydration of Portland cement with fly ash using electrical measurement," *Materials and Structures, RILEM*, **38**(5), 411–417.

Wei, X. S., Xiao, L. Z. and Li, Z. J. (2008) "Hyperbolic method to analyze the electrical resistivity curve of Portland cements with superplasticizer," *Journal of Wuhan University of Technology-Materials Science Edition*, **23**(2), 245–248.

Weil, S. (1995) "Non-destructive testing of bridge, highway and airport pavements." In Schickert, G. and Wiggerhanser, H., eds., *International Symposium Non-Destructive Testing in Civil Engineering(NDT-C, E)*, Sept. 26–28, Berlin, pp. 467–474

Whittington, H. W., McCarter, J., and Forde, M. C. (1981) "Conduction of electricity through concrete," *Magazine of Concrete Research*, **33**(114), 48–60.

Xiao, L. Z. and Li, Z. J. (2006) "Hydration monitoring of cementitious materials by using electrical resistivity measurement." In Reinhardt, H. W., ed., *Proceedings of Advanced Testing of Fresh Cementtitious Materials*, Aug. 3–4, Stuttgart, Germany, pp. 167–176.

Xiao, L. Z., Li, Z. J., and Wei, X. S, (2007) "Selection of superplasticizer in concrete mix design by measuring the early electrical resistivities of pastes," *Cement Concrete and Composites*, **29**, 350–356.

Zhang, J. and Li, Z. J. (2009) "Application of GEM equation in microstructure characterization of cement-based materials," *Journal of Materials in Civil Engineering*, **21**(11), 648–656.

CHAPTER 9

THE FUTURE AND DEVELOPMENT TRENDS OF CONCRETE

Due to the unique advantages of concrete, it will continue to be the most popular and most widely used material in the new century. The demand for concrete will keep increasing in the future. Subsequently, the research and development of concrete have to be advanced to meet the need and new requests from end users and to face new challenges. Hence, it is important to correctly predict the future and development trends of concrete in the 21st century. Here, the issues closely related to the topic are briefly discussed.

9.1 SUSTAINABILITY OF CONCRETE

Among all the future development trends, how to make concrete more sustainable is the most important issue. Sustainability can be defined as the "development that meets the needs of the present without compromising the ability of future generations to meet their own needs," according to the Brundtland Commission Report (1987). Sustainability includes all aspects of society, such as civil infrastructural systems, energy, environment, health, safety, and life-cycle analyses. Concrete is the most widely used material and consumes a great amount of resources. Contemporary concrete, typically, contains about 16–20 percent cementitious materials, 6–8 percent mixing water, 60–70 percent aggregate, and 2–3 percent of admixtures by mass. The most reliable way to estimate world production of concrete is to determine the amount of cement produced, calculate the amount of other composite utilizing the mass ratio of the common practice, and finally add them together. According to the amount of cement produced in 2007, it can be estimated that concrete consumes about 2.5 billion tonnes of cement, 1 billion tonnes of mixing water, 10 billion tonnes of aggregates together with 400 million tonnes of chemical admixtures annually. It makes that concrete becomes 14-billion-tonnes-a-year industry, the largest user of natural resources in the world. The mining, processing, and transport of huge quantities of aggregate, in addition to the billions of tonnes of raw materials needed for cement manufacturing, utilizes considerable energy and adversely affects the ecology of virgin lands. Moreover, a large amount of CO_2 is produced. Obviously, such a huge consumption of natural resources has a great impact on environment, and if not well controlled, will definitely compromise the ability of future generations to meet their own needs. The considerations on sustainability of concrete may contain three aspects: how to reduce gas emissions, especially CO_2 emissions; how to reduce energy consumption; and how to reduce raw materials consumption from natural resources during production, construction, and application of concrete. The three methods of achieving sustainability of concrete are reduce, reuse, and recycle.

9.1.1 Scientific utilization of more industry waste

One way to make concrete sustainable is to utilize industry waste or by-products to replace the raw materials for making concrete, such as cement and aggregates. The industry by-products utilized to replace cement are usually called supplementary cementitious materials (SCMs). Currently, blast furnace slag, fly ash, limestone powders, and silica fume are the most commonly used SCMs. These SCMs can be obtained in large and regular amounts with a relatively consistent composition. They can be added into cement during the final grinding process of cement production to reduce amount of clinker used, as in Europe. They can also be added into concrete mix during concrete production to reduce the amount of cement. No matter in which way it is done, the utilization of SCMs can reduce the amount of clinker or cement. The production of the clinker or Portland cement is an energy-intensive process and consumes 4 GJ per ton of cement. Production also emits a large amount of CO_2. The manufacture of one ton of Portland cement clinker releases 0.8 to 1 tons of CO_2 into the atmosphere, as indicated by the following calculations.

In cement manufacture, limestone has to be decomposed as

$$\underset{(100)}{\text{Limestone}(CaCO_3)}(1000^{\circ}C) \rightarrow \underset{(56)}{CaO} + \underset{(44)}{CO_2} \tag{9-1}$$

One ton of cement contains 620 kg CaO, and hence $CO_2 = 620 \times 44/56 = 487$ kg. CO_2 is also produced from fuel burning during the cement production. The amount is from 320 kg to about 450 kg and depends on the advances of the burning technique. The world's yearly cement output accounts for nearly 7 percent of global CO_2 emissions. Thus, utilization of SCMs can greatly reduce the environmental impact of the concrete industry. The concrete industry also recycles the waste products of the electric and steel industries as substitutes for virgin raw materials of concrete industries, thereby reducing the environmental impact of both. Moreover, these SCMs contain reactive silica that can react with CH in concrete to form secondary C–S–H and to improve concrete properties. Due to the incorporation of SCMs into concrete, the structure of concrete at the nanometer and micrometer levels becomes more complex. Thus, studies have to be carried out to reveal the influence of SCMs on to what extent and in what mechanism they can modify the structure of hydration products and subsequently the macroscopic properties of concrete. The optimized amount for cement replacement at which concrete can be benefited most should be investigated and proposed. In this way, the scientific utilization of current SCMs can be achieved. It should be pointed out that in many countries these SCMs are currently almost fully utilized in concrete. To further reduce the tonnage of Portland cement in concrete, new resources of SCMs have to be explored. Such resources should include other industry by-products that also contain reactive silica and/or reactive alumina, such as Pb/Zn mine tailing, phosphorous slag, coal gangue, and copper slag. It may be possible for them to achieve effects similar to those of currently used SCMs. However, extensive tests are needed for each new individual by-product before it can be readily used, because of their complex composition, some harmful elements, and unknown influence on concrete properties. Only with the better understanding of their reaction mechanisms and better techniques for their characterization can we open up new resources for SCMs and contribute to the sustainable development of concrete.

The natural mineral deposits provide a new promising resource for the SCMs. These include the natural pozzolans, such as volcano ash, which is ready to be used, and kaolin, which has to be activated by thermal treatment (Scrivener and Kirkpatrick, 2007). The product of kaolin that has been heat-activated is called metakaolin. Metakaolin has similar effect to that of silica

Figure 9-1 Recycled waste glass as an aggregate for concrete

fume, but is much cheaper. Hence, it has great potential for future application in concrete. More details on metakaolin can be found in Chapter 2.

Industrial waste that can be utilized to replace aggregates includes waste glass, demolished concrete, bottom ash, and large-size slag. Figure 9-1 shows crushed waste glass as a replacement of fine aggregate. Grading of waste glass particles is usually limited to 75 mm to 5 mm. The main concern about glass incorporation into concrete is the possibility of alkali–silica reaction. An alkali–silica reaction (ASR) is a reaction between alkalis in pores of cement paste and certain forms of aggregates, which results in excessive expansion of concrete sections and leads to severe cracking. Na_2O (sodium oxide) and K_2O (potassium oxide) are present in cement clinker in small amounts. It is thus conventional to express the results of chemical analysis of cement in terms of the oxides Na_2O and K_2O. Furthermore, the alkali content in cement is generally expressed as an equivalent percentage of Na_2O by mass of cement. Since the molecular weights of Na_2O and K_2O are respectively 62 and 94, the equivalent percentage of Na_2O is calculated with the formula

$$\%Na_2O_{eq} = \%Na_2O + 0.658 \cdot \%K_2O \tag{9-2}$$

In concrete, Na_2O and K_2O form hydroxides and raise the pH level from 12.5 to 13.5. The concentration of these hydroxides increases as Na_2O_{eq} increases. In such highly alkaline solutions, under certain conditions, the silica can react with the alkali to form an unlimited swelling gel, which draws in any free water from osmosis and expands, disrupting the concrete matrix. Expanding gel products exert internal stress within the concrete causing characteristic map cracking of unrestrained surfaces. Cracking resulting from alkali–silica reactions can lead to the loss of structural integrity.

It should be emphasized that as more and more concrete structures age, more and more demolished concrete will be produced. If it cannot be recycled and reused, the deposition of the construction waste will cause another environmental problem. However, aggregates recycled from demolished concrete are usually more porous and weak. Hence, it is important to develop

some technique to overcome the problem and ensure the quality of the concrete made of recycled aggregates.

9.1.2 Low energy and low CO_2 emission binders

To reduce the environmental impact of Portland cement, efforts have been made to search for other type of binders with low energy demand and less emission of carbon dioxide. One system along this line is alkaline-activated cementitious materials, in which geopolymer and alkaline-activated slag are two good examples. Geopolymer was discussed in detail in Chapter 2. Activated slag also utilizes water glass to trigger the chemical reaction with slag to form bonding. However, although the feasibility of alkaline-activated materials has been frequently demonstrated in the laboratory, their commercial exploitation has not been widespread due to variability of performance, especially with changes in temperature; the high cost of the most effective alkaline activators (e.g., water glass); and the lack of robustness with cheaper activators. Alkaline-activated systems are generally fast-setting and the use of superplasticizers is not effective. More research is needed to promote the practical use of alkaline-activated cementitious materials. Another system is MgO-based binder, such as magnesium phosphate cement, as introduced in detail in Chapter 2. As pointed out earlier, how to control the setting time is a big issue for such a material to be applied in a large scale. Other systems include new clinker types that contain higher amounts of alumina and sulfate than Portland cement. These clinkers include high aluminate cement, sulfate–aluminate cement, and high belite cement. A new high belite cement was developed recently in China (Sui et al., 2009). This type of belite-based Portland cement (high-belite cement, HBC) contains 45–60% C_2S, 20–30% C_3S, 3–7% C_3A, and 10–15% C_4AF. Laboratory research, industrial production, and field application of the resultant HBC concrete demonstrate that HBC compared with normal PC is a kind of low energy consumption, low CO_2 emission Portland cement with low hydration heat evolution, high later-age strength, and high performance. For example, the clinkering temperature of HBC is 1350°C, which is 100°C lower than normal PC. The CO_2 emission for clinkering HBC is reduced by 10% due to the low calcium design in the clinker mineral composition and low consumption of coal for clinker burning. The resultant HBC concrete shows excellent performance not only in better workability, higher mechanical strength, and excellent durability, but also in excellent thermal properties and crack resistance. Table 9-1 compares the energy consumption and CO_2 emission for C_2S and C_3S. Obviously, the low C_2S content in new HBC has led to energy savings and CO_2 emission reduction.

The concrete produced using HBC shows a better workability as compared to the one made of normal Portland cement when low w/c ratios are used, as shown in Table 9-2. Although the strength development of the concrete made from HBC is still slower at the early stage, up to an age of 7 days, it catches up to the strength of concrete made with ordinary Portland cement at the age of 28 days and exceeds it at 90 days, as shown in Table 9-3 for flexural, splitting, and compressive strengths. Compared to the existing low-heat Portland cement, which also contains

Table 9-1 Comparison of energy consumption and CO_2 emission for C_2S and C_3S

Mineral	Formation Enthalpy kJ/kg	Formation Temperature °C	CaO %	CO_2 Emission Coeeficient Per Unit Mass of Mineral
C_3S	1848	1450	73.7	0.578
C_2S	1336	1300	65.1	0.511

Table 9-2 Workability of HBC high-strength, high-performance concrete in comparison with OPC concrete

Concrete Type	Cement Amount (kg/m^3)	*W/B*	Fly Ash (kg/m^3)	Water (kg/m^3)	Superplasticizer (%)	Initial Slump (cm)	Slump at 90 min (cm)
C60 HBC	414	0.32	104	165	1.0	23.2	22.5
C60 OPC	414	0.32	104	165	1.0	22.4	20.3
C80 HBC	510	0.25	90	150	1.7	24.4	20.6
C80 OPC	510	0.25	90	150	1.7	0	0

Table 9-3 Strength comparison between HBC and OPC concretes

	Flexural Strength (MPa)			Splitting Strength (MPa)			Compressive Strength (MPa)		
Type	7 d	28 d	90 d	7 d	28 d	90 d	7 d	28 d	90 d
HPC-60	3.5	7.2	8.9	3.81	5.37	7.44	54.6	77.6	98.5
OPC-60	5.2	6.7	8.2	4.45	5.16	6.36	60.3	78.5	90.2
HPC-80	4.5	8.4	10.3	4.76	6.72	8.25	68.3	95.4	116.4
OPC-80	6.2	7.9	9.1	5.28	5.94	7.35	72.5	91.0	107.5

Table 9-4 Comparison of the Chinese standard with international standards for HBC

Standard	Compressive, 7 Days (MPa)	Compressive, 28 Days (MPa)
China GB200-2003	≥13.0	≥42.5
USA ASTM C150	≥7.0	≥17.0
Japan JIS R 521	≥7.5	≥22.5

a large amount of belite, the new binder has achieved a much higher strength at early ages, as shown in Table 9-4.

Concrete made of the new HBC has also demonstrated a better freeze–thaw resistance, smaller drying shrinkage, and lower heat release. The new HBC concrete has been applied in several major infrastructure projects in China, such as the third phase of Three Gorges Dam in Yichang, Zi Pingpu and Shenxigou dams in Sichuan province, Beijing International Airport, and the 5th Ring Road in Beijing. Figure 9-2 shows the application of new HBC concrete in Three Gorges Dam.

Obviously, such low-energy and low CO_2 emission binders have a great potential in future sustainable development of concrete.

9.1.3 Prolonging the service life of concrete

Of all the measures to make concrete sustainable, how to prolong the service life of a concrete structure is the most important. Prolonging the service life of a concrete structure not only saves the resources of raw materials for new buildings, but also reduces construction waste due to the demolishing of the existing buildings and infrastructure. Since durable concrete can reduce the frequency of replacement, improving durability of concrete contributes directly to its service life. Durability is especially important to contemporary concrete because that the contemporary

Figure 9-2 Application of new HBC concrete in the Three Gorges Dam

Portland cement concrete mixtures, which are usually designed to obtain high strength at early age, are very crack-prone. The interconnections between surface and interior cracks, microcracks, and voids in concrete provide the pathway for penetration of water and harmful ions that are implicated in of all kinds of durability problems.

To improve the durability of concrete, much research has been conducted in developing concrete mixes with incorporation of chemical and mineral admixtures. Along this line, a new concrete durability-enhancing admixture has been developed that utilizes natural polymer as a main admixture constituent (Li et al., 2000). Due to its natural renewability, low cost, ease of manufacture, and excellent durability improvement, the new admixture can be readily used to develop more durable concrete. Several concrete mixes with different formulae have been prepared to evaluate the effect of the concrete durability-enhancing admixture.

The cement used for the test was type I Portland cement (OPC) with a specific gravity of 3.15 and a fineness of 385 m^2/kg. River sand with a fineness modulus of 2.3 was employed as fine aggregate and a crushed limestone aggregate with a nominal maximum size of 10 mm was used as coarse aggregate. These concrete mix proportions are listed in Table 9-5.

The freeze–thaw test was performed to evaluate the effect of the new admixture on concrete properties. In the test, specimens were exposed to repeated cycles of freezing in air at $-18^{\circ}C$, and thawing in water at $6^{\circ}C$. After the freeze–thaw test, compression tests were conducted on the specimens.

Table 9-5 Mixture proportions (kg/m^3) of the concrete series used in this study

Code	Cement	Water	Sand	Aggregate
C1	415	250	625	1035
C2	Mixed with 0.1% effective solid content of natural polymer by weight of cement			
C3	Mixed with 0.5% effective solid content of natural polymer			
C4	Mixed with 1.0% effective solid content of natural polymer			
C5	With DAREX (75 mL/100 kg cement)			

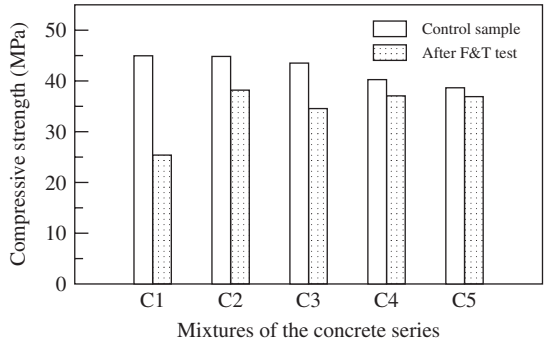

Figure 9-3 Comparison of compressive strengths of control samples and samples that underwent the freezing and thawing test for the concrete series

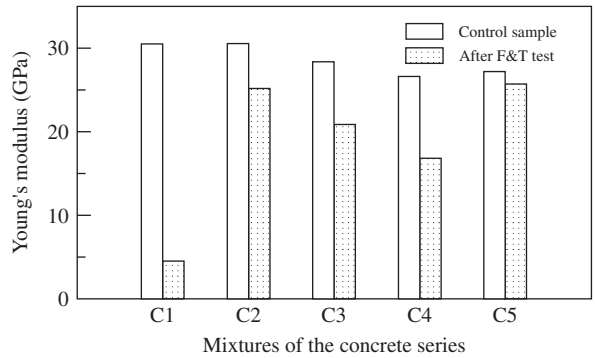

Figure 9-4 Comparison of the elastic modulus of control samples and samples that underwent the freezing and thawing test for the concrete series

Figures 9-3 and 9-4 show the strength and Young's modulus of the concrete mixtures following severe freezing and thawing cycles, and comparisons with the control specimens. The results show that the application of the durability-enhancing admixture in the concrete mixture leads to a significant improvement in the frost resistance of concrete. Even with only 0.1% effective solid content of the natural polymer, an obvious enhancement of concrete frost resistance in terms of less deficiency of compressive strength and elastic modulus was observed.

For the plain concrete mixture C1, the compressive strength and elastic modulus after a severe freezing and thawing process have largely deteriorated, by 43 and 85%, respectively, compared to control samples. For the air-entrained concrete mixture C5, there was a deficiency of only a few percent in both strength and modulus after the frost resistance test. This demonstrated the capability of improving the frost resistance of concrete by applying an air-entraining agent; however, the entrained air void system itself caused strength deficiency to a certain extent.

For the modified concrete C2, the reduction in compressive strength and elastic modulus after freezing and thawing tests were only 15 and 18%, respectively. This can be seen more clearly from Figure 9-5 which shows the representative stress–strain curves for the concrete series. It was shown that the incorporation of the durability-enhancing admixture can significantly improve the frost resistance of modified concrete in its unique ways.

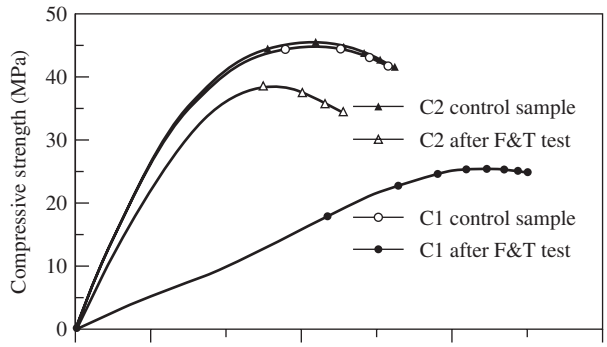

Figure 9-5 Representative stress–strain curves of the concrete series

The degradation of concrete materials under frost attack begins with the initiation of microcracks on the exposed concrete surface. Therefore, surface quality and cracking inspection of concrete that has under gone freez–thaw cycles also offers evidence of the improvement in the frost resistance of concrete employing the new admixture. In this study, wide and continuous cracks were observed on surfaces of the plain concrete mixture, while only a few thin cracks were found on surfaces of the natural polymer-modified concrete mixture. From the frost-resistance test results, it can be concluded that the optimal usage of the new admixture is about 0.1% the effective solid content of the natural polymer by weight of cement usage.

9.1.4 Efficiently utilizing materials—HSC and UHSC applications

Another way to make concrete sustainable is to explore its efficiency. Utilizing high-strength concrete (HSC) and ultra-high-strength concrete (UHSC) and a prestress technique during design and construction provides good ways of increasing the efficiency of concrete. It may be argued that HSC and UHSC utilize more cementitious materials and thus imply high energy consumption and high CO_2 emission. However, when HSC and UHSC are used in design and construction, the cross section of structural members such as column and beams can be largely reduced. Subsequently, the total amount of materials used for concrete structure can be reduced as compared to the case where normal-strength concrete is used. As a result, the cement amount is reduced and so is energy and CO_2 emission. Similarly, by utilizing a prestressing technique, steel tendons with higher tension strength can be effectively used and the total amount of steel can be reduced. The San Francisco Public Utilities Commission Building is a good example for this concept (Schokker, 2010). It is a concrete building of 14 stories above grade and 1 story below grade with a total area of 26,000 m^2. The building design and construction adopt a high-strength concrete that is vertically post-tensioned throughout the building core, which provides a 30% reduction in concrete and reinforcement over a normal-strength concrete system.

9.2 DEEP UNDERSTANDING OF THE NATURE OF HYDRATION

Durability enhancement of concrete requires a deep understanding of the nature of hydration products. One of the most important, long-standing needs in cement science (Powers and Brownyard, 1948) is a quantitative understanding of C–S–H on the atomic to 100 nm scale and how the structures on this scale control the mechanical, transport, and chemical properties

of hydrated cement paste. Numerical methods are commonly used to simulate the C–S–H structures. As mentioned earlier, the structure of C–S–H, the major hydration product of cement, has not been revealed yet. Moreover, as concrete is becoming more complex with the increased incorporation admixtures and SCMs, the hydration process and products become more complex. The phase assemblages formed from the reaction of the cement and different SCMs may be different from the hydration products of pure cement. The pore structure may also be changed and along with the cohesive forces between phases and the resulting mechanical properties. Understanding the structure of the hydration products of contemporary concrete is essential to improving them and hence the durability of concrete.

Fortunately, with the advancement of technology, a wide range of experimental and computational tools are available in recent decades for discovering the hydration of cementitious materials. Experimental methods such as atomic force microscopy (AFM), small-angle neutron and X-ray scattering, nuclear magnetic resonance (NMR), nanoindentation, and high-resolution scanning and transmission electron microscopies can be used to reveal at least part of the C–S–H at different scales. For example, AFM can be utilized to examine the aggregation shape of C–S–H at a tens of nanometer scale and to determine the cohesive force nature of the hydration products (Plassard et al., 2005). Small-angle neutron and X-ray scattering can be applied to probe "gel" porosity of C–S–H (Allen et al., 2004; Faraone et al., 2004; Fratini et al., 2006). NMR can be utilized to determine the C–S–H structure and the pore structure of cementitious materials (Richardson, 2004; McDonald et al., 2005). Nanoindentation can be used to measure the modulus of C–S–H and other hydrates (Ulm, 2007). And high-resolution scanning and transmission electron microscopies coupled with chemical microanalysis can be used to determine microstructural development and microchemistry of hydration phases (Richardson, 2002; Scrivener, 2004).

The data obtained from these experiments provide a predictive framework that spans the atomic to the macroscopic level to some extent. However, using only these experimental methods, it is still not possible to completely reveal the structure of concrete at the atomic and molecular level. Computational modeling and numerical simulation are needed in concrete science.

The numerical simulation methods at the atomic and molecular scale include quantum chemical and molecular potential based methods. Quantum (first principles) approaches involve solution of the Schrödinger equation describing the interaction of electrons and atomic nuclei. The electrons are described by their wave functions, and the challenge is to adequately describe these functions in a computationally accessible way. The Schrödinger equation cannot be solved exactly, except in the most limited cases. Hence, some approximation methods are needed. The Hartree-Fock approach involves an approximate solution of the exact solution to an approximate Schrödinger equation. Sherman (2001) provides an accessible introduction to quantum methods and illustrations of applications to aqueous solutions.

Potential-based methods such as the molecular dynamics (MD) approach, are based on empirical or semi-empirical potentials between or among atomic or molecular entities. They involve treating the atoms or molecules as classical (nonquantum) entities and computing their positions, motion, and energies as they interact with each other under the influence of potential functions. These functions can describe short-range atomic repulsion, van der Waals forces, and attractive and repulsive coulombic interactions. MD methods follow the time evolution of the structure and energy of the computed system, thus allowing calculation of dynamical properties, such as vibrational spectra. Kalinichev et al. (2002) provide a more detailed discussion of applications of potential-based, molecular dynamics simulations to cement systems. Quantum (Car-Parrinello) MD (CPMD) is a potentially useful hybrid that calculates the interactions among atoms by quantum (normally DFT) methods but follows their interactions through time the way MD does (Car and Parrinello, 1985; Remler and Madden, 1990; Marx and Hutter, 2000).

Each of these methods has advantages and disadvantages. The quantum methods are normally more accurate than the potential-based methods in describing atomic positions, interaction energies, and spectroscopic properties, but even with the most recent generation of supercomputers they are limited to a few hundred atoms. In contrast, MD and MC trade accuracy for increased system size and reaction time. They can now be used for systems of the order of 10^6 atoms for a few nanoseconds.

To build up an appropriate C–S–H model using simulation, the parameters have to be considered and utilized as objective functions to achieve a reasonable result. The first criterion is the Ca/Si ratio, which is ratio is the key factor that simulation has to be satisfy. Theoretically, as indicated in Chapter 5 by Equation 5-62, the stoichiometric equation for fully hydrated C_3S results in a Ca/Si ratio of 1.75. Experimentally, as summarized by Richardson (1999), the results of small-angle X-ray scattering (SAXS) and small-angle neutron scattering (SANS) have demonstrated that the values of the Ca/Si ratio range from 1.2 to 2.3, with a mean of 1.7–1.75. Thus, a value of 1.7 for the Ca/Si ratio is well accepted currently for numerical simulation.

Another important property for determining C–S–H structure is its density. In reality, the density depends on water content in C–S–H. Recently, Allen et al., (2007) obtained a value of 2604 kg/m^3 as the density of C–S–H by utilizing SANS and SAXS simultaneously with consideration of combined water. Such an estimation is thought to be closer to the natural property of C–S–H gel and hence can be adopted in the simulation.

Silicate connection is another important factor that has to be considered in interpreting the structure of C–S–H. Such information can be obtained utilizing ^{29}Si NMR. The basic unit of the silicates is the SiO_4 tetrahedron. When referring to ^{29}Si NMR, the peak in the spectrum for silicate can be classified by the number of bridging oxygen atoms in a specific SiO_4 unit. Theoretically, five categories of Q_n sites along with chemical shift (centered at) can be observed in NMR: Q_0 (−70 ppm), Q_1 (−80 ppm), Q_2 (−88 ppm), Q_3 (−98 ppm), and Q_4 (−110 ppm), where the subscript n represents the number of additional tetrahedra linked by sharing an oxygen atom with the base tetrahedron (Johansson, 1999). For C–S–H, it has been found that Q_1 and Q_2 Si sites are predominant; Q_3 and Q_4 Si sites are not expected to be seen (Kirkpatrick, 1996; Hewlett; 2004). As for Q_0, it is conventionally considered to be a surface hydroxylation of C_3S; however, it has been found that such monomers persisted in forming from the induction period to the late stages of the hydration reaction. The amount of Q_0 range from 2 to 10%. Therefore, the role of Q_0 silicate sites should also be taken into consideration for numerical simulation.

It is believed that only with the correct selection of a combination of Ca/Si ratio, density, and silicate connection projected as function in a numerical simulation, can meaningful and realistic results be obtained.

9.3 LOAD-CARRYING CAPABILITY–DURABILITY UNIFIED SERVICE LIFE DESIGN THEORY

It has been long realized that a concrete structure carryies the load while being exposed to various environmental conditions. The mechanical load and environmental condition influence each other during service period of concrete. Property degradation of concrete is caused by the coupling effect of loading and environment. However, traditionally, the design of concrete structure considers only the loading-carrying capability of the structure. Moreover, the design code treats the mechanical properties of concrete at the both material and structure levels as a constant having no variation with time. Since 1990s, durability issue has received more and more attention and some design codes concerning concrete durability have been developed. However, in these preliminary attempts, the durability of the concrete structure is taken care

of only by the details described in the code, such as the cover thickness of a structure under a certain environmental condition. There is no scientific formulation to quantify the effect of environmental conditions. In addition, the codes do not consider the dynamic changes of the properties and performance of concrete as either material or structure with time. Thus, the codes cannot reflect the true service conditions of a concrete structure.

In January 2001, the American Concrete Institute published a document, *Vision 2030: A vision for the US concrete industry* (ACI, 2001). In the document, it is stated that "The industry will make processing improvement throughout the life cycle of concrete, including design, manufacturing, transportation, construction, maintenance, and repair." The life cycle of concrete is emphasized.

In the 973 project started in 2009 in China, "Basic study on environmentally friendly contemporary concrete," a new design approach, a scientifically unified load-carrying capability and durability service life design theory has been proposed. It attempts to develop a brand new design philosophy in which the safety, durability, and serviceability of a concrete structure can be considered in a scientifically unified way and hence overcome the limitation of current design codes. The service life design theory has to resolve two fundamental issues. The first is how to introduce factors that influence concrete durability, such as environmental issues, into in a design code quantitively and couple it with mechanical loading effect. The second is how to consider the material properties and structure behavior dynamically as a function of time.

For the first issue, one solution is to develop a method that can transfer the environmental effect into an equivalent force or stress effect. This can be done by utilizing a plateform of thermodynamics and porous media theory. As an example, let us take a look at the representative volume element of cement-based material shown in the Figure 9-6. The element of concrete is being acted upon by mechanical load and chemical pores solution. The chemical reaction of pores solution can be transferred to a mechanical strain or stress based on thermodynamics and virtual energy calculation. With this conversion, it is possible to couple the environmental effect with the mechanical loading by superposition of its equivalent stress with the stress generated by mechanical load during the design procedures. Moreover, with this conversion, the traditional design formulations based on stress analysis can be continually utilized.

For the second issue, one approach is to find the mechanism and the regularity of material and structure degradation with time. This can be achieved through the study of the deterioration

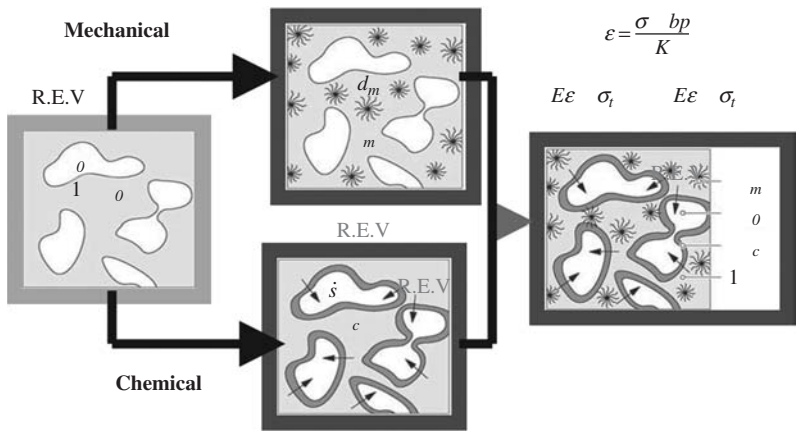

Figure 9-6 Conversion of chemical influence to mechanical effect

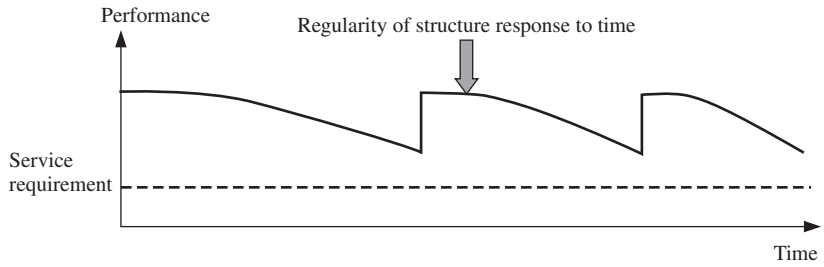

Figure 9-7 Regularity of concrete structure performance as function of time

of material and structure under the coupling effect of loading and environmental conditions, the study of structure exposed to real environmental conditions under the loading, the computer simulation of structural behavior under different combinations of loading and various environmental factors. Through these studies, the properties and behavior of concrete can be described as a function of time, as shown in Figure 9-7. With this function, the performance of a concrete structure at different service periods can be predicted and incorporated into the design accordingly. Figure 9-7 sketches the regularity of the performance of a concrete system as a function of time.

9.4 HIGH TOUGHNESS AND DUCTILE CONCRETE

Concrete has fatal disadvantages—low tensile strength, a quasi-brittle nature, tendency to crack, low toughness, and low ductility. Since concrete was invented in the 19th century, many attempts have been made to overcome these disadvantages. The development of reinforced concrete using steel bars to carry out tension has advanced the application of concrete greatly. The invention of prestressed concrete has further improved the crack resistance of concrete. Later, incorporating high-strength, small-diameter fibers into concrete was developed to improve the toughness and ductility of concrete. Two kinds of fibers are commonly used, continuous and short fiber. The use of short fibers seems to be preferable due to the simple and economical nature of the fabrication process. Experiments have verified that the response of the short fiber reinforced cement-based composites can be largely influenced by dispersion of the fiber. By adding the fibers to concrete, the toughness can be improved. However, due to increased cost and dispersion difficulties, short fibers cannot be added in a large amounts. Thus, the improvement on tensile strength and toughness of concrete is limited. Another attempt at toughness improvement is to incorporate polymer into concrete. There are three ways of doing this nowadays. One is to use polymer as the binder in concrete. This method uses a two-part polymer system, such as epoxy resin and hardener, premixed first and then mixed with aggregate to produce a hardened plastic material with aggregate as filler (polymer concrete). The second way is to impregnate polymer into concrete. This is usually done by impregnating a monomer and catalyst into a hardened concrete and polymerizing using steam or infrared heat in situ. The third way utilizes a polymer (usually latex) that is dispersed in water and then mixed with Portland cement and aggregate. This is identified as polymer-modified or latex-modified concrete. Polymer Concrete (PC) and polymer impregnated concrete (PIC) are very expensive and thus their use is limited to emergency concreting jobs in mines, tunnels, and highways as well as the production of high-strength, precast products, while Latex-modified concrete (LMC) is the most commonly used

in overlay practice. However, LMC does not offer much improvement in tensile strength and toughness for concrete. It is still a quasi-brittle material.

Even with these methodologies, the quasi-brittle nature of concrete is still there. Hence, to develop a brand new technology that can improve the toughness of concrete by eliminating its quasi-brittle nature is the dream of the researchers in the concrete field. If it becomes true, a new generation of concrete will be developed. Recently, many attempts have been made in this direction. In Europe, under the Nanocem project (www.nanocem.com), a new method has been proposed: a mineral organic composite having two poles, so that one end can chemically bond with hydrate of Portland cement, and the other end can polymerize. The hybrid organic–inorganic polymer dispersion based on emulsion polymerization of polyacrylate, polyurethane, vinyl acetate, or acrylates and siloxane molecular precursors. Hybrid organic–inorganic particles are functionlized with siloxane molecules $R'n\text{Si(OR)}4\text{-}n$, where R' can polymerize or copolymerize. Terminal trialxysyl groups undergo hydrolysis bonds with the mineral matrix of concrete (cement or aggregates). With this new composite, a new generation of concrete can be produced. The concrete will have high tensile strength, and be very ductile, which will be completely different from traditional concrete.

In China, under a national key research project on concrete, a study has been conducted to increase the toughness of concrete through incorporation of a new admixture. The new admixture is called concrete toughness enhancer. Its chemical composition is schematically shown in Figure 9-8.

To verify the effect of the newly developed admixture, two types of concrete specimens have been prepared for a three-point bending fracture test. One is made of regular concrete as reference and the other incorporates the new admixture. The test results of two specimens are listed in Table 9-6. With the incorporation of this admixture into concrete, the fracture toughness of the modified concrete is significantly increased.

Although preliminary investigation shows some promising results, it will take a long time to reach the final goal. However, with our understanding of the nature of the concrete hydrates, especially the C–S–H, it is possible to develop a method and a material that can react with

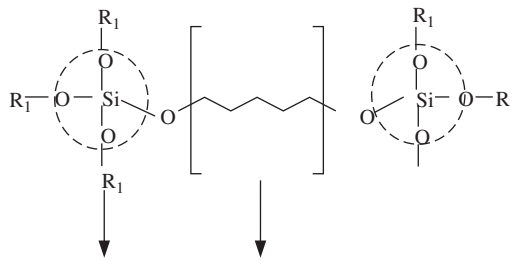

Figure 9-8 Schematic drawing of toughness enhancer structure

Table 9-6 Fracture test results for two types of specimens

Type (7 d)	Dosage (%)	P_{max} (kN)	K_{IC} (MPa · $\sqrt{m}$)	W_1 (N · m)	W_2 (N · m)	G_F (N · m^{-1})	Ratio (%)
Reference	0	4.12	1.03	0.54	0.23	91	100
Modified	1.5	5.53	1.38	0.89	0.99	220	242

C–S–H and self-polymerization to eliminate concrete's quasi-brittle nature and open an era for a new generation of concrete, i.e., the fourth generation of concrete.

REFERENCES

Allen A. J., et al. (2004), "In-situ quasi-elastic scattering characterization of particle size effects on the hydration of tricacium silicate," *J. Mater. Res.*, **19**, 3242–3254.

Allen, A. J., Thomas, J.J., and Jennings, H.M. (2007) "Composition and density of nanoscale calcium–silicate–hydrate in cement," *Nat. Mater.*, **6**, 311–316.

American Concrete Institute (2001) Vision 2030.

Bruntland, G., ed. (1987), *Our common future: The world commission on environment and development*, Oxford, U.K.: Oxford University Press.

Car, R. and Parrinello, M. (1985). "Unified approach for molecular dynamics and density-functional theory," *Phys. Rev. Lett.*, **55**, 2471–2474.

Faraone, A., et al. (2004) "Quasielatic and inelastic neutron scattering on hydrated calcium silicate pastes," *J. Chem Phys.*, **121**, 3212–3220.

Fratini, E., et al. (2006) "Hydration water and microstructure in calcium silicate and aluminium hydrates," *J. Phys.: Cond. Matter*, **18**, 2467–2483.

Hewlett, P. (2004) *Lea's chemistry of cement and concrete*. Oxford, UK: Elsevier Science & Technology Books.

Johansson K.C.L. (1999). "Kinetics of the hydration reactions in the cement paste with mechanochemically modified cement ^{29}Si magic-angle-spinning NMR study." *Cement Concrete Res.*, **29** (10), 1575–1581.

Kalinichev, A. G., et al. (2002) "Molecular dynamics modeling of chloride binding to the surfaces of Ca hydroxide, hydrated Ca-aluminate and Ca-silicate phases," *Chem. of Mater.*, **14**, 3539–3549.

Kirkpatrick, X. C. (1996). "^{29}Si and ^{17}O NMR investigation of the structure of some crystalline calcium silicate hydrates." *Adv. Cement Bas. Mat* **3**, 133–143.

Li, Z., Chau, C. K., Ma, B., and Li, F. "New natural polymer based durability enhancement admixture and corresponding concretes made with the admixture," US Patent No. 6,153,006.

Marx, D. and Hutter, J. (2000) In Grotendorst, J, ed., *Modern methods and algorithms of quantum chemistry.* NIC, FZ Julich, pp. 301–449.

McDonald, P. J., Korb, J-P, Mitchell, J. and Monteilhet, L. (2005) "Surface relaxation and chemical exchange in hydrating cement pastes: a two-dimensional NMR relaxation study". *Phys. Rev. E*, **72**, 011409.

Plassard, C., Lesniewska, E., Pochard, I., and Nonat, A. (2005), "Nanoscale experimental investigation of particle interactions at the origin of the cohesion of cement," *Langmiur*, **21**, 7263–7270.

Powers, T. C. and Brownyard, T. L. (1948) "Studies of the physical properties of hardened Portland cement paste," *Bulletin of the Portland Cement Association*, p. 22.

Remler, D. K. and Madden, P. A. (1990) "Molecular-dynamics without effective potentials via the Car-Parrinello approach," *Mol. Phys.*, **70**, 921–966.

Richardson, I. (1999) "The nature of C–S–H in hardened cements." *Cement Concrete Res.*, **29**, 1131–1147.

Richardson, I. G. (2002) "Electron microscopy of cement". In: Bensted, J. and Barnes, P., eds, *Structure and performance of cements.* London: Spon Press.

Richardson, I. G. (2004) "Tobermorite/jennite- and tonermorite/calcium hydroxide-based models for the structure of C–S–H: applicability to hardened pastes of tricalcium silicates, dicalcium silicate, Portland cement, and blends of Portland cement with blast-furnace slag, metakaolin, or silica fume." *Cement Concrete. Res.*, **34**, 1733–1777.

Schokker A. J. 2010, *The sustainable concrete guide: strategies and examples*, U.S. Green Concrete Council.

Scrivener, K. L., et al., 2004. "Quantitative study of Portland cement hydration by X-ray diffraction/ Rietveld analysis and independent methods." *Cement Concrete Res.*, **34** (9) 1541–1547.

Scrivener, K. L. and Kirkpatrick, R. J. (2007) "Innovation in use and research on cementitious material." In: Beaudoin, J.J., Makar, J.M., and Raki, L., eds., Proceedings of the 12th international congress on the chemistry of cement, July 8–13, 2007, Montreal, Canada. On CD.

Sherman, D. M. (2001) "Quantum chemistry and classical simulations of metal complexes in aqueous solutions." In: Cyan, R. T. and Kubicki, J. D. eds, *Molecular modeling theory: applications in the geosciences.* Washington, DC: Mineralogical Society of America, p. 531.

Sui, T.B., Fan, L., Wen, Z. J., and Wang, J. (2009) "Low energy and low emission cement with high performanceand low hydration heat and its concrete application," *Mater. China*, **28**(11), 46–52.

Ulm, F.J., et al. (2007) "Statistical indentation techniques for hydrated nanocomposites: concrete, bone, and shale." *J. Am. Ceramic Soc.*, **90**(9), 2677–2692. www.nanocem.com.

INDEX

B

C

D

E

F

O

P

T